AN ABSTRACT OF THE THESIS OF

<u>Brittain Eames Hill</u> for the degree of <u>Doctor of Philosophy</u> in <u>Geology</u> presented on <u>October 17, 1991.</u>

Title: <u>Petrogenesis of Compositionally Distinct Silicic Volcanoes in the Three Sisters Region of the Oregon Cascade Range: The Effects of Crustal Extension on the Development of Continental Arc Silicic Magmatism.</u>

Abstract Approved:

Signature redacted for privacy.

Edward M. Taylor

The Three Sisters region of the Oregon High Cascades has developed three compositionally and petrogenetically distinct silicic (i.e., $SiO_2 \geq 58\%$) magma systems within the last 600 k.y. These silicic systems evolved from the same High Cascade mafic magma system and developed in the same 20x30 km area of the arc, but did not interact. The Broken Top system (BT) evolved to 71% SiO_2 through a combination of plag + px + Fe-Ti oxides ± ap (PPFA) fractionation and 20%-35% mixing of rhyolitic (74% SiO_2) crustal melts. In contrast, part of the Three Sisters system (3S) evolved to 66% SiO_2 through PPFA fractionation alone, while other parts evolved to 66% SiO_2 through PPFA fractionation coupled with $\geq 40\%$ mixing of rhyolitic ($\geq 72\%$ SiO_2) crustal melts.

The 3S system was intermittently active from ≤ 340 ka to 2 ka. The petrogenesis of intermediate composition rocks at Middle Sister (<340 ka, >100 ka) was controlled by PPFA fractionation to $\leq 66\%$ SiO_2. Rhyolite (72%-76% SiO_2) was first erupted in the 3S system at ≈ 100 ka, at the start of South Sister (SS) volcanism. Major and trace element abundances preclude derivation of 3S rhyolite through crystal fractionation, but are consistent with 20-30% dehydration melting of mafic amphibolite. The petrogenesis of intermediate composition rocks at SS was controlled by PPFA fractionation coupled with 30-40% rhyolitic magma mixing. However, the rhyolitic magma mixed into an essentially mafic system, which limited intermediate differentiation at SS to $\leq 66\%$ SiO_2.

The BT system was active from ≈ 600 ka to at least 200 ka. Major and trace element abundances preclude derivation of BT rhyolite (74% SiO_2) through crystal fractionation, but are consistent with $\approx 30\%$ dehydration melting of older tonalitic intrusions. BT petrogenesis was controlled by PPFA fractionation accompanied by 10-20% mixing of rhyolitic magmas to $\approx 63\%$ SiO_2, with $\approx 30\%$ rhyolite mixing from 63% to 71% SiO_2. In contrast to the 3S system, differentiation proceeded beyond 66% SiO_2 because rhyolitic magma was mixed into a more evolved ($\approx 60\%$-65% SiO_2) system.

The observed temporal and spatial variations in petrogenesis were not controlled by regional changes in tectonic setting, crustal thickness or crustal composition. However, small-scale changes in the magnitude of crustal extension occurred in this area, and are thought to have controlled petrogenesis by localizing mid-crustal mafic magmatism and thus crustal heat flow.

Petrogenesis of Compositionally Distinct Silicic Volcanoes in the Three Sisters Region
of the Oregon Cascade Range: The Effects of Crustal Extension on the Development of
Continental Arc Silicic Magmatism.

by

Brittain Eames Hill

A THESIS

submitted to

Oregon State University

in partial fulfillment of
the requirements for the
degree of

Doctor of Philosophy

Completed October 17, 1991

Commencement June, 1992

ACKNOWLEDGEMENTS

TABLE OF CONTENTS

LIST OF FIGURES

LIST OF TABLES

PETROGENESIS OF COMPOSITIONALLY DISTINCT SILICIC VOLCANOES IN THE THREE SISTERS REGION OF THE OREGON CASCADE RANGE: THE EFFECTS OF CRUSTAL EXTENSION ON THE DEVELOPMENT OF CONTINENTAL ARC SILICIC MAGMATISM

1. INTRODUCTION

1.1 Overview of the Research Topic

This study was undertaken to examine the petrogenesis of silicic (i.e. $SiO_2 > 58\%$) rocks from the Three Sisters region of the Oregon Cascade Range, using modern analytical techniques to supplement detailed field studies of this geologically complex part of the High Cascades continental arc. Previous workers had shown that this area of the High Cascades was composed of at least 5 major volcanic centers, which had been active within the last ≈ 1 Ma and erupted a wide variety of volcanic rocks (e.g., Williams, 1944; Taylor, 1978, 1987; Hughes, 1983). Rhyolite was known to be unusually abundant in the Three Sisters area, compared to the rest of the Oregon High Cascades. Limited geochemical data from these studies indicated that there could be several distinct trends of silicic magma evolution, involving varying amounts of crystal fractionation and magma mixing. In addition, these trends occurred within a relatively small (600 km^2) area of the Oregon Cascades.

Petrogenetic trends in continental arcs can be influenced by marked changes in the physical conditions of the arc. Arc-length variations in subduction rate (e.g., Carr et al., 1982; Nye and Reid, 1986) and subduction angle (e.g., Kay et al., 1980; Carr et al., 1990) have been shown to control mafic arc magmatism. Compositional heterogeneities in the upper mantle, which may be primary (e.g., Hughes, 1990) or the result of subduction-related metasomatism (e.g. Hawkesworth et al., 1984; Arculus and Powell, 1986) can produce compositionally distinct mafic magmas through partial melting. Changes in the thickness or composition of the crust under the arc (Tilton and Barreiro, 1980; Kay et al., 1980; Thorpe et al., 1982; Hildreth and Moorbath, 1988) can produce distinct assimilation trends in the mafic magma system and compositionally distinct silicic magmas through partial crustal melting. Given these factors, it is often unrealistic to construct an arc-length petrogenetic model (e.g. Arculus and Johnson, 1978).

The Three Sisters area, however, is located in a relatively small area of the Oregon Cascades arc. It is extremely unlikely that any of the regional tectonic features listed above could control large variations in petrogenesis within a 20 km by 30 km segment of the Cascades arc. In addition, previous studies have shown that the mafic magma system in the Three Sisters area has the same degree of heterogeneity as in adjacent parts of the Oregon High Cascades, and that there are no spatial or temporal controls on mafic rocks within the Three Sisters area. If petrogenetically distinct silicic magma systems are present in the Three Sisters area, then these systems developed from and were influenced by the same mafic magma system.

Regional mapping in central Oregon has shown that the Three Sisters region of the Oregon Cascades was located in a structurally complex area, where regional north-striking extensional features merged with northwest-striking features (Taylor, 1981; Macleod et al., 1982). The effect of crustal stress on igneous petrogenesis is poorly known. Empirical (Nakamura, 1977; Hildreth, 1981) and theoretical (Shaw, 1980) models generally conclude that extension favors the ascent of mafic magma in the crust, but these models have not been previously applied to continental arc petrogenesis. Although the observed structural variations apparently did not effect mafic petrogenesis in the Three Sisters area, it was hypothesized that changes in the orientation of crustal stress could have influenced silicic petrogenesis by controlling the flux of mafic magma into the lower(?) crust. Recent work by Hildreth and Moorbath (1988) has demonstrated that lower crustal processes, and especially crustal composition, can strongly affect the petrogenesis of mafic and silicic arc rocks. The Three Sisters area thus represents an ideal locality to study the effects of local crustal processes on calc-alkaline continental arc petrogenesis.

The role of crystal fractionation versus magma mixing in arc petrogenesis cannot be explained by a simple model. It has been repeatedly shown that both of these petrogenetic processes can operate in arc environments (e.g., Bowen, 1928; Larsen, 1938; Anderson, 1976; Gill, 1981; Sakuyama, 1984; and many others). Additional complexities introduced through magma recharge (O'Hara, 1977, 1980; Nielsen, 1988) and crustal assimilation (DePaolo, 1981) further obscure the geochemical signatures of fractionation and mixing. Recent advances in experimental petrology, and the availability of powerful desk-top computers, have allowed the development of complex petrogenetic models. These models are constrained by experimentally determined phase relationships (e.g., Grove et al., 1982) and trace element distribution coefficients (e.g., Irving, 1978; Nielsen, 1985), and allow for realistic simulations of a variety of petrogenetic hypotheses. Tests of crystal fractionation hypotheses are no longer limited to simple mass balance and Rayleigh fractionation constraints. Although these procedures still result in useful petrogenetic limits, any real test of the importance of crystal fractionation in arc petrogenesis must account for open system processes as well (i.e., recharge, eruption and assimilation). The models developed in this study constrain some of the effects of open system processes on the High Cascades magmatic system.

1.2 Location and Methods

The study area encompasses 600 km^2 of the Oregon central High Cascades, and includes the Three Sisters and Broken Top composite volcanoes (figure 1.1). In keeping with historic usage, the term **Three Sisters area** will be used to describe the area from ≈5 km west of the Three Sisters peaks to ≈15 km east of Broken Top volcano (figure 1.1). In addition, the terms **Three Sister system** and **Broken Top system** will be used extensively throughout this study. The
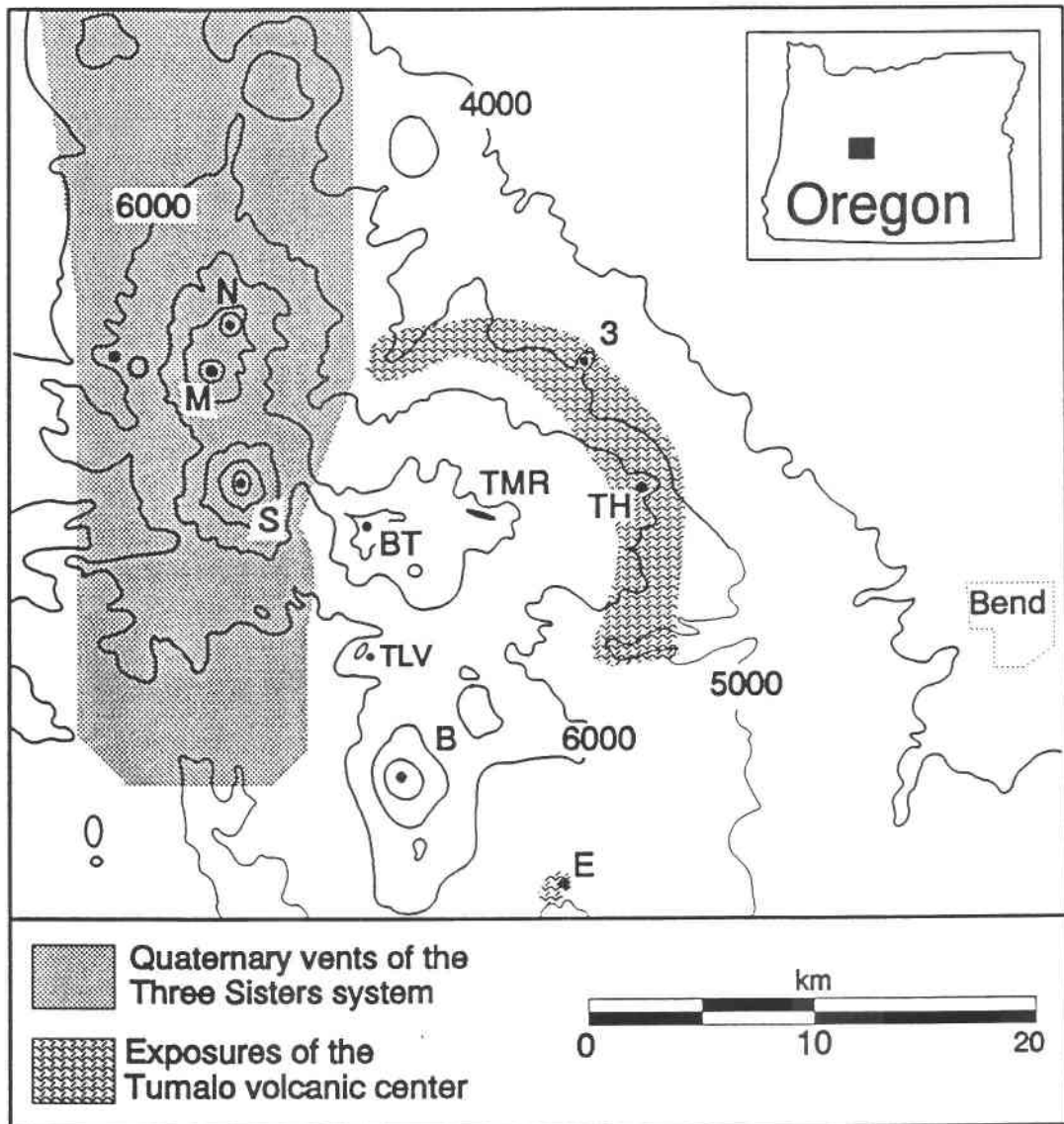
Figure 1.1: Location map of the Three Sisters region of the Oregon High Cascades. Major vents of the Three Sisters system: **N**: North Sister, **M**: Middle Sister, **S**: South Sister, **O**: Obsidian Cliffs. Major vents of the Broken Top system: **BT**: Broken Top, **TMR**: Tam MacArthur Rim, **TLV**: Todd Lake volcano, **B**: Mt. Bachelor. Prominent vents of the Tumalo volcanic center (Broken Top system): **3**: Three Creek Bu., **TH**: Triangle Hill, **E**: Edison Bu.

Three Sisters system refers to rocks associated with North, Middle and South Sister, including numerous silicic domes located within 5 km south and west of these composite volcanoes (figure 1.1). The **Broken Top system** refers to rocks associated with Broken Top, Tam MacArthur Rim, the Tumalo volcanic center (Hill, 1988), and Todd Lake volcano (Taylor, 1978)(figure 1.1).

Much of the study area is located in the Three Sisters Wilderness area of the Deschutes and Willamette National Forests; most parts of the area can be reached within a day's hike. Access to the rest of the area is provided by a myriad of logging roads. Field work was accomplished during the summers of 1986, 1987 and 1988, and consisted of selecting more than 200 samples for analysis, development of a stratigraphic section based on field relationships and published maps, and 1:62500 geologic mapping in the eastern Broken Top system. Sampling was guided by prior studies (Taylor, 1978, 1987, unpub. res.; Taylor et al., 1987; Wozniak, 1982; Clark, 1983; Hughes, 1983), and included all major silicic units within the study area.

A total of 127 High Cascade and 10 Deschutes Formation (Smith, 1986) rocks were selected for detailed geochemical analysis. Analytical methods are given in Appendix A. After completion of the geochemical analyses, 26 chemically-representative High Cascade units were selected for detailed mineralogical study with the O.S.U. Cameca SX-50 electron microprobe (Appendix A). Five K-Ar age determinations were also obtained to correlate and constrain the volcanic stratigraphy of the Three Sisters area (Chapter 3).

1.3 Summary of Previous Work

The Three Sisters area of the Oregon Cascade Range has been the subject of numerous reconnaissance geological studies since the late 1870's. A summary of early work, which focused on the geomorphology and glacial geology of this area, is presented in Hodge (1925). Mapping by Williams (1944, 1957) first characterized the major volcanos in the area, which were shown to be the products of discrete eruptions and not related to one "mega-volcano" (i.e., the Mt. Multnomah of Hodge, 1925). Williams also recognized that a large volume of pyroclastic material had been deposited east of the Three Sisters area prior to Quaternary volcanism. A 1:250000 reconnaissance map of the geology of Deschutes County by Peterson et al., 1976, included most of the study area. Detailed 1:62500 maps of the Three Sisters Wilderness area (Taylor et al., 1987), Mt. Bachelor area (Scott and Gardner, 1991), and the Broken Top area (Taylor, 1978,1987) cover much of the study area and were used extensively for sample selection.

There have been several petrologic studies on parts of the Three Sisters area. Anttonen (1972) characterized the major and trace element abundances of numerous rocks from the Three Sisters area, and modeled most of the variations through different amounts of partial melting in the descending oceanic plate. Taylor (1978,1987) mapped and analyzed rocks from the northwest and southwest parts of the Broken Top 15' quadrangle. Wozniak (1982) mapped the northern part

of South Sister and produced major element analyses for most map units. Clark's 1983 study of South Sister focused on Holocene activity, although older units were mapped and analyzed. Clark recognized the existence of a significant compositional gap at South Sister, which he concluded was produced through remobilization and mixing of previously evolved rhyolitic magmas into a fractionating magma system. Hughes (1983, 1990) and Hughes and Taylor (1986) have primarily examined the petrogenesis of 0-5 Ma mafic rocks in the central High Cascades. These studies conclude that much of the geochemical variations in the central Cascade mafic system is related to heterogeneities in the degree of mantle metasomatism or melting, and that mafic rocks erupted prior to ≈5 Ma are at times petrogenetically distinct from <0.7 Ma rocks. The pyroclastic deposits around Bend, Oregon, have been examined in detail by Peterson et al. (1976), Taylor (1981), Mimura (1984), Hill (1985, 1987, 1988) and Hill and Taylor (1989). These studies generally conclude that these pyroclastic rocks are the products of 4 major eruptions from the High Cascades west of Bend.

2. REGIONAL GEOLOGY OF THE CENTRAL HIGH CASCADES AREA

2.1 Crustal Composition

The best known exposures of pre-Tertiary crust are located over 100 km northeast of the Three Sisters area, and are primarily composed of greenschist-to-blueschist facies metavolcanics and metasediments (Swanson, 1969). A lawsonite-bearing blueschist from this terrane has an ^{40}Ar-^{39}Ar date of 223 ± 3 m.y., which is also the age of blueschist facies metavolcanic rocks in the east-central Klamath Mountains (Hotz et al., 1977). The occurrence in these two areas of blueschist facies rocks of the same age, with common structural trends and associated melange zones, supports continuation of Klamath Mountain-type rocks into central Oregon under the Tertiary volcanic cover (Hotz et al., 1977; Hietanen, 1981).

These greenschist facies rocks are likely part of a large, late Paleozoic-to-Jurassic suture system that extends from the northwestern Sierra Nevada through the Klamath Mountains, and which may possibly continue through Oregon and into the Idaho Batholith (Hietanen, 1981). Exposures in the Klamath Mountains of southwestern Oregon show that terranes associated with this suture zone are dominantly accreted island arc sequences of late Paleozoic to early Mesozoic age (e.g., Irwin, 1981).

A ≈50 km wide, regional gravity anomaly (figure 2.1) is coincident with the apparent northern boundary of the Klamath Mountain-central Oregon suture zone (Thiruvathukal et al., 1970; Riddihough et al., 1986). The gravity anomaly, referred to as the Klamath-Blue Mountain Lineament (KBL), marks a change in crustal density from relatively lower density, older(?) crust to the southeast and higher density, younger(?) crust to the northwest (Thiruvathukal et al., 1970; Riddihough et al., 1986). The KBL may reflect changes in crustal thickness due to Basin & Range extension (Thiruvathukal et al., 1970), but regional seismic studies have failed to detect any significant changes in crustal thickness where the KBL crosses the High Cascades (Leaver et al., 1984). High heat flow associated with High Cascade volcanism (Blackwell et al., 1982, 1990) obscures the exact location of the KBL in the Oregon Cascades, but a linear extrapolation of the KBL intersects the High Cascade axis in the Three Sisters area (figure 2.1).

Limited isotopic data support the argument that the KBL marks a change in crustal composition. Although the Oregon Cascades are characterized by relatively primitive lead isotopic ratios (Church and Tilton, 1973; Church et al., 1986; Conrey, 1991), lead isotopes from sulfide minerals in the western Cascades (Church, 1986) are slightly less radiogenic north of the KBL than to the south. Strontium isotopic ratios for Quaternary rhyolitic rocks, which were likely produced through partial crustal melts, are lower north of the KBL at Mt. Jefferson (≈0.7033; Conrey, 1991) than south of the KBL at the Three Sisters (≈0.7036; this study) and Mt. Mazama (≈0.7037; Bacon
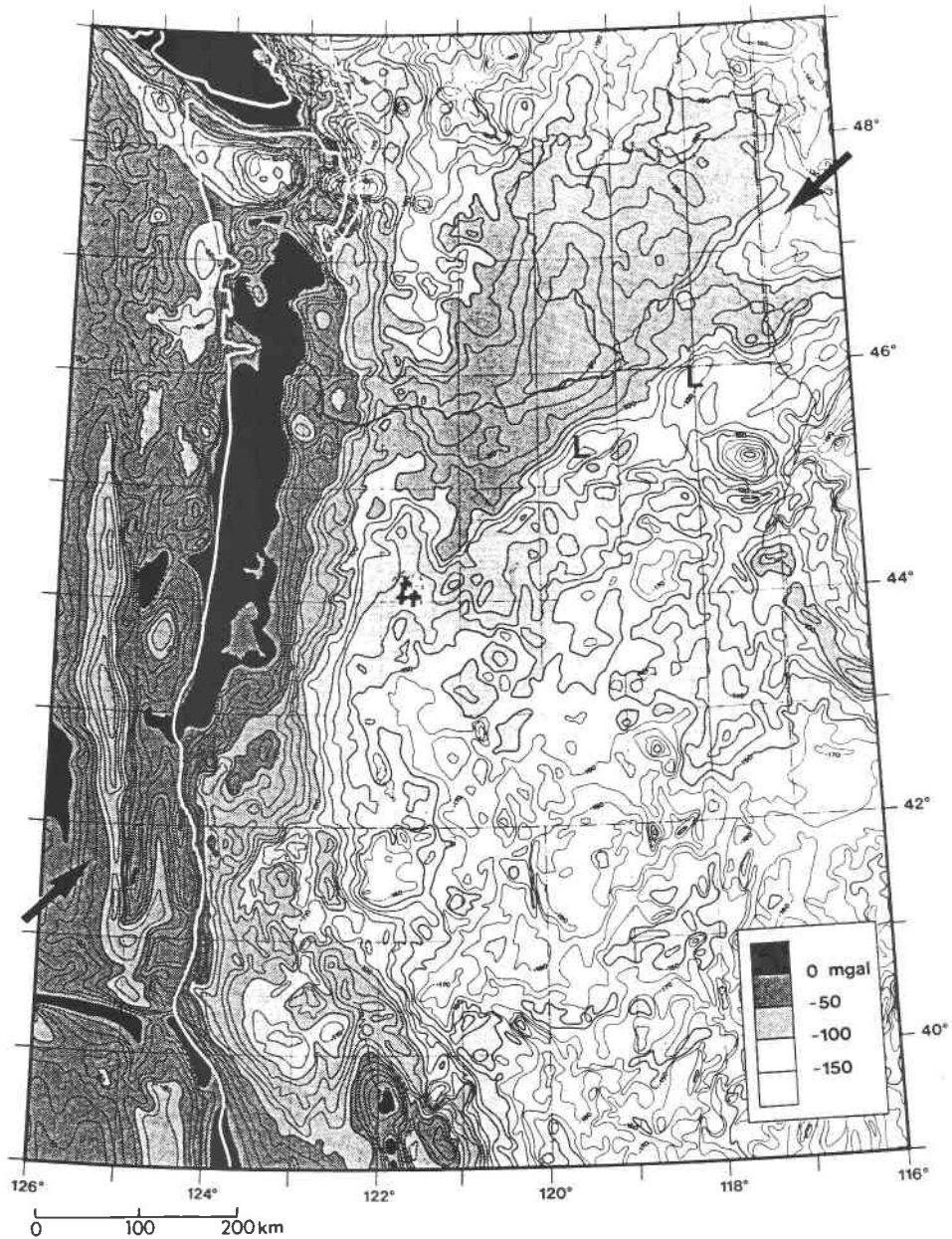
Figure 2.1: Regional Bouger gravity anomaly map of the Pacific Northwest, reproduced from Riddihough et al., 1986. Arrows indicate the Klamath-Blue Mountain gravity lineament (KBL) referred to in text. Small crosses at 122°W, 44°N represent North Sister, South Sister, and Broken Top volcanos. The KBL trends across the Oregon High Cascades in the Three Sisters area, although this relationship is obscured by the high heat flow (and thus a more negative Bouger anomaly) associated with High Cascade volcanism. It is possible that the Three Sisters area is located on, or very near to, the accretionary contact between older, Klamath Mtn.- type metamorphic rocks and younger meta-oceanic crust (Riddihough et al., 1986).

and Druitt, 1988). These isotopic data may indicate that slightly older, more isotopically evolved crust is located south of the KBL.

Metamorphic or older plutonic xenoliths have not been found in any rocks from the Three Sisters region, and thus the composition of the middle ($\approx$15-30 km) to lower ($\approx$30-45) crust under this part of the High Cascades remains unknown. Based on the above arguments, middle crustal lithologies under the Three Sisters area most likely consist of late Paleozoic accreted arc terranes. These terranes should be dominated by amphibolite-grade mafic metamorphic rocks, with relatively minor amounts of metamorphosed sedimentary and silicic igneous rocks.

2.2 Deep Crustal Structure

Magnetotelluric (Livelybrooks et al., 1989; Stanley et al., 1990) and seismic refraction (Leaver et al., 1984) studies have concluded that the crust beneath the central High Cascades consists of essentially four sub-horizontal layers (figure 2.2). Layer 1 is composed of $\leq$2 km of high resistivity Quaternary volcanic flows, which overlie 1-5 km of more conductive Tertiary volcanic rocks. Layer 2 extends to 11-12 km, and is composed of high resistivity, pre-Tertiary metamorphic rocks. The base of layer 2 is marked by a transition from brittle to ductile deformation, and represents the base of the upper crust (Stanley et al., 1990). Layer 3 (the middle crust) is highly conductive and is thought to represent amphibolite-facies rocks with small amounts of metamorphic fluid or partial melt (Stanley et al., 1990). Layer 3 extends to $\approx$30 km and is thought to be at temperatures of 500-600°C (Stanley et al., 1990; Blackwell et al., 1990). Layer 4 is only resolved seismically (Leaver et al., 1984), and extends from $\approx$30 km to a depth of 44 km along the length of the Oregon High Cascades. The deep crust (i.e., layer 4) is thought to consist of mafic granulite at temperatures of $\leq$1100°C, and mafic magma and intrusions (Stanley et al., 1990).

2.3 Regional tectonics

Most researchers in the last decade agree that the Oregon Cascade arc is the result of volcanism associated with subduction of the Juan de Fuca Plate (JDF) beneath the North American Plate (e.g., Priest et al., 1983; Taylor, 1990). Subduction of the JDF plate has likely occurred at a rate of $\approx$3 cm/yr since $\approx$5 Ma, although subduction rates as high as $\approx$8 cm/yr may have occurred between 5-35 Ma (Riddihough, 1984; Engebretson et al., 1986; Verplank and Duncan, 1987). The convergence direction between the JDF and North American plates has remained at about N50E since $\approx$10 Ma (Verplank and Duncan, 1987). Estimates for the dip of the subducting JDF plate beneath the Oregon Cascades are generally 65° ± 5° (Rasmussen and Humphries, 1988; Keach et al., 1989). Variations in subduction rate, convergence angle and possibly subduction angle with time are thought to have controlled many of the features of Cascade volcanism throughout the last 35 Ma (Priest et al., 1983; Verplank and Duncan, 1987; Taylor, 1990;
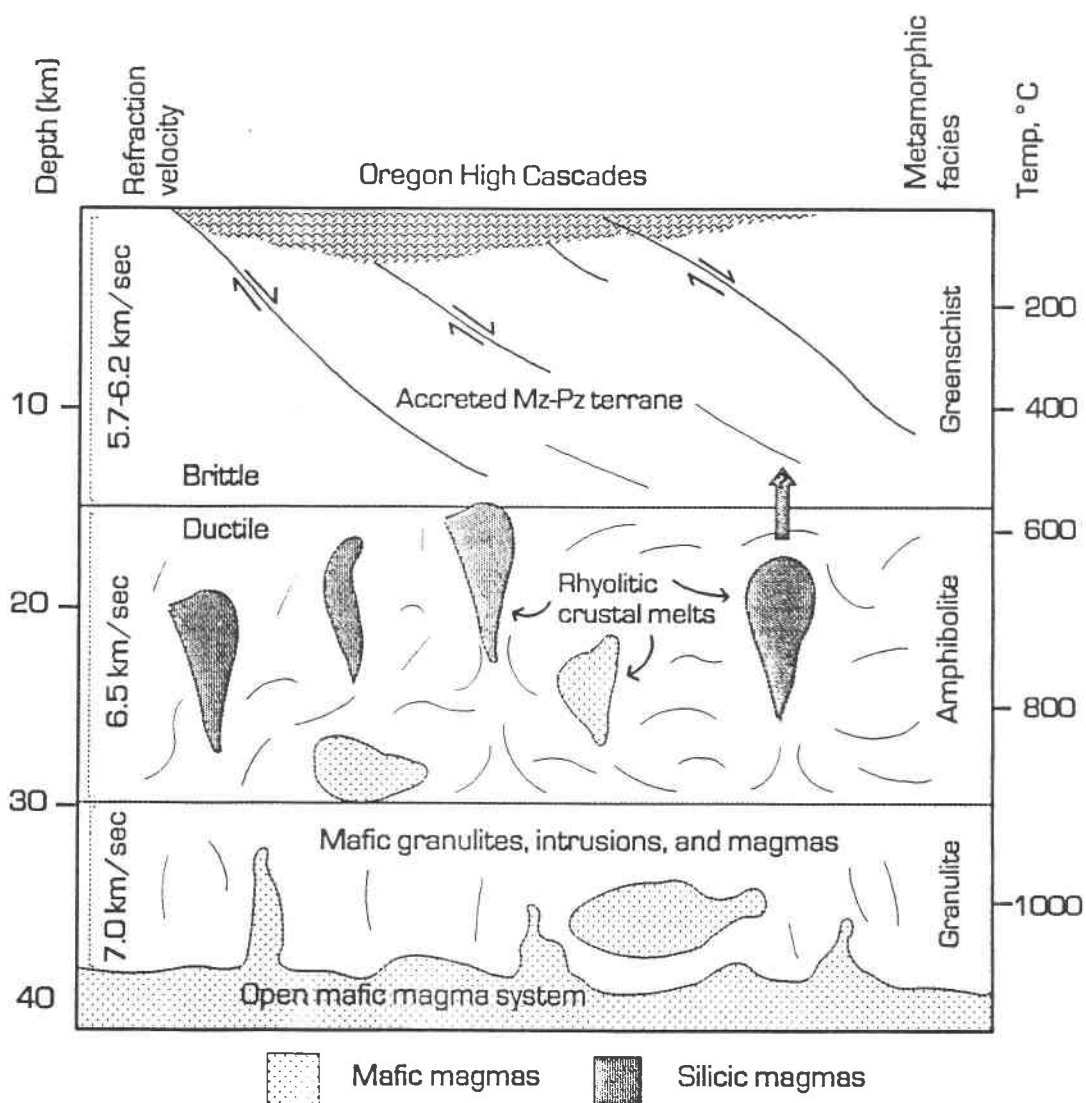
Figure 2.2: Schematic model of crustal structure in the Oregon High Cascades, based on magnetotelluric, seismic, heat flow, and petrologic data, slightly modified from Stanley et al., 1990. Mafic magmatism is focused in an essentially anhydrous deep ($\geq$30 km) crust. Magma segregation to middle crustal levels (15-30 km) permits differentiation to silicic compositions, and rhyolitic dehydration melts of amphibolitic crustal rocks. Magmas may pond at the brittle-ductile transition at $\approx$12 km (Stanley et al., 1990), and subsequently erupt through tectonically controlled magma conduits.

Priest, 1990). There is no evidence that any of these tectonic parameters have changed since 1 Ma, or would have resolvable variations along a 20 km segment of the High Cascades arc (i.e., within the Three Sisters area).

2.4 Regional Structure

The Oregon High Cascades are located in an area of active north-south compression and east-west horizontal extension of the crust, as shown (figure 2.3) by north-striking normal faults and vent alignments in this area (Nakamura, 1977; Zoback and Zoback, 1980). The orientation of regional horizontal extension has remained constant since ≈5 Ma, but was likely oriented to the northeast prior to ≈7 Ma (Sherrod and Pickthorn, 1989; Priest, 1990). Changes in the orientation (and probably the magnitude) of crustal extension in the Oregon Cascades have been linked to changes in the convergence angles between the Pacific and North American Plates (Atwater, 1970; Zoback and Zoback, 1980; Rogers, 1985; Priest, 1990), and to impingement of Basin and Range extension into the Cascades (Lawrence, 1976; Guffanti and Weaver, 1988; Wells, 1990).

The Brothers Fault Zone (BFZ) is expressed as a ≈200 km long zone of en-echelon normal faults that strike N40W to N50W (figure 2.3), and are thought to be the result of sub-surface dextral shear associated with Basin and Range extension (Lawrence, 1976). The BFZ may also represent a zone of transtensional shear associated with oblique subduction of the Juan de Fuca Plate (Gutmanis, 1989; Pezzopane and Weldon, 1990). Although the BFZ strikes towards the central part of the Oregon High Cascades, the BFZ is overlain by ≤0.7 to ≈3 Ma volcanic rocks near Newberry volcano (Peterson et al., 1976; MacLeod et al., 1982; Hawkins et al., 1988). The Tumalo Fault Zone (TFZ) (Peterson et al., 1976; Taylor, 1981) is a series of ≈N20W-striking normal faults that offsets units as young as 0.3-0.4 Ma (Peterson et al., 1976; Taylor, 1981; Sarna-Wojcicki et al., 1987). The TFZ offsets Newberry lavas, and strikes into the northwest fissure zone of Newberry volcano (Peterson et al., 1976; MacLeod et al., 1982; MacLeod and Sherrod, 1988). The TFZ does not merge with the BFZ, as has been occasionally reported (Lawrence, 1976; Guffanti and Weaver, 1988; Gutmanis, 1989), and has a markedly different orientation and age of deformation than the BFZ.

North-striking normal faulting at 5.4 to ≈4 Ma near the latitude of Mt. Jefferson (figure 2.3) resulted in the formation of a discontinuous intra-arc graben (Taylor, 1981; Smith, 1986). North-striking normal faults, which are thought to represent the western boundary of this graben, are exposed between Mt. Jefferson and the Three Sisters (figure 2.3). These faults mark the contact between Quaternary late High Cascade lavas on the east, and older (4-7 Ma) early High Cascade lavas on the west (Priest et al., 1987, 1988; Black et al., 1987). However, the contact between early and late High Cascade units south of the Three Sisters area is generally depositional (Sherrod, 1986). The eastern boundary of the graben is well exposed at Green Ridge (figure 2.3),
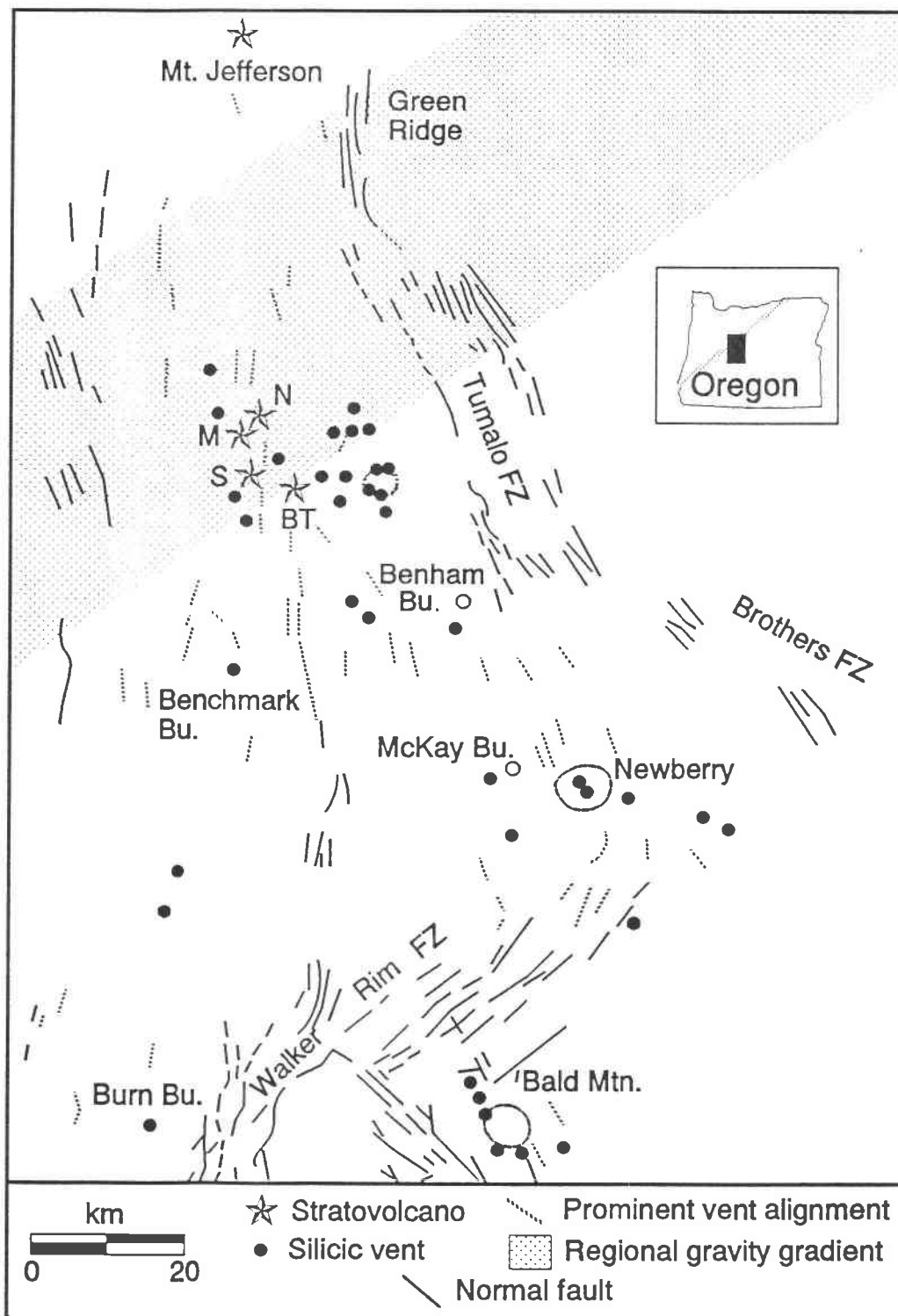
Figure 2.3: Faults and vent alignments of central Oregon, modified from MacLeod and Sherrod, 1988. Approximate boundaries of the regional gravity gradient from Thiruvathukal et al., 1970. **FZ** = Fault Zone. The strike of vent alignments changes from north to northwest in the Broken Top area. Northwest-striking vent alignments are parallel with the strike of the Tumalo FZ, which continues south to Newberry volcano and eventually merges with the Walker Rim FZ.

where at least 1 km of stratigraphic offset has occurred since 5.4 Ma (Conrey, 1985; Smith, 1986; Hill et al., 1991). Green Ridge faults apparently merge with the northern part of the Tumalo Fault Zone (Peterson et al., 1976; Conrey, 1985), suggesting that initial motion along the TFZ occurred during graben formation (Smith, 1986). However, numerous graben-forming faults had continued activity to 2.4-1.7 Ma (Priest et al., 1988; Priest, 1990; Taylor, 1990), suggesting that the TFZ may be primarily a Quaternary tectonic feature. Although there is no concrete evidence that the High Cascade graben is continuous (i.e., Allen, 1966; cf. Smith, 1986), north-striking normal faults may occur beneath the Quaternary volcanic cover in the subsurface west of the TFZ (Smith, 1986; Livelybrooks et al., 1989; Taylor, 1990).

2.5 A Brief History of the Oregon Cascades

The Oregon Cascades have been a locus of subduction-related calc-alkaline magmatism since ≈37 Ma (McBirney et al., 1974; White and McBirney, 1978; Taylor, 1981, 1990; Priest et al., 1983; Priest, 1990). Following the nomenclature of Priest et al., (1983), units older than 7.4 Ma are generally associated with the Western Cascades (i.e., Callagan, 1933; Peck et al., 1964). Units from 7.4 to 4 Ma are referred to as early High Cascades, with younger units belonging to the late High Cascades. Although it is likely that the position, width, and petrogenesis of the Cascade volcanic arc have changed considerably from ≈37 Ma to ≈7 Ma (e.g., Priest, 1990; Wells, 1990), much of the early geological history of the Western Cascades remains unstudied. Summaries of Western Cascade petrogenesis are presented in Taylor (1990), Priest et al., (1983), and Priest (1990).

Stratigraphic records of early High Cascade volcanism are preserved ≈20 km west and east of the late High Cascade volcanic axis. Lavas and volcaniclastic sediments of the Deschutes Formation (Smith, 1986) were deposited from 7.4 to 5.4 Ma in a broad basin located ≈10(?) to ≈50 km east of the early High Cascade volcanic axis. Mafic flows and intrusions, which are temporally correlative with the Deschutes Formation, are also exposed from ≈20 to ≈40 km west of the present volcanic axis (Sherrod, 1986; Black et al., 1987; Priest et al., 1987, 1988). Based on major element and limited trace element analysis, early High Cascade mafic rocks appear to be petrogenetically distinct from late High Cascade mafic rocks (Hughes, 1983, 1990; Conrey, 1985; Smith, 1986; Hughes and Taylor, 1986; Conrey and Sherrod, 1988). Early High Cascade mafic rocks are commonly diktytaxitic, and probably evolved from a mantle source that was more depleted in incompatible elements than the source of the late High Cascades (Hughes, 1990).

The transition from early to late High Cascade volcanism is marked by formation of the High Cascade graben, and uplift of the Western Cascades (Taylor, 1981, 1990; Priest, 1990). Graben formation was accompanied by the syntectonic(?) eruption of anomalously large amounts of relatively nonevolved high aluminum olivine tholeiite, possibly in response to increased amounts

of crustal extension (Taylor, 1981; Hughes and Taylor, 1986; Hughes, 1990). The dominance of basalt gradually yielded to basaltic andesite by about 2 Ma (Hughes, 1990; Conrey and Sherrod, 1988). Volcanism since ≈2 Ma has been characterized by the eruption of mafic rocks that are more incompatible element-enriched than those associated with either the early High Cascades or graben formation (Hughes, 1983, 1990; Hughes and Taylor, 1986). Most of the present Oregon central High Cascade volcanos are younger than ≈0.7 Ma, and have been erupted onto the post-graben mafic platform (White and McBirney, 1978; Taylor, 1981, 1987, 1990). However, Mt. Hood (Wise, 1969; Priest and Vogt, 1982) and Mt. Jefferson (Conrey, 1991) overlie silicic rocks that are penecontemporaneous with the mafic platform.

Late High Cascade silicic volcanism has been restricted to large stratovolcanic centers, although isolated silicic domes have been occasionally erupted >20 km from these centers (e.g., Hayrick Butte, Benchmark Butte). The major silicic vents in the Oregon High Cascades are spaced ≈100 km apart, which is similar to the spacing of the larger silicic intrusions in the Western Cascades (Peck et al., 1964). This spacing may reflect the thermal limits of maintaining hot magmatic conduits through continental crust of this thickness and composition (cf., Marsh, 1984).

3. GEOLOGY OF THE THREE SISTERS AREA

3.1 Introduction

The geology of the Three Sisters area reflects the complexities associated with the eruption of at least 7 major silicic vent complexes, and numerous monogenetic vents, within a 600 km^2 area. Previously reported stratigraphic relationships (Taylor, 1978, 1981, 1987; Wozniak, 1982; Clark, 1983) have been constrained with new K-Ar age determinations in this study. These relationships are summarized in figure 3.1, and will be expanded upon below.

This section also describes the geology and age of a poorly-documented section of the Deschutes Formation, informally known as the Bull Springs Inlier (Taylor, 1978; Smith, 1986), which occurs ≈5 km east of Triangle Hill. In addition, new data on the petrology and source of the voluminous pyroclastic deposits that occur in the Bend area, and previously unreported strontium isotopic analyses for rocks of the Three Sisters area, will be presented in this section.

3.2 Deschutes Formation

The Deschutes Formation is an assemblage of lavas, pyroclastic deposits and volcanogenic sediments derived from 7.4 to ≈4 Ma early High Cascade volcanism in the Mt. Jefferson-Three Sisters area (Hales, 1975; Taylor, 1978, 1981; Conrey, 1985; Smith, 1986; Smith et al., 1987). The Deschutes Fm. is best exposed ≈30 km northeast of the Three Sisters area in the Deschutes Basin (Smith, 1986), where it forms a ≈250 m thick section dominated by volcanogenic sediments and pyroclastic deposits. Deschutes Fm. mafic lavas are exposed as far south as Bend (Smith, 1986; McDannel, 1989), and it is likely that many of the mafic lavas and vents ≤10 km east of the Tumalo Fault Zone are of Deschutes Formation age (Taylor, 1981; Smith, 1986; McDannel, 1989).

Although most Deschutes Fm. igneous units were erupted from the area around Mt. Jefferson (Hales, 1975; Conrey, 1985; Smith, 1986), numerous Deschutes Fm. ignimbrites were erupted from the Three Sisters area (Cannon, 1985; Smith, 1986; McDannel, 1989). Deschutes Fm. ignimbrites range in composition from andesite to rhyodacite, and commonly contain banded pumice (Smith, 1986). Several small exposures of Deschutes Fm. ignimbrite are preserved in the Bend area, and include a poorly welded, banded rhyodacite-andesite vitric lapilli tuff near the confluence of Tumalo Creek and the Deschutes River (samples 3S088M,S), a non-welded rhyodacitic tuff on the northwest margin of Awbrey Butte (3S080), and a highly devitrified, moderately welded tuff near Tumalo Dam (3S077). Samples of the Buckhorn Canyon (3S141) and Deep Canyon (3S142) ignimbrites, which were erupted from the Three Sisters area, were also analyzed.

Analyzed Deschutes Fm. rhyodacitic ignimbrites are compositionally similar to rhyodacites from the Broken Top system (figure 3.2). Broken Top rhyodacites were produced though the
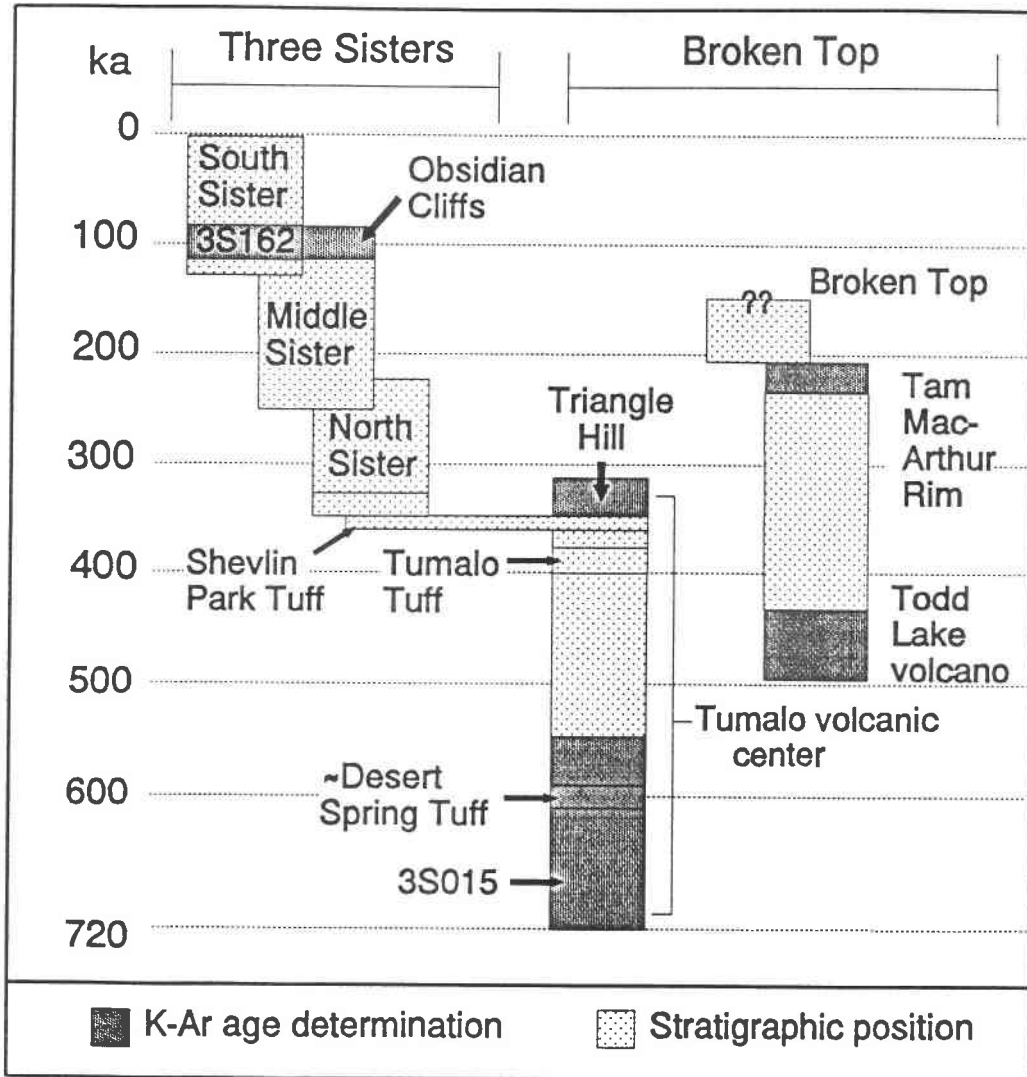
Figure 3.1: Generalized stratigraphy of the Three Sisters area, constrained with new K-Ar dates from this study. Stratigraphic positions are relative, and do not represent absolute ages. Size of K-Ar date symbol represents range of 1σ error. Positions of the Tumalo Tuff and Desert Spring Tuff constrained by data in Sarna-Wojcicki et al., (1987, 1989). K-Ar data presented in Table 3.1.

mixing of rhyolitic crustal melts into a fractionating intermediate composition magma system (Chapter 8). It is likely that a similar magma system existed in the Three Sisters area at ≈5 Ma, and produced these Deschutes Fm. rhyodacite ignimbrites. Although rhyolitic crustal melts were produced in this area at ≈5 Ma, these melts did not coalesce into a discrete rhyolitic magma chamber. Rhyolitic volcanism in the Broken Top system at ≈0.4 Ma thus reflects a set of geologic conditions that were unique to this particular time.

3.2.1 The Bull Springs Inlier of the Deschutes Formation

A noteworthy outcrop of Deschutes Fm. lavas, informally known as the Bull Springs Inlier (Taylor, 1981; Smith, 1986; Hill, 1988a), occurs ≈5 km east of Triangle Hill (figure 3.3). This ≈4 km^2 outcrop of basaltic andesite-to-dacite lavas occurs ≈5 km west of the Tumalo Fault Zone, and is important to understanding the structural history of this part of the Oregon Cascades.

The Bull Springs Inlier (BSI) is primarily composed of a series of andesitic to dacitic lavas, which have normal paleomagnetic directions and are nearly horizontal (figure 3.3). These lavas are capped by an aphyric basaltic andesite lava, which has a reversed paleomagnetic direction. This basaltic andesite lava has a K-Ar date of 4.7 ± 0.1 Ma, which corresponds to an upper Deschutes Fm. age (table 3.1). This date is also within a 4.47-4.85 Ma reverse polarity event in the Gilbert polarity epoch (Mankinen and Dalrylmple, 1979); normal polarity rocks underneath this unit are thus older than 4.85 Ma. Quaternary ignimbrites and mafic lavas (≤0.7 Ma) are also deposited around, and on, the BSI (figure 3.3). The distribution of Quaternary units on the western margin of the BSI suggests that the western face of the BSI is a pre-Quaternary fault scarp.

The BSI represents an isolated flank of a Deschutes Fm. volcanic center, with the main vent complex presumedly located further to the west. Normal faulting on the western margin isolated the BSI in a manner analogous to the formation of Green Ridge, and resulted in the formation of a basin west of the BSI. Offsets in shallow (≤5 km) crustal conductors observed ≈7 km northwest of the BSI (Livelybrooks et al., 1989) are consistent with this hypothesis. In addition, rotary drilling by UNOCAL Geothermal 6.5 km north-northwest of the BSI (Hole #79-9, T16S R10E, SWNE27) encountered >100 m of volcanic sediments underlying ≈100 m of Quaternary lavas and ignimbrites, further indicating that the area west to northwest of the BSI was a basin.

Formation of the High Cascade graben in the Green Ridge area began at ≈5.4 Ma, and likely continued until ≈5.3 Ma (Smith, 1986; Smith et al., 1987). If the BSI was created through the continuation of normal faulting south of Green Ridge, then this faulting did not reach the BSI area until <4.7 Ma. It is also unlikely that the >1 km of vertical displacement associated with the formation of Green Ridge (Conrey, 1985; Hill et al., 1991) was accommodated entirely by the Tumalo Fault Zone east of the BSI (Smith, 1986), or else the BSI would not have been preserved at the surface unless it had a pre-faulting elevation >2280 m (≈7500'). These relationships
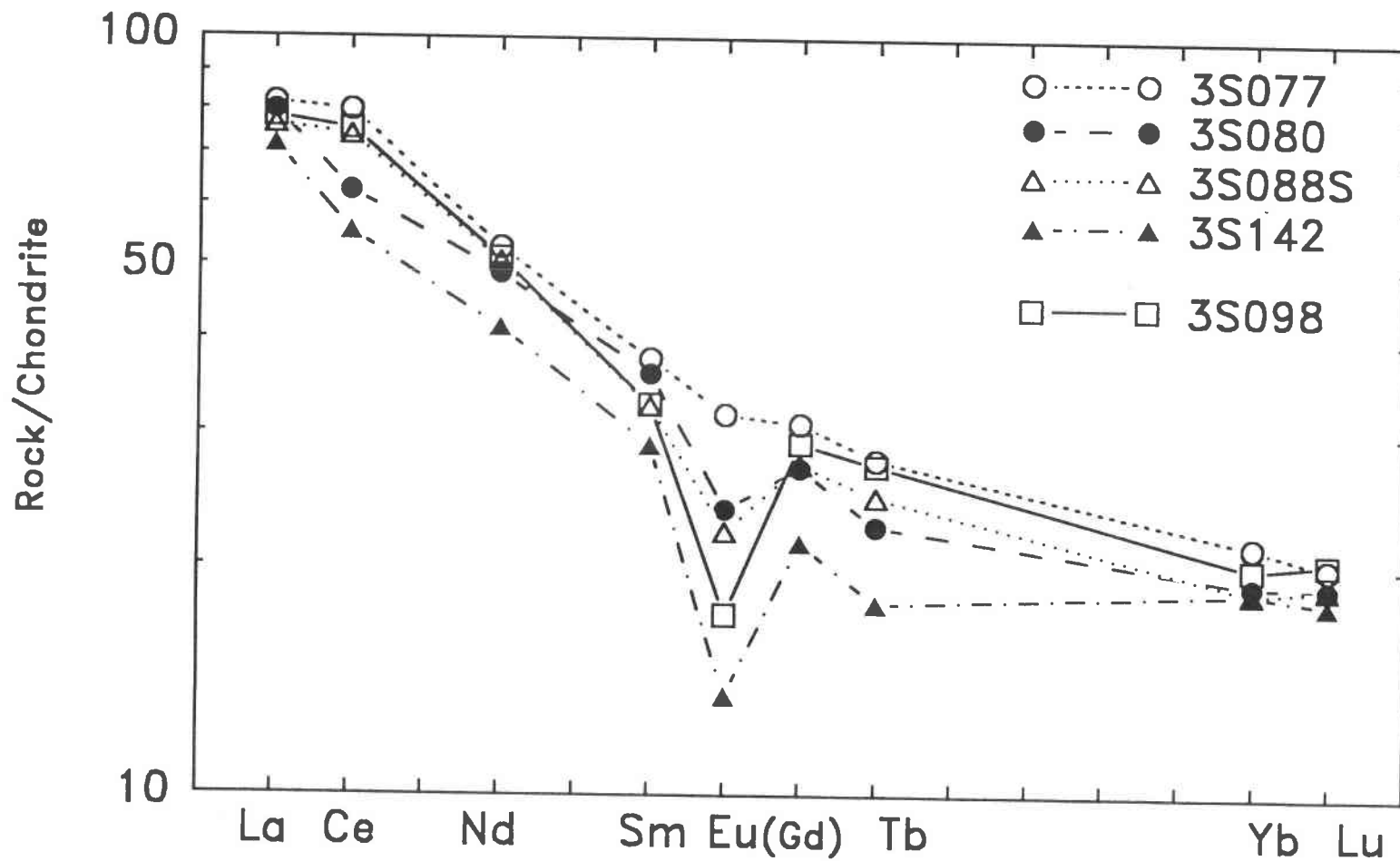
Figure 3.2: Chondrite-normalized (Anders and Ebihara, 1982) rare earth element diagram for Deschutes Formation (DF) rhyodacitic ignimbrites analyzed in this study. Broken Top (BT) rhyodacite 3S098 included for comparison. The similarity between DF and BT rhyodacites suggests that these units had a similar petrogenesis; rhyolitic magma was available for mixing during DF magmatism, but did not accumulate and form discrete rhyolitic magma chambers.

Figure 3.3: Geologic map of the Bull Springs Inlier.

Geology of the
Bull Springs Inlier

B. Hill, 1986, 1987

Description of Map Units
Qal: Quaternary alluvium
Qc: Colluvium
Qba: Quaternary High Cascade
     basaltic andesite lavas.
Qsp: Shevlin Park Tuff
Qds: Desert Springs Tuff
Tba: Pliocene basaltic andesite
Ta: Pliocene-Miocene andesite
Td: Pliocene-Miocene dacite

Contact, located ±50'
Contact, located ±200'

Numbers refer to analyzed
samples (3S00-).
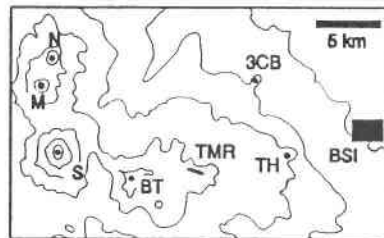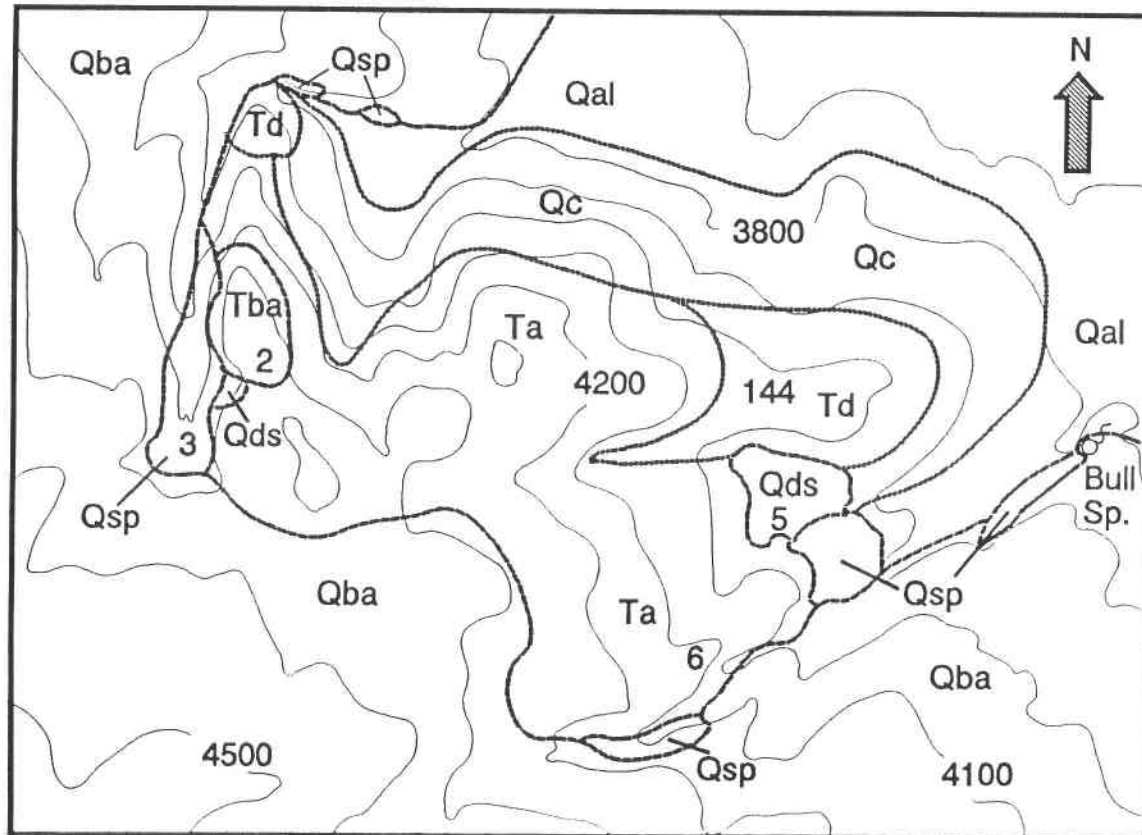
Base: NW 1/4, Shevlin Park 7.5' quadrangle
Deschutes County, Oregon.

Contour interval = 100'

Series[1]	Sample #	Sample wt (g)	K (wt %)[2]	$^{40}Ar_{rad}$ x10^{-12} mol/g	$^{40}Ar_{rad}$ (%)	Date ($\pm 1\sigma$)	Comments
DF	3S002	4.223	0.92	7.462	45.7	4.7 ± 0.1 Ma	Top of the Bull Springs Inlier, p-mag reversed.
BT[3]	3S015[3]	n/a	0.984	n/a	6.6	0.63 ± 0.09 Ma	Basaltic andesite cone, 1.5 km west of Triangle Hill.
BT	3S067	3.034	1.79	1.418	17.2	460 ± 30 ka	Todd Lake volcano, fresh dacite flow.
BT	3S010	4.115	1.05	0.619	13.8	340 ± 20 ka	Triangle Hill, non-vesiculated andesite bomb.
BT	3S046	2.499	2.33	0.859	13.8	213 ± 9 ka	Tam MacArthur Rim, glassy rhyodacite flow.
3S	3S159	4.021	0.59	0.373	1.8	0.4 ± 0.2 Ma	Middle Sister, vesicular porphyritic basalt.
3S	3S139	2.524	2.77	0.455	6.4	95 ± 10 ka	Obsidian Cliffs, fresh rhyolite obsidian.
3S	3S162	3.027	1.65	0.267	7.7	93 ± 11 ka	South Sister, glassy andesite flow 3S162.

Notes:

[1]Series: DF = Deschutes Fm.; BT = Broken Top system; 3S = Three Sisters system.

[2]K determined by Atomic Absorption Spectrometry at the University of Oregon, C. McBirney, analyst.

[3]Analysis at the University of Arizona Isotope Geochemistry Lab, 4/88, on feldspar concentrate from 3S015. Analysis courtesy of G. Priest, Or. Dept. Geol. Min. Ind., 1988. n/a = data not reported.

- Isotopic ratios determined at Oregon State University, R. Duncan, principal investigator.

- K-Ar ages calculated using the constants of Steiger and Jager (1977): $\lambda_e = 0.581 \times 10^{-10}$ yr^{-1}, $\lambda_B = 4.962 \times 10^{-10}$ yr^{-1}, and $^{40}K/K_{total} = 1.167 \times 10^{-4}$ mol/mol.

Table 3.1: Whole rock K-Ar age determinations for rocks from the Three Sisters area of the Oregon High Cascades. The date of Middle Sister basalt 3S159 is probably at the younger limits of 1σ error, based on stratigraphic relationships; empirical analysis of reported High Cascade K-Ar dates indicates that analyses with <2% radiogenic Ar are generally inaccurate as well as imprecise. Other dates correspond to the stratigraphic positions

indicate that normal faults of significant vertical displacement are probably buried under Quaternary units between the BSI and Triangle Hill (figure 3.3). These faults probably strike sub-parallel to the Tumalo Fault Zone; the BSI is located ≈10 km eastward of the projected strike of the Green Ridge faults, and pre-Quaternary rocks are not exposed in the area between the BSI and Triangle Hill.

3.3 Tumalo Volcanic Center

One of the more prominent topographic features of the Three Sisters area is a broad highland that extends east of Broken Top volcano (figure 1.1). This area was referred to as the "silicic highland" by Taylor (1978, 1981), but a more regionally descriptive name was needed to describe this highland and associated vents. The name "Tumalo volcanic center" was selected by Hill and Taylor (1988b) to describe both the "silicic highland", and a series of cogenetic andesitic cinder cones and rhyolitic domes that extend from Melvin Butte ≈25 km south to Edison Butte (figure 3.4).

Most of the TVC is covered by younger mafic lavas erupted from the Tam MacArthur Rim-Broken Top area, and by glacial deposits (Taylor, 1978, 1981). The most prominent feature of the TVC is a roughly circular arrangement of mafic cinder cones and silicic domes, centered on Triangle Hill (figure 3.4). This ≈3 km diameter feature is also coincident with a prominent negative Bouger gravity anomaly of 10 mgal (Couch et al., 1982), indicating that low density material underlies the Triangle Hill vent complex. Shallow crustal xenoliths form ≈1% of the ejecta of Triangle Hill, and range in size from <1 mm to ≈1 m in diameter. The most abundant xenoliths consist of fresh to hydrothermally(?) altered (mixed layer clays ± zeolite(?)) silicic lavas, which commonly do not resemble rocks exposed at the surface. Xenoliths of rhyolitic vent breccia are also common, as are mafic to intermediate lavas. Xenoliths of an intensely welded, crystal-rich silicic ignimbrite have also been erupted at Triangle Hill. These ignimbrite xenoliths are petrographically identical to samples of an intensely welded ignimbrite exposed ≈8 km south in the valley of Tumalo Creek (figure 3.4). This ignimbrite is probably associated with early volcanic activity at the TVC, and projects horizontally to ≈300 m beneath Triangle Hill. The abundance and composition of silicic xenoliths, combined with the negative gravity anomaly, indicates that the Triangle Hill vent complex overlies a major silicic vent.

All rocks exposed in the TVC area have normal paleomagnetic directions, and are likely younger than 720 ka. Based on limited stratigraphic information and the relatively steep slope of the cone, Triangle Hill appears to be the youngest vent in the Triangle Hill complex. Triangle Hill has a K-Ar date of 340 ± 20 ka, which probably represents the age of the last eruption of the TVC (Table 3.1). An additional K-Ar date of 0.63 ± 0.09 Ma was obtained (G. Priest, written comm.,

Figure 3.4: Geologic map of the Tumalo volcanic center and associat-
ed pyroclastic deposits. Data from Taylor (1981, 1987; unpub. res.
1974-1981), Hill (1985), Scott and Gardner (1991), and this study.
Geology of the Bull Springs Inlier (BSI) shown in detail in figure
BSI. Tumalo Tuff incorporates exposures of the Bend Pumice,
Tumalo Tuff, and Lava Island Tuff (Taylor, 1981).

Location symbols: **MB**: Melvin Butte; **TH**: Triangle Hill; **BB**: Bear-
wallow Butte; **BSI**: Bull Springs inlier; **TMR**: Tam MacArthur Rim;
BT: Broken Top; **TCk**: Tumalo Creek valley; **EB**: Edison Butte; **B**:
Mt. Bachelor.

Figure 3.4: Geologic map of the TVC.
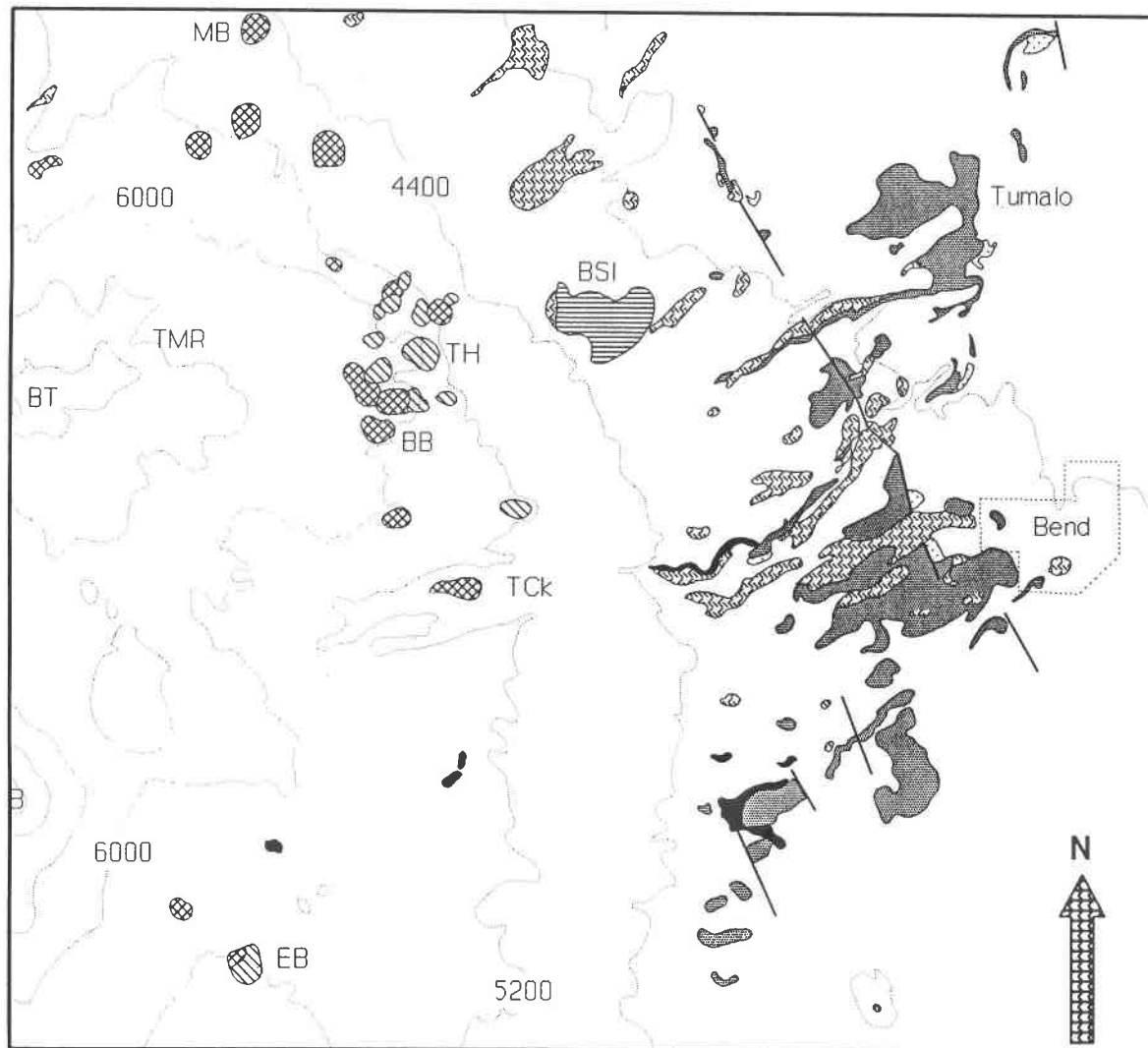
Geologic Map of the Tumalo
Volcanic Center & associated
Pyroclastic Deposits.

B.E. Hill & E.M.Taylor

Shevlin Park Tuff
Century Drive Tuff
Tumalo Tuff
Desert Spring Tuff

Rhyolite & Rhyodacite
Andesitic cinder cones

Deschutes Formation
Pliocene lavas of the Bull
Springs Inlier.

Major Fault

Contour interval = 800'

km
0   5

N

1988) on a plagioclase separate from an eroded basaltic andesite cone (3S015) 1.5 km northwest of Triangle Hill (Table 3.1). This date probably represents the age of early TVC volcanic activity, and is supported in the next section by evidence that the oldest TVC pyroclastic eruption occurred around 0.63 Ma.

3.3.1 Pyroclastic Deposits of the TVC

A sequence of four major pyroclastic deposits are exposed in the area extending east of the TVC to the town of Bend (figure 3.4). These deposits represent the eruption of ≥ 14 km^3 (dense rock equivalent, DRE) of andesitic-to-rhyolitic magma from the Tumalo volcanic center, from ≈ 600 ka to ≤ 320 ka. Although these deposits have been studied in some detail (Taylor, 1981; Mimura, 1984; Hill, 1985; Hill and Taylor, 1989), confusion remains as to the source and age of these rocks. Data presented in this section will show that these rocks were clearly related to late Quaternary eruptions from the Tumalo volcanic center.

3.3.1a Desert Spring Tuff

The Desert Spring Tuff (Taylor, 1981) probably is the oldest of the Pleistocene High Cascade pyroclastic deposits. Where the basal contact is exposed, the Desert Spring Tuff overlies rocks of the Deschutes Formation. The Desert Spring Tuff contains at least two distinct flow lobes that form one cooling unit. Although complete sections are not exposed, the Desert Spring Tuff has an average thickness of about 12 meters, with one preserved section 30 meters thick. Although preservation is generally poor and outcrops are widely scattered, the Desert Spring Tuff probably represents the eruption of ≈ 2 km^3 (DRE) of rhyodacitic magma.

The Desert Spring Tuff is characterized by black rhyodacitic pumice up to 0.5 m in diameter, which contains up to 15 wt. % phenocrysts of plagioclase (An_{45-40}), orthopyroxene ($Wo_3En_{55}Fs_{42}$), augite ($Wo_{40}En_{38}Fs_{22}$), magnetite, ilmenite, and apatite. Pyroxene phenocrysts are characterized by abundant inclusions of apatite. Although outcrops of the Desert Spring Tuff are scattered, the distribution of outcrops and the general westward increase in extent of welding indicates that this unit was erupted from the TVC area (Taylor, 1981; Mimura, 1984). In addition, the mineralogy and chemistry of the Desert Spring Tuff is very similar to several TVC domes such as Bearwallow Butte (table 3.2), which further supports a TVC source for this unit.

Glass shards from the Desert Spring Tuff have been correlated on the basis of major element geochemistry with the Rye Patch Dam ash bed (Davis, 1978), which is a widespread ash found in central Nevada and in core from Tulelake, northern California (Sarna-Wojcicki et al., 1989). The Rye Patch Dam ash has an age of ≈ 0.63 Ma, based on stratigraphic position in the Tulelake core (Sarna-Wojcicki et al., 1989). Paleomagnetic directions of the Desert Spring Tuff and Rye Patch Dam ash are also similar, further supporting a correlation between these two units

Sample	3S005	3S009	3SXBP	Avg Do	3S079	3S028	3S003
SiO2	68.0	68.2	74.2	74.6	67.0	58.5	61.5
TiO2	0.72	0.61	0.16	0.15	0.81	1.51	1.28
Al2O3	15.6	16.1	14.2	13.9	17.1	17.4	17.6
FeO*	4.24	3.44	1.82	1.63	4.12	7.88	6.53
MnO	0.09	0.09	0.07	0.06	0.13	0.16	0.22
MgO	0.45	0.87	0.08	0.05	0.83	2.26	1.50
CaO	2.12	2.35	0.81	0.69	2.39	5.36	3.83
Na2O	4.64	5.56	4.46	5.18	4.33	4.78	5.16
K2O	3.25	2.58	3.47	3.49	2.16	1.02	1.65
P2O5	0.19	0.16	0.03	0.02	0.16	0.37	0.47
TOTAL	99.86	101.16	99.63	99.77	98.01	100.09	99.92
Rb	77	52	84	84	44	16	26
Ba	755	732	794	796	616	503	519
Sr	209	237	65	50	278	498	396
Cs	1.40	0.95	3.10	1.37	1.60	0.80	1.20
Sc	9.52	8.72	4.29	4.30	11.05	21.82	18.33
V	25	23	0	3	36	159	105
Co	5.87	3.72	0.50	0.66	2.12	15.38	11.60
Ni	12	8	11	11	7	3	7
Cr	3	0	1	1	3	10	4
Zn	66	65	105	79	87	66	108
La	25.2	25.9	28.7	23.2	19.8	19.3	20.8
Ce	57.2	57.7	59.7	52.5	39.9	39.9	49.8
Nd	27.1	26.0	26.5	20.4	22.1	24.1	23.9
Sm	6.27	6.02	5.95	4.42	6.06	6.24	6.13
Eu	1.49	1.40	0.83	0.61	1.37	1.92	1.71
Tb	0.97	0.88	0.94	0.73	0.87	0.96	0.88
Yb	3.7	3.7	4.2	3.3	3.4	3.2	2.9
Lu	0.51	0.53	0.58	0.50	0.50	0.49	0.43
La/Sm	2.54	2.72	3.05	3.32	2.06	1.95	2.14
ΣHREE	54.09	52.75	57.77	46.72	50.23	51.02	45.99
Eu/Eu*	0.72	0.71	0.42	0.41	0.70	0.93	0.86
Zr	293	277	231	217	231	176	203
Hf	7.9	7.5	6.7	6.6	5.5	4.6	5.2
Ga	24	20	20	20	21	24	20
Y	34	33	36	28	36	32	30
Nb	18.6	16.1	16.9	17.4	14.3	9.5	12.9
Ta	1.01	0.98	1.20	1.02	0.66	0.61	0.72
Th	7.5	5.8	8.1	8.1	3.8	3.0	3.3
U	2.6	1.9	2.7	2.5	1.4	0.9	1.2

3S005: Desert Spring Tuff on eastern flank of Bull Springs Inlier.
3S009: Bearwallow Butte rhyodacite dome.
3SXBP: Bulk Bend Pumice, quarry ≈1mi SW Bend.
Avg Do: Average of 8 TVC rhyolite domes.
3S079: Columbia Canyon lapilli-fall tuff.
3S028: Century Drive Tuff, 2 mi NW. of Wanoga Butte.
3S003: Shevlin Park Tuff at west margin of Bull Springs Inlier.

Table 3.2: Compositions of pyroclastic units associated with the Tumalo volcanic center, and representative TVC silicic domes. Note that the composition of the Bend Pumice is nearly identical to the average composition of TVC rhyolite domes, and that the Desert Spring Tuff is compositionally similar to TVC rhyodacite domes.

(Gardner et al., 1992). If the Desert Spring Tuff represents the proximal equivalent of the 0.62 Ma Rye Patch Dam ash, then early TVC volcanism likely predated eruption of the Todd Lake volcano.

3.3.1b Tumalo Tuff

Previous workers (Taylor, 1981; Mimura, 1984; Hill, 1985; Hill and Taylor, 1989) have described a rhyolitic eruptive sequence consisting of a lapilli-fall tuff (Bend Pumice) directly overlain by a poorly welded ignimbrite (Tumalo Tuff), which is in turn overlain by a highly devitrified ignimbrite (Lava Island Tuff). Data presented in this section will support previous arguments (Hill, 1985; Hill and Taylor, 1989) that these units are the products of one eruptive event, and that the "Bend Pumice" (after Taylor, 1981) should be referred to as a member of the Tumalo Tuff.

The Bend Pumice member of the Tumalo Tuff (BP) is a rhyodacitic vitric lapilli-fall tuff that is best exposed along the roads leading to Tumalo State Park. The basal zone of the BP consists of pumice lapilli, ash, and perlitic obsidian, which have been locally reworked with alluvial gravels and sands. The basal zone ranges to 2 meters in thickness, and is thought to represent the preliminary stage of a climactic eruption (Hill, 1985). The basal zone is overlain by 3-13 meters of air-fall lapilli and ash, which progressively increases in average grain size up section except for a small reversal near the top of the deposit (Hill, 1985).

The median diameter of pumice-fall deposits generally shows an exponential decrease with distance from the vent (Fisher, 1964; Walker, 1971). The significant variations in median grain size and degree of sorting observed within the BP section require that samples used for granulometric analysis must be collected from a constant stratigraphic horizon in the deposit. Six $\approx$2 kg BP samples from 0.25 m below the contact with the overlying Tumalo Tuff were collected and manually sieved using standard sediment sieves (figure 3.5). These data were combined with grain-size data from Hill (1985) in order to better constrain the source of the Bend Pumice. The observed grain size distributions in the BP (figure 3.5) support the hypothesis that this unit was erupted from west of Bend (Hill, 1985). Comparison of the measured median grain sizes with distribution data from other pumice-fall deposits (Fisher, 1964; Walker, 1971) also suggests that the source of the BP was $\approx$10 to $\approx$20 km from these deposits (Hill, 1985).

A roughly 7x6x6-cm basaltic ($\rho \approx$2 g/cm^3) rock fragment was collected near the top of a Bend Pumice outcrop 9 km east-northeast of Triangle Hill (figure 3.4). Because rock fragments this size are generally transported ballistically, rather than convectively, from the vent, ballistic trajectories were calculated for this clast using the equations of Wilson (1972). The maximum ballistic transport distance for this clast is $\approx$2 km, which is unreasonably low. It is likely that this clast had components of both convective and ballistic transport (i.e., Walker, 1981), because the nearest reasonable vent locality was 9 km to the west at Triangle Hill. In essence, the occurrence
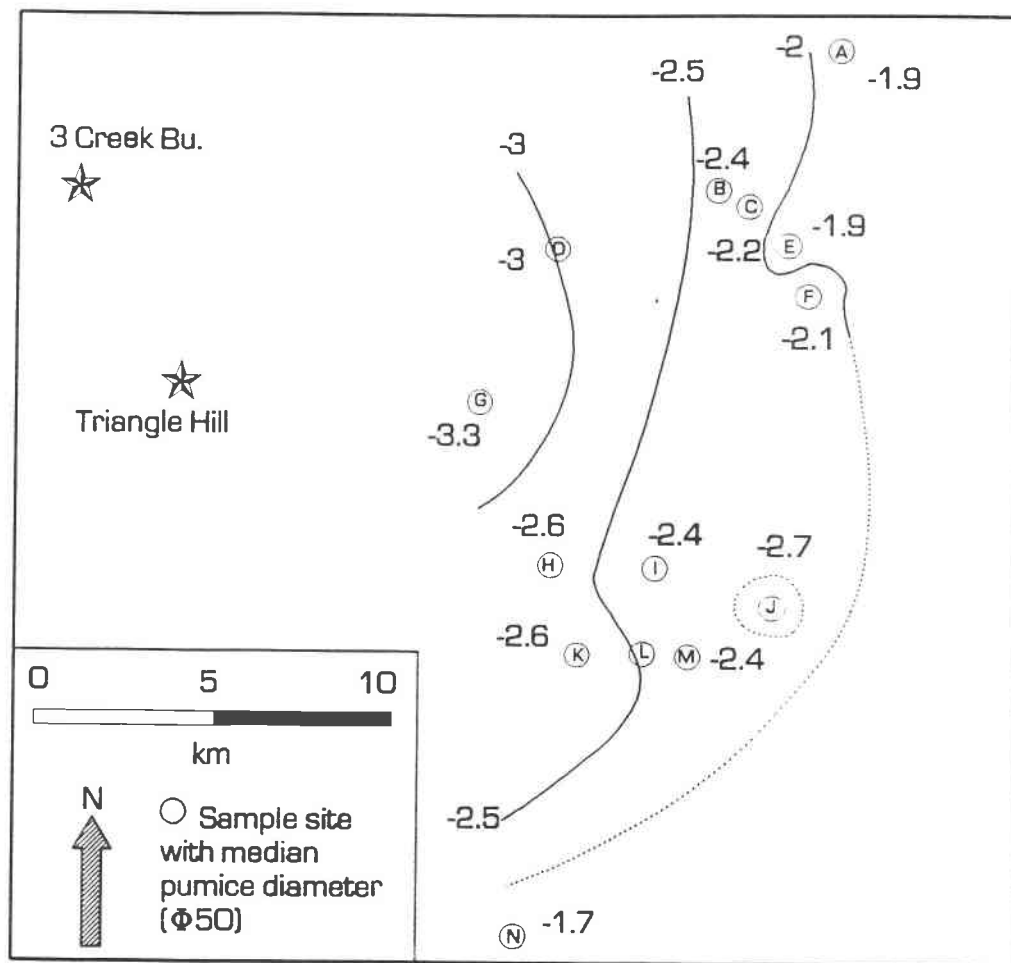
	D	M	G	H	C	E	M	L	K	I
-6φ	10.8	0.0	20.7	0.0	0.0	0.0	0.0	2.9	2.5	2.1
-5φ	17.1	4.0	6.6	10.0	3.2	3.0	3.8	3.7	4.8	4.0
-4φ	9.9	4.7	11.2	13.2	10.4	8.4	13.1	13.8	12.0	11.3
-3φ	12.5	14.3	16.7	18.9	17.6	15.2	19.6	19.8	21.1	20.2
-2φ	11.7	20.3	15.3	18.7	19.7	18.2	20.2	18.6	21.9	20.6
-1φ	13.5	24.6	13.6	16.8	20.6	21.5	19.6	18.4	20.7	20.4
0φ	8.9	17.3	6.9	8.9	12.5	13.3	11.9	10.6	9.5	10.8
1φ	7.5	9.1	4.5	7.0	9.3	10.4	8.3	8.5	5.1	6.4
>1φ	8.1	5.6	4.4	6.4	6.7	10.0	3.4	3.6	2.4	4.2
φ$_{50}$	3.0	1.7	3.3	2.6	2.2	1.8	2.4	2.5	2.6	2.4

Figure 3.5: Isopleth map of the median pumice diameter from the upper 0.25 m of the Bend Pumice member of the Tumalo Tuff. Sites A, B, F, and J from Hill (1985). Precision of these data is about ± 0.2φ, based on duplicate analyses from adjacent sites. Note the overall west-to-east decrease in median diameter, which suggests a source near Triangle Hill.

of this relatively large basaltic clast in the BP at this location clearly indicates proximity to the source vent.

Westward increases in average grain size, unit thickness (Hill, 1985), and size of volcanic rock fragments all indicate the BP was erupted from west of Bend, and most likely from the TVC area. In addition, the composition of the BP is nearly identical to the composition of TVC rhyolite domes (table 3.2). This rhyolite composition only occurs in the central High Cascades of Oregon at the TVC. The source of the BP (and cogenetic Tumalo and Lava Island Tuffs) was most likely the large silicic vent complex buried beneath Triangle Hill.

The Tumalo Tuff is a pink-to-tan rhyodacitic vitric ignimbrite that directly overlies the Bend Pumice. The absence of a normally graded top to the Bend Pumice, and the non-erosive basal contact of the Tumalo Tuff with the BP, indicates that the Tumalo Tuff was produced through collapse of a plinean eruption column (Hill, 1985). In addition, the compositions of the Bend Pumice and Tumalo Tuff are identical (Hill, 1985). It is thus misleading to refer to the Bend Pumice and Tumalo Tuff as separate units in the stratigraphy of the Bend, Oregon area. Eruption of the Tumalo Tuff was preceded by the deposition of a lapilli-fall tuff, which is herein referred to as the Bend Pumice member of the Tumalo Tuff.

The basal ≈ 1 m of the Tumalo Tuff consists of a coarse pumice-depleted zone (layer 2a) and occasional surge (layer 1p) deposits. The main nonsorted part of the Tumalo Tuff (layer 2b) is as thick as 22 meters, and was deposited as a single flow unit. Welding ranges from nonwelded to slightly welded (small amounts of pumice collapse). With the exception of the basal 1 meter and the interior of large pumice bombs, the Tumalo Tuff has undergone low-grade vapor phase alteration (Hill, 1985).

Imbrication of pumice clasts in the Tumalo Tuff indicates a northeast direction of flow (Mimura, 1984), which has been used to contend that the Tumalo Tuff was erupted from vents located 30-45 km southwest of Bend (Mimura, 1984). However, flow directions do not always indicate the direction to the source vent, because most ignimbrites are channeled by the pre-existing topography of the area (e.g., Suzuki and Ui, 1983). The direct association of the Tumalo Tuff with the Bend Pumice indicates that the Tumalo Tuff was erupted from the TVC, but was channeled by northeast-trending drainages as it flowed off of the TVC highland (Hill, 1985). The Tumalo Tuff represents the eruption of a minimum of 10 km^3 of nonzoned rhyodacitic magma (Hill, 1985).

The Tumalo Tuff has a distinct mineral assemblage: Plagioclase (An_{20}) > ferrohypersthene ($Wo_3En_{30}Fs_{57}$) $\geq$ pargasitic hornblende $\geq$ magnetite $\geq$ ilmenite $\geq$ apatite $\geq$ augite $\geq$ zircon (Appendix B). It is noteworthy that the Tumalo Tuff contains the most iron-rich orthopyroxenes that have been observed in the central High Cascades of Oregon. Banded pumice clasts, which

represent the mingling of rhyodacitic and unrelated dacitic magmas (Hill, 1985), are also found in proximal (western) exposures of the Tumalo Tuff ignimbrite.

The Tumalo Tuff eruption has been correlated on the basis of composition and paleomagnetic direction (Gardner et al., 1992) with the Loleta Ash, which has an estimated age of slightly less than 0.40 Ma (Sarna-Wojcicki et al., 1987). K-Ar age determinations for 4 plagioclase separates from the Tumalo Tuff yielded an average date of 0.29 ± 0.12 Ma (Sarna-Wojcicki et al., 1987). Fragments of rhyolite obsidian from the basal zone of the Bend Pumice have K-Ar dates of 0.39 ± 0.01 Ma and 0.41 ± 0.02 Ma (Sarna-Wojcicki et al., 1989), further indicating that the Tumalo Tuff is younger than 0.4 Ma. The age of the Tumalo Tuff is proabably 0.35-0.38 Ma, based on the stratigraphic position of the Loleta ash (Sarna-Wojcicki et al., 1987), age of similar composition rhyolite obsidian clasts in the basal BP (Sarna-Wojcicki et al., 1989), and age of overlying deposits (this study). A ≈0.35 Ma age for the Tumalo Tuff is at least 0.5 m.y. younger than previously reported ages (Armstrong et al., 1975).

3.3.1c Lava Island Tuff

The Lava Island Tuff is a purple-to-grey, intensely devitrified ignimbrite that in places overlies the Tumalo Tuff. The basal contact of the Lava Island Tuff with the Tumalo Tuff is sharp and erosive, with no intervening deposits. In contrast, the basal contact of the Tumalo Tuff with the unconsolidated Bend Pumice is non-erosive. The Lava Island Tuff has relative abundances of pumice, rock fragments and ash that appear similar to welded sections of the Tumalo Tuff. However, the Lava Island Tuff lacks a basal coarse-depleted 2a layer, which is present in the Tumalo Tuff. The intense devitrification and turbulent emplacement of the Lava Island Tuff indicates that this ignimbrite was emplaced with a higher gas content than the Tumalo Tuff. The Lava Island Tuff has a mineralogy that is similar to the Tumalo Tuff, except that the ferrohypersthene is rimmed with iron-rich augite ($Wo_{40}En_{20}Fs_{40}$) and both pyroxenes contain abundant apatite inclusions. The Lava Island Tuff probably represents a flow lobe of the Tumalo Tuff, which was derived from a deeper, less degassed part of the magma chamber during the waning stages of the Tumalo Tuff eruption (Taylor, 1981; Hill and Taylor, 1989).

3.3.1d Pumice of Columbia Canyon

This informally named (Hill and Taylor, 1989) dacitic, vitric lapilli-fall tuff occurs underneath the Shevlin Park Tuff in a steep canyon along the Columbia Canal (T17S R11E S17), and overlies several mafic flows north of the TVC. It has an average grain size (about 1 cm) that is similar to the Bend Pumice at the Columbia Canyon outcrop, and contains abundant angular fragments of black obsidian up to 4 cm in diameter, both of which suggest that this unit was erupted from a nearby TVC vent. The pumice contains phenocrysts of plagioclase (An_{40}) > augite

$(Wo_{40}En_{43}Fs_{35}) \approx$ hypersthene $(Wo_3En_{63}Fs_{34}) >$ amphibole $\geq$ magnetite $\geq$ ilmenite $>$ apatite (Appendix B). The moderately hydrated pumice of Columbia Canyon (sample 3S079) cannot be directly correlated with any other High Cascade dacite (table 3.2). Glass shards from the pumice of Columbia Canyon have a major element composition that is very similar to Summer Lake ash bed NN (Davis, 1985), which suggests that these two units are related (Sarna Wojcicki et al., 1989).

3.3.1e Century Drive Tuff

The Century Drive Tuff (Taylor, 1981) is a variably welded vitric ignimbrite that contains both rhyodacitic(?) and andesitic pumice. Andesitic pumice (table 3.2) contains phenocrysts of plagioclase $(An_{35}) >$ augite $(Wo_{41}En_{42}Fs_{17}) >$ olivine $(Fo_{71}) >$ hypersthene $(Wo_2En_{67}Fs_{31}) \geq$ magnetite $\geq$ ilmenite (Appendix B). Although the Century Drive Tuff is restricted to scattered outcrops in the area south and west of Bend (figure 3.4), it appears to be more densely welded in exposures closer to the TVC, suggesting eruption from a TVC vent. Outcrops of Century Drive Tuff also occur at elevations of 5600-5400' $\approx$25 km south of Triangle Hill, which further supports eruption from a TVC vent (figure 3.4). Eruption of the Century Drive Tuff probably involved $\leq$0.5 km^3 (DRE) of andesitic magma.

3.3.1f Shevlin Park Tuff

The Shevlin Park Tuff (Taylor, 1981) is an andesitic (table 3.2) ignimbrite that is distributed around a 180° sector east of and centered on Triangle Hill (Taylor, 1987; Hill and Taylor, 1989; Figure 3.4). The Shevlin Park Tuff forms a single cooling unit, and may contain two flow lobes and occasional base-surge deposits in more proximal exposures. The Shevlin Park Tuff contains plagioclase $(An_{36}) >$ augite $(Wo_{42}En_{43}Fs_{15}) \geq$ hypersthene $(Wo_3En_{65}Fs_{32}) >$ olivine $(Fo_{71}) >$ titanomagnetite (Appendix B). The distribution of the Shevlin Park Tuff, along with observed increases in degree of welding and average pumice size, clearly indicates this unit was erupted from the TVC. Imbrication of pumice lapilli in the Shevlin Park Tuff also indicates a radial direction of flow away from the Triangle Hill area (Mimura, 1984). Eruption of the Shevlin Park Tuff probably involved $\geq$1 km^3 (DRE) of andesitic magma.

A noteworthy Shevlin Park Tuff outcrop occurs in the upper reaches of the North Fork of Squaw Creek (T16S R9E S29-30). At this location the Shevlin Park Tuff is overlain by a normal polarity basaltic andesite flow, which is in turn overlain by the oldest basaltic andesites clearly associated with North Sister (Taylor, 1987). Because North Sister is the oldest stratovolcano of the Three Sisters, this exposure clearly demonstrates that pyroclastic volcanism associated with the TVC predated construction of the Three Sisters.

3.4 Todd Lake Volcano

Some of the oldest Quaternary-age rocks in the Broken Top system are associated with the Todd Lake volcano (Williams, 1944; Taylor, 1978; Figure 3SLOC). Todd Lake volcano (TLV) is a highly eroded composite volcano, which consists primarily of dacitic flows and intrusions; rhyodacite and basaltic andesite lavas were also erupted from the TLV (Taylor, 1978). A dacite flow from the middle section of TLV has a K-Ar date of 460 ± 30 ka (table 3.1), and all rocks associated with the TLV have normal paleomagnetic directions. TLV is overlain by mafic flows associated with Broken Top-Tam MacArthur Rim volcanism, and its stratigraphic relationship to the Tumalo volcanic center is not known.

3.5 Tam MacArthur Rim and Broken Top

Tam MacArthur Rim (TMR) represents a distinct volcanic center in the Broken Top system. Numerous basaltic andesite to rhyodacite dikes and vent breccias exposed by glaciation at TMR clearly demonstrate that this area was a locus of volcanic activity, even though these eruptions did not result in the construction of a stratovolcano (Taylor, 1978). Although stratigraphic relationships between TMR and the TVC are obscured by Pleistocene glacial deposits, it is likely that some mafic lavas from TMR partially cover the older TVC highland (Taylor, 1978).

A K-Ar date of 213 ± 9 ka was obtained on a glassy rhyodacite flow located at the top of the TMR section (table 3.1). This rhyodacite is also interbedded with a series of basaltic andesite flows that comprise the base of Broken Top volcano (Taylor, 1978). Although Broken Top volcano has been highly dissected by Pleistocene glaciation, this relatively large degree of erosion has developed in less than 200 k.y. In addition, a deposit of unconsolidated pumice lapilli from a small rhyodacite dome eruption on the northwest flank of Broken Top is preserved at an elevation of 7800'. A similar relationship is observed near North Sister, where lapilli from the ≈100 ka eruption of Obsidian Cliffs are preserved on the western flank of Little Brother at an elevation of 7400' (E.M. Taylor, pers. comm., 1986). This relationship suggests that Broken Top rhyodacitic volcanism may have continued until after early Wisconsin glaciation at ≈110 ka (Jouzel et al., 1987), assuming that early Wisconson glaciation covered these high-standing ridges.

3.6 The Three Sisters

North Sister is the oldest of the Three Sisters stratovolcanos (Taylor, 1981), and stratigraphically overlies the Shevlin Park Tuff (Taylor, 1987). North Sister is primarily constructed of basaltic andesite, although several small dikes of andesite are exposed on the northeast flank of the stratovolcano (E.M. Taylor, pers. comm., 1988). Uppermost North Sister lavas can be traced into

the lower parts of the Middle Sister stratigraphic section. Mafic volcanism at North Sister has not been studied in detail, although reconnaissance work by Hughes (1983) indicates that North Sister is a representative part of the Oregon High Cascades mafic magma system.

The lower parts of Middle Sister are primarily composed of mafic lavas, and andesitic to dacitic lavas are restricted to the upper parts of the Middle Sister section (Taylor, 1981; Taylor et al., 1987). Near the saddle between Middle and South Sister, a porphyritic basalt lava relatively high in the Middle Sister section (3S159) overlies dacite lava from the basal section of South Sister. A K-Ar date of 0.4 ± 0.2 Ma on this basalt has low precision and accuracy due to large amounts of atmospheric Ar (table 3.1). In addition, the youngest dacite from Middle Sister bifurcated around an early South Sister rhyolite dome in the saddle between Middle and South Sister. These stratigraphic relationships indicate that late Middle Sister and early South Sister volcanism was contemporaneous.

South Sister is the youngest of the Three Sisters stratovolcanos, and has erupted ≥ 1 km^3 of rhyolite as recently as ≈ 2 ka (Scott, 1987; Taylor, 1978). Geothermal drilling on the southern flanks of South Sister at Devils Lake encountered 0.15 ± 0.05 Ma basalt at 1819', near the base of the hole (Priest et al., 1989). Stratigraphic relations in the drill core indicate that this basalt is overlain by Devils Hill rhyolites, which are in turn overlain by South Sister andesites. In addition, a K-Ar date of 93 ± 11 ka was measured on an andesite flow near the base of the South Sister section. These data indicate that the bulk of South Sister is <100 ka.

3.7 Strontium Isotopes

There are few published strontium isotopic analyses for rocks from the Three Sisters area (table 3.3). A previously unreported ^{87}Sr/^{86}Sr analysis on the Tumalo Tuff (0.70375 ± 5) was provided by J. Dasch for this study (table 3.3). In addition, six ^{87}Sr/^{86}Sr analyses obtained by UNOCAL Geothermal as part of a regional geochemical study were released for this study (table SR76). These limited data suggest that mafic rocks in the Three Sisters area may have slightly higher ^{87}Sr/^{86}Sr (≈ 0.7035) than most Quaternary mafic rocks at Mt Jefferson (0.7028-0.7036; Conrey, 1991). Rhyolites from the Three Sisters and Broken Top systems have identical ^{87}Sr/^{86}Sr (≈ 0.7037). Petrogenetic models in chapter 9 show that these rhyolites were produced through partial crustal melts, indicating that the crust beneath this part of the Oregon Cascades is isotopically primitive. Rhyodacites at Mt. Jefferson, which were also inferred to have been produced through partial crustal melting (Conrey, 1991), have lower ^{87}Sr/^{86}Sr (≈ 0.7033). This relationship may indicate that Mt. Jefferson is located over relatively younger mafic crust than found under the Three Sisters area (Chapter 2).

Three Sisters area

Published $^{87}Sr/^{86}Sr$ analyses:

Location	%SiO$_2$	ppm Sr	$^{87}Sr/^{86}Sr \pm 1\sigma$	Source
Three Sisters	58%	355	0.7036 ± 6	Church & Tilton, 1970
Three Sisters	54%	330	0.704 ± 1	Church & Tilton, 1970
South Sister	<53->64	n/a	0.7034-0.7039	Leeman, 1982

New $^{87}Sr/^{86}Sr$ analyses:

Location	Sample#	%SiO$_2$	ppm Sr	ppm Rb	$^{87}Sr/^{86}Sr \pm 1\sigma$	Source
Tumalo Tuff	3245	74	68.3	79.2	0.70375 ± 5	Dasch, 1984
Three Ck. Bu.	[1]3S032	74	52	86	0.70368 ± 2	UNOCAL, 1989
Obsidian Cliffs	[1]3S139	76	119	79	0.70363 ± 3	UNOCAL, 1989
Sister Sp.	[1]3S136	64	392	28	0.70370 ± 3	UNOCAL, 1989
Yapoah lava	[2]TFJ-437	56	650	21	0.70346 ± 1	UNOCAL, 1989
E. N. Sister	[2]TS-692	53	530	4	0.70351 ± 2	UNOCAL, 1989
Older Belknap	C-1	53	n/a	n/a	0.70345 ± 2	UNOCAL, 1989

- Dasch: Analysis at Johnson Space Center, 1984.

- UNOCAL: Analyses at U.C.S.B. by J. Mattinson, 1985. Relative to NBS 987 Sr standard: 0.710254.

1: Sample numbers correspond to equivalent samples from this study.
2: Sample numbers correspond to equivalent samples Hughes, 1983.

Table 3.3: Compilation of published and new $^{87}Sr/^{86}Sr$ isotopic analyses for rocks from the Three Sisters area. Tumalo Tuff sample from Hill (1985), analysis courtesy of J. Dasch, written comm., 1984. UNOCAL samples are previously unreported data from UNOCAL Geothermal, Santa Rosa, California, and published with permission of UNOCAL (D. Carrier, written comm., 1989). Samples are correlated with equivalent whole-rock analyses, as other geochemical data are not available. These data indicate that mafic samples contain less radiogenic Sr than silicic samples, but still have enriched $^{87}Sr/^{86}Sr$ relative to most samples from Mt. Jefferson (Conrey, 1991), and some samples from the flanks of Newberry volcano (Goles and Lambert, 1990). Rhyolite analyses have identical $^{87}Sr/^{86}Sr$ at 1σ, which indicates that these units did not sample isotopically distinct or highly evolved crustal compositions.

4. MINERALOGY

Rocks from the study area display a wide variety of textures and mineral abundances, which systematically with rock composition. Phenocryst abundances range from trace amounts in some rhyolites to greater than 35% in some andesites and dacites (figure 4.1), and all rock compositions have samples that vary from nearly aphyric (< 1%) to moderately phyric (> 20%). The phenocryst assemblage is dominated by plagioclase for all rock compositions, with subordinate amounts of clinopyroxene, orthopyroxene, olivine, Fe-Ti oxides, and amphibole in relative proportions that are compositionally controlled. The mineralogy of Three Sisters and Broken Top systems can be characterized, however, as an anhydrous, plagioclase - two pyroxene assemblage; hydrous phenocrysts are restricted to trace amounts of amphibole in some rhyodacites and rhyolites. Disequilibrium crystallization features, such as complex plagioclase zoning, abundant glass inclusions in plagioclase phenocrysts, reaction rims around mafic phases, and multiple phenocryst populations within single units, are also common in rocks from the study area. These textural features are important characteristics of both the Three Sisters and Broken Top volcanic systems, and are evidence of the dynamic, open-system differentiation that produced these rocks.

Thin sections from 115 samples were studied in detail, and the petrographic data are summarized in appendix B. Of these samples, 21 were selected for detailed microprobe analysis. Most of these samples represented typical compositions from the study area, based on geochemical abundances and petrographic characteristics, while other samples had unusual petrographic features (i.e. complex zoning, multiple phenocryst populations) that warranted additional study. In addition, the compositions of minerals separated from 5 pyroclastic units in the Bend area were determined with the microprobe.

4.1 Feldspar

Phenocrysts and microlites of plagioclase are ubiquitous in the studied units, and range in abundance from 25% in some dacites and basaltic andesites to trace amounts in nearly aphyric rhyolites (Appendix B). Plagioclase usually occurs as 1-2 mm-long euhedral to subhedral crystals, but ranges in length up to 4 mm. Anorthoclase has been recognized through microprobe analysis as a rare groundmass phase in a Tam MacArthur Rim dacite (3S036), and as a 10 μm rim on several andesine phenocrysts in a South Sister dacite (3S123) (table 4.1).

Variations in plagioclase composition determined through microprobe analysis are plotted in figures 4.2a-c for each rock type. Rhyolites from the Three Sisters system (figure 4.2a) contain plagioclase that is consistently more calcic (An_{50-25}) than found in Broken Top rhyolites (An_{25-15}). This compositional difference is probably controlled by bulk composition and not by temperature, as the Three Sisters rhyolites are consistently more calcic than Broken Top rhyolites: molar
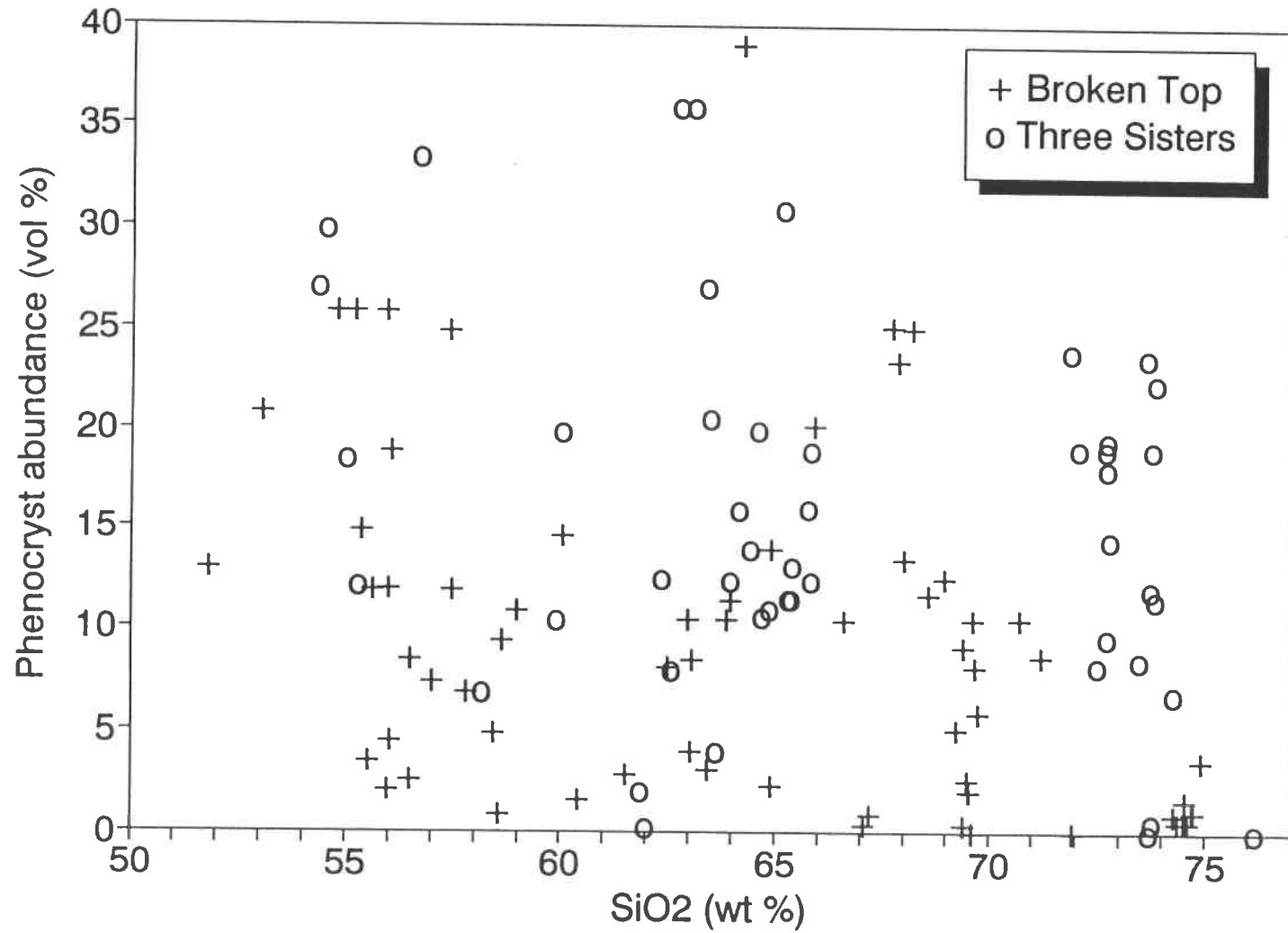
Figure 4.1: Visual estimates of phenocryst modal abundance versus silica content of the host rock. Note that Three Sisters rhyolites are more phyric than Broken Top rhyolites.

Sample	SiO2	Al2O3	FeO	MgO	CaO	Na2O	K2O	BaO	Total	Ab	Or	An
3S003 rim (2)	57.75	25.99	0.43	0.02	7.83	6.96	0.28	0.07	99.33	60.60	1.62	37.79
3S005 rim (2)	56.02	25.78	0.34	0.01	8.26	6.71	0.39	0.04	97.53	58.21	2.22	39.58
3S009 rim (2)	60.11	24.01	0.24	0.02	5.57	7.71	0.69	0.08	98.41	68.63	4.00	27.38
3S017 GM (3)	53.09	28.39	1.01	0.09	11.42	4.63	0.18	0.01	98.82	41.88	1.06	57.06
3S028b rim	57.39	25.65	0.34	0.06	7.37	7.49	0.30	0.05	98.65	63.67	1.69	34.64
3S030 GM & R (4)	54.57	27.86	1.00	0.02	10.62	5.01	0.31	0.02	99.40	45.21	1.82	52.97
3S030 #3 rim	59.95	24.35	0.74	0.00	6.30	7.16	0.70	0.06	99.26	64.49	4.15	31.36
3S036 HiK GM (2)	64.90	21.14	0.58	0.02	4.04	6.66	2.01	0.06	99.41	65.23	12.91	21.85
3S036 GM (2)	58.76	25.29	0.78	0.00	7.26	6.60	0.67	0.06	99.42	59.69	3.99	36.33
3S042 GM (4)	64.68	21.15	0.33	0.00	2.26	8.83	1.23	0.25	98.73	81.07	7.43	11.49
3S045 GM & R (5)	55.62	27.25	1.14	0.04	9.60	5.57	0.36	0.01	99.60	50.13	2.14	47.73
3S049 GM & R (3)	52.78	29.09	0.92	0.07	12.04	4.45	0.33	0.02	99.70	39.33	1.91	58.76
3S058 GM & R (3)	59.40	25.23	0.24	0.00	6.64	7.19	0.44	0.06	99.19	64.49	2.57	32.94
3s061 GM & R (2)	55.97	27.01	0.57	0.01	9.38	5.73	0.39	0.03	99.09	51.32	2.29	46.40
3S069 GM (2)	50.73	30.36	1.02	0.01	13.55	3.70	0.21	0.00	99.57	32.68	1.22	66.10
3S074 GM & R (3)	53.46	28.11	1.18	0.06	11.30	4.45	0.43	0.01	99.01	40.53	2.59	56.88
3S079 rim (3)	58.70	25.46	0.42	0.02	7.72	7.04	0.25	0.04	99.63	61.38	1.41	37.22
3S090 GM (5)	53.66	28.71	0.82	0.05	11.24	4.82	0.21	0.01	99.53	43.15	1.24	55.62
3S098 GM & R (4)	62.10	23.72	0.36	0.01	4.82	8.18	0.53	0.09	99.80	73.09	3.12	23.78
3S112 GM & R (3)	57.13	26.47	0.87	0.01	8.56	6.09	0.45	0.04	99.62	54.78	2.68	42.54
3S114 GM & R (3)	57.27	26.50	0.29	0.02	8.43	6.40	0.34	0.03	99.27	56.73	1.97	41.30
3S115 GM low An	59.69	25.09	0.88	0.03	6.48	7.15	0.53	0.06	99.91	64.54	3.13	32.33
3S115 GM high An	55.15	28.45	0.69	0.03	10.40	5.11	0.22	0.01	100.06	46.45	1.33	52.22
3S122 GM & R (5)	60.72	24.70	0.27	0.01	6.36	7.10	0.58	0.08	99.82	64.53	3.50	31.97
3S123 GM	59.20	24.94	0.76	0.01	6.79	7.17	0.68	0.08	99.62	63.04	3.95	33.01
3S123z rim (2)	62.60	22.01	0.69	0.01	4.07	7.16	2.16	0.04	98.73	66.13	13.02	20.85
3S131 GM & #3 rim	61.45	23.12	0.50	0.01	4.68	7.97	0.79	0.09	98.59	71.95	4.65	23.40
3S131 GM & R (4)	54.51	27.33	0.96	0.07	10.13	5.37	0.26	0.03	98.66	48.18	1.56	50.26
3S134 GM (2)	60.08	24.34	0.57	0.00	5.78	7.57	0.51	0.08	98.93	68.22	3.01	28.78
3S137 GM (3)	58.66	25.62	0.51	0.01	7.23	6.99	0.39	0.06	99.47	62.20	2.26	35.54
3SXBP rim (3)	62.47	22.33	0.24	0.02	4.05	8.49	0.76	0.10	98.46	75.60	4.48	19.92
LI rim (2)	63.52	23.08	0.19	0.00	4.32	8.48	0.57	0.10	100.27	75.39	3.33	21.28

Table 4.1: Average compositions of groundmass feldspars (GM) and plagioclase rim compositions (R), determined through microprobe analysis. Number of samples averaged shown in parenthesis. All averages have standard deviations ≤ 7%.
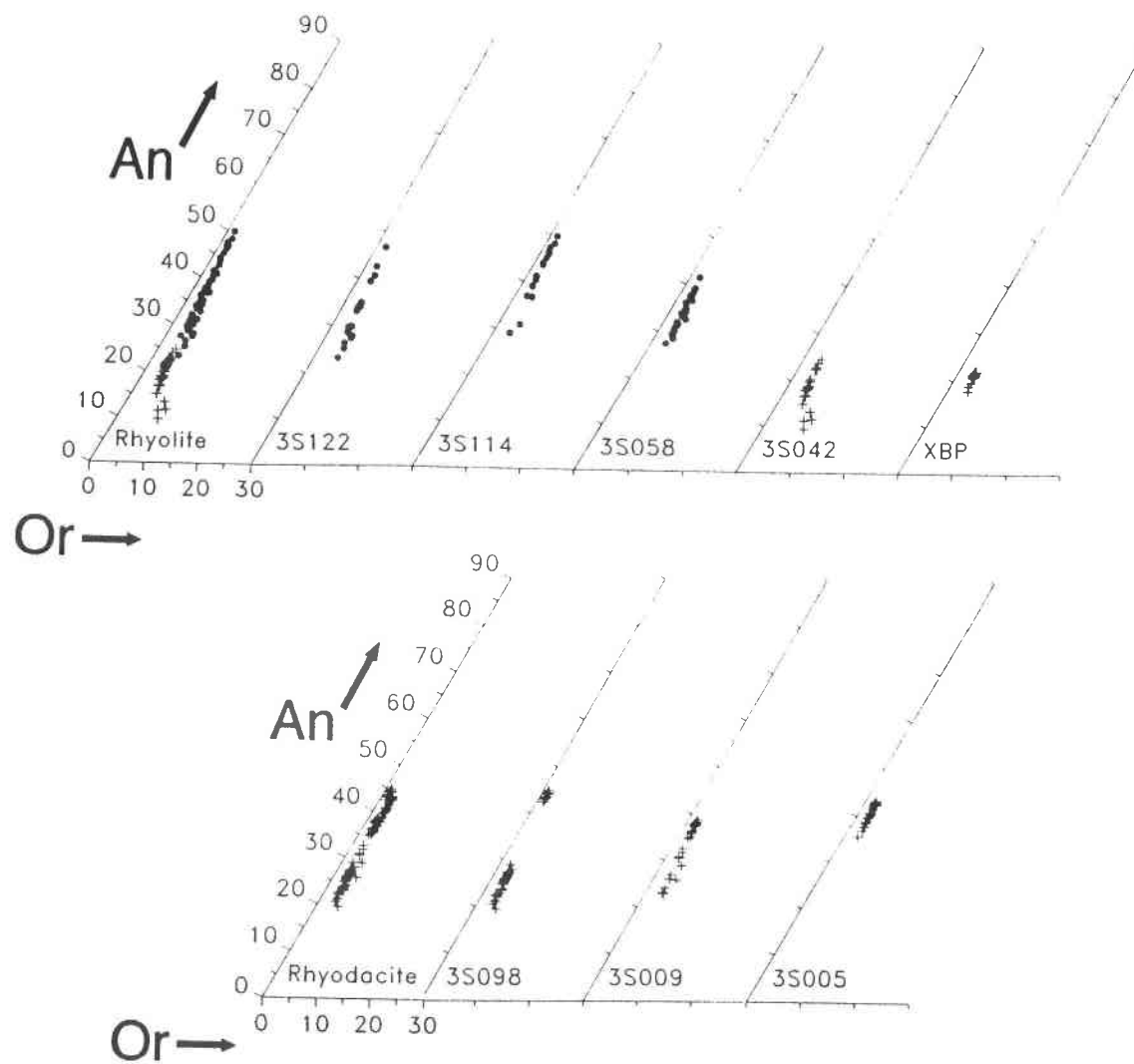
Figure 4.2a: Compositional range of plagioclase phenocrysts and microlites for individual rhyolite and rhyodacite samples, plotted on part of the Ab-An-Or feldspar ternary. + Broken Top system, o Three Sisters system. **Rhyolite** and **Rhyodacite** are combined plots of all samples.

36
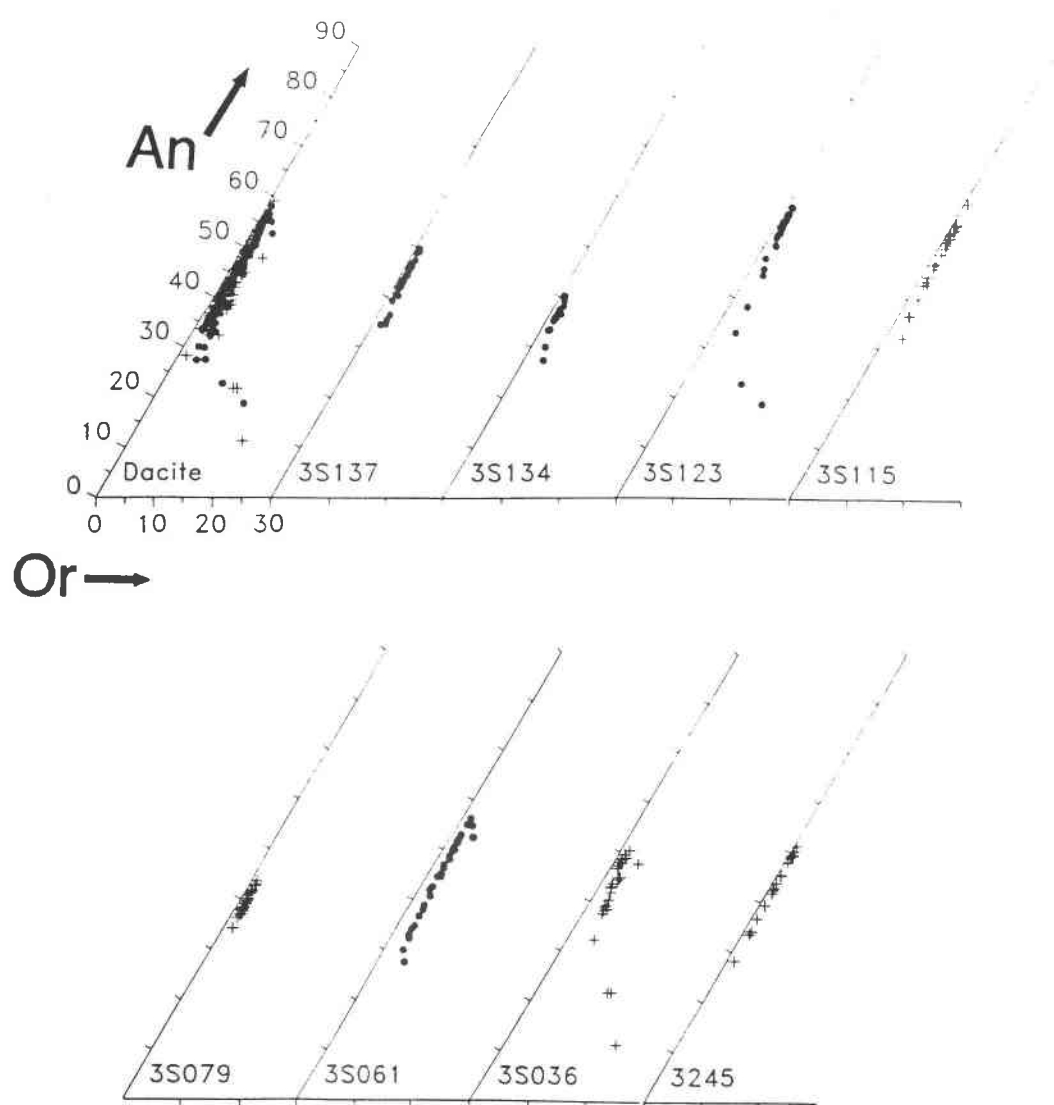
Figure 4.2b: Compositional range of plagioclase phenocrysts and microlites for individual dacite samples, plotted on part of the Ab-An-Or feldspar ternary. Dacite is a plot of all dacitic samples, symbols the same as in figure 4.2a.
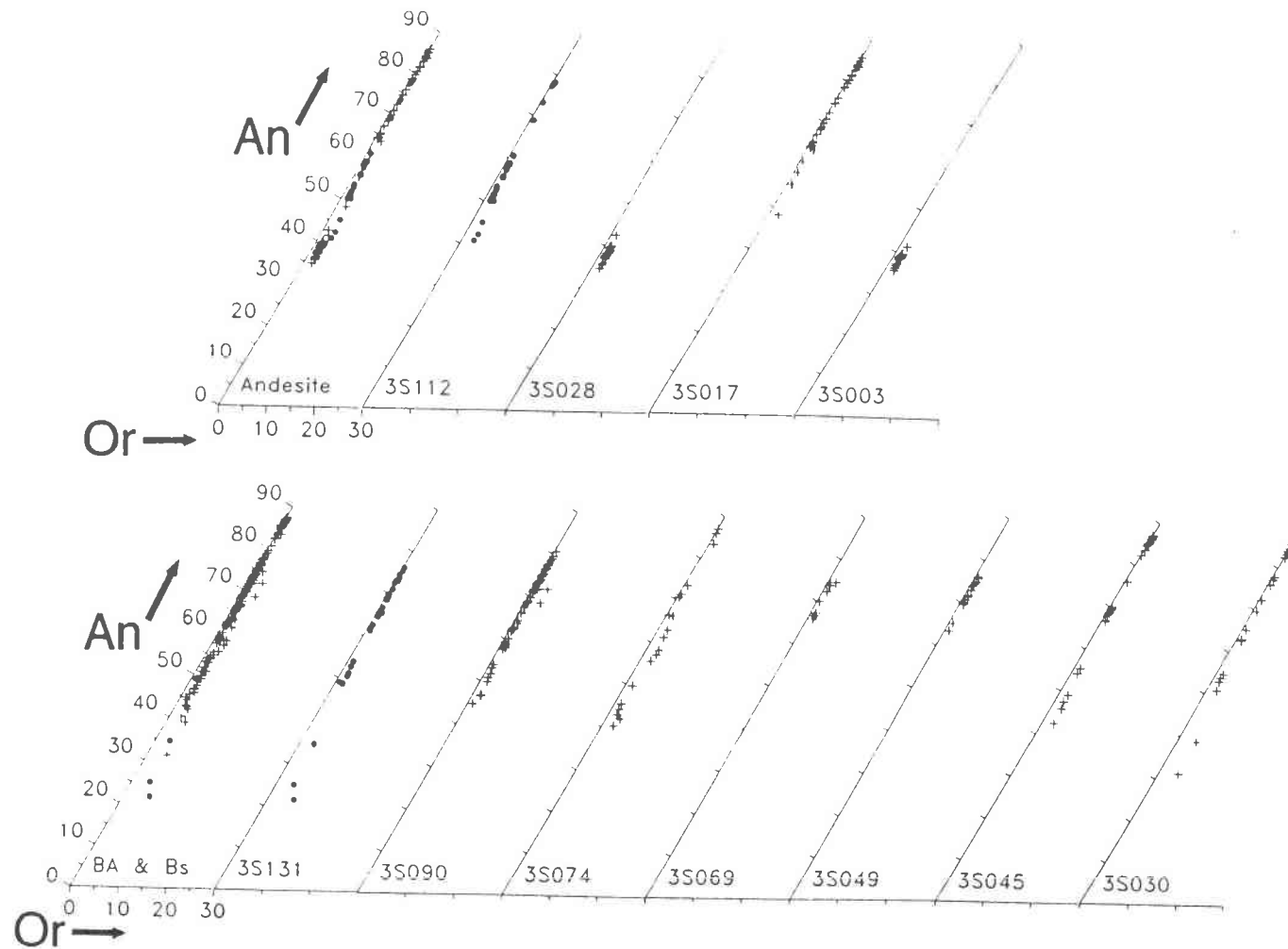
Figure 4.2c: Compositional range of plagioclase phenocrysts and microlites for individual andesite, basaltic andesite, and basalt samples, plotted on part of the Ab-An-Or feldspar ternary. Symbols as in figure 4.2a. **Andesite** and **BA & Bs** are combined plots of all samples.

CaO/Na_2O = 0.52 vs. 0.25 at 72% SiO_2, and 0.24 vs. 0.15 at 76% SiO_2, respectively. The largest range in plagioclase composition tends to occur in basaltic andesites, although each rock type contains samples with small (≤ 10 An) and samples with large (10-50 An) compositional variations. Plagioclase phenocrysts with the largest compositional range generally contain an anomalously calcic core, strongly zoned sodic rims, and tend to be the larger crystals in a seriate distribution.

Average phenocryst rim and groundmass plagioclase compositions (table 4.1), which should represent compositions that are relatively close to equilibrium with the magma at the time of eruption, are compared with rock SiO_2 in figure 4.3a. The expected trend (cf. Gill, 1982; Ewart, 1982) of more albitic plagioclase with increasing rock SiO_2 is present, along with variations of ± 10 An for similar composition rocks. As expected, most mafic units have groundmass plagioclase more calcic than An_{50}. The groundmass plagioclase in basaltic andesites 3S030 and 3S131, however, is unusually albitic; both of these units have a coarsely crystalline, sub-ophitic groundmass, which indicates that these units cooled slowly at the surface and that the groundmass plagioclase probably crystallized at a temperature that was significantly lower than in the pre-eruptive magma.

Most of the studied plagioclase phenocrysts display complex oscillatory zoning, which is characteristic of most calc-alkaline systems (Ewart, 1982). Both oscillatory and simply zoned plagioclase tend to be normally zoned, with rim An 10-60% less than core An (figure 4.3a). Reverse zoning is uncommon, but is observed both optically and analytically in several units (figure 4.3b). The most strongly zoned plagioclase phenocrysts also tend to have at least one zoning reversal (i.e. normal→reverse→normal) and complex oscillatory zoning. Both simple and oscillatory normal zoning is the expected result of equilibrium fractionation of a slowly cooled magma, and is supported by experimental studies (Lofgren, 1980), numerical simulations (Loomis, 1982), and by its common occurrence in most calc-alkaline volcanic systems (Ewart, 1982; Gill, 1982).

Strong compositional zonation is also a characteristic of plagioclase phenocrysts that contain abundant glass inclusions. While a variety of terms such as "sieved", "dusty", "fritted" or "spongy" have been applied to plagioclase with glass inclusions, two genetically distinct types of plagioclase glass inclusions are generally recognized. The first type, herein referred to as *fritted*, consists of irregularly-shaped sodic cores mantled by a zone of fine (μm-scale) glass inclusions in a more calcic rim (figure 4.4a). Fritted plagioclase has been reported in a variety of igneous rocks (e.g. Larsen et al., 1938; MacDonald & Katsura, 1965; Koyaguchi, 1986; Glazner et al., 1990), and is generally thought to represent dissolution of albitic plagioclase that has been incorporated into a more anorthitic melt with subsequent crystallization of a reversely zoned rim (do.; Sakuyama, 1981; Tsuchiyama & Takahashi, 1983; Donaldson, 1985; Tsuchiyama, 1985). Fritted plagioclase, however, is uncommon and poorly developed in this part of the High Cascades; only 4% of 114 examined rocks have more than 50% of the plagioclase with some evidence of weak fritting, and between 5%
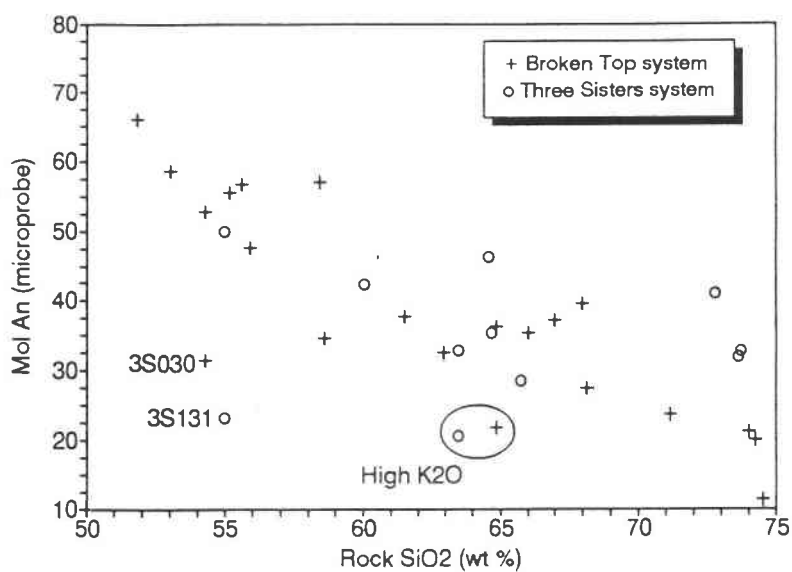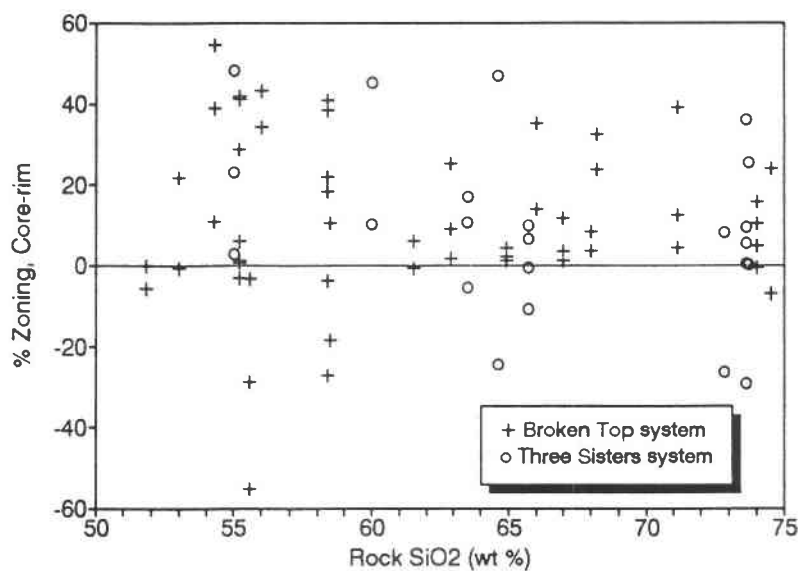
Figure 4.3: **A)** Average composition of groundmass plagioclase and rim of phenocrysts, plotted against silica content of the host rock. Compositions listed in table 4.1. **B)** Percent change in core-to-rim An content of plagioclase phenocrysts, versus silica content of the host rock. Plagioclase compositions determined through microprobe analysis. Negative values indicate reversed zoning.
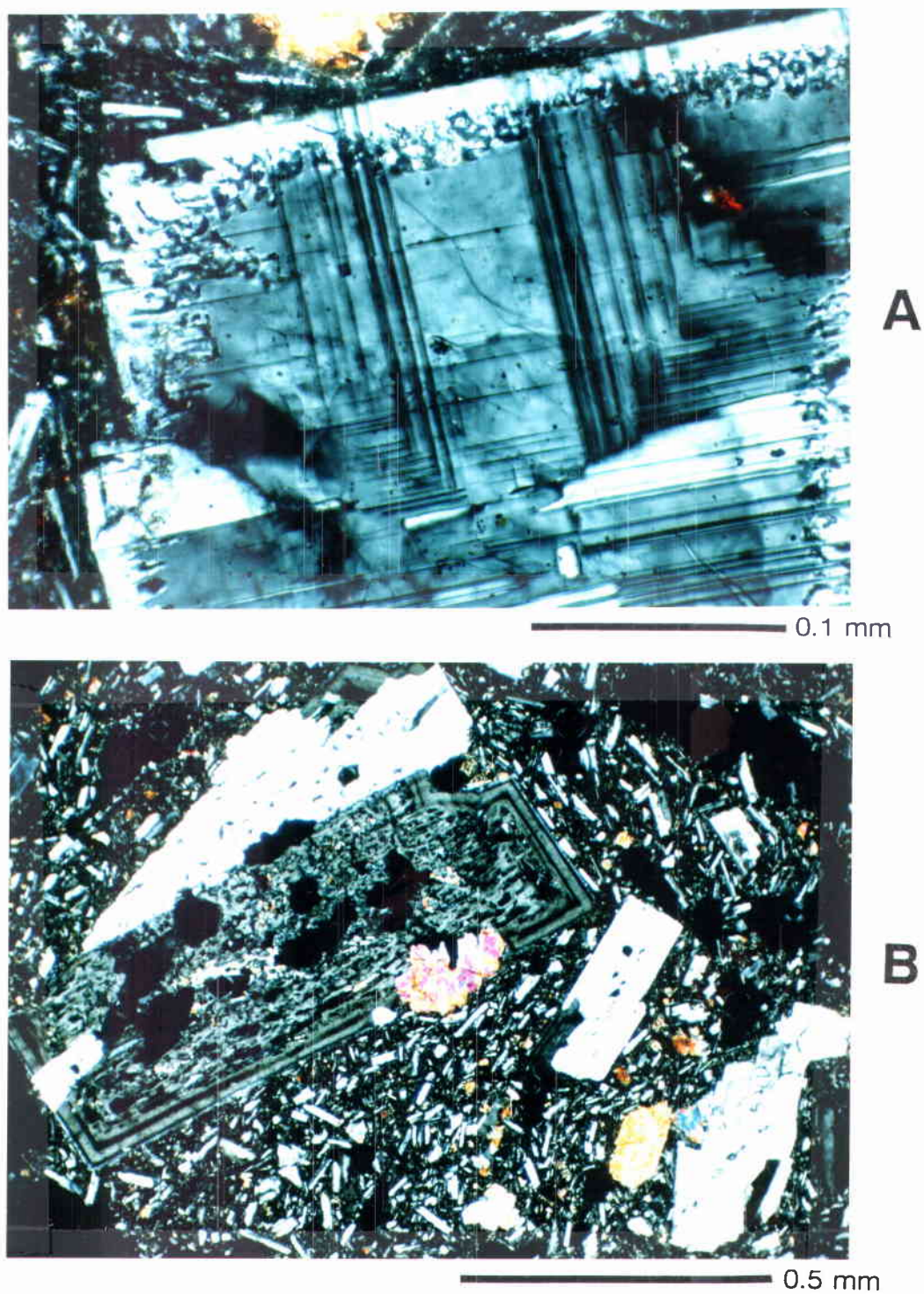
Figure 4.4: **A)** Poorly developed fritted rim (An_{61}) on An_{40} plagioclase phenocryst, basaltic andesite 3S074. This sample is one of few in the study area that contains fritted or resorbed plagioclase. **B)** Typical sieved plagioclase phenocryst, with nonzoned An_{74} core and normally zoned, glass-free rim (An_{73-58}). Sample from basaltic andesite 3S090.

and 50% of the plagioclase displays some evidence of fritting in 18% of these rocks (Appendix B). In addition, half of the samples that are identified as fritted contain highly rounded sodic cores and glass-free, reversely zoned calcic rims. These samples clearly indicate dissolution of albitic plagioclase in an anorthitic melt (Donaldson, 1985), but lack the fine glass inclusions that are characteristic of a fritted texture.

The second type of plagioclase is referred to as *sieved*, which consists of calcic cores that are nonzoned to weak normal zoned and contain abundant, large (generally $\geq 10\mu m$) glass inclusions, mantled by a normally zoned, glass-free, more sodic rim (figure 4.4b). Unlike fritted plagioclase, sieved plagioclase is a common petrographic feature in the studied rocks; between 5% and 50% of the plagioclase phenocrysts are significantly sieved in 64% of these rocks, and $\geq$ 50% of the plagioclase is sieved in 11% of the rocks. Sieved plagioclase has also been reported in a large variety of igneous rocks (do., Luhr & Carmichael, 1980), and is most likely produced through disequilibrium crystallization produced by undercooling of the melt (Lofgren, 1980; Swanson, 1977; Corrigan, 1982; Glazner et al., 1990). Lofgren (1974) observed that a transition from tabular to skeletal (i.e. sieved) plagioclase morphology generally occurred between 40°C and 140°C undercooling, and that larger amounts of undercooling produced acicular, dendritic plagioclase. Isothermal cooling experiments by Lofgren (1973) also produced sieved plagioclase when cooling rates were roughly 2°C/hr, but an increase in cooling rate to 32°C/hr produced acicular, dendritic plagioclase. Growth rates of about 10^{-7} cm/sec for skeletal plagioclase in undercooled tholeiitic melts were determined by Corrigan (1982). While this rate will presumedly decrease with decreasing temperature and increasing viscosity of the melt, it is likely that the 1-2 mm sieved plagioclase commonly observed in the studied rocks crystallized on the order of tens of days.

Magma mixing is the most common mechanism that is thought to produce the large degrees of undercooling necessary for the crystallization of sieved plagioclase (e.g. Larsen et al., 1938; Dungan & Rhodes, 1978; Hibbard, 1981; Ussler and Glazner, 1989). Evidence for some degree of magma mixing occurs in most arc volcanic systems (e.g. Eichelberger, 1975; Gill, 1982), and there is little reason to doubt that magma mixing is capable of producing the degree of cooling necessary to crystalize sieved plagioclase. Because at least 5% of the plagioclase is sieved in 75% of the studied rocks, understanding its petrogenetic connotations is obviously important. Large amounts ($\geq$ 50%) of sieved plagioclase, however, are only observed in some basaltic andesites and in Holocene South Sister rhyolites. Previous studies by Hughes (1983) and Clark (1983) have indicated that basaltic andesites in this part of the High Cascades can be generated through a variety of open-system magmatic processes. This model will also be supported in the following chapter. It is thus not surprising that basaltic andesites in the study area contain abundant sieved plagioclase, which was likely produced through magma mixing.

However, roughly 90% of the plagioclase in Holocene South Sister rhyolites is sieved, but less than 20% of the plagioclase in all other Three Sisters rhyolites is sieved (figure 4.4C-D). This is significant because Holocene South Sister rhyolites have nearly the same composition as other Three Sisters rhyolites, and minor compositional differences between these rhyolites types cannot be attributed to mixing of compositionally distinct magmas (Chapter 9). It is possible that chemically similar but *thermally* distinct rhyolitic magmas were mixed to produce the necessary undercooling for sieved plagioclase crystallization in the Holocene units, as temperature drops of only about 100°C have been shown to produce sieved plagioclase (Lofgren, 1974; Swanson, 1977). Although work by Nelson and Montana (1989) has shown that plagioclase resorption (i.e., fritted) in anhydrous basaltic melts can be induced by drops in pressure of 2-6 kbar, the effects of decompression on plagioclase morphology in hydrous silicic systems have not been studied. However, the relatively lower position of the plagioclase liquidus under hydrous conditions (Kushiro, 1979; Sekine et al., 1979) may result in the formation of sieved plagioclase with isothermal decompression. Sieved plagioclase in the Holocene South Sister rhyolites thus may have recorded the recharge of a Holocene magma chamber by a fresh batch of cooler but compositionally similar rhyolitic magma, or may indicate that an episode of decompression occurred in the Holocene magma chamber.

4.2 Pyroxenes

Pyroxenes are the most abundant ferromagnesian silicate minerals in the central High Cascades, and an anhydrous, two-pyroxene assemblage characterizes the mineralogy in the study area for rocks with 55% to 72% SiO_2. Abundances of pyroxene phenocrysts, which were determined through visual estimation of thin sections, typically range from 1-5% for mafic rocks, 3-10% for intermediate rocks, and 1-3% for silicic rocks. Petrographic data for the occurrence of pyroxenes are summarized in figure 4.5. Clinopyroxene (augite) is the most abundant pyroxene in rocks having 53% to ≈58% SiO_2, with the exception of a Middle Sister basaltic andesite (3S030). Augite is essentially a trace phase by 72% SiO_2, which is where the ferromagnesian assemblage changes to orthopyroxene ± amphibole. Pyroxenes from 27 representative mafic to silicic rocks from the study area were analyzed with the electron microprobe (Appendix C-2), and their compositional range is shown in figure 4.6.

4.2.1 Clinopyroxene

Phenocrysts of clinopyroxene (augite) are commonly coarser-grained (1-2 mm) and more irregularly formed (subhedral to anhedral) than orthopyroxene. Augite compositions are plotted in
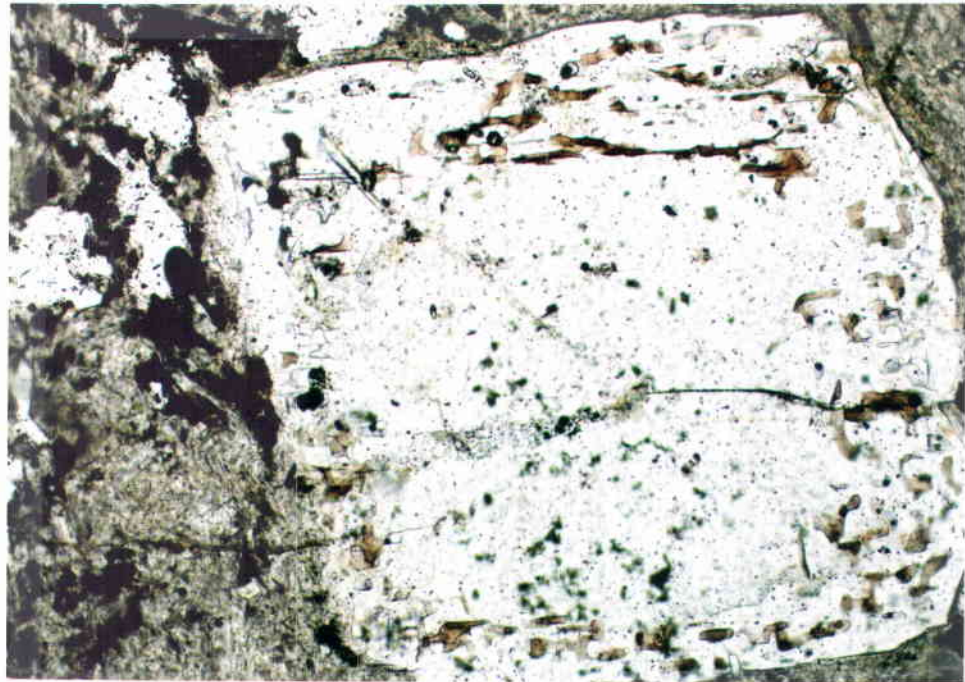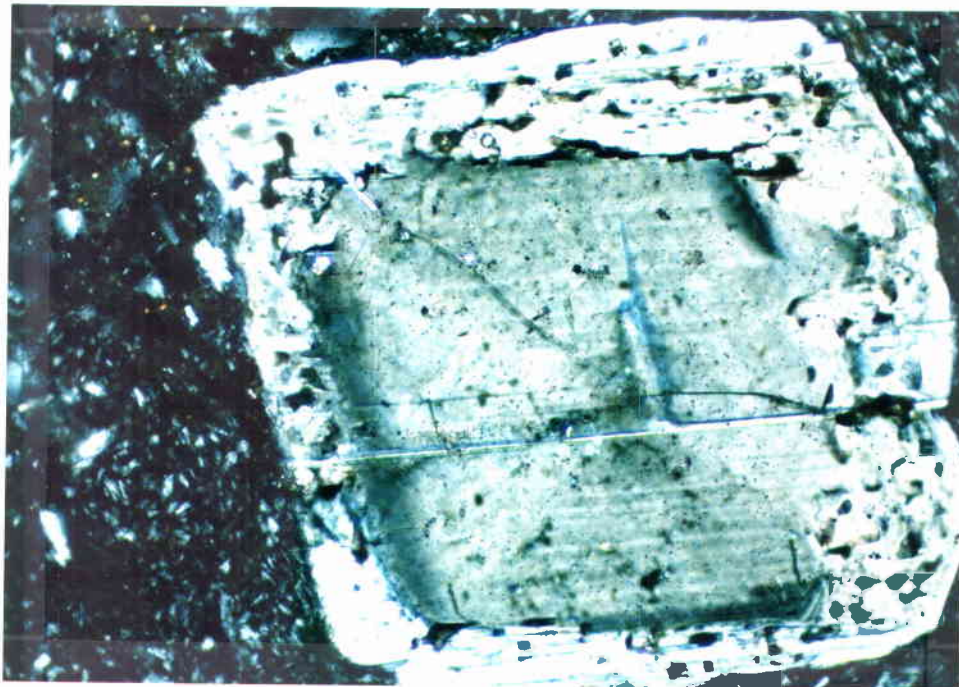
Figure 4.4: C) Non-polarized and D) plane-polarized photomicrographs of Holocene South Sister rhyolite 3S122. Plagioclase phenocrysts in Holocene Three Sisters rhyolites have complex normal oscillatory zoning ($\approx An_{40-30}$) and contain abundant coarse glass inclusions. However, Pleistocene Three Sisters rhyolites typically contain <10% sieved plagioclase but display the same complex normal oscillatory zoning ($\approx An_{40-30}$) as the Holocene rhyolites.
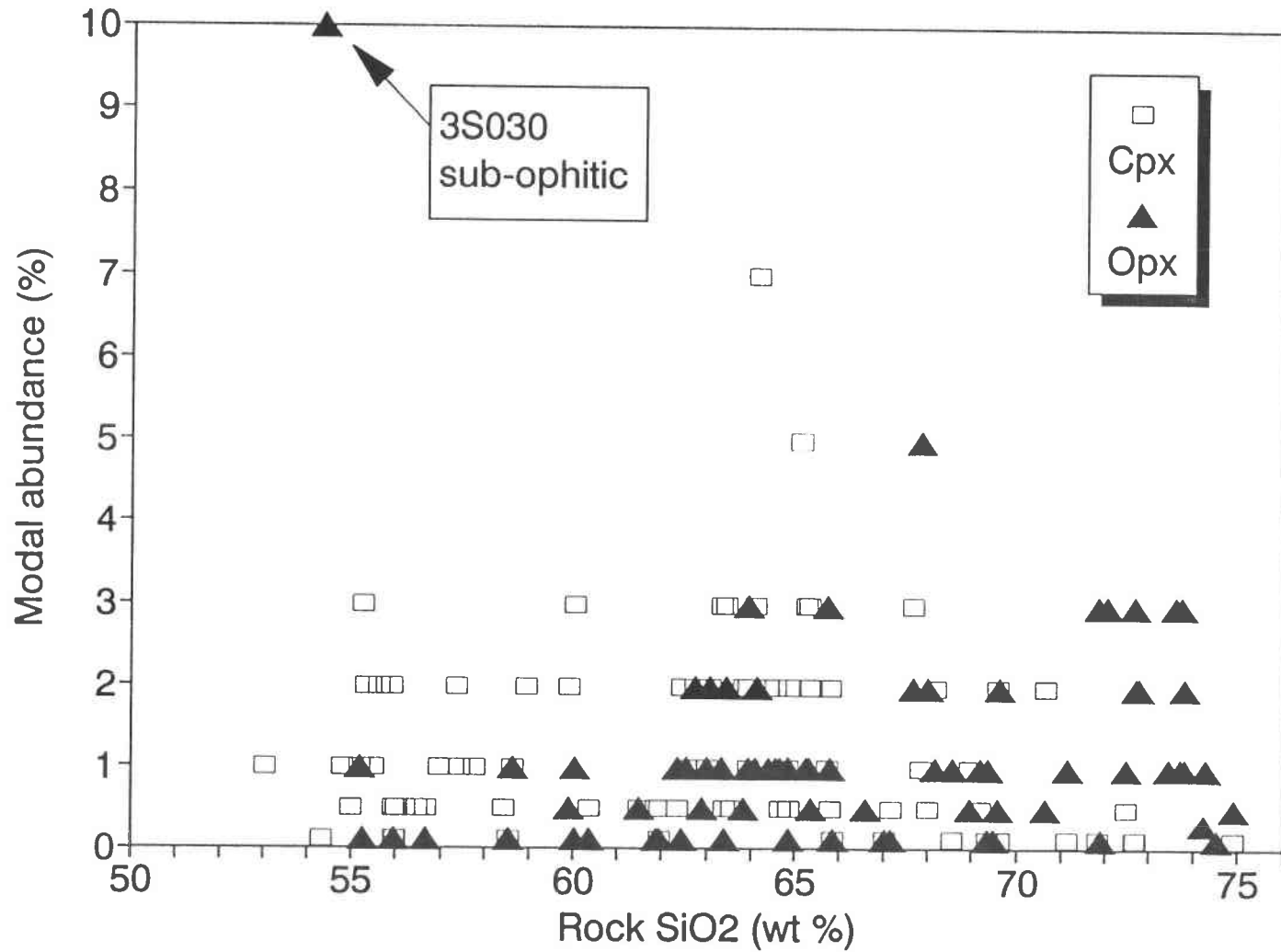
Figure 4.5: Visual estimates of clinopyroxene and orthopyroxene modal abundances versus silica content of the host rock. The high content of opx in basaltic andesite 3S030 is due to abundant 1-2mm sub-ophitic opx in the sample.
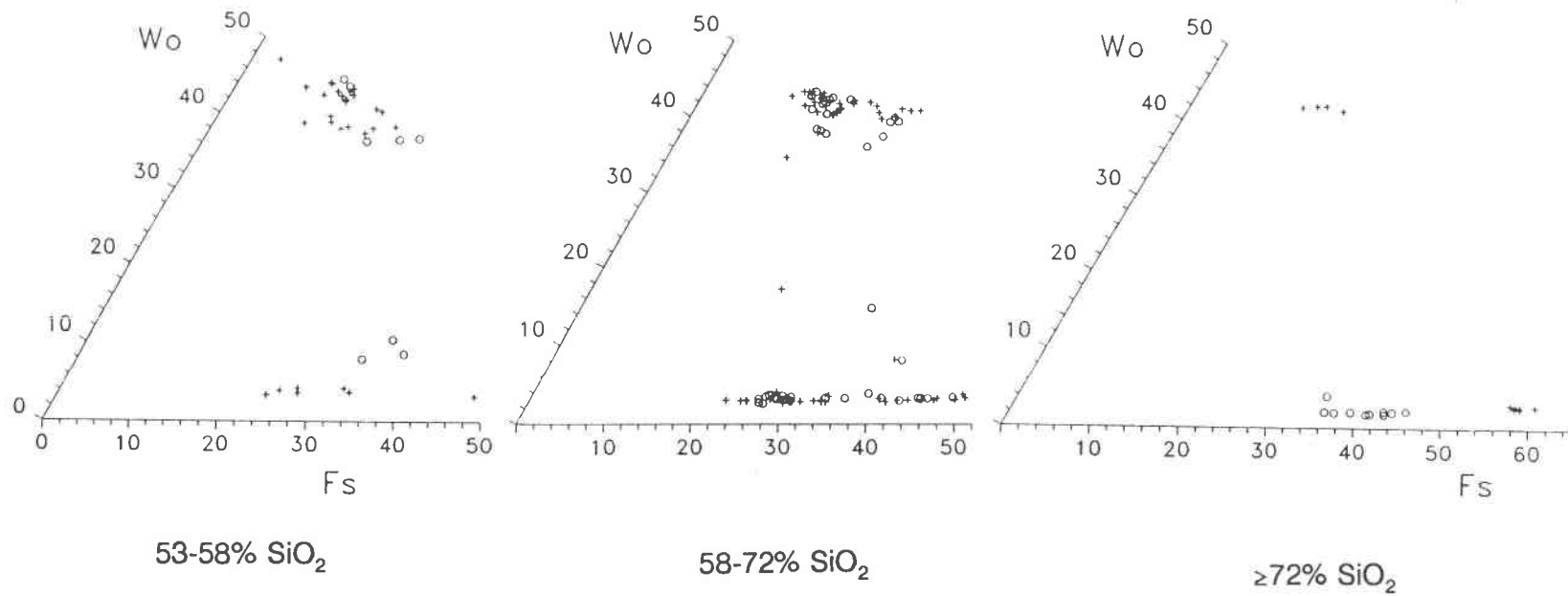
Figure 4.6: Compositional range of clinopyroxene and orthopyroxene for all samples, plotted on part of the Wo-En-Fs ternary. Compositions in mol % Wo and Fs. Samples grouped according to range in SiO$_2$ of the host rock.

figure 4.6, and representative augite analyses are given in table 4.2. Augite compositions tend to be less magnesian with increasing SiO_2 in the host rock, and range from $\approx En_{50}$ at 53% SiO_2 (3S049) to $\approx En_{34}$ at 72% SiO_2 (3S098). Visible sector zoning and concentric zoning is scarce in augites from mafic rocks. Core-to-rim zonation in En content of more than $\approx 10\%$ was not found in any of the augites (figure 4.7; augites $> \approx 50\%$ En). Nonetheless, small degrees of zonation are probably significant, owing to the limited amount of variability that can occur in iron and magnesium abundances in the pyroxene crystal lattice while calcium content remains relatively constant (i.e. 16-19%). Augite rim compositions that differ by at least 5% from core compositions probably represent non-equilibrium crystallization and may be evidence of open system differentiation, although no apparent correlation between degree of zoning and either rock composition or augite composition was observed.

Some of the augites in numerous intermediate composition rocks (Appendix B) have thin overgrowth rims of a finely crystalline, low birefringence mineral that is probably a low-Ca pyroxene. Microprobe analysis of rimmed augites in dacites from South Sister (3S061) and Broken Top (3S115) determined that these overgrowths are pigeonite. A South Sister andesite (3S112) also had several phenocrysts of hypersthene with thin rims of pigeonite. The transition from augite-orthopyroxene to augite-pigeonite generally occurs at either temperatures greater than $\approx 1000°C$ for these composition rocks (Lindsley, 1983), or in the more iron-enriched (calcium-poor) members of a comagmatic suite (cf. Huebner, 1980). The pigeonite rims probably formed on pyroxene xeno-crysts that were introduced into a more silicic (i.e. calcium-poor) melt through magma mixing. As rimmed pyroxenes do not normally develop during closed-system fractionation (e.g. Huebner, 1980), their occurrence is another petrographic indicator of open-system magmatic processes.

4.2.2 Orthopyroxene

Subhedral to euhedral phenocrysts of orthopyroxene generally range up to 2 mm in length, and are the dominant ferromagnesian mineral in most rocks with $SiO_2 \geq 64\%$ (figure 4.5). Orthopyroxene compositions are also plotted in figure 4.6, and representative orthopyroxene compositions are in table 4.2. Analyzed orthopyroxenes show an overall decrease in En content with increasing rock SiO_2, and range from $\approx En_{74}$ at 58% (3S003) to $\approx En_{39}$ at 74% SiO_2 (BPb). Unlike augites, orthopyroxene compositions in rhyolites are distinct for the Broken Top and Three Sisters magmatic systems (figure 4.6). The orthopyroxenes in Broken Top rhyolites are ferro-hypersthenes with Wo contents that are typical for High Cascade orthopyroxenes (Wo_3), while Three Sisters rhyolites contain hypersthenes with consistently low Wo contents (Wo_2). It is not surprising that ferrohypersthenes are found in Broken Top rhyolites, as these rocks are highly iron enriched: Fe' [= molar Fe/(Fe + Mg)] ≥ 0.9; Three Sisters rhyolites have Fe' ≤ 0.9 and thus contain hypersthene. Lindsley (1983) observed that with constant rock composition and decreasing

Clinopyroxenes

Sample	3S049b	3S045a	3S028b	3S112b	3S115b	3S134c	3S098c
Rx SiO2	53.0	56.0	58.5	60.0	62.9	65.7	71.1
SiO2	51.94	51.23	50.83	52.88	52.44	51.15	51.95
TiO2	0.48	0.82	0.64	0.75	0.64	0.41	0.26
Al2O3	2.96	3.06	1.93	3.12	1.65	1.37	0.62
FeO	6.00	10.54	9.26	13.08	9.71	13.28	14.41
Fe2O3	0.71	0.00	1.84	0.00	0.74	0.95	0.35
MgO	17.44	14.47	14.23	12.73	15.09	12.38	11.79
MnO	0.21	0.30	0.64	0.39	0.33	0.78	0.71
CaO	18.34	17.45	19.00	16.77	19.29	18.60	19.33
Na2O	0.38	0.47	0.38	0.78	0.35	0.34	0.31
Cr2O3	0.25	0.03	0.01	0.03	<0.01	0.01	<0.01
TOTAL	98.71	98.36	98.75	100.53	100.22	99.26	99.73
Wo	38.7	37.9	40.8	37.3	40.1	39.7	40.7
En	51.1	43.7	42.6	39.4	43.6	36.8	34.5
Fs	10.2	18.4	16.6	23.4	16.3	23.5	24.8

Orthopyroxenes

Sample	3S028c	3S112c	3S115a	3S134b	3S098b	BPb	3S058a
Rx SiO2	58.5	60.0	62.9	65.7	71.1	74.0	73.7
SiO2	51.97	52.14	53.94	51.55	51.02	49.07	52.43
TiO2	0.27	0.54	0.32	0.21	0.20	0.10	0.12
Al2O3	0.69	0.53	0.98	0.67	0.40	0.22	0.39
FeO	14.64	23.38	18.36	26.72	28.56	31.78	24.43
Fe2O3	5.01	0.44	0.34	0.06	0.30	2.24	0.00
MgO	25.12	20.25	24.68	17.73	16.11	12.97	20.01
MnO	0.90	0.63	0.52	1.22	1.40	1.98	1.17
CaO	1.45	1.92	1.37	1.61	1.85	1.29	0.92
Na2O	0.04	0.06	0.04	0.05	0.03	0.05	0.01
Cr2O3	0.02	<0.01	0.04	<0.01	<0.01	<0.01	0.02
TOTAL	100.12	99.89	100.58	99.81	99.88	99.70	99.50
Wo	2.99	3.9	2.7	3.3	3.9	2.8	1.9
En	72.00	57.7	68.1	51.3	47.0	39.5	57.1
Fs	25.01	38.4	29.2	45.4	49.1	57.7	41.0

Pigeonites

	3S131 (3)	3S061b Core	3S061b Rim	3S112d Core	3S112d Rim	3S115c Core	3S115c Rim
SiO2	52.30	52.30	51.67	53.88	52.22	52.51	52.24
TiO2	0.45	0.52	0.40	0.30	0.62	0.66	0.36
Al2O3	0.66	1.67	0.37	0.86	0.85	1.81	0.40
FeO	21.14	7.34	23.66	17.04	20.15	9.54	23.26
Fe2O3	0.27	1.62	0.36	1.48	0.00	0.88	0.00
MgO	19.82	15.47	17.95	25.04	18.11	15.14	18.26
MnO	0.58	0.37	1.06	0.51	0.59	0.45	0.99
CaO	4.38	20.42	3.93	1.89	7.14	19.38	3.99
Na2O	0.06	0.34	0.08	0.02	0.12	0.34	0.10
Cr2O3	0.02	<0.01	<0.01	0.02	0.03	0.03	0.04
TOTAL	99.68	100.05	99.48	101.03	99.82	100.73	99.62
Wo	9.0	42.6	8.2	3.8	14.7	40.2	8.2
En	56.4	44.9	51.8	69.1	51.9	43.7	52.6
Fs	34.7	12.6	40.1	27.2	33.4	16.2	39.2

Table 4.2: Representative pyroxene microprobe analyses. Rx SiO2 refers to SiO_2 in host rock, mol% Wo, En and Fs. Pigeonite sample 3S131 is an average of 3 30-50μ groundmass crystals, others samples are single-crystal rim compositions unless otherwise stated.
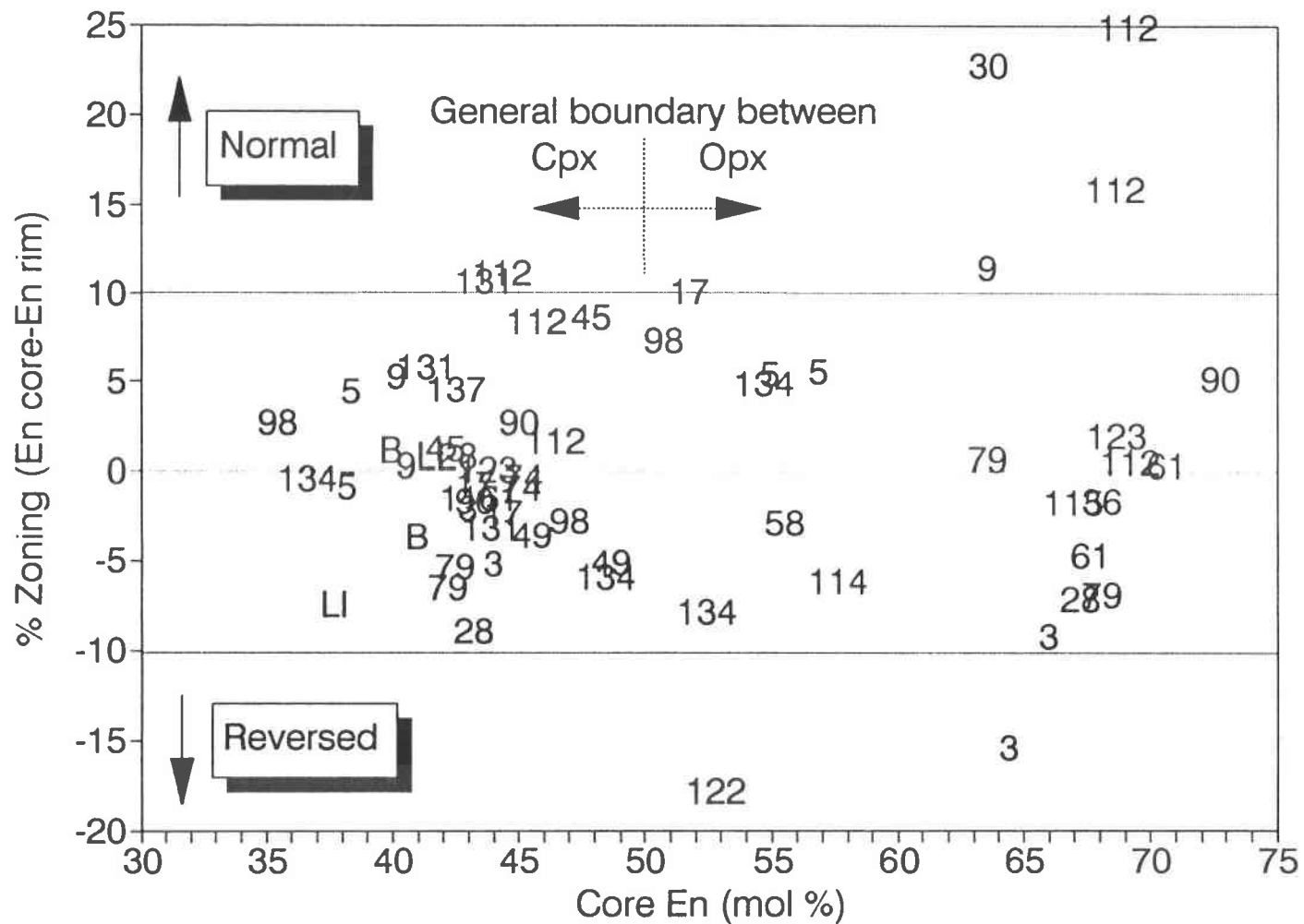
Figure 4.7: Range of core-to-rim zoning measured in pyroxene phenocrysts. Zoning is expressed as the percent change from core to rim En (mol %) content, with negative numbers indicating reversed zoning. Clinopyroxenes are generally $<En_{50}$, and orthopyroxenes are generally $>En_{50}$.

temperature, the Ca content of orthopyroxene will decrease while the Ca content of augite will increase. The anomalously low Wo contents of hypersthene in Three Sisters rhyolites suggests that these minerals may have crystallized at lower temperatures than Broken Top system ferrohypersthenes.

In general, analyzed orthopyroxenes are more strongly zoned with respect to Fe & Mg than augites, and have core-to-rim changes in En content of up to 25% (figure 4.7). There is also a general tendency, which was not observed for augites, for the strongest zonation in Fe & Mg to occur in more magnesian orthopyroxenes. This is probably due to the greater range in iron and magnesium contents that can be accommodated in orthopyroxene, relative to augite, for the same series of rocks (i.e., En_{74-39} vs. En_{52-34}).

4.2.3 Pigeonite

Pigeonite (i.e. Wo_5 to Wo_{15}) has been recognized through microprobe analysis as both a stable groundmass mineral in basaltic andesite 3S131, and as occasional 5-15μ rims around other pyroxenes, as stated above. Representative pigeonite analyses are in table 4.2. Basaltic andesite 3S131 is slightly iron enriched (Fe' = 0.58) relative to other High Cascade basaltic andesites (Fe' $\approx$ 0.4-0.5) (Hughes, 1983; this study). As pigeonite is generally the stable low-calcium pyroxene phase for mafic magmas with Fe' greater than $\approx$0.45 (Huebner, 1980), it is not surprising that the pyroxene assemblage in 3S131 is augite + pigeonite.

4.3 Olivine

Phenocrysts of olivine range in abundance from 5% to 10% in basalts, from 2% to 5% in most basaltic andesites, and $\leq$1% in some andesites (Appendix B). Olivine phenocrysts are generally subhedral and $\leq$ 2mm in diameter, and euhedral phenocrysts are only observed in some basalts. Xenocrysts of olivine are found in several dacites and rhyodacites, and are always embayed and rimmed with orthopyroxene.

Opacitic olivine was found in some vesicular mafic rocks. The formation of opacitic olivine is a deuteric process involving the oxidation of olivine to magnetite $\pm$ enstatite at low pressures (Haggerty & Baker, 1967), and does not indicate that olivine was out of equilibrium with the magma. Microprobe analysis of olivine in basalt 3S049 (table 4.3) shows that fresh phenocrysts of $\approx$Fo$_{80}$ olivine alter to Fo$_{95}$ olivine (3S049b) and a symplectite of magnetite + orthopyroxene (3S049b opacite). Lesser degrees of deuteric alteration ($\pm$ hydration) results in the formation of iddingsite on olivine rims and fractures, which is commonly observed in mafic rocks.

	SiO2	FeO	MgO	MnO	CaO	NiO	Total	Fo	Fa	Mo	Li	Te	FM
3S003a core	37.15	25.12	36.24	0.46	0.13	0.00	99.09	71.76	27.91	0.19	0.00	0.52	0.28
3S003a rim	37.92	24.99	35.55	0.42	0.16	0.01	99.05	71.54	28.21	0.23	0.01	0.48	0.29
3S003b core	37.34	25.53	35.98	0.42	0.15	0.00	99.41	71.34	28.40	0.21	0.00	0.47	0.29
3S003b rim	38.08	24.78	37.77	0.30	0.19	0.02	101.14	73.05	26.88	0.26	0.02	0.33	0.27
3S017a 150μm core	37.81	21.81	39.01	0.35	0.16	0.10	99.24	75.99	23.84	0.22	0.10	0.39	0.24
3S017a rim	37.09	25.57	36.08	0.38	0.15	0.14	99.39	71.40	28.39	0.21	0.14	0.42	0.29
3S028 core	37.33	25.49	35.81	0.45	0.17	0.04	99.28	71.26	28.46	0.24	0.04	0.51	0.29
3S028 rim	36.87	27.17	37.34	0.37	0.16	0.00	101.91	70.88	28.94	0.22	0.00	0.40	0.29
3S028 rim 2nd point	38.52	24.88	36.57	0.37	0.21	0.04	100.59	72.29	27.59	0.30	0.04	0.42	0.28
3S045 120μm euhed	36.84	26.44	35.01	0.54	0.16	0.08	99.06	69.96	29.65	0.22	0.09	0.62	0.30
3S045 60μm subh	36.88	25.74	35.46	0.57	0.19	0.04	98.88	70.79	28.84	0.27	0.05	0.65	0.29
3S045a 250μm core	37.73	22.04	38.73	0.44	0.22	0.06	99.22	75.67	24.16	0.31	0.06	0.49	0.25
3S049 30μm GM	35.95	31.72	30.47	0.53	0.24	0.00	98.91	62.96	36.77	0.35	0.00	0.62	0.37
3S049 50μm GM	35.77	33.33	29.82	0.67	0.19	0.01	99.79	61.15	38.35	0.28	0.01	0.78	0.39
3S049a core	38.62	16.99	42.67	0.31	0.16	0.19	98.94	81.64	18.24	0.22	0.20	0.34	0.19
3S049a rim	36.47	27.92	33.36	0.45	0.17	0.05	98.41	67.85	31.87	0.24	0.05	0.53	0.32
3S049b By opacite	41.40	5.24	53.14	0.19	0.07	0.12	100.16	94.66	5.24	0.09	0.11	0.20	0.05
3S049b Opacite	37.61	32.80	26.81	0.33	0.62	0.18	98.35	59.64	40.94	0.99	0.22	0.42	0.41
3S049c core	38.79	17.29	42.88	0.23	0.17	0.22	99.59	81.55	18.44	0.24	0.23	0.25	0.19
3S049c rim	38.65	18.76	40.84	0.33	0.16	0.11	98.85	79.41	20.46	0.23	0.11	0.37	0.21
3S069a 200μm core	39.91	14.93	45.13	0.29	0.18	0.15	100.60	84.29	15.65	0.24	0.16	0.31	0.16
3S069a rim	39.46	15.49	44.56	0.38	0.10	0.12	100.10	83.45	16.28	0.13	0.12	0.40	0.17
3S069b 200μm core	40.22	12.68	46.89	0.24	0.14	0.34	100.50	86.77	13.16	0.18	0.34	0.25	0.13
3S069b rim	39.52	15.76	44.10	0.33	0.13	0.17	100.01	83.14	16.67	0.17	0.17	0.36	0.17
3S074 30μm opacitic rim	37.70	23.20	37.68	0.55	0.10	0.08	99.31	73.97	25.55	0.14	0.08	0.61	0.26
3S074a core	39.41	17.11	42.75	0.35	0.15	0.27	100.03	81.52	18.30	0.20	0.28	0.38	0.19
3S074a rim	39.17	16.55	42.28	0.29	0.18	0.16	98.63	81.93	18.00	0.25	0.17	0.32	0.18
3S090a 120μm core	37.50	23.86	36.77	0.40	0.16	0.07	98.75	73.14	26.63	0.22	0.07	0.46	0.27
3S090a rim	35.74	33.97	28.92	0.56	0.23	0.08	99.50	60.08	39.61	0.35	0.09	0.66	0.40
3S090b 300μm core	37.17	25.65	35.90	0.44	0.15	0.10	99.41	71.18	28.54	0.21	0.11	0.49	0.29
3S090b rim	35.98	30.27	32.11	0.52	0.20	0.03	99.11	65.20	34.49	0.29	0.03	0.60	0.35
3S131 150μm core	35.05	39.89	24.84	0.61	0.25	0.10	100.72	52.42	47.23	0.38	0.11	0.73	0.48
3S131a 100μm core	35.75	35.87	28.24	0.51	0.24	0.00	100.61	58.25	41.51	0.36	0.00	0.59	0.42
3S131a rim	35.24	39.05	25.56	0.68	0.22	0.05	100.81	53.59	45.94	0.33	0.06	0.81	0.47
3S131b 15M GM	34.16	44.49	20.15	0.71	0.31	0.03	99.85	44.49	55.11	0.49	0.04	0.89	0.56
3S131b rim	33.91	45.61	20.02	0.80	0.31	0.02	100.66	43.67	55.82	0.48	0.02	0.99	0.57

Table 4.3: Olivine compositions determined through microprobe analysis. FM = Molar Fe / (Fe + Mg + Mn); mol %'s Fo, Fa, Mo, Li and Te. Opacite refers to a symplectic intergrowth of magnetite ± enstatite produced through deuteric alteration.

Olivine phenocrysts in basaltic andesites and andesites commonly have embayed rims, which are either opacitic or rimmed by a $\leq$ 0.1mm zone of orthopyroxene. Embayed rims in olivine do not indicate resorption, but are probably a growth feature characteristic of an increased cooling rate in the magma (Donaldson, 1976). Orthopyroxene rims formed subsequent to embayment, due to the reaction of a silica-undersaturated phase with a more silicic melt. Embayed and rimmed olivines are thus one of the expected products of magma mixing.

Olivine compositions determined through microprobe analysis ranged from Fo_{87} chrysolite in basalt 3S069 to $\approx Fo_{45}$ hortonolite in basaltic andesite 3S131 (table 4.3). Forsterite content generally decreases with increasing silica in the host rock (figure 4.8), although unusually Fe-rich olivines were found in basaltic andesites 3S049 and 3S131; Olivine in most calc-alkaline basaltic andesites is generally between Fo_{85} and Fo_{70} (Ewart, 1982). The high Fe content of olivine (Fo_{45}) in basaltic andesite 3S131 reflects the anomalously high Fe content of the rock (Fe' = 0.58) compared to average High Cascade basaltic andesites (Fe' $\leq$ 0.5; Hughes, 1983).

4.4 Iron-Titanium Oxides

Phenocrysts to microphenocrysts of opaque minerals from the system FeO-Fe_2O_3-TiO_2, which will be referred to as Fe-Ti oxides, occur in all of the studied units. Fe-Ti oxide abundances typically range from 2-5% in mafic rocks, 1-3% in intermediate units, and $\leq$ 1% in silicic rocks. The Fe-Ti oxides commonly occur as inclusions in all other major phases, and phenocryst sizes typically range to 0.5 mm. Analyses of representative Fe-Ti oxides from the study area are in table 4.4. Microprobe analysis of 27 representative mafic to silicic rocks from the study area (Appendices C-4 and C-5) confirmed the ubiquitous occurrence of titanomagnetite (magnetite-ülvospinel solid solution) when opaque minerals are present. The occurrence of ilmenite (ilmenite-hematite solid solution) was restricted to samples with $SiO_2 \geq 59\%$.

Exsolution lamellae are present in titanomagnetites from ignimbrites 3S005 and the Lava Island Tuff, rhyolite dome 3S042, and in ilmenites from rhyodacite dome 3S009. All of the units with exsolved Fe-Ti oxides also have light to moderate deuteric vapor-phase(?) alteration, indicating that the exsolution lamellae were produced through oxidation and not through slow cooling (Buddington & Lindsley, 1964). Because oxidation-induced exsolution can alter the Ti/Fe ratio in iron-titanium oxides (Furuta et al., 1985), these oxides with exsolution lamellae do not represent magmatic compositions.

Coexisting titanomagnetite-ilmenite pairs from most units have Mg/Mn ratios that plot within the 2σ limits of equilibrium distribution of Bacon & Hirschmann (1988) (figure 4.10). This equilibrium relationship has been calibrated with high-silica rhyolite data, but the compositions and temperatures of formation of the Fe-Ti oxides in this study are comparable to the data used by
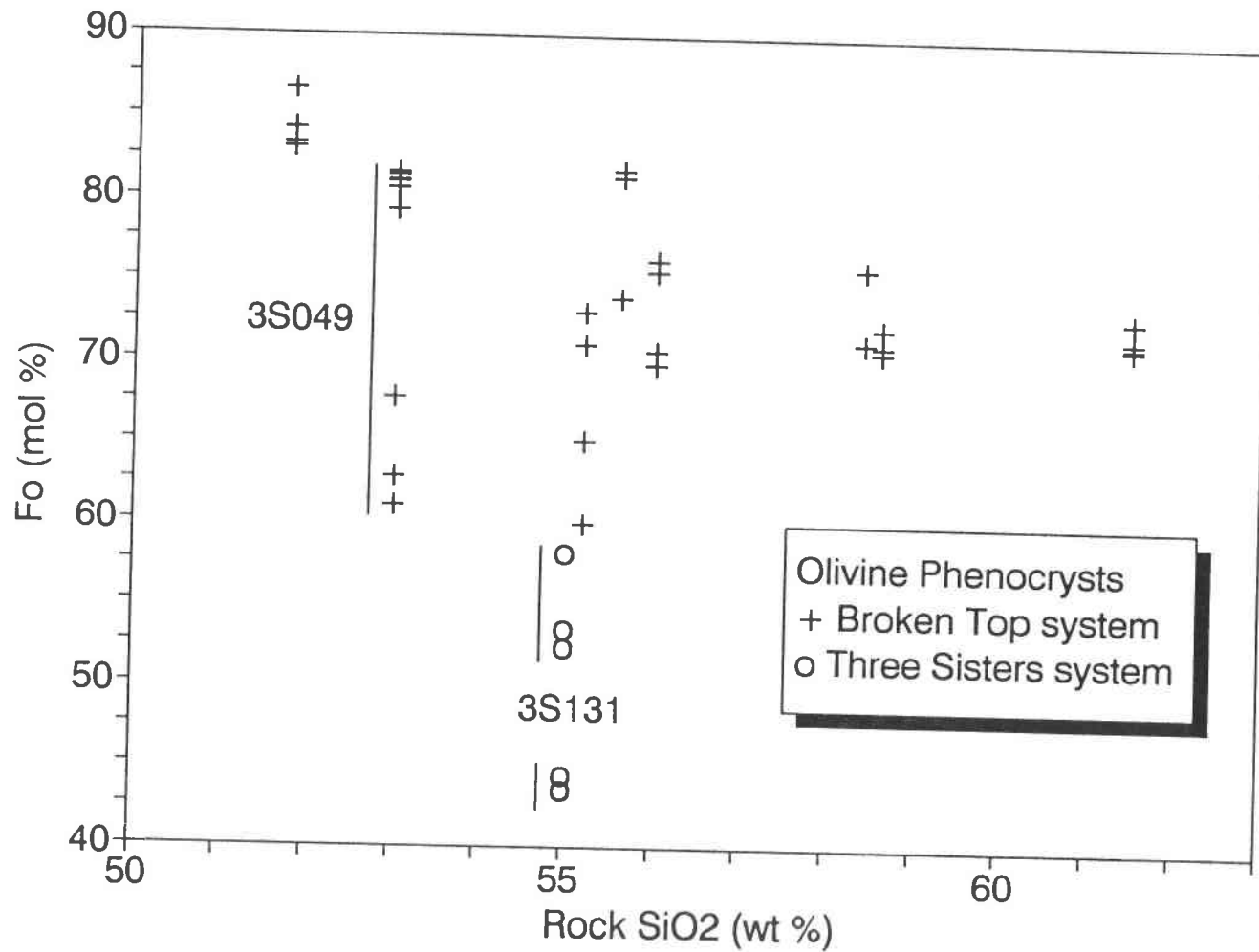
Figure 4.8: Compositional range of olivine phenocrysts and microlites versus silica content of the host rock. Note that high Fe olivine (hortonolite) is associated with unusually Fe-rich basaltic andesite 3S131. Fe-rich olivines in 3S049 are groundmass microlites.

Titanomagnetites

Sample #	3S049	3S045	3S028	3S123	3S098	3S058	BP-b
Rx SiO2	53.0	56.0	58.5	63.5	71.1	73.7	74.0
SiO2	0.07	0.10	0.06	0.05	0.08	0.09	0.11
TiO2	10.00	15.53	13.66	14.49	17.32	8.49	14.42
Al2O3	0.77	0.57	2.24	2.17	1.30	1.82	1.35
FeO	35.35	44.04	40.23	42.41	45.38	37.58	43.24
Fe2O3	48.22	36.84	41.27	39.61	35.73	51.29	40.31
MnO	0.28	0.34	0.60	0.47	0.72	0.54	0.93
MgO	2.57	0.30	2.18	1.42	1.15	0.86	0.50
Cr2O3	0.02	0.02	0.03	0.00	0.01	0.07	0.11
TOTAL	97.28	97.73	100.27	100.63	101.68	100.74	100.97
XÜsp	29.2	45.7	38.2	40.6	48.3	24.3	41.0

Fe-Ti-Cr spinels

Sample #	3S030	3S069	3S069	3S112	3S045
Rx SiO2	54.3	51.8	51.8	60.0	56.0
SiO2	0.05	0.07	0.04	0.07	0.07
TiO2	18.39	1.78	1.44	20.46	2.03
Al2O3	1.40	3.51	2.26	1.53	20.60
FeO	44.13	27.85	27.06	47.45	21.50
Fe2O3	31.01	50.79	61.95	24.66	20.02
MnO	0.44	0.43	0.51	0.38	0.32
MgO	2.18	3.19	3.27	1.20	9.38
Cr2O3	0.96	11.52	2.84	2.15	24.04
TOTAL	98.56	99.14	99.37	97.89	97.95
XÜsp	52.1	5.2	4.2	58.7	5.2

Ilmenites

Sample #	3S028	3S123	3S098	3S058	BPb-a
Rx SiO2	58.5	63.5	71.1	73.7	74.0
SiO2	0.01	0.05	0.01	0.00	0.03
TiO2	44.41	45.79	48.60	42.68	49.69
Al2O3	0.00	0.07	0.00	0.00	0.00
FeO	35.16	35.99	39.90	34.73	40.99
Fe2O3	17.64	14.99	8.87	19.24	6.40
MnO	0.68	0.50	1.08	0.76	1.42
MgO	2.31	2.66	1.53	1.60	1.29
Cr2O3	0.06	0.04	0.02	0.05	0.08
Nb2O5	0.02	0.00	0.18	n/a	0.24
TOTAL	100.27	100.09	100.19	99.06	100.13
XHem	16.63	14.18	8.39	18.44	6.12

Table 4.4: Representative Fe-Ti oxide compositions, and compositions of unusually Cr-rich (Cr_2O_3 ≥1 wt%) Fe-Ti oxides, determined by microprobe analysis. RxSiO2 refers to SiO_2 in host rock. Ferric-ferrous iron partitioning, mole fractions ülvospinel (XÜsp) and hematite (XHem) calculated according to Carmichael (1967). Sample locations in appendix D-1.
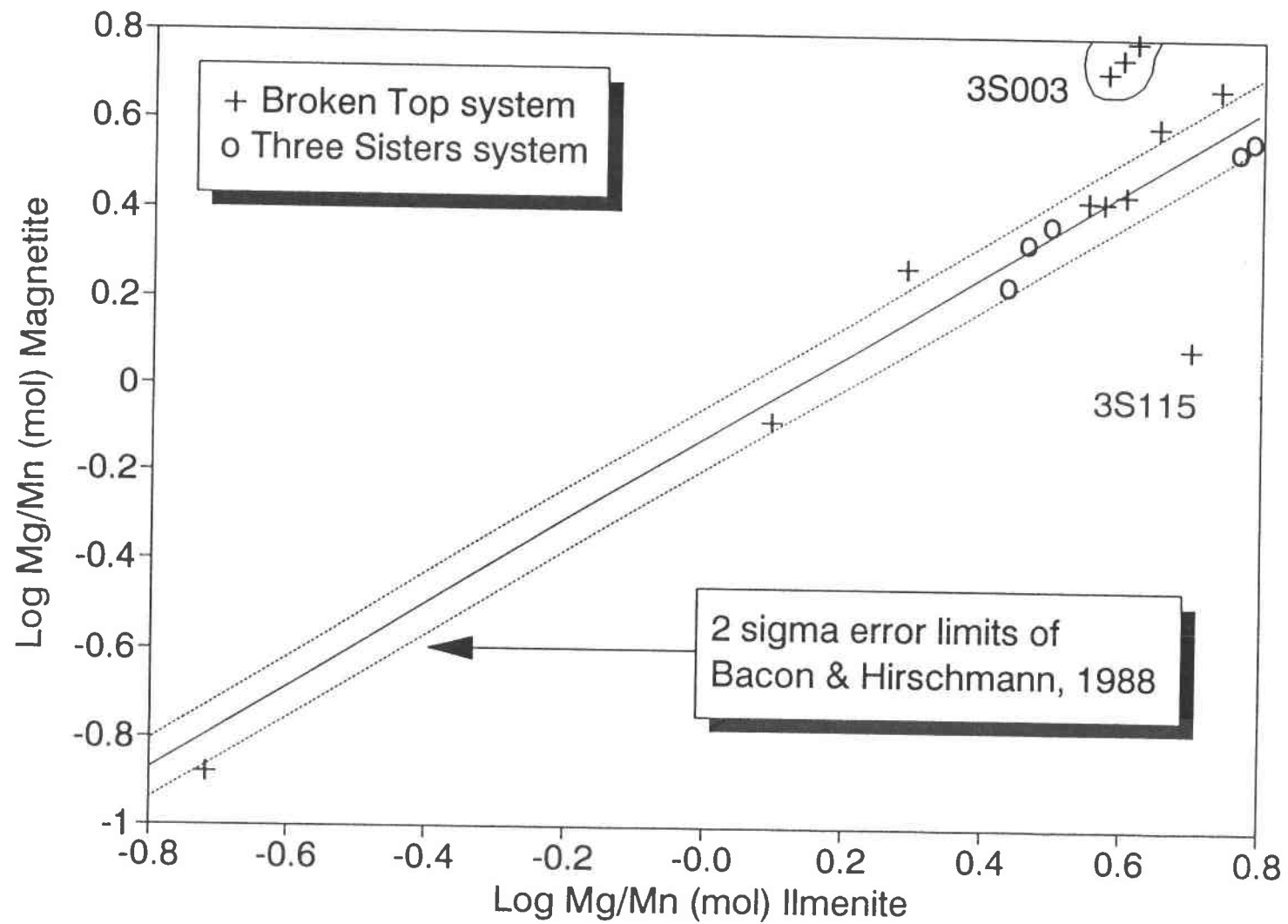
Figure 4.9: Molar Mg/Mn ratios for coexisting magnetite-ilmenite pairs. Equilibrium between magnetite and ilmenite is indicated by Mg/Mn ratios that plot within the 2σ error limits of Bacon and Hirschmann (1988); samples 3S003 and 3S115 are clearly out of equilibrium.

Bacon & Hirschmann (1988). Although a slight compositional dependence on Mg/Mn partitioning has been suggested by Grunder & Mahood (1988), the distribution of most of the analyses from this study within the 2σ equilibrium limits strongly indicates that these titanomagnetite-ilmenite pairs are in equilibrium. Fe-Ti oxides from dacite 3S115 and andesite 3S003, however, are strongly out of equilibrium with respect to Mg/Mn abundances, which suggests that one or both of these phases are xenocrysts.

Chromian titanomagnetites (cf., Haggerty, 1976) were analyzed in basalt 3S069, basaltic andesite 3S030, and andesite 3S112 (table 4.4). Chromian titanomagnetite phenocrysts are commonly observed in relatively non-evolved (i.e. high Cr, Ni, Co) basalts (Haggerty, 1976). Basalt 3S069 has a very high Cr abundance (415 ppm), which supports petrographic evidence that chromian titanomagnetite was a phenocryst in this unit. Bulk rock samples 3S030 and 3S112 both have Cr $\leq$100 ppm, indicating a more evolved composition than 3S069. Other analyzed Cascade mafic units with Cr $\leq$100 ppm contain titanomagnetite as the main Fe-Ti oxide, indicating that the chromian titanomagnetites in 3S030 and 3S112 are likely xenocrysts from less evolved basaltic melts.

An inclusion of titanian chromite (table 4.4) was also found in a plagioclase glomerocryst (An_{85}) from basaltic andesite 3S045. Both the unusually high calcium content of the plagioclase and the titanian chromite inclusion strongly indicate that this glomerocryst was derived from a composition that is much more primitive than observed in exposed rocks in this part of the High Cascades.

4.5 Amphibole

Trace amounts of amphibole phenocrysts are found in about half of the studied rhyolites and occasionally in some rhyodacites (Appendix B). Amphibole phenocrysts range in size up to 5 mm, are generally euhedral, and have brown to brownish-green pleochroism. Glomerocrysts containing partially to wholly opacitized amphibole, and fine-grained glomerocrysts of orthopyroxene + opaque minerals pseudomorphically replacing amphibole (i.e. ghosts), are also found in three basaltic andesites and a dacite (Appendix B). As amphibole phenocrysts have only been observed in rhyolites, discrete amphibole "ghosts" are probably direct evidence of magma mixing with rhyolitic melts.

Amphiboles from 9 units (55 points) were analyzed on the microprobe, and representative analyses are summarized in table 4.5. Cation distributions were calculated on the basis of 23 oxygens according to the method of Spear and Kimball (1984), using the average of the highest and lowest acceptable values for Fe^{3+} to calculate the amphibole formula. Following the terminology of Leake (1978), all amphiboles in the study area are calcic and have a general composition of Magnesian Hastingsite, but range in composition to Edenite and Pargasitic Hornblende (table 4.5). There is a surprising degree of variation in amphibole composition; amphiboles from individual

Label	3S053-A core 53A	3S053-A rim 53a	3S053-B core 53B	3S053-B rim 53b	BPT-C core BC	BPT-C rim Bc	3S060-A core 60A	3S060-A rim 60a
SiO2	44.18	43.45	47.80	47.29	42.15	43.20	42.68	41.41
TiO2	1.47	1.81	1.30	1.98	3.29	3.13	3.17	3.78
A12O3	9.94	9.28	5.57	8.03	10.00	10.05	11.77	11.51
FeO	12.74	10.19	14.74	15.77	15.92	19.14	11.61	8.73
Fe2O3	3.32	6.10	2.45	0.00	3.62	0.00	0.97	5.70
FeO*	15.73	15.68	16.95	15.77	19.18	19.14	12.48	13.86
MgO	13.10	13.71	13.48	13.12	10.81	10.06	13.81	13.28
MnO	0.33	0.20	0.48	0.28	0.52	0.52	0.16	0.19
CaO	10.77	10.94	10.87	10.71	10.17	10.06	11.24	11.20
Na2O	1.57	1.81	0.98	1.56	2.22	2.07	1.89	2.01
K2O	0.34	0.43	0.74	0.41	0.29	0.28	0.43	0.36
H2O	1.74	1.88	1.96	1.92	1.88	1.77	1.92	1.93
F-	0.54	0.21	0.04	0.24	0.21	0.46	0.24	0.17
Cl-	0.09	0.08	0.19	0.09	0.04	0.05	0.02	0.01
Total	100.14	100.10	100.59	101.41	101.10	100.79	99.90	100.29

Cations on the basis of 23 Oxygen, average Fe3+

	3S053-A core 53A	3S053-A rim 53a	3S053-B core 53B	3S053-B rim 53b	BPT-C core BC	BPT-C rim Bc	3S060-A core 60A	3S060-A rim 60a
Si	6.53	6.42	7.04	6.89	6.29	6.48	6.27	6.08
Al(IV)	1.47	1.58	0.96	1.12	1.71	1.52	1.73	1.92
Ti	0.16	0.20	0.14	0.22	0.37	0.35	0.35	0.42
Al(VI)	0.26	0.03	0.01	0.26	0.05	0.26	0.31	0.07
Fe2+	1.57	1.27	1.81	1.92	1.99	2.40	1.43	1.07
Fe3+	0.37	0.67	0.28	0.00	0.41	0.00	0.11	0.64
Mg	2.89	3.02	2.96	2.85	2.10	2.25	3.02	2.90
Mn	0.04	0.03	0.06	0.04	0.07	0.07	0.02	0.02
Ca	1.71	1.73	1.72	1.67	1.63	1.62	1.77	1.76
Na	0.00	0.06	0.02	0.05	0.09	0.05	0.00	0.13
Na(IV)	0.45	0.46	0.26	0.39	0.55	0.55	0.54	0.45
K	0.06	0.08	0.14	0.08	0.06	0.05	0.08	0.07
OH	1.73	1.88	1.93	1.87	1.89	1.77	1.88	1.92
Cl	0.02	0.02	0.05	0.02	0.01	0.01	0.01	0.00
F	0.25	0.10	0.02	0.11	0.10	0.22	0.11	0.08
Fe3+/Fe*	0.19	0.35	0.13	0.00	0.17	0.00	0.07	0.37
Mg/Mg+Fe2+	0.65	0.70	0.62	0.60	0.51	0.48	0.68	0.73

Amphibole types

3S053-A Edenitic Hornblende, Holocene Devils Hill pumice.
3S053-A Magnesian Hastingsitic Hornblende.
3S053-B Magnesio-Hornblende.
3S053-B Edenite.
BPT-C Magnesian Hastingsitic Hornblende, top of Bend Pumice.
BPT-C Edenitic Hornblende.
3S060-A Pargasitic Hornblende, Holocene Rock Mesa pumice.
3S060-A Magnesio-Hastingsite.

Table 4.5: Representative microprobe analyses of amphiboles from rhyolites. Recalculations using the method of Spear & Kimball (1984), using average values of Fe^{3+} on a 23-O basis; water calculated on a 15 cation, 2(OH, F, Cl) basis. Amphibole types from Leake (1978).

Three Sisters units generally have a larger compositional variation than found in Broken Top units, and amphiboles from each system plot in discrete to partially overlapping fields (e.g. figure 4.10a-d). All amphiboles, with the exception of 3S090 and 3S009, were analyzed during the same microprobe run and no significant drift in probe calibration occurred; the compositional variations are not due to analytical error.

Increases in the Al content of igneous amphiboles can be produced through increases in temperature (Blundy & Holland, 1990), or through increases in total pressure at a relatively fixed temperature (Hollister et al., 1987; Hammarstron & Zen, 1986; Johnson & Rutherford, 1989). While most of the analyzed amphiboles have a consistent linear decrease in total Al with increasing Si (figure 4.10b), 7 points have significantly higher total Al. Excess Al will be in octahedral coordination, and will generally substitute for Fe^{3+}, Ti or (Fe^{2+} + Mg) on the M2 site (Hawthorne, 1981). If the observed increases in total Al are a function of pressure or temperature, there should be a positive correlation between Al(IV) and another M2 cation. No correlation between Mg, Fe^{2+}, or Ti and Al is observed (e.g. figure 4.10c), although a slight negative correlation is observed with Fe^{3+} (figure 4.10d). This strongly suggests that the observed variation in Al content of amphiboles in the same rock was not produced through changes in magmatic pressure or temperature. In addition, all of the analyzed amphiboles have very similar anion abundances (Appendix C-3). Consequently, it is difficult to appeal to variations in magmatic water content that shifted the compositional field into a more aluminous range.

It is unclear why there is such a wide range of amphibole composition, both within individual rocks and between rocks of very similar composition. The Bend Pumice has no significant compositional zonation from the base to the top of the unit (Hill, 1985), yet the Bend Pumice amphiboles show a large amount of compositional variation. The amphibole variations are not systematic, and do not reflect progressive core to rim differences in composition. Given the high degree of ordering in the amphibole structure (Hawthorne, 1981; Blundy & Holland, 1990), it is speculated that the observed compositional variations may have been produced through variations in chemical diffusion rates, much in the same way that oscillatory zoning can be formed in plagioclase (Loomis, 1982; Grove et al., 1985).

4.6 Accessory Minerals

Apatite occurs as small (≤ 0.1 mm) inclusions in plagioclase and pyroxene phenocrysts in most units with SiO2 ≥ 57% (Appendix B), and can be recognized as a groundmass mineral in many dacites and rhyodacites. Based on experimental studies on a Cascade-Aleutian rock suite, Green and Watson (1982) concluded that apatite saturation could occur in this system at ≥57% SiO2, but that the temperatures necessary for apatite crystallization in more mafic magmas were unrealistically low (≈800 °C at 7.5 kb). Green and Watson suggested that the apatite inclusions
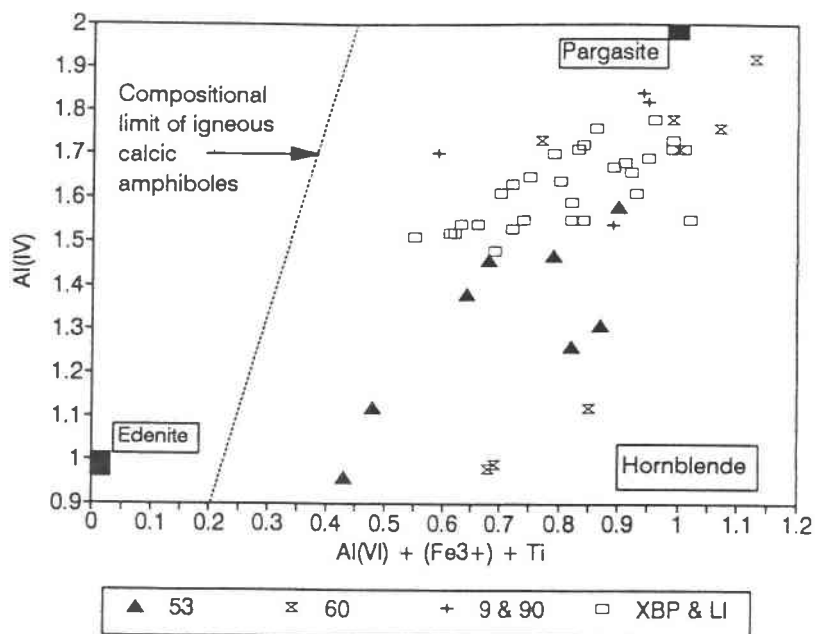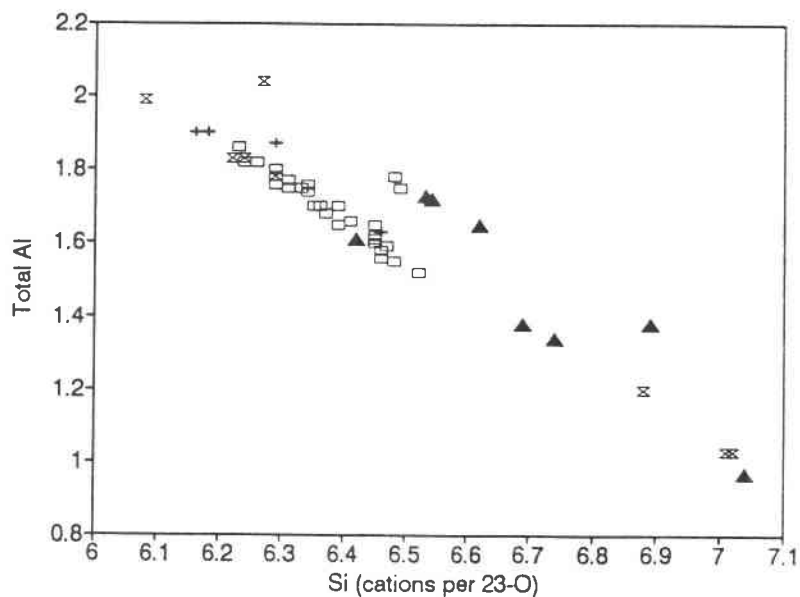
Figure 4.10: **A)** Compositional range of amphibole for all samples. Analyses in appendix C-3, normalized to 23-O and average Fe^{3+} (Spear and Kimball, 1984) and nomenclature from Leake (1978). Note the wider range of scatter for Three Sisters samples (53 & 60) than for Broken Top samples. **B)** Total Al versus Si variations for analyzed amphiboles. Note the two distinct fields of total Al at constant Si.
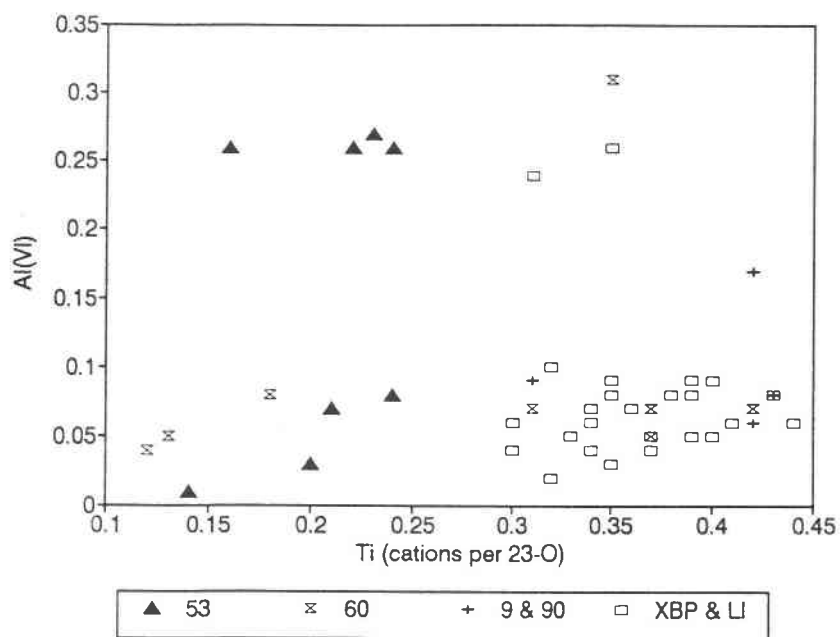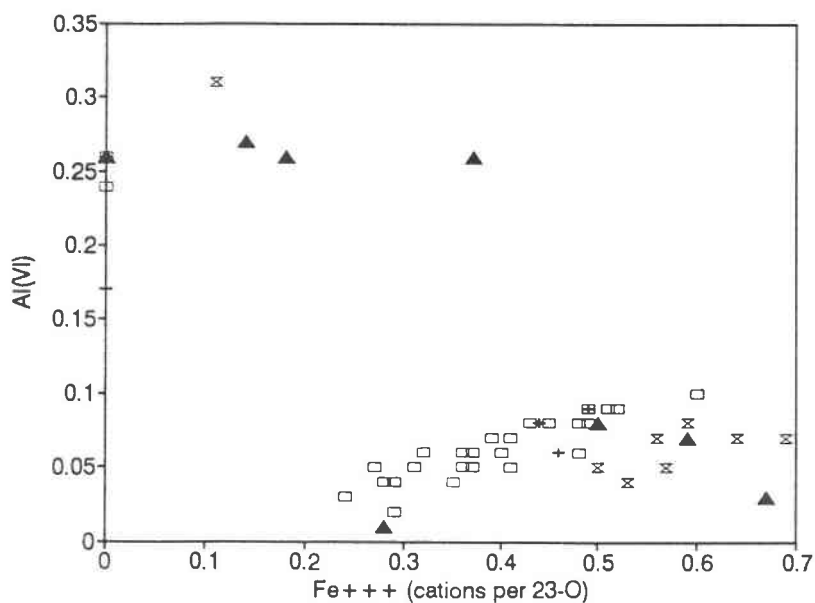
Figure 4.10: C) & D) Cation abundances for analyzed amphiboles. Samples with excess Al(VI) do not show a correlation with Ti, $Mg + Fe^{2+}$, or Fe^{3+} abundance. If the excess Al(VI) contents of these amphiboles was a function of temperature or pressure, then there should be a positive correlation between AL(VI) and another M2 cation (Ti, $Mg + Fe^{2+}$, or Fe^{3+}) (cf., Blundy and Holland, 1990).

were produced through local saturation of P_2O_5 at the phenocryst-melt interface, and that the common occurrence of apatite inclusions in most mafic rock minerals does not indicate that the bulk melt was saturated in P_2O_5. Experimental studies by Harrison and Watson (1984) confirmed that the relatively slow rate of phosphorus diffusion in these melts would result in local saturation of apatite at the phenocryst-melt boundary. The magmas in the study area were probably not saturated with apatite until about 62% SiO2 (Green & Watson, 1982), although local saturation in apatite probably occurred by 57% SiO2. Petrogenic models for the interval 57% to 62% SiO2 thus need to account for the effect of apatite fractionation, even though apatite is not saturated in the melt.

Zircon was recognized in the groundmass of several rhyodacites and rhyolites as a very small (< 0.1 mm), highly birefringent crystal (Appendix B). It is likely that most other rhyolites contained zircon, but it was not present in the thin section due to its very low abundance in the rock.

Small (≤ 0.2 mm) xenocrysts of biotite, associated with plagioclase glomerocrysts, were occasionally found in thin sections of Three Sisters rhyolites. The biotite xenocrysts generally had faint opacitic rims, and only rarely occurred as a discrete phase. A 30μm shred of biotite was also analyzed in dacite 3S036 (table 4.6). Single xenocrysts of quartz (0.3 mm) and sanidine (0.5 mm) were found in dacite 3S036.

Rounded inclusions of pyrrhotite ($\approx Fe_{0.89}S$) were found in an orthopyroxene from rhyodacite 3S005, and in an ilmenite from rhyolite 3S114 (table 4.6). The pyrrhotite inclusion were probably trapped as immiscible sulfide blebs, as they are rounded and wholly enclosed by the host mineral. It is likely that sulfide blebs in silicic rock minerals represent local saturation of sulfur at the crystal-melt interface (Bacon, 1989).

Phlogopite was recognized as a vapor phase mineral in two rocks that had undergone small amounts of deuteric alteration: rhyodacite 3S009 and basaltic andesite 3S074. Vapor phase phlogopite is characterized by high F contents (R. Nielsen, pers. comm., 1990), which are found in the analyzed phlogopites (table 4.6). Although many other vapor phase minerals undoubtably occur in some rocks in the study area, these deuterically altered rocks were generally not sampled.

MICAS

	3S009	3S074	3S036
SiO2	46.30	41.80	53.87
TiO2	0.14	0.85	1.20
Al2O3	11.02	10.79	15.39
FeO	1.80	4.99	8.30
MgO	24.12	26.29	9.65
MnO	0.18	0.05	0.06
CaO	0.03	0.00	0.70
Na2O	0.95	0.74	3.35
K2O	8.05	8.83	7.56
Cr2O3	0.00	0.00	0.03
H2O	0.11	0.18	3.35
F-	8.71	8.39	2.43
Cl-	0.05	0.10	0.18
Total	101.46	103.01	106.07
O=F,Cl	3.69	3.56	1.06
TOTAL	97.77	99.45	105.01

3S009 15μm clot of vapor phase phlogopite.
3S074 30μm vapor phase(?) phlogopite by plagioclase glomerocryst.
3S036 30μm biotite shred in groundmass.

SULFIDES

	Weight %		Atomic %	
	3S005	3S114	3S005	3S114
S	38.61	37.97	53.17	52.52
Fe	58.56	59.61	46.29	47.34
Cu	0.18	0.00	0.12	0.00
Ni	0.40	0.15	0.30	0.11
Co	0.13	0.04	0.10	0.03
Zn	0.03	0.00	0.02	0.00
Total	97.904	97.767		

3S005 10μm rounded pyrrhotite inclusion in opx.
3S114 15μm rounded pyrrhotite inclusion in ilmenite.

Table 4.6: Microprobe analyses of micas and sulfides found in rocks from the study area. High F contents of the micas indicates a deuteric origin. Sulfide inclusions probably represent the effects of local saturation of the melt with sulfur (Bacon, 1989).

5. ESTIMATES OF INTENSIVE VARIABLES

5.1 Fe-Ti Oxide Temperatures and Oxygen Fugacities

Temperatures and oxygen fugacities for equilibrium pairs of titanomagnetite-ilmenite were derived according to the method of Buddington and Lindsley (1964), using the recalculation procedure of Carmichael (1967) to account for the distribution of minor components (table 5.1). Temperatures and oxygen fugacities were also calculated from the solution model of Ghiorso and Sack (1991). The Ghiorso and Sack solution model accounts for the significant variations in thermodynamic parameters that are produced by nonideal mixing of minor components in the spinel structure, which have not been accounted for in previous solution models for Fe-Ti oxide geothermometry (e.g. Anderson and Lindsley, 1988).

Temperatures derived from Buddington and Lindsley (1964) are plotted against temperatures from Ghiorso and Sack (1991) in figure 5.1. Most of the temperatures derived from Ghiorso and Sack (1991) are within 30°C of the temperatures derived from Buddington and Lindsley (1964), which corresponds to the 1σ analytical uncertainty reported by Buddington and Lindsley (1964). Calculated differences in temperatures of >30°C are restricted to some Broken Top series pyroclastic units, which also have titanomagnetite-ilmenite Mg/Mn ratios that are close to the 2σ limits of equilibrium (Bacon and Hirschmann, 1988). However, the temperatures calculated for these two units using the method of Ghiorso and Sack are unreasonably low (<750°C), based on the lack of low temperature phases (i.e., sanidine and quartz) in these units. This may indicate that temperature-fO_2 equilibria relationships in Ghiorso and Sack's formulations are more sensitive to disequilibriation effects at low temperatures. Fe-Ti oxide temperatures and oxygen fugacities determined from Buddington and Lindsley's calibration curves will be used in this study, as these temperatures correspond more closely to the observed modal mineralogies in silicic rocks from the study area.

Temperatures and oxygen fugacities for equilibrium titanomagnetite-ilmenite pairs are plotted in figure 5.2. Equilibrium data are limited in this study, but several important trends can be recognized. Most of the samples plot within the field of orthopyroxene-bearing silicic rocks recognized by Carmichael and others (1974), which correlates with the 2-pyroxene mineralogy found in most of the studied rocks. Broken Top rhyolites that plot within the orthopyroxene field, however, contain phenocrysts of amphibole along with orthopyroxene. These amphibole-bearing rhyolites either had oxygen fugacities that were lower, or temperatures that were higher, than found in the orthopyroxene-amphibole field of Carmichael and others (chapter 6, 1974). In addition, Three Sisters rhyolites had oxygen fugacities that were significantly higher than Broken Top rhyolites (figure 5.2), and plot near the amphibole-biotite field or in the extrapolated ortho-pyroxene-amphibole field.

Titanomagnetite		Mols Usp	Mols Mgt	Mols X +++	Mol% Usp	Ilmn	Mols Ilmn	Mols Hem	Mol% R2O3	Buddington & Lindsley (1964) T(°C)	fO₂	Ghiorso & Sack (1991) T(°C)	fO₂
3S005* Avg (2)	R	0.154	0.286	0.289	35.0	(4)	0.62	0.05	7.04	780	−14.9	743	−15.92
3S028* Avg (6)	A	0.179	0.267	0.269	40.1	(3)	0.55	0.11	16.97	960	−10.4	1012	−9.47
3S058 50μ, euhed	h	0.108	0.336	0.339	24.3	(1)	0.53	0.12	18.44	825	−12.3	864	−11.46
3S079* Avg (2)	D	0.180	0.274	0.277	39.7	(2)	0.56	0.11	16.49	965	−10.4	1016	−9.37
3S098* Avg (3)	R	0.220	0.233	0.236	48.6	(1)	0.61	0.06	8.39	885	−12.7	862	−13.35
3S114 50μ fresh	h	0.122	0.327	0.330	27.1	(1)	0.53	0.13	19.68	900	−11.1	917	−10.47
3S123* Avg (2)	d	0.185	0.265	0.268	41.1	(2)	0.57	0.09	13.86	925	−11.4	964	−10.54
3S134* Avg (2)	d	0.232	0.204	0.208	53.2	(1)	0.61	0.05	7.58	910	−12.4	872	−13.41
3S137* Avg (2)	d	0.251	0.197	0.201	56.0	(2)	0.60	0.07	10.51	1005	−10.6	988	−10.90
BP* Avg (7)	H	0.183	0.259	0.263	41.4	(2)	0.62	0.04	6.12	820	−14.2	738	−16.59
Lava Is* Avg (2)	H	0.142	0.299	0.303	32.1	(1)	0.58	0.08	12.03	830	−13.0	833	−13.11

Table 5.1: Average compositions of Fe-Ti oxides used in calculations. End-member compositions calculated using the procedure of Carmichael (1967), and the number of samples averaged for each calculation shown in parantheses. Temperatures and oxygen fugacities for equilibrium Fe-Ti oxide pairs calculated from the curves of Buddington & Lindsley (1964), and the solution model of Ghiorso & Sack (1991).
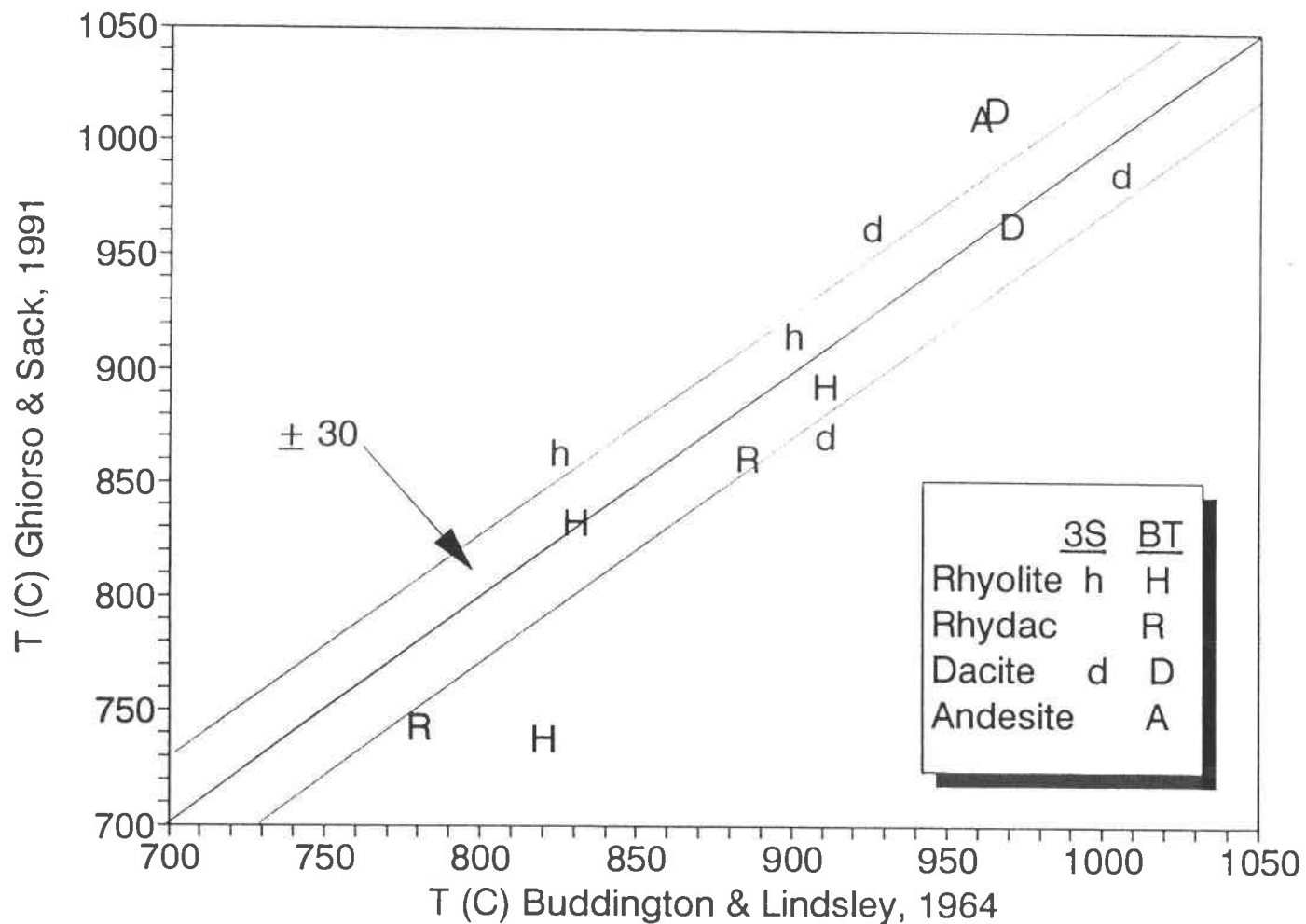
Figure 5.1: Temperatures for titanomagnetite-ilmenite pairs. Temperatures determined through the solution model of Ghiorso and Sack (1991) plotted against temperatures determined from the experimental curves of Buddington and Lindsley (1964). Error field of ± 30°C corresponds to reported 1σ error for each method.
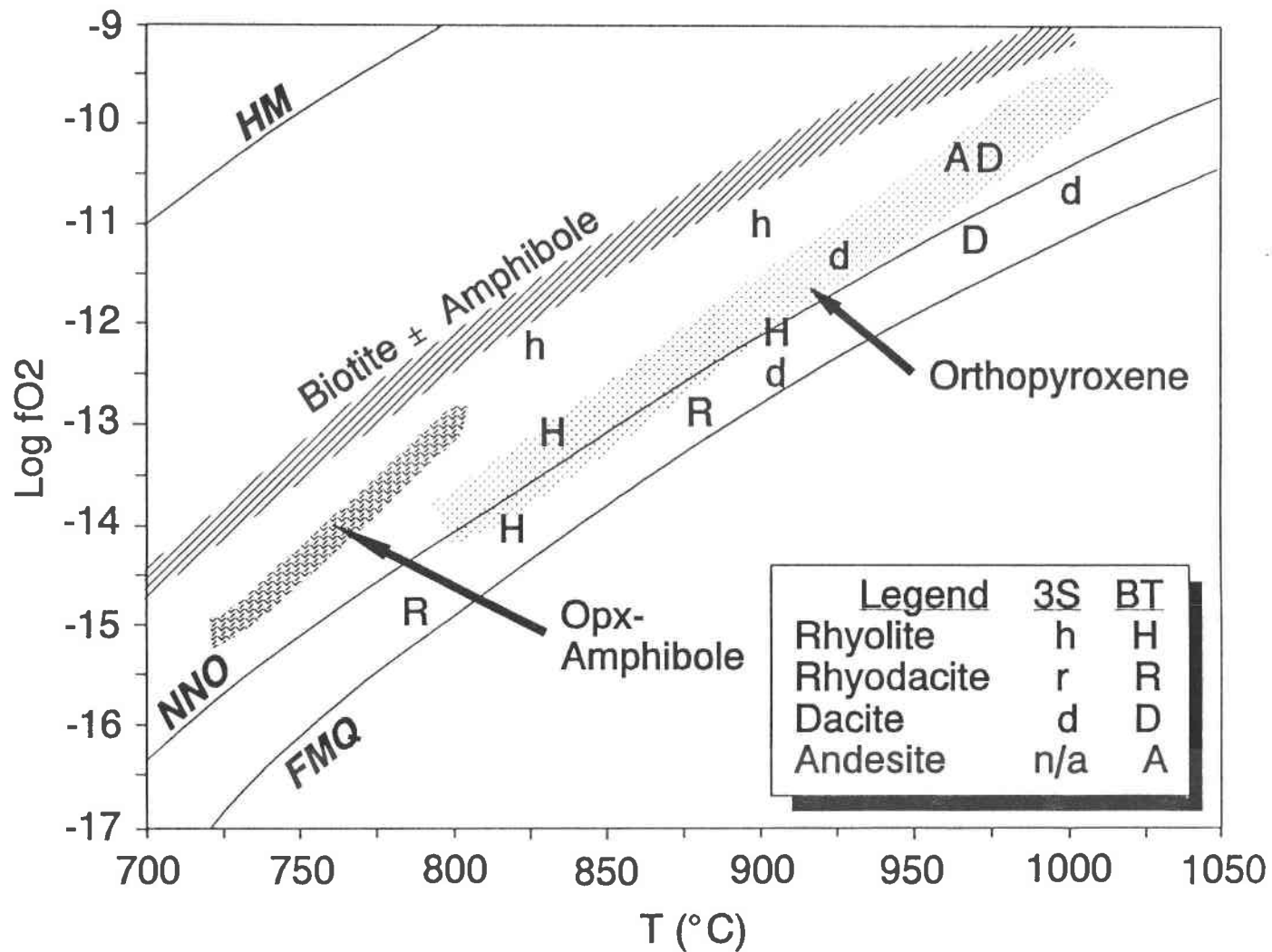
Figure 5.2: Temperatures and oxygen fugacities for titanomagnetite-ilmenite pairs. T and fO$_2$ data derived from the curves of Buddington and Lindsley (1964). Fields of orthopyroxene, opx-amphibole and biotite ± amphibole stability from Carmichael et al., 1974.

5.2 2-Pyroxene Geothermometry

Many of the analyzed units with $SiO_2 > 55\%$ contain phenocrysts of both clinopyroxene and orthopyroxene. Pyroxene phenocrysts in these units are commonly subhedral to euhedral with fresh, nonreacted rims, indicating equilibrium crystallization between the two pyroxenes. Rocks with visibly equilibrated pyroxenes are appropriate for use in pyroxene geothermometry.

Pyroxene thermometry is based on the relationship that with increasing temperature, the Ca content of clinopyroxenes (i.e. augite) generally decreases while the Ca content of orthopyroxene or pigeonite increases (Lindsley, 1983). Relatively simple graphical and solution models (e.g. Wood and Banno, 1973) have been developed into experimentally constrained thermodynamic solution models (Davidson and Lindsley, 1985). The Davidson and Lindsley (1985) solution model is preferred as it accounts for the effect of pressure on calculated temperatures ($\approx 8°C$/kbar), and for the effects of minor components (esp. Ti and Al) on the activities of Wollastonite (Wo), Enstatite (En), and Ferrosilite (Fs).

Major element pyroxene analyses are recalculated into mol percent Wo, En, and Fs using the projection of Lindsley and Anderson (1983), which accounts for the distribution of the minor components Ti, Al, Cr, Mn, and Na. Lindsley (1983) observed that only pyroxenes with Wo + En + Fs ≥ 90% are suitable for use in 2-pyroxene geothermometry. Numerous pyroxenes analyzed for this study that had $Al_2O_3 \geq 2.5$ wt.% or $TiO_2 \geq 0.8\%$ (Appendix C-2) had Wo + En + Fs ≤ 90% and were thus not suitable for pyroxene thermometry calculations.

Lindsley (1983) observed an analytical + experimental error of ± 50°C for pyroxenes with ≤ 2 mol% minor components, with an increase in error of + 5°C for each mol percent increase in minor components. These errors also apply to the solution model of Davidson and Lindsley (1985). There is also a pressure dependence of ≤ 8°C/kbar for the Davidson and Lindsley (1985) pyroxene geothermometer. Whereas total pressure is a poorly constrained intensive variable for the systems in this study, it seems reasonable to assume that most of the phenocrysts in the studied rocks crystallized between 5 kbars (rhyolites?) to 10 kbars (andesites?) total pressure. Temperatures calculated from the Davidson and Lindsley (1985) solution model, using estimated pressures of 5 kbars and 10 kbars, are shown in table 5.2, along with appropriate estimated uncertainties and pyroxene compositions. An increase of 5 kbars in estimated pressure generally results in an increase of ≈30°C in temperature, which is always less than the ±50°C analytical error (table 5.2). Reasonable (i.e. ± 5 kbars) variations in total pressure will not significantly change the temperatures calculated from this model.

The Davidson and Lindsley (1985) solution model uses the measured augite composition to iteratively calculate the temperature and low-Ca pyroxene composition that should be in equilibrium with the analyzed augite. Relative equilibration between augite and coexisting orthopyroxene or pigeonite can thus be evaluated by comparing the Wo and En abundances calculated by the solution

Sample	Pair	Augite (mol%) En	Wo	Others	Opx (mol%) En	Wo	Others
3S003 avg & c	Cpx-Opx	48.1	38.2	9.0	73.1	3.1	5.7
3S005	Cpx-Opx	39.3	39.1	6.7	53.6	3.2	3.1
3S009	Cpx-Opx	40.6	40.6	5.6	57.2	3.0	3.3
3S028 avg & c-core	Cpx-Opx	47.4	38.6	9.7	68.3	2.9	6.0
3S030	Cpx-Opx	46.4	36.6	7.4	69.2	4.3	4.3
3S036	Cpx-Opx	47.5	39.2	9.1	69.5	3.5	5.4
3S045	Cpx-Opx	45.5	35.7	9.3	71.4	4.1	4.1
3S061 orthopyroxene	Cpx-Opx	46.7	39.2	8.4	71.2	2.8	4.9
3S061 pigeonite	Cpx-Pig	46.7	39.2	8.4	51.2	11.0	3.9
3S079 c rim & avgs	Cpx-Opx	49.0	37.6	5.4	68.9	3.0	5.8
3S090c w/ a-core	Cpx-Opx	45.1	41.2	7.2	73.1	3.5	8.3
3S090c w/ a-rim	Cpx-Opx	45.1	41.2	7.2	69.6	3.7	5.0
3S098 glomero opx	Cpx-Opx	35.4	40.1	5.0	51.3	3.6	3.9
3S098 phenocrysts	Cpx-Opx	35.4	40.1	5.0	48.7	3.6	3.7
3S112 opx-C rim	Cpx-Opx	45.5	35.5	8.9	58.3	4.0	3.8
3S112 phenocrysts	Cpx-Opx	45.5	35.5	8.9	69.7	3.7	4.8
3S112 pigeonite	Cpx-Pig	45.5	35.5	8.9	50.9	17.3	4.2
3S115 phenocrysts	Cpx-Opx	45.2	38.6	7.7	65.8	3.2	4.1
3S115 pigeonite	Cpx-Pig	45.2	38.6	7.7	51.8	11.1	3.4
3S123 glomerocryst	Cpx-Opx	45.0	40.0	8.2	68.4	3.2	4.7
3S123 phenocrysts	Cpx-Opx	46.5	39.3	8.9	67.6	3.4	4.4
3S131 pigeonite	Cpx-Pig	42.9	35.6	6.7	55.7	11.0	3.7
3S134	Cpx-Opx	38.8	38.1	7.2	54.0	3.4	4.1
3S137	Cpx-Opx	44.3	39.3	9.7	62.5	3.5	6.0
3SXPB	Cpx-Opx	44.2	38.9	8.2	41.2	2.9	7.5
3SXBPa rim & avg	Cpx-Opx	45.8	38.2	8.8	41.2	2.9	7.5
Lava Island	Cpx-Opx	42.9	39.3	9.8	40.4	3.1	6.8

Sample	5 kbars En	Wo	T(°C)	10 kbars En	Wo	T(°C)	Error ±1σ	B&L T(°C)
3S003 avg & c	73.9	3.4	1098	74.3	3.6	1129	69	
3S005	57.2	3.0	960	57.8	3.1	988	55	780 ± 30
3S009	60.2	2.6	922	60.9	2.6	949	57	
3S028 avg & c-core	73.0	3.3	1078	73.4	3.4	1109	70	960 ± 30
3S030	69.3	3.8	1116	69.6	4.0	1149	61	
3S036	73.8	3.1	1062	74.2	3.2	1092	67	
3S045	66.9	4.0	1125	67.2	4.2	1159	61	
3S061 orthopyroxene	72.2	3.1	1051	72.7	3.2	1081	64	
*3S061 pigeonite	68.1	6.9	1013	68.4	7.1	1026	60	
3S079 c-rim & avgs	74.9	3.6	1125	75.2	3.8	1156	69	965 ± 30
*3S090c w/ a-core	70.3	2.4	959	70.9	2.5	987	81	
*3S090c w/ a-rim	70.3	2.4	959	70.9	2.5	987	65	
*3S098 glomero opx	49.4	2.7	881	50.0	2.7	906	59	
*3S098 phenocrysts	49.4	2.7	881	50.0	2.7	906	59	885 ± 30
3S112 opx-c rim	66.7	4.1	1129	67.0	4.2	1163	59	
3S112 phenocrysts	66.7	4.1	1129	67.0	4.2	1163	64	
*3S112 pigeonite	61.9	9.8	1095	62.0	9.9	1107	61	
3S115 phenocrysts	68.8	3.2	1049	69.3	3.3	1080	60	
*3S115 pigeonite	64.7	7.3	1014	64.9	7.5	1026	57	
3S123 glomerocryst	69.4	2.8	1002	70.0	2.9	1031	64	
3S123 phenocrysts	71.9	3.1	1046	72.4	3.2	1075	62	925 ± 30
*3S131 pigeonite	57.7	9.6	1065	57.9	9.8	1076	58	
3S134	55.9	3.3	984	56.5	3.4	1013	60	910 ± 30
3S137	67.5	3.0	1016	68.1	3.1	1046	70	1005 ± 30
*3SXBP	67.0	3.1	1027	67.6	3.2	1057	78	820 ± 30
*3SXBPa rim & avgs	69.6	3.4	1069	70.1	3.5	1099	78	820 ± 30
*Lava Island	64.6	3.0	998	65.2	3.1	1027	74	830 ± 30

Table 5.2: 2-pyroxene thermometry (Davidson and Lindsley, 1985). *Sample = pyroxene pairs out of equilibrium, B&L = temperatures using curves of Buddington and Lindsley (1964). See text for additional explanations of data.

model for the low Ca pyroxene with the measured Wo and En abundance. Most of the calculated compositions are within ± 0.5 mol% Wo and ± 5 mol% En of the measured Wo and En abundances (table 5.2), which corresponds to the qualitative limits of "equilibrium" of the Davidson and Lindsley (1985) model. Pyroxene pairs that are apparently out of equilibrium fall into two groups: calculated En contents that are higher than measured En (9113, 9113a, MTT, LI, 65p, 112p, 115p), or calculated Wo contents that are lower than measured Wo (all pigeonite samples and 90c, 90r, 98, 98g). These samples do not yield accurate temperatures, and are not used in the following discussions. In addition, naturally occurring pigeonites with the same En contents as the studied pigeonites (En_{51} to En_{56}) are stable at temperatures greater than $\approx 1000°C$ (Lindsley, 1983), which can thus be used as a minimum temperature for pigeonite-bearing rocks in this study.

5.3 Combined Estimates of Temperature

Equilibrium temperatures calculated from the 2-pyroxene thermometer of Davidson and Lindsley (1985) at 5 kbars pressure are equivalent within 1σ error limits to the corresponding Fe-Ti oxide temperatures of Buddington and Lindsley (1964) (column BL&, table 5.2) for most samples. Temperatures calculated from either the Fe-Ti oxide equilibration curves of Buddington and Lindsley or 2-pyroxene thermometer of Davidson and Lindsley are plotted against rock SiO_2 in figure 5.3; Fe-Ti oxide temperatures are preferred, as these temperatures are generally more precise than 2-pyroxene temperatures. The Fe-Ti oxide temperature for rhyodacite 3S005, however, is unreasonably low (780°); low temperature minerals such as sanidine and quartz, which are normative for this composition, are not observed. The 2-pyroxene temperature (960°C) is thus used for 3S005. Based on these limited data, there are no significant differences in temperature between the Broken Top and Three Sisters systems for rocks of similar composition. Temperatures are apparently continuous from $\approx 1150°C$ at 55% SiO_2 to $\approx 850°C$ at 74% SiO_2, although there is significant variation in temperature (± 50-75°C) for rocks of similar composition (figure 5.3). These temperatures should be viewed as good approximations, as many of the analyzed mineral pairs were out of equilibrium and additional microprobe analysis is needed before temperature relationships can be adequately described.

5.4 Estimates of Pressure

There are no mineralogical relationships in any of the studied rocks that are known to be uniquely pressure dependent. The Al content of calcic amphiboles has been proposed as an empirical geobarometer for silica saturated igneous rocks (e.g. Hammarstrom and Zen, 1986). This geobarometer may be reasonably accurate at temperatures of $\approx 750°C$ for calcic amphiboles in equilibrium with melt, fluid, biotite, quartz, sanidine, plagioclase, sphene and titanomagnetite (i.e.
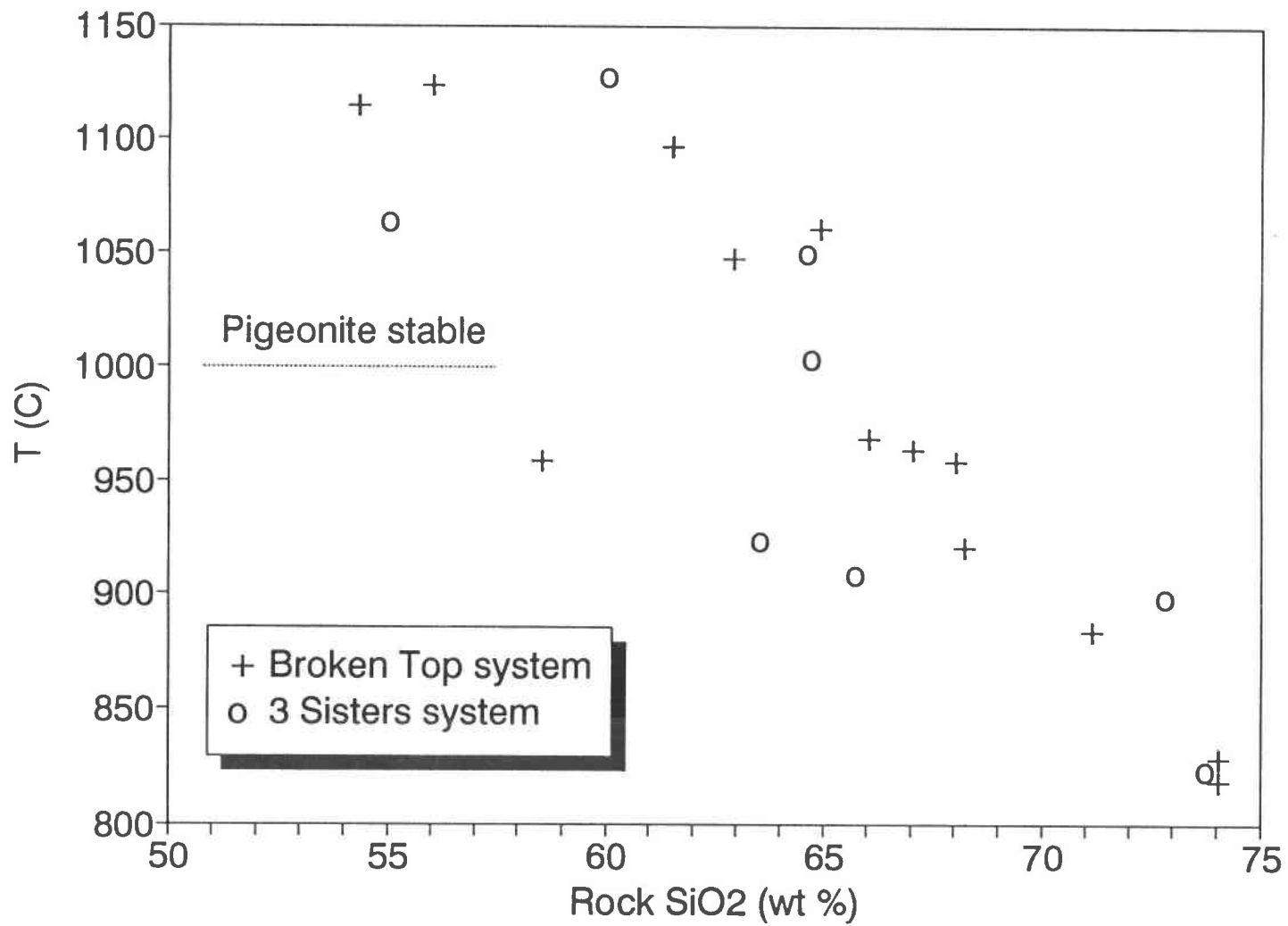
Figure 5.3: Temperatures calculated from Fe-Ti oxide or 2-pyroxene data plotted against silica content of the host rock. Approximate range of pigeonite stability from Lindsley (1983).

Johnson and Rutherford, 1989). High Cascade rhyolites lack many of these phases, indicating that the Al content of amphibole may not reflect an equilibrated, pressure-dependent condition. The Al-in-amphibole geobarometer is also strongly temperature dependent (Blundy and Holland, 1990), and has an associated error of ± 4 kbars when used with well-constrained temperature data.

The recent development of a thermodynamically constrained solution model of Al siting in amphibole by Blundy and Holland (1990) removes many of the mineralogical constraints imposed by the amphibole geobarometer of Hammarstrom and Zen (1986). This solution model is valid for plagioclase-bearing, silica saturated rocks, and is best applied as a geothermometer. Although the pressure dependence of the model is poorly constrained, independently determined temperatures may be applied to the model to derive estimates of total pressure (±4 kbars) (Blundy and Holland, 1990). The solution model was applied to amphibole-bearing silicic rocks in the study area, in an attempt to provide some limits on total pressure. Estimated temperatures from table 5.2, which have uncertainties of at least ± 50°C, were used in the model, along with the upper and lower limits of Si found in the amphiboles of each unit (table 5.3). Calculated pressures ranged from -2 ± 4 kbars to 6 ± 4 kbars (figure 5.4), and serve only to indicate that the magmas probably equilibrated last at upper to middle crustal levels.

Pressures calculated for amphiboles with excess Al are no greater than those calculated for amphiboles from the same unit that lack excess Al (figure 5.4). This relationship supports the previous hypothesis (Chapter 4.5) that the excess Al in some amphiboles was not produced through higher pressure or higher temperature crystallization; increasing the estimated crystallization temperature of the excess Al amphiboles would have the effect of lowering the calculated pressure, and it is not intuitive why potentially higher pressure crystallization should have occurred at lower temperature (i.e. 750°C).

Amphiboles from Broken Top system rhyolites cluster at 2 ± 2 kbars (figure 5.4), whereas Three Sisters amphiboles show a much wider range of calculated pressure (i.e. 2 ± 4 kbars). Three Sisters amphiboles that are magnesio-hornblendes also have consistently lower pressures than other amphiboles (table 5.3). The magnesio-hornblendes may have crystallized at a temperature lower than 850°C; when the estimated temperature of these amphiboles is lowered to 750°C, their calculated pressures are comparable to other Three Sisters amphiboles. Whereas the excess Al in some amphiboles may be an artifact of the method used to calculate Fe^{3+}/Fe^{2+} (Spear and Kimball, 1984), the magnesio-hornblendes may represent a lower temperature stage of crystallization in some Three Sisters rhyolites.

Rocks from the study area can be compared to other calc-alkaline systems that have experimentally constrained phase relationships. If a magma system is evolving primarily through crystal fractionation, then the fractionating assemblage will reflect the temperature, pressure and composition of the system. The effects of pressure and water content on phase relationships of

	Si	Al$_{VI}$	T °C	X$_{ab}$	P kbars	Label	Amphibole type
3S009 core	6.46	0.09	900	0.69	0.6	9	Magnesian Hastingsitic Hornblende
3S053-A 250μm core	6.53	0.26	850	0.65	2.3	53A	Edenitic Hornblende
3S053-A rim	6.42	0.03	850	0.65	3.2	53a	Magnesian Hastingsitic Hornblende
3S053-B 100μm	7.04	0.01	850	0.65	-2.4	53B	Magnesio-Hornblende
3S053-B rim	6.89	0.26	850	0.65	-0.9	53b	Edenite
3S053-C 200μm core	6.62	0.27	850	0.65	1.6	53C	Edenitic Hornblende
3S053-C rim	6.54	0.26	850	0.65	2.2	53c	Edenitic Hornblende
3S053-D 100μm	6.74	0.08	850	0.65	0.5	53*	Magnesio-Hornblende
3S053-E 50μm FRAG rim	6.69	0.07	850	0.65	1.0	53	Magnesio-Hornblende
3S060-A 250μm core	6.27	0.31	850	0.65	4.4	60A	Pargasitic Hornblende
3S060-A rim	6.08	0.07	850	0.65	5.9	60a	Magnesio-Hastingsite
3S060-B 200μm FRAG	6.29	0.07	850	0.65	4.2	60*	Magnesio-Hastingsitic Hornblende
3S060-C 250μm core	6.22	0.05	850	0.65	4.8	60C	Magnesio-Hastingsite
3S060-C rim	6.24	0.07	850	0.65	4.6	60c	Magnesio-Hastingsite
3S060-D >250μm core	7.01	0.04	850	0.65	-2.0	60D	Magnesio-Hornblende
3S060-D rim	7.02	0.05	850	0.65	-2.1	60d	Magnesio-Hornblende
3S060-E 200μm FRAG	6.88	0.08	850	0.65	-0.8	60	Magnesio-Hornblende
3S090 glomero	6.16	0.06	1000	0.5	2.5	90	Magnesio-Hastingsite
3S090a 2ND POINT	6.29	0.17	1000	0.5	1.4	90a	Pargasitic Hornblende
3S090a glomero	6.18	0.08	1000	0.5	2.3	90a	Magnesio-Hastingsite
BP LRZ-A >250μm core	6.41	0.07	850	0.76	2.1	lA	Magnesian Hastingsitic Hornblende
BP LRZ-A rim	6.47	0.06	850	0.76	1.6	la	Magnesian Hastingsitic Hornblende
BP LRZ-B >250μm core	6.48	0.03	850	0.76	1.5	lB	Magnesian Hastingsitic Hornblende
BP LRZ-B rim	6.45	0.05	850	0.76	1.8	lb	Magnesian Hastingsitic Hornblende
BP LRZ-C core	6.46	0.04	850	0.76	1.7	lC	Magnesian Hastingsitic Hornblende
BP LRZ-C rim	6.26	0.09	850	0.76	3.3	lc	Magnesian Hastingsitic Hornblende
BPB-A core	6.23	0.08	850	0.76	3.5	bA	Magnesian Hastingsitic Hornblende
BPB-A rim	6.31	0.08	850	0.76	2.9	ba	Magnesian Hastingsitic Hornblende
BPB-B 200μm core	6.34	0.08	850	0.76	2.7	bB	Magnesian Hastingsitic Hornblende
BPB-B rim	6.45	0.06	850	0.76	1.8	bb	Magnesian Hastingsitic Hornblende
BPB-C 250μm core	6.39	0.09	850	0.76	2.3	bC	Magnesian Hastingsitic Hornblende
BPB-C rim	6.29	0.06	850	0.76	3.0	bc	Magnesian Hastingsitic Hornblende
BPB-D >250μm core	6.24	0.06	850	0.76	3.4	bD	Magnesian Hastingsitic Hornblende
BPB-D rim	6.29	0.09	850	0.76	3.0	bd	Magnesian Hastingsitic Hornblende
BPB-E core	6.36	0.06	850	0.76	2.5	b	Magnesian Hastingsitic Hornblende
BPT-A core	6.52	0.04	850	0.76	1.2	BA	Magnesian Hastingsitic Hornblende
BPT-A rim	6.45	0.07	850	0.76	1.8	Ba	Magnesian Hastingsitic Hornblende
BPT-B >250μm core	6.37	0.05	850	0.76	2.4	BB	Magnesian Hastingsitic Hornblende
BPT-B rim	6.35	0.05	850	0.76	2.6	Bb	Magnesian Hastingsitic Hornblende
BPT-C core	6.29	0.05	850	0.76	3.0	BC	Magnesian Hastingsitic Hornblende
BPT-C rim	6.48	0.26	850	0.76	1.5	Bc	Edenitic Hornblende
BPT-D core	6.31	0.05	850	0.76	2.9	BD	Magnesian Hastingsitic Hornblende
BPT-D rim	6.33	0.08	850	0.76	2.7	Bd	Magnesian Hastingsitic Hornblende
LI-A 200μm core	6.46	0.02	850	0.75	1.8	LA	Magnesian Hastingsitic Hornblende
LI-A rim	6.45	0.10	850	0.75	1.9	La	Magnesian Hastingsitic Hornblende
LI-B >250μm core	6.39	0.04	850	0.75	2.4	LB	Magnesian Hastingsitic Hornblende
LI-B rim	6.49	0.24	850	0.75	1.6	Lb	Edenitic Hornblende
LI-C >200μm core	6.34	0.08	850	0.75	2.8	LC	Magnesian Hastingsitic Hornblende
LI-C rim	6.29	0.09	850	0.75	3.1	Lc	Magnesian Hastingsitic Hornblende

Table 5.3: Estimated pressures of crystallization of amphibole-bearing rocks, using the geobarometer of Blundy and Holland (equation 5, 1990). All pressures have a minimum uncertainty of ± 4 kbars. Si and Al(VI) cation abundances calculated from Spear and Kimball (1984) (Appendix C-5), estimated temperatures from table 5.2, mol fraction albite from table 4.1, and amphibole types from Leake (1978).
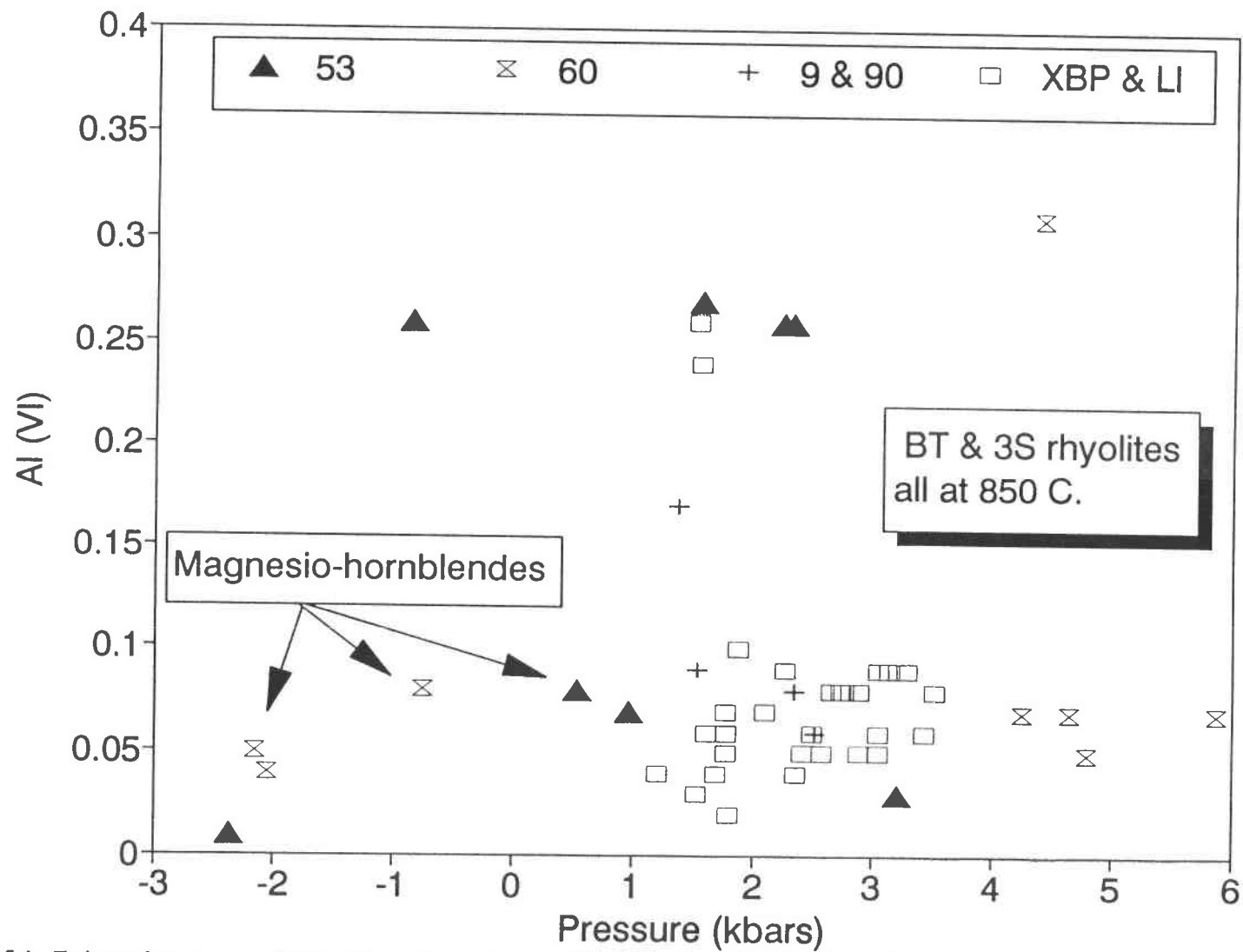
Figure 5.4: Estimated pressures calculated from the solution model of Blundy and Holland (1990) for the Al content of amphibole. Amphibole data described in text and given in table 5.3. Al(VI) calculated from the method of Spear and Kimball (1984).

calc-alkaline rocks from the oceanic part of the Aleutian arc have been investigated by Baker and Eggler (1983, 1987). Because the mafic systems in the High Cascades and Aleutians have similar compositions (calc-alkaline, parental high alumina basalt) and range of temperatures, the pressure-dependent phase relationships determined on the Aleutian system should be applicable to the High Cascades system. However, the following chapter on mafic petrogenesis will show that differentiation of the High Cascades mafic system involved significant amounts of silicic magma mixing, which could potentially alter the phase relationships between the High Cascades and Aleutian systems.

Using the pseudo-ternary phase projections from Baker and Eggler (1983), mafic rocks from this part of the High Cascades plot (figure 5.5) close to the anhydrous 8 kbar phase boundaries of Baker and Eggler (1983, 1987). Andesites and dacites plot between the 8 kbar and 5 kbar-2% H_2O boundaries. Extrapolation of the 5 kbar-2% H_2O boundary to mafic compositions (cf., Baker, 1987) also indicates that the High Cascade mafic magmas may have contained <2% H_2O, although it is possible that higher water contents (>2% H_2O) combined with higher pressures (>8 kbars) might result in similar phase relationships. These data suggest that the evolution of High Cascade mafic magmas probably occurred at deep crustal levels (30-40 km) and relatively low water contents (≤2% H_2O).

5.5 Estimates of Water Content

Although water content is an extensive variable, it is rarely measured directly and must be estimated by comparison with experimental systems. This part of the High Cascades is character-ized by an anhydrous mineral assemblage from basalt to rhyodacite, with trace amounts of amphibole in most rhyolites (chapter 4). In contrast, andesites, dacites and rhyodacites at Mt. Mazama contain significant amounts of amphibole, which probably indicates a relatively higher H_2O content (Bacon and Druitt, 1988).

5.5.1 Amphibole equilibria

Magmas that were in presumed equilibrium with plag + opx + cpx can be used to infer H_2O contents by comparison with the experimental data of Merzbacher and Eggler (1984) for Mt. St. Helens andesites and dacites. These experiments were run between 1 atm. and 4 kbars, and show that amphibole saturation occurs at higher water contents at both higher pressures and temperatures. Andesites, dacites and rhyodacites from the study area generally plot (figure 5.6) in the area of ≥4% H_2O, but at water contents below the amphibole stability field. The lack of amphibole phenocrysts in rocks that plot close to or within the amphibole stability field of Merzbacher and Eggler (1983) suggests that crystallization might have occurred at pressures > 4 kbars, which would shift the amphibole stability field away from the opx apex. In contrast, rocks
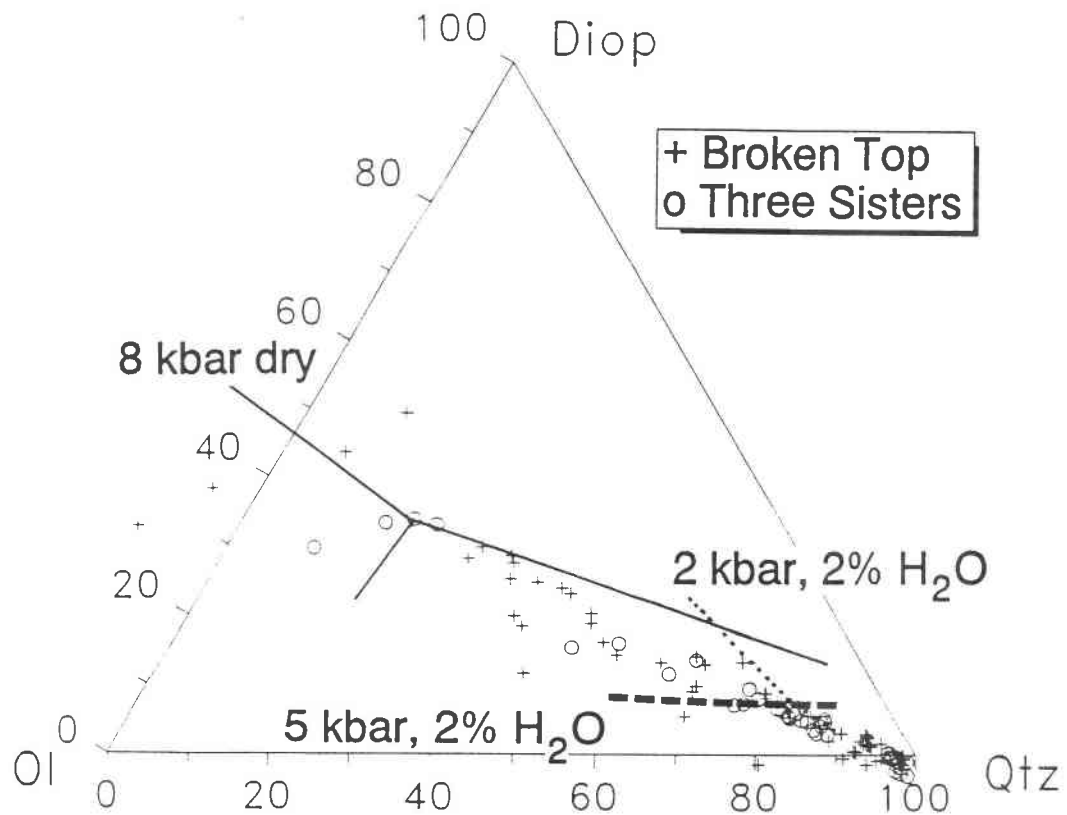
Figure 5.5: Pseudoternary projection from plag + mgt of all High Cascade rocks from the study area, after Baker and Eggler (figure 1, 1983). Phase boundaries determined from melting experiments of Aleutian calc-alkaline arc rocks at 8 kbars anhydrous (solid line), 5 kbars, 2 wt% H_2O (dashed line), and 2 kbars, 2 wt% H_2O (dotted line), from Baker and Eggler (1983,1987). High Cascade mafic rocks plot near the 8 kbars anhydrous boundaries. Note that the mafic data plot above an extrapolated 5 kbars hydrous boundary; increasing pressure at constant water content would effectively raise this boundary towards the diopside apex. Mafic rocks may have thus evolved at pressures >8 kbars, if estimated water contents of 1-2 wt% are correct. Although the trend of the silicic data is toward lower pressures or higher water contents, more evolved compositions may reflect mixing between rhyolites and mafic rocks.
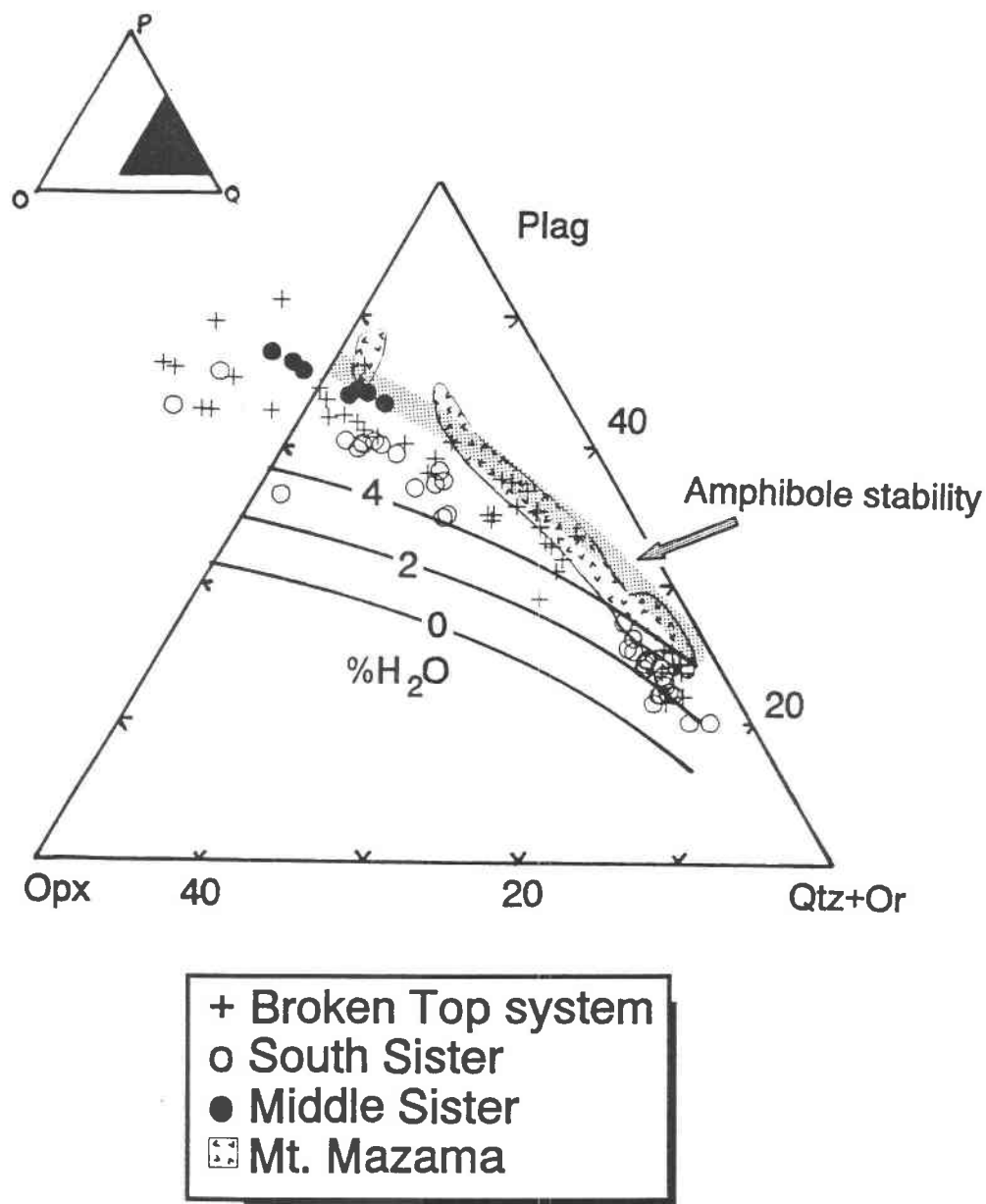
Figure 5.6: Intermediate and silicic rocks from the study area projected onto part of the plag-opx-qtz+or pseudoternary of Merzbacher and Eggler (figure 3, 1984). Projection is from diopside + mgt, and is modified from Baker and Eggler (1983) to include opx instead of ol. Contours = position of the opx-plag cotectic at a given melt H_2O content. Field of amphibole stability is for intermediate to silicic calc-alkaline rocks to 4 kbars pressure (Merzbacher and Eggler, 1984). Note that the trend of amphibole-bearing rocks from Mt. Mazama (Bacon and Druitt, 1988) corresponds to the amphibole stability field, but that rocks from the study area generally plot below the Mazama data and lack amphibole. Andesitic and dacitic magmas from Middle Sister (filled circles) had apparently higher water contents than similar rocks from South Sister (open circles).

from Mt. Mazama generally plot within the amphibole stability field (figure 5.6), contain significant amounts of amphibole, and are characterized by differentiation involving amphibole fractionation (Bacon and Druitt, 1988). Climactic rhyodacites from Mt. Mazama also plot at higher water contents than rhyolites from the study area, even though both groups contain amphibole phenocrysts (figure 5.6). Lower temperatures in the rhyolites would stabilize amphibole at lower water contents than in Mazama rhyodacites, although differences in pressure and composition should also control the stability of amphibole.

The composition of amphiboles from the study area is very similar to the composition of Mazama amphiboles (Druitt and Bacon, 1989) and amphiboles produced experimentally from Mt. St. Helens dacite (Rutherford and Devine, 1988). However, some of the amphiboles in the study area are more Mg-depleted (Mg' = $Mg/Mg + Fe^{2+} \approx 0.5$-$0.7$) than Mazama (Mg' ≈ 0.6-0.7) or Mt. St. Helens (Mg' ≈ 0.6-0.7) amphiboles. This relationship is consistent with the restriction of amphibole in the study area to silicic rhyodacites and rhyolites, and indicates that these magmatic systems are comparable.

5.5.2 Plagioclase equilibria

Plagioclase-melt equilibrium is a function of temperature, composition, and water content of the melt (Kudo and Weill, 1970; Housh and Luhr, 1991). Synthetic, 1 atm. relationships (Kudo and Weill, 1970) have been modified by experimental data on natural systems by Housh and Luhr (1991), who have developed albite and anorthite exchange reactions between plagioclase and melt. These exchange reactions can be used to estimate the water content of the melt, if the temperature, pressure and plagioclase composition are known. The minimum uncertainties in estimated water contents derived from the exchange reactions are ±0.54 wt% for albite and ±0.33 wt% for anorthite.

The plagioclase exchange reactions were applied to representative samples from the study area, using the BASIC program TWATER from Housh and Luhr (1991). Variations in total pressure between 10 kbar and 3 kbar had no significant effect (±0.1 wt%) on calculated water contents, and estimated pressures of 8 kbars were used in all calculations. Uncertainties in temperature of ± 30°C, however, resulted in changes of ± ≈1 wt% in calculated water content. Water contents for South Sister rhyolite 3S114 (An_{41}, T=900°C) were (Ab) 2.8 ± 0.6 and (An) 2.9 ± 0.4 wt%, which corresponds to the water content derived from figure 5.6 (≈3%). Broken Top rhyolite 3SXBP (An_{24}, T=820°C) water contents were (Ab) 4 ± 1 and (An) 5 ± 1 wt%. Both Broken Top and Three Sisters rhyolites contain trace amounts of amphibole and project onto the same area in figure 5.6, and should have similar water contents (≈4%). Broken Top rhyodacite 3S009 (An_{38}, T=950°C), which contains a trace of amphibole, had calculated water contents of

(Ab) 3 ± 1 and (An) 4 ± 1 wt%, and dacite 3S115 (An$_{54}$) had lower water contents: (Ab) 1.6 ± 0.9, (An) 2.7 ± 0.8 wt%. South Sister dacite 3S123 (An$_{50}$, T = 925°C) had higher calculated water contents (Ab: 4.0 ± 0.7, An: 5.4 ± 0.6 wt%) than either Broken Top dacite or Middle Sister dacite 3S137 (An$_{45}$, T = 1000°C), (Ab) 2.5 ± 0.6, (An) 3.6 ± 0.5 wt%. However, Middle Sister dacites and andesites plot in an area of **higher** water content (figure 5.6) than South Sister andesites and dacites. The lower estimated temperature of SS dacite 3S123 may be in part responsible for the higher calculated water content in this unit. Application of the Housh and Luhr (1991) plagioclase exchange model to rocks in the study area is limited by the relatively large uncertainties in estimated temperature associated with these rocks.

Although andesites, dacites and rhyodacites from the study area probably contained ≥4% H_2O, amphibole was not stable in these melts and was not a fractionating phase. If these rocks evolved primarily through crystal fractionation, the parental mafic rocks must have been hydrous, and probably contained 1-2% H_2O (assuming H_2O is incompatible and >50% crystallization to derive andesite from high alumina basalt). Rhyolitic magmas probably contained 3-4% H_2O, and crystallized trace amounts of amphibole. Petrogenetic models developed in the following chapters must consider the effects of elevated pressure and water content, in relation to commonly used anhydrous, 1 atmosphere petrogenetic models.

6. GEOCHEMISTRY

6.1 Introduction

One hundred and twenty-seven High Cascade samples were analyzed with standard X-ray fluorescence and instrumental neutron activation analysis techniques for this study. Details of these analytical methods are in Appendix A, and geochemical analyses are listed in Appendix D. Analyzed elements and associated analytical errors are summarized in table 6.1. Analytical precision is primarily a function of the concentration of an element in the sample; higher concentrations give larger signals above background "noise", and thus result in more precise analyses. The range of the 1σ errors in table 6.1 combines errors due to the precision of the analytical technique with errors of accuracy in reproducing standard values.

The analyzed High Cascade samples are all younger than 720 ka, and were all produced under the same regional tectonic conditions. Ten rocks from the Deschutes Formation were also analyzed. These samples were discussed in Chapter 3, but are not included in the following geochemical models of High Cascade petrogenesis because they probably formed under different tectonic conditions than the late High Cascades (e.g., Priest et al., 1983). An additional 28 analyses of late High Cascade mafic to intermediate composition rocks from the Three Sisters area, which are from Hughes (1983, 1990), are also included in the data set used for geochemical modeling.

6.2 Terminology

The general classification of aphanitic calc-alkaline rocks is at times confusing and arbitrary, but is generally based on silica content and significant changes in modal mineralogy. The classification scheme used in this study (figure 6.1a) is a modification of the total alkali-silica variation diagram of Le Maitre (1984), which generally conforms to historical use of volcanic rock names in the Cascades and preserves petrologically significant distinctions between silicic rock types. The major difference between the classifications in this study (figure 6.1a) and Le Maitre (1984) is the addition of the term "rhyodacite" for rocks with 68-72% SiO_2. Rhyodacite is usually the most silicic rock at other Oregon High Cascade volcanos (Wise, 1969; Conrey, 1991; Bacon and Druitt, 1988), but higher silica rocks are common in the Three Sisters area. It is thus appropriate to reserve the term "rhyolite" for aphanitic calc-alkaline rocks with $\geq$72% SiO_2. In this study, mafic refers to rocks with $\leq$ 58% SiO_2 and silicic to rocks with >58% SiO_2.

6.3 General Major Element Trends

Quaternary rocks of the Three Sisters area form a typical calc-alkaline assemblage, following the widely accepted definitions of Peacock (1931) (figure 6.1b), and Irving and Barager (1971)

Element	Method	Range of 1σ analytical error[1]
SiO_2	XRF	± 0.5 wt%
TiO_2	XRF	± 0.05 wt%
Al_2O_3	XRF	± 0.5 wt%
FeO	XRF	± 0.3 wt%
MnO	XRF	± 0.01 wt%
MgO	XRF	± 0.05 wt%
CaO	XRF	± 0.1 wt%
Na_2O	XRF	± 0.1 wt%
K_2O	XRF	± 0.05 wt%
P_2O_5	XRF	± 0.01 wt%
Rb	XRF	3% – 3%
Ba	XRF	7% – 3%
Sr	XRF	3% – 3%
Cs	INAA	15% – 3%
Sc	INAA	3% – 3%
V	XRF	3% – 3%
Co	INAA	3% – 3%
Ni	XRF	5% – 10%
Cr	INAA	3% – 15%
Zn	INAA	10% – 6%
La	INAA	3% – 3%
Ce	INAA	4% – 3%
Nd	INAA	7% – 5%
Sm	INAA	3% – 3%
Eu	INAA	3% – 3%
Tb	INAA	4% – 3%
Yb	INAA	4% – 4%
Lu	INAA	3% – 3%
Zr	XRF	3% – 3%
Hf	INAA	4% – 3%
Ga	XRF	7% – 5%
Y	XRF	6% – 4%
Nb	XRF	10% – 5%
Ta	INAA	6% – 3%
Th	INAA	5% – 3%
U	INAA	6% – ≥20%

[1] Range of analytical error for mafic to silicic samples. Error incorporates counting statistics and accuracy in reproduction of standards during analytical runs. XRF accuracy determined through analyses of standard samples by W.S.U., U.S.G.S., and other labs.

Table 6.1: Summary of analytical methods and associated 1σ errors for mafic-to-silicic samples. XRF = X-ray fluorescence, INAA = instrumental neutron activation analysis. Details of analytical procedures are explained in Appendix A.
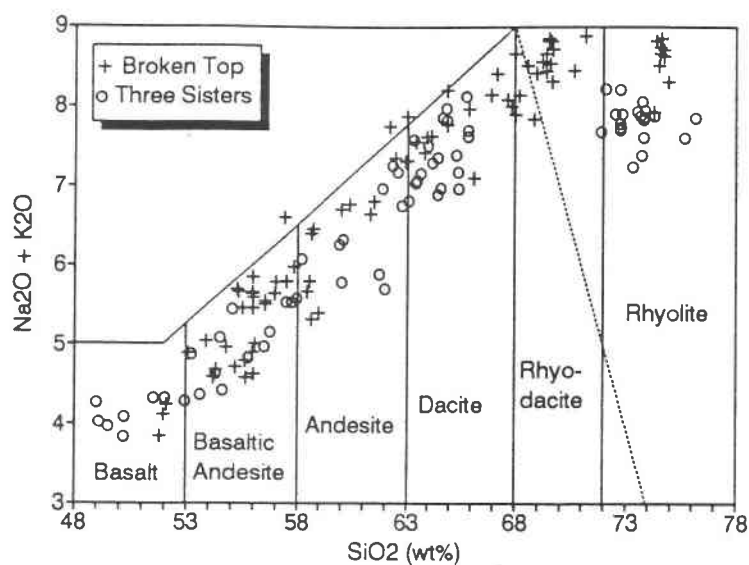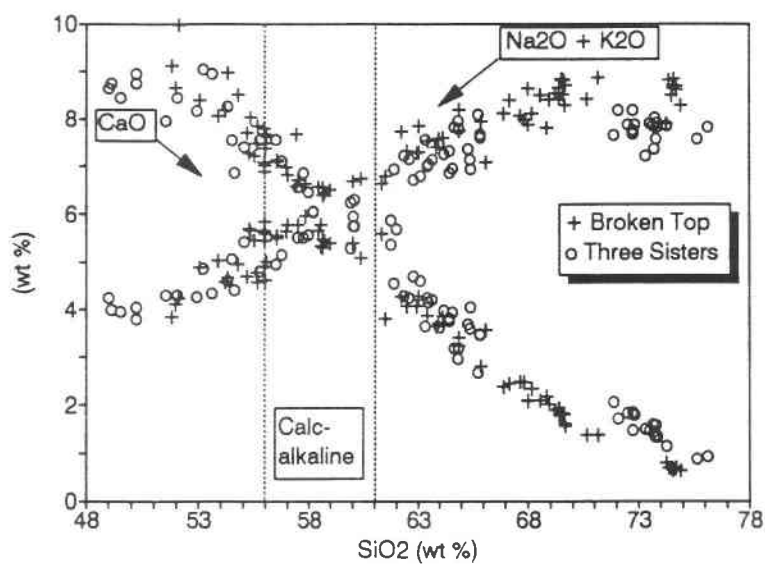
Figure 6.1: **A)** Total alkalies versus silicia classification diagram, modified from Le Maitre (1984). Dashed diagonal line represents original dacite-rhyolite boundary, which has been subdivided into a rhyodacite field. **B)** Peacock diagram showing variations in total alkalies and lime that intersect in the calc-alkaline field (dashed lines).

(figure 6.2a). Rocks from the study area are primarily metaluminous (molar $Al/Ca+Na+K \leq$ 1)(Shand, 1947), but some rhyolites are slightly peraluminous (molar $Al/Ca+Na+K = 1$-1.2) (figure 6.2b). Eight analyses of rhyodacitic to dacitic pumice from unconsolidated surficial deposits (3S001, 3S007, 3S014, 3S018, 3S024, 3S041, 3S044, 3S079) appeared strongly peraluminous but had low major element totals (98%-96%) and were anomalously low in alkalies due to hydration (Appendix D). These hydrated samples are not used in the following major element discussions, but will be included in models utilizing relatively immobile trace elements.

Major element variation diagrams in figure 6.3 provide useful first-order constraints on the petrogenesis of the Broken Top and Three Sisters magmatic systems, and define the key petrologic problems in the study area. Many inter-element variations are relatively well constrained from 76% to $\approx$58% SiO_2, but significantly less constrained from $\approx$58% to 48% SiO_2. In the most general sense, the mafic system appears to be more open (i.e. greater amounts of recharge, assimilation and mixing) than the silicic system.

Most of the 48% to 54% SiO_2 samples are from the Three Sisters system, as basalts are relatively uncommon in the Broken Top system. Studies of mafic magmatism by Hughes (1983, 1990), and Hughes and Taylor (1986) have not identified any spatial distinctions among Quaternary basalts from the Three Sisters to Mt. Jefferson area. Basalts and basaltic andesites from the Broken Top system plot within the same compositional range as mafic rocks from the Three Sisters system; there is no evidence to suggest that either magmatic system has compositionally distinct mafic rocks.

There is, however, a significant compositional gap in the Three Sisters system between 66% and 72% SiO_2, but the same interval in the Broken Top system shows continuous elemental variations (figure 6.3). A similar compositional gap was also recognized by Clark (1983) at South Sister volcano. There is also a small but significant compositional gap in the Broken Top system between 72% and 74% SiO_2. This compositional gap is not only expressed by a 2 wt% gap in SiO_2, but other major and trace element variations have a similar compositional gap between rhyodacites and rhyolites in the Broken Top system. I must emphasize that sampling throughout the study area focused on silicic rocks, and was guided by the detailed studies of Wozniak (1982), Clark (1983), Hughes (1983) and Taylor (1978, 1987, unpub. res.). It is thus extremely unlikely that the compositional gaps represent inadequate sampling of the silicic rock suite exposed at the surface.

Broken Top rhyolites often plot off of the trend defined by $\approx$65% to 72% SiO_2 Broken Top rocks. It will be shown that the 72% to 74% SiO_2 compositional gap in this system is petrologically significant. In contrast, Three Sisters rhyolites generally form linear trends from 72% to 76% SiO_2, which always project to more poorly defined trends at $\leq$65% SiO_2.

These observations of major element distributions define the main petrologic problems that will be addressed in this study:
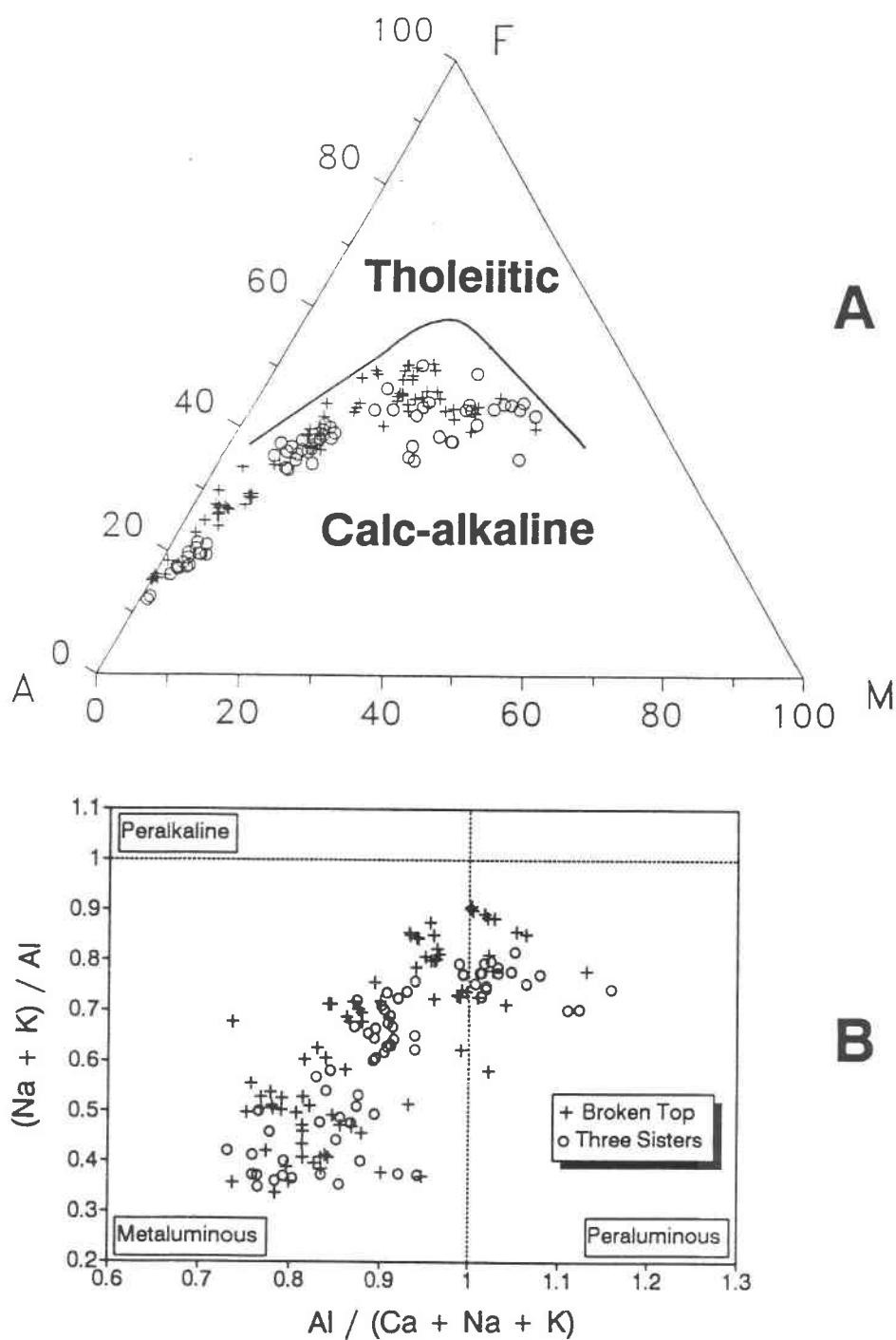
Figure 6.2: **A)** AFM diagram defining the boundary between tholeiitic and calc-alkaline series rocks, from Irving and Barager (1971). A = Na$_2$O+K$_2$O, F = FeO, M = MgO, all in weight percent. **B)** Alumina saturation diagram, after Shand (1947). The rocks that appear to be slightly peraluminous (i.e., corundum normative) are rhyolites.
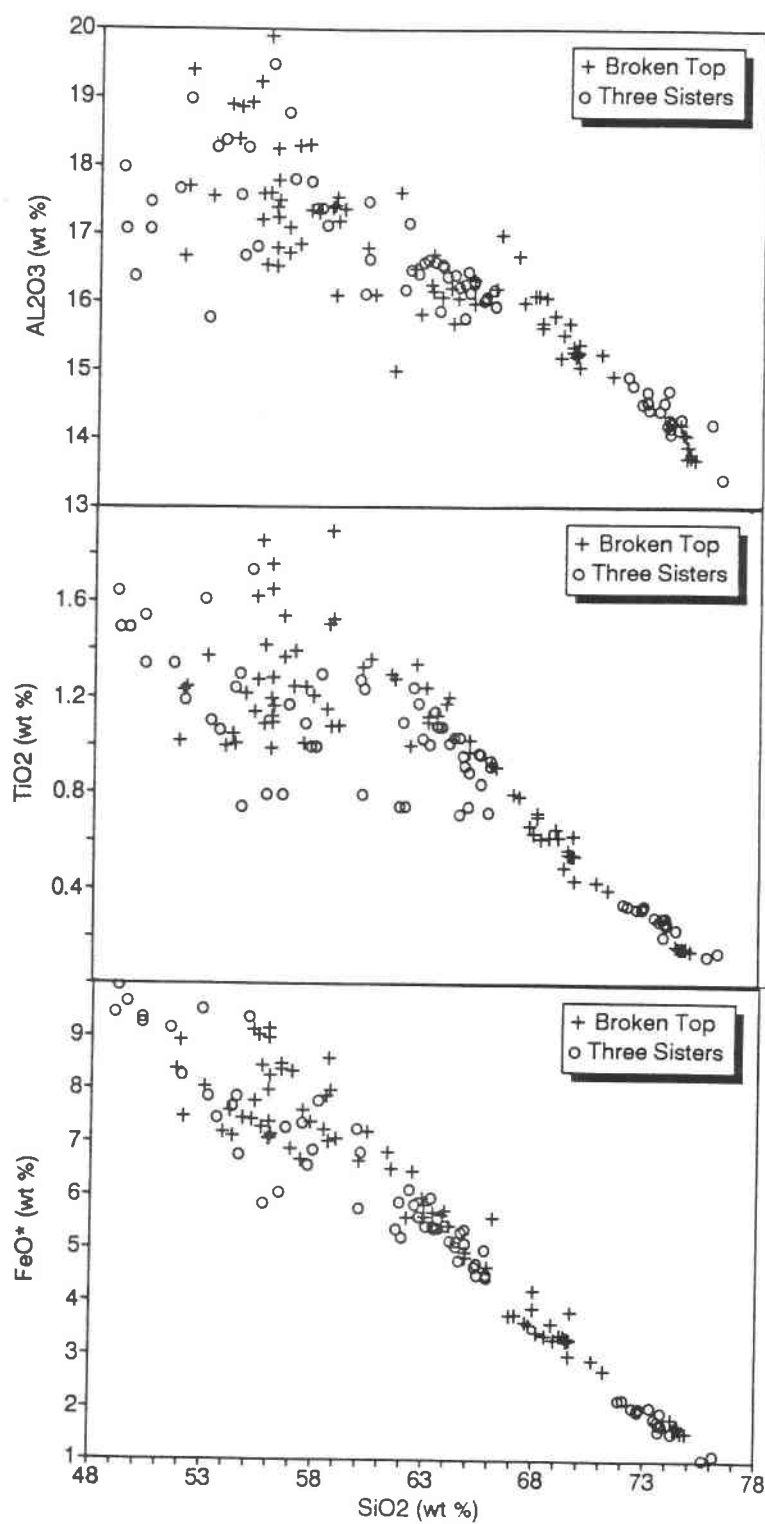
Figure 6.3: Major element-silica variation diagrams.
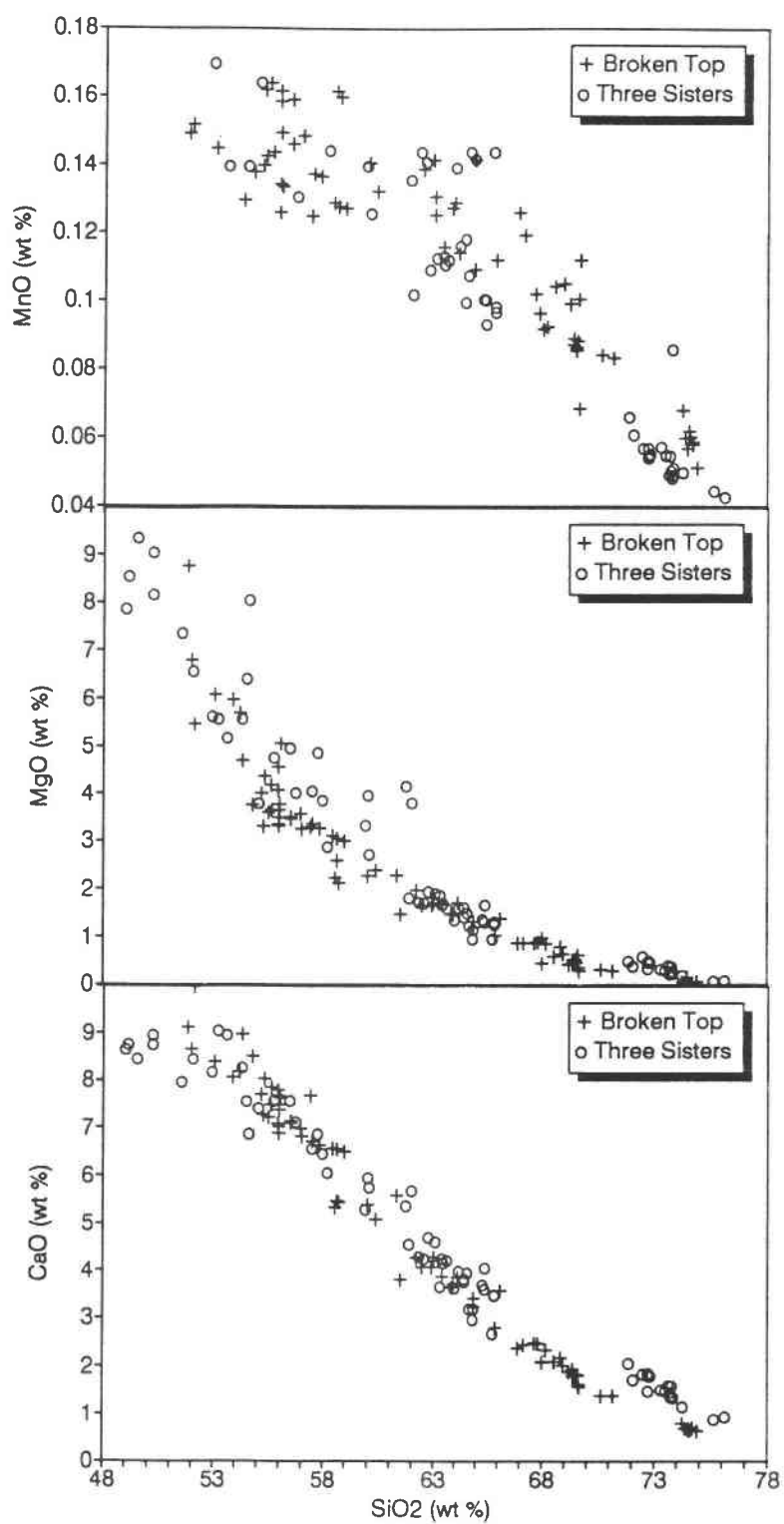
Figure 6.3: Major element-silica variation diagrams (continued).
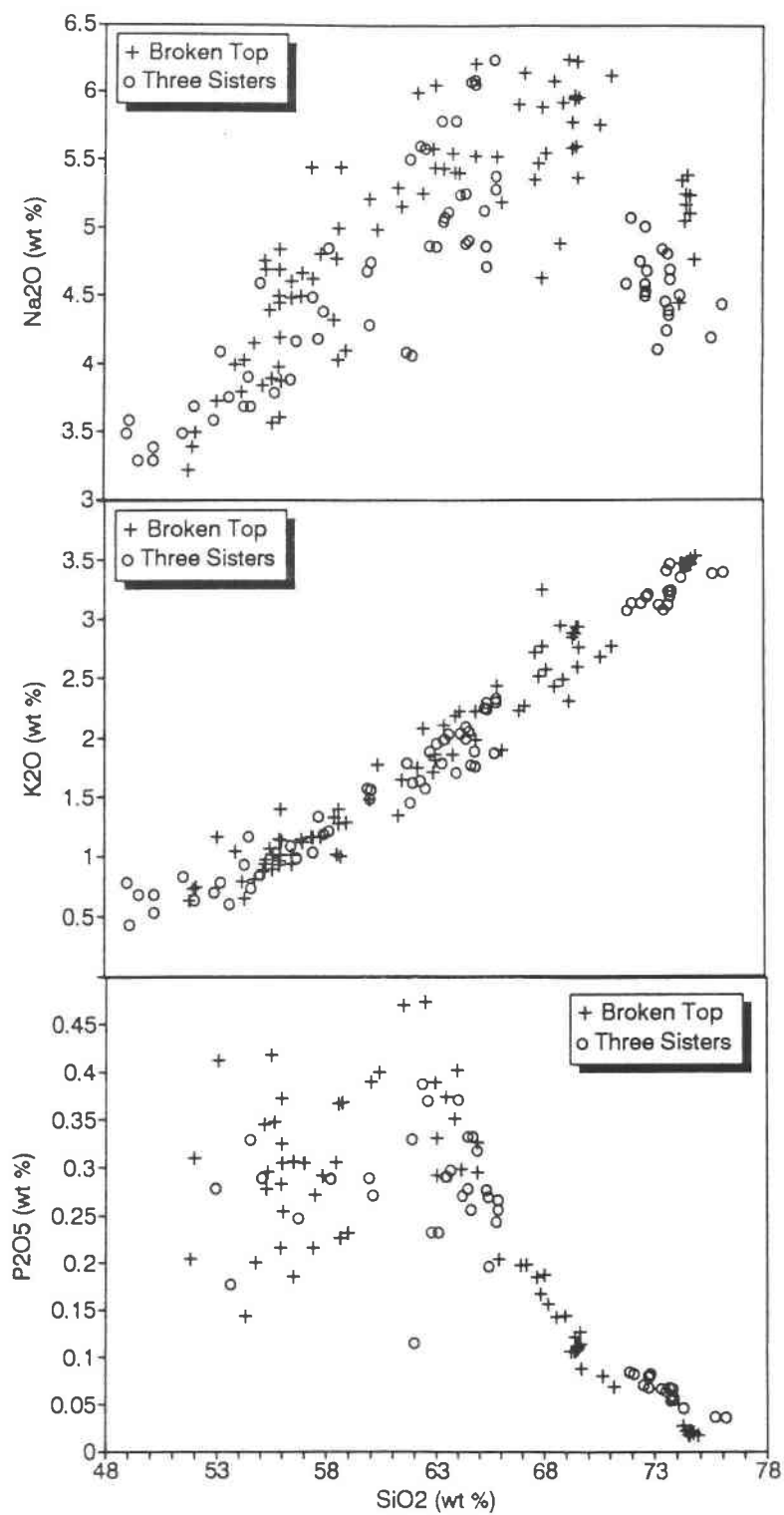
Figure 6.3: Major element-silica variation diagrams (continued).

1) Why are Broken Top rhyolites compositionally distinct from Three Sisters rhyolites?

2) What is the contribution (if any) of each rhyolite type to the geochemical evolution of their associated systems? Did rhyolites from one system interact with the other system?

3) Why are rhyolites relatively abundant in this part of the Oregon Cascades, but rarely found at other Oregon Cascade volcanos?

4) Why does the Three Sisters system have a compositional gap from 66% to 72% SiO_2, but this interval in the Broken Top system represents continuous elemental variations? What is the significance of the compositional gap in the Broken Top system between 72% and 74% SiO_2?

5) Why does the amount of inter-element variation apparently decrease with increasing silica content? Is this simply a matter of closure, that is, does increasing the percentage of silica result in a decrease in the abundance and possible variations of other elements (cf., Chayes, 1964). Or does this trend reflect other magmatic processes?

All of these questions must be evaluated in light of the close spatial and temporal associations of these two magmatic systems. The primary goal of this study is to explain the physical processes that led to the development of two distinct silicic magma systems in this part of the Oregon Cascades. Silicic magmatism cannot be studied, however, without first considering the petrogenesis of associated mafic rocks that are likely progenitors to the silicic series.

7. MAFIC PETROGENESIS

7.1 Introduction

The petrogenesis of mafic rocks in the central part of the Oregon Cascades has been examined in detail by Hughes (1983, 1990) and Hughes and Taylor (1986). These studies have examined late Miocene to Holocene basalts, basaltic andesites, and andesites that have been generated in sometimes different tectonic regimes, and erupted at spatially and compositionally distinct volcanic complexes. The fundamental conclusions of their research can be summarized as follows: High Cascade basalts erupted since the late Pliocene were generated from an ocean island basalt-like mantle that was variably enriched in large ion lithophile elements. Variable (but undefined) amounts of mantle metasomatism are required to generate the chemically distinct types of basaltic andesite they recognized in the High Cascades, along with lesser amounts of crystal fractionation and crustal assimilation.

This study was designed to examine silicic magmatism in detail, and the data base is not representative enough of the mafic system to allow for rigorous evaluation of the model presented above. The following sections will, however, impose significant constraints on the general magmatic processes invoked by Hughes (1983, 1990), and Hughes and Taylor (1986).

7.2 Crystal Fractionation

The simplest model of mafic petrogenesis to test is whether or not a series of rocks are related through crystal fractionation. Crystallization is probably the single most important petrogenetic process in the compositional evolution of a magma, as it is the inescapable result of the loss of heat from a magmatic system. Assimilation of wall rocks and the mixing of magmas must also result in some crystallization of the parental magma, as crystallization supplies the heat required to raise an assimilant to its solidus and produce melting (Bowen, 1928). It will be shown that even in a dynamic, open magmatic system, the crystallizing mineral assemblage will exert the most control on the major element evolution of the system (cf., Defant and Nielsen, 1990).

The mineralogy, and inferred crystallization sequence, of mafic rocks in the study area is olivine (ol) ± plagioclase (plag) to ≈53% SiO_2, clinopyroxene (cpx) + ol + plag for 53%-56% SiO_2, cpx + ol + plag ± orthopyroxene (opx) for 56%-58% SiO_2, and cpx + opx + plag (± trace ol) to 63% SiO_2. Phenocrysts of Fe-Ti oxides are also present in all mafic rocks, and apatite occurs as a trace phenocryst in rocks with ≥ 57% SiO_2. The modal proportions of these phases in a rock, however, do not necessarily reflect the fractionating mineral assemblage. Crystal sorting by size and density in a convecting magma body (Marsh and Maxey, 1985) can readily change the phenocryst proportions observed in a rock. In-situ crystallization (Langmuir, 1989; McBirney and Noyes, 1979) can also involve the apparent nonmodal fractionation of minerals. In addition, some basalts from

the study area and many other calc-alkaline continental arcs (cf. Gill, 1981; Thorpe, 1981) show evidence of clinopyroxene crystallization, yet lack that mineral in the mode.

Recent experimental work on the phase relationships of different types of basaltic melts, under variable pressures and water contents, can be used to constrain crystal fractionation models more accurately than with the modal mineralogy. Much of the work on natural systems has focused on anhydrous melts at 1 atmosphere pressure (Walker et al, 1979; Grove et al., 1982; Grove and Bryan, 1983), which are used to define the cotectics in figure 7.1. The general effects of increasing pressure under anhydrous conditions on some basaltic phase relationships has been studied by Thompson (1974, 1975), Stolper (1980), Takahashi and Kushiro (1983), and Elthon and Scarfe (1984). These studies show that increasing pressure will generally expand the orthopyroxene and clinopyroxene phase volumes at the expense of olivine ± plagioclase. Low pressure ($\leq$ 2.5 kbar) experiments on water-undersaturated basalts by Spulber and Rutherford (1983) indicate the olivine phase volume is expanded while the plagioclase volume contracts. Increasing water content will also increase the anorthite content of the liquidus plagioclase (Eggler, 1972; Sekine et al., 1979) and stabilize magnetite as an early crystallizing phase (Grove and Sisson, 1991).

Rocks from the study area and 1 atmosphere cotectics from Grove et al. (1982) are plotted in figure 7.1. The samples plot well off of the 1 atmosphere cotectics, but note that the low-Ol end of the data is sub-parallel to these cotectics, especially for higher silica compositions. This may be due to the effect of closure at higher silica compositions, but similar offsets at Medicine Lake volcano were interpreted by Grove and Baker (1984) to represent high pressure (5-10 kbars?) fractionation at water undersaturated conditions. Under these conditions olivine should be the liquidus phase, with early crystallization of magnetite, augite and calcic plagioclase. Olivine and augite dominate the crystallizing assemblage, with lesser amounts of plagioclase and magnetite (Grove and Baker, 1984; Grove and Kinzler, 1986; Grove and Sisson, 1991), leading to a calc-alkaline mafic fractionation trend.

Anhydrous, high pressure experiments on high magnesium (MgO $\geq$ 9 wt%) basalt (Elthon and Scarfe, 1984; Gust and Perfit, 1987) and high aluminum ($Al_2O_3 \geq$ 17 wt%) basalt (Baker and Eggler, 1983, 1987; Johnston, 1986) can also provide useful constraints on the effects of pressure on basalt crystallization, and generally confirm the above mineralogical relationships. It is not possible, however, to rigorously apply the phase relationships from these studies to the mafic rocks in the study area, as differences in composition will change the phase relationships. For example, higher MgO contents will greatly expand olivine stability for P $\leq$ 20 kbars (figure 7.2). Compositional differences in studied high aluminum basalts also results in changes in liquidus temperatures and garnet stability fields (figure 7.3). While liquidus temperatures and exact orders of crystallization cannot be determined for High Cascade rocks from these data, the experimental data confirm that higher pressures will result in early crystallization of augite in anhydrous basaltic melts.
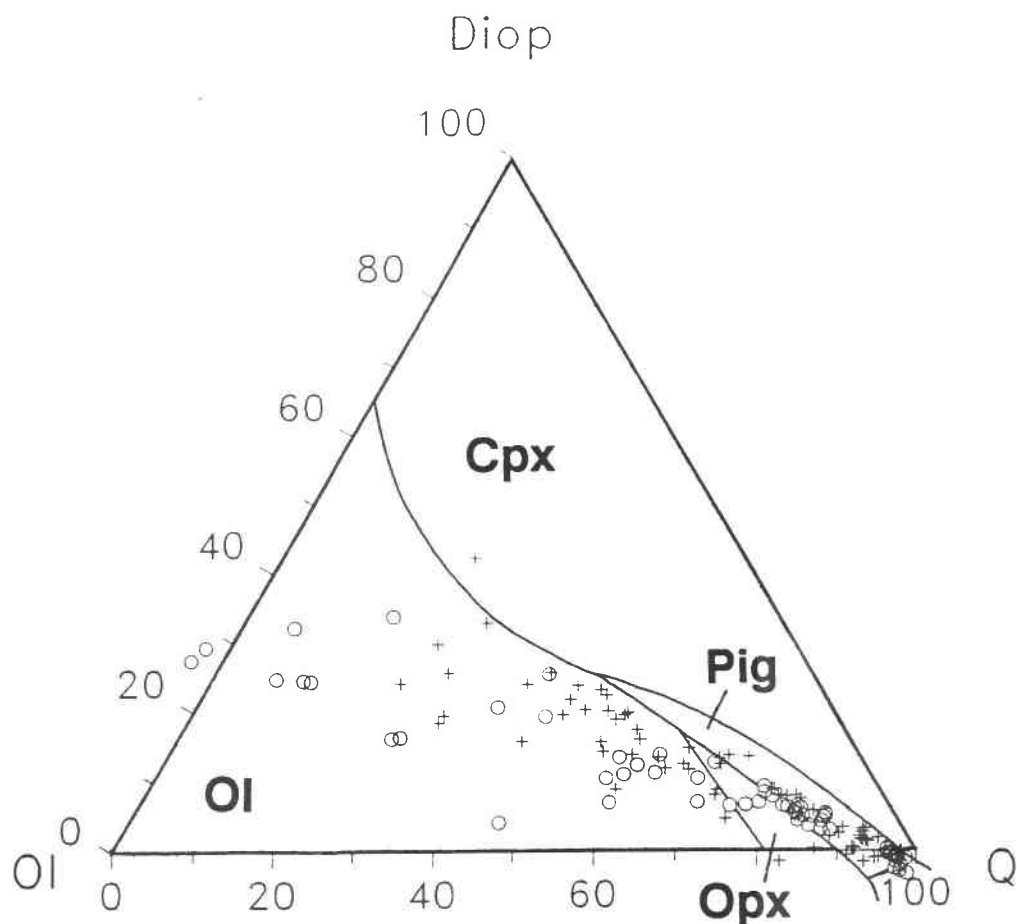
Figure 7.1: Low pressure phase relationships in the system olivine (Ol)- diopside (Di)- quartz (Qtz)- plagioclase, projected from plagioclase following the method of Grove et al., 1982: Wt % oxide is converted to mole %, and cation normalized. Mineral components:

$SUM = SiO_2 - CaO - 2(KO_{0.5} + NaO_{0.5}) + Cr_2O_3 + TiO_2$

$Qtz = (SiO_2 - 0.5(FeO + MgO) - 1.5CaO - 0.25AlO_{1.5} - 2.75(KO_{0.5} + NaO_{0.5}) + Cr_2O_3 + 0.5TiO_2)/SUM$

$Plag = 0.5(AlO_{1.5} - KO_{0.5} + NaO_{0.5})/SUM$

$Oliv = 0.5(FeO + MgO + 0.5(AlO_{1.5} - KO_{0.5} - NaO_{0.5}) - CaO - 2TiO_2 - Cr_2O_3)/SUM$

$Diop = CaO - 0.5AlO_{1.5} + 0.5(KO_{0.5} + NaO_{0.5})/SUM$

$Or = KO_{0.5}/SUM$

$Sp = (Cr_2O_3 + TiO_2)/SUM$

Normalize Qtz+Plg+Oliv+Diop = 100%, then normalize Qtz+Oliv+Diop = 100% for a plagioclase projection.

+ = Broken Top system rocks, o = Three Sisters system rocks.
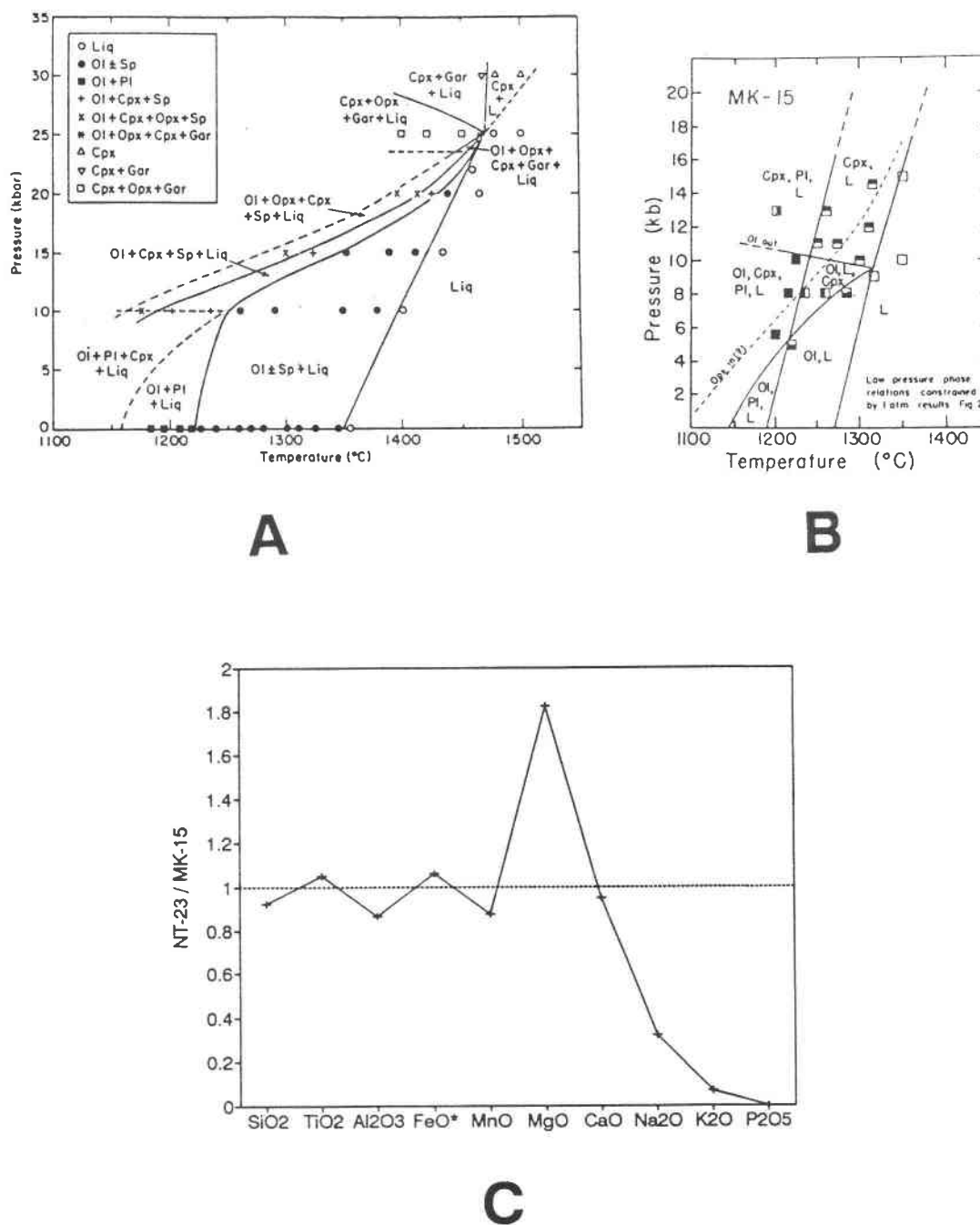
Figure 7.2: Comparison of high pressure phase relationships for high-Mg basalts NT-23 (**A**) (Elthon and Scarfe, 1984) and MK-15 (**B**) (Gust and Perfit, 1987). Significant differences in MgO, CaO, Na$_2$O and K$_2$O (**C**) result in different phase relationships. High-Mg basalts in the High Cascades are significantly different from these compositions, which precludes direct application of these high pressure phase relationships to the Cascade mafic system.

Figure 7.3: Comparison of high pressure phase relationships for high-Al basalts AT-1 (**A**) (Baker and Eggler, 1983) and SSS.1.4 (**B**) (Johnston, 1986). Significant differences in composition (**C**) result in different phase relationships for these rocks. High-Al basalts in the High Cascades are also significantly different from these compositions, which again precludes direct application of these high pressure phase relationships to the Cascade mafic system.

Pearce element ratios (PER) (Pearce, 1968) are commonly used to test if a series of rocks are cogenetic (cf. Russell and Nicholls, 1988). In order to quantitatively model with PERs, however, the extensive properties of one of the constituents in the system must not change; assimilation or mixing in the magma system will change the extensive properties of all the components in the system, and remove the constraints necessary for robust PER modeling. Disequilibrium mineral features, such as sieved plagioclase and rimmed pyroxenes (Chapter 4), indicate that the mafic magma system undoubtedly evolved with a significant component of mixing or assimilation. Most continental arc mafic systems are open magmatic systems (cf. Hildreth et al., 1986; Grove and Kinzler, 1986), and that rigorous application of PER models to these systems is not justified. PER models can, however, provide useful limits on the types and relative proportions of minerals that may have fractionated in the mafic magma system.

PER discrimination diagrams show the effects of fractionating different minerals on major element abundances. The hypothesis that clinopyroxene is a significant fractionating phase in the mafic system, along with olivine, plagioclase, and magnetite, was tested using numerator coefficients from Stanley and Russell (1989) and assuming that potassium was a conserved element. Plagioclase and olivine + oxide (figure 7.4a) fractionate in roughly equal proportions ($\approx$1:1), olivine + oxide and clinopyroxene (figure 7.4b) fractionate at roughly 1.5:1, and plagioclase fractionates at roughly 2:1 with clinopyroxene (figure 7.4c). A combination of these trends results in a fractionating assemblage of plag:ol+ox:cpx of $\approx$40:35:25, which is very similar to the assemblages used by Grove and Baker (1984) to generate numerous mafic calc-alkaline trends (i.e. plag > ol+ox $\geq$ cpx with ol+ox+cpx > plag).

Simple mass balance calculations, however, (table 7.1) show that fractionating these mineral proportions from a representative parental high MgO Cascade basalt (TFJ-438) fails to reproduce depletions in FeO* and TiO_2 observed in Cascade rocks (figure 7.5a). Mass balance models using these mineral proportions and more iron-rich olivine (Fo_{70}) and augite (En_{40}) also fail to produce the observed FeO* and TiO_2 depletions. However, simple mass balance models using Ol:Cpx:-Plag:Mgt of 25:22:40:13 produce the best fit to the observed trends for all major elements except Na_2O, which is relatively enriched in the model (figure 7.5b); elevated Na_2O was expected because in the model a plagioclase composition is fixed at An_{85}.

The role of magnetite fractionation in the petrogenesis of calc-alkaline arc rocks is at times controversial. A common problem involves the necessity of having 10%-15% magnetite in the fractionating assemblage in order to prevent titanium enrichment and create a silica enrichment trend (Gill, 1981; Grove and Baker, 1984; Grove and Kinzler, 1986). Cumulate gabbroic xenoliths from island arc volcanos, however, rarely contain $\geq$ 5% magnetite (Beard and Day, 1988). It is often assumed that if $\geq$5% of the fractionating assemblage were magnetite, then the cumulate xenoliths should also contain $\geq$5% magnetite (cf., Conrey, 1990). This argument against $\geq$5%
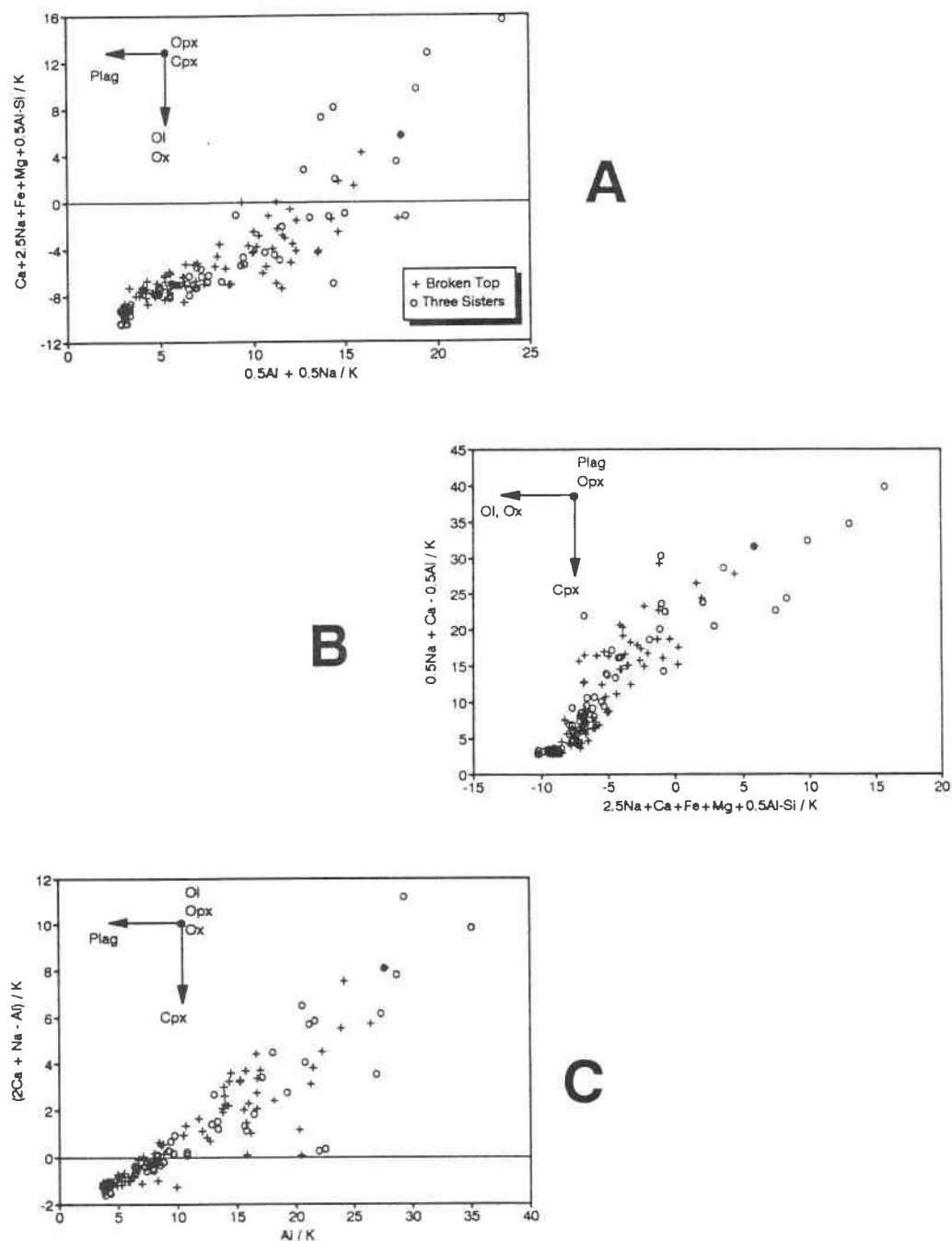
Figure 7.4: Pearce element discrimination diagrams, using numerator coefficents from Stanley and Russell (1989) and assuming K is a conserved element. Slope of the trends gives fractionation ratio for tested minerals. **A)** Plag-Ol + Oxide fractionation occurred at ≈1:1. **B)** Ol + Oxide - Cpx fractionation at ≈1.5:1. **C)** Plag - Cpx fractionation at ≈2:1. Combination of these fractionation relationships gives an assemblage of Plag:Ol+Ox:Cpx of ≈40:35:25.

Mineral		SiO2	TiO2	Al2O3	FeO*	MnO	MgO	CaO	Na2O	K2O	P2O5
Olivine	Fo85	39.9			14.9	0.3	45.1	0.2			
Augite	En51	51.9	0.5	3.0	6.6	0.2	17.4	18.3	0.4		
Plag	An85	46.6		34.0	0.5		0.1	17.1	1.6	0.0	
Magnetite		0.1	15.5	0.6	77.2	0.3	0.3				

Starting composition

	SiO2	TiO2	Al2O3	FeO*	MnO	MgO	CaO	Na2O	K2O	P2O5
TFJ-438	49.8	1.5	16.5	9.8	0.1	9.5	8.6	3.3	0.7	0.2

Ending Compositions

Ol:Cpx:Plg:Mgt	SiO2	TiO2	Al2O3	FeO*	MnO	MgO	CaO	Na2O	K2O	P2O5	F
1) 30:25:40:05	54.0	1.9	18.0	9.5	0.1	4.0	6.7	5.0	1.2	0.3	0.50
2) 25:22:40:13	59.0	0.9	18.5	4.5	0.1	4.0	6.4	5.5	1.4	0.4	0.66

Observed range in composition at 4% MgO

SiO2	TiO2	Al2O3	FeO*	MnO	MgO	CaO	Na2O	K2O	P2O5
58	1.0	18	6	0.13	4	6.5	4	1.3	0.4
±3	±0.2	±1	±1	±0.02	±1	±0.5	±0.5	±0.4	±0.1

Table 7.1: Mineral compositions used in mafic mass balance calculations, determined through microprobe analysis of phenocrysts in basalts and basaltic andesites (magnetite). F: Fraction crystallized. Simple mass balance calculations used a 2% crystallization interval, in which fixed proportions of the above minerals were removed from the parental composition. The derivative composition was re-normalized to 100%, and crystallization was modeled until MgO reached ≈4%, which is the point orthopyroxene appears as a phenocryst phase. Ending compositions for (1) calc-alkaline fractionation bounded by Pearce element plots, and (2) best fit to observed trends.
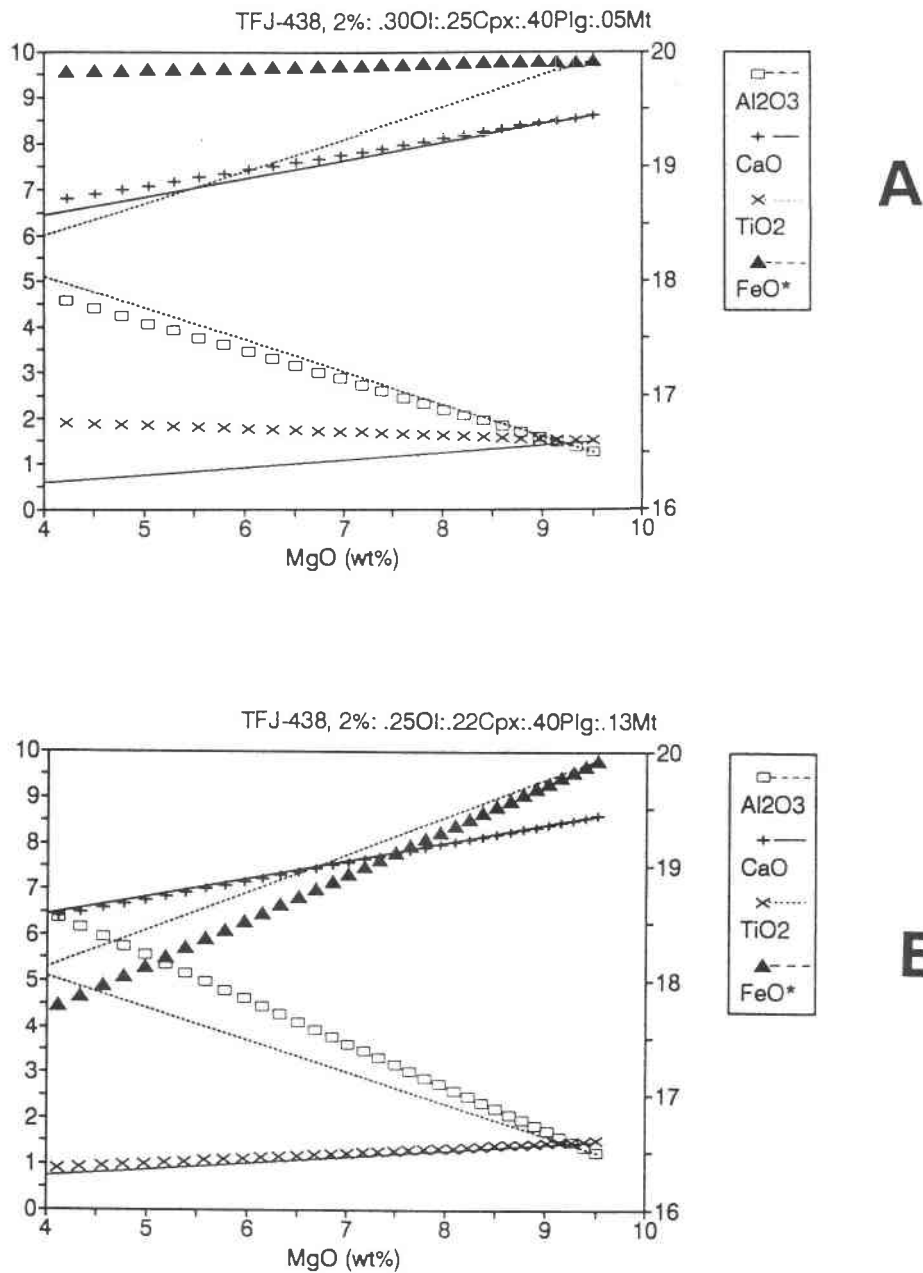
Figure 7.5: Results of simple mass balance models (symbols) plotted with best-fit trends for High Cascade mafic rock (lines). Right y-axis corresponds to Al_2O_3, other oxides on left y-axis. A) Test of model bounded by Pearce element calculations, using an Ol:Cpx:Plag:Mgt of 30:25:40:05. Note the poor fit of the model to observed FeO and TiO_2 trends. B) Best-fit mass balance model using TFJ-438 as a starting composition and a Ol:Cpx:Plag:Mgt at 25:22:40:13. Calculations discussed in table 7.1.

magnetite fractionation assumes that the gabbroic xenoliths actually represent cumulates from the studied fractionation interval. Mafic magmas, however, have low viscosity ($\approx 10^2$-10^3 poise, Murase and McBirney, 1973) and thus have a limit on the density of a xenolith that can be entrained and erupted. With all other factors being equal (i.e., size, composition, temperature, ascent rate etc.), a gabbroic xenolith with an Ol:Cpx:Plg:Mgt of 25:21:40:14 ($\rho \approx 3.4$) will have about a 33% greater settling velocity in a basaltic magma ($\rho \approx 2.7$) that a xenolith with an Ol:Cpx:Plg:Mgt of 30:25:40:5 ($\rho \approx 3.2$). The lack of gabbroic cumulate xenoliths with $\geq 5\%$ magnetite in many arc rocks may thus reflect the inability of basaltic magma to transport a relatively high density xenolith to the surface, and the absence of these xenoliths does not necessarily invalidate fractionation models involving $\geq 5\%$ magnetite.

The major element variation diagrams (figure 6.3) have a large degree of scatter at mafic compositions, which indicates that the mafic series is not the product of a uniform petrologic process. Simple mass balance calculations, however, show that the overall **trends** in the mafic system are consistent with a general petrogenetic model **dominated** by fractionation of calcic plagioclase, sub-equal amounts of olivine and augite, and $\geq 10\%$ magnetite. Similar degrees of major element scatter in fractionating mafic systems are often explained by invoking loosely constrained "open system processes", such as magma mixing, recharge, and assimilation (e.g., Hildreth et al., 1986; Hildreth and Moorbath, 1988; Hughes, 1990). However, limits can be imposed on the effect of open system processes using numerical mixing, recharge and assimilation models (e.g., O'Hara, 1980; DePaolo, 1981; Nielsen 1985, 1988, 1990; Langmuir, 1989).

7.3 Open System Models

The composition and proportion of minerals fractionating from an evolving magma are controlled primarily by temperature, pressure and the composition of the melt. Experimental data for the temperature and compositional dependence on phase equilibria can be used to model liquid lines of descent in anhydrous magma systems at low pressure (Nielsen and Dungan, 1983; Nielsen, 1985, 1988, 1990; Defant and Nielsen, 1990). The essence of this approach is to use experimental data to construct temperature-composition expressions that relate the composition of the studied system to a calculated liquidus mineralogy, and to crystallize the system under various conditions of recharge, eruption and mixing.

Trace element partitioning is strongly dependent on the composition of the system and temperature, and to much lesser extent on pressure (Irving, 1978; Mysen and Virgo, 1980; Nielsen, 1985). In order to account for compositional effects on trace element partitioning, the Nielsen (1985,1988) model assumes that the melt consists of two components: network formers (Si, NaAl, and KAl) and network modifiers (Al in excess of Na+K, all other elements). The use of a two

lattice melt model permits estimation of the activity of trace elements in the melt from their concentrations. The partitioning of the element into the fractionating mineral is then related to mineral component reactions, which account for substitution and siting effects (e.g., Gallahan and Nielsen, in press). This approach relates the activity of the trace element in the melt to it's activity in the fractionating phase, which results in compositionally compensated distribution coefficients.

The advantage of this model (referred to as CHAOS by Nielsen, 1990) is that the behavior of all components in the system is allowed to vary as the system evolves, as opposed to remaining fixed for relatively long intervals of differentiation (i.e. mass balance calculations or Rayleigh fractionation). The distribution coefficients used in the model are calculated for the phases that are in equilibrium with the evolving melt, and are thus more accurate than the general mineral/matrix distribution coefficients commonly used in trace element modeling. This approach permits detailed calculation of major and trace element liquid lines of descent, and allows quantitative assessment of magma recharge, mixing, assimilation and eruption effects on the evolving system.

The experimental data that constrain CHAOS models, however, are from anhydrous melts at 1 atmosphere. Previous arguments have indicated that the mafic system in this part of the Oregon Cascades evolved at elevated pressures ($\approx$10 kbars), and that the system was not anhydrous but water undersaturated. CHAOS models will thus be dominated by the plagioclase + olivine cotectic, with later crystallization of augite and magnetite; the Oregon Cascades mafic system should have early crystallization of all four of these phases, and the plagioclase should be more calcic than modeled with CHAOS. For this reason, the following CHAOS models are not presented as rigorous simulations of Oregon Cascade mafic petrogenesis, but rather as a useful test of what **degrees** of elemental variation can be expected from different open system processes.

7.3.1 Crystal fractionation

Differences between liquid lines of descent modeled with CHAOS and those observed in the studied mafic system are represented in figure 7.6. The closed system CHAOS model with TFJ-438 (Hughes, 1983) as the starting composition used a 2% crystallization interval and was produced with no recharge, assimilation or eruption, which is referred to as a 0-0-0 model. Early crystallization of plag + ol results in little silica enrichment until the appearance of augite on the liquidus at $\approx$60% crystallization. A 0-0-0 model was also calculated using basalt 3S069 as the starting composition; augite fractionation occurred at only $\approx$40% crystallization in this model. It is apparent that simple mass balance models more accurately account for the observed major element variations in this system than 0-0-0 CHAOS models using either TFJ-438 or 3S069 as parental compositions (figure 7.6).

It is also apparent from figure 7.6 that there are numerous "parental" compositions that can be used as starting compositions in these models. Primitive basalts (i.e. close to equilibrium with
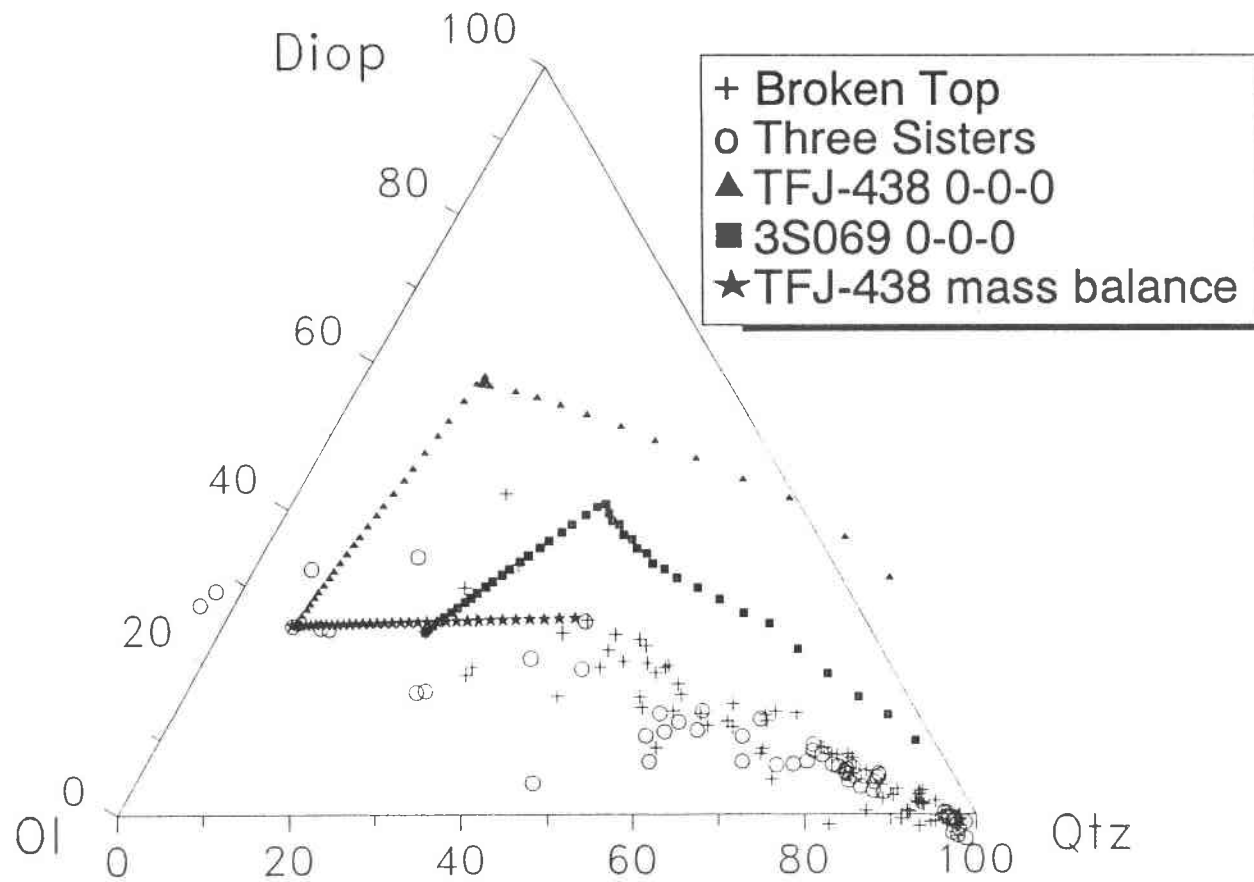
Figure 7.6: Closed system (0-0-0) models projected from plagioclase (Grove et al., 1982). Note that an unreasonably large amount of crystallization (≈60%) is needed to reach the olivine-augite cotectic using TFJ-438 as the starting composition. If 3S069 is used as the starting composition, only ≈40% crystallization is necessary to reach the olivine-augite cotectic. The simple mass balance model, however, more closely corresponds to the High Cascade mafic trend than either 0-0-0 model.

mantle peridotite) are rarely found in volcanic arcs (Nye and Reid, 1987), and have not been reported in the Oregon Cascades. High Cascade basalts that are high in MgO, Ni and Cr have higher incompatible element abundances than some High Cascade basaltic andesites (Hughes, 1983), which further obscures parental relationships. The geochemical diversity observed in this area (e.g., figure 6.3) shows that there are many basalts in this part of the High Cascades that can serve as parental compositions. The purpose of the following models is not to rigorously describe the liquid line of descent for one parent to a specific daughter, but rather to understand the geological processes that are acting on the magma system as a whole. Given the current uncertainties in the composition of parental melts, the effects of pressure and water content on the liquid line of descent, trace element distribution coefficients, and the composition of possible crustal assimilants, rigorous geochemical modeling of the High Cascade mafic system is not justified. For the purposes of this study, a relatively primitive basalt was used as a parental composition in the petrogenetic models; basalt 3S069 has relatively high MgO (8.8%), Ni (148 ppm) and Cr (451 ppm), low incompatible element abundances, and phenocryst modes of 10% olivine but only 0.1% plagioclase.

7.3.2 Magma recharge and eruption

Although the **absolute** elemental abundances produced by CHAOS models will not accurately simulate the High Cascade magmatic system, due to the low pressure data used to construct the models, the **relative** abundances generated by CHAOS yield valuable information on the geochemical effects of various open system processes. These CHAOS models provide the means to test various open system hypotheses that are frequently invoked, but rarely constrained, in most mafic petrogenetic studies.

Fractionation paired with magma recharge and eruption is a relatively simple open-system model that can be simulated with CHAOS. A steady state model can be constructed by setting the recharge rate to twice the crystallization rate and the rate of eruption equal to the rate of crystallization, which is referred to as a 2-0-1 model. Randomized recharge events were set to occur after 20% of the system had been crystallized and erupted, using 5% crystallization increments. The modeled system was randomly sampled after every 15% interval of crystallization; variations in the periodicity of recharge (10%-40%), crystallization increment (1%-10%) and sampling (10%-40%) only produced small deviations from the above model.

A 2-0-1 model for 3S069 (figure 7.7) illustrates the main features of a recharging mafic magma system. The most significant feature is the inability of a recharging mafic system to routinely fractionate to compositions more silicic than basaltic andesite. Recharge rates that permit a steady state (i.e., long lived) magma chamber continuously drive the bulk composition of the system back towards a parental composition, and constrain the system to higher temperature
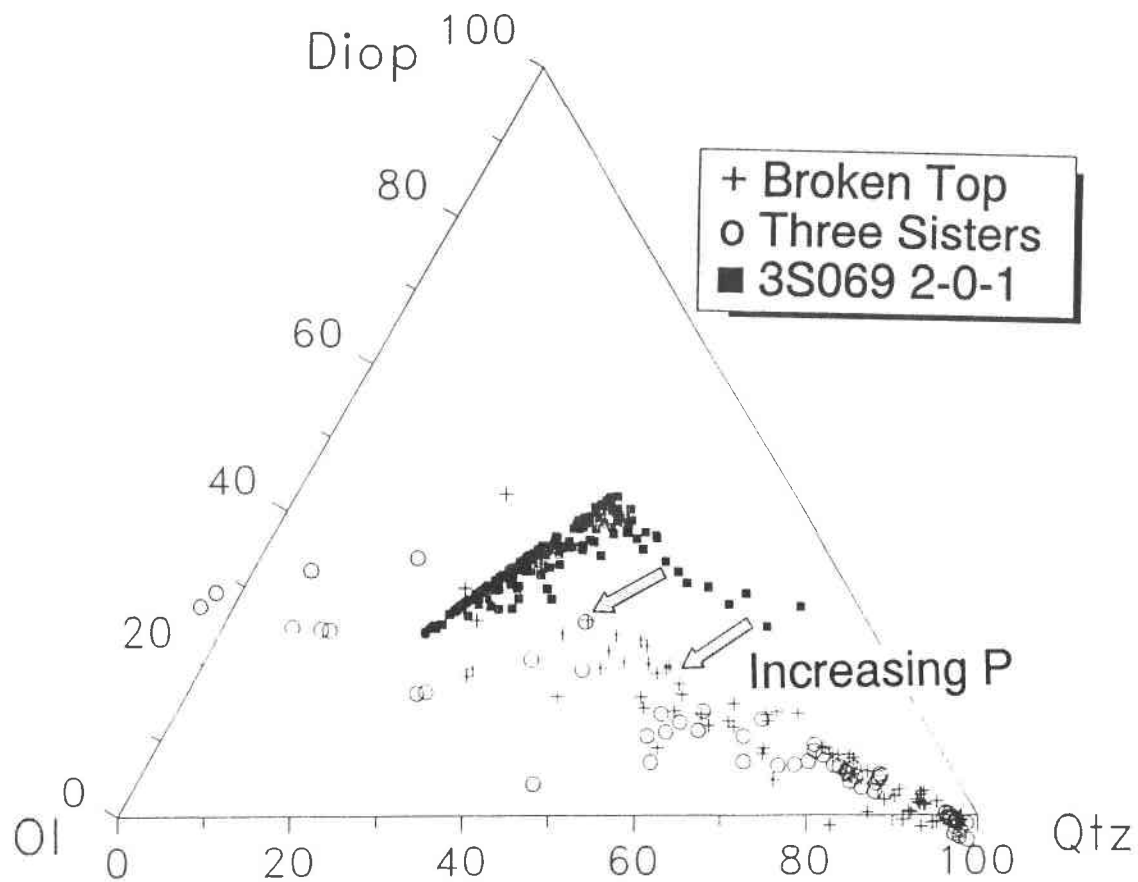
Figure 7.7: 2-0-1 recharge model using 3S069 as the starting composition. Note that the overall trend of the model parallels the 1 atmosphere cotectics (cf., figure 7.6), with significant deviations produced through the mixing of parental and evolved magmas. Increased pressure should expand the augite stability field at the expense of olivine, and lower the augite-olivine cotectic into the High Cascade data field (arrows). Much of the observed variation in the High Cascade mafic series can be accounted for by the 2-0-1 recharge model.

cotectics (O'Hara and Mathews, 1981; Nielsen, 1988). Thus the only way to generate silicic melts from a basaltic parent through crystal fractionation (i.e., without assimilation) is to close the system to significant amounts of recharge, which greatly limits the amount of evolved magma that can be produced (e.g., >50-60% crystallization necessary for andesite).

The liquid line of descent in the 2-0-1 model, however, is still controlled by the position of the 1 atm. cotectics, with only minor deviations off the cotectics produced through mixing (figure 7.7). This is in part an artifact of the anomalously large 1 atm. olivine-plagioclase stability field used in the models, which limits the fractionation of augite to intervals of >40% crystallization. Previous discussions have shown the necessity of augite and magnetite crystallization early in the fractionation sequence. Early fractionation of augite would result in more apparent scatter in the modeled 2-0-1 trends because the augite-olivine cotectic would be reached at much lower degrees of crystallization. Increasing the sampling, mixing interval and simulation length could also produce a little more apparent scatter off of the cotectics in modeled systems (Nielsen, 1988).

Most models of continental arc magmatism contain a large, long lived mafic magma reservoir near the base (40-60 km) of the crust (e.g., Gill, 1981; Marsh, 1984; Hildreth and Moorbath, 1988; Bergantz, 1990). Magmatic differentiation in this reservoir is probably dominated by recharge, with lesser amounts of wall rock assimilation due to a large volume-to-surface ratio of the magma reservoir and the difficulty in mixing silicic partial melts down into the mafic reservoir (Huppert and Sparks, 1988). The relative importance of fractionation versus assimilation in mafic differentiation cannot be rigorously tested until additional experimental work on high pressure (≈ 10 kbars) phase relationships is completed. With that caveat in mind, some of the major (figure 7.7) and trace (figure 7.8a) element variations observed in High Cascade rocks from 49% to about 58% SiO_2 are reproduced by a 2-0-1 recharge and eruption model, once the effects of higher pressure fractionation are qualitatively accounted for. One effect of recharge is to maintain compatible element abundances at higher levels than observed in closed-system fractionation models (Defant and Nielsen, 1990). Some High Cascade mafic rocks have compatible element abundances (e.g., Ni, Cr, V, Co) that are consistent with a 2-0-1 model (figure 7.8a). Although magma recharge and eruption must exert a significant degree of control on the mafic differentiation trends in this part of the High Cascades, these processes do not explain all of the variations observed within the High Cascade mafic system (e.g., figure 7.8a-b). Further complexities must be introduced by recharge of different primary melt compositions (i.e., Hughes, 1983, 1990; Hughes and Taylor, 1986), or by crustal assimilation, in order to account for the observed geochemical variations.

Pearce (1983) recognized that incompatible elements with low ionic potentials (Cs, Rb, Sr, Ba, large ion lithophiles (LIL) and light rare earths (LRE)) are characteristically enriched in subduction zone magmas, relative to heavy rare earth (HRE) and high field strength (HFS) elements. The low ionic potentials of the enriched elements favor aqueous mobility, which has lead
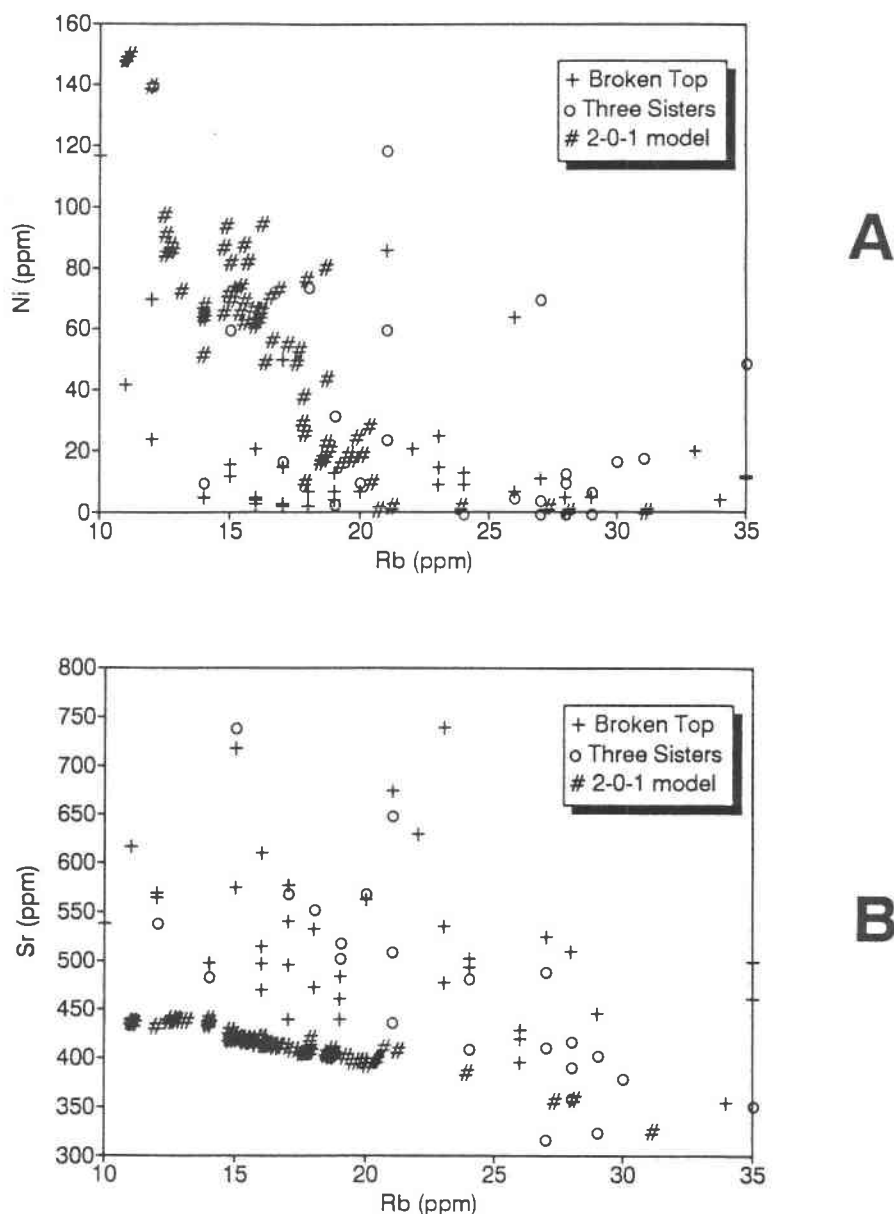
Figure 7.8: **A)** Representative compatible-incompatible trace element diagram for High Cascade
mafic samples. Note that modeled element distributions are very similar to some
observed compositions; most trace elements that are compatible in olivine (± augite)
follow this pattern. Although modeled abundances will at times deviate from observed
abundances, due to the 1 atm. crystallization path in the model, the modeled **patterns**
generally reflect the observed distribution patterns. **B)** Representative compatible-
incompatible element diagram for modeled elements that do not follow observed trends.
The large amount of observed Sr variation is not explained by the modeled degrees of
magma recharge and eruption, and must have been produced through another open
system processes. The 2-0-1 model also over estimates the amount of plagioclase
fractionation, due to the large stability field of plagioclase in 1 atm. anhydrous mafic
systems.

Pearce (1983) and others (e.g., Hawkesworth and Ellam, 1989; Hughes, 1990) to speculate that heterogeneities in primary melt composition may be produced by variable degrees of fluid enrichment in the mantle wedge. This hypothesis, however, is difficult to test, as there are few constraints placed on the degree and types of enrichments that are possible in the mantle wedge. The effects of fluid enrichment in subduction zone magmatism is a fundamental problem in igneous petrology, and one that cannot be adequately addressed by the data in this study. The elements that are most strongly enriched in a metasomatized mantle source, however, are also the elements that are incompatible in the major rock forming silicate minerals. Incompatible element enrichments can also be produced through mixing silicic partial melts into the mafic system. The next section will show that this hypothesis is valid for the High Cascades mafic magma system.

7.3.3 Assimilation

Experimental work has shown that silicic melts can be produced through partial melting of basaltic and metabasaltic rocks under a wide range of temperatures, pressures, and water contents (e.g. Helz, 1976; Spulber and Rutherford, 1983; Ellis and Thompson, 1986; Rutter and Wyllie, 1988; Beard and Lofgren, 1989). Low degrees ($\approx$10-30%) of melting generally produces rhyolitic partial melts, which are broadly similar in composition to rhyolites in the study area (chapter 9) and resemble granitic minimum melts (cf., Tuttle and Bowen, 1958).

Rhyolitic partial melts may be abundant near the base of the crust, where the ponding and crystallization of mafic magmas will generate sufficient heat for crustal fusion (e.g., Patchett, 1980; Huppert and Sparks, 1988; Bergantz, 1989). Assuming a geothermal gradient of 20°C/km and the base of the crust at $\approx$40 km, lower crustal rocks should be at $\approx$800°C. Metabasalt should have a specific heat of $\approx$0.3 cal/g °C, a heat of fusion (or latent heat of crystallization) of $\approx$100 cals/g and a solidus at $\approx$1000°C (after Grove et al., 1982). A melt-to-wallrock ratio of $\approx$1.5:1 should thus result in partial melts of the metabasaltic wallrock; if the melts convect, this ratio will be lower (cf. Huppert and Sparks, 1988).

It is likely that the temperature of these rhyolitic melts was close to the liquidus. Petrographic study has shown that plagioclase phenocrysts with resorbed, low An cores and reversely-zoned rims are rarely found in mafic rocks from the study area. Such reversely-zoned phenocrysts are most likely xenocrysts from the mixing or assimilation of partially crystalline silicic magmas or wall rocks. For example, Conrey (1991) has shown that mixing a silicic magma into the Mt. Jefferson mafic system usually resulted in abundant resorbed and reversely-zoned plagioclase phenocrysts. The absence of abundant reversely-zoned phenocrysts does not prove that the mixed silicic magma was aphyric, however, because the lower temperature phenocrysts may have been completely resorbed during homogenization. The repeated absence of these phenocrysts, however, may indicate that mixing involved sparsely phyric silicic magmas. Sparsely phyric rhyolites from the

study area have phenocryst equilibrium temperatures of around 850°C (Chapter 5), and may thus have had a liquidus temperature in excess of 900°C.

The experimental and thermal data support the hypothesis that rhyolitic partial melts should be associated with any large, long-lived mafic magma system ponded near the base of the crust. The effects of assimilation/mixing of these rhyolitic melts into the mafic magma system can be modeled using CHAOS. Because the rhyolitic melts are assumed to be cooler (≈900°C) than the mafic melts (≥1100°C), mixing will result in crystallization of the evolving magma. In order to produce a steady-state simulation, recharge was set to 2, assimilation (i.e., mixing of rhyolite) to 0.3, and eruption at 1.3, with mixing events randomized at 35% intervals of fractionation. Larger amounts of assimilation resulted in very short simulations, presumably due to the quenching effect of the rhyolitic assimilant. Small rates of assimilation (10-20%) generally resembled 2-0-1 models, and rarely evolved to andesitic compositions. Ranges of assimilation-to-crystallization for AFC-type models in the literature range up to 1:1 (DePaolo, 1981), although 0.3-0.5:1 is probably more realistic (Taylor, 1980; Hildreth and Moorbath, 1988; Grunder and Mahood, 1988).

The main results of a 2-0.3-1.3 model using rhyolite 3S032 as the assimilant are shown in figures 7.9-7.11. The primary effect of assimilation is to drive the evolving system off of the cotectics to a much greater extent than observed for 2-0-1 recharge models (figure 7.9). The assimilating system will still be bounded by the cotectics, especially the cpx-opx-plag cotectic, but the higher temperature cotectics should be less well defined. The degree of major element variation for the assimilation model more closely corresponds to the observed variations than found in 2-0-1 models (figure 7.9), although this may be in part due to the limited mafic data set. More importantly, this model allows the mafic system to routinely evolve beyond 58% SiO_2, which was not possible with a 2-0-1 recharge model.

Trace elements that are compatible in olivine and pyroxene, as represented by Ni in figure 7.10a, are generally enriched in the assimilation model relative to 2-0-1 models. Ni bulk distribution coefficients will not be strongly affected by changes in pressure, because Ni remains highly compatible in high and low pressure mafic assemblages due to the early crystallization of olivine. The assimilation model can directly account for numerous samples that lie off of the main recharge-fractionation trend (figure 7.10a). However, Sc-Rb variations (figure 7.10b) are not duplicated by CHAOS models, because augite does not fractionate early in anhydrous, 1 atmosphere mafic systems. The lack of a Sc enrichment trend in High Cascade basalts indicates that augite is an early fractionating phase in this system, which is consistent with differentiation at pressures of ≈5-10 kbars (cf., Elthon and Scarfe, 1984). Note that although the absolute abundances of Sc and Rb from CHAOS models in figure 7.10b are higher than observed in the High Cascade rocks, the degree of scatter in the 2-0.3-1.3 model is very similar to the scatter in the mafic High Cascade rocks.
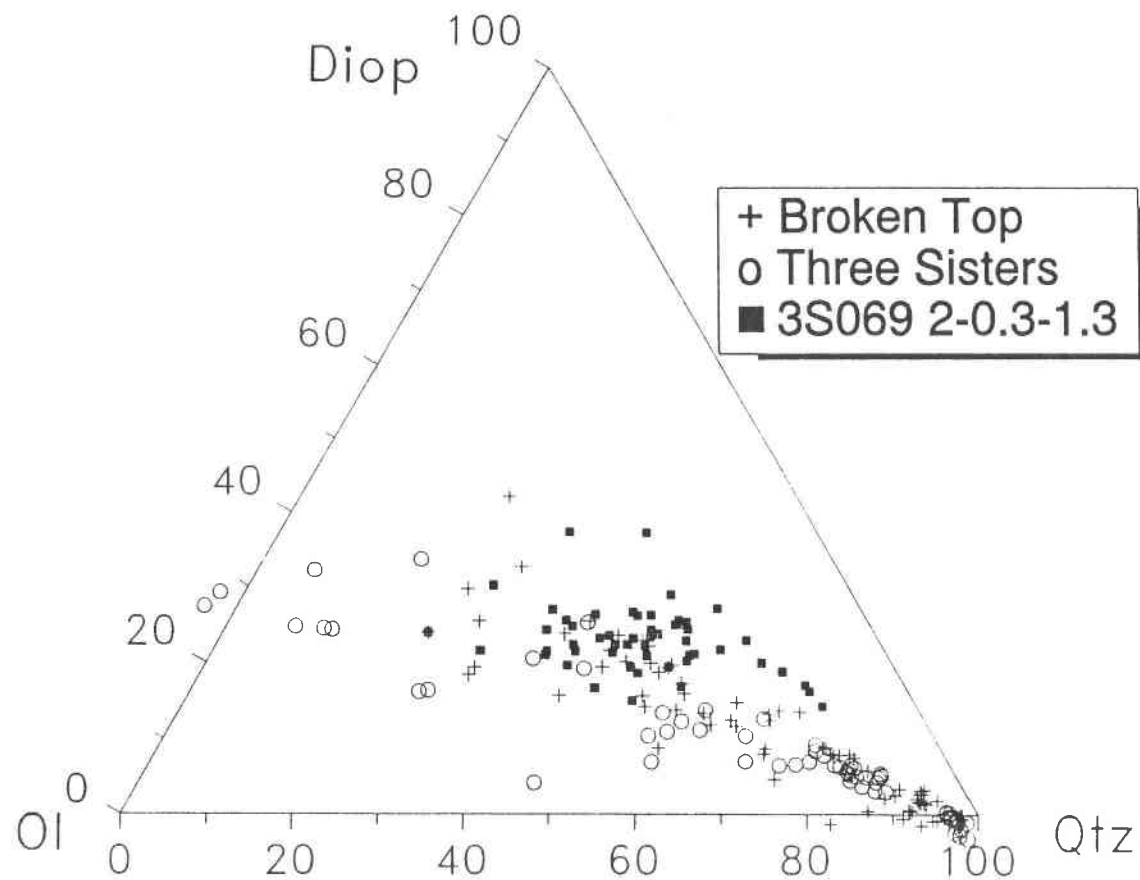
Figure 7.9: 2-0.3-1.3 assimilation model using 3S069 as the starting composition, and rhyolite 3S032 as the assimilant. Note that the evolving system is much more offset from the cotectics than observed in the 2-0-1 recharge model. The degree of variation in the assimilation model closely corresponds to observed variations in the mafic system. The mixing of rhyolitic melts into the mafic system is necessary for the mafic system to evolve beyond 58% SiO_2, and to explain some of the observed variations that cannot be accounted for through recharge or closed system fractionation.
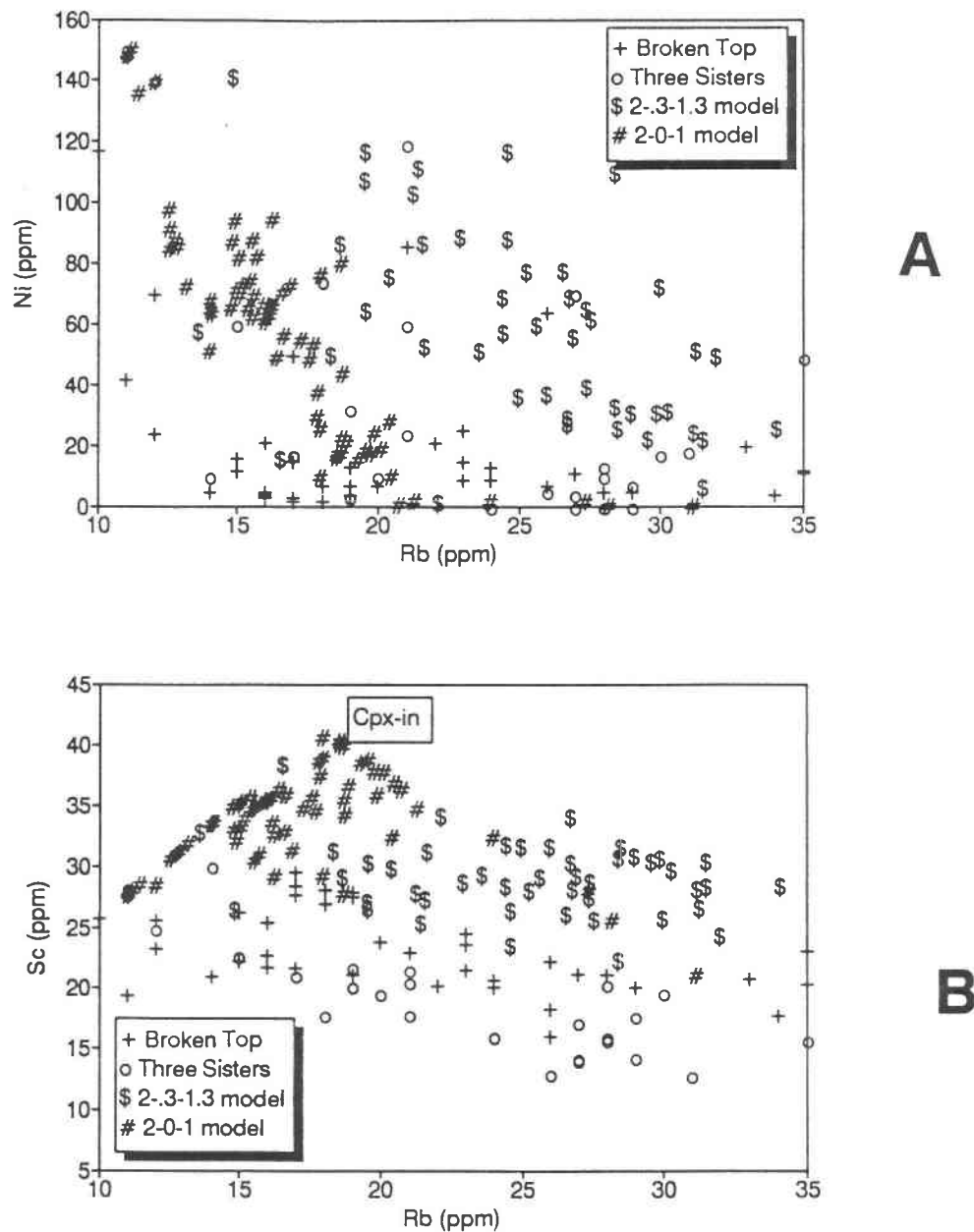
Figure 7.10: Representative compatible-incompatible trace element diagram for High Cascade mafic samples. **A)** Note that the assimilation model accounts for numerous samples that lie above the main recharge (2-0-1) trend, and the greater degree of variation shown by the assimilation model. Trace elements that are compatible in olivine follow this pattern. **B)** Assimilation is also required to explain many of the distributions of trace elements that are compatible in augite. Although the absolute abundances of Sc and Rb do not match observed abundances due to the late crystallization of cpx in 1 atm. models, the overall patterns in the 2-0.3-1.3 model closely match much of the observed distribution.

The distribution of other incompatible to moderately compatible trace elements (figure 7.11), which are poorly constrained by 2-0-1 models, can be accounted for by a 2-0.3-1.3 assimilation model. Ba/La and La/Sm ratios will not be strongly affected by the fractionation of olivine, pyroxene, magnetite or plagioclase. The large degree of variation in these elemental ratios (figure 7.11) also indicates that assimilation must be occurring with fractionation and recharge.

However, neither recharge or assimilation CHAOS models adequately account for the relatively high observed abundances of Sr and Al_2O_3 (figure 7.12). This may be in part due to the unusually low abundance of Sr (440 ppm) in 3S069 relative to other analyzed basalts (550-600 ppm). Simple mass balance models discussed above required ≈40% plagioclase in the fractionating assemblage to match the observed Al_2O_3 distributions. The observed enrichments in Sr (figure 7.12) are consistent with 50% crystallization of an assemblage containing 40% plagioclase (Sr distribution coefficient of 1.5 to 2), assuming the initial concentration of Sr was 550 ppm. CHAOS models consistently over estimate the degree of plagioclase fractionation (≈60% plagioclase in the fractionating assemblage), due to the relatively large stability field of plagioclase at 1 atmosphere, anhydrous conditions.

7.4 Summary of Mafic Petrogenesis

The High Cascade mafic magma system cannot be described by any single petrogenetic model. Profound uncertainties in mineralogic relationships at 10 kbars pressure and water undersaturated conditions precludes a rigorous evaluation of the role of crystal fractionation in the evolution of mafic rocks. The possibility of metasomatic enrichments in mantle-derived basaltic melts and heterogeneities in crustal assimilants further obfuscates general paradigms for mafic petrogenesis. There are, however, certain limits that can be placed on the evolution of mafic rocks in the study area.

The models presented above have shown the versatility of crystal fractionation and recharge in explaining some of the observed geochemical variations, even though these models are limited by the lack of high pressure mineralogical constraints. The High Cascade mafic system undoubtedly has numerous parental compositions (cf. Hughes, 1990), each of which can evolve a separate "micro-system" or blend into the larger magma system. To simply choose a basalt and differentiate it through Rayleigh fractionation is not a realistic test of the crystal fractionation hypothesis. The effects of magma recharge and eruption, which must occur in any open long-lived system, must be accounted for before the crystal fractionation hypothesis can be fully tested.

Silicic magmas must also at times be mixed into the mafic system, in order to account for many of the observed trace element variations from 49% to ≈58% SiO_2, and to differentiate above 58% SiO_2. Thermal and experimental data show that silicic magmas can be generated through partial melts of essentially mafic lower crust. Indeed, it is difficult to envision how a large, long-
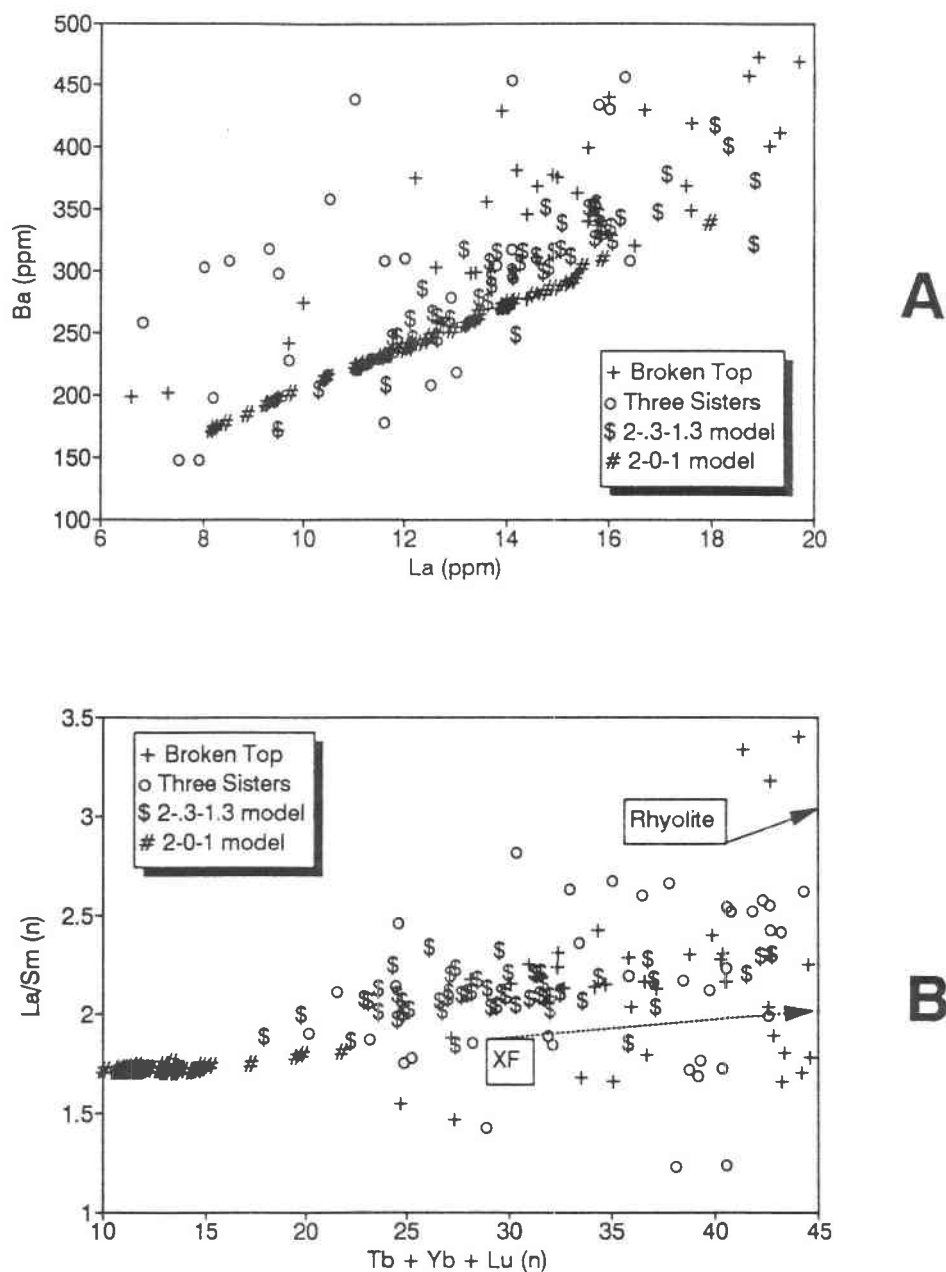
Figure 7.11: Representative incompatible trace element diagams. **A)** The degree of variation between elements with similar geochemical behavior can be successfully described with the 2-0.3-1.3 assimilation model. Note that the 2-0-1 recharge model cannot significantly fractionate Ba from La, because these elements have very similar mineral/melt distribution coefficients ($\approx$0.1-0.2) in the fractionating mafic system. The assimilation model, however, results in significant Ba/La fractionation, due to the mixing of a rhyolitic melt with a different Ba/La than the starting composition. **B)** Fractionation of plag + px + mgt cannot significantly change the La/Sm ratio. Mixing of a rhyolitic melt with a different La/Sm is required to produce many of the observed REE distributions.
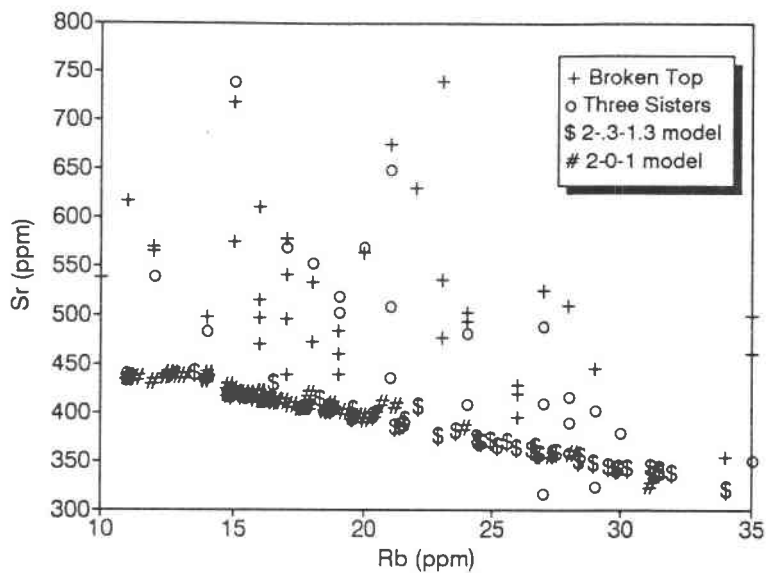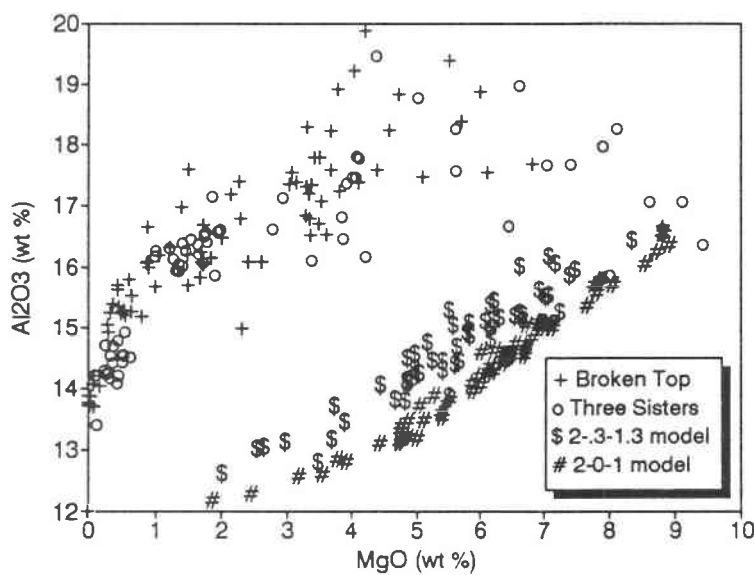
Figure 7.12: Sr-Rb (**A**) and Al$_2$O$_3$-MgO (**B**) variations cannot be accounted for by either recharge or assimilation CHAOS models. CHAOS models over estimate the amount of plagioclase fractionation at 60%; simple mass balance and Rayleigh fractionation are consistent with ≈40% plagioclase fractionation. Over fractionation of plagioclase results in anomalously low values of Sr and Al$_2$O$_3$, and limits the degree of Sr-Rb variation.

lived mafic magma system could be located in crustal rocks and not produce partial melts! The absence of restitic xenoliths or xenocrysts in presumedly mixed magmas indicates that either the interval of time after mixing was long enough to permit complete resorption of the incorporated material, or that the incorporated silicic magma was aphyric. Incompatible element enrichments, which are often explained as metasomatic enrichments in the mantle source, also can be produced in mafic magmas through reasonable amounts of silicic magma mixing paired with recharge. Metasomatic enrichments in the mantle are thus not a prerequisite for mafic magmatism in this part of the High Cascades.

The observed decrease in geochemical variation with increasing silica is not simply a matter of closure, but reflects fundamental changes in the processes that control magma evolution. A large mafic system that is open to recharge by parental basaltic melts cannot differentiate past $\approx 58\%$ SiO_2; recharge rates that permit a long-lived system also drive that system continuously back towards a parental composition. Routine differentiation to compositions more silicic than andesite must require either stopping the input of primary basaltic melts into the system, or increased rates of silicic magma mixing/crustal assimilation. Magma evolution above $\approx 58\%$ SiO_2 must proceed without recharge, which removes an important "randomizing" factor from the magma system. The relatively lower degrees of geochemical variation above $\approx 58\%$ SiO_2 thus reflects the lower number of "randomizing" magmatic processes. Crystal fractionation may occur in a system that is essentially closed to mafic input, and the mixing of silicic partial melts may become a more important petrogenetic process. The next chapter will test these hypothesis, and start to define more narrow evolutionary paths towards rhyolitic magmatism.

Finally, it is important to note that the Quaternary High Cascades mafic magma system does not display any apparent spatial or temporal controls on petrogenesis. For example, rocks that were apparently produced with relatively large amounts of assimilation (i.e., $\approx 30\%$) are not restricted to any specific location or time; they occur throughout the Quaternary High Cascades section. The petrogenetically distinct silicic magma systems in this part of the High Cascades (chapters 8 & 9) thus evolved from the same mafic magma system.

8. PETROGENESIS OF ANDESITES, DACITES AND RHYODACITES

8.1 Introduction

Models of mafic petrogenesis in the preceding chapter have demonstrated the importance of open system magmatic processes in generating the observed major and trace element variations for mafic rocks in this part of the Oregon High Cascades. Although the dynamics of magma recharge and assimilation of crustal melts produces distinct compositional trends, neither of these processes appears to be spatially or temporally controlled for mafic rocks in the Quaternary Oregon Cascades. A lack of spatial or temporal control supports the argument that the evolution of mafic rocks in this part of the High Cascades occurred in a large, long-lived magma system ponded at the base of the lower crust.

Compositional trends associated with more silicic rocks, however, often show spatial and temporal controls. This chapter will examine the petrogenesis of andesites, dacites and rhyodacites, and show that there are at times distinct spatial and temporal controls on the distribution of these rock types within the study area. For convenience, andesites, dacites, and rhyodacites will be referred to as the **intermediate** series throughout this chapter.

Unlike basalts and basaltic andesites, the andesites, dacites and rhyodacites were almost exclusively erupted from large vent complexes in the study area (stratovolcanos and the TVC). Exceptions are limited to small dacitic domes like Kokostick Butte (figure 1.1), which are as much as 5-10 km away from a central vent complex. This relationship is true for other volcanic centers in the High Cascades (cf., Conrey, 1991; Bacon and Druitt, 1988; Leeman et al., 1990), and for most other continental arcs (e.g. Gill, 1981; Thorpe, 1982; Grove and Kinzler, 1986).

There is a distinct temporal progression to the intermediate series in the Three Sisters system. The oldest stratovolcano, North Sister, consists primarily of basalt and basaltic andesite, with only a few small andesitic dikes emplaced in the upper part of the northwestern flank (Taylor, 1981; pers. comm., 1987). Middle Sister contains relatively abundant andesite and dacite, but basalt and basaltic andesite comprise the bulk of the volcano (Taylor, 1981). The youngest stratovolcano, South Sister, consists primarily of andesite and dacite, with lesser amounts of basaltic andesite and rhyolite (Taylor, 1981; Wozniak, 1982; Clark, 1983); rhyodacite (i.e. 68-72% SiO_2) is not found at any vents in the Three Sisters system. In addition, andesites and dacites associated with Middle Sister (MS) are also compositionally and texturally distinct from South Sister (SS) andesites and dacites. The Three Sisters thus show increasing amounts of different types of intermediate magmatism with both time and southward progression of volcanism. In contrast, there is no apparent spatial or temporal correlation among intermediate composition rocks associated with Broken Top (Taylor, 1978, 1987) or the TVC; intermediate series rocks, including rhyodacite, were erupted throughout the history of each of these two vent complexes.

Petrogenetic models for intermediate composition rocks will ultimately address the following points:

1) Did the same petrogenetic processes found in the High Cascade mafic system act in the intermediate system, or did these processes change?

2) Why did the intermediate series in the Three Sisters system only evolve to ≈66% SiO_2, but evolved to 72% SiO_2 in the Broken Top system?

3) Why are Middle Sister intermediate rocks compositionally distinct from South Sister intermediate rocks?

This chapter will begin to examine the compositional differences between the Three Sisters and Broken Top magmatic systems, and present models to explain these differences. The preceding chapter has identified the two dominant petrogenetic processes that control magma evolution within the High Cascades: The mixing of silicic partial melts into the evolving magma system, and crystal fractionation associated with mafic recharge.

Useful boundaries can be placed on the relative importance of open system fractionation versus silicic magma mixing through semi-qualitative modeling. The strength of these models lies not in the absolute values derived, but rather in the relative changes that are observed both within and between the studied magmatic systems. However, the geochemical behavior of trace elements in andesites and dacites is only moderately well constrained by experimental and empirical data. Large variations in many reported mineral/matrix distribution coefficients for intermediate composition rocks (Appendix E) precludes detailed trace element modeling. Phase relationships in intermediate composition rocks are also poorly constrained, as are the effects of water content and pressure. With these uncertainties, no useful purpose is served by presenting rigorously quantitative (i.e., grossly oversimplified) petrogenetic models.

8.2 Three Sisters System

Andesites and dacites associated with Middle Sister (MS) are compositionally and texturally distinct from South Sister (SS) andesites and dacites. Less than 5% of the plagioclase phenocrysts in MS intermediate rocks contain abundant glass inclusions, but ≥50% of the plagioclase pheno-crysts in SS intermediate rocks are usually sieved (Appendix B). Numerous SS dacites contain ≈0.1-0.5% olivine phenocrysts, but MS dacites lack olivine (Appendix B). Intermediate series rocks from MS also tend to be less phyric (10-15% total phenocrysts) than SS rocks (10-35% total phenocrysts). These mineralogical features at SS suggest disequilibrium crystallization associated with magma mixing, and MS textures indicate equilibrium crystallization.

Although dacites from both MS and SS range to 66% SiO_2, MS dacites are characterized by generally lower compatible and incompatible trace elements (table 8.1). The textural and geochemical differences between these two systems may indicate that the MS intermediate series was produced dominantly through crystal fractionation, and the SS intermediate series through mixing between mafic and rhyolitic melts.

If crystal fractionation controlled the petrogenesis of intermediate composition rocks, then the crystallizing phases should be represented by the minerals observed in these rocks. Intermediate composition rocks from both the Three Sisters and Broken Top systems have contain phenocrysts of plag + cpx + opx + mgt ± ol from ≈56% to ≈63% SiO_2, with trace amounts of olivine observed in some SS dacites to 66% SiO_2. Augite and orthopyroxene occur in nearly equal proportions in the intermediate series rocks. Amphibole phenocrysts are only observed in intermediate rocks as a trace phase (1 crystal per thin section) in two TVC rhyodacite (68% SiO_2) domes. Trace amounts of highly resorbed, opacitic amphibole xenocrysts were found in TVC andesite 3S090 and SS dacite 3S150. There is, however, no mineralogical evidence to support resolvable amounts of amphibole fractionation in the intermediate series. Apatite occurs as inclusions in phenocrysts for most units with ≥57% SiO_2, which is interpreted to represent local saturation in P_2O_5 at the mineral-melt interface (Chapter 4). Small (≤0.5 mm) groundmass crystals of apatite are often observed in rocks with SiO_2 ≥62-63%. This observation, and the experimental work of Green and Watson (1982), indicates that apatite fractionation did not occur in the intermediate series until ≈62% SiO_2.

Simple mass balance calculations (table 8.2) using the above anhydrous phenocrysts show that any fractionation hypothesis must involve a significant amount of plagioclase (>50%) to deplete the system in Al_2O_3 and CaO. Magnetite must also be present (≥5%) to prevent TiO_2 enrichment and, in conjunction with olivine, give a silica enrichment trend. The best-fit to the observed intermediate major element trends is obtained with a fractionating assemblage of 8% ol, 15% cpx, 10% opx, 60% plag (An_{75}), 7% mgt and 0.4% apatite (table 8.2). Although small variations in either the fractionating proportions or in mineral compositions can have a significant effect on the dacite generated through simple mass balance models (table 8.2), these models support a fractionation hypothesis for the MS intermediate series.

Trace element variations also support a fractionation-dominated origin for MS dacites, but indicate that the fractionating system was probably open to some amounts of recharge and assimilation. Observed depletions in Sc relative to Rb enrichment (figure 8.1a) are consistent with ≈40% equilibrium fractionation of an assemblage having a bulk distribution coefficient for Sc (D_{Sc}) ≈2, with D_{Rb}=0.01. Experimentally determined Sc distribution coefficients for pyroxenes in intermediate composition melts can be calculated from Nielsen et al., (in press), giving a

	Middle Sister		S Sister	
	3S132	**3S134**	**3S130**	**3S119**
SiO2	61.9	65.7	62.0	65.8
TiO2	1.10	0.73	0.75	0.91
Al2O3	17.2	16.2	16.5	16.0
FeO*	5.91	5.03	5.25	4.49
MnO	0.14	0.14	0.10	0.10
MgO	1.86	0.99	3.85	1.35
CaO	4.59	2.72	5.72	3.52
Na2O	5.52	6.26	4.08	5.30
K2O	1.47	1.89	1.64	2.34
P2O5	0.33	0.25	0.12	0.26
Rb	24	31	35	46
Ba	508	607	456	653
Sr	483	272	352	329
Cs	0.68	0.85	0.69	1.27
Sc	16.01	12.81	15.68	11.45
V	58	12	109	67
Co	9.76	3.56	20.66	7.73
Ni	<40	18	49	<40
Cr	3	<6	84	5
Zn	152	208	≈60	140
La	18.6	21.3	14.1	20.6
Ce	44.1	53.8	28.5	47.1
Nd	23.1	28.0	15.0	20.4
Sm	5.29	6.75	3.15	4.95
Eu	1.61	1.80	0.90	1.28
Tb	1.04	1.27	0.57	0.90
Yb	2.7	4.2	2.0	2.6
Lu	0.41	0.62	0.28	0.41
La/Sm	2.22	1.99	2.83	2.63
ΣHREE	47.68	66.22	30.32	44.22
Eu/Eu*	0.86	0.77	0.83	0.75
Zr	176	241	110	206
Hf	4.6	7.0	2.9	5.6
Ga	20	21	13	22
Y	27	38	19	26
Nb	10.2	12.7	7.4	10.9
Ta	0.54	0.62	0.45	0.74
Th	2.3	2.9	3.0	4.7
U	0.9	1.3	1.1	1.7

3S132	Andesite lava 1 mi. east of Linton Spring, elevation = 7000'.
3S134	Lane Mesa dacitic flow dome, east margin, 6460'.
3S130	Andesite flow 0.5 mi. SW of Obsidian Falls.
3S119	Dacite flow(?) in SSE flank S. Sister, 7320'.

Table 8.1: Comparision of representative Middle Sister and South Sister andesites and dacites. Note the significant differences in compatible (V, Co, Cr) element and REE abundances between MS and SS types. ΣHREE = chondrite-normalized Tb + Yb + Lu.

Mineral compositions

		SiO2	TiO2	Al2O3	FeO*	MnO	MgO	CaO	Na2O	K2O	P2O5
Oliv	Fo85	39.9			14.9	0.3	45.1	0.2			
Cpx	En51	51.9	0.5	3.0	6.6	0.2	17.4	18.3	0.4		
Plag	An75	47.8		33.1	0.6		0.1	16.2	2.2	0.1	
Opx	En72	52.0	0.3	0.7	19.2	0.9	25.1	1.5	0.0		
Mgt	BA45	0.1	15.5	0.6	77.2	0.3	0.3				
Ap								56.0			43.0

Starting composition

	SiO2	TiO2	Al2O3	FeO*	MnO	MgO	CaO	Na2O	K2O	P2O5
3S106	55.9	1.0	18.3	7.1	0.1	4.6	7.8	4.0	0.9	0.2

BEST FIT
Model 1:   8% Ol, 15% Cpx, 10% Opx, 60% Plag, 7% Mgt, 0.4% Ap

	SiO2	TiO2	Al2O3	FeO*	MnO	MgO	CaO	Na2O	K2O	P2O5
F=0.40	65.6	0.8	16.3	4.7	0.1	0.9	3.6	6.3	1.7	0.3
MS 3S134	65.7	0.7	16.2	5.0	0.1	1.0	2.7	6.3	1.9	0.3

Model 2: 10% Ol, 13% Cpx, 5% Opx, 62% Plag, 10% Mgt, 0% Ap

	SiO2	TiO2	Al2O3	FeO*	MnO	MgO	CaO	Na2O	K2O	P2O5
F=0.44	65.8	0.7	16.2	5.0	0.1	1.9	4.3	5.9	1.6	0.4
MS 3S134	65.7	0.7	16.2	5.0	0.1	1.0	2.7	6.3	1.9	0.3

Model 3: Same mineral %'s as model 1,
8% Ol, 15% Cpx, 10% Opx, 60% Plag, 7% Mgt, 0.4% Ap
But more evolved compositions:

		SiO2	TiO2	Al2O3	FeO*	MnO	MgO	CaO	Na2O	K2O	P2O5
Oliv	Fo70	36.8			26.4	0.5	35.0	0.2			
Cpx	En39	52.9	0.8	3.1	13.1	0.4	12.7	16.8	0.8		
Plag	An60	52.7		29.1	0.9		0.1	12.1	4.5	0.3	
Opx	En68	53.9	0.3	1.0	18.7	0.5	24.7	1.4	0.0		

	SiO2	TiO2	Al2O3	FeO*	MnO	MgO	CaO	Na2O	K2O	P2O5
F=0.26	65.5	0.7	17.9	1.8	0.1	1.6	4.9	5.6	1.8	0.3
MS 3S134	65.7	0.7	16.2	5.0	0.1	1.0	2.7	6.3	1.9	0.3

Table 8.2: Simple mass balance models used to test the crystal fractionation hypothesis for Middle Sister dacites, using the mass balance method described in table 7.1. Starting composition is a representative High Cascade basaltic andesite, and mineral compositions are from analyzed samples in this study. Model 1 represents best fit to observed MS compositions. Models 2 and 3 show how small changes in the fractionating proportions (2) or mineral compositions (3) can significantly change the modeled dacite composition.
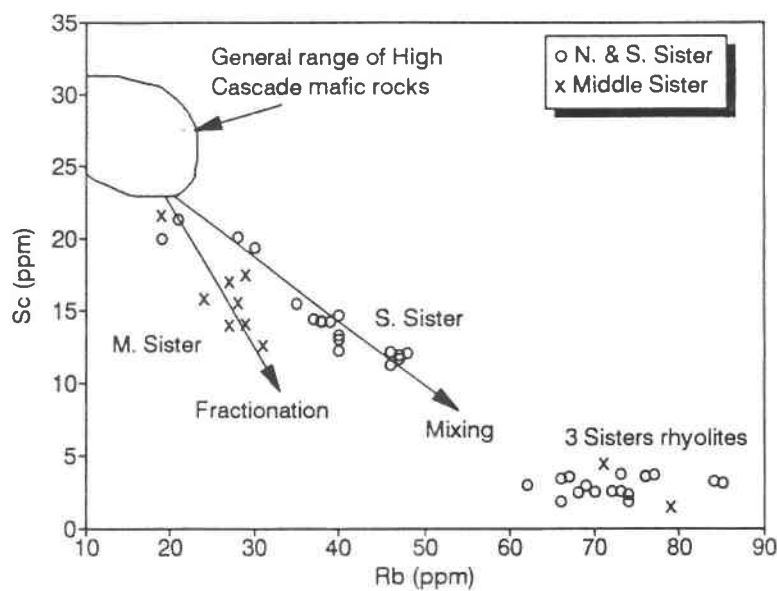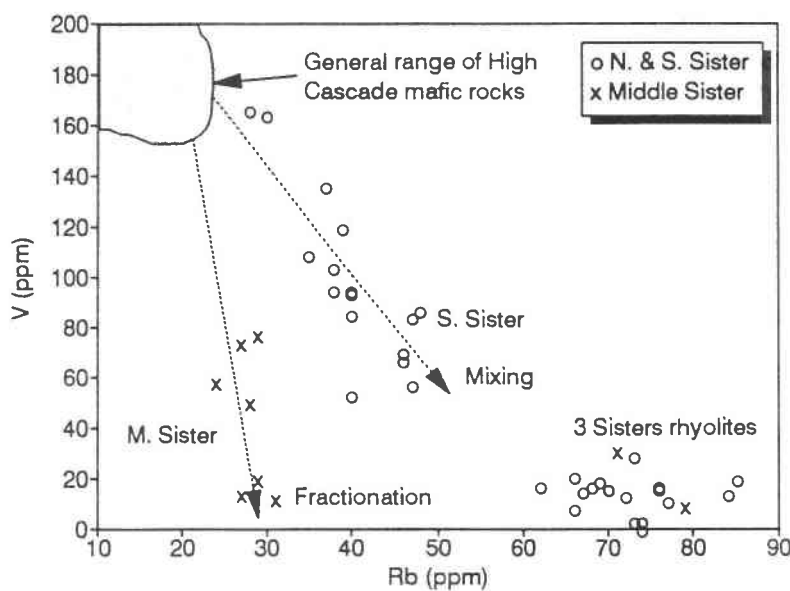
Figure 8.1: Representative compatible-incompatible element plots for Three Sisters rocks. **A)** Depletions in Sc relative to Rb enrichment in the MS intermediate series are consistent with open system fractionation of a typical High Cascade basaltic andesite, involving ≈20% pyroxene. Note the relatively low depletions in Sc relative to Rb enrichment for the SS intermediate series. **B)** Depletions in V relative to Rb enrichment in the MS intermediate series also are consistent with open system fractionation of a typical High Cascade basaltic andesite, involving ≈7% magnetite. Note the relatively low depletions in V relative to Rb enrichment for the SS intermediate series.

cpx K_{dSc} = 5 and opx K_{dSc} ≈ 2. The resulting D_{Sc}≈1 (using mass balance %'s) is too low to have produced the observed depletions in Sc relative to Rb enrichment in figure 8.1a, using simple equilibrium fractionation.

Steady-state recharge of the fractionating system by basaltic andesite melt, however, will produce larger incompatible element enrichments relative to compatible element depletions than are possible through simple equilibrium fractionation (Nielsen, 1988; Defant and Nielsen, 1990). This relationship is shown in figure 8.2 for Sc and V, two elements that are strongly compatible in px + mgt. Opening the evolving system to recharge (2-0-1) by parental basaltic andesite melts results in mixed compositions that are lower in compatible elements, relative to a closed system (0-0-0) model. Combining recharge with modest amounts of silicic magma mixing (≈20%) also results in incompatible element enrichments, relative to both closed system fractionation and recharge. Thus, if only 5 ppm of the observed Rb enrichments were due to simple fractionation effects and the other 5 ppm were due to open system recharge and eruption, the resulting depletions in Sc for the MS intermediate series could be produced with an effective D_{Sc}≈1.

The same arguments can be applied to V depletions in figure 8.1b. To produce the observed depletions in V through simple equilibrium fractionation would necessitate a D_V≈7 and a magnetite K_{dV}≈80, which is twice as high as generally measured in andesitic rocks (Appendix E). Open system processes indicated by Rb enrichments, however, would lower the necessary magnetite K_{dV} to ≈40, which corresponds to published mineral/matrix distribution coefficients.

The distribution of Zr versus Rb also clearly shows that the MS intermediate series was produced primarily through fractionation and recharge of a basaltic andesite to dacite system, but that a significant amount of silicic magma mixing is required to account for the observed SS patterns (figure 8.3). Zr remains an incompatible element during fractionation until zircon saturation is reached, which is a function of both temperature and composition of the melt (Watson and Harrison, 1983). Application of Watson and Harrison's experimental results shows that zircon saturation for Three Sisters (and BT) intermediate compositions requires >500 ppm Zr in the melt for temperatures >930°C, but ≤250 ppm Zr at temperatures of ≤860°C. Zr should thus behave incompatibly during fractionation of the intermediate series, as temperatures are likely ≥930°C (Chapter 5). The Zr/Rb of the MS series is very close to the Zr/Rb produced by CHAOS 0-0-0 and 2-0-1 models, indicating that fractionation paired with basaltic andesite recharge can produce the MS intermediate series (figure 8.3). The buffering of Zr with respect to increasing Rb in the SS series cannot be produced through zircon fractionation, and must represent a significant amount (≥20%) of rhyolite mixing into the evolving intermediate system.

Rare earth element (REE) trends are also consistent with a fractionation hypothesis for MS intermediate series rocks. Fractionation of cpx + opx + ol + plag + mgt will have little effect on La/Sm, due to the low distribution coefficients for these elements (Nielsen, 1990; Nielsen et al., in
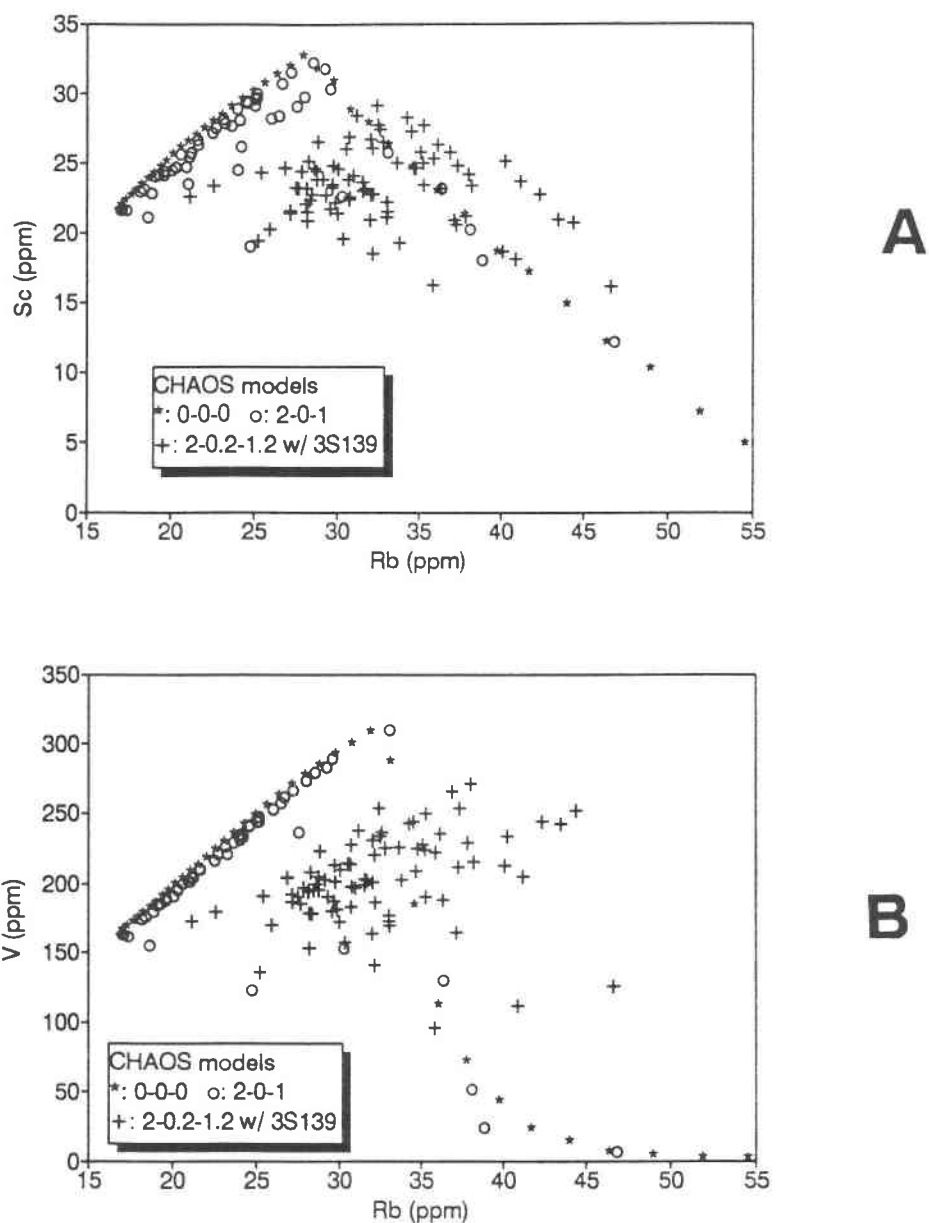
Figure 8.2: Results of intermediate system CHAOS models. Models used a typical High Cascade basaltic andesite (3S106) under closed system fractionation (0-0-0, F=0.24), steady-state fractionation with randomized recharge events (2-0-1) and fractionation paired with recharge and mixing of Three Sisters rhyolite magmas (2-0.2-1.2). Both open system models were run until F=800. Relative to the High Cascades, the models are enriched in compatible elements due to the late crystallization of augite (Sc) and magnetite (V) in CHAOS simulations. These models show that incompatible elements are relatively enriched when the system is open to rhyolite mixing, and that magma recharge will result in lower compatible element abundances relative to simple fractionation.
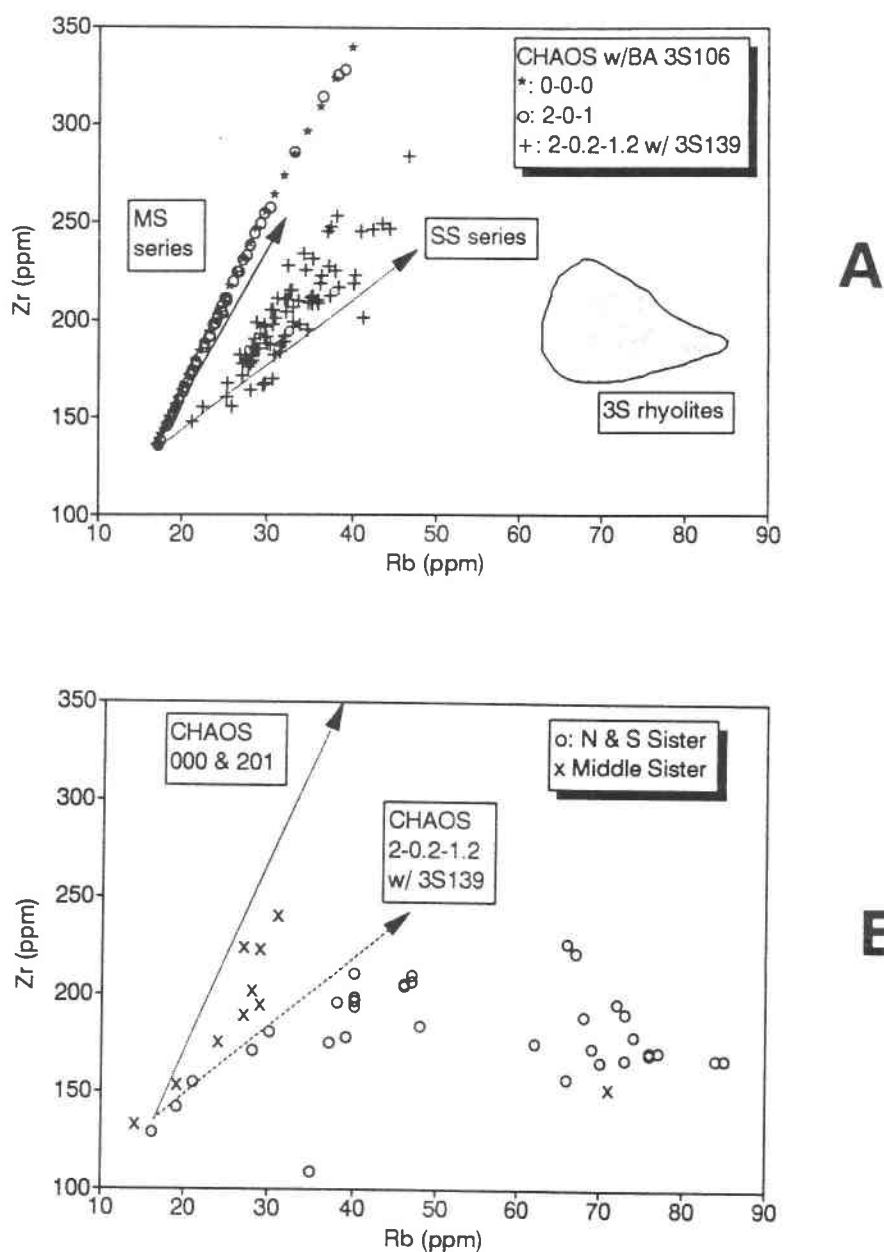
Figure 8.3: Results of CHAOS models showing variations in Zr vs. Rb. **A)** Closed system fractionation (0-0-0) or recharge (2-0-1) models account for the observed variation between Zr and Rb in the MS system, as zircon is not a fractionating phase for these compositions. Open system (2-0.2-1.2) models using rhyolite 3S139 are necessary to successfully model Zr vs. Rb variations in the SS system. **B)** CHAOS trends superimposed on Three Sisters data. Note that the 2-0.2-1.2 model is relatively enriched in Zr, indicating that higher assimilation rates are probably necessary to account for the SS data. Higher assimilation rates, however, quench the system during CHAOS simulations.

press). The incompatible heavy REE's Tb, Yb, and Lu (cpx $K_d \approx 0.8$) will also be enriched in the melt, with negligible fractionation between these elements (Nielsen et al., in press). The fractionation of apatite, however, can potentially alter La/Sm, due to the relatively high compatibility of the MREE's (Appendix E). However, apatite fractionation is limited to differentiation above 62% SiO_2, and constrained by mass balance calculations to involve ≤0.5% of the fractionating assemblage. REE trends observed for MS intermediate rocks are consistent with the fractionation hypothesis, with little MREE depletion or La/Sm fractionation occurring with differentiation from a basaltic andesite parent (figure 8.4). The trends observed for SS rocks, however, are not consistent with a fractionation hypothesis; the large increases in La/Sm and depletions in HREE abundances necessitate ≥5% apatite in the fractionating assemblage, which is not supported by either mass balance or experimental models (Green and Watson, 1982).

The intermediate rocks at Middle Sister are thus the products of open-system differentiation from a periodically recharged basaltic andesite to dacite magma system. Although small amounts of rhyolite magma mixing may have contributed to some of the geochemical variations observed in the MS intermediate series, this series was essentially produced through crystal fractionation. In addition, this system must have been closed to large amounts of recharge by parental **basaltic** melts or else it would not have been able to differentiate into intermediate compositions. Because mafic volcanism has occurred throughout the history of this area, it is highly unlikely that closure of the evolving MS intermediate system to mafic recharge was due to a cessation of mafic magmatism at depth. Segregation of the MS intermediate magmatic system to shallower crustal levels (20-30 km??), however, may have served to effectively isolate the system from basaltic recharge.

In contrast to Middle Sister, crystal fractionation is not capable of generating the South Sister intermediate series. Fractionation of pyroxene, plagioclase, olivine and magnetite cannot generate the observed La/Sm enrichments, which are associated with little increase in HREE abundance (figure 8.4). Fractionation of ≥5% apatite might produce some of the observed HREE depletions, but P_2O_5 generally **increases** with differentiation in the SS intermediate series (table 8.1), precluding any significant amount of apatite fractionation; simple mass balance calculations show that crystallization of only 0.5% apatite will buffer the melt in P_2O_5. The observed decreases in Zr/Rb (figure 8.3) could have been produced through zircon fractionation, but the SS intermediate series was too hot (≥950°C) to have been saturated in zircon at only ≈200 ppm Zr (Watson and Harrison, 1983).

South Sister intermediate rocks generally plot along mixing lines between basaltic andesite and Three Sisters rhyolite (figures 8.1 and 8.3). Linear mixing of ≈50% basaltic andesite (e.g., 3S106) with ≈50% rhyolite (e.g., 3S140) reproduces many of the general major and trace element abundances of SS intermediate rocks, including REE patterns (figure 8.5a). Crystallization must have accompanied mixing, as the rhyolite was probably at a significantly lower temperature
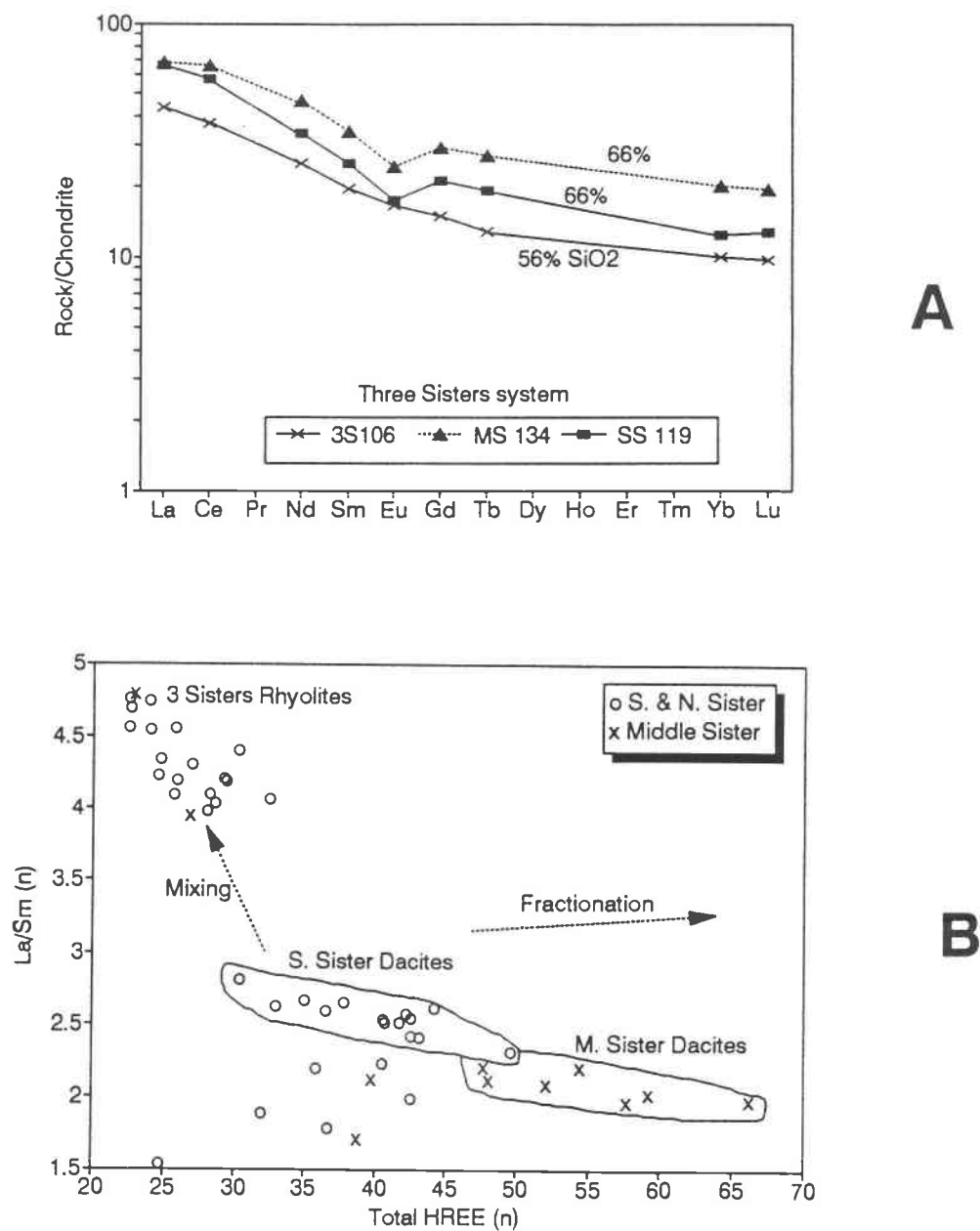
Figure 8.4: Rare earth element plots for Three Sisters rocks. **A)** Chondrite-normalized (Anders and Ebihara, 1982) REE diagram for a typical High Cascade basaltic andesite (3S106), MS dacite (MS 134) and SS dacite (SS 119). Note that the REE trends for the MS dacite and basaltic andesite are parallel, but the SS dacite has distinct HREE and LREE slopes. **B)** Chondrite-normalized La/Sm (i.e. LREE slope) versus normalized Tb+Yb+Lu (HREE abundance) for Three Sisters rocks. Fractionation will produce little change in La/Sm with increasing HREE abundance (MS dacites). Mixing with Three Sisters rhyolites must have occurred for SS dacites in order to produce the observed increases in La/Sm with little change in HREE abundance.
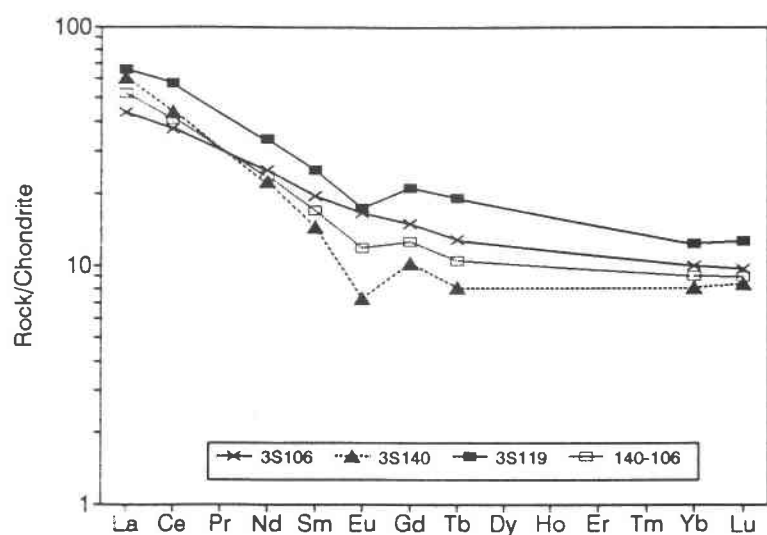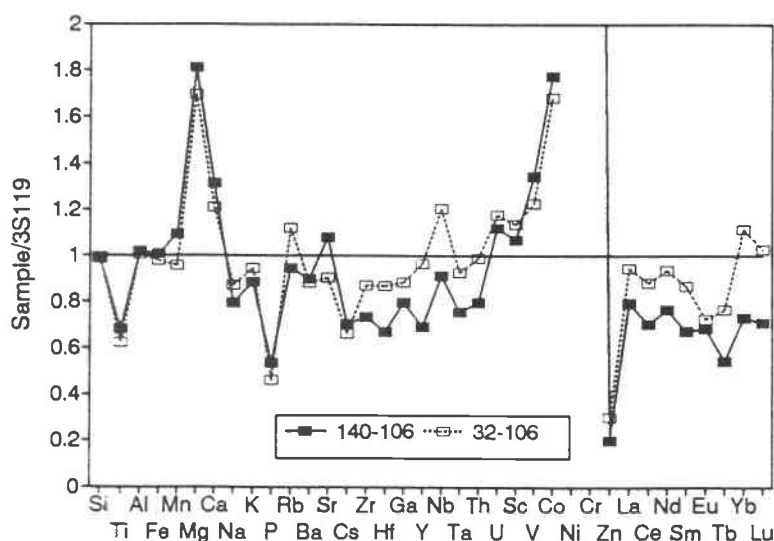
Figure 8.5: Mixing diagrams for South Sister dacite petrogenesis. **A)** Chondrite-normalized REE diagram for a 50% mixture of basaltic andesite 3S106 with 50% Three Sisters rhyolite 3S140. The resulting mixture (140-106) has a REE pattern that is parallel (very slight MREE depletion) to SS dacite 3S119. Fractionation of plag + px + mgt ± ap will enrich all REEs to SS dacite levels. **B)** Enrichment-depletion diagram for Three Sisters (140-106) and Broken Top (32-106) rhyolite mixes with basaltic andesite 3S106, plotted relative to SS dacite 3S119. Although both mixtures have similar major element characteristics, a mix with Broken Top rhyolite results in anomalously high incompatible element abundances (Ta, Rb, Th, HREE), which precludes developing the observed compatible element depletions in 3S119 through crystal fractionation. A mixture with a Three Sisters rhyolite permits subsequent fractionation of trace elements to observed abundances.

($\approx 900\,^{\circ}$C) than the basaltic andesite ($\approx 1100\,^{\circ}$C). As shown by CHAOS models, the effect of crystallization will be to shift the mixing vectors towards MS fractionation trends, which is observed for SS intermediate rocks in figures 8.1 and 8.3. Mixing paired with ≈ 20-30% fractionation of pyroxene, plagioclase and magnetite will also increase total REE abundances without REE fractionation, and produce relative depletions in Eu (cf., Middle Sister dacites). This type of fractionation will increase the REEs in the rhyolite-basaltic andesite mixture to the levels observed in SS dacites (figure 8.5a).

The mixing hypothesis for the SS intermediate series was also tested using rhyolite 3S032 from the Broken Top system as the silicic component. Although the overall patterns obtained with a BT rhyolite mix were similar to the 3S rhyolite mix (figure 8.5b), incompatible element abundances were generally too high (especially HREE) and compatible element abundances too low to allow for any significant amount of fractionation subsequent to mixing; the depletions in Mg, Ca, Sr and transition metals observed in SS dacites require that mixing is accompanied by ≈ 20-30% fractionation of pyroxene and plagioclase (figure 8.5b).

Evolution of the South Sister intermediate series must have been dominated by mixing subequal amounts of basaltic andesite and rhyolite magmas, with subordinate amounts of crystal fractionation. A detailed study of mafic-silicic magma mixing by Frost and Mahood (1987) in the Lamarck pluton, and the theoretical models of Sparks and Marshall (1986), concluded that homogenization of similarly mixed magmas would only occur if the mass fraction of mafic magma was ≥ 0.5; smaller mass fractions result in quenching of the mafic magma. Mixing lesser amounts of mafic magma into a rhyolitic magma body should thus result in mafic enclaves (cf., Bacon, 1986; Linneman and Meyers, 1990) and **not** a homogenous dacite or rhyodacite. Trace amounts of small (≤ 1 mm) mafic clots were observed in the most silicic SS dacites (3S119 and 3S150), but were absent from other studied intermediate rocks. The occurrence of these mafic clots in only the most silicic SS dacites further indicates that these compositions represent the upper silica limit for mafic mixing/homogenization. Restriction of the SS intermediate system to $\leq 66\%$ SiO_2 is not an arbitrary boundary, but most likely reflects the lowest percentages of mafic magma that could be homogenized in a Three Sisters rhyolitic melt. In addition, ≈ 50:50 mixing of a more silicic magma (i.e. 61% SiO_2 andesite) into the rhyolitic magma would result in a mixture that was more silicic than 66% SiO_2. Pyroxene and plagioclase fractionation coupled with mixing would further increase the SiO_2 content of the mixture, resulting in the formation of a rhyodacitic magma (i.e., $\geq 68\%$ SiO_2). The absence of any rocks at South Sister with $SiO_2 \geq 66\%$ indicates that the lower silica component of mixing was mafic and not intermediate in composition.

The lack of distinct mixing trends between MS intermediate rocks and Three Sisters rhyolites may indicate that rhyolitic melts were not sufficiently abundant during MS evolution to generate intermediate compositions through extensive mafic-rhyolitic magma mixing. The previous discussion

of mafic magmatism has shown the necessity of ≈20-30% silicic magma mixing/assimilation to produce many of the observed open-system trends. These silicic partial melts, however, were likely generated in the lower crust adjacent to a large, long-lived mafic system, and subsequently homogenized into that system. The effects of silicic magma mixing are not restricted to mafic rocks associated with silicic volcanic centers, but are present in mafic rocks throughout the Oregon High Cascades (cf., Conrey and Sherrod, 1988; Conrey, 1991; Hughes, 1990; this study). This observation suggests that silicic mixing is a regional (i.e., deep crustal) feature, and can occur in areas that lack intermediate to silicic volcanos.

Geochemical modeling also indicates that it is unlikely that the regional High Cascades mafic system could differentiate to intermediate compositions, due to the large amounts of basaltic recharge necessary to maintain thermal balance. The MS intermediate system must have segregated from the large mafic system near the base of the crust, and probably resided at some intermediate crustal level (30-20 km?). The lack of abundant rhyolite mixing could indicate that the rhyolitic magmas resided at a different crustal depth, or that there were no effective connections between the rhyolite and MS intermediate system. It is also possible that rhyolitic magmas were not present at mid-crustal levels during MS evolution. Stratigraphic correlations and K-Ar dates (Chapter 3) strongly indicate that rhyolitic volcanism in the Three Sisters is a relatively young (≈90 ka) feature, and probably post-dates most Middle Sister activity. The lack of petrologic evidence for rhyolite mixing, which is so abundant at South Sister, further supports the argument that rhyolitic magmatism was not appreciably developed during the evolution of Middle Sister.

Although it cannot be proven with the present data, it is likely that Middle Sister volcanism was contemporaneous (± 50 ka) with Broken Top volcanism. There is, however, no evidence to suggest that the MS intermediate system interacted in any way with the Broken Top magmatic system. In addition, there is no evidence to suggest that the Broken Top and South Sister magmatic systems interacted to generate intermediate composition rocks, supporting the argument that South Sister is probably younger that the Broken Top system (≤100 ka vs. ≈100-200 ka).

8.3 Broken Top Intermediate System

The mineralogy of the Broken Top system intermediate series is the same as observed in the Three Sisters system: plag + cpx + opx + mgt ± ol from ≈56% to ≈63% SiO_2, with no ol and subequal amounts of cpx and opx from ≈63% to 72% SiO_2. Apatite is a groundmass phase for $SiO_2 \geq 62\%$, and amphibole is only observed as a rare trace phase in two rhyodacites. Unlike the Three Sisters system, there are no textural or mineralogical distinctions among similar composition rocks from different vents within the Broken Top system, i.e., rocks from the TVC show the same phases and textures as rocks from Tam MacArthur Rim or Broken Top vents.

Major elements usually vary linearly with increasing SiO_2 for Broken Top system basaltic andesites through rhyodacites (cf., figure 6.3), with the exceptions of Al_2O_3, Na_2O, and P_2O_5. These elements show relatively large degrees of scatter to 65% SiO_2, but more linear distributions from 65% to 72% SiO_2. The small degree of scatter observed for most elements above 65% SiO_2 could possibly represent a liquid line of descent along a well-defined cotectic, or a mixing trend between rhyolite and less silicic magmas. Representative analyses of Broken Top intermediate series rocks are given in table 8.3.

The fractionation hypothesis can first be tested through simple mass balance models (table 8.4). Differentiation from 63% to 65% SiO_2 always results in increasing Na_2O when the fractionated plagioclase is at least as calcic as andesine. A fractionating assemblage of 54% An_{60} plag, 20% cpx, 14% opx, 9% mgt, 1.5% ilmn and 1.5% ap (model #1) duplicates the composition of those Broken Top dacites that have unusually high Na_2O (>5.5 wt.%). High Na_2O produced through crystal fractionation is also a characteristic of Middle Sister dacites (figure 8.6).

In contrast, differentiation for most of the Broken Top intermediate series (lower Na_2O) cannot be modeled through crystal fractionation. Above 65% SiO_2, fractionation models must account for decreasing Na_2O with increasing SiO_2, which necessitates ≥75% An_{25} plagioclase in the crystallizing assemblage (models 2-4, table 8.4). Phenocrysts more sodic than ≈An_{30} are rarely found in Broken Top rhyodacites, and it is highly unlikely that relatively hydrous (3-4% H_2O; chapter 5) dacitic to rhyodacitic magmas would have crystallized oligoclase rather than andesine. Even when ≥75% oligoclase is used in mass balance models, fractionation of opx ± hb ± cpx cannot produce the observed variations in CaO, MnO and MgO (table 8.4) above 65% SiO_2.

Assimilation of rhyolitic crust (i.e. mixing with rhyolitic magma) paired with crystal fractionation (cf., DePaolo, 1981) is necessary to produce most of the Broken Top intermediate series. Models were constructed (table 8.5) using Broken Top rhyolite 3S032 as the assimilant, which has higher SiO_2 and K_2O than all other Broken Top intermediate series rocks. Although crystal fractionation of basaltic andesite can produce Broken Top low silica (≈63% SiO_2) dacites (table 8.4), smaller proportions of rhyolite assimilation (R = mass assimilated / mass fractionated = 0.1 to 0.2) with plag + ol + cpx + opx + mgt + ilmn + ap fractionation can also produce many Broken Top series low-silica dacites (table 8.5). However, the low silica dacites did not evolve to high Na_2O dacite compositions with any significant amounts of rhyolite mixing, because mixing these compositions would result in lower Na_2O abundances.

The main Broken Top intermediate series above 63% SiO_2 is characterized by decreasing Na_2O with increasing SiO_2, which cannot be produced through realistic crystal fractionation models (table 8.4). However, assimilation of rhyolitic magma at R = 0.3 paired with fractionation can reproduce the main Broken Top intermediate trend to rhyodacitic compositions (table 8.5, model #2). A second, higher Na_2O trend (≥65% SiO_2) can also be generated from the high-Na_2O dacites

Sample	3S107	High Na		Main Series	
		3S100	3S098	3S036	3S037
SiO2	63.0	64.9	71.1	64.9	69.6
TiO2	1.10	0.97	0.40	1.02	0.54
Al2O3	16.2	16.3	14.9	16.0	15.4
FeO*	5.84	4.85	2.74	4.94	3.31
MnO	0.13	0.14	0.08	0.11	0.07
MgO	1.84	1.22	0.30	1.33	0.36
CaO	4.23	3.26	1.40	3.43	1.64
Na2O	5.45	6.22	6.13	5.54	5.38
K2O	1.87	1.99	2.77	2.23	2.93
P2O5	0.33	0.30	0.07	0.33	0.11
Rb	37	39	58	41	59
Ba	558	548	721	649	736
Sr	375	300	135	363	181
Cs	1.10	1.29	2.04	0.50	0.90
Sc	16.27	14.07	9.25	13.60	8.73
V	98	24	1	58	15
Co	9.63	3.84	1.59	7.14	2.50
Ni	4	6	10	9	10
Cr	8	4	2	<5	<5
Zn	135	207	135	80	54
La	21.8	24.6	24.4	24.1	22.2
Ce	51.5	62.6	61.3	50.4	53.7
Nd	28.6	34.0	30.8	27.9	24.0
Sm	6.50	7.84	6.46	6.59	5.99
Eu	1.58	2.04	1.28	1.65	1.28
Tb	1.00	1.45	1.28	0.95	0.84
Yb	3.6	4.8	4.2	3.4	3.5
Lu	0.51	0.77	0.66	0.51	0.50
La/Sm	2.12	1.98	2.38	2.31	2.34
ΣHREE	54.21	77.55	67.67	52.10	50.02
Eu/Eu*	0.74	0.75	0.56	0.77	0.66
Zr	222	272	274	250	308
Hf	5.8	7.7	8.3	6.3	8.4
Ga	21	19	20	18	19
Y	34	42	37	34	30
Nb	14.4	20.0	15.5	15.7	16.8
Ta	0.71	1.03	0.90	0.80	1.00
Th	3.3	3.8	5.5	4.0	5.4
U	1.5	1.3	2.2	1.6	2.2

3S107: Representative High Cascade low silica dacite, Broken Top.
3S100: High Na₂O dacite, S. Fork Squaw Ck., 6600'.
3S098: High Na₂O rhyodacite, older dome at Squaw Ck. Falls.
3S036: Main series dacite, east Tam MacArthur Rim.
3S037: Main series rhyodacite, east Tam MacArthur Rim.

Table 8.3: Representative Broken Top system intermediate series rocks, with examples of high Na$_2$O dacite and rhyodacite. Differentiation to high Na$_2$O is a feature of crystal fractionation, as assimilation of relatively low Na$_2$O (≈5%) rhyolite will lower Na$_2$O in the evolving magmas. Note that evolution to high Na$_2$O dacite results in increasing HREE's, but that main series differentiation is characterized by relatively constant HREE abundances.
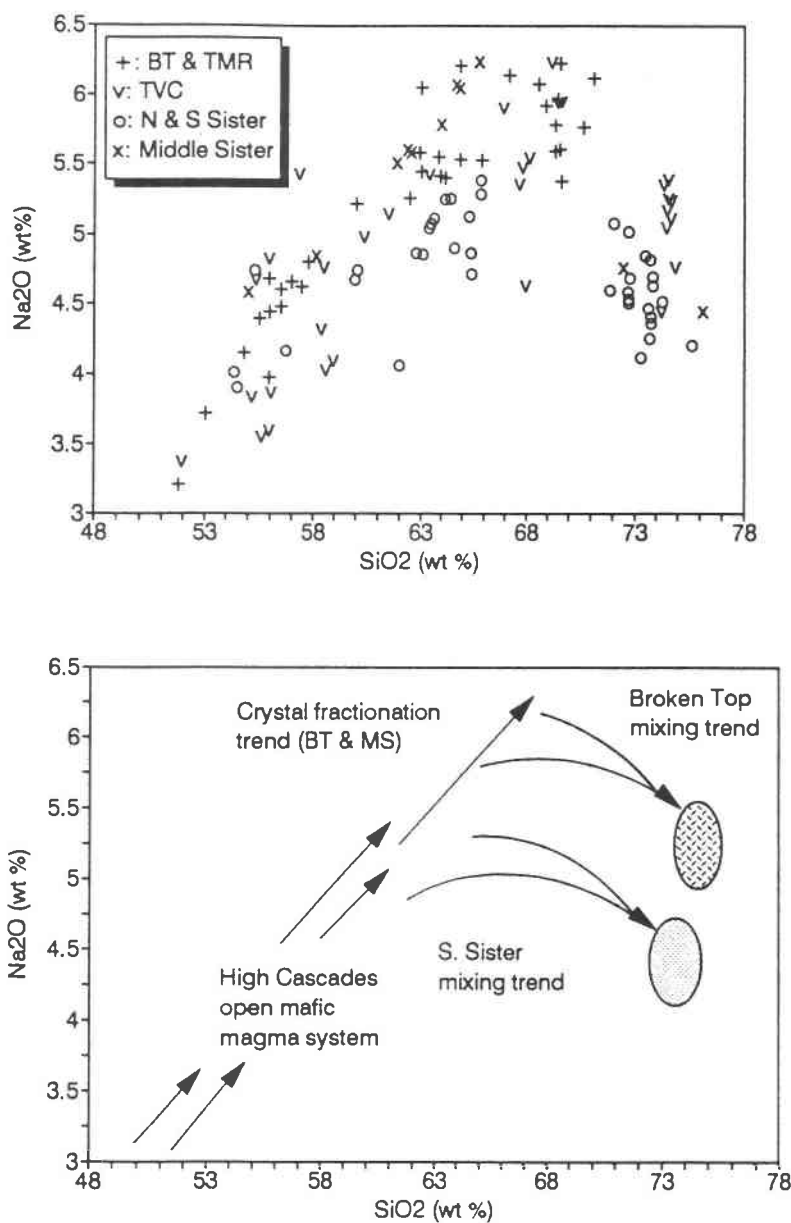
Figure 8.6: Variations in Na_2O and SiO_2 for High Cascades rocks in this study. Crystal fraction-ation with plagioclase as sodic An_{30} will produce a Na_2O enrichment trend; significant amounts of rhyolite mixing ($\approx$20-30%) and fractionation of sodic plagiocase (An_{25-30}) is necessary to buffer or deplete Na_2O in the intermediate series. Note that several Broken Top dacites have the same elemental abundances as Middle Sister dacites, and that the South Sister and Broken Top series follow different mixing paths due to the different rhyolite compositions in each system.

		SiO2	TiO2	Al2O3	FeO*	MnO	MgO	CaO	Na2O	K2O	P2O5
Cpx	En37	51.2	0.4	1.4	13.5	0.8	12.4	18.6	0.3		
Plag	An60	52.7		29.1	0.9		0.1	12.1	4.5	0.3	
Plag	An35	58.7		25.6	0.5		0.0	7.2	7.0	0.4	
Plag	An20	62.5		22.3	0.2		0.0	4.1	8.5	0.8	
Opx	En68	53.9	0.3	1.0	18.7	0.5	24.7	1.4	0.0		
Mgt		0.1	14.5	2.2	78.1	0.7	1.4				
Ilmn		0.0	42.2		51.5	0.6	2.5				
Apt								56.0			43.0
Hb		42.1	3.8	10.4	14.7	0.3	12.9	10.7	2.3	0.3	

Model #1: Starting composition

	SiO2	TiO2	Al2O3	FeO*	MnO	MgO	CaO	Na2O	K2O	P2O5
3S107	63.0	1.10	16.2	5.84	0.13	1.84	4.23	5.45	1.87	0.33

54% An$_{60}$, 20% Cpx, 14% Opx, 9% Mgt, 1.5% Ilmn, 1.5% Ap

	SiO2	TiO2	Al2O3	FeO*	MnO	MgO	CaO	Na2O	K2O	P2O5
F=0.88	65.1	0.97	16.1	4.85	0.12	1.28	3.37	5.82	2.09	0.29
3S100	64.9	0.97	16.3	4.85	0.14	1.22	3.26	6.22	1.99	0.30

Models #2-#4: Starting composition

	SiO2	TiO2	Al2O3	FeO*	MnO	MgO	CaO	Na2O	K2O	P2O5
3S100	64.9	0.97	16.3	4.85	0.14	1.22	3.26	6.22	1.99	0.30

76% An$_{25}$, 14% Hb, 7.3% Mgt, 1% Ilmn, 1.7% Ap

	SiO2	TiO2	Al2O3	FeO*	MnO	MgO	CaO	Na2O	K2O	P2O5
F= 0.56	71.8	0.39	14.6	2.80	0.16	0.81	1.59	6.10	2.79	0.06
3S098	71.1	0.40	14.9	2.74	0.08	0.31	1.40	6.13	2.77	0.07

Model #3: 3S100 with
76% An$_{25}$, 7% Hb, 7.3% Mgt, 1% Ilmn, 1.7% Ap

	SiO2	TiO2	Al2O3	FeO*	MnO	MgO	CaO	Na2O	K2O	P2O5
F= 0.56	71.4	0.53	15.0	2.40	0.13	0.53	1.97	6.19	2.80	0.06
3S098	71.1	0.40	14.9	2.74	0.08	0.31	1.40	6.13	2.77	0.07

Model #4: 3S100 with
77% An$_{25}$, 13% Opx, 5.3% Mgt, 3% Ilmn, 1.7% Ap

	SiO2	TiO2	Al2O3	FeO*	MnO	MgO	CaO	Na2O	K2O	P2O5
F= 0.58	70.6	0.40	15.3	2.58	0.11	0.39	2.39	6.23	2.77	0.07
3S098	71.1	0.40	14.9	2.74	0.08	0.31	1.40	6.13	2.77	0.07

Model #5, main trend: 3S107 with
71% An$_{30}$, 12% Cpx, 9% Opx, 3.5% Mgt, 3% Ilmn, 1.5% Ap

	SiO2	TiO2	Al2O3	FeO*	MnO	MgO	CaO	Na2O	K2O	P2O5
F= 0.44	69.7	0.53	15.4	4.32	0.09	0.32	2.06	5.34	2.96	0.09
3S037	69.6	0.54	15.4	3.31	0.07	0.36	1.64	5.38	2.93	0.11

Table 8.4: Simple mass balance models for Broken Top dacite to rhyodacite differentiaion. Model #1 shows that crystal fractionation from 63% to 65% SiO$_2$ produces a high Na$_2$O trend. Continued fractionation above 65% SiO$_2$ fails to produce the Broken Top main intermediate series compositions (Models 2-4); note that An$_{25}$ plag is required to buffer Na$_2$O, and the poor correspondence between observed and modeled CaO, MnO and MgO. Anhydrous assemblages (model #4) produce the best fit for most elements, but fail to account for CaO abundances. Using a lower Na$_2$O parent still requires An$_{30}$ plag (model #5) to buffer Na$_2$O in the main trend; plag phenocrysts <An$_{30}$ are rarely found in rhyodacites. Magma differentiation above 65% SiO$_2$ in the Broken Top system was not controlled by crystal fractionation.

	SiO2	TiO2	Al2O3	FeO*	MnO	MgO	CaO	Na2O	K2O	P2O5
Olv Fo70	36.8			26.4	0.5	35.0	0.2			
Cpx En39	52.9	0.8	3.1	13.1	0.4	12.7	16.8	0.8		
Plg An60	52.7		29.1	0.9		0.1	12.1	4.5	0.3	
Plg An40	59.2		26.1	0.4		0.0	8.1	6.2	0.5	
Plg An35	58.7		25.6	0.5		0.0	7.2	7.0	0.4	
Plg An20	62.5		22.3	0.2		0.0	4.1	8.5	0.8	
Opx1 En68	53.9	0.3	1.0	18.7	0.5	24.7	1.4	0.0		
Opx2 En55	52.4	0.1	0.4	24.8	1.1	20.2	0.9	0.1		
Mgt	0.1	14.5	2.2	78.1	0.7	1.4				
Ilmn	0.0	42.2		51.5	0.6	2.5				
Apt							56.0			43.0
Hb	42.1	3.8	10.4	14.7	0.3	12.9	10.7	2.3	0.3	
3S032	74.5	0.15	13.7	1.70	0.06	0.01	0.71	5.26	3.48	0.02

Starting composition

	SiO2	TiO2	Al2O3	FeO*	MnO	MgO	CaO	Na2O	K2O	P2O5
3S093	57.5	1.25	17.4	7.60	0.14	3.37	6.73	4.63	1.17	0.27

AFC Model #1 R = 0.1

65% An$_{57}$ Plag, 5% Ol, 15% Cpx, 8% Opx1, 5.6% Mgt, 1% Ilmn, 0.4% Ap

	SiO2	TiO2	Al2O3	FeO*	MnO	MgO	CaO	Na2O	K2O	P2O5
3S107	63.0	1.10	16.2	5.84	0.13	1.84	4.23	5.45	1.87	0.33
F = 0.54	63.4	1.08	16.1	5.79	0.13	1.82	4.29	5.49	1.85	0.31

AFC Model #2 main series, R = 0.3

69% An$_{30}$ Plag, 14% Cpx, 9% Opx2, 3.5% Mgt, 3% Ilmn, 1.5% Ap

Starting Composition

	SiO2	TiO2	Al2O3	FeO*	MnO	MgO	CaO	Na2O	K2O	P2O5
3S107	63.0	1.10	16.2	5.84	0.13	1.84	4.23	5.45	1.87	0.33
F = 0.50	70.6	0.48	15.4	3.40	0.05	0.39	1.76	5.40	3.03	0.09
3S037	69.6	0.54	15.4	3.31	0.07	0.36	1.64	5.38	2.93	0.11

AFC Model #3, R = 0.35

75% An$_{25}$ Plag, 8% Cpx, 8% Opx2, 4.5% Mgt, 3% Ilmn, 1.5% Ap

Starting composition

	SiO2	TiO2	Al2O3	FeO*	MnO	MgO	CaO	Na2O	K2O	P2O5
3S100	64.9	0.97	16.3	4.85	0.14	1.22	3.26	6.22	1.99	0.30
F = 0.62	71.0	0.42	15.2	2.84	0.10	0.37	1.58	6.16	2.86	0.09
3S098	71.1	0.40	14.9	2.74	0.08	0.31	1.40	6.13	2.77	0.07

Table 8.5: Mass balance models of assimilation with crystal fractionation for Broken Top intermediate series magmatism. Assimilation of rhyolite 3S032 was modeled by addition of R * F (Ratio of mass assimilated/mass fractionated * 2% Fractionation increment) of 3S032 to each fractionation increment. Model #1 shows that small amounts (R = 0.1-0.2) of crustal assimilation paired with fractionation of basaltic andesite can produce Broken Top low silicia dacites. Main series rhyodacites (Model #2) can be produced through AFC of low silica dacites, with assimilation rates of 0.3. Model #3 shows that AFC involving higher assimilation rates and fractionation of more sodic plagioclase may generate high Na$_2$O rhyodacites from high Na$_2$O dacites.

through slightly higher assimilation proportions (R = 0.35) and increased fractionation of more sodic plagioclase (table 8.5, model #3).

Compatible element variations (e.g., Sc and V, figure 8.7) in the main Broken Top intermediate series also do not support a simple fractionation hypothesis. Using the arguments developed for the Middle Sister series, incompatible element abundances in the main BT intermediate series are too high (relative to compatible element depletions) to have originated through simple crystal fractionation of the mass-balance constrained mineral assemblage. The observed variations are also not consistent with the effects of recharge by andesitic melts, which will maintain essentially constant compatible element abundances but increase incompatible element abundances. The compatible element variations are consistent, however, with a model similar to the one developed for SS, which requires 20-30% of silicic magma mixing to account for the observed variations. The amount of mixing should be less than at South Sister, as much of the main BT series is intermediate between the MS (fractionation dominated) and SS (mixing dominated) fields (figure 8.7). Broken Top units that plot closest to the MS fields are part of the high Na_2O trend, which was apparently produced through crystal fractionation.

The distribution of Zr versus Rb also clearly shows that mixing of rhyolitic magma is required to account for the observed variations (figure 8.8). It has been shown that Zr remained an essentially incompatible element during intermediate series fractionation, due to the elevated temperatures ($\geq 930°C$) and low concentrations of Zr (≤ 350 ppm) that prevented zircon saturation in the BT melts. CHAOS models show that neither simple fractionation (0-0-0) nor recharge (2-0-1) can account for the observed Zr-Rb distributions, but that a model involving $\approx 20\%$ mixing of rhyolite (2-0.2-1.2) reproduces the observed scatter and relative increases in Zr and Rb to 72% SiO_2 (figure 8.8). Note that mixing of $> 20\%$ rhyolite with the differentiating basaltic andesite system would probably result in lower Zr/Rb than observed in the Broken Top system.

Variations in REE's also show that rhyolite mixing is required to produce the BT intermediate series. The REE's form essentially sub-parallel patterns, increase in overall abundance, and develop small negative Eu anomalies from basaltic andesite to $\approx 63\%$ SiO_2 (figure 8.9a), which is characteristic of plagioclase-pyroxene fractionation with small (R ≈ 0.1) rhyolite assimilation rates. However, two distinct REE trends develop above 63% SiO_2 in the Broken Top system. In the high Na_2O trend, the REE's continue to enrich until 65% SiO_2 (figure 8.9a), which is consistent with plagioclase-pyroxene fractionation and results in high Na_2O dacites. Differentiation in the high Na_2O trend from 65% to 72% SiO_2 results in small MREE and HREE depletions, which was produced by apatite fractionation (model 3, table 8.5) paired with magma mixing (figure 8.9a). In contrast, the main trend has essentially constant REE abundances from 63% to $\approx 65\%$ SiO_2, and only minor LREE and HREE enrichments developed by $\approx 70\%$ SiO_2 (figure 8.9b).
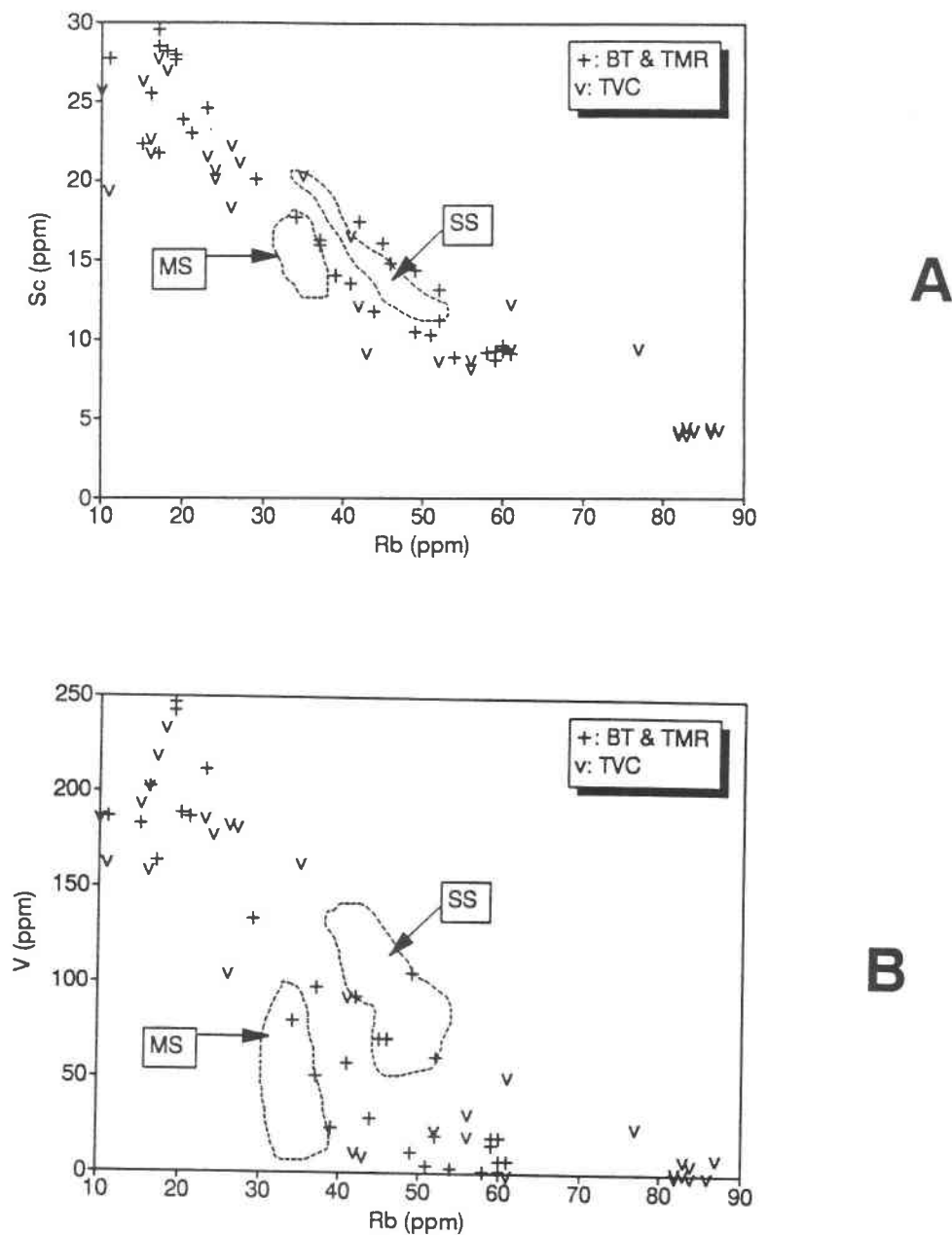
Figure 8.7: Compatible-incompatible element trends for Broken Top and Three Sisters rocks. Variations in Sc **(A)** and V **(B)** indicate that the main BT intermediate series contains components of fractionation (i.e., Middle Sister) and rhyolite mixing (i.e., South Sister). Observed compatible element depletions are consistent with a model involving fractionation paired with ≈20-30% rhyolite mixing in an open basaltic andesite system. Note that intermediate samples from the TVC are indistinguishable from BT-TMR samples. Samples with ≤40 ppm Rb that plot close to the MS field are part of the high Na_2O series.
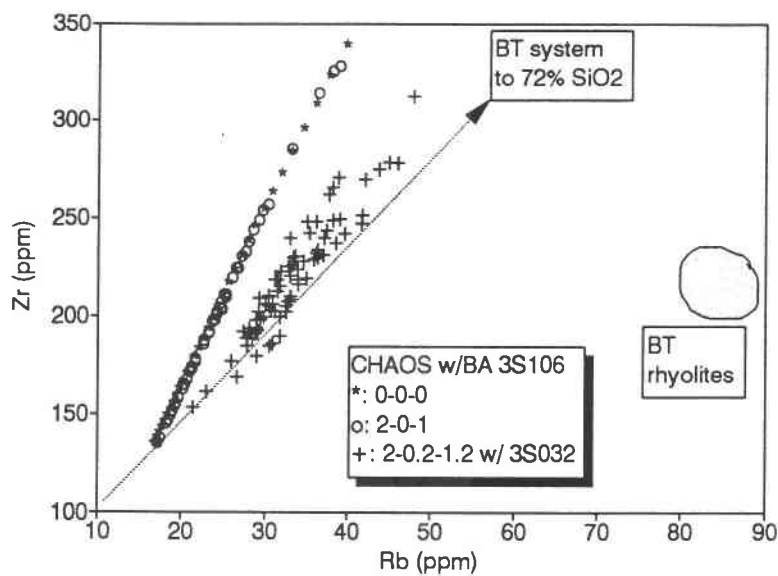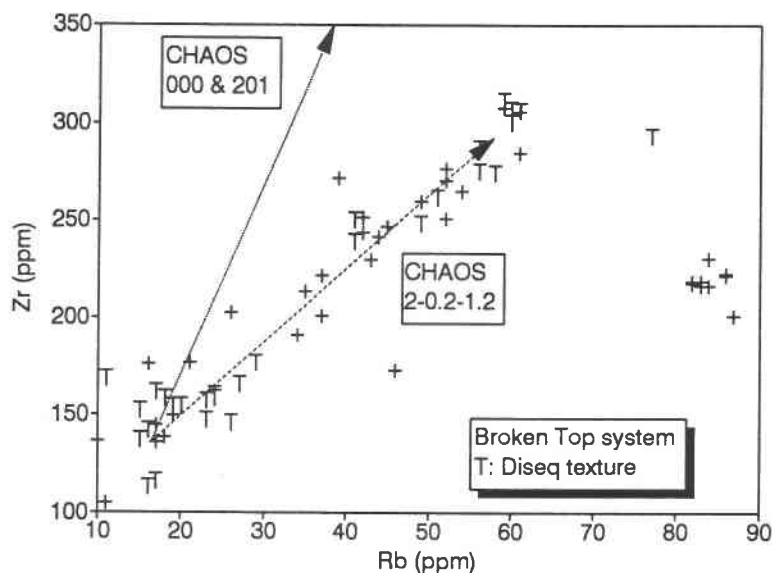
Figure 8.8: Results of CHAOS models showing variations in Zr vs. Rb. **A)** Closed system fractionation (0-0-0) or recharge (2-0-1) models cannot account for the observed fractionation between Zr and Rb, as zircon is not a fractionating phase for these compositions. Open system (2-0.2-1.2) models using rhyolite 3S032 successfully model Zr vs. Rb variations. **B)** CHAOS trends superimposed on BT system data. Note that samples with significant disequilibrium mineral textures do not form distinct groups.
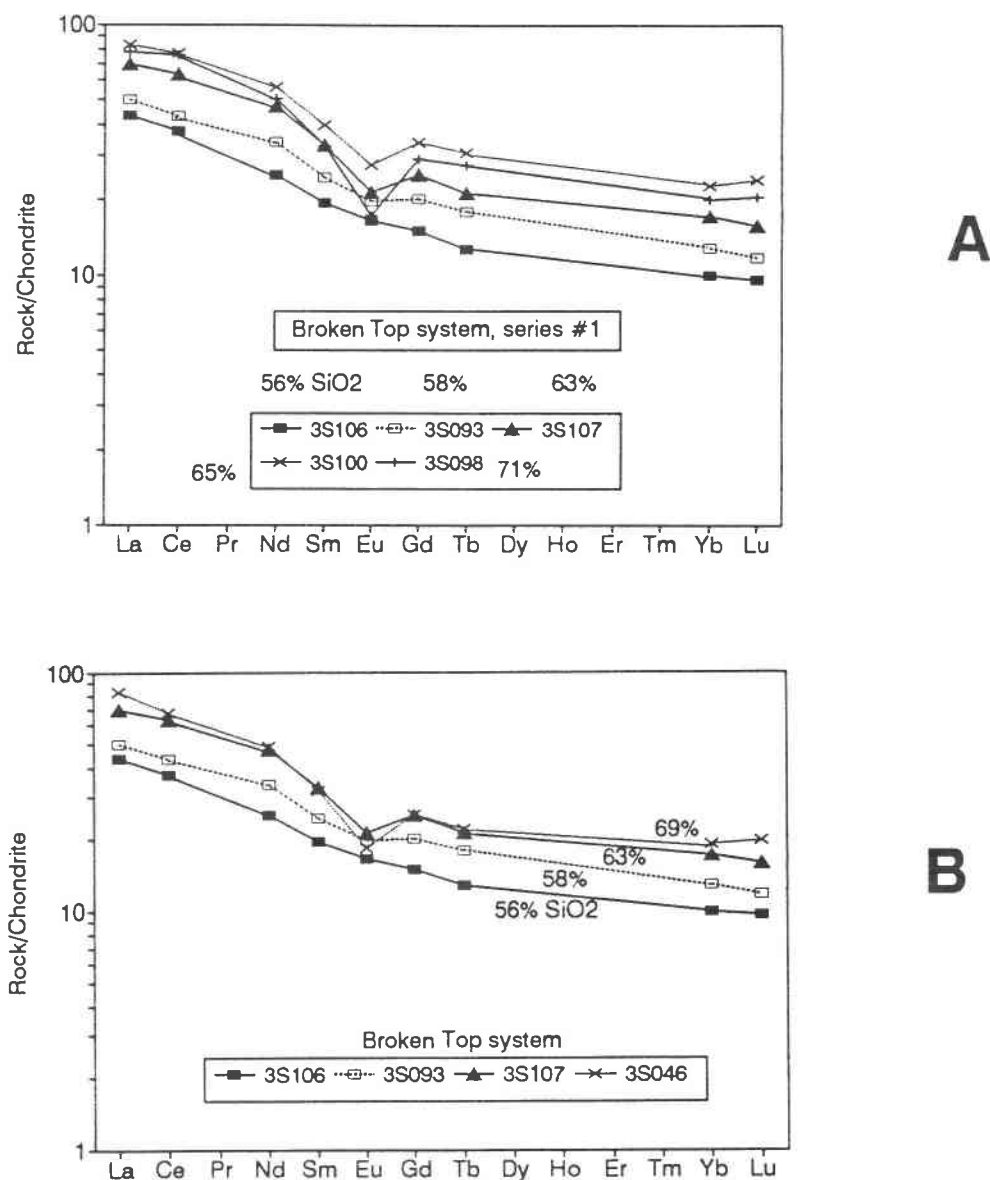
Figure 8.9: Rare earth element diagrams for Broken Top system petrogenesis. **A)** Broken Top intermediate series differentiation to 63% SiO_2 is characterized by increasing REE content with little REE fractionation, and development of small negative Eu anomalies. Above 63% SiO_2, the high Na_2O series is characterized by increasing REE to 65% SiO_2, which is thought to represent differentiation without rhyolite mixing. Depletions in the HREE and increases in La/Sm above 65% SiO_2 are the product of ≈35% rhyolite mixing paired with apatite fractionation. The main series **(B)** is characterized by constant MREE to ≈70% SiO_2, with small enrichments in LREE and HREE. This feature indicates small amounts of apatite fractionation paired with ≈30% rhyolite mixing.

The increase in La/Sm and depletions in the HREE's and MREE's in the high Na_2O trend might be a feature of apatite fractionation. Large amounts (10-20%) of amphibole fractionation could produce similar REE features (cf. Grove and Donnelly-Nolan, 1986; Bacon and Druitt, 1988), but none of the BT intermediate series rocks contain more than a rare trace of amphibole. Augite REE K_d's are only ≈ 0.1-0.5 (Nielsen et al., in press), and 20% augite fractionation will not significantly affect the REE's. Apatite distribution coefficients for the REE's in silicic compositions are in the range of 10 for La and 20 to 30 for the MREE's (Watson and Green, 1981; Fujimaki, 1986; Appendix E), with the MREE's having the highest K_d's. The observed depletions in the REE's from 65% to 71% SiO_2 would require $\approx 30\%$ fractionation (determined by Rb and Th enrichment) with bulk distribution coefficients of $D_{La}=1$, $D_{Sm}=1.5$, $D_{Eu}=2.3$, $D_{Tb}=1.4$, and $D_{Yb}=1.4$, and thus 5-10% apatite in the fractionating assemblage. Mass balance constraints limit apatite to $\approx 1.5\%$ of the fractionating assemblage, which can not produce the observed REE patterns unless apatite distribution coefficients are much larger than reported. Magma evolution above 65% SiO_2 in the high Na_2O requires significant amounts of mixing with rhyolitic magmas (R = 0.35, table 8.5) in order to generate the observed REE patterns.

In contrast to the first trend, the increases in La/Sm and buffering of the MREE's in the main trend could have been produced by relatively lesser amounts of magma mixing along with apatite fractionation. The observed depletions in the REE's from 63% to 70% SiO_2 would require $\approx 40\%$ fractionation with bulk distribution coefficients of $D_{La}=0.7$, $D_{Sm}=1.1$, $D_{Eu}=1.3$, $D_{Tb}=1.0$, and $D_{Yb}=0.8$, and thus ≈ 5-3% apatite in the fractionating assemblage; note that although the interval of fractionation has increased relative to the first trend, the bulk distribution coefficients have decreased. Mass balance calculations constrain apatite to $\approx 1.5\%$, and the fractionation of apatite $\pm$ pyroxene (+ plag) is incapable of producing the REE variations observed in the second series. Mixing of rhyolite magma at R = 0.3 paired with apatite fractionation (cf., table 8.5) is capable of buffering the REE's in the main intermediate series. CHAOS (2-0.2-1.2) models involving 20% mixing of rhyolite 3S032 into an open basaltic andesite system (figure 8.10) confirm that the mixing of rhyolite with a parental basaltic andesite magma system, and subsequent fractionation of pyroxene $\pm$ apatite, is capable of producing the observed REE features of the main BT intermediate series to 72% SiO_2.

Intermediate series dacites and rhyodacites with elevated REE's and Na_2O are not temporally or spatially distinct from intermediate rocks of the main trend. Rocks from both trends have the same range in mineralogy, texture, and degree of crystallinity. Unlike the Three Sisters system, the Broken Top system does not show any spatial or temporal constraints on intermediate series petrogenesis. There are, however, only two high Na_2O dacites in the sample set (3S100 and 3S008) for comparison. Both of these samples lack disequilibrium mineral features (Appendix B), which supports a crystal fractionation hypothesis.
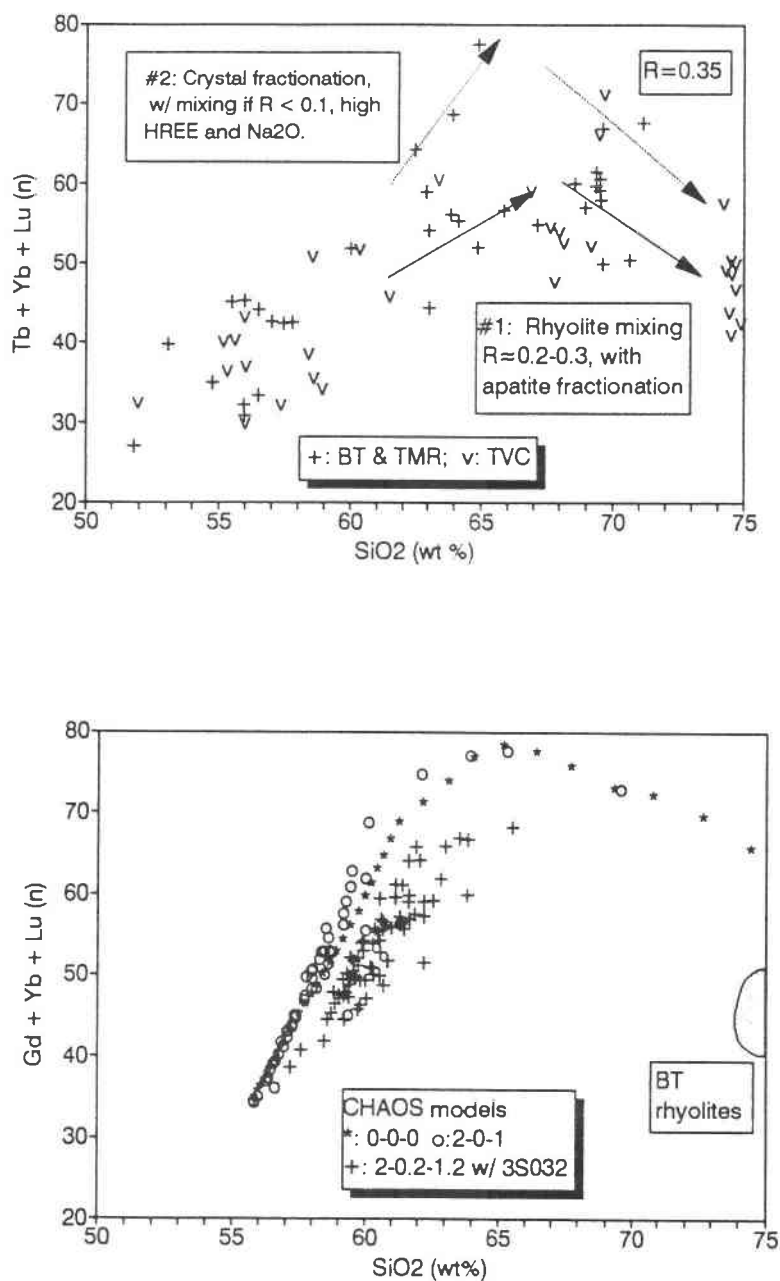
Figure 8.10: Results of a CHAOS 2-0.2-1.2 model involving periodic mixing of 20% rhyolite 3S032. Fractionation of apatite associated with mixing generally buffers the intermediate series HREE's at rhyolite abundances. High HREE, high Na_2O dacites and rhyodacites are the result of crystal fractionation without rhyolite mixing to 65% SiO_2, and higher rates of rhyolite mixing and fractionation above 65% SiO_2. Although all the rhyolites are associated with the older Tumalo volcanic center (TVC), younger Broken Top & Tam MacArthur Rim magmatism involved mixing with this type of rhyolite.

8.4 Summary of Intermediate Series Petrogenesis

In summary, magma evolution to 63% SiO_2 in the Broken Top series was characterized by open system crystal fractionation with small amounts (R ≈ 0.1) of rhyolite mixing. Above 63% SiO_2, two chemically distinct trends developed in the Broken Top system. Magma evolution from 63% to 72% SiO_2 in the main Broken Top trend was characterized by crystal fractionation paired with ≈30% rhyolite mixing, which maintained fairly constant levels of Na_2O and the REE's during differentiation. A second, high Na_2O and high HREE trend was produced through crystal fractionation from 63% to 65% SiO_2, and higher rates of rhyolite mixing (R = 0.35) paired with fractionation from 65% to 72% SiO_2. Unlike the Three Sisters intermediate system, rocks from both Broken Top intermediate trends are spatially, temporally and mineralogically identical.

It is important to note that crystal fractionation as a dominant evolutionary process is limited in occurrence to ≤65% SiO_2 in both the Middle Sister and Broken Top systems. Magma evolution above 65% SiO_2 in the Middle Sister system probably did not occur because rhyolitic magmas were not available for mixing into the fractionated system. In contrast, intermediate series differentiation probably continued above 65% SiO_2 in the Broken Top system because rhyolitic magmas were available for mixing into an evolved, intermediate composition magma system. Arguments developed for South Sister petrogenesis showed that rhyolite is probably limited to ≤50% of any magma mixture, or else the mafic component would be thermally quenched (i.e., Frost and Mahood, 1987). South Sister intermediate compositions were thus limited to ≤65% SiO_2, which represents the limit of 50% rhyolite - 50% basaltic andesite mixing. In the Broken Top system, fractionation continued beyond basaltic andesite (58% SiO_2) to 65% SiO_2, thus increasing the SiO_2 content of potentially mixing system 7 wt.% SiO_2 above the South Sister system. The fact that the Broken Top system evolved through mixing + fractionation to 72% SiO_2 but the same process in the South Sister system was limited to 65% SiO_2 is probably a function of the degree of evolution of the mafic mixing component. Because the Broken Top "mafic" mixing component had evolved up to ≈65% SiO_2 instead of ≈58% SiO_2 (i.e., +7 wt% higher), 50:50 mixtures with rhyolite could produce rhyodacitic (i.e., +7 wt% SiO_2 higher) instead of dacitic melts.

9. PETROGENESIS OF RHYOLITES

9.1 Three Sisters Rhyolites

Rhyolites associated with the Three Sisters are texturally and compositionally heterogeneous. Holocene rhyolites show relatively small degrees of geochemical variation (table 9.1), which is thought to have been produced through "small" amounts of crystal fractionation (Clark, 1983; Scott, 1987). Pleistocene low-silica ($\approx 72\%$ SiO_2) rhyolites are similar to the Holocene rhyolites, but range to more evolved high-silica (76% SiO_2) compositions (table 9.1). There are also subtle trace element distinctions between Holocene and Pleistocene rhyolites. The Holocene rhyolites tend to plot in more closely spaced, distinct groups, and have relatively higher incompatible element abundances (figure 9.1).

Although both rhyolite types have the same range in mineral chemistry and degrees of crystallinity, plagioclase phenocrysts from each type are texturally distinct. Both rhyolite types contain $\leq 20\%$ plagioclase, which has oscillatory zonation from $\approx An_{40}$ to $\approx An_{30}$. However, most plagioclase phenocrysts in all of the Holocene rhyolites contain 10-40% clear-to-light-brown coarse glass inclusions (figure 4.4C-D), but plagioclase from Pleistocene rhyolites rarely contains glass inclusions. This sieved texture in the Holocene rhyolites cannot be simply the product of magma mixing; assuming that the Holocene rhyolites were originally a Pleistocene rhyolite composition, the Holocene geochemical trends point **away** from both mafic and more silicic mixing components (figure 9.1). It is also not clear how magma mixing could have produced texturally distinct but compositionally identical phenocrysts. A rapid decrease in pressure might produce sieved plagio-clase (e.g., Nelson and Montana, 1989), but the Holocene plagioclase should be more sodic (Blundy and Shimizu, 1991) if it were produced through decompression of a hydrous melt. The plagioclase textures and geochemical variations indicate that the Holocene rhyolites were produced from a different magma chamber than the Pleistocene rhyolites.

Geochemical variations within both rhyolite suites can be explained through relatively small amounts of crystal fractionation. Although the range in geochemical variation and crystallinity is small, there is a rough correlation between variations in CaO, Al_2O_3 and FeO and degree of crystallinity for Three Sisters rhyolites (figure 9.2a). Simple mass balance models (table 9.2) show that variations between Pleistocene low-silica and high-silica rhyolite can be accounted for by the fractionation of 5-18 wt% of the observed minerals (plag + opx + mgt + ilmn + ap ± hb) in modal proportions. The smaller degrees of geochemical variation observed in the Holocene rhyolites also can be accounted for with 5% modal fractionation (cf., Clark, 1983; Scott, 1987). REE variations are consistent with these mass balance models. Small depletions in Eu and generally increasing REE abundances reflect plag + opx ± hb fractionation (figure 9.2b, table 9.2); small HREE and Zr depletions in high-silica rhyolite 3S139 require the addition of 0.4% zircon to

Sample	Middle Sister	Holocene Low	Holocene High	Pleistocene Low	Pleistocene High
	3S134	3S145	3S060	3S148	3S139
SiO2	65.7	71.8	73.7	72.5	76.1
TiO2	0.73	0.35	0.29	0.33	0.14
Al2O3	16.2	14.9	14.1	14.5	13.4
FeO*	5.03	2.20	1.75	2.06	1.16
MnO	0.14	0.07	0.05	0.06	0.04
MgO	0.99	0.53	0.41	0.61	0.11
CaO	2.72	2.11	1.62	1.86	0.97
Na2O	6.26	4.61	4.38	4.77	4.46
K2O	1.89	3.09	3.48	3.15	3.41
P2O5	0.25	0.09	0.07	0.07	0.04
Rb	31	73	85	71	79
Ba	607	755	809	742	876
Sr	272	251	185	193	119
Cs	0.85	1.93	2.20	2.02	1.94
Sc	12.81	3.92	3.29	4.60	1.63
V	12	29	20	31	9
Co	3.56	3.53	2.44	3.75	0.58
Ni	18	16	<10	9	<10
Cr	<6	7	2	9	1
Zn	208	90	47	180	64
La	21.3	18.8	21.0	19.2	20.0
Ce	53.8	43.1	38.4	38.6	44.6
Nd	28.0	16.7	16.0	17.4	14.9
Sm	6.75	2.97	3.07	3.06	2.63
Eu	1.80	0.70	0.59	0.64	0.42
Tb	1.27	0.54	0.41	0.41	0.39
Yb	4.2	1.7	1.8	1.9	1.5
Lu	0.62	0.27	0.31	0.29	0.24
La/Sm	1.99	4.00	4.32	3.96	4.80
ΣHREE	66.22	27.94	26.89	26.75	22.87
Eu/Eu*	0.77	0.68	0.60	0.65	0.49
Zr	241	168	168	153	96
Hf	7.0	4.6	4.5	4.5	3.2
Ga	21	16	13	17	15
Y	38	17	18	18	15
Nb	12.7	10.6	12.1	8.7	10.0
Ta	0.62	0.68	0.79	0.67	0.74
Th	2.9	7.2	8.2	7.0	7.3
U	1.3	2.6	3.2	2.4	2.6

3S134: Middle Sister dacite, Lane Mesa.
3S145: Holocene low-silica rhyolite, Carver Lake dome.
3S060: Holocene high-silica rhyolite, Rock Mesa.
3S148: Pleistocene low-silica rhyolite, Chambers Lake dome.
3S139: Pleistocene high-silica rhyolite, Obsidian Cliffs.

Table 9.1: Analyses of representative Three Sisters rhyolite types, showing range of geochemical variation observed in Holocene and Pleistocene rhyolites. Middle Sister dacite is shown for comparison. Note the extreme depletions in HREE and high La/Sm that characterize all Three Sisters rhyolites.
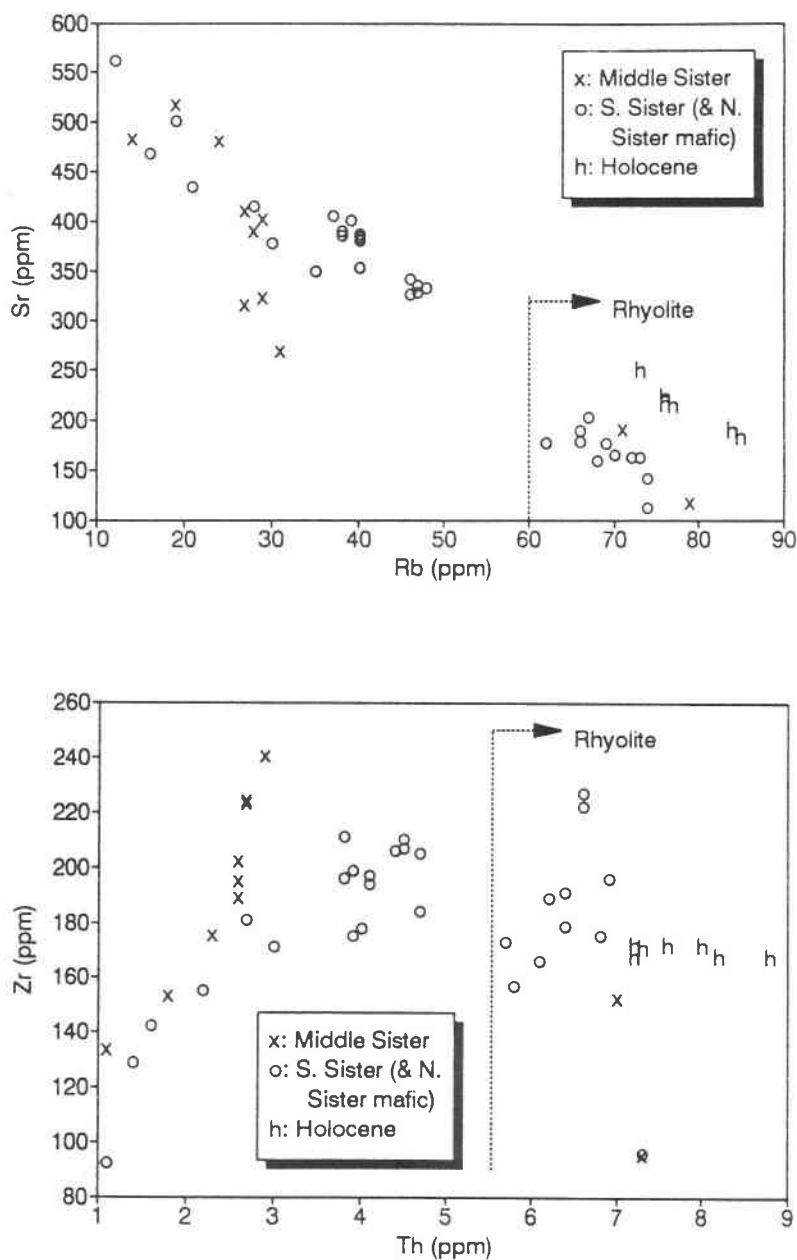
Figure 9.1: Compatible-incompatible element plots for the Three Sisters system. Holocene and Pleistocene rhyolites plot in distinct groups; note the consistently higher Sr in the Holocene rhyolites. Holocene rhyolites do not plot along mixing lines with observed compositions, and the geochemical differences are not the products of crystal fractionation. Fractionation of modal minerals can, however, account for intra-suite variations.
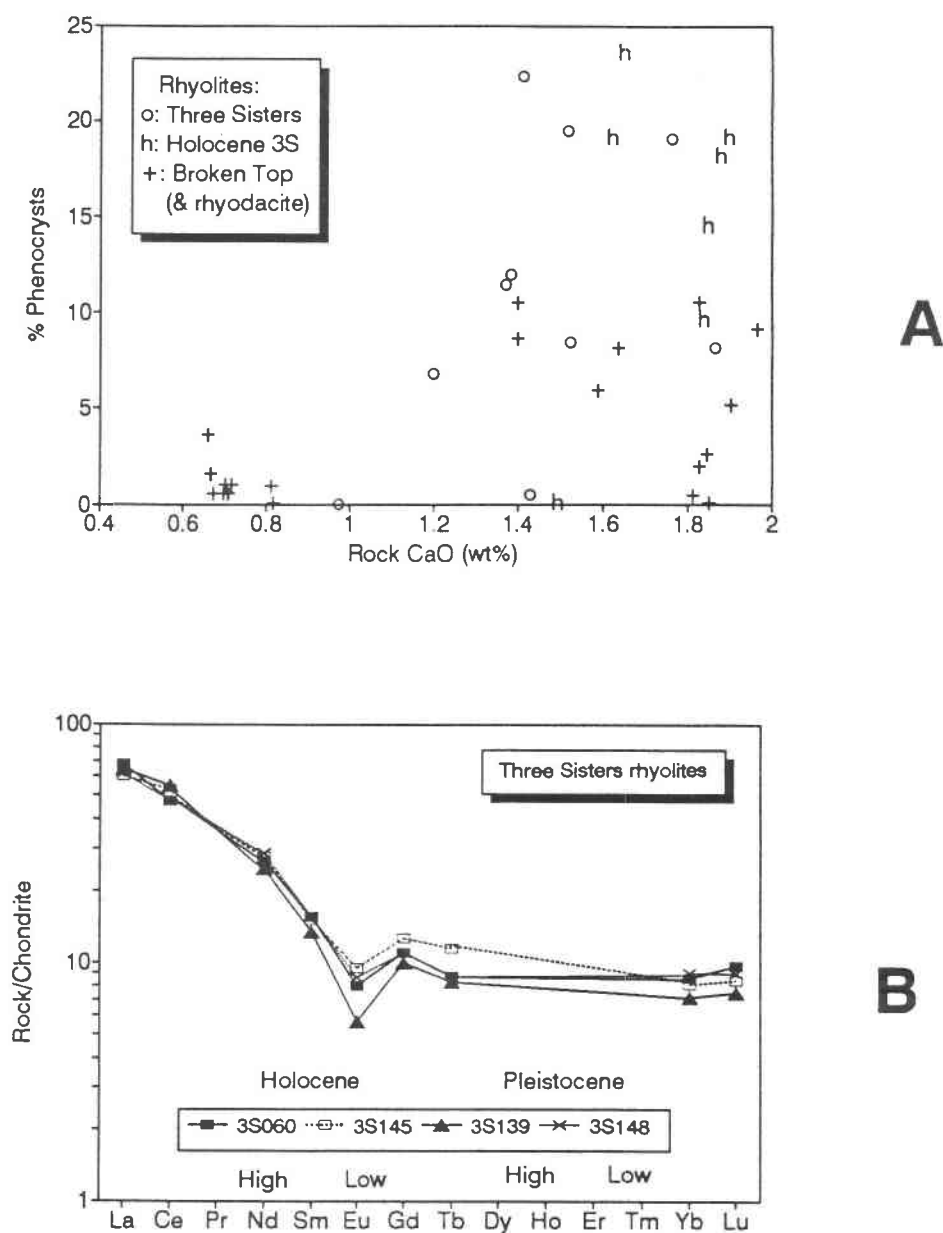
Figure 9.2: Comparisons of Holocene and Pleistocene Three Sisters rhyolites. **A)** Three Sisters rhyolites show a very rough correlation between CaO content and modal % phenocrysts in the rock, suggesting that fractionation or accumulation of the modal minerals may have controlled geochemical evolution. **B)** Chondrite-normalized REE patterns for the range of Holocene and Pleistocene rhyolite compositions. The most evolved rhyolites of each group are characterized by higher La/Sm and Eu/Eu*, and lower HREE. These features can be modeled with <1% apatite and <0.4% zircon fractionation, which is supported by mass balance calculations.

Mineral		SiO2	TiO2	Al2O3	FeO*	MnO	MgO	CaO	Na2O	K2O	P2O5
Plag	An31	61.1		24.7	0.3		0.0	6.2	7.2	0.5	
Opx	En58	52.4	0.1	0.4	24.8	1.1	20.2	0.9	0.1		
Mgt		0.1	9.6	1.8	82.7	0.5	1.4				
Ilmn		0.0	42.2		51.5	0.6	2.5				
Apt								56.0			43.0
Hb		42.1	3.8	10.4	14.7	0.3	12.9	10.7	2.3	0.3	

Pleistocene parental composition

	SiO2	TiO2	Al2O3	FeO*	MnO	MgO	CaO	Na2O	K2O	P2O5
3S148	72.5	0.33	14.5	2.06	0.06	0.61	1.86	4.77	3.15	0.07

Pleistocene 7% model: Fractionation of
6% Plag, 0.6% Opx, 0% Hb, 0.35% Mgt, 0.15% Ilmn, 0.03% Ap

	SiO2	TiO2	Al2O3	FeO*	MnO	MgO	CaO	Na2O	K2O	P2O5
7% model:	74.7	0.23	14.0	1.58	0.05	0.21	1.30	4.58	3.20	0.05
3S054	74.2	0.24	14.3	1.58	0.05	0.23	1.20	4.53	3.37	0.05

Pleistocene 18% model: Fractionation of
15% Plag, 2.2% Opx, 0.5% Hb, 0.35% Mgt, 0.35% Ilmn, 0.1% Ap

	SiO2	TiO2	Al2O3	FeO*	MnO	MgO	CaO	Na2O	K2O	P2O5
18% Model	72.6	0.32	14.7	2.08	0.07	0.61	1.86	4.73	2.86	0.07
3S139	76.1	0.14	13.4	1.16	0.04	0.11	0.97	4.46	3.41	0.04

Holocene parental composition

	SiO2	TiO2	Al2O3	FeO*	MnO	MgO	CaO	Na2O	K2O	P2O5
3S145	71.8	0.35	14.9	2.20	0.07	0.53	2.11	4.61	3.09	0.09

Holocene 11% model: Fractionation of
9% Plag, 0.7% Opx, 0.5% Hb, 0.35% Mgt, 0.10% Ilmn, 0.06% Ap

	SiO2	TiO2	Al2O3	FeO*	MnO	MgO	CaO	Na2O	K2O	P2O5
11% Model	71.9	0.35	14.9	2.18	0.06	0.58	2.10	4.57	3.15	0.09
3S060	73.7	0.29	14.1	1.75	0.05	0.41	1.62	4.38	3.48	0.07

Table 9.2: Crystal fractionation models for Three Sisters rhyolites. Models used mineral compositions from Three Sisters rhyolites 3S114 and 3S122. Removal of 7% to 18% of the observed modal minerals from the lowest silica rhyolite (3S148) reproduces the geochemical variations found in Three Sisters Pleistocene rhyolites. The range of composition in the Holocene rhyolites can be produced though the fractionation of 11% modal minerals from the least evolved Holocene rhyolite (3S145). These features strongly indicate that the members of each rhyolite type were erupted from a common magma chamber, which was compositionally zoned due to crystal fractionation.

the fractionating assemblage. Trace element distributions also show that the Holocene rhyolites cannot be derived from the Pleistocene rhyolites through crystal fractionation (figure 9.1), and must have originated as a discrete batch of rhyolitic magma.

9.1.1 Crystal fractionation

Previous models have shown that differentiation to 65% SiO_2 at Middle Sister was primarily controlled by crystal fractionation, but the petrogenesis of andesites and dacites at South Sister was controlled by magma mixing. South Sister intermediate composition rocks could not have been parental to Three Sisters rhyolites, because the formation of these intermediate rocks required an independent source of rhyolitic magma. However, continued fractionation at Middle Sister may have resulted in the formation of Three Sisters rhyolite magmas and a 7% SiO_2 compositional gap (cf., Grove and Donnelly-Nolan, 1986).

Other High Cascade volcanos, which are also thought to represent fractionating magmatic systems, contain large (i.e., greater than the 7% SiO_2 gap in the Three Sisters) compositional gaps. The climactic eruption at Mt. Mazama contained a 9% SiO_2 compositional gap, which was produced through a combination of fractionation and accumulation of crystals in the underlying high-Sr andesitic magmas (Bacon, 1983; Druitt and Bacon, 1989). The Mt. Mazama rhyodacites can be successfully modeled by fractionation of the accumulated anhydrous minerals from andesitic compositions, with minor assimilation of granitic wall rocks (Bacon and Druitt, 1988). Rhyolites at Medicine Lake were apparently derived through extensive (50-60%) amphibole + plagioclase fractionation from andesite, with small amounts of wall-rock assimilation (Grove et al., 1982; Grove and Donnelly-Nolan, 1986). Due to the shallow slope of the amphibole liquidus, an 11% SiO_2 compositional gap developed at Medicine Lake with only small decreases in temperature of the system (Grove and Donnelly-Nolan, 1986). However, both Medicine Lake and Mt. Mazama are characterized by abundant intermediate composition rocks that are highly phyric (30-55% crystals) and contain significant amounts of amphibole (10-20%). Intermediate composition rocks in the Three Sisters generally contain ≤30% phenocrysts and lack amphibole (Chapter 4), yet the Three Sisters system still contains a 7% SiO_2 compositional gap. It is possible that the Three Sisters rhyolites were produced through fractionation of Middle Sister dacites, but that the fractionating minerals remained on the walls of the magma chamber (cf. McBirney and Noyse, 1979) and were not erupted as cumulate intermediate rocks. This fractionation hypothesis can be tested through mass balance and trace element models.

Mass balance models indicate that Three Sisters rhyolites (table 9.1) cannot be derived from Middle Sister dacites through the fractionation of plag ± opx ± hb ± cpx ± mgt ± ilmn ± ap. Increases in K_2O necessitate >50% crystallization, as K_2O will remain essentially incompatible using the observed mineral compositions (table 9.3). The low abundance of Na_2O in the rhyolites

Mineral	SiO2	TiO2	Al2O3	FeO*	MnO	MgO	CaO	Na2O	K2O	P2O5
Plag An20	62.5		22.3	0.2		0.0	4.1	8.5	0.8	
Opx En51	51.6	0.2	0.7	26.8	1.2	17.7	1.6	0.1		
Mgt	0.1	14.5	2.2	78.1	0.7	1.4				
Ilmn	0.0	44.4		51.1	0.7	2.3				
Apt ≈							56.0			43.0
Hb	42.1	3.8	10.4	14.7	0.3	12.9	10.7	2.3	0.3	

Starting composition

MS Dacite	SiO2	TiO2	Al2O3	FeO*	MnO	MgO	CaO	Na2O	K2O	P2O5
3S134	65.7	0.73	16.2	5.0	0.14	1.0	2.7	6.3	1.9	0.25

Best fit using anhydrous assemblage
83% An$_{20}$ Plag, 8% Opx, 8% Mgt, 1% Ap

	SiO2	TiO2	Al2O3	FeO*	MnO	MgO	CaO	Na2O	K2O	P2O5
F ≈ 0.40:	73.9	0.35	14.1	2.1	0.13	0.5	1.6	5.6	2.9	0.09
3S148	72.5	0.33	14.5	2.1	0.06	0.6	1.9	4.8	3.2	0.07

Model #2, Medicine Lake:
After Grove and Donnelly-Nolan, 1986

Mineral	SiO2	TiO2	Al2O3	FeO*	MnO	MgO	CaO	Na2O	K2O	P2O5
Plag An35	58.7		25.6	0.5		0.0	7.2	7.0	0.4	
Opx En51	51.6	0.2	0.7	26.8	1.2	17.7	1.6	0.1		
Mgt	0.1	14.5	2.2	78.1	0.7	1.4				
Apt ≈							56.0			43.0
Hb	42.1	3.8	10.4	14.7	0.3	12.9	10.7	2.3	0.3	

Fractionation with above minerals,
66% An$_{35}$ Plag, 8% Opx, 17% Hb, 7% Mgt, 1% Ap

	SiO2	TiO2	Al2O3	FeO*	MnO	MgO	CaO	Na2O	K2O	P2O5
F = 0.50	75.9	0.07	14.4	1.2	0.10	-0.9	-0.4	7.1	2.9	0.04
3S148	72.5	0.33	14.5	2.1	0.06	0.6	1.9	4.8	3.2	0.07

Model #3, Medicine Lake, same compositions as above:
69% An$_{35}$ Plag, 6% Opx, 15% Hb, 10% Mgt, 1% Ap

	SiO2	TiO2	Al2O3	FeO*	MnO	MgO	CaO	Na2O	K2O	P2O5
F = 0.50	76.3	-0.08	14.1	0.8	0.12	-0.4	-0.3	7.0	2.9	0.12
3S148	72.5	0.33	14.5	2.1	0.06	0.6	1.9	4.8	3.2	0.07

Table 9.3: Simple mass balance calculations used to model petrogenesis of Three Sisters low-silica rhyolites through crystal fractionation of Middle Sister dacite. Calculation method explanation in table 7.1. Fractionation of an anhydrous assemblage (model 1) can only approximate 3S rhyolite compositions if unreasonably large amounts of anomalously sodic plagioclase are crystallized. Note that 60% crystallization with 83% An$_{20}$ plagioclase still results in anomalously high Na$_2$O in the modeled rhyolite; using An$_{30}$ plagioclase does not result in significant Na$_2$O depletions. Medicine Lake models use the fractionating assemblages of Grove and Donnelly-Nolan (1986), but fail to approximate 3S rhyolite compositions. Any model involving fractionation of >5% Hb results in CaO, MgO and Al$_2$O$_3$ depletions that are much greater than observed in 3S rhyolites. Hydrous and anhydrous mass balance models of Middle Sister dacites fail to reproduce Three Sisters rhyolite compositions, indicating that crystal fractionation is not a valid hypothesis for Three Sisters rhyolite petrogenesis.

can not be modeled even with fractionating an assemblage containing >80% An_{20} plagioclase. Because plagioclase phenocrysts in 3S rhyolites are generally more calcic than An_{30} and 3S amphiboles contain ≤2% Na_2O, it is not possible to deplete Na_2O to the observed levels by fractionation from Middle Sister dacites.

Amphibole fractionation is critical in the petrogenesis of rhyolitic magmas at Medicine Lake, and is thought to control the development of many intermediate-to-rhyolite compositional gaps (Grove and Donnelly-Nolan, 1986). Mass balance models involving >5% hornblende fractionation are anomalously depleted in MgO and CaO (Medicine Lake models, table 9.3), as are models containing >5% cpx. The inability to fit hornblende fractionation into the mass balance models supports the conclusion that amphibole was not a liquidus phase in the Three Sisters intermediate system, and fractionation of amphibole did not control the development of a compositional gap.

Apatite fractionation is critical to evaluating REE distributions, as apatite is the only mineral in these rocks that has high REE compatibility (Appendix E). Three Sisters rhyolites are characterized by low HREE (≈10X chondrite), high La/Sm (4-5) and moderate Eu/Eu* (0.7-0.5) (figure 9.3a). These REE characteristics require a D_{La} = 1.1, D_{Ce} = 1.4, D_{Tb} = 2.4 and D_{Lu} = 2, with F≈0.4 (Rb & Th). Apatite is the only observed mineral that has high La and Ce distribution coefficients (≈10-30) (Watson and Green, 1981; Appendix E); hornblende K_d's are <1 for La, and <2 for Ce. In situ fractionation of a LREE-silicate such as allanite or sphene (Gromet and Silver, 1983) would also result in significant Th depletions and LREE-HREE fractionation, which is not observed (table 9.1). In addition, mass balance calculations limit apatite to 1% of the fractionating assemblage. This amount of apatite fractionation is insufficient to deplete the LREE and HREE to observed levels in the rhyolites. Fractionation would thus have to involve unreasonably large amounts of hornblende (>50%, with apatite constrained to ≈1%) to produce the observed rhyolite REE patterns (figure 9.3a).

Petrogenetic models at Medicine Lake require <20% hornblende fractionation, which is supported by mass balance and petrographic constraints (Grove and Donnelly-Nolan, 1986). Andesite to rhyolite differentiation at Medicine Lake is characterized by increasing LREE and constant HREE (figure 9.3b), which is consistent with ≈15% hb + ≈1% ap fractionation. Dacite to rhyolite differentiation at the Three Sisters, however, involves large LREE and HREE depletions that can only be produced through >50% amphibole fractionation. There is no evidence to indicate that amphibole fractionation occurred in the Three Sisters system, which had lower water contents than either Mt. Mazama or Medicine Lake (Chapter 5) and lacks hornblende-bearing intermediate rocks. The observed rhyolite REE abundances cannot be produced by any reasonable model involving crystal fractionation from Middle Sister dacite. Unlike many other calc-alkaline arc volcanos (Grove and Donnelly-Nolan, 1986), the dacite-rhyolite compositional gap at the Three
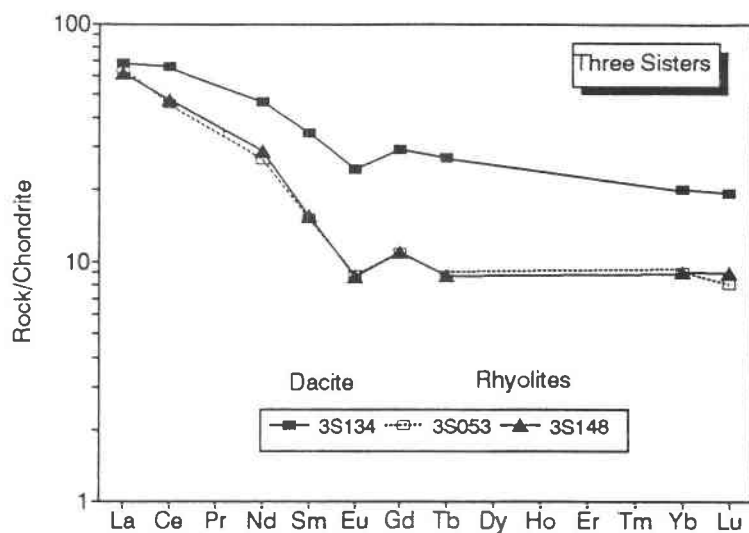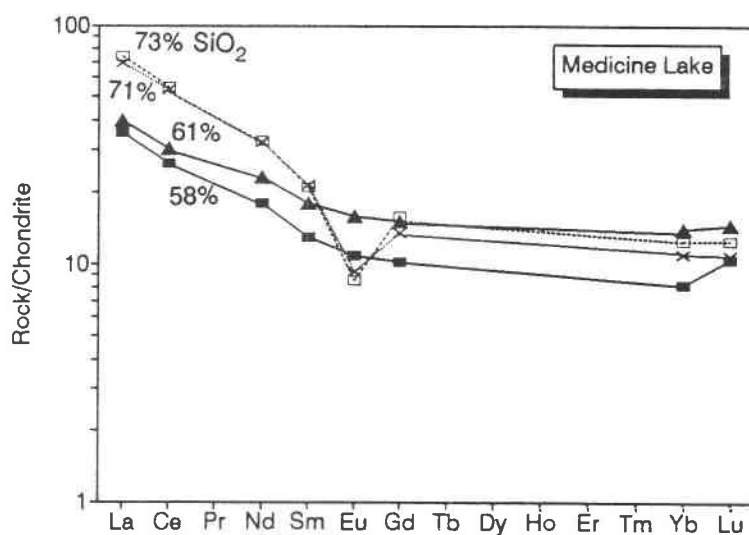
Figure 9.3: Rare earth element plots for Three Sisters rhyolite petrogenesis. **A)** Comparison of evolved Middle Sister dacite REE pattern with least evolved Three Sisters rhyolite REE's. Derivation of the rhyolites through crystal fractionation from the dacite would require >50% amphibole fractionation, as apatite is limited to 1% by mass balance. This model is not reasonable for the essentially anhydrous Three Sisters system. **B)** Variations in REE at Medicine Lake are consistent with fractionation of plag ($\approx$70%) + hb ($\approx$20%) + ap ($\approx$1%) from andesite to produce rhyolite (Grove and Donnelly-Nolan, 1986). Note that the Medicine Lake model produces large increases in LREE, La/Sm, Eu/Eu*, and relatively constant HREE; Three Sisters dacite-rhyodacite differentiation is characterized by significant depletions in LREE and HREE, and constant Eu/Eu*, which is not consistent with the Medicine Lake model.

Sisters cannot be the product of crystal fractionation. If the Three Sisters rhyolites cannot be produced through fractionation of less evolved magmas, then they must ultimately be derived from partial melts of crustal rocks.

9.1.2 Partial melting

Previous discussions have concluded that relatively dense, mafic crust is located from ≈ 30 to ≈ 45 km beneath this part of the High Cascades, with a more heterogeneous (but predominately mafic) crust between ≈ 12 and ≈ 30 km (e.g., Leaver et al., 1984; Riddihough et al., 1984; Chapter 2). Temperatures at middle (15-30 km) crustal depths are not certain, but temperatures of around 500°C at 10 km are justified through extrapolation of surficial heat flow values (Blackwell et al., 1982; 1990). Assuming that the "meta-mafic" country rock is at 500°C with a solidus at 1000°C, a specific heat of ≈ 0.25 cal/g °C, and a heat of fusion equivalent to the latent heat of crystallization of nearby mafic to intermediate magmas (at ≈ 1100°C), then $\approx 50\%$-25% of the volume of the intrusive rocks can be produced as 100% melt of the country rock. In reality, smaller volumes of intrusive rock are required to generate the same volume of melt, because melting will only involve 30%-50% of the country rock (cf. Bergantz, 1990). Although there is a large uncertainty on each of the values used in this calculation, it is reasonable to conclude that volumes of rhyolitic crustal melt of at least 1-10 km^3 could be generated at mid-crustal depths under the High Cascades.

Although isotopic data are extremely limited for this part of the High Cascades, Three Sisters rhyolite 3S139 has the same relatively low $^{87}Sr/^{86}Sr$ (0.70363 ± 3) as Broken Top rhyolite 3S032 (0.70368 ± 2), indicating that isotopically evolved crust (i.e. ≥ 0.705) does not underlie this area (table 3.3). Three Sisters rhyolites are characterized by flat HREE patterns, indicating that garnet and amphibole were not restitic minerals (Barker and Arth, 1976; Drummond and Defant, 1990). Garnet is a stable mineral in many basalt melting experiments at pressures > 10 kbars (Ellis and Thompson, 1986; Rutter and Wyllie, 1988; Rapp, 1990), which strongly indicates that Three Sisters rhyolites were not produced at depths > 35-40 km. Three Sisters rhyolites are also metaluminous, and only contain trace amount of normative corundum (cf. Chapter 6). Partial melts of peraluminous metasediments always produce peraluminous melts (Thompson, 1982; Conrad et al., 1988; Patiño-Douce and Johnston, 1990), and as such could not generate the Three Sisters rhyolites. Water saturated melts of basalt that leave amphibole in the residuum are also mildly to strongly peraluminous (Helz, 1976; Spulber and Rutherford, 1983; Ellis and Thompson, 1986; Beard and Lofgren, 1989, 1991; Winther, 1989), and do not resemble most silicic rock compositions.

Dehydration melting experiments (i.e. the only H$_2$O in the sample is contained in the hydrous minerals) of basalt have generally focused on the origin of island arc silicic rocks (e.g. tonalites and low-K$_2$O granitoids). These studies have used a variety of mafic starting materials: Unaltered MORB's and Hawaiian tholeiites (Holloway and Burnham, 1972; Helz, 1976; Spulber

and Rutherford, 1983; Wolf and Wyllie, 1989), tholeiitic metabasalts and metabasaltic andesite (Beard and Lofgren, 1989, 1991), and the synthetic CMASH system (Ellis and Thompson, 1986).

The rocks used by Beard and Lofgren (1991) were greenschist facies metavolcanics from the late Jurassic Smartville Complex of northern California (Beard and Day, 1987), which may be broadly correlative to the metavolcanic rocks that probably underlie this part of the High Cascades (Chapter 2). Samples were partially melted at pressures (1, 3, 6.9 kbars) and temperatures (850°C to 1000°C) that correspond to the most likely conditions for partial crustal melting underneath the High Cascades. Although the concentrations of TiO_2, Na_2O, K_2O, and P_2O_5 in the partial melts will be controlled by the concentrations of these elements in the parental rock, the metavolcanic rocks are reasonably similar to High Cascade mafic compositions.

The results of Beard and Lofgren (1991), using starting compositions that most closely resemble High Cascade compositions, are given in table 9.4. Partial melts produced by ≈15-25% melting of the metabasalts at ≈900°C, and ≈25% melting of basaltic andesite at 950°C, most closely resemble the composition of Three Sisters rhyolites. Overall enrichments in TiO_2 and P_2O_5 and depletions in alkalies systematically reflect the relative abundances of these elements in the metabasaltic rocks (Beard and Lofgren, 1991). The partial melts are also higher in CaO and FeO than the Three Sisters rhyolites, which is probably due to the relative enrichment of these elements in the starting compositions. The initial melt-forming reaction for the dehydration melts at 3 kbars is: 9 Qtz + 33 Amph + 5 Plag = 2 Mgt + 6 Opx + 20 Cpx + 19 Melt, and is terminal for both quartz and amphibole (Beard and Lofgren, 1991). Rocks that contain more CaO and FeO will thus produce melts with higher CaO and FeO. Above 900°C, the melt-forming reaction is : 13 Plag + 1 Cpx + 1 Opx + 1 Ilmn + 1 Mgt = 18 Melt, and most of the melt is produced through the breakdown of plagioclase (Beard and Lofgren, 1991). Because the normative plagioclase composition is similar for both the metabasaltic and mafic High Cascade rocks (≈An_{50}), differences in CaO content are probably controlled by amphibole and not by plagioclase.

Dehydration melting of metabasaltic rocks at pressures of 3 to 7 kbars and temperatures of ≈900°C can produce ≈20% melt that has the general characteristics of Three Sisters rhyolites, once the differences in source composition are accounted for. The mineralogy of the metabasaltic source rock will change from an amphibole-rich greenstone (40-50% amphibole) to a pyroxene hornfels (≈50% plag, ≈40% pyroxene, table 9.4) restite, which is observed in the Smartville Complex (Beard and Day, 1987). The experimental data of Beard and Lofgren (1991) show that apatite was also a restitic mineral up to 1000°C; P_2O_5 contents in the melt increase with increasing temperature, and mass balance calculations indicate that the restite contains ≈0.5 wt.% apatite (table 9.4).

Trace elements from experimentally produced partial melts are not determined, due to the difficulty in analyzing small (≤100 mg), heterogeneous glass samples. These data are also not

Sample:	478							571					557				
P (kbar)		3	3	3	6.9	6.9	6.9		3	6.9	6.9	6.9		3	3	3	6.9
T (°C)		900	950	1000	850	900	950		900	850	900	950		900	950	1000	1000
SiO2	52.5	76.6	73.1	62.9	75.6	72.3	71.0	51.4	73.2	74.7	73.0	70.4	57.0	76.2	72.6	69.1	69.1
TiO2	1.74	0.43	0.67	1.56	0.16	0.59	0.64	1.55	0.49	0.12	0.41	0.64	0.60	0.40	0.74	0.90	0.93
Al2O3	15.3	13.1	13.9	15.5	14.5	15.3	15.6	15.8	15.2	14.7	15.6	17.3	15.4	13.0	14.5	16.0	16.3
FeO*	11.79	2.39	3.59	7.91	2.10	2.93	3.81	12.23	2.07	1.96	2.30	2.18	8.01	2.29	3.44	4.55	4.20
MnO	0.26	0.08	0.10	0.16	0.06	0.06	0.06	0.26	0.08	0.08	0.07	0.09	0.17	0.08	0.05	0.08	0.04
MgO	4.74	0.49	0.83	2.08	0.24	0.87	0.47	4.42	0.47	0.38	0.72	0.30	5.52	0.60	0.69	0.51	0.50
CaO	10.90	2.72	3.40	5.61	2.76	3.76	3.63	8.95	2.11	2.42	3.20	2.67	9.20	2.67	3.13	3.71	3.80
Na2O	1.96	3.21	3.43	3.15	2.83	3.05	3.50	3.30	3.77	3.10	2.58	3.63	2.54	3.01	3.13	3.46	3.36
K2O	0.15	0.92	0.85	0.58	1.76	0.96	1.02	0.37	2.56	2.49	1.98	2.33	0.44	1.66	1.48	1.52	1.48
P2O5	0.30	0.07	0.15	0.58	na	0.18	0.27	0.30	0.08	0.09	0.11	0.37	0.18	0.08	0.25	0.25	0.24
H2O	≈1	4.9	3.0	3.8	5.7	4.8	3.8	≈1	6.0	3.5	8.1	5.2	≈1	5.2	3.4	4.3	4.4
XMELT		21	26	39	6	21	20		16	7	12	17		23	28	35	28
Restite																	
Plg		40	36	29	36	37	38		48	49	48	44		39	38	30	33
Cpx		19	22	21		23	24		23		24	26		25	22	21	29
Opx		11	7	6		12	12		0.3		8	3		8	7	10	9
Amph	46				46.2			50		38	Tr		40				
Qtz					6												
Mgt		4	4	4	1	3	2		11	4	5	8		5	6	4	2
Ilmn		6	5	3	4	4	4		1	3	4	2					2

	3S069	3S045	3S148
SiO2	51.8	56.0	72.5
TiO2	1.02	1.12	0.33
Al2O3	16.7	18.3	14.5
FeO*	8.39	7.41	2.06
MnO	0.15	0.13	0.06
MgO	8.79	3.66	0.61
CaO	9.14	7.70	1.86
Na2O	3.22	4.45	4.77
K2O	0.64	1.02	3.15
P2O5	0.21	0.28	0.07

Restite, recalculated to 100%

Plag	47	58	52
Cpx	29	28	30
Opx	15	0.4	10
Mgt	4	13	8
Ilmn	5	1	-
Ap*	0.56	0.67	0.53

Ap* by mass balance, CaO = 55.4 wt.%, P2O5 = 42.1 wt.%

Table 9.4: Composition of dehydration melts of metabasaltic rocks, from Beard and Lofgren (1991). 3S148 is the least evolved Pleistocene Three Sisters rhyolite, with representative High Cascade mafic compositions shown for comparison. The general effect of increasing pressure is to lower the melt fraction and overall variations in melt composition, and to produce slightly more aluminous melts. Increasing temperature lowers SiO$_2$ and K$_2$O contents, with large increases in MgO, FeO, CaO and Al$_2$O$_3$ as more refractory phases (plag + px) melt. Dehydration melts of basalt 478 (6.9 kbars) and 571 (3 kbars) at 900°C, and basaltic andesite 557 (3 kbars) at 950°C, most closely resemble Three Sisters rhyolite 3S148. Elevated FeO and CaO contents of the melts relative to 3S148 probably reflects the enrichment of these element in the starting compositions; differences in TiO$_2$, alkalis and P$_2$O$_5$ between 3S148 and the melts are directly controlled by the source composition (Beard and Lofgren, 1991).

reported for the starting compositions used in the dehydration melting experiments. Trace element abundances can, however, be estimated by using High Cascade compositions from this study, melting models constrained by Beard and Lofgren's data, and distribution coefficients representative of a silicic (i.e. low silica rhyolite) melt in equilibrium with an anhydrous restite. Equilibrium batch melting models of High Cascade basalt 3S069, using melt fractions and restite mineralogies from Beard and Lofgren (1991), support the origin of Three Sisters rhyolites through dehydration melting of metabasaltic rocks between 3 and 6.9 kbars (table 9.5). The models are limited by the uncertainties associated with most trace element distribution coefficients in low silica rhyolite melts (cf., Appendix E), and potential ranges in source rock composition. In general, successful trace element models require small amounts of apatite (≤0.5%) in the restite to buffer REE abundances and produce flat HREE patterns, which is supported by mass balance calculations (table 9.5). Melts that strongly resemble Three Sisters rhyolites can be produced through 16-20% equilibrium batch melting of basalt 3S069, leaving a residual mineralogy of plag + px + oxides + apatite. Differences between observed and calculated trace element abundances are within reasonable uncertainties in trace element distribution coefficients and source composition (i.e., ± 10% variation in each parameter).

Holocene Three Sisters rhyolites generally contain more Al_2O_3, FeO*, CaO and Sr, and lower MgO and Sc, than Pleistocene rhyolites (table 9.1). Basaltic dehydration melt reactions above 900°C are dominated by the dissolution of plagioclase (Beard and Lofgren, 1991). The geochemical differences between the Holocene and Pleistocene rhyolites may thus be due to slightly higher melting temperatures (≥900°C) during production of the Holocene rhyolites; enhanced dissolution of plagioclase would increase the melt in Al_2O_3, CaO and Sr, and lower MgO and Sc through relatively lower degrees of augite dissolution (i.e., increased augite in the restite). Although the geochemical variations are too small to be rigorously modeled, there is no compelling evidence to indicate that the Holocene rhyolites were produced through partial melts of a crust that was compositionally distinct from the source of the Pleistocene rhyolites.

9.1.3 Summary of Three Sisters rhyolite petrogenesis

In summary, Three Sisters rhyolites cannot be produced through crystal fractionation from dacitic compositions. The Three Sisters silicic system lacks abundant amphibole, which is commonly required to produce compositional gaps and rhyolitic melts through crystal fractionation. Major and trace element models demonstrate that the Three Sisters rhyolites were most likely produced through dehydration melting of metabasaltic crust at 3-7 kbars (≈10-25 km) and around 900°C. Magma at ≈1100°C intruded into an ≈500°C crust at these depths can likely produce partial melt volumes roughly equivalent to the volume of the intrusions. Because the volume of rhyolite is much smaller than the volume of basaltic andesitic to andesitic rocks, this model is thermally valid.

Model #1, Metabasalt 571, 3 kbars, 900°C

Distribution Coefficients

	Restite	Rb	Sr	Sc	V	La	Sm	Eu	Tb	Lu
Plag	0.58	0.3	4.4			0.3	0.1	2.5	0.2	0.1
Cpx	0.28		0.4	33	3	0.5	2.9	2.5	3.8	3.0
Opx	0.004			7	1	0.4	0.8	0.6	0.9	0.9
Ap	0.007		1			15.0	46.0	26.0	38.0	14.0
Mgt	0.13			5	40					
Ilmn	0.01			1	10					
Bulk D:		0.17	2.67	9.93	6.14	0.4	1.2	2.3	1.4	1.0
Cs (3S069)		11	439	27.7	187	30.4	16.1	15.1	10.9	8.7
Model #1, F=0.16		36	183	3.3	35	59.7	13.9	7.1	8.1	8.7
3S148		71	193	4.6	31	61.5	15.5	8.6	8.7	9.0

Model #2, Metabasalt 478, 6.9 kbars, 900°C

Distribution Coefficients

	Restite	Rb	Sr	Sc	V	La	Sm	Eu	Tb	Lu
Plag	0.47	0.3	4.4			0.3	0.1	2.5	0.2	0.1
Cpx	0.29		0.4	33	3	0.5	2.9	2.5	3.8	3.0
Opx	0.15			7	1	0.4	0.8	0.6	0.9	0.9
Ap	0.005		1			15.0	46.0	26.0	38.0	14.0
Mgt	0.04			5	40					
Ilmn	0.05			1	10					
Bulk D:		0.14	2.19	10.87	3.12	0.4	1.2	2.1	1.5	1.1
Cs (3S069)		11	439	27.7	187	30.2	16.1	15.1	10.9	8.7
Model #2, F=0.20		34	226	3.1	70	55.7	13.5	8.0	7.8	7.9
3S148		71	193	4.6	31	61.5	15.5	8.6	8.7	9.0

Table 9.5: Estimated trace element abundances from partial melting of High Cascade basalt 3S069, using melt fractions and restite modal mineralogies from the dehydration melting experiments of Beard and Lofgren (1991). Model #1 uses a melt composition from metabasalt 571 that most closely matches the composition of Three Sisters rhyolite 3S148 (cf., table 9.4); the partial melt from metabasalt 478 (Model #2) also approximates 3S148. Both models use representative distribution coefficients for rhyodacitic magmas, and trace element abundances are calculated assuming equilibrium batch melting ($C_l = C_s / [D (1 - F) + F]$). The correspondence between modeled and observed trace element abundances are within the uncertainty associated with the rhyodacitic distribution coefficients and reasonable variations in source composition. For example, models underestimate Rb abundances; lowering the plag Rb K_d to 0.1 and increasing Rb in the source to 15 ppm duplicates 3S rhyolite abundances. Residual apatite is required to buffer the REE's, and to produce flat HREE patterns. Models that lack residual apatite fail to account for observed P_2O_5 and REE trends. REE abundances in the models are also lower than observed in 3S rhyolites, but a 10% increase in the source concentration duplicates 3S rhyolite abundances. Partial melting of High Cascade basalts leaving a restite of essentially plag + pyroxene can generate Three Sisters rhyolite compositions.

Holocene rhyolites were probably generated at slightly higher temperatures than the Pleistocene rhyolites, resulting in a relatively larger plagioclase component in the Holocene melts. Variations within the Holocene and Pleistocene rhyolite suites can be accounted for by 6-15% crystal fractionation of modal minerals, but variations between these suites cannot be modeled through either crystal fractionation or mixing with any known composition. The Holocene rhyolites represent a compositionally distinct batch of magma, which thus had the potential to interact with the South Sister system differently than the Pleistocene rhyolites.

9.2 Broken Top System Rhyolites

Rhyolites in the Broken Top system are restricted in occurrence to domes and pyroclastic deposits associated with the Tumalo volcanic center (Chapter 3). Although the ages of most of these rhyolites are poorly constrained, the main pulse of rhyolitic volcanism occurred around 380 ± 20 ka. However, previous discussions have demonstrated the necessity of rhyolite magma mixing in the petrogenesis of Broken Top rhyodacites and dacites (Chapter 8). Rhyolitic magma must thus have been present in the Broken Top system to at least ≈200 ka, which is the age of the base of Broken Top volcano (Chapter 3).

Broken Top rhyolites are aphyric to sparsely phyric and contain ≤1% phenocrysts of plagioclase (An_{25-20}) > hypersthene (En_{40}) > amphibole ≥ magnetite + ilmenite > apatite > zircon. In contrast to the more phyric Three Sisters rhyolites, Broken Top rhyolites contain more sodic plagioclase (3S = An_{40-30}) and less magnesian hypersthene (3S ≈ En_{55}) (figure 4.6). Broken Top rhyolites are also compositionally distinct from Three Sisters rhyolites (table 9.6), and contain lower amounts of TiO_2, MgO, CaO, Sr, and Co. Broken Top rhyolites also contain significantly more Na_2O, Sc, Zn, REE's (esp. HREE) and HFSE's than Three Sisters rhyolites (figure 9.4). These compositional distinctions have been used in previous petrogenetic models (Chapters 7-8) to show that rhyolites from each magmatic system did not interact with less evolved magmas from the other system.

9.2.1 Crystal fractionation

Models of Broken Top intermediate system petrogenesis have demonstrated the necessity of rhyolite mixing to evolve most dacites and rhyodacites; high Na_2O dacite is the most evolved Broken Top composition that can be attributed to predominantly crystal fractionation. If the Broken Top rhyolites were produced through crystal fractionation, then high Na_2O dacite should have been the parental composition. Amphibole fractionation over a small temperature interval has been demonstrated to produce compositional gaps between dacite and rhyolite at Medicine Lake volcano (Grove and Donnelly-Nolan, 1986). A possible model for Broken Top magmatism could

	3S098	3S037	3SXBP	3S032	Avg	1σ	3S054
SiO2	71.1	69.6	74.2	74.5	74.6	± 0.2	74.2
TiO2	0.40	0.54	0.16	0.15	0.15	± 0.01	0.24
Al2O3	14.9	15.4	14.2	13.7	13.9	± 0.1	14.3
FeO*	2.74	3.31	1.82	1.70	1.63	± 0.05	1.58
MnO	0.08	0.07	0.07	0.06	0.06	± 0.00	0.05
MgO	0.30	0.36	0.08	0.01	0.05	± 0.05	0.23
CaO	1.40	1.64	0.81	0.71	0.69	± 0.02	1.20
Na2O	6.13	5.38	4.46	5.26	5.18	± 0.18	4.53
K2O	2.77	2.93	3.47	3.48	3.49	± 0.03	3.37
P2O5	0.07	0.11	0.03	0.02	0.02	± 0.00	0.05
Rb	58	59	84	86	84	± 2	74
Ba	721	736	794	796	796	± 11	840
Sr	135	181	65	52	50	± 3	144
Cs	2.04	0.90	3.10	1.50	1.37	± 0.27	1.30
Sc	9.25	8.73	4.29	4.25	4.30	± 0.18	2.51
V	1	15	0	0	3	± 4	3
Co	1.59	2.50	0.50	0.54	0.66	± 0.15	1.47
Ni	10	10	11	10	10	± 1	<1
Cr	2	<5	1	<3	1	± 1	<2
Zn	135	54	105	84	79	± 11	49
La	24.4	22.2	28.7	25.3	23.2	± 2.8	19.8
Ce	61.3	53.7	59.7	52.6	52.5	± 8.8	36.2
Nd	30.8	24.0	26.5	20.4	20.4	± 2.3	14.0
Sm	6.46	5.99	5.95	4.77	4.42	± 0.44	2.62
Eu	1.28	1.28	0.83	0.64	0.61	± 0.03	0.49
Tb	1.28	0.84	0.94	0.78	0.73	± 0.08	0.35
Yb	4.2	3.5	4.2	3.7	3.3	± 0.2	1.6
Lu	0.66	0.50	0.58	0.53	0.50	± 0.03	0.24
La/Sm	2.38	2.34	3.05	3.35	3.32	± 0.19	4.77
ΣHREE	67.67	50.02	57.77	50.62	46.74	± 3.39	22.50
Eu/Eu*	0.56	0.66	0.42	0.40	0.41	± 0.03	0.59
Zr	274	308	231	222	217	± 6	180
Hf	8.3	8.4	6.7	6.5	6.6	± 0.5	4.6
Ga	20	19	20	20	20	± 2	15
Y	37	30	36	31	28	± 3	16
Nb	15.5	16.8	16.9	17.8	17.4	± 0.7	11.5
Ta	0.90	1.00	1.20	1.00	1.02	± 0.03	0.77
Th	5.5	5.4	8.1	7.9	8.1	± 0.4	6.4
U	2.2	2.2	2.7	2.7	2.5	± 0.2	2.6

3S098: Squaw Ck. dome, high Na_2O rhyodacite.
3S037: E. Tam MacArthur Rim, main series rhyodacite.
3SXBP: Average Bend Pumice; bulk pumice sample.
3S032: Three Ck. Butte dome, from summit.
AVG: Average of 8 TVC rhyolites, excluding 3SXBP.
3S054: Pleistocene Three Sisters rhyolite, E. flank Devils Hill.

Table 9.6: Representative analyses of Broken Top system rhyodacites and rhyolites, with Three Sisters rhyolite 3S054 for comparison. 3S098 and 3S037 show range in composition of Broken Top system rhyodacites, which represents range of compositions parental to the rhyolites. Note that 3S032 is representative of average TVC rhyolite compositions, but that many elemental abundances in 3SXBP are outside of average TVC rhyolite compositions. This is most apparent for Na_2O and Cs, which are highly succeptable to deuteric alteration or weathering. 3SXBP is also relatively enriched in REE and Ta, which may indicate that the Bend Pumice was somwhat more evolved than other TVC rhyolites.
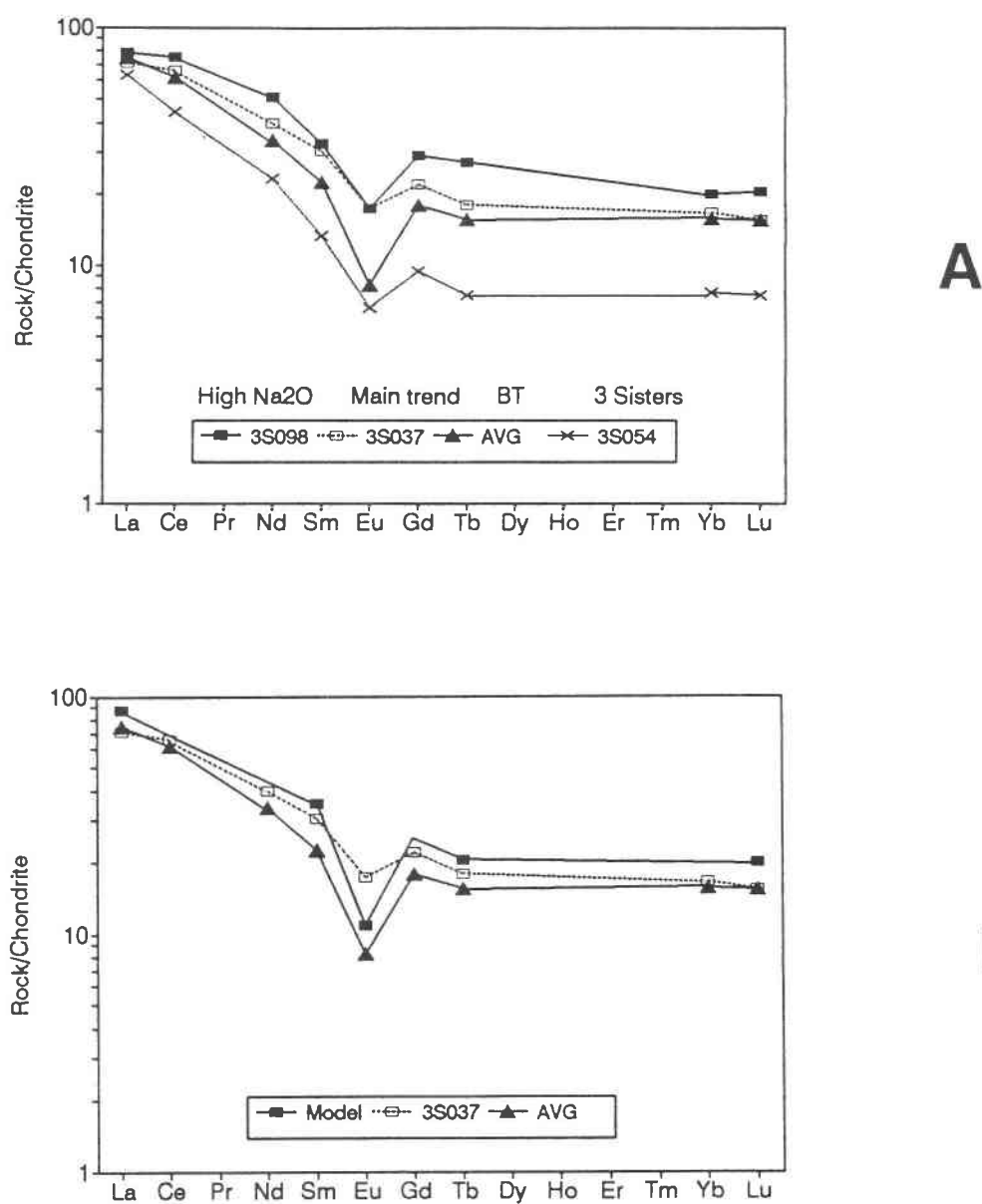
Figure 9.4: Chondrite normalized REE patterns for Broken Top rhyolite petrogenesis. **A)** Plot of high Na₂O and main trend rhyodacites, with Broken Top and Three Sisters rhyolites shown for comparison (table 9.6). If these rhyodacites were parental to Broken Top rhyolites, then fractionation involved significant REE depletions. These depletions cannot be modeled from high Na₂O dacites and rhyodacites, as models require unrealistically high bulk distribution coefficients for the REE's. **B)** Modeled REE abundances resulting from fractionation of main trend rhyodacite 3S037, using a mass-balance constrained assemblage. All fractionation models that reproduce observed major element trends fail to produce observed REE depletions. Crystal fractionation is not a valid hypothesis for the origin of Broken Top rhyolites.

thus involve production of rhyolite through crystal fractionation of dacite, with subsequent magma mixing and fractionation to produce the main dacite-rhyodacite trend.

Mass balance calculations show that the Broken Top rhyolites cannot be produced through crystal fractionation of high Na_2O dacite (table 9.7). Anhydrous fractionation involving 90% An_{20} plagioclase cannot lower Na_2O contents to observed rhyolite levels without severely depleting the melt in CaO and Al_2O_3. The addition of amphibole to the fractionating assemblage results in further CaO and Al_2O_3 depletions, and raises FeO, MnO and MgO contents in the modeled rhyolite (table 9.7). Fractionation of high Na_2O dacite, which was derived predominantly through crystal fractionation, does not produce Broken Top rhyolite compositions.

Mass balance models using rhyodacite from the main Broken Top series can produce Broken Top rhyolites (table 9.7). However, it has been demonstrated that the petrogenesis of these rhyodacites involves ≈30% mixing with Broken Top rhyolite. If rhyolite was a prerequisite for the evolution of the main series rhyodacites, then the rhyolite must have been independently produced and thus these rhyodacites could not have been parental to the Broken Top rhyolites.

Trace element distributions also clearly demonstrate that fractionation of the main series rhyodacites could not have resulted in Broken Top rhyolite compositions. Observed enrichments in incompatible elements required a minimum of 30% crystallization, but mass balance constraints limit crystallization to 22%. The crystallizing mineral assemblage is dominated by plagioclase, which is capable of producing the observed depletions in Sr and Eu (rhyodacite distribution coefficients from table 9.5). However, REE distributions are inconsistent with crystal fractionation of the mass balance constrained mineral assemblage (figure 9.4b). Rhyodacite to rhyolite fractionation is characterized by depletions in all the REE's, but bulk distribution coefficients are ≈50% too low to have depleted the REE's in the rhyolite. Crystal fractionation of 82% plag, 7% opx, and 1% ap results in elevated REE contents in the modeled rhyolite (figure 9.4b). In conclusion, Broken Top rhyolites cannot be produced through crystal fractionation of either type of Broken Top rhyodacite. These rhyolites must thus also be the products of partial crustal melts.

9.2.2 Partial melting

Three Sisters rhyolites were produced through ≈20% melting of metabasaltic crustal rocks, leaving a plagioclase + pyroxene + apatite restite. The restite mineralogy resulted in REE patterns that have relatively high La/Sm (≈4), modest Eu/Eu* (≈0.6) and low HREE (cf. 3S054 in figure 9.4a). Relative to Three Sisters rhyolites, Broken Top rhyolites have similar major element concentrations, but have elevated REE contents, lower La/Sm (≈3) and larger Eu/Eu* (≈0.4) (table 9.6). These REE distributions indicate the residual mineralogy probably contained more plagioclase and less apatite than observed for Three Sisters rhyolites. The restites from dehydration melting of metabasaltic rocks (Beard and Lofgren, 1991) always contained ≤60% plag ≤15% mgt +

		SiO2	TiO2	Al2O3	FeO*	MnO	MgO	CaO	Na2O	K2O	P2O5
Plag	An35	58.7		25.6	0.5		0.0	7.2	7.0	0.4	
Plag	An20	62.5		22.3	0.2		0.0	4.1	8.5	0.8	
Opx	En55	52.4	0.1	0.4	24.8	1.1	20.2	0.9	0.1		
Mgt		0.1	9.6	1.8	82.7	0.5	1.4				
Ilmn		0.0	42.2		51.5	0.6	2.5				
Apt								56.0			43.0
Hb		42.1	3.8	10.4	14.7	0.3	12.9	10.7	2.3	0.3	

Starting composition: high Na$_2$O rhyodacite, models 1 & 2

	SiO2	TiO2	Al2O3	FeO*	MnO	MgO	CaO	Na2O	K2O	P2O5
3S098	71.1	0.40	14.9	2.74	0.08	0.30	1.40	6.13	2.77	0.07

Model #1: 28% anhydrous fractionation of
90% An$_{20}$ Plag, 4% Opx, 3.5% Mgt, 2% Ilmn, 0.5% Ap

	SiO2	TiO2	Al2O3	FeO*	MnO	MgO	CaO	Na2O	K2O	P2O5
Model #1:	75.3	0.14	13.2	1.96	0.08	0.10	0.56	5.63	3.44	0.02
AVG RHYO	74.6	0.15	13.9	1.63	0.06	0.05	0.69	5.18	3.49	0.02

Model #2: 28% hydrous fractionation of
90% An$_{20}$ Plag, 4% Hb, 4% Mgt, 1.5% Ilmn, 0.5% Ap

	SiO2	TiO2	Al2O3	FeO*	MnO	MgO	CaO	Na2O	K2O	P2O5
Model #2:	75.4	0.15	13.0	2.04	0.09	0.19	0.43	5.61	3.44	0.02
AVG RHYO	74.6	0.15	13.9	1.63	0.06	0.05	0.69	5.18	3.49	0.02

Model #3: 22% fractionation of main series rhyodacite 3S037,
81.5% An$_{30}$ Plag, 7% Opx, 7% Mgt, 3.5% Ilmn, 1% Ap

Starting composition

	SiO2	TiO2	Al2O3	FeO*	MnO	MgO	CaO	Na2O	K2O	P2O5
3S037	69.9	0.54	15.4	3.31	0.07	0.36	1.64	5.38	2.93	0.11
Model #3:	74.2	0.14	14.2	1.73	0.05	0.05	0.66	5.19	3.55	0.03
AVG RHYO	74.6	0.15	13.9	1.63	0.06	0.05	0.69	5.18	3.49	0.02

Table 9.7: Mass balance models involving crystal fractionation of Broken Top system rhyodacites to produce Broken Top rhyolite. Although most rhyodacite petrogenesis requires ≈30% mixing of rhyolite magma, the Broken Top rhyodacites that were most directly related to crystal fractionation are part of a high Na$_2$O trend. These rhyodacites (e.g., 3S098) are the most likely parental compositions for rhyolite differentiation. Simple mass balance models (#1 & #2) demonstrate that fractionation of 90% An$_{20}$ plagioclase will not produce the required depletions in Na$_2$O. The fractionation of hornblende in place of orthopyroxene (model #2) also results in CaO and Al$_2$O$_3$ depletions that are too large, and FeO and MgO depletions that are too small, relative to average rhyolite compositions. Broken Top rhyolites cannot be produced through fractionation of high Na$_2$O rhyodacites. Valid mass balance models can be produced by using a main series rhyodacite (e.g., 3S037) as the parental composition. Orthopyroxene can also be replaced by up to 2% hornblende and still result in rhyolite compositions at 22% fractionation. Note the large amounts of plagioclase (An$_{30}$) and Fe-Ti oxides required by the model, which will strongly affect trace element distributions.

ilmn, and cpx ≥ opx. Equilibrium batch melting models (table 9.8) using these mineralogical constraints fail to reproduce Broken Top rhyolite trace element abundances using typical basaltic starting compositions. These models always resulted in melt concentrations of Sr and V were too high, and Rb and REE that were too low, when elemental abundances representative of High Cascade mafic rocks were used as the starting composition (table 9.8). The source rocks of Broken Top rhyolite partial melts must be depleted in Sr, Sc and V, and contain elevated REE's with higher La/Sm, relative to High Cascade mafic rocks.

There are few detailed partial melting experiments over a range of pressures (3-10 kbars) and water contents (highly undersaturated) that would be appropriate for the High Cascades that use intermediate composition igneous rocks as starting materials. A detailed study by Conrad et al. (1988) on Taupo volcanic zone silicic magmatism utilized dacitic and greywacke starting compositions, which were melted at water-saturated and water-undersaturated conditions at 10 kbars. Partial melts of greywacke were always strongly peraluminous, and do not resemble High Cascade silicic rock. Partial melts of dacite under water-saturated to moderately undersaturated (X_{H2O} = 0.5) conditions also resulted in peraluminous rhyolitic melts. Metaluminous rhyolitic melts were only produced at water-undersaturated conditions (X_{H2O} = 0.25), which corresponds to ≈4 wt.% H_2O (Conrad et al., 1988).

This water content is probably higher than expected for the High Cascades magma system; dehydration melts typically occur at ≈1 wt.% H_2O, if the source rock contains ≈50% amphibole (cf., Beard and Lofgren, 1991). The overall effect of elevated water content will be to increase the solubility of anorthitic plagioclase in the melt, resulting in higher Al_2O_3 and CaO contents (Conrad et al., 1988). Partial melts of Taupo dacite are higher in Al_2O_3 and CaO, and lower in Na_2O, than Broken Top rhyolites (table 9.9). Although some of these differences were likely controlled by differences in the source composition, partial melting of the Taupo dacite under relatively elevated water contents would result in more anorthitic plagioclase in the melt, and thus higher Al_2O_3 and CaO, and lower Na_2O. In order to account for these differences, it is likely that the generation of Broken Top rhyolites occurred at lower water contents (< 4 wt% H_2O) than used by Conrad et al. (1988). It is thus highly unlikely that Broken Top melting occurred with residual amphibole, because amphibole was only stable in the residua at >4 wt.% H_2O (X_{H2O} = >0.25) in the Conrad et al. experiments. Lower water contents might also stabilize apatite in the residua by limiting P_2O_5 diffusion into the melt (Harrison and Watson, 1984), which is supported by low P_2O_5 contents and REE characteristics of the Broken Top rhyolites (table 9.9).

Major element concentrations of Taupo dacite partial melts at 850°C, ≈45% melting, are broadly similar to Broken Top rhyolites, once the effects of presumedly higher experimental water contents are accounted for (table 9.9). Trace element models, however, do not directly support the origin of Broken Top rhyolites though partial melting of dacitic rocks with the constraints of

Equilibrium Batch Melting: $C_l = C_s / [D(1-F) + F]$

Distribution Coefficients

	Restite	Rb	Sr	Sc	V	La	Sm	Eu	Tb	Lu
Plag	0.6	0.3	4.4			0.3	0.1	2.5	0.2	0.1
Cpx	0.14		0.4	33	3	0.5	2.9	2.5	3.8	3.0
Opx	0.12			7	1	0.4	0.8	0.6	0.9	0.9
Ap	0		1			15.0	46.0	26.0	38.0	14.0
Mgt	0.09			5	40					
Ilmn	0.05			1	10					
Bulk D:		0.18	2.70	5.96	4.64	0.3	0.6	1.9	0.7	0.6
Cs (3S069)		11	439	27.7	187	30.2	16.1	15.1	10.9	8.7
Model #1, F = 0.2		32	186	5.6	48	68.9	24.4	8.7	13.9	13.0
Cl (3S032)		86	52	4.3	3	81.1	24.2	8.6	16.6	16.4

Distribution Coefficients

	Restite	Rb	Sr	Sc	V	La	Sm	Eu	Tb	Lu
Plag	0.6	0.3	4.4			0.3	0.1	2.5	0.2	0.1
Cpx	0.14		0.4	33	3	0.5	2.9	2.5	3.8	3.0
Opx	0.12			7	1	0.4	0.8	0.6	0.9	0.9
Ap	0		1			15.0	46.0	26.0	38.0	14.0
Mgt	0.09			5	40					
Ilmn	0.05			1	10					
Bulk D:		0.18	2.70	5.96	4.64	0.3	0.6	1.9	0.7	0.6
Cs (estimated)		30	125	22	15	35.0	16.1	15.1	13.0	11.0
Model #2, F = 0.2		87	53	4.4	4	79.8	24.4	8.7	16.6	16.4
Cl (3S032)		86	52	4.3	3	81.1	24.2	8.6	16.6	16.4

Table 9.8: Equilibrium batch melting models for Broken Top rhyolite petrogenesis, using mineralogical constraints from Beard and Lofgren (1991). **Model #1:** Restites from dehydration melts of metabasaltic rocks contain ≤60% plag and ≤15% mgt + ilmn (cf., Table 9.4; Beard and Lofgren , 1991). These mineral proportions are insufficent to lower Sr and V in a basaltic partial melt to rhyolite abundances, even at 10% melting. Note that apatite in the restite would result in additional HREE depletions, but would likely increase La/Sm to rhyolitic values. **Model #2:** Estimated source composition constrained by 60% plag and 15% mgt + ilmn in the restite, 20% melting. Note the low abundances of Sr and V necessary in the source to produce the observed rhyolitic concentrations; variations in F from 0.1 to 0.3 results in small variations in Sr and V abundances, but large variations in less compatible elements. Models #1 and #2 clearly demonstrate that Broken Top rhyolites were not produced through partial melts of metabasaltic rocks. Relative to basalts, potential source rocks must be depleted in Sr, Sc, and V, and contain elevated REE's with higher La/Sm.

	SiO2	TiO2	Al2O3	FeO*	MnO	MgO	CaO	Na2O	K2O	P2O5
TVZ exp.	65.2	0.60	15.7	5.0	0.1	2.5	5.3	3.6	1.7	0.10
3S107	63.0	1.10	16.2	5.8	0.1	1.8	4.2	5.5	1.9	0.33

Run 617A, X_{H2O}=0.25, T=850°C, Residual Mineralogy:
44.5% Glass, 6.6% Qtz, 31.7% An_{44} Plag, 8.8% Cpx, 8.3% Opx, 0.2% Ilmn

	SiO2	TiO2	Al2O3	FeO*	MnO	MgO	CaO	Na2O	K2O	P2O5
Glass 617A	72.0	0.29	15.3	2.1	0.05	0.49	2.6	3.6	3.5	0.10
Avg BT	74.6	0.15	13.9	1.6	0.06	0.05	0.7	5.2	3.5	0.02

Model #1, distribution coefficients

	Restite	Rb	Sr	Sc	V	La	Sm	Eu	Tb	Lu
Plag	0.65	0.3	4.4			0.3	0.1	2.5	0.2	0.1
Cpx	0.18		0.4	33	3	0.5	2.9	2.5	3.8	3.0
Opx	0.17			7	1	0.4	0.8	0.6	0.9	0.9
Ap	0		1			15.0	46.0	26.0	38.0	14.0
Mgt	0			5	40					
Ilmn	0.004			1	10					
Bulk D:		0.20	2.93	7.13	0.75	0.4	0.7	2.2	0.9	0.8
Cs (3S107)		37	375	16.3	98	70.0	33.0	21.4	21.3	15.8
Model #1, F=0.45		67	181	3.7	114	109.2	38.7	12.9	22.1	18.3
Cl (3S032)		86	52	4.3	3	81.1	24.2	8.6	16.6	16.4

Model #2, distribution coefficients

	Restite	Rb	Sr	Sc	V	La	Sm	Eu	Tb	Lu
Plag	0.64	0.3	4.4			0.3	0.1	2.5	0.2	0.1
Cpx	0.16		0.4	33	3	0.5	2.9	2.5	3.8	3.0
Opx	0.15			7	1	0.4	0.8	0.6	0.9	0.9
Ap	0.02		1			15.0	46.0	26.0	38.0	14.0
Mgt	0.01			5	40					
Ilmn	0.02			1	10					
Bulk D:		0.19	2.90	6.40	1.23	0.6	1.6	2.6	1.6	1.0
Cs (3S107)		37	375	16.3	98	70.0	33.0	21.4	21.3	15.8
Model #2, F=0.45		67	183	4.1	87	88.0	25.0	11.3	16.0	16.2
Cl (3S032)		86	52	4.3	3	81.1	24.2	8.6	16.6	16.4

Model #3, same residual mineralogy as in #2

		Rb	Sr	Sc	V	La	Sm	Eu	Tb	Lu
Cs estimated:		47	105	17	5	64.5	32.0	16.0	22.0	16.0
Model #3, F=0.45		85	51	4.3	4	81.1	24.2	8.4	16.5	16.4
Cl (3S032)		86	52	4.3	3	81.1	24.2	8.6	16.6	16.4

Table 9.9: Partial melt models for Broken Top rhyolite petrogenesis, using experimental data on melts of Taupo volcanic zone dacite from Conrad et al., 1988. Average TVZ dacite used in melting experiments is broadly similar to dacite 3S107, but is more magnesian and has a higher Ca/Na than High Cascades dacites. Melting experiment 617A (850°C, 45% melt) was water-undersaturated ($\approx$4 wt% H_2O) and resulted in an anhydrous restite and a rhyolitic melt. Differences between experimental melt and Broken Top rhyolite compositions are probably a function of differences in source composition and high water content of the partial melts stabilizing more calcic plagioclase. Trace element models show that the expermental restite is unlikely to have produced Broken Top rhyolite compositions. The REE's in model #1 are too high, and probably indicate residual apatite (model #2). Model #3 uses estimated trace element abundances that result in a Broken Top rhyolite composition, using an experimentally-constrained melt fraction and residual mineralogy.

Conrad et al., 1988. Sr abundances in the modeled melt are extremely high, even when rhyolitic distribution coefficients are used in the models (table 9.9). Major element distributions indicate that if partial melting occurred at lower water contents, the residuum should contain a more calcic plagioclase, which will have a lower distribution coefficient for Sr and thus higher Sr contents in the melt. The source of Broken Top rhyolites was limited to ≈100 ppm Sr (model #3), if ≈60% of the residuum contains plagioclase. Apatite must also have been a residual mineral, to produce the observed La/Sm and REE patterns in the Broken Top rhyolites (model #2, table 9.9). In addition, ilmenite ± magnetite must be more abundant (i.e., >0.2%) in the residuum to account for the low TiO_2, FeO^* and V contents in the Broken Top rhyolites. Even when the effects of lower water content and increased abundances of minor mineral phases are accounted for, it is highly unlikely that partial melts of dacitic rocks could have produced the Broken Top rhyolites. In general, the estimated source composition (model #3, Table 9.9) needs to be somewhat more evolved than typical High Cascades dacites.

The climactic eruption of Mt. Mazama ejected medium-grained tonalitic blocks as large as 4 m, which contain 1-5 mm thick veins of rhyolitic glass (Bacon and Druitt, 1988). The tonalitic blocks are thought to represent fragments of the deep walls of the Mazama magma chamber, which had remained at high temperatures (≤950°C) for sufficient time to produce rhyolitic partial melts (Druitt and Bacon, 1989). The compositions of these rhyolitic partial melts are very similar to the composition of Broken Top rhyolites (table 9.10 and figure 9.5). Silicic rocks at Mt. Mazama are thought to have been produced mainly through crystal fractionation of High Cascades andesite (Bacon and Druitt, 1988), and are thus petrogenetically distinct from Broken dacites and rhyo-dacites. These tonalites may be analogous to older silicic plutonic rocks that potentially underlie this part of the Cascade Range, which may be correlative with plutonic rocks of the Klamath Mountains or related to older episodes of Cascades arc magmatism (Chapter 2-3).

The tonalite blocks had an original mineralogy dominated by plag + opx + cpx + mgt + ilmn, accessory ap + zr, and minor amounts of qtz + hb + bio + kfelds. Partial melting resulted in dissolution of hb + kfelds + bio (± plag + qtz), with a restite of relict plag + qtz and new kfelds + opx + cpx + mgt + ilmn (Druitt and Bacon, 1989). Recrystallized, euhedral Fe-Ti oxides in tonalite blocks with high melt fractions (≈10-35%) yield equilibration temperatures of 950-980°C, which suggests that melting occurred at very low water contents (Druitt and Bacon, 1989). Rhyolitic melts in the tonalite blocks likely represent dehydration melts that were produced at relatively high temperatures (≥950°C) and low pressures (≈2-5 kbars).

Although the Mazama rhyolites are chemically similar to the Broken Top rhyolites (table 9.10), there are significant differences between the compositions of these rhyolites that must be explained. The Mazama rhyolites are more enriched in K_2O, Rb, and Cs than possible through ≈50% partial melting of a tonalitic source, which Bacon and Druitt attribute selective enrichment

Sample	Broken Top Avg	1σ	Mazama: 1023 CGR	Glass	Mazama: 799 CGR	Glass
SiO2	74.6 ±	0.2	67.4	75.8	67.3	75.4
TiO2	0.15 ±	0.01	0.57	0.49	0.53	0.58
Al2O3	13.9 ±	0.1	15.9	11.9	16.2	12.2
FeO*	1.63 ±	0.05	3.28	2.02	3.24	2.14
MnO	0.06 ±	0.00	0.05	0.04	0.06	0.03
MgO	0.05 ±	0.05	1.52	0.24	1.42	0.23
CaO	0.69 ±	0.02	3.40	0.66	3.51	0.67
Na2O	5.18 ±	0.18	5.13	4.03	5.15	3.91
K2O	3.49 ±	0.03	2.21	4.68	2.26	4.65
P2O5	0.02 ±	0.00	0.13	0.04	0.13	0.07
Rb	84 ±	2	41	117	47	113
Ba	796 ±	11	671	567	674	547
Sr	50 ±	3	390	54	379	52
Cs	1.37 ±	0.27	2.50	7.70	3.00	7.90
Sc	4.30 ±	0.18	9.32	7.48	8.95	9.03
V	3.25 ±	3.56	–	–	64	–
Co	0.66 ±	0.15	7.80	4.20	7.80	4.10
Ni	11.13 ±	0.93	–	–	13	–
Cr	0.50 ±	0.66	13	2	13	–
Zn	79 ±	11	38	40	57	50
La	23.2 ±	2.8	17.0	22.0	19.0	28.0
Ce	52.53 ±	8.78	25.0	46.0	38.0	63.0
Nd	20.36 ±	2.34	19.0	22.0	22.0	29.0
Sm	4.42 ±	0.44	4.20	5.60	4.90	7.40
Eu	0.61 ±	0.03	0.90	0.50	0.90	0.49
Tb	0.73 ±	0.08	0.51	0.83	0.63	1.03
Yb	3.3 ±	0.2	2.0	3.1	2.1	4.1
Lu	0.50 ±	0.03	0.33	0.45	0.32	0.61
La/Sm	3.32 ±	0.19	2.56	2.48	2.45	2.39
ΣHREE	46.72 ±	3.39	30.59	46.35	33.31	60.32
Eu/Eu*	0.41 ±	0.03	0.68	0.27	0.58	0.20
Zr	217 ±	6	195	202	197	367
Hf	6.6 ±	0.5	5.1	5.8	5.0	10.6
Ga	20 ±	2	–	–	19	–
Y	28 ±	3	25	30	25	38
Nb	17.4 ±	0.7	5.0	–	5.2	–
Ta	1.02 ±	0.03	0.43	0.70	0.46	0.95
Th	8.10 ±	0.42	4.4	8.2	4.7	11.3
U	2.48 ±	0.18	1.8	3.5	2.2	5.0

Estimated
melt fraction (Th K_D= 0.01)   0.54   0.42

Table 9.10: Comparison of average Broken Top rhyolite with glass compositions from partially melted tonalitic xenoliths (CGR) from the climactic eruption of Mt. Mazama (Bacon and Druitt, 1988). Rhyolitic glass from tonalite 1023 most closely resembles Broken Top rhyolite compositions. Relative depletions in Broken Top rhyolites of TiO_2, FeO and MgO can be modeled by adding 1.3% ilmn and 2.8% cpx to the Mazama restite. Large enrichments in K_2O, Rb and Cs are not consistent with incompatible element enrichments during partial melting, and probably indicate enrichment during hydrothermal alteration. Melt fractions calculated by assuming that Th was incompatible and immobile during hydrothermal alteration. Note how relativley small variations in melt fraction and starting composition between 799 and 1023 result in large REE variations in the melt.
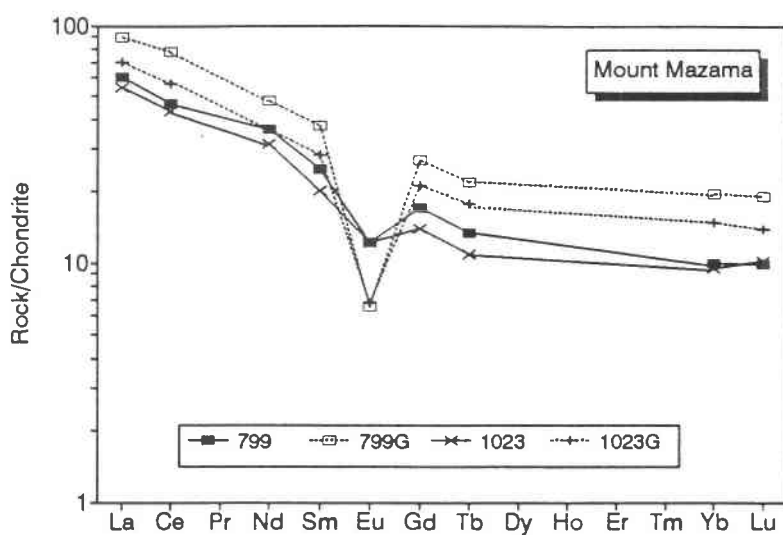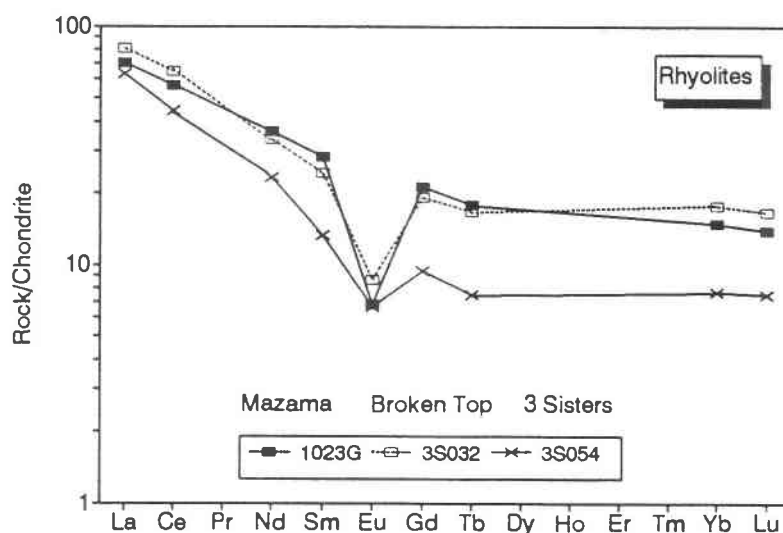
Figure 9.5: Chondrite normalized REE plots comparing Mt. Mazama and Broken Top rhyolites.
A) Comparison of Mt. Mazama tonalitic xenoliths (799 and 1023) and rhyolitic partial
melts from these xenoliths (799G and 1023G)(Bacon and Druitt, 1988). Melts occurred at
water-undersaturated conditions at ≈950°C and 2-5 kbars, with a plag + px + fe-oxide +
ap residuum. B) Comparison of Mazama rhyolite 1023G with Broken Top and Three
Sisters rhyolites. Mazama rhyolite 1023G closely resembles Broken Top rhyolites; small
variations in La/Sm and Eu/Eu* can be accounted for by small variations in the amount
of residual apatite and in the anorthite content of residual plagioclase. Three Sisters
rhyolites are petrogenetically distinct, and were produced through partial melts of basaltic
rocks.

during alteration. Oxygen isotopic exchange between plagioclase and quartz in the tonalitic blocks indicates that hydrothermal alteration of these rocks preceded high temperature (>900°C) isotopic re-equilibration (Bacon et al., 1989). If melting first occurred along altered joints and selvages, it would be possible to selectively enrich the melt in relatively mobile K_2O, Rb and Cs. Assuming that Rb and K_2O behave incompatibly, partial melts (F=0.54) of tonalite 1023 should contain 76 ppm Rb and 4.01 wt.% K_2O, which corresponds to Broken Top rhyolite compositions (table 9.10). Additional depletions in TiO_2, FeO* and MgO in the Mazama rhyolite could be produced by the addition of 1.3% ilmn and 2.8% cpx in the restite.

Mazama rhyolites (esp. 1023G) contain REE and HFSE abundances that are very close to the composition of Broken Top rhyolites (figure 9.5a). Although 0.3% residual apatite is required to balance P_2O_5, the slightly lower La/Sm in the Mazama rhyolite probably reflects a relatively lower amount of apatite in the tonalitic residuum. The slightly larger Eu/Eu* and lower Al_2O_3 + Na_2O in the Mazama rhyolite may also reflect a larger amount of sodic plagioclase in the restite.

9.2.3 Summary of Broken Top rhyolite petrogenesis

Broken Top rhyolites are spatially, temporally, mineralogically and compositionally distinct from Three Sisters rhyolites. Crystal fractionation of high Na_2O dacites is not a valid model for Broken Top rhyolite petrogenesis, and other fractionation models require the pre-existence of rhyolite to create the parental compositions. Trace element abundances also invalidate many petrogenetic models, in part because amphibole was not a significant fractionating phase. The Broken Top rhyolites are petrogenetically distinct from high silica melts at Medicine Lake and Mt. Mazama, which were produced essentially through crystal fractionation.

Partial melts of metabasaltic rocks do not result in Broken Top rhyolite trace element compositions. Although experimental data are scarce for partial melts of intermediate composition rocks at low water contents, dehydration melts of dacitic rocks do not apparently produce Broken Top rhyolite compositions. Enrichments in incompatible trace elements, and depletions of compatible trace elements, in the Broken Top rhyolites requires the melting of a source more evolved than typical High Cascade dacites.

Rhyolitic partial melts in tonalitic ejecta from the climactic eruption of Mt. Mazama are very similar to Broken Top rhyolite compositions. The Mazama rhyolites were apparently produced through ≈50% dehydration melts of the tonalite at ≈950°C and 2-5 kbars pressure. Geochemical differences between the Mazama and Broken Top rhyolites can be accounted for by alteration in the Mazama source rocks, and small variations in the residual mineralogy. The Mazama tonalites may be analogous to older silicic plutons that likely underlie this part of the central High Cascades. The Broken Top rhyolites could have been produced independently from the High Cascades magma system through partial melts of older silicic plutons that likely occur in the upper-to-middle(?) crust.

10. SUMMARY OF CENTRAL HIGH CASCADE PETROGENESIS

10.1 Petrogenesis of Volcanoes in the Three Sisters Area Since ≈600 ka

Continental arc magmatism in the Three Sisters region of the central High Cascades reflects a complex interrelationship between crystal fractionation, magma recharge, and the mixing of rhyolitic crustal melts. Although these relationships are certainly not unique to the High Cascades (cf., Hildreth and Moorbath, 1988), significant temporal and spatial variations in the expression of these petrogenetic processes have developed in only a 600 km^2 area of the Oregon Cascades arc since ≈500 ka.

Previous studies of central Cascades mafic petrogenesis (Hughes, 1983, 1990; Priest et al., 1983; Hughes and Taylor, 1986; Conrey and Sherrod, 1988; Conrey, 1991) have generally recognized that rocks older than ≈5 Ma are often petrogenetically distinct from rocks younger than ≈2 Ma, which also may be distinct from rocks younger than ≈0.7 Ma. This study further supports the conclusions of previous researchers that there are no discernable spatial or temporal controls on mafic petrogenesis for rocks younger than ≈0.7 Ma within the Three Sisters region of the Oregon High Cascades.

Major and trace element variations for Three Sisters area mafic rocks clearly indicate that clinopyroxene and titanomagnetite are early fractionating phases, which is the general characteristic of relatively high pressure (7-10 kbars), water-undersaturated (≈1 wt.%) mafic systems. Although experimental data on phase relationships and trace element partitioning are available for anhydrous, 1 atm. mafic systems, there are only limited data for high pressure (7-10 kbars), water-undersaturated systems that most closely correspond to the High Cascades mafic system. Even with these limitations, there are certain conclusions on mafic petrogenesis reached in this study.

Crystal fractionation coupled with magma recharge was an important petrogenetic process for mafic rocks in the study area. In essence, any long-lived (10^5-10^6 years) mafic magma system must have had a recharge rate equal to the crystallization + eruption ± assimilation rate, in order to maintain thermal and mass balance. It is reasonable to conclude that the High Cascades mafic system has been recharged with relatively primitive, mantle-derived melts, because:

1) Parental mafic compositions have been erupted throughout the last ≈700 k.y.

2) The subduction-related processes that result in mafic arc magmatism have continued to operate during the last ≈700 k.y.

3) High Cascades mafic petrogenesis cannot be explained by a model involving closed system mafic fractionation or assimilation.

The primary effect of mafic recharge is to shift the evolving system back towards parental compositions, resulting in compatible element buffering with incompatible element enrichments. This feature is commonly observed in the central Cascades mafic system, and in many other magmatic

arcs (cf., Conrey, 1990). It is also likely that recharge involved different types of primary basaltic melts, which may have been produced by different degrees of peridotite melting, mantle metasomatism, or compositional heterogeneities in the mantle source (e.g., Hughes, 1990).

Recharge rates that result in a steady-state magma system (i.e. recharge = crystallization + eruption rates) apparently limits differentiation in that system to roughly 58% SiO_2 (cf., Nielsen, 1988); magma systems that evolve andesite and dacite through crystal fractionation are probably closed to mafic recharge. Rocks with >58% SiO_2 are rarely observed in the High Cascades except at large, stratovolcanic centers; the most abundant rocks in the High Cascades, including the Plio-Pleistocene mafic platform, are basaltic andesite (e.g., Hughes and Taylor, 1986). This observation also supports the hypothesis that the High Cascades mafic magma system has remained open to large amounts of recharge through time. This mafic system most likely resided at deep crustal levels (35-45 km), and ponded at the crust-mantle boundary due to density contrasts (cf., Marsh, 1985; Hildreth and Moorbath, 1988).

A large, recharging, mafic magma system located in the deep crust has sufficient heat to generate partial melts of adjacent mafic crustal rocks. If 10-30% melting occurs at water-undersaturated conditions, then these melts are broadly rhyolitic. Many of the geochemical features of the High Cascades mafic system, which cannot be explained by recharge + fractionation, can be accounted for by periodically mixing 10-20 vol.% High Cascades rhyolite into the mafic magma system. Mixing also should have resulted in crystal fractionation, because the rhyolitic magma was likely cooler ($\approx 900°C$) than the mafic magma ($> 1100°C$).

In summary, a large mafic magma system probably extends along the length of the Oregon Cascades arc at the base of the crust. Parental basaltic magmas of this system were generated through subduction-induced melting of upper mantle peridotite, which was possibly metasomatized and undoubtedly heterogenous. Periodic recharge coupled with crystal fractionation of plag + ol + pyroxene + Fe-Ti oxides can explain many of the geochemical features of the High Cascades mafic system since ≈ 700 ka. Other geochemical features are consistent with periodically mixing 10-20% rhyolitic crustal melts into the mafic magma system. Although it is possible that portions of this mafic system could remain isolated from the main system in both space and time, there is no evidence to suggest that any part of the central High Cascades mafic system has been petrogenetically distinct since ≈ 700 ka. The petrogenetically distinct silicic magma systems found in this part of the High Cascades thus evolved from the same mafic magma system.

In contrast to the mafic system, spatial and temporal petrogenetic controls are observed for intermediate composition rocks in this part of the High Cascades. These controls are best expressed in the petrogenesis of the Three Sisters. North Sister, which is the oldest of the Three Sisters ($\leq \approx 350$ ka), is an essentially mafic stratovolcano; the most evolved compositions at North Sister are several small dikes of low silica andesite (E.M. Taylor, pers. comm., 1987). At Middle

Sister (younger than NS, ≥100 ka.), intermediate rocks were produced almost exclusively through the fractionation of plag + px + Fe-Ti oxides ± ol ± ap, resulting in elevated Na_2O and REE's to 66% SiO_2. In addition, the evolving system was essentially closed to mafic recharge, or else fractionation would not have proceeded beyond ≈58% SiO_2. It is not clear why fractionation was limited to 66% SiO_2 at Middle Sister. Other High Cascade volcanoes, such as Mt. Mazama and Medicine Lake, evolved >66% SiO_2 magmas through crystal fractionation and minor amounts of silicic wall-rock assimilation from similar mafic systems. A lack of evolution above 66% SiO_2 may indicate that the Middle Sister magma system was smaller and more closed to recharge than these other systems. If the Middle Sister system was smaller, then magma volumes could have been insufficient to maintain a fractionating chamber beyond 65% SiO_2 before conductive heat loss resulted in ≈50% crystallization (i.e. a non-contiguous magma (cf., Bergantz, 1990)). Small amounts of rhyolite mixing (i.e., Mazama) or amphibole fractionation (i.e. Medicine Lake), neither of which occurred during Middle Sister petrogenesis, may also be a prerequisite to differentiation above 66% SiO_2. It is important to note that rhyolitic magmas were present <10 km to the southeast in the contemporaneous (≈380-200 ka) Broken Top system, but these rhyolites did not interact with either the North or Middle Sister magma system. The progression from NS to MS probably reflects the temporal evolution of a relatively closed magma system from essentially mafic (NS) to more andesitic and dacitic compositions (MS) through the fractionation of anhydrous minerals (figure 10.1).

At ≈100 ka, volcanism had shifted ≈5 km south of Middle Sister to South Sister, and the first rhyolites were erupted in the Three Sisters system. In contrast to the fractionation origin of the Middle Sister intermediate series, the petrogenesis of South Sister is characterized by the mixing of ≥≈40% rhyolite into an essentially mafic (58%-60%?) system to produce intermediate composition rocks to 66% SiO_2; mixing 30% rhyolite with fractionation-produced dacite would have resulted in compositions more silicic than 66% SiO_2, which are not observed at South Sister. If dacitic magmas produced through crystal fractionation (i.e. MS) were present in the Three Sisters system at ≈100 ka, they did not mix with rhyolitic magma to produce rocks with >66% SiO_2, nor were they erupted at South Sister. The petrogenetic changes that occurred at ≈100 ka between Middle and South Sister were not caused exclusively by the addition of rhyolitic partial melts into a Middle Sister-type fractionating magma system; the main magma system was re-established ≈5 km to the south, became more mafic, and generated rhyolitic magmas through dehydration melting of metabasaltic crustal rocks. These features are consistent with the emplacement of a new, essentially mafic system into the thermally-mature middle crust beneath South Sister at ≈100 ka (figure 10.1). It is speculated that the South Sister mafic system was probably quite similar to the older North Sister mafic system, but that rhyolitic partial melts were produced at South Sister because the mafic system was emplaced into crust that was relatively hotter due to Middle Sister magmatism. South
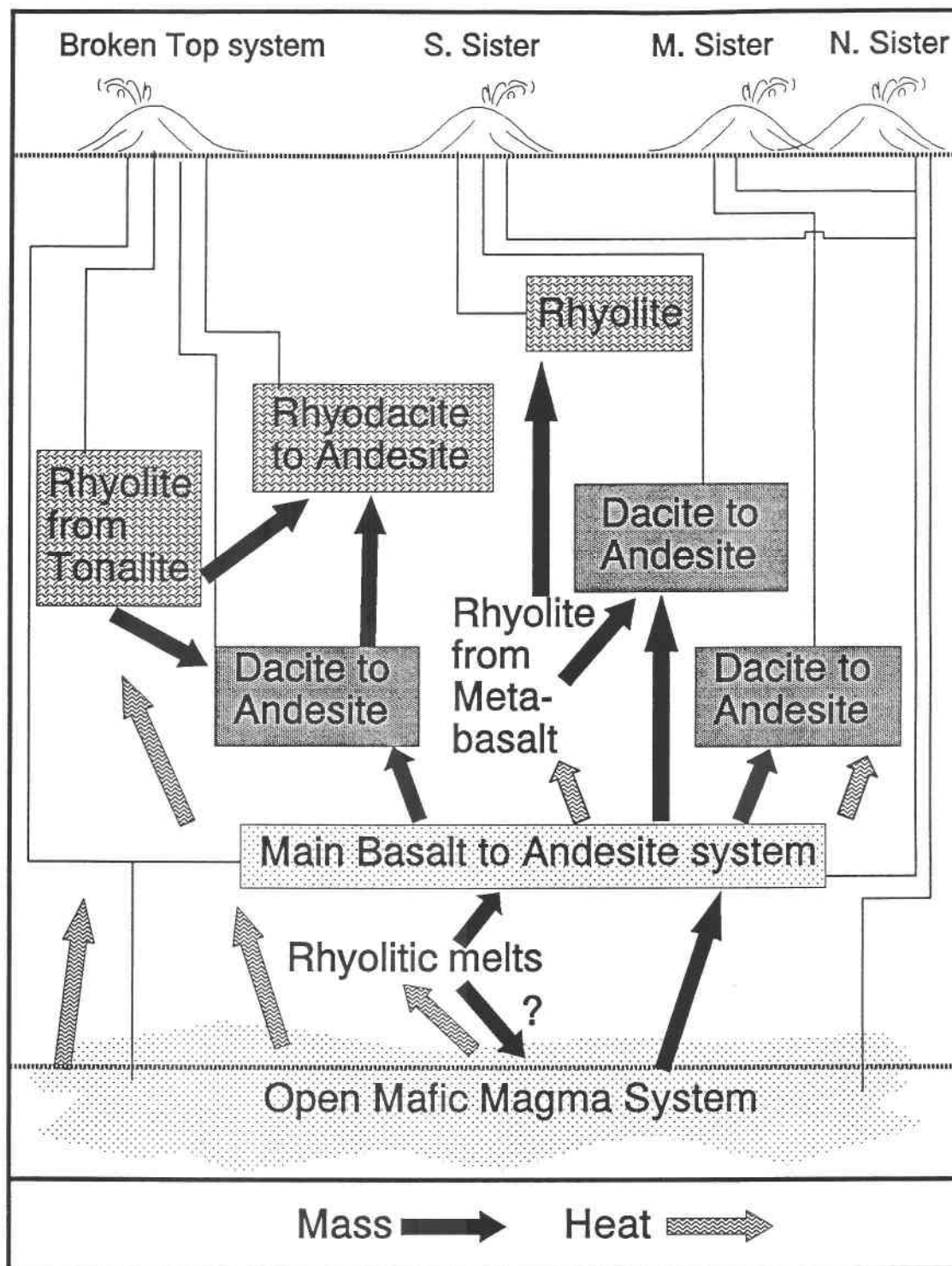
Figure 10.1: Schematic diagram of petrogenetic development in the Three Sisters region of the Oregon High Cascades. Arrows indicate direction of mass and heat transfer, solid lines are eruption paths, and boxes represent fractionating magma bodies. Vertical and horizontal distances are schematic and do not imply actual positions of these magma systems.

Sister can be thought of as a primarily bimodal system, with intermediate composition magmatism controlled by magma mixing and crystal fractionation. With increasing time, more evolved intermediate compositions will likely become available to mix with the rhyolite at South Sister, resulting in dacitic-to-rhyodacitic magmas and a reduction in the observed 66%-72% compositional gap (i.e., ≈Broken Top system).

Crystal fractionation to intermediate compositions (≈65% SiO_2) combined with ≈30% rhyolite mixing resulted in dacitic-to-rhyodacitic magmatism in the Broken Top system from ≈500 ka to at least ≈200 ka. In contrast to Middle Sister, only a few Broken Top rocks that evolved to 65% SiO_2 through anhydrous crystal fractionation were erupted; differentiation above 63% SiO_2 generally required the mixing of ≈30% rhyolite into the magma system. In contrast to South Sister, dacitic magmas were available for mixing with 30-35% rhyolite, resulting in the evolution of rhyodacite and only a small (≈2% SiO_2) compositional gap in the Broken Top system (figure 10.1)

Rhyolites from the Three Sisters and Broken Top systems were produced from partial melts of different crustal compositions. Observed major and trace element abundances in both of these rhyolites are not consistent with evolution from intermediate compositions through crystal fraction-ation. Three Sisters rhyolites most closely resemble dehydration melts of metabasaltic rocks, with ≈20% melt produced at ≈3-7 kbars and ≈900°C. Although intra-suite variations (72-76% SiO_2) can be accounted for through 6-15% fractionation of modal minerals, inter-suite variations between Holocene and Pleistocene rhyolites cannot be related through crystal fractionation or magma mixing. Holocene rhyolites were generated from the same type of metabasaltic crustal rocks as Pleistocene rhyolites, but melting probably occurred at slightly higher temperatures and resulted in a larger plagioclase component in the Holocene melts. The compositional differences between the Holocene and Pleistocene rhyolites may thus reflect an increase in crustal temperature with time due to continued magmatism beneath South Sister.

In contrast to the Three Sisters rhyolites, Broken Top rhyolites were likely produced through partial melts of tonalitic crustal rocks, and do not resemble dehydration melts of metabasaltic rocks, or melts of associated restites. Although there are only limited experimental data on the water-undersaturated melting of silicic crustal rocks, partial melts from tonalitic blocks in the climactic ejecta of Mt. Mazama closely resemble Broken Top rhyolites. The Mt. Mazama rhyolites were apparently produced through 40-50% dehydration melts of tonalite at ≈950°C and ≈2-5 kbars. The tonalites at Mt. Mazama were also produced through crystal fractionation, and could be analogous to older silicic intrusions that may underlie the Broken Top system.

Most, and possibly all, of the Broken Top rhyolite was associated with the Tumalo volcanic center and erupted at 380 ± 20 ka. The continuous eruption of rhyodacites and dacites from ≈600 ka to at least 200 ka in the Broken Top system, however, indicates that rhyolitic magmas must have been present in this system from at least ≈600 ka to ≈200 ka. Rhyolitic volcanism in the Three

Sisters system, however, is constrained to the last ≈100 k.y. There may thus have been a ≈100 k.y. hiatus between Broken Top and Three Sisters rhyolitic volcanism, although more age data are needed to evaluate this relationship. Stratigraphic and K-Ar age data in this study clearly demonstrate that petrogenetically distinct rhyolites can be produced, and can control the development of distinct intermediate composition magma systems, in contemporaneous and adjacent parts of a 600 km^2 area of the Oregon High Cascades.

10.2 The Occurrence of Rhyolite in the Oregon High Cascades

Rhyolitic volcanism of any significant magnitude or duration in the Oregon High Cascades is restricted to the Three Sisters region. No rocks with >68% SiO_2 have been reported from Mt. Hood (figure 10.2) (Wise, 1969; Priest and Vogt, 1982). Rhyolite at Mt. Jefferson is restricted to several small (<1 km^3) domes; partial crustal melts at Mt. Jefferson are primarily rhyodacitic (Conrey, 1991). Mt. Mazama produced large amounts of rhyodacite through crystal fractionation and minor crustal assimilation (Bacon and Druitt, 1988), but rhyolite is restricted at Mt. Mazama to small melt zones in tonalitic xenoliths.

Appreciable volumes of rhyolite have been erupted from Newberry volcano since ≈500 ka (MacLeod and Sherrod, 1988). However, Newberry is petrogenetically distinct from other major volcanoes in the Oregon High Cascades, and is not strictly a High Cascade volcano (Waters, 1962; Higgins, 1973; Goles and Lambert, 1990):

1) Newberry is predominantly a bimodal shield volcano, and lacks the abundant intermediate composition rocks that characterize High Cascade stratovolcanoes (cf., Beyer, 1973; Higgins, 1973; MacLeod et al., 1982; MacLeod and Sherrod, 1988).

2) Newberry rhyolites are petrologically similar to a series of rhyolitic domes and flows that extend ≈300 km to the southeast (MacLeod et al., 1975; MacLeod and Sherrod, 1988; Goles and Lambert, 1990; Draper, 1991). These rhyolites become progressively younger as they approach Newberry, and are thought to be associated with the Brothers Fault Zone (Walker, 1974; MacLeod et al., 1975; Draper, 1991). Volcanism associated with the Brothers Fault Zone since ≈10 Ma is probably related to Basin & Range extension and not subduction (Carlson and Hart, 1987; Draper, 1991).

3) Newberry is located at the convergence of 3 major fault zones (figure 10.3), in an area of thinner crust than the rest of the Oregon High Cascades (37 km vs. 44 km; Fitterman, 1988; Leaver et al., 1984). Mafic eruption rates at Newberry are appreciably higher than in the adjacent part of the High Cascades (Sherrod and Smith, 1990).

Newberry is located in an area that has apparently undergone greater amounts of Pleistocene crustal extension than any part of the Oregon High Cascades. Even if Newberry has a petrogenetic component related to subduction, Newberry petrogenesis must have been strongly influenced by the
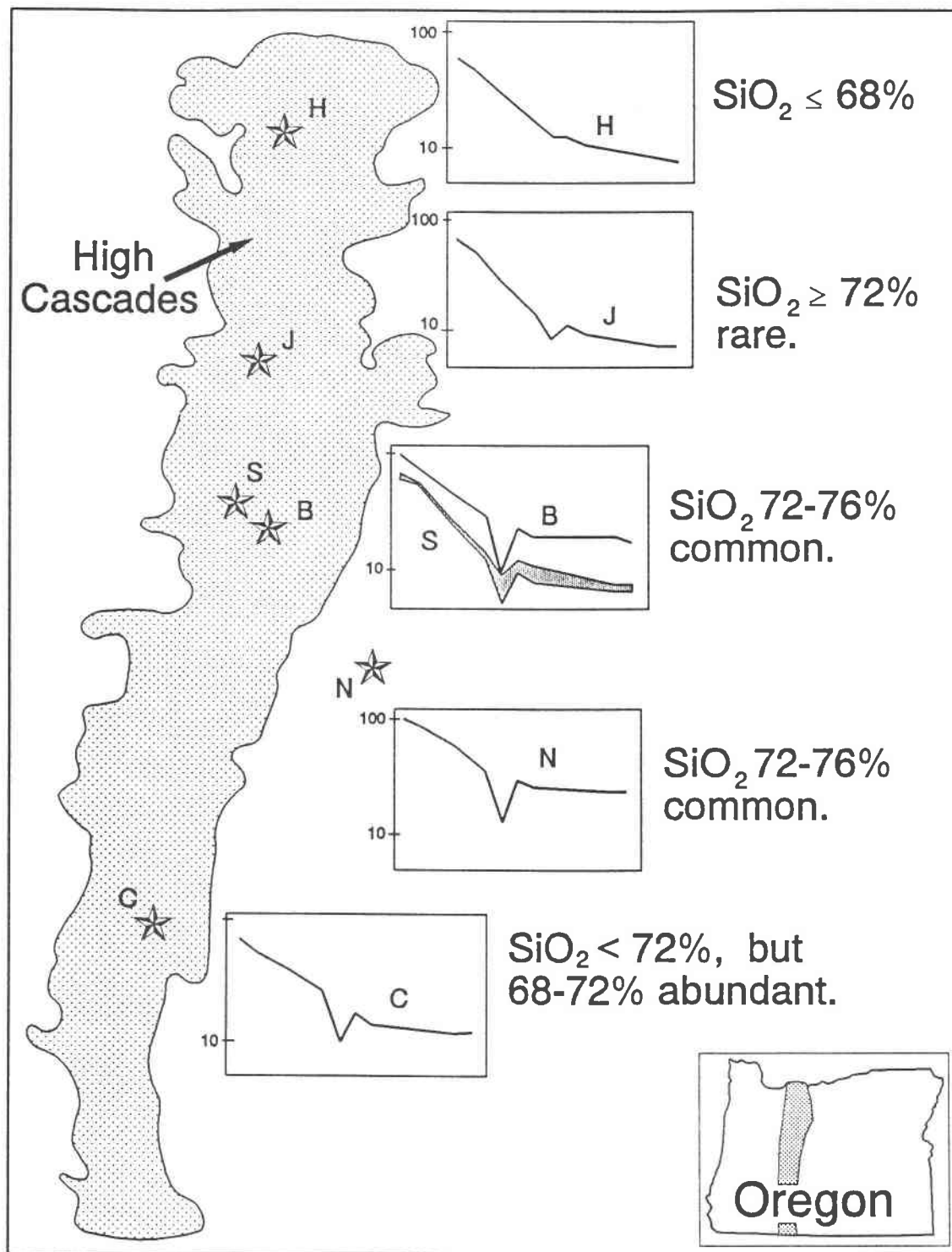
Figure 10.2: Distribution of silicic Quaternary vents in the Oregon High Cascades, and chondrite-normalized REE patterns for the most evolved compositions at each volcano. See text for data sources. Rhyolite in the High Cascades is restricted to the Three Sisters area, where two distinct types of rhyolite are erupted. Rhyolite at Newberry is not directly related to High Cascade volcanism, and is probably influenced by Basin and Range extension.
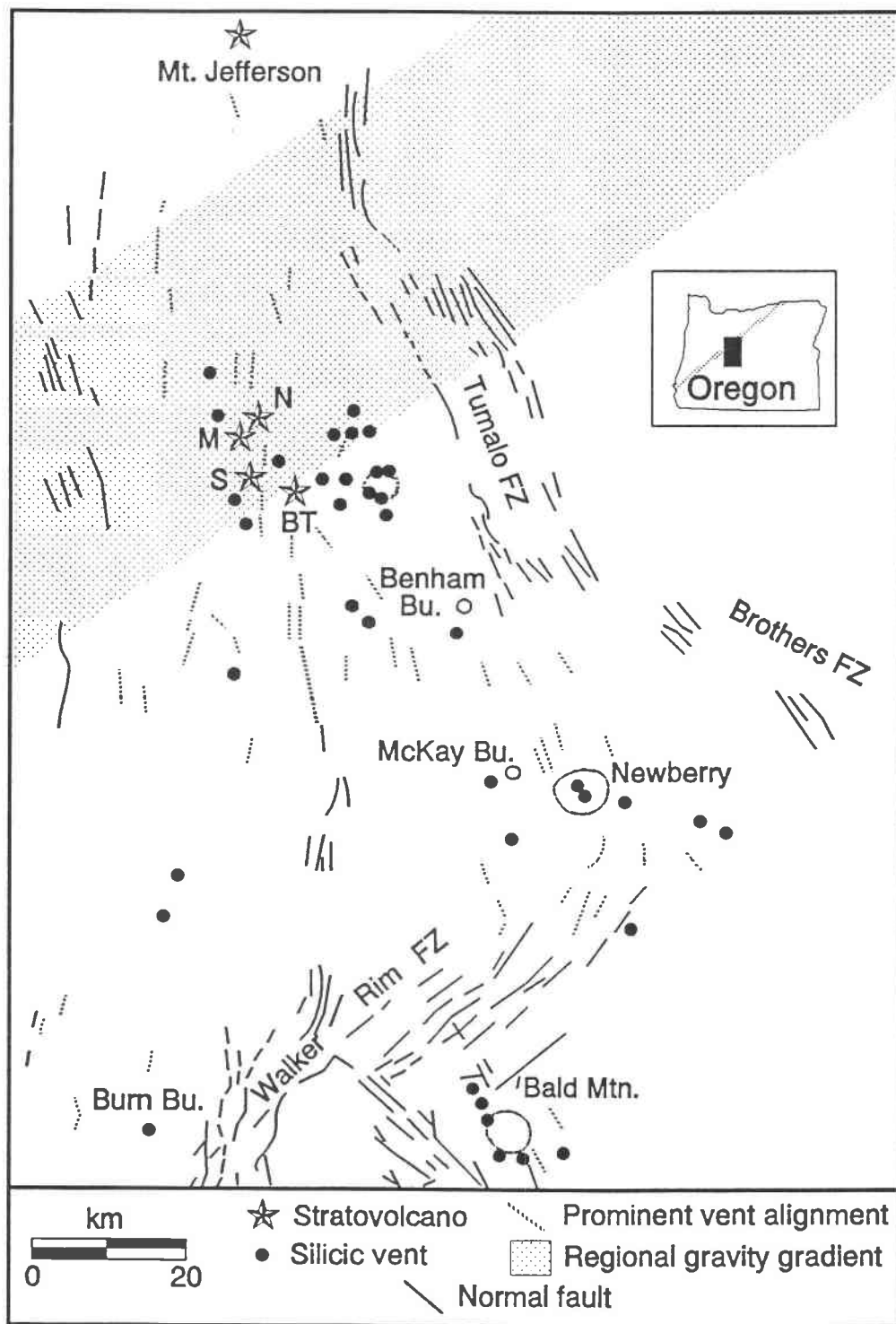
Figure 10.3: Faults and vent alignments of central Oregon, modified from MacLeod and Sherrod, 1988. Approximate boundaries of the regional gravity gradient from Thiruvathukal et al., 1970. **FZ** = Fault Zone. Note the change in structural trend from north to northwest that occurs east of the Three Sisters.

relatively higher heat flow associated with Basin and Range-style crustal thinning and increased mafic volcanism (cf., MacLeod and Sherrod, 1988). Although the relationships between crustal extension and petrogenesis are poorly constrained, intuitively an increase in crustal heat flow should favor the production of rhyolitic crustal melts (cf., Marsh, 1985; Bergantz, 1989).

10.3 Tectonic Controls on Continental Arc Petrogenesis

Arc-length variations in the petrogenesis of continental calc-alkaline volcanic rocks have been reported for the Cascades (Hughes et al., 1980), Aleutians (Kay et al., 1982), Central America (Carr et al., 1982) and the Andes (Thorpe et al., 1982; Hildreth and Moorbath, 1988). These studies have shown that variations in subduction rate, angles of plate convergence, age of volcanism, crustal thickness and composition can strongly influence the petrogenesis of continental arc rocks (i.e., Arculus and Johnson, 1978).

The Oregon High Cascades south of Mt. Hood are thought to represent a single tectonic segment of the High Cascades magmatic arc (Guffanti and Weaver, 1988). Although crustal thickness remains essentially constant at 44 km along the length of this segment (Leaver et al., 1984), it is likely that a small change in crustal composition or age occurs between Mt. Jefferson and the Three Sisters area (Chapter 2). Two rhyodacites ($\approx 70\%$ SiO_2) at Mt. Jefferson, which were produced through partial melts of mafic crustal rocks, have $^{87}Sr/^{86}Sr \leq 0.7034$ (Conrey, 1991). These rhyodacites are petrogenetically similar to rhyolites in the Three Sisters, which were produced through dehydration melts of metabasalt and have $^{87}Sr/^{86}Sr = 0.7036$ (table 3.3). These data support the argument that metabasaltic crust in the northern part of this arc segment is potentially younger (early Cenozoic to late Mesozoic) than metabasaltic crust in the southern part of the segment (early Mesozoic to late Paleozoic) (e.g., Riddihough et al., 1986). However, the isotopic (and presumably geochemical) differences between these crustal types are relatively small, compared to crustal variations reported in other studies (i.e. $^{87}Sr/^{86}Sr = 0.7036$-0.7057, Hildreth and Moorbath, 1988). In addition, rhyodacites and granitoid xenoliths at Mt. Mazama also have $^{87}Sr/^{86}Sr = 0.7037$ (Bacon et al., 1989), yet Mt. Mazama did not erupt rhyolite. It is unlikely that the petrogenetic differences between the Three Sisters area and other Oregon High Cascade volcanoes originated from these small presumed changes in crustal age or composition.

The Three Sisters region apparently is located on crust of similar composition and thickness as the rest of the Oregon Cascades arc segment. There is no evidence to indicate that subduction rates or convergence angles were different in the Three Sisters area than for the rest of this arc segment. Mafic extrusion rates have also remained relatively constant within this arc segment since ≈ 2 Ma (Sherrod and Smith, 1990). In spite of these similarities, the Three Sisters area is petrogenetically distinct from the other stratovolcanic centers in this segment of the Cascades arc. Previous models involving large-scale tectonic or crustal controls on the petrogenesis of continental

arc volcanism cannot explain the petrologic features of the Three Sisters area. In addition, differences between the Broken Top and Three Sisters systems have developed contemporaneously from the same mafic magma system, in the same 600 km^2 area of the Cascades arc. Clearly, these features cannot be the result of regional tectonic or crustal heterogeneities.

10.4 A Paradigm of Crustal Stress and Igneous Petrogenesis

The Oregon High Cascades are located in an area of regional east-west extension (Zoback and Zoback, 1980), which is in part related to the dynamics of oblique subduction of the Juan de Fuca plate (Wells et al., 1984; Rodgers, 1985; Pezzopane and Weldon, 1990). North-south alignments of Quaternary vents in the Three Sisters area parallel the strike of older ($\leq$5 Ma) normal faults, especially north and west of the Three Sisters (figure 10.3; cf., Bacon, 1985, figure 2). These orientations reflect a Quaternary east-west extensional stress regime (cf., Nakamura, 1977). East and southeast of the Three Sisters, vent alignments strike to the northwest and parallel the trend of the Tumalo Fault Zone (figure 10.3), which was active in the Quaternary (Peterson et al., 1976; Taylor, 1981).

It has long been recognized that the Brothers Fault Zone (BFZ) may intersect the Oregon High Cascades in the Three Sisters area, and that the BFZ is related to Basin and Range extension (Lawrence, 1976; Bacon, 1983, 1985; Guffanti and Weaver, 1988). The timing of BFZ impingement into the Cascades, however, is not clear. BFZ impingement might have influenced development of the Oregon Cascades graben at $\approx$5.4 Ma (Guffanti and Weaver, 1988), but there is evidence that the Cascades graben may not be a Basin and Range structure (Taylor, 1981; Smith, 1986; Smith et al., 1987). The Oregon Cascades graben developed well north of the Basin and Range province, and there is little evidence of major crustal extension in the intervening area (Smith et al., 1987). The location of the graben near the Basin and Range province may be coincidental; discontinuous intra-arc grabens can develop under a variety of tectonic or volcanic conditions (see summary by Smith, 1986), and their formation does not require back-arc extension. It is also possible that the formation of the Cascades graben may be related to differential crustal loading between the Miocene Cascades volcanic axis and the Deschutes Basin (Smith et al., 1989). In addition, if rhyolitic volcanism in southeastern Oregon was related to northwesterly progression of the BFZ (Walker, 1974; MacLeod et al., 1975), then $\approx$5 Ma volcanism was located $\approx$100 km east of Newberry volcano (figure 10.4). These data suggest that the BFZ did not impinge upon the Oregon Cascades arc until later than 5 Ma, and that the Oregon Cascades graben may not be directly related to Basin and Range extension (Smith, 1986; Smith et al., 1987).

Newberry volcano is thought to represent the termination of northwest-younging rhyolitic volcanism associated with the BFZ (Walker, 1974; MacLeod et al., 1975; MacLeod and Sherrod, 1988), based in part on the abundance of $\leq$1 Ma to Holocene rhyolitic eruptions located at
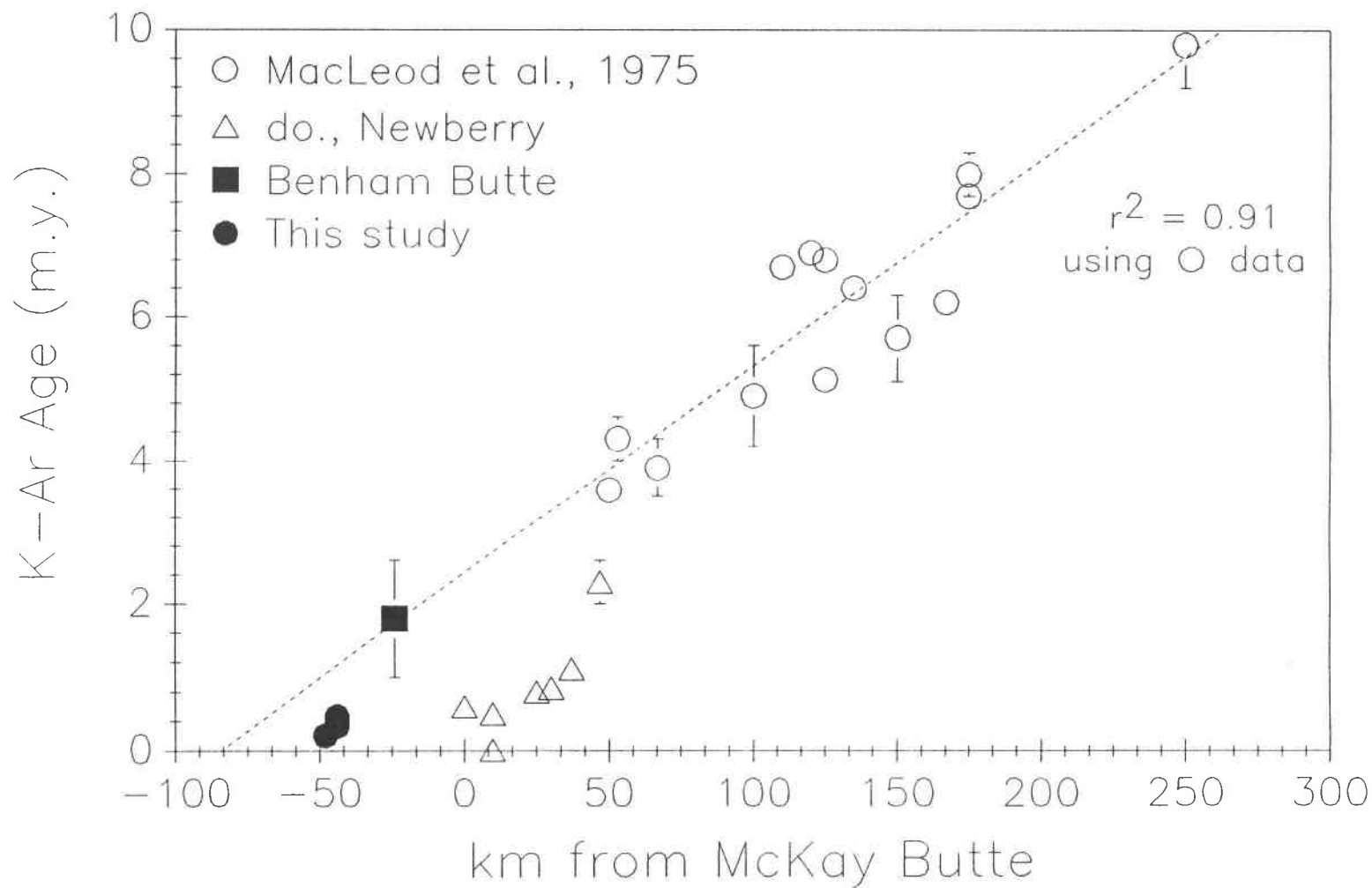
Figure 10.4: Age of rhyolitic domes and flows ≤10 Ma in eastern Oregon plotted against distance from McKay Butte (Newberry volcano), using age data from MacLeod et al., 1975, Fiebelkorn et al., 1983, and this study. The "Newberry" trend (triangles) may have separated from the main trend at ≈3 Ma, while the main trend continued on to Benham Butte and the Three Sisters area.

Newberry. MacLeod et al. (1975) concluded that the rate of northwesterly age progression changed at ≈5 Ma from ≈3 cm/yr to ≈1 cm/yr (figure 10.4), and that the lower rate terminated at Newberry volcano. However, the timing of this rate change may be as young as ≈2-3 Ma, given the degree of variation (r=0.91) in the age-position data (figure 10.4). In addition, Fiebelkorn et al. (1983) report a K-Ar age of 1.8 ± 0.8 Ma on sanidine from Benham Butte (figure 10.3), which has a reversed paleomagnetic direction (i.e. >0.72 Ma) and a composition more similar to Newberry rhyolite than adjacent High Cascades rhyolite (Appendix D). Benham Butte is also located ≈30 km northwest of Newberry, and thus cannot simply be related to the younger "Newberry" trend. However, the linear extrapolation of a best-fit (r=0.91) line through the older (≈3 cm/yr) trend intersects the position of Benham Butte at its age (figure 10.4). It is speculated that the Newberry trend is superimposed upon, or a branch of, the older(?) ≈3 cm/yr trend, and that rhyolitic volcanism at Newberry is only in part related to the BFZ; either Cascade magmatism or extension associated with the Walker Rim-Tumalo Fault Zones could have influenced the development of Newberry volcano.

If the ≈3 cm/yr trend continued northwest of Newberry and on past Benham Butte, it would have intersected the Three Sisters area (Walker, 1974) at ≈500 ka (figure 10.4). This corresponds to the age of early Broken Top system silicic volcanism. Although this relationship may be coincidental, it probably indicates that rhyolitic volcanism in this area may be a direct result of more recent impingement of "BFZ-tectonics+volcanism" onto the Oregon High Cascades. This does not imply that the BFZ actually intersects the High Cascades or merges with the Tumalo Fault Zone, as the last motion on the BFZ probably occurred prior to ≈3 Ma (MacLeod et al., 1982; Hawkins et al., 1988). Instead, this relationship suggests that the regional tectonic forces that controlled faulting and volcanism along the BFZ could have begun to operate in this part of the High Cascades at ≈500 ka.

It is not clear whether the BFZ represents a zone of dextral shear related to Basin and Range extension (Lawrence, 1976) or transtensional motion linked to oblique subduction of the Juan de Fuca Plate (Gutmanis, 1989; Pezzopane and Weldon, 1990). In either case, the Three Sisters region is apparently located in a zone of greater crustal extension than occurs within 75 km to the north or south (figure 10.3). The western boundary of the central High Cascades is marked by north to north-northwest striking faults and vent alignments, which were produced through both older extensional events (i.e., ≈5.4 Ma graben formation) and a regional east-west extensional stress field in the Quaternary (e.g., Zoback and Zoback, 1980; Smith et al., 1987). However, east and south of Broken Top volcano, faults and vent alignments strike to the northwest (figure 10.3). The northeast-to-northwest change in strike of the Walker Rim-Tumalo Fault Zones at Newberry volcano, coupled with essentially northern strike along and west of the High Cascades axis, must

have resulted in an area of relatively greater crustal extension east of the Three Sisters in order to accommodate this shift from east-west to northeast-southwest extension.

The effects of crustal extension on the petrogenesis of calc-alkaline volcanic rocks are poorly constrained. Empirical (Nakamura, 1977; Hildreth, 1981) and theoretical (Shaw, 1980) models of the effects of crustal stress on magmatism generally conclude that extension favors the vertical ascent of mafic magma in the crust. Bimodal (i.e. lacking intermediate composition rocks) volcanism is often characteristic of extensional terranes (e.g., Smith, 1979; Hildreth, 1981). The production of rhyolitic crustal melts should be enhanced by increased mafic intrusion accompanying extension, although magma residence times in the crust are insufficient to develop intermediate compositions through fractionation or mixing. However, these general models were developed for volcanic systems in highly extended terranes, such as the Basin and Range. The High Cascades represent a slightly extensional terrane, and the proposed variations in crustal extension are small relative to the adjacent Basin and Range province.

10.5 A Tectonomagmatic Model of Three Sisters Area Petrogenesis

The above general concepts can be used to construct a hypothesis on the effects of small-scale changes in the magnitude of crustal extension. If a zone of northeast-southwest extension intersects a region of overall east-west extension, then the area of intersection is relatively more extended that surrounding area, regardless of the absolute amount of extension. Mafic intrusion should be somewhat favored in the more extended area, resulting in a higher potential for recharge of crustal magma chambers and additional thermal input into the crust. Elevated recharge rates and wall rock temperatures should favor the production of fractionating magma chambers, which would have larger volumes and less conductive heat loss and could thus differentiate to more evolved (i.e. intermediate) compositions. In addition, these factors would enhance the production of rhyolitic crustal melts, which could then interact with the fractionating magma chambers.

This hypothesis explains many of the observed temporal and spatial controls on petrogenesis in the Broken Top and Three Sisters systems. The Broken Top system is characterized from ≈500 ka to ≤200 ka by significant amounts of andesite to rhyodacite, which were produced through a combination of crystal fractionation and rhyolite mixing. However, the only large eruption (≥10 km^3) of rhyolite in this system occurred at ≈380 ka, and was associated with the Tumalo volcanic center. Some geological event must have triggered this production of anomalously large volumes of rhyolitic crustal melt. The most efficient process would have been an increase in crustal heat-flow produced by mafic intrusion into the thermally mature middle(?) crust. It is thus speculated that the impingement of an extensional stress regime related to Brothers Fault Zone tectonics onto the central High Cascades magmatic arc at ≈500-400 ka triggered the production of anomalously large volumes of Broken Top rhyolite. After the eruption of this rhyolite at ≈380 ka, the locus of Broken

Top system volcanism shifted west of the Tumalo volcanic center to the Tam MacArthur Rim area. Eruption of rocks as silicic as rhyodacite continued in the Broken Top system to at least 200 ka, indicating that sufficient volumes of rhyolitic magma remained in the system to mix with a differentiating intermediate system.

Although North Sister is the oldest of the Three Sisters stratovolcanoes (≤340 ka), remnants of older mafic composite volcanoes (Little Brother, Sphinx Butte, The Wife) have been exposed beneath the Three Sisters. It is thus likely that mafic magmatism in the Three Sisters system occurred contemporaneously with silicic magmatism in the Broken Top system prior to ≈340 ka. Three Sisters mafic magmatism became focused at North Sister around 340 ka, after the large rhyolite eruption in the Broken Top system. Differentiation at North Sister was limited to low silica andesite, probably due to a significant amount of recharge into the mafic magma system. Between ≈340 and ≈100 ka, the locus of Three Sisters volcanism shifted from North Sister ≈2 km south to Middle Sister. It is possible that this shift was tectonically controlled, but there are no data that directly support this hypothesis. Andesite and dacite were produced at Middle Sister through crystal fractionation from mafic compositions, indicating that the magma system was essentially closed to mafic recharge. Migration of the magma system to shallower crustal depths (≈20-30 km?) might have effectively closed the system to mafic recharge. Although Middle Sister volcanism was probably contemporaneous with Broken Top volcanism, there is no evidence that rhyolite from the Broken Top system interacted with the North or Middle Sister systems.

At ≈100 ka, the locus of Three Sisters volcanism shifted ≈5 km south to South Sister. Although data are limited, stratigraphic relations suggest the shift from Middle to South Sister volcanism occurred over a short interval of time. Limited stratigraphic relationships also indicate that Broken Top system volcanism had essentially ceased by ≈100 ka. South Sister petrogenesis is characterized by the first eruptions of rhyolite in the Three Sisters system, and the mixing of rhyolite into a fractionating magma system that was more mafic than the Middle Sister system. The fractionating magma system associated with South Sister probably represents a new batch of mafic magma, which had likely segregated from the regional Cascades mafic system into the thermally mature middle(?) crust at ≈100 ka. The shift in High Cascade rhyolitic magmatism from the Broken Top system to South Sister is also consistent with northwesterly age progression of tectonically-influenced rhyolitic magmatism in this area. Holocene rhyolites at South Sister are petrogenetically distinct from Pleistocene South Sister rhyolites, and probably reflect a small increase in the temperature of crustal melting with continued volcanic activity at South Sister.

11. CONCLUSIONS

Petrogenetic models in this thesis have demonstrated that fractionation of plagioclase, pyroxene, Fe-Ti oxides ± apatite (PPFA) can effectively produce intermediate composition magmas from typical High Cascade mafic compositions. In order to fractionate to intermediate compositions, the relative amount of recharge into the system must be lower than in an essentially mafic magma system; magma systems having recharge rates capable of sustaining a steady state system (i.e., recharge = fractionation + eruption) are generally restricted to $\leq 58\%$ SiO_2. Low recharge rates at Middle Sister thus enabled PPFA fractionation to proceed to intermediate compositions, but the degree of magma evolution at Middle Sister was limited to $\approx 66\%$ SiO_2 due to the relatively small size of the differentiating magma system.

PPFA fractionation can also explain some of the intermediate composition rocks ($\leq 65\%$ SiO_2) in the Broken Top system. However, most of the intermediate composition rocks in the Broken Top system were produced through mixing 20%-35% rhyolite into the fractionating magma system. The rhyolite in this system cannot be produced from less evolved compositions through crystal fractionation, and was likely produced through partial melts of tonalitic crustal rocks. Magma mixing coupled with PPFA fractionation in the Broken Top system also resulted in a small compositional gap from 72-74% SiO_2.

In contrast to the Broken Top system, rhyolite associated with the Three Sisters system was produced through partial melts of mafic amphibolite. Rhyolitic magma chambers also developed in the Three Sisters system, and evolved from 72% to 76% SiO_2 through PPFA + minor amphibole fractionation. Intermediate composition rocks at South Sister were produced by mixing $\geq 40\%$ rhyolitic magma into a PPFA-fractionating mafic system. In spite of the marked petrogenetic differences between Middle and South Sister, the degree of differentiation at South Sister also was limited to $\approx 66\%$ SiO_2. Magma mixing coupled with PPFA fractionation in the South Sister system also resulted in a compositional gap from 66-72% SiO_2.

Intermediate composition rocks at South Sister and in the Broken Top system reflect the degree of evolution in the less evolved magma that is mixed with rhyolite. At South Sister, the less evolved magma was essentially mafic ($SiO_2 \approx 58-60\%$). Mixing (+ PPFA fractionation) between roughly equal amounts of essentially mafic and rhyolitic magma can only generate magmas with $\leq 66\%$ SiO_2. In contrast, the less evolved magma in the Broken Top system was essentially intermediate ($SiO_2 \approx 60-65\%$). Mixing (+ PPFA fractionation) between intermediate and rhyolitic magma can result in compositions with $\leq 72\%$ SiO_2. Although intermediate composition magmas were present during the construction of Middle Sister, the lack of rhyolitic magma precluded differentiation beyond 66% SiO_2 through magma mixing (i.e., Broken Top system).

The petrogenesis of the Three Sisters region of the Oregon High Cascades can be summarized in the following sequence:

1) Volcanism from ≈600(?) to ≈350 ka occurred at the Tumalo volcanic center and Todd Lake volcano. Rhyolite was produced in the Broken Top system through the partial melting of tonalitic crustal rocks, with sufficient volumes of melt produced to erupt ≥10 km^3 of rhyolite at ≈380 ka. Intermediate composition magmas were produced in the Broken Top system through the mixing of 20-35% rhyolite into a PPFA-fractionating magma system. Rhyodacites in the early Broken Top system also closely resemble rhyodacites in the Deschutes Formation, which suggests that similar petrogenetic processes occurred in the Pliocene Oregon Cascades (cf., Conrey, 1991).

2) Volcanism from ≈350 to ≈100 ka shifted to the west, and was localized at Tam MacArthur Rim and Broken Top, and at North-Middle(?) Sister. Petrogenesis at Tam MacArthur Rim and Broken Top volcano involved the same petrogenetic processes as earlier Broken Top system magmatism. However, petrogenesis in the contemporaneous Three Sisters system involved the development of an intermediate composition system (Middle Sister) from the Cascades mafic system (North Sister) through PPFA fractionation. Although rhyolitic magmas were present in the Broken Top system, these rhyolites did not interact with the Three Sisters system.

3) Volcanism younger than ≈100 ka was probably localized at South Sister. Rhyolites were first erupted in the Three Sisters system at this time, and were produced through partial melts of mafic amphibolites. In contrast to Middle Sister, South Sister petrogenesis was controlled by mixing ≥40% rhyolite into a magma system that was more mafic than at Middle Sister.

This study has clearly shown that profound changes in the petrogenesis of silicic rocks can occur within a relatively small area of a continental arc over a period of ≈10^5 years. Previous models of continental arc petrogenesis have demonstrated the ability of marked or regional changes in tectonic setting, crustal thickness, and crustal composition to control regional variations in the petrogenesis of mafic and silicic volcanic rocks. However, these parameters did not change in the 20x30 km^2 area of the Three Sisters region, and thus could not have controlled petrogenesis in this area within the last ≈600 k.y.

The subtle influences of crustal extension on the petrogenesis of igneous rocks are poorly understood. Bimodal volcanism is often thought to be characteristic of moderately extended terranes such as the Basin and Range, and highly extended rifts such as the Rio Grande Rift erupt prodigious amounts of basaltic lava. But what about areas that are less extended than the Basin and Range? Most continental arcs, like the Oregon Cascades, are located in areas of modest crustal extension (i.e. σ_3 is perpendicular to the arc axis), and many contain discontinuous intra-arc

grabens. Could small variations in the orientation or magnitude of crustal extension have influenced the petrogenesis of these arcs? Empirically, these variations in extension could effect the magma supply rate into the crust, which would control the crustal heat flux. Relatively small increases in extension could thus result in relatively small increases in the volume of mafic magma intruding into the crust. However, when these increases are superimposed on a previously steady-state magma system (e.g., North-Middle Sister), the resulting perturbations may result in significant petrogenetic shifts in the system. Increases in crustal heat may trigger significant amounts of crustal melting, and result in the establishment of rhyolitic magma chambers. The increase in heat would also favor the establishment of longer lived (i.e. more differentiated) magma chambers (e.g., Broken Top system), because the thermal contrast between the magma and wall rock would be lowered. Recharge by mafic magmas during extension could also shift a fractionating intermediate magma system back towards more mafic compositions (e.g., South Sister). All of these features are characteristic of petrogenesis in the Three Sisters region, as is the location of this region in an area of slightly greater crustal extension than the rest of the Oregon Cascades. The amount of petrogenetic diversity that occurred within this area since ≈ 600 ka requires the addition of small scale variations in crustal extension to the list of geological processes that can control continental arc petrogenesis.

12. REFERENCES

Allen, J.E., 1966. The Cascade Range volcano-tectonic depression of Oregon. *in* Staples, L.W., Green, J., eds., Lunar Geological Field Conference Trans., Or. Dept. Geol. Min. Ind., p. 21-23.

Anders, E., Ebihara, M., 1982. The chemical composition of C1 chondrites; a new estimate for pre-solar elemental abundances. Geochim. Cosmochim. Acta, 46:2363-2380.

Arculus, R.J., 1987. The significance of source versus process in the tectonic controls of magma genesis. J. Volcan. Geotherm. Res., 32:1-12.

Arculus, R.J., Johnson, R.W., 1978. Criticism of generalised models for the magmatic evolution of arc-trench systems. Earth Planet. Sci. Lett., 39:118-126.

Armstrong, R.L., Taylor, E.M., Hales, P.O., Parker, D.J., 1975. K-Ar dates for volcanic rocks, central Cascade Range of Oregon. Isochron/West, 13:5-7.

Arth, J.G., 1976. Behavior of trace elements during magmatic processes - A summary of theoretical models and their applications. J. Res. U.S. Geol. Surv., 4-1:41-47.

Atwater, T., 1970. Implications of plate tectonics for the Cenozoic tectonic evolution of western North America. Geol. Soc. Am. Bull., 81:3513-3535.

Bacon, C. R., 1983. Eruptive history of Mount Mazama and Crater Lake caldera, Cascade Range, U.S.A. J. Volcan. Geotherm. Res., 18:57-115.

___, 1985. Implication of silicic vent patterns for the presence of large crustal magma chambers. J. Geophys. Res., 90:11243-11252.

___, 1986. Magmatic inclusions in silicic and intermediate volcanic rocks. J. Geophys. Res., 91:6091-6112.

Bacon, C.R., Adami, L.H., Lanphere, M.A., 1989. Direct evidence for the origin of low-18O silicic magmas: quenched samples of a magma chamber's partially-fused granitoid walls, Crater Lake, Oregon. Earth Planet. Sci. Lett., 96:199-208.

Bacon, C.R., Druitt, T.H., 1988. Compositional evolution of the zoned calcalkaline magma chamber of Mount Mazama, Crater Lake, Oregon. Contrib. Min. Pet., 98:224-256.

Bacon, C.R., Hirschmann, M.M., 1988. Mg/Mn partitioning as a test for equilibrium between coexisting Fe-Ti oxides. Am. Min., 73:57-61.

Baker, D.R., 1987. Depths and water content of magma chambers in the Aleutian and Mariana island arcs. Geology, 15:496-499.

Baker, D.R., Eggler, D.H., 1983. Fractionation paths of Atka (Aleutians) high-alumina basalts: Constraints from phase relations. J. Volcan. Geotherm. Res., 18:387-404.

___, 1987. Composition of anhydrous and hydrous melts coexisting with plagioclase, augite, and olivine or low-calcium pyroxene from one atmosphere to 8 kbar: Application to the Aleutian volcanic center of Atka. Am. Min., 72:12-28.

Barker, F., Arth, J.G., 1976. Generation of trondhjemitic-tonalitic liquids and Archean bimodal trondhjemite-basalt suites. Geology, 4:596-600.

Beard, J.S., Day, H.W., 1987. The Smartville intrusive complex, northern Sierra Nevada, California: The core of a rifted volcanic arc. Geol. Soc. Am. Bull., 99:779-791.

___, 1988. Petrology and emplacement of reversely zoned gabbro-diorite plutons in the Smartville complex, northern California. J. Pet., 29:965-995.

Beard, J.S., Lofgren, G.E., 1989. Effect of water on the composition of partial melts of greenstone and amphibolite. Science, 244:195-197.

___, 1991. Dehydration melting and water-saturated melting of basaltic and andesitic greenstones and amphibolites at 1, 3, and 6.9 kb. J. Pet., 32:365-4001.

Bergantz, G.W., 1989. Underplating and partial melting: Implications for melt generation and extraction. Science, 245:1093-1095.

___, 1990. Melt fraction diagrams: The link between chemical and transport models *in* Reviews in Mineralogy, vol. 24, J. Nicholls, J.K. Russell, eds., Mineralogical Society of America, Washington, D.C., pp. 239-258.

Beyer, R.L., 1973. Magma differentiation at Newberry crater in central Oregon. Ph.D. diss., U. Oregon, 93 p.

Black, G.L., Woller, N.M., Ferns, M.L., 1987. Geologic map of the Crescent Mountain area, Linn County, Oregon, scale 1:62500. Or. Dept. Geol. Min. Ind. Map GMS-47.

Blackwell, D.D., Bowen, R.G., Hull, D.H., Riccio, J., Steele, J.L., 1982. Heat flow, arc volcanism, and subduction in northern Oregon. J. Geophys. Res., 87:8735-8754.

Blackwell, D.D., Steele, J.L, Frohme, M.K., Murphey, C.F., Priest, G.R., Black, G.L., 1990. Heat flow in the Oregon Cascade Range and its correlation with regional gravity, Curie point depths, and geology. J. Geophys. Res., 95:19475-19493.

Blundy, J.D., Holland, T.J.B., 1990. Calcic amphibole equilibria and a new amphibole-plagioclase geothermometer. Contrib. Min. Pet., 104:208-224.

Blundy, J.D., Shimizu, N., 1991. Trace element evidence for plagioclase recycling in calc-alkaline magmas. Earth Planet. Sci. Lett., 102:178-197.

Bowen, N.L., 1928. The evolution of the igneous rocks. Dover Publications, New York. 251 p.

Buddington, A.F., Lindsley, D.H., 1964. Iron-titanium oxides and synthetic equivalents. J. Pet., 5:310-357.

Callagan, E., 1933. Some features of the volcanic sequence in the Cascade Range in Oregon. Am. Geophys. Union Trans, 14th Ann. Meeting, p. 243-249.

Cannon, D.M., 1985. The stratigraphy, geochemistry and mineralogy of two ash-flow tuffs in the Deschutes Formation, central Oregon. M.S. Thesis, Oregon State Univ., Corvallis. 142 p.

Carlson, R.W., Hart, W.K., 1987. Crustal genesis on the Oregon Plateau. J. Geophys. Res., 92: 6191-6206.

Carmichael, I.S.E., 1967. The iron-titanium oxides of sialic volcanic rocks and their associated ferromagnesian silicates. Contrib. Min. Pet., 14:36-64.

Carmichael, I.S.E., Turner, F.J., Verhoogen, J., 1974. Igneous petrology. McGraw-Hill International., New York.

Carr, M.J., Feigenson, M.D., Bennett, E.A., 1990. Incompatible element and isotopic evidence for tectonic control of source mixing and melt extraction along the Central American arc. Contrib. Min. Pet., 105:369-380.

Carr, M.J., Mayfield, D., Walker, J., 1982. Relation of lava compositions to volcano size and structure in El Salvador. J. Volcan. Geotherm. Res., 10:35-48.

Catchings, R.D., Mooney, W.D., 1988. Crustal structure of east central Oregon: Relation between Newberry Volcano and regional crustal structure. J. Geophys. Res., 93:10081-10094.

Chayes, F., 1964. Variance-covariance relations in some published Harker Diagrams of volcanic suites. J. Pet., 5:219-237.

Church, S.E., 1976. The Cascade Mountains revisited: A re-evaluation in light of new lead isotopic data. Earth Planet. Sci. Lett., 29:175-188.

Church, S.E., LeHuray, A.P., Grant, A.R., Delevaux, M.H., Gray, J.E., 1986. Lead-isotopic data from sulfide minerals from the Cascade Range, Oregon and Washington. Geochim. Cosmochim. Acta, 50:317-328.

Church, S.E., Tilton, G.R., 1973. Lead and strontium isotopic studies in the Cascade Mountains: Bearing on andesite genesis. Geol. Soc. Am. Bull., 84:431-454.

Clark, J.G., 1983. Geology and petrology of South Sister Volcano, High Cascade Range, Oregon. Ph.D. Diss., U. Oregon, 236 p.

Clemens, J.D., Holloway, J.R., White, A.J.R., 1986. Origin of A-type granite: Experimental constraints. Am. Min., 71:317-324.

Conrad, W.K., Nicholls, I.A., Wall, V.J., 1988. Water-saturated and -undersaturated melting of metaluminous and peraluminous crustal compositions at 10 kb: Evidence for the origin of silicic magmas in the Taupo Volcanic Zone, New Zealand, and other occurrences. J. Pet., 29:765-803.

Conrey, R.M., 1985. Volcanic stratigraphy of the Deschutes Formation, Green Ridge to Fly Creek, north-central Oregon. M.S. Thesis, Oregon State Univ., Corvallis, 349 p.

____, 1990. Comments on a paper by Jon. D. Woodhead titled 'The origin of geochemical variations in Mariana Lavas: A general model for petrogenesis in intra-oceanic island arcs?'. Contrib. Min. Pet., 31:957-962.

____, 1991. Geology and petrology of the Mt. Jefferson area, High Cascade Range, Oregon. Ph.D. Diss,, Washington State Univ., 357 p.

Conrey, R.M., Sherrod, D.R., 1988. Stratigraphy of drill holes and geochemistry of surface rocks, Breitenbush Hot Springs 15-minute quadrangle, Cascade Range, Oregon. Or. Dept. Geol. Min. Ind. OFR O-88-5, p. 15-31.

Corrigan, G.M., 1982. The crystal morphology of plagioclase feldspar produced during isothermal supercooling and constant rate cooling experiments. Mineral. Mag., 46:433-439.

Couch, R.W., Pitts, G.S., Gemperle, M., Braman, D.E., Veen, C.A., 1982. Gravity anomalies in the Cascade Range in Oregon: Structural and thermal implications. Or. Dept. Geol. Min. Ind. OFR O-82-9.

Davidson, J.P., Dungan, M.A., Ferguson, K.M., Colucci, M.T., 1987. Crust-magma interactions and the evolution of arc magmas: The San Pedro-Pellado volcanic complex, southern Chilean Andes. Geology, 15:443-446.

Davidson, P.M., Lindsley, D.H., 1985. Thermodynamic analysis of quadrilateral pyroxenes. Part II. Model calibration from experiments and applications to geothermometry. Contrib. Min. Pet., 91:390-404.

Davis, J.O., 1985. Correlation of late Quaternary tephra layers in a long pluvial sequence near Summer Lake, Oregon. Quat. Res., 23:38-53.

Defant, M.J., Drummond, M.S., 1990. Derivation of some modern arc magmas by melting of young subducted lithosphere. Nature, 347:662-665.

Defant, M.J., Nielsen, R.L., 1990. Interpretation of open system petrogenetic processes: Phase equilibria constraints on magma evolution. Geochim. Cosmochim. Acta, 54:87-102.

DePaolo, D.J., 1981. Trace element and isotopic effects of combined wallrock assimilation and fractional crystallization. Earth Planet. Sci. Lett., 53:189-202.

Donaldson, C.H., 1976. An experimental investigation of olivine morphology. Contrib. Min. Pet., 57:187-213.

___, 1985. A comment on crystal shapes resulting from dissolution in magmas. Min. Mag., 49:129-132.

Donnelly-Nolan, J.M., 1988. A magmatic model of Medicine Lake Volcano, California. J. Geophys. Res., 93:4412-4420.

Dostal, J., Dupuy, C., Carron, J.P., Le Guen de Kerneizon, M., Maury, R.C., 1982. Partition coefficients of trace elements: Application to volcanic rocks of St. Vincent, West Indes. Geochim. Cosmochim. Acta, 47:525:533.

Draper, D.S., 1991. Late Cenozoic bimodal volcanism in the northern Basin and Range Province of southeastern Oregon. J. Volcan. Geotherm. Res., 47:299-328.

Druitt, T.H., Bacon, C.R., 1989. Petrology of the zoned calcalkaline magma chamber of Mount Mazama, Crater Lake, Oregon. Contrib. Min. Pet., 101:245-259.

Drummond, M.S., Defant, M.J., 1990. A model for tondhjemite-tonalite-dacite genesis and crustal growth via slab melting: Archean to modern comparisons. J. Geophys. Res., 95:21503-21521.

Dudas, M.J., Schmitt, R.A., Harward, M.E., 1971. Trace element partitioning between volcanic plagioclase and dacitic pyroclastic matrix. Earth Planet. Sci. Lett., 11:440-446.

Dungan, M.A., Rhodes, J.M., 1978. Residual glass and melt inclusions in basalts from DSDP Legs 45 and 46: evidence for magma mixing. Contrib. Min. Pet., 67:417-431.

Eggler, D.H., 1972. Water-saturated and undersaturated melting relations in a Paricutin andesite and an estimate of water content in the natural magmas. Contrib. Min. Pet., 34:261-271.

Eichelberger, J.C., 1975. Origin of andesite and dacite; evidence of magma mixing at Glass Mountain in California and the other Circum-Pacific volcanos. Geol. Soc. Am. Bull., 86:1381-1391.

Ellis, D.J., Thompson, A.B., 1986. Subsolidus and partial melting reactions in the quartz-excess $CaO + MgO + Al_2O_3 + SiO_2 + H_2O$ system under water-excess and water-deficient conditions to 10 kb: Some implications for the origin of peraluminous melts from mafic rocks. J. Pet., 27:91-121.

Elthon, D., Scarfe, C.M., 1984. High-pressure phase equilibria of a high-magnesia basalt and the genesis of primary oceanic basalts. Am. Min., 69:1-15.

Engebretson, D.C., Cox, A., Gordon, R.G., 1986. Relative motions between oceanic and continental plates in the Pacific Basin. Geol. Soc. Am. Sp. Paper 206, 59 p.

Ewart, A., 1982. The mineralogy and petrology of Tertiary-Recent orogenic volcanic rocks: with special reference to the andesitic-basaltic compositional range. *in* Thorpe, R.S. ed., Andesites, Wiley & Sons, New York. p. 25-95.

Fiebelkorn, R.B., Walker, G.W., MacLeod, N.S., McKee, E.H., Smith, J.G., 1983. Index to K-Ar determinations for the state of Oregon. Isochron West, 37:3-60.

Fink, D.R., Manley, 1987. Origin of pumiceous and glassy textures in rhyolite flows and domes. Geol. Soc. Am. Sp. Paper 212, 77-88.

Fisher, R.V., 1964. Maximum size, median diameter, and sorting of tephra. J. Geophys. Res., 69:341-355.

Fitterman, D.V., 1988. Overview of the structure and geothermal potential of Newberry Volcano, Oregon. J. Geophys. Res., 93:10059-10066.

Flanagan, F.J., 1976. Descriptions and analyses of eight new U.S.G.S. Rock Standards. U.S. Geol. Surv. Pro. Paper 840, p. 131-184.

Frost, T.P., Mahood, G.A., 1987. Field, chemical, and physical constraints on mafic-felsic magma interaction in the Lamarck Granodiorite, Sierra Nevada, California. Geol. Soc. Am. Bull., 99:272-291.

Fujimaki, H., 1986. Partition coefficients of Hf, Zr, and REE between zircon, apatite, and liquid. Contrib. Min. Pet., 94:42-45.

Furuta, T., Otsuki, M., Akimoto, T., 1985. Quantitative electron probe microanalysis of oxygen in titanomagnetites with implications for oxidation processes. J. Geophys. Res., 90:3145-3150.

Gallahan, W.E., Nielsen, R.L., 1991. The partitioning of Sc, Y and the rare earth elements between Ca pyroxene and natural mafic to intermediate magmas. Geochim. Cosmochim. Acta, in press.

Gardner, C.A., Hill, B.E., Negrini, R.M., Sarna-Wojcicki, A.M., Davis, J.O., 1992. Paleomagnetic correlation of late Pleistocene ignimbrites from the Bend, Oregon area with distal ash beds. Quat. Res., in press.

Ghiorso, M.S., Sack, R.O., 1991. Fe-Ti oxide geothermometry: thermodynamic formulation and the estimation of intensive variables in silicic magmas. Contrib. Min. Pet., in press.

Gill, J.B., 1982. Orogenic Andesites and Plate Tectonics. Springer-Verlag, New York. 390 p.

Glazner, A.F., Ussler, W. III, Mathis, A.C., 1990. Interpretation of plagioclase texture in volcanic rocks. EOS, 71-43:1678.

Goles, G.G., Lambert, R.S.J., 1990. A strontium isotopic study of Newberry volcano, central Oregon: Structural and thermal implications. J. Volcan. Geotherm. Res., 43:159-174.

Green, T.H., Pearson, N.J., 1985. Rare earth element partitioning between clinopyroxene and silicate liquid at moderate to high pressure. Contrib. Min. Pet., 91:24-36.

Green, T.H., Watson, E.B., 1982. Crystallization of apatite in natural magmas under high pressure, hydrous conditions, with particular reference to 'orogenic' rock series. Contrib. Min. Pet., 79:96-105.

Gromet, L.P., Silver, L.T., 1983. Rare earth element distributions among minerals in a granodiorite and their petrogenetic implications. Geochim. Cosmochim. Acta, 47:925-939.

Grove, T.L., Baker, M.B., 1985. Phase equilibrium controls on the tholeiitic versus calc-alkaline differentiation trends. J. Geophys. Res., 89:3253-3274.

Grove, T.L., Baker, M.B., Kinzler, R.J., 1985. Coupled CaAl-NaSi diffusion in plagioclase feldspar: Experiments and applications to cooling rate speedometry. Geochim. Cosmochim. Acta 48:2113-2121.

Grove, T.L., Bryan, W.B., 1983. Fractionation of pyroxene-phyric MORB at low pressure: An experimental study. Contrib. Min. Pet., 84:293-309.

Grove, T.L., Donnelly-Nolan, J.M., 1986. The evolution of young silicic lavas at Medicine Lake Volcano, California: Implications for the origin of compositional gaps in calc-alkaline series lavas. Contrib. Min. Pet., 92:281-302

Grove, T.L., Gerlach, D.C., Sando, T.W., 1982. Origin of calc-alkaline series lavas at Medicine Lake Volcano by fractionation, assimilation and mixing. Contrib. Min. Pet., 80:160-182.

Grove, T.L., Kinzler, R.J., 1986. Petrogenesis of andesites. Ann. Rev. Earth Planet. Sci., 14:417-454.

Grove, T.L., Sisson, T.W., 1991. Water and the role of magnetite in the generation of calc-alkaline rock series. EOS, 72:292.

Grunder, A.L., Boden, D.R., 1987. Comment on '...Magmatic conditions of the Fish Canyon Tuff, Central San Juan Field, Colorado' by Whitney & Stormer (1985). J. Pet., 28:737-746.

Grunder, A.L., Mahood, G.A., 1988. Physical and chemical models of zoned silicic magmas: The Loma Seca Tuff and Calabozos Caldera, southern Andes. J. Pet., 29:831-867.

Guffanti, M., Weaver, C.S., 1988. Distribution of late Cenozoic volcanic vents in the Cascade Range: Volcanic arc segmentation and regional tectonic considerations. J. Geophys. Res., 93:6513-6529.

Gust, D.A., Perfit, M.R., 1987. Phase relations of a high-Mg basalt from the Aleutian Island Arc: Implications for primary island arc basalts and high-Al basalts. Contrib. Min. Pet., 97:7-18.

Haggerty, S.E., 1976. Opaque mineral oxides in terrestrial igneous rocks. in M.S.A. Short Course Notes vol 3, ed. D. Rumble III., p. Hg101-Hg300.

Haggerty, S.E., Baker, I., 1967. The alteration of olivine in basaltic and associated lavas. Part I: High temperature alteration. Contrib. Min. Pet., 16:233-257.

Hales, P.O., 1975. Geology of the Green Ridge area, Whitewater River quadrangle, Oregon. M.S. thesis, Oregon State Univ., 90 p.

Hammarstrom, J.M., Zen, E-an, 1986. Aluminum in hornblende: An empirical igneous geobarometer. Am. Min., 71:1297-1313.

Harrison, T.M., Watson, E.B., 1984. The behavior of apatite during crustal anatexis: Equilibrium and kinetic considerations. Geochim. Cosmochim. Acta, 48:1467-1477.

Hart, S.R., Brooks, C., 1974. Clinopyroxene-matrix partitioning of K, Rb, Cs, Sr and Ba. Geochim. Cosmochim. Acta, 38:1799-1806.

Hawkesworth, C., Ellam, R., 1989. Chemical fluxes and wedge replenishment rates along recent destructive plate margins. Geology, 17:46-49.

Hawkins, F.F., LaForge, J.A., Templeton, M., Gilbert, J.D., 1988. Seismotectonic study for Arthur R. Bowman and Ochoco Dams, Crooked River project, Oregon. U.S. Bur. Rec. Seismotectonic Report 88-10, 52 p.

Hawthorne, F.C., 1981. Crystal chemistry of amphiboles. in Veblen, D.R., & Ribbe, P.H., eds., Reviews in mineralogy, vol. 9A, p. 1-102.

Hietanen, A., 1981. Extension of Sierra Nevada-Klamath suture system into eastern Oregon and western Idaho. U. S. Geol. Surv. Pro. Paper 1226-C, 11p.

Helz, R.T., 1976. Phase relations of basalts in their melting ranges at PH2O = 5 kb. Part II. Melt compositions. J. Pet., 17:139-193.

Hibbard, M.J., 1981. The magma mixing origin of mantled feldspars. Contrib. Min. Pet, 76:158-170.

Higgins, M.W., 1973. Petrology of Newberry Volcano, central Oregon. Geol. Soc. Am. Bull., 84:455-488.

Higuchi, H., Nagasawa, H., 1969. Partition of trace elements between rock-forming minerals and the host volcanic rocks. Earth Planet. Sci. Lett., 7:281-287.

Hildreth, W., 1981. Gradients in silicic magma chambers: Implications for lithospheric magmatism. J. Geophys. Res., 86:10153-10192.

Hildreth, W., Grove, T.L., Dungan, M.L., 1986. Introduction to special section on open magmatic systems. J. Geophys. Res., 91:5887-5890.

Hildreth, W., Moorbath, S., 1988. Crustal contributions to arc magmatism in the Andes of central Chile. Contrib. Min. Pet., 98:455-489.

Hill, B.E., 1985. Petrology of the Bend pumice and Tumalo tuff; A Pleistocene Cascade eruption involving magma mixing. M.S. Thesis, Oregon State University, Corvallis. 101p.

___, 1988a. The Bull Springs Inlier and its significance to Oregon central High Cascade tectonics. Proc. Or. Acad. Sci., 24:62 (Abstr).

___, 1988b. The Tumalo Volcanic Center: A large Pleistocene vent complex on the east flank of the Oregon central High Cascades. Geol. Soc. Am. Abstr., 20-7:398.

___, 1989. Significance of distinct rhyodacitic provinces within the Three Sisters region of the Oregon central High Cascades (abstr). N. M. Bur. Mines. Min. Res., Bulletin 131, p. 130.

Hill, B.E., Priest, G., Blackwell, D., 1991. Initial results from the 1990 geothermal drilling program at Santiam Pass, Cascade Range, Oregon. Or. Geol., 53-5:101-103.

Hill, B.E., Taylor, E.M., 1989a. The significance of Quaternary pyroclastic volcanism on the eastern flank of the Oregon central High Cascades. Geol. Soc. Am. Abstr., 21-5:92.

Hill, B.E., Taylor, E.M., 1989b. Oregon central High Cascade pyroclastic units in the vicinity of Bend, Oregon. U.S. Geol. Survey Open file report 89-645:51-54.

Hollister, L.S., Grissom, G.C., Peters, E.K., Stowell, H.H., Sisson, V.B., 1987. Confirmation of the empirical correlation of Al in hornblende with pressure of solidification of calc-alkaline plutons. Am. Min., 72:231-239.

Holloway, J.R., Burnhan, C.W., 1972. Melting relations of basalt with equilibrium water pressure less than total pressure. J. Pet., 13:1-29.

Hotz, P.E., Lanphere, M.A., Swanson, D.A., 1977. Triassic blueschist from northern California and north-central Oregon. Geology, 5:659-663.

Housh, T.B., Luhr, J.F., 1991. Plagioclase-melt equilibria in hydrous systems. Am. Min., 76:477-492.

Huebner, S.J., 1980. Pyroxene phase equilibria at low pressure. *in* Prewitt, C.T., ed., Reviews in mineralogy, vol. 7., p. 213-288.

Hughes, J.M., Stoiber, R., Carr, M.J., 1980. Segmentation of the Cascade volcanic chain. Geology, 8:15-17.

Hughes, S.S., 1983. Petrochemical evolution of the High Cascade volcanic rocks in the Three Sisters region, Oregon. Ph.D. Diss., Oregon St. Univ., 199p.

___, 1990. Mafic magmatism and associated tectonism of the central High Cascade Range, Oregon. J. Geophys. Res., 95:19623-19638.

Hughes, S.S. and Taylor, E.M., 1986. Geochemistry, petrology and tectonic implications of central High Cascade mafic platform lavas. Geol. Soc. Am. Bull., 97:1024-1036.

Huppert, H.E., Sparks, R.S.J., 1980. The fluid dynamics of a basaltic magma chamber replenished by influx of hot, dense ultrabasic magma. Contrib. Min. Pet., 75:279-289.

___, 1988. The generation of granitic magma by intrusion of basalt into continental crust. J. Pet., 29:599-624.

Irvine, T.N., Barager, W.R.A., 1971. A guide to the chemical classification of the common volcanic rocks. Can. J. Earth Sci., 8:523-548.

Irving, A.J., 1978. A review of experimental studies of crystal/liquid trace element partitioning. Geochim. Cosmochim. Acta., 42:543-770.

Irwin, W.P., 1981. Tectonic accretion of the Klamath Mountains in Ernst, W.G., ed., The geotectonic development of California: Rubey Volume No. 1, 29-49.

Johnson, M.C., Rutherford, M.C., 1989. Experimental calibration of the aluminum-in-hornblende geobarometer with application to Long Valley caldera (California) volcanic rocks. Geology, 17:837-841.

Johnston, A.D., 1986. Anhydrous P-T phase relations of near-primary high-aluminia basalt from the South Sandwich Islands. Contrib. Min. Pet., 92:368-382.

Johnston, A.D., Wyllie, P.J., 1988. Interaction of granitic and basic magmas: experimental observations on contamination processes at 10 kbar with H2O. Contrib. Min. Pet., 98:352-362.

Jouzel, J., Lorius, C., Petit, J.R., Genthon, C., Barkov, N.I., Kotlyakov, V.M., Petrov, V.M., 1987. Vostok ice core: A continuous isotope temperature record over the last climatic cycle (160,000 years). Nature, 329:403-408.

Kay, S.M., Kay, R.W., Citron, G.P., 1982. Tectonic controls on tholeiitic and calc-alkaline magmatism in the Aleutian arc. J. Geophys. Res., 87:4051-4072.

Keach, W.R., Oliver, J.E., Brown, L.D., Kaufman, S., 1989. Cenozoic active margin and shallow Cascades structure: COCORP results from western Oregon. Geol. Soc. Am. Bull., 101:783-794.

Kelemen, P.B., Johnson, K.T.M., Kinzler, R.J., Irving, A.J., 1990. High-field strength element depletions in arc basalts due to mantle-magma interaction. Nature, 345:521-524.

Koyaguchi, T., 1986. Textural and compositional evidence for magma mixing and its mechanism, Abu volcanic group, southwestern Japan. Contrib. Min. Pet., 93:33-45.

Kudo, A.M., Weill, D.F., 1970. An igneous plagioclase thermometer. Contrib. Min. Pet., 25:52-65.

Kuo, L.C., Kirkpatrick, R.J., 1982. Pre-eruption history of phyric basalts from DSDP Legs 45 and 46: Evidence from morphology and zoning patterns in plagioclase. Contrib. Min. Pet., 79:13-27.

Kushiro, I., 1979. Fractional crystallization of basaltic magma. *in* Yoder, H.S., ed., The evolution of igneous rocks, fiftieth anniversary perspectives. Princeton Univ. Press, Princeton. p. 171-204.

Langmuir, C.H., 1989. Geochemical consequences of in situ crystallization. Nature, 340:199-205.

Larsen, E.S., Irving, J., Gonyer, F.A., Larsen, E.S., 3rd., 1938. Petrologic results of a study of the minerals from the Tertiary volcanic rocks of the San Juan region, Colorado. Am. Min., 23:227-257.

Laul, J.C., 1979. Neutron activation analysis of geological materials. Atomic Energy Rev., 17-3:603-695.

Lawrence, R.L., 1976. Strike-slip faulting terminates the Basin and Range province in Oregon. Geol. Soc. Am. Bull., 87:846-850.

Leake, B.E., 1978. Nomenclature of amphiboles. Canadian Mineral., 16:501-520.

Leaver, D.S., Mooney, W.D., Kohler, W.M., 1984. A seismic refraction study of the Oregon Cascades. J. Geophys. Res., 89:3121-3134.

Leeman, W.P., 1982. Tectonic and magmatic significance of strontium isotopic variations in Cenozoic volcanic rocks from the western United States. Geol. Soc. Am. Bull., 93:487-503.

Leeman, W.P., Scheidegger, K.F., 1977. Olivine/liquid distribution coefficients and a test for crystal-liquid equilibrium. Earth Planet. Sci. Lett., 35:247-257.

Leeman, W.P., Smith, D.R., Hildreth, W., Palacz, Z., Rogers, N., 1990. Compositional diversity of late Cenozoic basalts in a transect across the southern Washington Cascades: Implications for subduction zone magmatism. J. Geophys. Res., 95:19561-19582.

Le Maitre, R.W., 1984. A proposal by the IUGS Subcommission on the Systematics of Igneous Rocks for a chemical classification of volcanic rocks based on the total alkali silica (TAS) diagram. Austrl. J. Earth Sci., 31:243-255.

Lindsley, D.H., 1983. Pyroxene thermometry. Am. Min., 68:477-493.

Lindsley, D.H., Anderson, D.J., 1983. A two-pyroxene thermometer. Proc. 13th Lunar Planet. Sci. Conf. Pt. 2 (supplement). J. Geophys. Res., 88:A887-A906.

Linneman, S.R., Meyers, J.D., 1990. Magmatic inclusions in the Holocene rhyolites of Newberry Volcano, central Oregon. J. Geophys. Res., 95:17677-17691.

Livelybrooks, D.W., Clingman, W.W., Rygh, J.T., Urquhart, S.A., Waff, H.S., 1989. A magneto telluric study of the High Cascade graben in central Oregon. J. Geophys. Res., 94:14173-14184.

Lofgren, G.E., 1974. An experimental study of plagioclase crystal morphology: isothermal crystallization. Am. J. Sci., 274:243-273.

____, 1980. Experimental studies on the dynamic crystallization of silicate melts. *in* Hargraves, ed., Physics of magmatic processes, Princeton University Press, p. 487-551.

Loomis, T.P., 1982. Numerical simulations of crystallization processes of plagioclase in complex melts: the origin of major and oscillatory zoning in plagioclase. Contrib. Min. Pet., 81:219-229.

Luhr, J.F., Carmichael, I.S.E., 1980. The Colima Volcanic Complex, Mexico. Contrib. Min. Pet. 71:343-372.

MacDonald, G.A., Katsura, T., 1965. Eruption of Lassen Peak, Cascade Range, California, in 1915: example of mixed magma. Geol. Soc. Am. Bull., 76:475-482.

MacLeod, N.S., Sherrod, D. R., 1988. Geologic evidence for a magma chamber beneath Newberry Volcano, Oregon. J. Geophys. Res., 93-B9:10067-10079.

MacLeod, N.S., Sherrod, D.R., Chitwood, L.A., 1982. Geologic map of Newberry Volcano, Deschutes, Klamath, and Lake Counties, Oregon. U.S. Geol. Surv. Open File Report 82-847.

MacLeod, N.S., Walker, G.W., McKee, E.H., 1975. Geothermal significance of eastward increase in age of upper Cenozoic rhyolite domes in southeastern Oregon. Proc. U.N. Symp. Dev. Geotherm. Res. 2nd., 465-474.

Mankinen, E.A., Dalrymple, G.B., 1979. Revised geomagnetic polarity time scale for the interval 0-5 m.y. B.P. J. Geophys. Res., 84:615-626.

Marsh, B.D., 1984. Mechanics and energetics of magma formation and ascension. in F.R. Boyd., ed., Explosive Volcanism: Inception, Evolution, and Hazards. National Academy Press, Washington, D.C., pp. 67-83.

Marsh, B.D., Maxey, M.R., 1985. On the distribution and separation of crystals in convecting magma. J. Volcan. Geotherm. Res., 24:95-150.

McBirney, A.R., Noyse, 1979. Crystallization and layering of the Skaergaard Intrusion. J. Pet. 20:487-554.

McBirney, A.R., Sutter, J.F., Naslund, H.R., Sutton, K.G., White, C.M., 1974. Episodic volcanism in the central Oregon Cascade Range. Geology, 2:585-589.

McDannel, A.K., 1989. Geology of the southernmost Deschutes Basin, Tumalo quadrangle, Deschutes County, Oregon. M.S. Thesis, Oregon State Univ., Corvallis. 166 p.

Merzbacher, C., Eggler, D.H., 1984. A magmatic geohygrometer: Application to Mount St. Helens and other dacitic magmas. Geology, 12:587-590.

Meyers, J.D., Marsh, B.D., 1981. Geology and petrogenesis of the Edgecumbre Volcanic Field, SE Alaska: The interaction of basalt and sialic crust. Contrib. Min. Pet., 77:272-287.

Mimura, K., 1984. Imbrication, flow direction and possible source areas of the pumice-flow tuffs near Bend, Oregon. J. Volcan. Geotherm. Res., 21:45-60.

Murase, T., McBirney, A.R., 1973. Properties of some common igneous rocks and their melts at high temperatures. Geol. Soc. Am. Bull., 84:3563-3592.

Mysen, B.O., Virgo, D., 1980. Trace element partitioning and melt structure: An experimental study at 1 atm. pressure. Geochim. Cosmochim. Acta, 44:1917-1930.

Nagasawa, H., Schnetzler, C.C., 1971. Partitioning of rare earth, alkali and alkaline earth elements between phenocrysts and acidic igneous magma. Geochim. Cosmochim. Acta, 35:953-968.

Nash, W.P., Crecraft, H.R., 1985. Partition coefficients for trace elements in silicic magmas. Geochim. Cosmochim. Acta, 49:2309-2322.

Nelson, S.T., Montana, A., 1989. Plagioclase-resorption textures as a consequence of the rapid isothermal decompression of magmas. N. M. Bureau Mines Min. Res. Bull. 131., p. 202.

Nielsen, R.L., 1985. A method for the elimination of the compositional dependence of trace element distribution coefficients. Geochim. Cosmochim. Acta, 49:1775-1779.

___, 1988. A model for the simulation of combined major and trace element liquid lines of descent. Geochim. Cosmochim. Acta, 52:27-38.

___, 1990. Simulation of igneous differentiation processes. *in* Nicholls, J., Russell, J.K., eds., Reviews in Mineralogy, vol. 24, Mineralogical Society of America, Washington, D.C., pp. 65-106.

Nielsen, R.L., Dungan, M.A., 1983. Low pressure mineral-melt equilibria in natural anhydrous mafic systems. Contrib. Min. Pet., 84:310-326.

Nielsen, R.L., Fisk, M.R., Forsythe, L., Gallahan, W.E., in press. Variable REE and HFSE partition coefficients: Implications for magma differentiation and mantle evolution. Nature.

Nielsen, R.L., Gallahan, W.E., Newberger, F., in press. Experimentally determined mineral-melt partition coefficients for Sc, Y and REE for olivine, orthopyroxene, pigeonite, magnetite and ilmenite. Geochim. Cosmochim. Acta.

Nye, C.J., Reid, M.R., 1986. Geochemistry of primary and least fractionated lavas from Okmok volcano, central Aleutians: Implications for arc magmatism. J. Geophys. Res., 44:287-308.

O'Hara, M.J., 1980. Nonlinear nature of the unavoidable long-lived isotopic, trace and major element contamination of a developing magma chamber. Phil. Trans. Royal Soc. Lond., 297:215-227.

O'Hara, M.J., Mathews, R.E., 1981. Geochemical evolution in an advancing, periodically replenished, periodically tapped, continuously fractionating magma chamber. J. Geol. Soc. Lond., 138:237-289.

Onouma, N., Higuchi, H., Wakita, H., Nagasawa, H., 1968. Trace element partition between two pyroxene and the host lava. Earth Planet. Sci. Lett., 5:47-51.

Patchett, P.J., 1980. Thermal effects of basalt on continental crust and crustal contamination of magmas. Nature, 283:559-561.

Patiño-Douce, A.E., Johnston, A.D., 1991. Phase equilibria and melt productivity in the pelitic system: Implications for the origin of peraluminous granitoids and aluminous granulites. Contrib. Min. Pet., 107:202-214.

Peacock, M.A., 1931. Classification of igneous rocks. J. Geol., 39:54-67.

Pearce, J.A., 1983. Role of the sub-continental lithosphere in magma genesis at active continental margins, *in* Hawkesworth, C.J., and Norry, M.J., eds., Continental Basalts and Mantle Xenoliths: Nantwich, England, Shiva Publishing Ltd., p. 230-249.

Pearce, T.H., 1968. A contribution to the theory of variation diagrams. Contrib. Min. Pet., 19:142-157.

Peck, D.L., Griggs, A.B., Schlicker, H.G., Wells, F.G., Dole, H.M., 1964. Geology of the central and northern parts of the Western Cascade Range in Oregon. U.S. Geol. Surv. Pro. Paper 449, 56p.

Peterson, N.V., Groh, E.A., Taylor, E.M., Stensland, D.E., 1976. Geology and mineral resources of Deschutes County, Oregon. Or. Dept. Geol. Min. Ind. Bull. 89, 66p.

Pezzopane, S.K., Weldon, R.J., 1990. Holocene fault activity between the Basin and Range and High Cascades, Oregon (abstr). EOS, 71:1608.

Philpotts, J.A., Schnetzler, C.C., 1970. Phenocryst-matrix partition coefficients for K, Rb, Sr and Ba, with applications to anorthosite and basalt genesis. Geochim. Cosmochim. Acta, 34:302-322.

Presnall, D.C., Bateman, P.C., 1973. Fusion relations in the system $NaAlSi_3O_8$-$CaAl_2Si_2O_8$-$KAlSi_3O_8$-SiO_2-H_2O and the generation of granitic magmas in the Sierra Nevada Batholith. Geol. Soc. Am. Bull., 84:3181-3202.

Priest, G.R., 1990. Volcanic and tectonic evolution of the Cascade volcanic arc, central Oregon. J. Geophys. Res., 92:19583-19599.

Priest, G.R., Black, G.L., Woller, N.M., Taylor, E.M., 1988. Geologic map of the McKenzie Bridge quadrangle, Lane County, Oregon, scale 1:62500. Or. Dept. Geol. Min. Ind. Map GMS-48.

Priest, G.R., Mattinson, J.M., Damon, P.E., 1989. Implications of new isotopic age data from drill holes in the Oregon Cascades (abstr). EOS, 71:1299.

Priest, G.R., Vogt, B.A., 1982. Geology and geothermal resources of the Mount Hood area, Oregon. Or. Dept. Geol. Min. Ind. Sp. Paper 14, 100 p.

Priest, G.R., Woller, N.M, Black, G.L., Evans, S.H., 1983. Overview of the Geology of the central Oregon Cascade Range *in* Priest, G.R., Vogt, B.F., eds., Geology and geothermal resources of the central Oregon Cascade Range, Or. Dept. Geol. Min. Ind. Sp. Paper 15, 123 p.

Priest, G.R., Woller, N.M, Ferns, M.L., 1987. Geologic map of the Breitenbush River area, Linn and Marion Counties, Oregon, scale 1:62500. Or. Dept. Geol. Min. Ind. Map GMS-46.

Rapp, R.P., 1990. Partial melting of metabasalt at low water contents and the origin of the Archean continental crust: Summary of experimental evidence (abstr.). EOS, 71:1720.

Rasmussen, J., Humphries, E., 1988. Tomographic image of the Juan de Fuca plate beneath Washington and western Oregon using teleseismic P-wave travel times. Geophys. Res. Lett., 15:1417-1420.

Riddihough, R., 1984. Recent movements of the Juan de Fuca plate system. J. Geophys. Res., 89:6980-6994.

Riddihough, R., Finn, C., Couch, R., 1986. Klamath-Blue Mountain lineament, Oregon. Geology, 14:528-531.

Rogers, G.C., 1985. Variation in Cascade volcanism with margin orientation. Geology, 13:495-498.

Russell, J.K., Nicholls, J., 1988. Analysis of petrologic hypotheses with Pearce element ratios. Contrib. Min. Pet., 99:25-35.

Russell, J.K., Stanley, C.R., 1990. A theoretical basis for the development and use of chemical variation diagrams. Geochim. Cosmochim. Acta, 54:2419-2431.

Rutherford, M.J., Devine, J.D., 1988. The May 18, 1980, eruption of Mount St. Helens 3. Stability and chemistry of amphibole in the magma chamber. J. Geophys. Res., 93:11949-11959.

Rutter, M.J., Wyllie, P.J., 1988. Melting of vapor-absent tonalite at 10 kbar to simulate dehyd ration-melting in the deep crust. Nature, 331:159-160.

Sakuyama, M., 1981. Petrological study of the Myoko and Kurohime volcanos, Japan: Crystalliza-tion sequence and evidence for magma mixing. J. Pet., 22:553-583.

____, 1984. Magma mixing and magma plumbing systems in Island arcs. Bull. Volc., 47-4: 685-703.

Sarna-Wojcicki, A.M., Morrison, S.D., Meyer, C.E., Hillhouse, J.W., 1987. Correlation of upper Cenozoic tephra layers between sediments of the western United States and eastern Pacific Ocean and comparison with biostratigraphic and magnetostratigraphic age data. Geol. Soc. Am. Bull., 98:207-223.

Sarna-Wojcicki, A.M., Meyer, C.E., Nakata, J.K., Scott, W.E., Hill, B.E., Slate, J.L., Russell, P.C., 1989. Age and correlation of mid-Quaternary ash beds and tuffs in the vicinity of Bend, Oregon. U.S. Geol. Survey Open file report 89-645:55-62.

Schnetzler, C.C., Philpotts, J.A., 1968. Partition coefficients of Rare-earth elements and Barium between igneous matrix material and rock-forming-mineral phenocrysts - I. in Ahrens, L.H., ed., Origin and distribution of the elements, p. 929-938. Pergammon, New York.

Schnetzler, C.C., Philpotts, J.A., 1970. Partition coefficients of rare-earth elements and between igneous matrix material and rock-forming mineral phenocrysts - II. Geochim. Cosmochim. Acta, 34:331-340.

Scott, W.E., 1987. Holocene rhyodacite eruptions on the flank of South Sister volcano, Oregon. G.S.A. Sp. Paper 212, 35-56.

____, 1990. Temporal variations between eruptions of the Mount Bachelor volcanic chain and fluctuations of late Quaternary glaciers. U.S. Geol. Surv. Open file report 89-645, p. 10-18.

Scott, W.E., Gardner, C.A., 1990a. Southern part of Mount Bachelor volcanic chain and late Holocene rhyolite eruptions of South Sister. U.S. Geol. Survey Open file report 89-645:36-48.

____, 1990b. Geologic map of the Mount Bachelor volcanic chain and surrounding area, Cascade Range, Oregon. U.S. Geol. Survey Misc. Inv. Map I-1967, scale 1:50,000.

Sekine, T., Katsura, T., Aramaki, S., 1979. Water saturated phase relationships of some andesites with application to the estimation of the initial temperature and water pressure at the time of eruption. Geochim. Cosmochim. Acta, 43:1367-1376.

Shand, S.J., 1947. Eruptive Rocks. Third edition, Wiley and Sons, New York. pp. 206-224.

Shaw, H.R., 1980. The fracture mechanism of magma transport from the mantle to the surface. *in* Hargraves, R.B., ed., Physics of magmatic processes, Princeton Univ. Press, New Jersey. p. 201-264.

Sherrod, D.R., 1986. Geology, petrology, and volcanic history of a portion of the Cascade Range between latitudes 43°-44° N, central Oregon, U.S.A. Ph.D. Diss., Univ. Calif. Santa Barbara, 320 p.

Sherrod, D.R., Pickthorn, L.B.G., 1989. Some notes on the Neogene structural evolution of the Cascade Range in Oregon. U.S. Geol. Surv. Open File Rept. 89-179, 351-368.

Sherrod, D.R., Smith, J.G., 1990. Quaternary extrusion rates of the Cascade Range, northwestern United States and southern British Columbia. J. Geophys. Res., 95:19465-19474.

Singer, B.S., Meyers, J.D., 1990. Intra-arc extension and magmatic evolution in the central Aleutian Arc, Alaska. Geology, 18:1050-1053.

Smith, G.A., 1986. Stratigraphy, sedimentology and petrology of Neogene rocks in the Deschutes Basin, central Oregon: A record of continental-margin volcanism and its influence on fluvial sedimentation in an arc-adjacent basin. Ph.D. Diss., Or. St. Univ., 467 p.

Smith, G.A., Snee, L.A., Taylor, E.M., 1987. Stratigraphic, sedimentologic, and petrologic record of late Miocene subsidence of the central Oregon High Cascades. Geology, 15:389-392.

Smith, G.A., Vincent, K.R., Snee, L.W., 1989. An isostatic model for basin formation in and adjacent to the central Oregon High Cascade Range. U.S. Geol. Surv. OFR 89-178:411-429.

Smith, R.L., 1979. Ash-flow magmatism. Geol. Soc. Am. Sp. Paper 180, 5-27.

Sparks, R.S.J., Marshall, L.A., 1986. Thermal and mechanical constraints on mixing between mafic and silicic magmas. J. Volcan. Geotherm. Res., 29:99-124.

Spear, F.S., Kimball, K.L., 1984. RECAMP - a FORTRAN IV program for estimating Fe3+ contents in amphiboles. Computers & Geosci., 10:317-325.

Spulber, S.D., Rutherford, M.J., 1983. The origin of rhyolite and plagiogranite in oceanic crust: an experimental study. J. Petrol., 24:1-25.

Stanley, C.R., Russell, J.K., 1989. Petrologic hypothesis testing with Pearce element ratio diagrams: Derivation of diagram axes. Contrib. Min. Pet., 103:78-89.

Stanley, W.D., Mooney, W.D., Fuis, G.S., 1990. Deep crustal structure of the Cascade Range and surrounding regions from seismic refraction and magnetotelluric data. J. Geophys. Res., 95:19419-19438.

Steiger, R.H., Jäger, E., 1977. Subcommission on geochronology: Convention on the use of decay constants in geo- and cosmochronology. Earth. Planet. Sci. Lett., 36:359:362.

Stolper, E., 1980. A phase diagram for mid-ocean ridge basalts: preliminary results and implications for petrogenesis. Contrib. Min. Pet., 74:13-27.

Suzuki, K., Ui, T., 1983. Factors governing the flow lineation of a large-scale pyroclastic flow - An example in the Ata pyroclastic flow deposit, Japan. Bull. Volcan., 46-1:71-81.

Swanson, D.A., 1969. Lawsonite blueschist from north-central Oregon. U. S. Geol. Surv. Pro. Paper 650B, B8-B11.

Swanson, S.E., 1977. Relation of nucleation and crystal-growth rate to the development of granitic textures. Am. Min., 62:966-978.

Takahashi, E., Kushiro, I., 1983. Melting of a dry peridotite at high pressures and basalt magma genesis. Am. Min., 68:859-79.

Tatsumi, Y., Hamilton, D.L., Nesbitt, R.W., 1986. Chemical characteristics of fluid phase released from a subducted lithosphere and origin of arc magmas: Evidence from high-pressure experiments and natural rocks. J. Volcan. Geotherm. Res., 29:293-309.

Taylor, E.M., 1978. Field geology of the S.W. Broken Top quadrangle, Oregon. Or. Dept. Geol. Min. Ind. Sp. Paper 2, 50p.

___, 1981. Central High Cascade roadside geology--Bend, Sisters, McKenzie Pass, and Santiam Pass, Oregon in D.A. Johnston and J.Donnelly-Nolan, eds., Guides to some volcanic terranes in Washington, Idaho, Oregon and Northern California. U.S. Geol. Survey Circ. 838, p. 55-58.

___, 1987. Field geology of the northwest quarter of the Broken Top 15' quadrangle, Deschutes County, Oregon. Or. Dept. Geol. Min. Ind. Sp. Paper 21, 20p.

___, 1990. Volcanic history and tectonic development of the central High Cascade Range, Oregon. J. Geophys. Res., 95:19611-19622.

Taylor, E.M., MacLeod, N.S., Sherrod, D.R., Walker, G.W., 1987. Geologic map of the Three Sisters Wilderness, Deschutes, Lane, and Linn Counties, Oregon. U.S. Geol. Survey Map MF-1952.

Taylor, E.M., Smith, G.A., 1987. Record of early High Cascade volcanism at Cove Palisades, Oregon: Deschutes Formation volcanic and sedimentary rocks. Geol. Soc. Am. Centennial Field Guide - Cordilleran Section, p. 313-315.

Taylor, H.P. Jr., 1980. The effects of assimilation of country rocks by magmas on $^{18}O/^{16}O$ and $^{87}Sr/^{86}Sr$ systematics in igneous rocks. Earth. Planet. Sci. Lett., 47:243-257.

Thiruvathukal, J.V., Berg, J.W., Heinrichs, D.F., 1970. Regional gravity of Oregon. Geol. Soc. Am. Bull., 81:725-738.

Thompson, A.B., 1982. Dehydration melting of pelitic rocks and the generation of H_2O-undersaturated granitic liquids. Am. J. Sci., 282:1567-1595.

Thompson, R.N., 1974. Primary basalts and magma genesis, I, Skye, north-west Scotland. Contrib. Min. Pet., 45:317-341.

Thompson, R.N., 1975. Primary basalts and magma genesis, II, Snake River Plain, Idaho, U.S.A. Contrib. Min. Pet., 52:157-164.

Thorpe, R.S., 1982. Andesites: Orogenic andesites and related rocks. Wiley and Sons, New York, 724 p.

Thorpe, R.S., Francis, P.W., Hammill, M., Baker, M.C.W., 1982. The Andes. *in* Thorpe, R.S., ed., Andesites, Wiley and Sons, New York. p. 187-205.

Trial, A.F., Spera, F.J., 1990. Mechanisms for the generation of compositional heterogeneities in magma chambers. Geol. Soc. Am. Bull., 102:353-367.

Tsuchiyama, A., 1985. Dissolution kinetics of plagioclase in the melt of the system diopside-albite-anorthite, and the origin of dusty plagioclase in andesite. Contrib. Min. Pet., 89:1-16.

Tsuchiyama, A., Takahashi, E., 1983. Melting kinetics of a plagioclase feldspar. Contrib. Min. Pet., 84:345-354.

Tuttle, O.F., Bowen, N.L., 1958. Origin of granite in light of experimental studies in the system $NaAlSi_3O_8$-$KAlSi_3O_8$-SiO_2-H_2O. Geol. Soc. Am. Mem. 74.

Ussler, W. III, Glazner, A.F., 1989. Phase equilibria along a basalt-rhyolite mixing line: Implications for the origin of calc-alkaline intermediate magmas. Contrib. Min. Pet. 101:232-244.

Verplank, E.P., Duncan, R.A., 1987. Temporal variations in plate convergence and eruption rates in the Western Cascades, Oregon. Tectonics, 6:197-209.

Walker, D., Shibata, T., DeLong, S.F., 1979. Abyssal tholeiites from the Oceanographer Fracture Zone. II. Phase equilibrium and mixing. Contrib. Min. Pet., 70:111-125.

Walker, G.P.L., 1971. Grain-size characteristics of pyroclastic deposits. J. Geol., 79:696-714.

Walker, G.W., 1974. Some implications of late Cenozoic volcanism to geothermal potential in the High Lava Plains of south-central Oregon. U.S. Geol. Surv. Open File Report, 14 p.

Waters, A.C., 1962. Basalt magma types and their tectonic associations: Pacific Northwest of the United States. *in* MacDonald, G.A., and Kuno, H, eds., The crust of the Pacific Basin. Am. Geophys. Union Monogr. 6:158-170.

Watson, E.B., 1982. Basalt contamination by continental crust: Some experiments and models. Contrib. Min. Pet., 80:73-87.

Watson, E.B., Capobianco, C.J., 1981. Phosphorus and the rare earth elements in felsic magmas: An assessment of the role of apatite. Geochim. Cosmochim. Acta., 45:2349-2358.

Watson, E.B., Green, 1981. Apatite/liquid partition coefficients for the rare earth elements and strontium. Earth Planet. Sci. Lett., 56:405-421.

Watson, E.B., Harrison, T.M., 1983. Zircon saturation revisited: Temperature and composition effects in a variety of crustal magma types. Earth Planet. Sci. Lett., 64:295-304.

Wells, R.E., 1990. Paleomagnetic rotations and the Cenozoic tectonics of the Cascade arc, Washington, Oregon, and California. J. Geophys. Res., 95:19409-19417.

Wells, R.E., Engebretson, D.C., Snavley, P.D., Coe, R.S., 1984. Cenozoic plate motions and the volcano-tectonic evolution of western Oregon and Washington. Tectonics, 3:275-294.

White, C.M, McBirney, A.R., 1978. Some quantitative aspects of orogenic volcanism in the Oregon Cascades. Geol. Soc. Am. Mem. 152, p. 369-388.

Williams, H., 1944. Volcanoes of the Three Sisters region, Oregon Cascades. Univ. of Calif. Pubs., Berkeley, 27-3:37-84.

___, 1957. A geologic map of the Bend quadrangle, Oregon and a reconnaissance geologic map of the central portion of the High Cascade Mountains. Or. Dept. Geol. Min. Ind. Map.

Wilson, L., 1972. Explosive volcanic eruptions - II The atmospheric trajectories of pyroclasts. Geophys. J. R. Astr. Soc., 30:381-392.

Wise, W.S., 1969. Geology and petrology of the Mt. Hood area: A study of High Cascade volcanism. Geol. Soc. Am. Bull., 80:969-1006.

Wolf, M.B., Wyllie, P.J., 1989. The formation of tonalitic liquids during the vapor-absent partial melting of amphibolite at 10kb (abstr). EOS, 70:506.

Wood, B., Banno, S., 1973. Garnet-orthopyroxene and orthopyroxene-clinopyroxene relations in simple and complex systems. Contrib. Min. Pet., 42:109-124.

Wozniak, K.C., 1982. Geology of the northern part of the southeast Three Sisters quadrangle, Oregon. M.S. Thesis, Oregon St. Univ., 98p.

Zoback, M.L., Zoback, M., 1980. State of stress in the conterminous United States. J. Geophys. Res.,85:6113-6156

APPENDICES

APPENDIX A: ANALYTICAL METHODS

Instrumental Neutron Activation Analysis

Facilities at the Oregon State University Radiation Center were used to obtain trace element abundances through instrumental neutron activation analysis (INAA). Experimental design follows the procedures outlined in Laul (1979) and Hughes (1983). Two analytical runs were made for this study: 71 samples (3S001-3S080, 3S140-3S144) in the spring of 1987, and 65 samples (3S086-3S152) in the spring of 1988. All samples were prepared from the fresh interiors of field samples, crushed in an alumina-ceramic jaw-crusher to ≈0.5 cm, split, and ≈20 g powdered in a alumina-ceramic shatter box. In-house standards CRB-3 (equivalent to U.S.G.S. BCR-1) and CSG-1 (Champion Stock Granodiorite), and N.B.S. standard 1633-a (Fly ash) were used as standards. About 0.8 g of rock powder was sealed in 2/5d polyvials, which were then sealed into a 2d polyvial. The 2d polyvials were double-stacked in the rotating rack of the O.S.U. TRIGA reactor, and irradiated for 6 hours at 1 MW. Gamma-ray counts were obtained using high (≈20%) efficiency Ge(Li) detectors coupled with 4096-channel analyzers. Data storage and reduction was accomplished with DOS-based desk top computers. First counts of 4k to 10k seconds occurred 6 to 14 days after irradiation, and obtained Na, Ba, La, Sm, Yb, Lu, and U abundances. Long counts of 15k to 20k seconds occurred 30 to 45 days after irradiation, and measured Fe, Sc, Co, Ni, Rb, Sr, Cs, Ce, Nd, Eu, Tb, Zr, Hf, Ta and Th abundances.

Duplicate sample analyses were obtained in each analytical run, and are given in table A-1. The high precision of the INAA technique is shown by the small degree of variation shown in analyzing sample splits under different irradiation and counting conditions. Accuracy was tested by running a CRB-3 standard as an unknown; elemental abundances were generally within ±5% of accepted standard values.

X-Ray Fluorescence

X-ray fluorescence (XRF) analyses were accomplished during the summer of 1988 at Washington State University. Previously crushed samples (≈0.5 cm) were split, and ≈15 g were ground in a tungsten carbide (WC) shatter box for 2 minutes. 3.5000 ± 3 g of rock powder and 7.0000 ± 3 g of lithium tetraborate flux were combined and mechanically homogenized for 10 minutes. The powder was then fused in graphite crucibles at 1000°C for 35 minutes, cooled, reground and refused. The glass beads were then ground flat with 240 and 600 SiC grit, cleaned in an ultrasonic cleaner and washed in lab-grade alcohol. Glass beads were analyzed in a fully automated Rigaku 3370 X-ray spectrometer, with all analyses accomplished in one week-long run.

	XRF + INAA 3S046	3S046B	INAA 3S136	INAA 3S136B	XRF 3S136	Std CRB-3*	INAA 1987 CRB3	INAA 1988 CRB3	XRF 1988 CRB3
SiO2	69.5	69.5				54.35			55.1
TiO2	0.55	0.55				2.22			2.25
Al2O3	15.2	15.3				13.63			13.8
FeO*	3.30	3.27	5.41	5.28	5.47	12.07	12.01	12.23	12.34
MnO	0.09	0.09				0.18			0.22
MgO	0.54	0.51				3.45			3.64
CaO	1.85	1.82				6.95			7.16
Na2O	5.98	5.97	5.80	5.90	5.80	3.27	3.26	3.29	3.40
K2O	2.88	2.88				1.69			1.74
P2O5	0.11	0.11				0.36			0.36
TOTAL	101.27	101.39				98.17			100.00
Rb	60	60	20	30	28	47.1	35	n/a	48
Ba	740	725	610	612	583	678	626	705	634
Sr	182	182	360	390	392	330	310	320	326
Cs	1.90	1.80	0.95	0.82		0.97	0.99	1.00	
Sc	9.45	9.31	15.75	14.86	15	32.8	33.04	32.1	28
V	1	7				404			403
Co	2.89	2.89	7.12	6.59		36.3	36.1	36.6	
Ni	8	8	<40	<60	4	13	<50	30	3
Cr	<4	<4	3	4	0	16	14	13	29
Zn	89	86	191	275	95	129	130	136	148
La	25.9	25.8	22.0	21.6		25	25.7	24.8	
Ce	55.1	54.6	53.2	48.1		53.7	55.2	54.9	
Nd	29.5	28.6	26.0	26.2		28.7	32.3	28.4	
Sm	6.30	6.37	6.27	6.35		6.58	6.64	6.7	
Eu	1.36	1.31	1.82	1.75		1.96	1.97	1.91	
Tb	1.03	1.01	1.13	1.15		1.05	1.01	1.1	
Yb	4.0	4.0	3.2	3.3		3.39	3.37	3.37	
Lu	0.64	0.61	0.49	0.49		0.51	0.49	0.52	
Zr	307	307	130	180	203	131	150	190	173
Hf	8.5	8.4	5.8	5.3		4.9	5.1	5.2	
Ga	20	18							21
Y	37	37							34
Nb	17.7	17.4							12.6
Ta	0.92	0.94	0.59	0.58		0.79	0.8	0.81	
Th	5.6	5.4	2.6	2.5		6.04	6.12	5.9	
U	2.0	2.1	1.2	1.1		1.71	1.7	1.6	

*CRB-3 is equivalent to U.S.G.S. Standard BCR-1; values for BCR-1 from Flanagan (1976).

Table A-1: Replicate analyses for samples 3S046 (1987) and 3S136 (1988) using INAA. Sample splits were irradiated at different levels in the reactor, counted on different Ge(Li) detectors and reduced with different calibration standards. Note the high degree of precision indicated by these analyses. Accuracy for INAA and XRF shown by blind analysis of standard CRB-3 (i.e., BCR-1). Note the close correspondence between analyzed and reported values for CRB-3; actual abundance of FeO* in CRB-3 may be 12.25 wt. % (R. Walker, pers. comm., 1988).

A 2:1 flux-to-rock ratio was used to increase the precision of trace element analyses. However, this ratio results in larger matrix corrections during XRF analysis, which may introduce a bias towards higher SiO_2 (+0.5 wt.%) and lower FeO*, CaO, and TiO_2 (-0.5 wt.% total) in W.S.U. analyses (Conrey, 1991). Precision and accuracy of the XRF analyses was evaluated through replicate analysis of sample 3S046, and analysis of standard CRB-3 as an unknown (table A-1). These analyses confirm the relative degree of precision and accuracy reported by Conrey (1991) for W.S.U. XRF analyses.

Electron Microprobe

Mineral compositions were determined with the fully automated Cameca SX-50 microprobe at O.S.U. during 1989-1990. Twenty one samples were selected for detailed microprobe analysis, which represented the major geochemical trends observed in the study area for basalt to rhyolite. In addition, mineral separates from 5 Quaternary pyroclastic units in the Bend area were analyzed with the microprobe.

Operating conditions of the microprobe were 15 kV accelerating voltage with a current of 20 nA. A beam width of 2μm was used for all minerals except plagioclase, which used a 5μm beam width. Calibrations used mineral standards, and were checked during each analytical run by successful analysis of standard reference minerals. Mineral compositions and structural formulae were calculated for all minerals except amphiboles and Fe-Ti oxides with standard Cameca software. Amphibole compositions were calculated using the program AMPREC.FOR by Spear and Kimball (1984), which calculates an average value of Fe^{3+} based on the structural limits of Fe^{3+} in the appropriate composition amphibole. Fe-Ti oxides were recalculated using the method of Carmichael (1967).

APPENDIX B: Visual estimates of phenocryst abundances and additional petrographic information for studied rocks. 0.1 = Trace amounts, other numbers = estimated percents. **Phno**: Total phenocryst abundance. **An**: Plagioclase An determined through the Michel-Levy method. **Zon**: Plagioclase zoning, **W** = weak (<10 An), **M** = moderate (10-20 An), **S** = strong (> 20 An), **N** = normal, **R** = reverse. **Siv**: % of plagioclase phenocrysts with coarse glass inclusions. **Frt**: % plagioclase phenocrysts with evidence of resorption or fine glass inclusions on rim. **GM**: Groundmass features: **C** = coarse (> 0.2 mm), **M** = medium (0.1-0.2 mm), **F** = fine (< 0.1 mm), **X** = holocrystalline, **V**, hyalocrystalline, **G** = glassy, **D** = devitrified. Other notes: **Rsbd**: resorbed; **Gloms**: Glomerocrysts

SAMPLE	Plag	Cpx	Opx	Ol	Hb	Opq	Ap	Zr	Phno	An	Zon	Siv	Frt	GM	Additional notes
3SXBP	0.5		0.3		0.1	0.1	0.1	0.1	1.0	22		0		G	Rhyolite pumice
3S001	0.1		0.1			0.1			0.1			0		G	Rhyodacite pumice
3S003	1.0	0.5	0.5	0.5		0.5			3.0	46	WN	10		G	Andesite pumice
3S005	10.0	0.5	2.0			1.0	0.1		13.6	45	WN	50		G	Rhyodacite pumcie
3S008	2.0	1.0				1.0	0.1		4.1	45	WN	10		MX	Gloms, coarse plag sieved
3S009	20.0	2.0	1.0		0.1	1.0	0.1		25.1	42	MN	5	1	MD	Devitrified, cpx & opx oxidized
3S010	7.0	2.0				2.0			11.0	48	MN	50	5	MV	Aphyr. rhyo(?) xenoliths
3S010X	5.0					1.0			6.0	30	WN	5		CD	Devit, FeMg's -> Opaques
3S011	7.0	2.0		1.0		5.0			15.0	80	SN	50	10	FX	Sieved=An35, Felty GM
3S012	0.5						0.1		0.6	20	WN	0		FV	Devitrified
3S015	20.0	2.0		1.0		2.0			25.0	46	WN	75		CX	Sieved=An80 cpx rimmed
3S017	3.0	0.5		1.0		0.5			5.0	68	WN	25	10	FX	Pilotax; tr. ol Rimmed
3S019	20.0	3.0	2.0		0.1		0.1		25.2	45	WN	25		MX	Sieved=An30
3S022	15.0	0.5		3.0		0.5			19.0	68	SN	25	25	FX	An68-30; Felty
3S023	15.0	1.0	5.0			2.0	0.5		23.5	22	WR	5	100	CX	Wk Fritted Rims, Oxidized Opx
3S027	20.0	0.1	0.1			0.1			20.3	22		5		DG	Eutaxitic, Devitrified
3S028	0.5	0.1	0.1	0.1		0.1			1.0	45	WN	10		G	Andesite pumice
3S029	3.0	0.5	1.0			0.5	0.1	0.1	5.2	22	MN	0		MX	Cpx rimmed
3S030	10.0	0.1	10.0			7.0			27.1	55	SN	0	100	CX	Subophitic, Plg Rims
3S031	5.0	3.0	0.1	2.0	0.1	2.0			12.2	48	WN	50	25	CX	Opacitic Hb, Ol rimmed (opx?)
3S032	0.5					0.1			0.6	20	WN	0		FD	Devitrified
3S033	3.0	0.1		1.0		0.5			4.6	52	WN	25	25	FX	Ol rimmed (opx?)
3S034	1.0					0.1			1.1	12	WN	0		FD	Devitrified
3S035	1.0					0.1			1.1	20	WN	0		FD	Devitrified
3S036	1.0	0.5	0.1			0.5	0.1		2.4	33	MN	10	50	FV	Sanid, Qtx, Bio. An40-33
3S037	5.0	0.1	2.0			1.0	0.1		8.2	22	MN	5		FX	An38-22
3S038	2.0	1.0		0.1		0.5			3.6	75	WN	50	10	MX	Cpx Rimmed (opx?)
3S040A	7.0	0.1	1.0			1.0	0.1		9.2	38	WN	25	25	FX	An44-34 Siv, Embayed opx
3S042	1.0		0.1			0.5	0.1		1.7	15	WN	0		FV	Freshest TVC Rhyolite Dome
3S043	0.1								0.1			0		G	Fresh obsidian
3S044	10.0		0.5						10.5	40	WN	0		G	Dacitic pumice
3S045	10.0	0.1		1.0		1.0			12.1	46	SN	10	40	MX	An73-46, Skeletal ol
3S046	1.0		0.1			0.5	0.1		2.7	36	WN	50		FV	Coarsely sieved plag

SAMPLE	Plag	Cpx	Opx	Ol	Hb	Opq	Ap	Zr	Phno	An	Zon	Siv	Frt	GM	Additional notes
3S048	0.5		0.1						0.5			50		G	Rhyodacite pumice, ≈3S046
3S049	10.0	1.0		5.0		5.0			21.0	49	SN	10		MX	Visible banding; An78-48
3S050	10.0	1.0	0.5			1.0	0.1		12.6	39	MN	50		FV	An44-39
3S051	7.0	2.0	0.5			1.0	0.1		10.6	35	WN	5		FV	Banded; Oscillatory Plag
3S052	7.0	3.0	1.0			0.1	0.5		11.6	32	SN	50		MX	An55-32; Glomerocrysts
3S053	15.0	0.1	3.0			1.0	0.1		19.2	36	WN	70		MV	Biotite Shreds in GM
3S054	5.0		1.0			0.5	0.4		6.9	22	MN	0		MV	An26-22; Glomerocrysts
3S057	15.0	0.1	2.0			1.0	0.1		18.2	36	WN	90		MV	Hyalopilitic dome
3S058	10.0		1.0		0.1	0.5	0.5		12.1	35	WR	10	10	MV	An30-35;Oxy opx, Rsbd Plg
3S059	7.0	3.0	1.0			0.1	0.5		11.6	32	SN	25	20	MX	AN55-32; Gloms, Ol rims (opx?)
3S060	15.0		3.0		0.1	1.0	0.1		19.2	20	WN	75	10	FV	Tr. Biotite; Highly sieved plag
3S061	15.0	2.0	1.0			2.0	0.1		20.1	24	WN	25		FV	Cpx Rimmed; Sieved=An41
3S062	10.0		1.0			0.5	0.1		11.6	23	WN	25		MX	Biotite; An28-23; Gloms
3S063	25.0	5.0				1.0			31.0	28	WN	5		FV	GM%'s; An34-28, cpx rims (opx?)
3S064	25.0	2.0	2.0			5.0	2.0		36.0	35	WN	50		CV	An35-30; Gloms; Zonation
3S065	25.0	2.0	2.0			5.0	2.0		36.0	35	WN	50		CV	An35-30; Gloms; Zonation
3S066	10.0			10.0		10.0			30.0	48	MN	10	90	CX	Fritted Plg, resorbed Ol
3S067	25.0	7.0	2.0			5.0	0.1		39.1	42	WR	50	5	FV	An36-42; Glomerocrysts
3S069	0.1			10.0		3.0			13.1	75	WN	0		CX	Embayed & Opacitic Ol
3S073	7.0	1.0	1.0			0.5			9.5	45	WN	25		FX	Phenos An35
3S074	7.0	2.0		1.0		2.0			12.0	55	MN	50	25	MV	An65-55; Sieved=An55-35; Ol Rims
3S075	3.0	0.1	0.5					0.1	3.7	20	WN	10		FX	Glomerocrysts
3S078	0.1								0.1			0		FV	Aphyric, Hyalopilitic
3S079	0.5	0.1	0.1			0.1			0.5			0		G	Rhyodacite pumice
3S085	2.0	0.5	0.1			0.5	0.1		3.2	45	WN	25		FX	Gloms, Lgst Plags sieved
3S090	20.0	1.0	1.0	3.0		1.0			26.0	45	WN	75		CX	Sieved=An35-25
3S091	2.0					0.1			2.1	35	WN	50		FV	Almost Aphyric
3S092	5.0	1.0		0.5		1.0			7.5	45	WN	50		FV	Sieved=An20; Ol w/ opx Rims
3S093	7.0	1.0		3.0		1.0			12.0	34	MN	90	10	CX	An45-34; Rsbd Plag
3S094	1.0	0.5	0.1			0.1			1.0	45	WN	0		G	Rhyodacite pumice
3S095	5.0	2.0	0.1			1.0	0.1		8.2	37	WN	0		FV	Moderately Vesicular
3S096	7.0	2.0	0.5			1.0	0.1		10.6	33	WN	0		FV	Glomerocrysts
3S097	10.0	3.0	0.1	0.5		1.0	0.1		14.7	35	MN	25		FV	Sieved=An62; Oxidized Opx
3S098	7.0	0.1	1.0			0.5	0.1		8.7	30	WN	25		FV	Highly pleochroic opx
3S099	7.0	0.5		1.0		0.1			8.6	64	WN	0		FX	Glomerocrysts
3S100	10.0	2.0	1.0			1.0	0.1		14.1	24	WN	10		FV	An30-24; Glomerocrysts
3S101	5.0	1.0		0.5		0.5			7.0	42	SN	50	10	FX	Sieved=An80
3S102	1.0	0.5	0.1			0.1			1.7	80	WR	0		FX	Cognate Xenoliths
3S104	10.0	0.1	1.0			0.5	0.1	0.1	11.8	35	WN	10		FV	Devitrified; Zr incs Plag
3S105	20.0	1.0		3.0		2.0			26.0	40	MN	25		FX	An52-40, Skeletal Ol
3S106	20.0	2.0		3.0		1.0			26.0	52	WN	10		FX	An58-52; Glomerocrysts

SAMPLE	Plag	Cpx	Opx	Ol	Hb	Opq	Ap	Zr	Phno	An	Zon	Siv	Frt	GM	Additional notes
3S107	7.0		1.0			0.5	0.1		8.6	40	WN	5		FV	An45-40
3S108	7.0	2.0	1.0			1.0	0.5		11.5	32	MN	5		FX	An44-32
3S109	2.0	0.5		0.1		0.1			2.7	60	MN	50		FX	AutoBxx; Ol Opacitic
3S110	7.0	2.0	0.5			1.0	0.1		10.6	35	WN	10		FV	Hyalopilitic
3S111	10.0	3.0	1.0			2.0	0.1		16.1	38	WN	5		MV	Glomerocrysts
3S112	15.0	3.0	1.0			1.0			20.0	41	MN	10		CX	An58-41; Px Rimmed; Gloms
3S113	15.0		3.0		0.1	1.0	0.1		19.2	36	WN	0		FV	Oxidized Opx; Oscil Plg
3S114	12.0		2.0			0.5	0.1		14.6	33	MN	90		FV	An33-20
3S115	7.0	2.0	0.5			1.0	0.1		10.6	36	WN	10		CX	Cpx rimmed
3S116	0.5					0.1			0.6	20	WN	0		FV	Devitrified
3S117	0.5					0.1			0.6	20	WN	0		FV	Devitrified
3S118	20.0		2.0			0.5			22.5	27	WN	5		G	Slightly hydrated glass
3S119	15.0	2.0	1.0			1.0	0.1		19.1	45	MR	50		MV	An36-45; Mafic Clot; Gloms
3S120	20.0	3.0	1.0			3.0	0.1		27.1	38	SN	10		FX	An70-38; Gloms; Opqs rimmed
3S122	20.0		3.0			0.5	0.1	0.1	23.7	26	MN	90		FV	Trace of Biotite in GM
3S123	15.0	3.0	2.0	0.1		0.5	0.1		20.7	37	WN	10		FX	Ol Rims; Brecciated
3S124	15.0		2.0		0.5	2.0	0.1		19.6	30	MN	10		FV	Glomerocrysts, Abund Hb
3S125	10.0	2.0	1.0			1.0	0.1		14.1	36	WN	5		FV	Glomerocrysts
3S126	7.0		1.0			0.5	0.1		8.6	42	WN	10		FV	Weathered
3S127	7.0		2.0		0.1	0.5	0.1		9.7	33	MN	90		FV	An41-33
3S128	1.0	0.5	0.1			0.5	0.1		2.2	45	WN	0		MX	Felty
3S130	0.5	0.1	0.1			0.1	0.5		0.3	40	WN	50	25	FX	Tr Bio in plg, Fritted
3S131	10.0	0.5		5.0		3.0	0.1		18.6	45	WN	100		CX	Dikty; Ol Zoned, Wk Sievs
3S132	1.0	0.5	0.1			0.5			2.1	38	WN	0		MV	Glassy; Mafic Xenoliths
3S133	5.0			1.0		1.0			7.0	60	MN	10		CV	An70-60; Seriate; Ol Rims
3S134	10.0	1.0	3.0			2.0	0.2		16.2	43	WN	5		MV	Cpx rimmed (opx?)
3S135	5.0	1.0	1.0			1.0	0.1		8.1	42	WN	0		FV	Cpx rimmed (opx?)
3S136	7.0	1.0	3.0			1.0	0.5		12.5	33	WN	0		FV	Brn AP; Gloms; cpx rims (opx?)
3S137	7.0	0.5	1.0			2.0	0.2		10.7	37	MN	5		FV	cpx rims, Brown apatite
3S138	10.0	0.5	1.0			1.0	0.1		12.6	44	WN	0		FV	cpx rims, Glomerocrysts
3S139	0.1			0.1					0.1		WN	0		G	Fresh Obsidian
3S140	0.5					0.1			0.6	15	WN	10	10	FV	Consertal Plg+Gls Xenos
3S145	20.0	0.1	3.0		0.1	1.0	0.1		24.0	29	WN	90		FV	Complex oscillatory zoning
3S146	7.0	2.0	0.5			1.0			10.5	33	MN	5		FX	Cpx rims, Low An plg
3S147	7.0	1.0	1.0			2.0	0.1		11.1	38	WN	5		CX	Cpx rimmed
3S148	5.0	0.5	1.0	0.1	0.5	0.1	0.1		8.3	21	MN	50	25	FV	Ol Xenos, V. complx Gloms
3S149	30.0	0.5	0.1	2.0		1.0			33.6	48	SN	75	10	CV	Cpx Rimmed, An70-48
3S150	10.0	2.0	0.5	0.1		0.5	0.1		13.2	38	SN	50		MV	Hb Relicts, Mafic clots
3S151	10.0	0.5	1.0			1.0			12.5	42	WN	10		FV	Slight hydration
3S152	3.0	0.5		0.1		0.5			4.1	34	MN	25	5	CX	Skeletal Ol in GM

Appendix C-1: Feldspar compositions determined through electron microprobe analysis. Mol percents anorthite (An), albite (An) and orthoclase (Or) calculated using standard CAM-ECA software. **GM:** groundmass crystal; **glom:** glomerocryst; **acic:** acicular crystal; **siv:** coarse glass inclusions (sieved); **intmed:** significant reversal in core to rim zoning.

Sample	SiO2	Al2O3	FeO	MgO	CaO	Na2O	K2O	BaO	TOTAL	An	Ab	Or
3SXBP core	62.51	23.52	0.19	0.00	4.46	8.41	0.55	0.09	99.73	21.95	74.85	3.21
3SXBP rim	62.13	23.24	0.20	0.01	4.35	8.70	0.60	0.09	99.31	20.90	75.68	3.42
3SXBP core	62.14	23.39	0.25	0.02	4.48	8.42	0.58	0.09	99.36	21.95	74.69	3.36
3SXBP rim	61.53	22.30	0.14	0.00	4.06	8.77	0.62	0.14	97.57	19.65	76.78	3.58
3S003a core	57.69	25.83	0.46	0.02	7.79	6.66	0.27	0.02	98.74	38.63	59.78	1.59
3S003a rim	56.41	25.03	0.44	0.02	7.82	7.41	0.30	0.09	97.53	36.26	62.10	1.65
3S003b core	56.85	25.83	0.49	0.01	7.91	6.63	0.28	0.05	98.05	39.10	59.25	1.65
3S003b rim	59.10	26.95	0.42	0.02	7.84	6.51	0.27	0.04	101.14	39.32	59.10	1.59
3S005a core	57.54	26.55	0.35	0.00	8.49	6.26	0.37	0.04	99.59	41.90	55.91	2.19
3S005a rim	56.73	25.57	0.33	0.00	7.78	6.63	0.41	0.05	97.50	38.38	59.24	2.38
3S005b core	56.57	26.71	0.38	0.01	8.62	6.24	0.37	0.03	98.93	42.38	55.47	2.16
3S005b rim	55.30	25.99	0.35	0.01	8.75	6.78	0.37	0.02	97.56	40.77	57.18	2.05
3S009a core	58.59	25.90	0.33	0.01	7.81	6.87	0.29	0.04	99.84	37.94	60.37	1.69
3S009a rim	59.53	24.19	0.23	0.02	5.83	7.49	0.63	0.04	97.96	28.94	67.35	3.71
3S009b core	57.99	26.01	0.26	0.01	7.67	6.59	0.31	0.03	98.87	38.41	59.75	1.84
3S009b rim	60.68	23.83	0.25	0.01	5.30	7.93	0.74	0.11	98.85	25.81	69.90	4.29
3S017a core	46.93	33.11	0.67	0.04	16.44	2.03	0.05	0.01	99.28	81.51	18.20	0.29
3S017a rim	55.40	26.52	0.96	0.07	9.66	5.53	0.34	0.02	98.50	48.11	49.88	2.01
3S017b core	51.36	29.86	0.64	0.08	12.76	3.90	0.10	0.00	98.69	64.01	35.39	0.60
3S017b rim	46.74	32.88	0.63	0.07	16.56	2.07	0.07	0.00	99.03	81.24	18.36	0.40
3S017c core	49.05	31.49	0.70	0.06	15.02	2.80	0.06	0.00	99.17	74.52	25.13	0.35
3S017c rim	53.22	28.47	0.88	0.08	11.63	4.54	0.16	0.00	98.98	58.06	41.00	0.94
3S017d core	46.50	33.32	0.59	0.04	16.70	1.88	0.05	0.01	99.08	82.86	16.83	0.32
3S017d rim	45.82	33.71	0.56	0.05	17.23	1.56	0.03	0.02	98.98	85.73	14.07	0.20
3S017e core siv	49.91	30.73	0.66	0.05	13.98	3.15	0.07	0.00	98.56	70.71	28.87	0.42
3S017e edge siv	50.24	30.16	0.65	0.06	13.39	3.70	0.10	0.00	98.31	66.25	33.16	0.60
3S017e rim	52.78	28.45	0.87	0.09	11.48	4.52	0.20	0.04	98.44	57.68	41.11	1.21
3S017f core siv	46.61	33.56	0.52	0.07	16.85	1.68	0.05	0.00	99.33	84.52	15.20	0.28
3S017f edge siv	46.18	33.18	0.65	0.06	16.70	1.97	0.04	0.00	98.78	82.22	17.57	0.22
3S017f rim	54.54	23.12	4.14	2.53	9.12	4.39	0.43	0.05	98.31	51.92	45.20	2.88
3S017 30µm	52.60	29.57	0.80	0.07	11.94	4.21	0.15	0.00	99.32	60.51	38.62	0.88
3S017 50µm acic GM	53.12	27.77	1.11	0.10	11.09	4.82	0.21	0.03	98.24	55.31	43.44	1.24
3S017 50µm acic GM	53.56	27.82	1.13	0.12	11.22	4.88	0.18	0.00	98.90	55.37	43.57	1.06
3S028a core	57.54	25.33	0.46	0.04	7.28	6.97	0.30	0.04	97.97	35.95	62.28	1.77
3S028a rim	57.52	27.45	0.45	0.07	8.85	6.47	0.23	0.06	101.09	42.51	56.21	1.29
3S028b core	57.41	25.85	0.42	0.04	7.82	6.63	0.28	0.03	98.47	38.80	59.53	1.67
3S028b rim	57.39	25.65	0.34	0.06	7.37	7.49	0.30	0.05	98.65	34.64	63.67	1.69
3S030a core	45.78	34.36	0.54	0.01	17.51	1.50	0.03	0.06	99.79	86.42	13.38	0.20
3S030a rim	54.31	28.01	1.16	0.02	10.65	5.07	0.30	0.01	99.52	52.76	45.50	1.74
3S030b core	45.22	34.14	0.51	0.04	17.49	1.49	0.03	0.05	98.96	86.53	13.32	0.15
3S030b rim	47.87	32.39	0.60	0.00	15.78	2.53	0.11	0.03	99.31	77.01	22.35	0.64
3S030c siv	50.15	30.74	0.84	0.05	14.36	3.39	0.17	0.02	99.71	69.40	29.63	0.98
3S030c edge siv	54.35	27.93	1.06	0.04	10.87	5.01	0.26	0.04	99.56	53.70	44.77	1.53
3S030c rim	59.95	24.35	0.74	0.00	6.30	7.16	0.70	0.06	99.26	31.36	64.49	4.15
3S030 30µm GM	55.31	27.62	0.84	0.00	10.10	5.17	0.38	0.03	99.45	50.76	46.96	2.28
3S030 50µm GM	51.88	29.75	0.99	0.02	12.92	4.13	0.22	0.02	99.92	62.57	36.19	1.24
3S030 60µm acic GM	54.30	27.89	0.95	0.01	10.85	4.79	0.29	0.00	99.07	54.65	43.62	1.73
3S036a core	64.71	20.95	0.48	0.02	2.30	7.68	3.27	0.17	99.58	11.47	69.17	19.37
3S036a rim	56.67	26.87	0.41	0.04	8.78	5.82	0.46	0.07	99.12	44.22	53.04	2.75
3S036b core	57.97	26.34	0.37	0.05	7.96	6.45	0.56	0.06	99.75	39.24	57.50	3.26
3S036b rim	58.40	25.77	0.34	0.03	7.38	6.42	0.58	0.07	98.98	37.50	59.02	3.48
3S036c core	47.25	23.82	0.52	0.05	9.30	5.21	0.29	0.01	86.45	48.76	49.43	1.80
3S036c rim	56.42	27.21	0.65	0.04	9.33	5.17	0.76	0.05	99.64	47.61	47.78	4.61
3S036 50µm acic GM	57.85	25.86	0.78	0.01	8.02	6.21	0.53	0.04	99.30	40.30	56.50	3.20
3S036 50µm acic GM	59.66	24.72	0.77	0.00	6.51	6.99	0.81	0.09	99.54	32.35	62.87	4.78
3S036 50µm GM	67.06	19.68	0.51	0.02	3.69	6.12	1.79	0.03	98.90	21.84	65.54	12.62
3S036 75M acic	62.74	22.61	0.66	0.02	4.38	7.20	2.23	0.09	99.92	21.86	64.93	13.21
3S042a core	62.80	22.58	0.13	0.00	3.87	8.67	0.67	0.09	98.80	19.00	77.09	3.90
3S042a rim	63.07	22.85	0.26	0.00	4.09	8.49	0.61	0.10	99.48	20.28	76.11	3.61
3S042b core	61.77	23.59	0.20	0.00	5.00	8.06	0.57	0.04	99.23	24.67	71.97	3.37
3S042b rim	62.80	22.36	0.20	0.00	3.80	8.71	0.65	0.11	98.63	18.68	77.53	3.79
3S042 30µm acic	64.88	21.24	0.43	0.00	2.28	8.61	1.33	0.31	99.07	11.71	80.15	8.14

Sample	SiO2	Al2O3	FeO	MgO	CaO	Na2O	K2O	BaO	TOTAL	An	Ab	Or
3S042 50μm acic GM	66.09	20.85	0.21	0.00	1.94	9.20	1.30	0.22	99.82	9.65	82.68	7.68
3S042 60μm	62.71	21.37	0.30	0.00	2.58	8.57	1.15	0.24	96.92	13.25	79.69	7.06
3S042 GM acic	65.06	21.12	0.37	0.00	2.24	8.92	1.14	0.24	99.10	11.37	81.77	6.86
3S045a glom core	46.24	34.07	0.48	0.06	17.09	1.58	0.05	0.00	99.56	85.48	14.25	0.28
3S045a glom rim	53.84	28.59	0.99	0.07	11.10	4.79	0.25	0.01	99.64	55.31	43.20	1.49
3S045b core	50.56	31.30	0.52	0.11	13.98	3.27	0.09	0.00	99.83	69.91	29.56	0.53
3S045b rim	56.25	27.07	1.00	0.05	9.08	5.67	0.40	0.00	99.53	45.80	51.78	2.42
3S045c core	20.69	16.52	0.00	0.07	17.17	1.84	0.04	0.00	56.33	83.58	16.22	0.20
3S045c edge	47.43	33.32	0.55	0.09	16.48	1.94	0.04	0.00	99.85	82.20	17.55	0.25
3S045c rim	55.66	27.28	1.09	0.04	9.59	5.66	0.34	0.00	99.66	47.37	50.62	2.01
3S045 30μm acic GM	53.92	28.41	1.24	0.04	10.96	4.97	0.25	0.02	99.81	54.10	44.40	1.50
3S045 30μm acic GM	55.36	27.52	1.25	0.01	9.88	5.44	0.36	0.04	99.87	49.04	48.83	2.14
3S045 40μm acic GM	56.91	25.99	1.12	0.06	8.50	6.10	0.44	0.01	99.13	42.36	55.01	2.62
3S049 core	49.02	31.73	0.49	0.05	15.07	2.80	0.12	0.00	99.29	74.29	24.99	0.72
3S049 intmed	53.81	29.08	0.55	0.08	12.73	3.68	0.17	0.00	100.10	65.01	33.97	1.02
3S049 rim	49.21	31.93	0.68	0.03	15.02	2.72	0.14	0.01	99.73	74.74	24.46	0.80
3S058a core	58.37	24.87	0.34	0.00	6.88	7.01	0.50	0.06	98.03	34.11	62.93	2.96
3S058a intmed	54.34	22.36	0.28	0.01	6.10	8.53	0.51	0.05	92.17	27.56	69.72	2.73
3S058a rim	58.78	25.27	0.26	0.00	6.91	7.18	0.39	0.04	98.83	33.91	63.79	2.30
3S058b core siv	57.64	26.29	0.22	0.00	7.87	6.52	0.38	0.09	99.00	39.11	58.64	2.25
3S058b rim	60.60	24.43	0.26	0.00	5.84	7.54	0.54	0.09	99.29	29.01	67.80	3.19
3S058 125M acic GM	58.83	25.98	0.20	0.00	7.19	6.84	0.37	0.04	99.45	35.91	61.87	2.22
3S061a core	54.23	28.56	0.30	0.00	10.51	5.14	0.27	0.00	99.02	52.20	46.20	1.60
3S061a rim	64.67	23.65	0.38	0.00	5.31	7.20	0.80	0.06	102.07	27.55	67.54	4.92
3S061b core siv	58.17	25.43	0.72	0.04	7.88	6.57	0.46	0.01	99.28	38.79	58.52	2.69
3S061b rim	55.31	27.34	0.62	0.01	9.73	5.55	0.36	0.02	98.94	48.13	49.73	2.14
3S061 50μm GM	56.64	26.67	0.53	0.02	9.03	5.91	0.41	0.04	99.25	44.67	52.91	2.43
3S069a core	49.40	31.66	0.73	0.09	15.01	2.78	0.11	0.00	99.78	74.40	24.96	0.64
3S069a rim	53.14	14.55	4.89	8.01	14.34	2.53	0.30	0.05	97.82	74.38	23.76	1.87
3S069b core	49.98	30.88	0.51	0.12	14.37	3.35	0.10	0.02	99.32	69.93	29.50	0.57
3S069b rim	48.53	32.27	0.58	0.09	15.32	2.93	0.12	0.00	99.83	73.75	25.55	0.69
3S069 30μm GM acic	50.59	30.18	1.10	0.02	13.47	3.74	0.20	0.00	99.29	65.79	33.04	1.17
3S069 50μm GM	50.87	30.53	0.94	0.00	13.62	3.66	0.22	0.00	99.85	66.41	32.31	1.28
3S074a core siv	56.25	26.58	0.46	0.01	9.12	5.92	0.26	0.00	98.59	45.30	53.20	1.51
3S074a rim	53.11	28.58	1.06	0.07	11.58	4.31	0.44	0.01	99.16	58.17	39.21	2.63
3S074b glom core	50.29	30.81	0.52	0.09	14.02	3.18	0.07	0.04	99.03	70.56	28.99	0.44
3S074b rim	52.53	28.74	0.84	0.07	12.09	4.02	0.35	0.01	98.64	61.15	36.76	2.09
3S074c core siv	48.29	31.74	0.82	0.00	15.40	2.62	0.17	0.01	99.05	75.72	23.31	0.97
3S074c rim	47.84	32.59	0.63	0.02	15.79	2.40	0.08	0.02	99.38	78.05	21.48	0.47
3S074d core rsbd	58.36	25.48	0.56	0.06	7.90	6.33	0.48	0.03	99.20	39.64	57.52	2.84
3S074d edge rsbd	58.01	25.56	0.55	0.01	8.00	6.05	0.90	0.04	99.13	39.96	54.67	5.37
3S074d rim	51.01	28.54	0.74	0.06	11.98	3.95	0.33	0.00	96.59	61.41	36.59	2.00
3S074 30μm GM	53.67	28.11	1.03	0.04	11.18	4.69	0.41	0.00	99.15	55.49	42.11	2.40
3S074 30μm	53.59	27.65	1.44	0.05	11.15	4.35	0.45	0.04	98.71	56.99	40.26	2.75
3S074 50μm acic GM	52.15	29.46	0.84	0.05	12.58	3.90	0.33	0.00	99.31	62.82	35.20	1.98
3S079a core	57.87	26.60	0.49	0.02	8.45	6.15	0.21	0.07	99.85	42.63	56.12	1.25
3S079a rim	58.62	26.57	0.40	0.03	8.41	6.51	0.22	0.00	100.75	41.13	57.59	1.28
3S079b core	59.03	26.08	0.37	0.01	7.90	6.69	0.25	0.05	100.37	38.93	59.63	1.45
3S079b rim	59.81	24.99	0.41	0.03	7.14	7.40	0.27	0.07	100.11	34.25	64.20	1.55
3S079c core	59.54	25.60	0.28	0.04	7.38	6.83	0.26	0.00	99.93	36.78	61.66	1.56
3S079c rim	57.66	24.82	0.45	0.00	7.60	7.22	0.24	0.14	98.04	36.27	62.34	1.38
3S090a core glom	52.11	29.97	0.50	0.09	12.66	4.21	0.11	0.00	99.66	62.01	37.32	0.67
3S090a rim	49.22	31.73	0.66	0.06	14.58	2.93	0.09	0.05	99.31	72.97	26.52	0.51
3S090b core	47.58	32.79	0.55	0.05	15.89	2.24	0.08	0.03	99.20	79.31	20.23	0.46
3S090b edge	48.68	31.79	0.71	0.08	15.04	2.78	0.08	0.00	99.15	74.58	24.95	0.47
3S090b rim	55.73	26.89	0.71	0.06	9.42	5.78	0.32	0.01	98.92	46.49	51.65	1.85
3S090c core siv	46.88	33.01	0.69	0.04	16.23	2.12	0.07	0.02	99.05	80.58	19.03	0.40
3S090c edge siv	51.71	29.74	0.61	0.04	12.68	3.92	0.17	0.00	98.87	63.47	35.51	1.02
3S090c rim	48.82	31.55	0.64	0.07	14.77	2.86	0.09	0.01	98.82	73.63	25.83	0.54
3S090d core	50.21	31.45	0.56	0.06	14.38	3.12	0.07	0.02	99.86	71.51	28.10	0.39
3S090d intmed	49.70	32.33	0.66	0.05	15.24	2.78	0.06	0.00	100.81	74.93	24.72	0.36
3S090d rim	55.49	28.23	0.63	0.03	10.29	5.38	0.23	0.04	100.32	50.71	47.96	1.33
3S090e core siv	50.07	26.93	4.13	1.30	13.21	3.03	0.54	0.06	99.26	68.33	28.33	3.34
3S090e rim	50.93	31.40	0.66	0.06	13.82	3.60	0.06	0.06	100.19	67.72	31.95	0.33
3S090f core siv	48.30	28.74	2.93	0.79	13.71	2.67	0.51	0.05	97.71	71.56	25.25	3.20
3S090f edge siv	49.29	32.05	0.60	0.05	15.08	2.76	0.07	0.01	99.91	74.86	24.75	0.39
3S090f rim	51.14	31.02	0.52	0.02	13.63	3.64	0.09	0.00	100.06	67.10	32.38	0.52
3S090 30μm acic GM	52.66	29.13	0.84	0.04	11.88	4.62	0.23	0.02	99.41	57.91	40.76	1.33
3S090 30μm acic GM	55.40	27.60	1.12	0.04	10.10	5.45	0.27	0.00	99.99	49.82	48.59	1.60
3S090 30μm acic GM	53.53	29.31	0.66	0.05	11.62	4.65	0.17	0.05	100.03	57.42	41.56	1.02

Sample	SiO2	Al2O3	FeO	MgO	CaO	Na2O	K2O	BaO	TOTAL	An	Ab	Or
3S090 30μm acic GM	54.86	28.23	0.86	0.07	10.48	5.25	0.24	0.00	99.99	51.68	46.91	1.41
3S090 50μm acic GM	52.98	29.29	0.69	0.08	11.66	4.42	0.18	0.00	99.29	58.67	40.27	1.06
3S090 60μm GM	52.55	28.72	0.74	0.04	11.71	4.53	0.17	0.00	98.47	58.22	40.78	1.00
3S098a core	56.40	26.89	0.39	0.02	8.64	6.33	0.22	0.01	98.89	42.44	56.25	1.31
3S098a intmed	56.81	27.26	0.30	0.02	8.97	6.07	0.23	0.01	99.67	44.36	54.31	1.33
3S098a rim	61.50	24.09	0.36	0.00	5.23	8.03	0.45	0.06	99.73	25.76	71.58	2.65
3S098b core	61.19	24.38	0.24	0.03	5.68	8.01	0.43	0.03	99.98	27.46	70.05	2.49
3S098b rim	61.39	24.32	0.28	0.01	5.38	8.05	0.48	0.05	99.95	26.21	71.00	2.79
3S098c core	61.05	23.97	0.23	0.01	5.43	7.80	0.44	0.07	98.99	27.03	70.34	2.63
3S098c rim	62.16	23.46	0.32	0.02	4.76	8.16	0.51	0.06	99.44	23.64	73.33	3.03
3S098 100μm	60.23	24.40	0.38	0.01	5.93	7.84	0.36	0.06	99.22	28.85	69.07	2.08
3S098 50μm acic GM	63.33	23.02	0.48	0.00	3.92	8.49	0.68	0.18	100.09	19.52	76.47	4.02
3S112a core siv	48.79	32.82	0.54	0.06	15.64	2.46	0.08	0.00	100.38	77.53	22.01	0.46
3S112a edge siv	50.49	31.14	0.47	0.09	13.81	3.37	0.14	0.00	99.51	68.79	30.38	0.83
3S112a rim	57.06	26.31	0.83	0.02	8.57	6.20	0.49	0.00	99.47	42.06	55.07	2.88
3S112b core glom	54.60	27.82	0.69	0.06	10.37	5.22	0.22	0.00	98.98	51.65	47.05	1.30
3S112b rim	54.17	28.43	0.67	0.06	11.02	4.74	0.21	0.00	99.30	55.49	43.24	1.27
3S112c core	54.03	28.96	0.66	0.07	11.46	4.86	0.22	0.00	100.25	55.87	42.87	1.26
3S112c rim	55.31	27.71	0.79	0.05	10.02	5.29	0.37	0.00	99.54	50.01	47.82	2.17
3S112 30μm acic GM	56.50	26.78	1.04	0.02	9.07	5.86	0.41	0.06	99.72	44.98	52.61	2.41
3S112 30μm acic GM	57.82	26.33	0.76	0.00	8.04	6.20	0.46	0.07	99.67	40.60	56.67	2.74
3S114a core	56.95	26.81	0.49	0.03	9.06	5.92	0.29	0.06	99.61	45.05	53.24	1.71
3S114a rim	56.74	26.36	0.22	0.03	8.45	6.44	0.31	0.04	98.57	41.26	56.95	1.79
3S114b core siv	61.27	24.22	0.26	0.01	6.07	7.02	0.66	0.07	99.58	31.01	64.95	4.04
3S114b rim	57.90	26.25	0.30	0.03	8.06	6.69	0.39	0.04	99.66	39.07	58.69	2.24
3S114 50μm acic	57.17	26.89	0.35	0.01	8.77	6.06	0.32	0.01	99.59	43.59	54.54	1.88
3S115a core	54.65	28.81	0.52	0.05	10.65	5.13	0.13	0.00	99.93	53.00	46.21	0.79
3S115a edge	53.73	29.39	0.56	0.03	11.94	4.49	0.12	0.00	100.26	59.07	40.20	0.73
3S115a rim	55.18	28.37	0.65	0.04	10.52	5.24	0.17	0.00	100.17	52.06	46.92	1.02
3S115b core	54.24	28.67	0.63	0.02	10.89	5.11	0.19	0.00	99.75	53.46	45.41	1.14
3S115b rim	57.96	26.40	0.57	0.02	8.11	6.51	0.33	0.01	99.91	39.99	58.08	1.94
3S115c core siv	54.64	27.84	0.49	0.04	10.16	5.30	0.21	0.01	98.68	50.79	47.94	1.27
3S115c rim	56.23	27.42	0.74	0.03	9.29	5.83	0.25	0.00	99.77	46.13	52.41	1.47
3S115 30μm GM	55.15	28.45	0.69	0.03	10.40	5.11	0.22	0.01	100.06	52.22	46.45	1.33
3S115 40μm acic	57.12	26.30	0.90	0.19	8.57	6.06	0.33	0.04	99.52	42.99	55.02	1.99
3S115 acic 20μm	59.69	25.09	0.88	0.03	6.48	7.15	0.53	0.06	99.91	32.33	64.54	3.13
3S122a core	60.01	24.41	0.17	0.00	6.06	7.52	0.56	0.08	98.80	29.80	66.92	3.28
3S122a rim	62.33	23.18	0.31	0.00	5.44	7.19	0.80	0.06	99.30	28.04	67.08	4.88
3S122b core siv	59.48	25.46	0.17	0.00	7.05	6.89	0.53	0.09	99.67	35.02	61.88	3.11
3S122b rim	60.36	25.35	0.29	0.00	7.03	6.96	0.53	0.11	100.62	34.68	62.19	3.13
3S122c core siv	62.84	23.84	0.14	0.00	5.21	7.65	0.69	0.06	100.43	26.22	69.63	4.15
3S122c rim	60.49	25.53	0.20	0.02	6.68	6.93	0.48	0.03	100.36	33.77	63.33	2.90
3S122d core siv	59.53	25.43	0.21	0.00	6.92	6.86	0.51	0.08	99.54	34.71	62.24	3.05
3S122d rim	61.07	24.65	0.29	0.00	6.24	7.20	0.53	0.10	100.08	31.35	65.48	3.17
3S122e core	54.12	28.71	0.35	0.00	11.01	4.85	0.23	0.05	99.32	54.86	43.75	1.39
3S122e rim	60.35	25.50	0.26	0.01	6.79	6.69	0.47	0.06	100.13	34.90	62.23	2.87
3S123a core	53.48	29.09	0.50	0.06	11.45	4.72	0.18	0.02	99.50	56.66	42.29	1.05
3S123a rim	55.17	28.02	0.65	0.05	10.23	5.34	0.33	0.00	99.79	50.43	47.61	1.95
3S123b core	55.08	27.97	0.74	0.03	10.24	5.36	0.37	0.02	99.80	50.24	47.61	2.16
3S123b rim	54.34	28.33	0.56	0.06	10.66	5.09	0.27	0.04	99.35	52.79	45.61	1.60
3S123c core	53.32	28.86	0.45	0.07	11.32	4.94	0.19	0.01	99.16	55.27	43.61	1.13
3S123c rim	56.17	27.05	0.58	0.04	9.26	5.82	0.41	0.01	99.33	45.67	51.95	2.39
3S123d core glom	53.83	29.05	0.50	0.05	11.21	4.93	0.16	0.00	99.73	55.14	43.92	0.95
3S123d rim glom	62.82	21.84	0.73	0.02	4.33	7.01	1.62	0.05	98.43	22.85	66.94	10.20
3S123d rim glom	56.56	26.99	0.74	0.00	9.00	5.90	0.49	0.05	99.74	44.41	52.73	2.86
3S123 30μm acic GM	57.67	25.46	1.14	0.37	7.76	6.58	0.58	0.04	99.59	38.11	58.47	3.42
3S123 50μm acic GM	59.20	24.94	0.76	0.01	6.79	7.17	0.68	0.08	99.62	33.01	63.04	3.95
3S131a core siv	50.42	31.04	0.63	0.05	14.23	3.15	0.10	0.03	99.66	70.94	28.44	0.62
3S131a edge siv	59.34	24.77	0.65	0.02	7.10	7.05	0.52	0.04	99.49	34.67	62.31	3.03
3S131a rim	50.53	30.65	0.58	0.04	13.83	3.44	0.08	0.05	99.20	68.64	30.92	0.45
3S131b core siv	50.21	31.05	0.62	0.05	14.19	3.45	0.12	0.02	99.70	68.99	30.32	0.69
3S131b rim	53.79	27.46	0.95	0.03	10.67	5.14	0.23	0.03	98.29	52.70	45.97	1.34
3S131c core siv	55.22	27.08	0.61	0.10	9.81	5.55	0.16	0.03	98.57	48.91	50.12	0.97
3S131c edge siv	52.02	29.46	0.80	0.07	12.61	4.10	0.15	0.04	99.24	62.41	36.72	0.87
3S131c rim	61.13	23.28	0.48	0.02	4.97	7.77	0.63	0.06	98.33	25.13	71.10	3.77
3S131 30μm GM	54.76	27.64	0.83	0.07	10.18	5.21	0.27	0.04	99.00	51.07	47.31	1.62
3S131 30μm GM	54.83	27.16	0.98	0.07	9.92	5.59	0.28	0.04	98.86	48.72	49.67	1.61
3S131 30μm GM	61.78	22.96	0.51	0.00	4.40	8.16	0.94	0.11	98.86	21.67	72.79	5.54
3S131 75M acic GM	54.65	27.06	1.09	0.11	9.75	5.53	0.28	0.01	98.47	48.55	49.78	1.66
3S134a core	60.01	25.38	0.29	0.00	6.68	7.22	0.23	0.01	99.81	33.39	65.26	1.35

Sample	SiO2	Al2O3	FeO	MgO	CaO	Na2O	K2O	BaO	TOTAL	An	Ab	Or
3S134a rim	58.77	25.97	0.30	0.01	7.37	6.84	0.24	0.02	99.52	36.77	61.78	1.45
3S134b core glom	59.03	25.80	0.38	0.00	7.41	6.86	0.35	0.04	99.87	36.64	61.32	2.04
3S134b rim	57.68	25.24	0.40	0.00	7.34	6.38	0.27	0.00	97.32	38.21	60.11	1.68
3S134 30μm acic GM	60.51	23.97	0.64	0.00	5.53	7.69	0.59	0.07	98.99	27.45	69.06	3.49
3S134 50μm GM	59.65	24.71	0.51	0.01	6.03	7.45	0.42	0.09	98.87	30.10	67.38	2.52
3S137a core	55.65	27.10	0.47	0.03	9.35	6.04	0.17	0.01	98.82	45.65	53.38	0.97
3S137a rim	55.34	27.02	0.35	0.03	8.96	5.75	0.20	0.02	97.66	45.68	53.09	1.23
3S137b core	56.49	26.75	0.40	0.02	8.81	6.25	0.18	0.02	98.92	43.32	55.61	1.07
3S137b rim	57.36	26.33	0.48	0.01	8.37	6.65	0.31	0.05	99.55	40.28	57.95	1.77
3S137c core	56.34	26.99	0.35	0.01	9.20	6.08	0.20	0.03	99.20	45.02	53.81	1.18
3S137c rim	56.61	25.95	0.48	0.04	8.15	6.48	0.22	0.04	97.98	40.47	58.25	1.28
3S137 50μm acic GM	58.46	25.54	0.49	0.01	7.43	6.91	0.38	0.04	99.26	36.45	61.31	2.24
3S137 50μm acic GM	58.89	25.59	0.53	0.02	7.06	7.08	0.41	0.05	99.61	34.68	62.93	2.39
3S137 100μm acic	58.64	25.73	0.52	0.01	7.20	6.99	0.37	0.09	99.54	35.50	62.36	2.15
Lava Is. 1 core	62.81	23.28	0.19	0.00	4.72	8.22	0.56	0.05	99.83	23.30	73.43	3.27
Lava Is. 1 rim	62.19	22.19	0.21	0.00	4.11	8.90	0.62	0.14	98.35	19.60	76.85	3.55
Lava Is. 2 core	63.03	23.34	0.21	0.00	4.67	8.33	0.56	0.09	100.23	22.90	73.85	3.25
Lava Is. 2 rim	64.86	23.98	0.18	0.00	4.53	8.07	0.52	0.05	102.19	22.95	73.93	3.12

Appendix C-2: Compositions of pyroxenes determined by electron microprobe analysis. FeO and
Fe$_2$O$_3$, and mol percents wollastonite (Wo), enstatite (En) and ferrosilite (Fs) calculated with
standard CAMECA software. Groundmass crystals denoted by size with sample number.
Glom: glomerocryst; **edge:** analysis next to overgrowth rims.

	SiO2	TiO2	Al2O3	FeO	Fe2O3	MnO	MgO	CaO	Na2O	Cr2O3	TOTAL	Wo	En	Fs
3SXBPa core	51.31	0.42	1.18	10.25	1.61	0.49	13.85	19.43	0.30	0.00	98.84	41.26	40.92	17.82
3SXBPa rim	50.90	0.38	1.10	8.86	2.70	0.51	14.23	19.53	0.31	0.00	98.52	41.88	42.43	15.69
3SXBPb core	49.72	0.09	0.27	31.92	2.80	1.97	13.27	1.35	0.05	0.00	101.44	2.91	39.89	57.20
3SXBPb rim	49.07	0.10	0.22	31.78	2.24	1.98	12.97	1.29	0.05	0.00	99.70	2.83	39.47	57.70
3SXBPc core	49.97	0.14	0.29	32.56	0.67	1.90	13.27	1.24	0.03	0.03	100.09	2.66	39.61	57.73
3SXBPc rim	49.19	0.11	0.22	31.69	2.34	1.81	13.26	1.23	0.05	0.01	99.91	2.68	40.23	57.09
3SXBP	51.17	0.99	3.06	8.14	1.99	0.60	14.64	19.56	0.47	0.00	100.61	41.84	43.56	14.60
3SXBP	51.18	0.94	2.64	7.30	2.46	0.50	15.26	19.49	0.45	0.00	100.20	41.64	45.36	13.01
3S003a core	51.13	0.64	1.84	7.63	3.40	0.62	14.74	19.71	0.42	0.01	100.13	42.23	43.95	13.81
3S003a rim	51.88	0.42	1.07	6.98	3.55	0.59	15.78	19.62	0.34	0.00	100.22	41.31	46.24	12.45
3S003b core	51.60	0.47	1.28	9.16	1.89	0.75	14.55	19.12	0.39	0.03	99.21	40.60	42.98	16.42
3S003b rim	51.62	0.49	1.32	8.54	1.49	0.48	14.89	19.48	0.36	0.00	98.67	41.24	43.85	14.91
3S003c core	52.53	0.19	1.10	18.64	1.07	0.95	23.32	1.42	0.00	0.02	99.24	2.90	65.98	31.12
3S003c rim	52.11	0.26	0.55	14.59	4.67	0.93	25.22	1.49	0.03	0.00	99.86	3.06	72.05	24.89
3S003d core	52.37	0.25	0.64	19.28	1.28	1.17	22.68	1.48	0.01	0.00	99.18	3.02	64.38	32.60
3S003d rim	50.66	0.25	0.67	12.68	7.05	1.01	25.28	1.46	0.04	0.03	99.12	3.09	74.31	22.60
3S005a core	51.58	0.25	0.59	23.76	2.11	0.88	19.67	1.56	0.05	0.01	100.44	3.25	56.81	39.94
3S005a rim	52.56	0.22	0.61	25.96	0.00	0.94	18.74	1.51	0.03	0.00	100.56	3.10	53.66	43.24
3S005b core	51.25	0.21	0.40	24.78	2.20	0.99	18.89	1.47	0.03	0.00	100.21	3.06	54.91	42.03
3S005b rim	52.40	0.19	0.49	27.14	0.00	0.93	18.28	1.58	0.01	0.00	101.02	3.23	51.98	44.79
3S005c core	50.83	0.36	1.04	12.55	1.95	0.61	12.83	18.43	0.32	0.00	98.92	39.58	38.35	22.07
3S005c rim	51.47	0.35	0.96	13.66	0.00	0.48	12.41	18.78	0.24	0.00	98.35	39.88	36.67	23.45
3S005d core	50.68	0.39	1.18	12.15	1.85	0.60	12.79	18.85	0.27	0.04	98.81	40.45	38.18	21.37
3S005d rim	50.30	0.34	1.10	11.06	2.63	0.59	12.77	19.25	0.30	0.00	98.33	41.75	38.52	19.74
3S009a core	52.36	0.28	0.97	10.42	1.21	0.58	13.97	19.93	0.31	0.00	100.03	41.56	40.52	17.92
3S009a rim	52.16	0.27	1.10	10.26	1.40	0.55	13.87	20.00	0.32	0.05	99.98	41.90	40.41	17.69
3S009b core	51.71	0.52	1.69	10.33	1.27	0.45	13.67	19.89	0.36	0.01	99.90	42.03	40.17	17.80
3S009b rim	52.19	0.21	0.81	12.02	0.11	0.61	13.10	19.75	0.28	0.00	99.08	41.28	38.09	20.63
3S009c core	52.54	0.32	1.00	20.35	2.45	0.78	22.45	1.42	0.03	0.00	101.34	2.88	63.54	33.58
3S009c rim	52.67	0.16	0.49	24.74	0.23	0.98	19.89	1.42	0.03	0.02	100.63	2.89	56.27	40.84
3S017a core	50.59	0.95	3.27	7.82	1.99	0.39	14.45	20.00	0.38	0.03	99.87	42.99	43.22	13.78
3S017a rim	49.60	1.13	3.72	7.79	2.93	0.39	14.36	19.49	0.34	0.05	99.78	42.51	43.56	13.93
3S017b core	49.70	1.14	4.32	7.82	3.04	0.34	17.18	15.92	0.28	0.19	99.92	34.47	51.75	13.79
3S017b rim	48.86	1.21	4.86	8.79	2.68	0.33	15.19	17.14	0.29	0.05	99.40	37.76	46.54	15.70
3S017c core	50.87	0.77	3.13	7.26	1.54	0.20	14.96	20.27	0.31	0.10	99.40	43.22	44.37	12.41
3S017c rim	50.65	0.84	3.38	6.62	2.96	0.21	15.20	20.13	0.35	0.05	100.40	43.18	45.37	11.45
3S028 core	51.79	0.40	1.17	8.38	1.93	0.63	14.59	19.83	0.40	0.02	99.12	42.05	43.04	14.92
3S028a core	51.95	0.42	1.18	8.60	1.72	0.55	14.76	19.84	0.35	0.00	99.37	41.75	43.20	15.05
3S028a rim	49.87	0.47	1.34	5.40	6.04	0.59	15.34	19.33	0.42	0.01	98.82	42.62	47.06	10.32
3S028b core	50.83	0.64	1.93	9.26	1.84	0.64	14.23	19.00	0.38	0.01	98.75	40.84	42.55	16.62
3S028b rim	52.50	0.40	1.26	9.78	0.30	0.52	14.55	19.68	0.36	0.02	99.36	41.03	42.21	16.77
3S028c core	52.53	0.26	0.71	17.91	1.77	0.97	23.75	1.37	0.02	0.00	99.29	2.79	67.22	30.00
3S028c rim	51.97	0.27	0.69	14.64	5.01	0.90	25.12	1.45	0.04	0.02	100.12	2.99	72.00	25.01
3S030 20μm	52.22	0.78	0.92	12.44	0.18	0.40	14.15	18.31	0.35	0.05	99.79	38.13	41.00	20.87
3S030 30μm	51.72	0.69	1.93	9.11	0.84	0.30	15.92	18.18	0.30	0.09	99.06	38.13	46.46	15.41
3S030 GM 30μm	52.05	0.61	2.19	8.77	1.13	0.24	16.37	18.15	0.29	0.14	99.94	37.85	47.48	14.68
3S030 Ophitic	53.87	0.34	1.20	17.03	0.30	0.42	24.90	2.12	0.04	0.03	100.24	4.21	68.75	27.05
3S030a core	53.00	0.39	1.01	19.92	0.00	0.48	22.59	2.10	0.04	0.04	99.55	4.25	63.56	32.20
3S030a rim	51.46	0.21	0.13	28.28	0.00	0.84	16.83	1.56	0.04	0.06	99.40	3.26	49.08	47.66
3S036a core	53.21	0.40	1.23	17.61	1.30	0.67	24.34	1.62	0.05	0.03	100.46	3.26	68.05	28.69
3S036a rim	53.07	0.35	1.08	16.95	1.67	0.62	24.73	1.59	0.02	0.02	100.08	3.21	69.20	27.59
3S036 30μm	51.82	0.58	1.56	8.37	1.68	0.33	15.48	19.28	0.32	0.00	99.43	40.48	45.24	14.28
3S036 30μm	53.38	0.45	1.16	17.24	0.44	0.51	24.72	1.78	0.03	0.00	99.71	3.57	68.74	27.70
3S036 50μm	52.68	0.68	1.71	13.25	2.84	0.44	21.42	8.39	0.21	0.00	101.63	17.16	60.97	21.88
3S045 20μm	54.17	0.43	0.82	15.79	0.59	0.51	25.83	2.03	0.05	0.00	100.21	4.01	70.88	25.11
3S045a core	50.54	0.85	3.63	7.33	2.14	0.24	16.00	18.40	0.33	0.03	99.48	39.51	47.81	12.68
3S045a rim	51.23	0.82	3.06	10.54	0.00	0.30	14.47	17.45	0.47	0.03	98.36	37.90	43.71	18.39
3S045b core	52.88	0.49	1.48	10.27	0.00	0.46	14.53	19.47	0.33	0.00	99.90	40.50	42.06	17.44
3S045b rim	51.69	0.80	2.34	10.63	0.00	0.46	14.18	19.05	0.33	0.04	99.51	40.17	41.58	18.25
3S049 50μm	52.35	0.60	1.81	7.98	0.16	0.22	16.77	18.81	0.21	0.23	99.14	38.75	48.07	13.18
3S049 30μm	48.48	1.52	4.10	1.38	6.56	0.46	15.64	20.56	0.71	0.05	99.46	46.99	49.72	3.29
3S049a core	50.65	0.82	3.50	6.07	1.45	0.20	15.77	19.74	0.36	0.49	99.05	42.39	47.11	10.50

	SiO2	TiO2	Al2O3	FeO	Fe2O3	MnO	MgO	CaO	Na2O	Cr2O3	TOTAL	Wo	En	Fs
3S049a rim	50.49	0.91	3.75	6.02	1.04	0.23	15.23	20.52	0.33	0.35	98.87	44.05	45.48	10.47
3S049b core	50.27	0.66	4.35	4.52	2.02	0.20	16.11	20.00	0.36	0.79	99.28	43.37	48.63	8.00
3S049b rim	51.94	0.48	2.96	6.00	0.71	0.21	17.44	18.34	0.38	0.25	98.71	38.66	51.12	10.22
3S058 50μm	51.65	0.13	0.46	25.17	0.49	1.03	19.18	1.08	0.02	0.00	99.21	2.23	55.34	42.43
3S058a core	52.68	0.11	0.33	24.86	0.00	1.24	19.04	0.86	0.01	0.00	99.13	1.80	55.50	42.70
3S058a rim	52.43	0.12	0.39	24.43	0.00	1.17	20.01	0.92	0.01	0.02	99.50	1.88	57.11	41.01
3S061 glom	51.52	0.69	2.22	7.23	1.89	0.36	15.25	21.19	0.35	0.00	100.70	42.66	44.82	12.52
3S061 glom	53.75	0.21	0.63	18.46	0.00	0.65	24.10	1.52	0.03	0.04	99.39	3.03	67.11	29.86
3S061 glom	53.88	0.24	0.81	16.41	1.93	0.71	25.66	1.39	0.00	0.00	101.03	2.76	70.74	26.50
3S061a core	54.37	0.27	0.63	16.52	0.83	0.52	25.76	1.63	0.05	0.00	100.58	3.21	70.58	26.21
3S061a rim	53.78	0.27	0.98	16.73	0.72	0.62	25.40	1.34	0.05	0.00	99.89	2.67	70.36	26.97
3S061b core	51.54	0.69	2.48	9.16	0.22	0.29	15.09	19.11	0.31	0.00	98.89	40.24	44.22	15.54
3S061b rim	51.67	0.40	0.37	23.66	0.36	1.06	17.95	3.93	0.08	0.00	99.48	8.15	51.80	40.05
3S061b by rim	52.30	0.52	1.67	7.34	1.62	0.37	15.47	20.42	0.34	0.00	100.05	42.58	44.87	12.55
3S061c core	52.85	0.38	1.41	17.65	1.01	0.57	24.03	1.80	0.04	0.01	99.75	3.64	67.61	28.76
3S061c rim	53.63	0.29	0.93	16.45	1.33	0.51	25.52	1.40	0.03	0.00	100.09	2.79	70.80	26.41
3S074 50μm	53.20	0.21	0.34	20.29	0.92	0.73	22.51	1.86	0.06	0.00	100.11	3.75	63.16	33.10
3S074a core	51.44	0.81	2.66	7.42	1.39	0.25	15.37	20.00	0.34	0.00	99.67	42.22	45.14	12.64
3S074a rim	48.99	1.20	5.02	6.65	2.77	0.27	14.79	19.45	0.32	0.05	99.49	42.82	45.29	11.90
3S074b core	50.91	0.94	3.05	7.65	1.73	0.39	15.16	19.41	0.39	0.02	99.65	41.50	45.08	13.42
3S074b rim	50.42	0.96	4.14	6.15	1.94	0.22	15.29	20.50	0.28	0.38	100.26	43.86	45.51	10.64
3S079a core	53.33	0.46	1.65	17.08	1.22	0.72	24.45	2.06	0.03	0.00	100.99	4.12	68.06	27.82
3S079a rim	54.47	0.39	1.27	15.23	2.46	0.59	26.63	1.53	0.05	0.00	102.63	3.01	72.73	24.26
3S079b core	52.26	0.63	2.02	9.62	1.68	0.64	14.58	19.51	0.39	0.04	101.37	40.81	42.43	16.76
3S079b rim	51.58	0.47	1.35	6.89	3.57	0.62	15.12	20.16	0.39	0.05	100.20	42.84	44.69	12.47
3S079c core	53.46	0.45	1.22	9.68	0.06	0.53	14.87	20.43	0.31	0.07	101.07	41.61	42.15	16.24
3S079c rim	52.43	0.42	1.13	7.54	3.30	0.65	15.44	19.98	0.38	0.00	101.28	41.75	44.89	13.37
3S079d core	53.45	0.29	0.65	20.25	1.31	1.10	22.79	1.54	0.05	0.00	101.43	3.08	63.52	33.40
3S079d rim	53.48	0.31	0.66	20.66	0.17	1.12	22.69	1.44	0.03	0.00	100.54	2.88	63.11	34.01
3S090 20μm	50.27	1.18	3.10	10.23	1.59	0.38	15.04	17.38	0.32	0.01	99.49	37.31	44.92	17.77
3S090a core	53.32	0.46	2.16	14.88	1.70	0.41	26.14	1.69	0.03	0.02	100.80	3.39	72.75	23.87
3S090a rim	53.88	0.34	0.81	17.04	1.30	0.55	24.97	1.84	0.06	0.00	100.78	3.66	69.04	27.30
3S090b glom	50.60	1.04	3.54	7.61	2.04	0.31	15.08	19.49	0.36	0.03	100.11	41.77	44.97	13.27
3S090b rim	50.14	1.09	3.37	7.94	1.56	0.29	14.55	19.57	0.36	0.03	98.90	42.33	43.78	13.89
3S090c core	52.47	0.50	1.77	8.08	0.70	0.26	14.96	20.79	0.33	0.01	99.86	43.20	43.26	13.54
3S090c rim	49.21	1.06	4.02	7.43	3.70	0.26	14.35	19.45	0.35	0.08	99.90	42.83	43.96	13.21
3S098	52.01	0.20	0.64	14.51	0.78	0.87	11.69	19.40	0.28	0.01	100.38	40.70	34.11	25.90
3S098 glom	51.20	0.23	0.46	27.13	0.13	1.30	17.27	1.60	0.04	0.00	99.34	3.34	50.23	46.43
3S098a core	51.16	0.23	0.40	29.04	0.20	1.28	16.12	1.63	0.05	0.00	100.11	3.42	46.98	49.60
3S098a rim	51.37	0.21	0.33	28.49	0.00	1.24	16.60	1.52	0.06	0.06	99.87	3.17	48.28	48.55
3S098b core	51.38	0.18	0.38	27.11	0.69	1.25	17.48	1.49	0.03	0.05	100.04	3.11	50.71	46.18
3S098b rim	51.02	0.20	0.40	28.56	0.30	1.40	16.11	1.85	0.03	0.00	99.88	3.88	47.03	49.09
3S098c core	51.43	0.35	0.88	13.57	1.06	0.70	11.98	19.26	0.32	0.02	99.58	40.92	35.41	23.67
3S098c rim	51.95	0.26	0.62	14.41	0.35	0.71	11.79	19.33	0.31	0.00	99.73	40.66	34.49	24.84
3S112	54.35	0.29	0.89	17.03	0.96	0.47	25.40	1.80	0.04	0.00	101.23	3.54	69.56	26.89
3S112a core	52.07	0.72	1.97	9.91	1.12	0.32	15.69	17.98	0.36	0.04	100.18	37.61	45.68	16.72
3S112a rim	51.52	0.87	1.32	13.25	0.44	0.36	14.36	17.12	0.27	0.06	99.55	35.88	41.86	22.26
3S112b core	51.30	0.78	2.23	9.02	1.62	0.34	14.98	18.91	0.38	0.00	99.56	40.18	44.29	15.53
3S112b edge	51.59	0.66	2.14	9.38	0.85	0.33	15.75	18.08	0.29	0.14	99.19	38.02	46.05	15.93
3S112b rim	52.88	0.75	3.12	13.08	0.00	0.39	12.73	16.77	0.78	0.03	100.53	37.27	39.36	23.37
3S112c core	53.50	0.37	1.08	17.45	1.15	0.66	24.70	1.63	0.02	0.00	100.55	3.25	68.55	28.20
3S112c rim	52.14	0.54	0.53	23.38	0.44	0.63	20.25	1.92	0.06	0.00	99.89	3.93	57.69	38.39
3S112d core	53.88	0.30	0.86	17.04	1.48	0.51	25.04	1.89	0.02	0.02	101.03	3.75	69.08	27.17
3S112d rim	52.22	0.62	0.85	20.15	0.00	0.59	18.11	7.14	0.12	0.03	99.82	14.71	51.92	33.37
3S112e core	52.57	0.54	1.39	9.14	0.43	0.38	16.15	18.49	0.29	0.02	99.38	38.21	46.42	15.37
3S112e rim	51.69	0.72	2.40	7.99	0.90	0.25	15.65	19.46	0.30	0.12	99.47	40.83	45.68	13.49
3S112f core	54.03	0.39	1.15	17.22	0.00	0.43	25.15	1.86	0.01	0.00	100.25	3.67	69.11	27.22
3S112f rim	53.38	0.38	0.96	17.03	1.20	0.53	24.68	1.88	0.05	0.04	100.12	3.76	68.78	27.46
3S114 glomo	52.26	0.15	0.89	20.93	1.36	0.88	21.33	2.01	0.05	0.08	99.94	4.12	60.92	34.96
3S114 gm	52.66	0.14	0.50	23.37	0.00	0.98	20.96	1.03	0.00	0.00	99.64	2.10	59.26	38.64
3S114a core	52.34	0.10	0.36	24.21	0.59	1.13	20.18	0.89	0.05	0.00	99.85	1.83	57.58	40.59
3S114a rim	52.35	0.17	0.70	22.08	0.00	0.76	21.28	0.99	0.01	0.00	98.34	2.05	61.15	36.83
3S115 50μm	52.76	0.48	1.06	20.86	0.00	0.72	22.19	1.78	0.01	0.01	99.86	3.60	62.37	34.04
3S115a core	53.49	0.35	1.23	18.56	1.43	0.74	24.07	1.47	0.04	0.00	101.38	2.94	66.93	30.13
3S115a rim	53.94	0.32	0.98	18.36	0.34	0.52	24.68	1.37	0.04	0.04	100.58	2.72	68.07	29.22
3S115b core	52.11	0.70	1.81	9.76	0.39	0.44	14.82	19.38	0.32	0.00	99.73	40.40	42.99	16.61
3S115b rim	52.44	0.64	1.65	9.71	0.74	0.33	15.09	19.29	0.35	0.00	100.22	40.08	43.63	16.29
3S115c core	52.51	0.66	1.81	9.54	0.88	0.45	15.14	19.38	0.34	0.03	100.73	40.17	43.66	16.18
3S115c rim	52.24	0.36	0.40	23.26	0.00	0.99	18.26	3.99	0.10	0.04	99.62	8.25	52.57	39.18
3S122 50μm	51.10	0.16	1.06	25.49	0.89	1.09	18.68	1.01	0.02	0.00	99.50	2.11	54.41	43.48

	SiO2	TiO2	Al2O3	FeO	Fe2O3	MnO	MgO	CaO	Na2O	Cr2O3	TOTAL	Wo	En	Fs
3S122a core	51.07	0.10	0.37	26.00	0.00	1.37	18.01	1.04	0.03	0.02	98.01	2.19	52.78	45.03
3S122a rim	52.64	0.09	0.93	21.66	0.26	0.82	21.99	1.03	0.01	0.02	99.45	2.10	62.21	35.70
3S123 glom	53.72	0.33	1.00	18.08	0.70	0.64	24.46	1.56	0.05	0.00	100.53	3.12	67.78	29.11
3S123 core	51.31	0.67	2.23	7.45	2.04	0.34	14.95	20.40	0.30	0.00	99.67	43.15	43.99	12.86
3S123 50µm	51.96	0.57	1.76	8.39	1.54	0.38	15.11	19.80	0.34	0.00	99.84	41.54	44.10	14.36
3S123 50µm	53.76	0.30	0.63	18.59	0.68	0.57	24.11	1.75	0.04	0.00	100.43	3.49	66.75	29.77
3S123 glom	52.02	0.70	1.92	8.79	0.99	0.34	14.84	20.25	0.28	0.03	100.15	42.17	42.99	14.84
3S123a core	53.50	0.33	0.94	17.39	1.83	0.54	24.74	1.72	0.01	0.00	101.00	3.43	68.64	27.93
3S123a rim	53.58	0.36	1.08	18.41	1.07	0.52	24.31	1.61	0.01	0.02	100.99	3.21	67.36	29.44
3S123b core	52.07	0.56	1.76	8.43	1.32	0.32	15.02	20.06	0.33	0.01	99.88	41.97	43.73	14.30
3S123b rim	51.89	0.58	1.67	8.17	1.73	0.40	15.02	20.23	0.28	0.02	99.99	42.30	43.70	14.00
3S131 20µm	51.83	0.53	0.78	20.96	0.00	0.58	19.09	5.03	0.07	0.06	98.93	10.39	54.86	34.75
3S131 50µm	52.77	0.48	0.76	19.94	0.05	0.53	21.17	3.92	0.07	0.01	99.68	7.94	59.68	32.38
3S131 50µm	52.32	0.35	0.44	22.52	0.76	0.62	19.18	4.19	0.04	0.01	100.43	8.56	54.52	36.92
3S131a core	50.03	1.04	3.96	6.73	2.51	0.20	14.57	20.54	0.33	0.02	99.93	44.44	43.85	11.72
3S131a rim	51.80	0.70	1.49	11.03	1.12	0.36	15.61	17.38	0.24	0.02	99.75	36.22	45.25	18.54
3S131a rim	51.37	0.97	1.45	13.14	0.00	0.39	14.11	17.31	0.31	0.00	99.05	36.44	41.33	22.23
3S131b core	50.60	0.97	3.70	7.49	1.25	0.27	14.69	20.37	0.29	0.09	99.70	43.47	43.62	12.92
3S131b rim	51.49	0.89	1.25	14.41	0.13	0.47	13.36	17.45	0.29	0.00	99.74	36.62	39.00	24.38
3S134 core	51.65	0.35	1.19	13.36	0.93	0.74	12.80	18.57	0.30	0.02	99.90	39.19	37.57	23.24
3S134 50µm	51.70	0.24	0.55	26.51	0.01	1.10	18.15	1.58	0.01	0.02	99.86	3.27	52.17	44.56
3S134a core	51.42	0.19	0.45	26.04	0.33	1.16	18.09	1.63	0.02	0.00	99.33	3.38	52.40	44.22
3S134a rim	52.16	0.33	0.88	24.05	0.23	0.97	19.80	1.65	0.05	0.00	100.12	3.39	56.51	40.10
3S134b core	51.15	0.31	0.75	28.30	0.37	1.16	16.64	1.66	0.04	0.00	100.37	3.47	48.41	48.12
3S134b rim	51.55	0.21	0.67	26.72	0.06	1.22	17.73	1.61	0.05	0.00	99.81	3.34	51.29	45.37
3S134c glom	51.98	0.32	1.03	14.03	0.00	0.66	12.50	18.62	0.29	0.00	99.41	39.22	36.62	24.16
3S134c rim	51.15	0.41	1.37	13.28	0.95	0.78	12.38	18.60	0.34	0.01	99.26	39.74	36.79	23.47
3S134d core	51.89	0.37	0.90	25.34	0.88	0.93	19.07	1.48	0.05	0.01	100.92	3.06	54.67	42.28
3S134d rim	51.40	0.22	0.62	26.23	0.27	1.13	17.92	1.61	0.06	0.00	99.46	3.35	52.04	44.61
3S137 core	52.30	0.34	1.47	20.38	1.22	0.80	22.11	1.65	0.03	0.00	100.30	3.36	62.84	33.80
3S137a core	51.32	0.52	1.53	8.60	2.79	0.50	14.37	19.96	0.34	0.01	99.93	42.41	42.48	15.10
3S137a edge	51.48	0.52	1.80	9.87	1.67	0.50	13.70	19.78	0.41	0.00	99.73	42.14	40.60	17.26
3S137a rim	52.17	0.27	0.89	21.70	1.09	0.81	21.24	1.65	0.03	0.01	99.85	3.37	60.59	36.04
LI-A core	50.55	0.13	0.22	34.03	0.33	1.91	12.79	1.37	0.01	0.00	101.33	2.89	37.68	59.43
LI-A edge	49.53	0.12	0.30	31.26	3.28	2.14	13.45	1.41	0.03	0.07	101.58	3.06	40.48	56.47
LI-a rim	49.75	0.04	0.22	23.88	1.37	3.52	7.22	14.52	0.14	0.00	100.63	31.58	21.83	46.59
LI-B edge	49.76	0.09	0.39	32.55	1.68	1.88	12.99	1.45	0.02	0.01	100.84	3.13	38.94	57.93
LI-b rim	49.56	0.11	0.67	20.23	2.31	2.50	6.87	17.86	0.32	0.04	100.47	39.53	21.15	39.32
LI-C core	52.57	0.30	0.88	11.23	1.48	0.78	14.28	18.67	0.38	0.00	100.56	38.97	41.46	19.57
LI-c rim	52.12	0.33	0.96	10.38	1.61	0.66	14.02	19.29	0.40	0.00	99.77	40.69	41.14	18.18

Appendix C-3: Composition of amphiboles determined through electron microprobe analysis. Capitol letter suffix on sample number indicates analysis was from the core of the crystal, lower case suffix indicates rim was analyzed. Size of the crystal is approximate. Iron partitioning and cation abundances determined through program AMPREC.FOR (Spear and Kimball, 1984), using the "average Fe" algorithm. Water calculated on the basis of 2(OH, F, Cl) and 15 cations; F and Cl abundances by microprobe analysis. BP samples from the top (t), base (b) or lower reworked zone (l) of the Bend Pumice (Hill, 1985), whole rock analysis 3SXBP in appendix D-1.

	3S009	3S053A	3S053a	3S053B	3S053b	3S053C	3S053c	3S053D	3S053E	3S060A	3S060a	3S060B	3S060C	3S060c	3S060D	3S060d	3S060E
Wt. %	$100\mu m$	$250\mu m$	rim	$100\mu m$	rim	$200\mu m$	rim	$100\mu m$	$50\mu m$	$250\mu m$	rim	$200\mu m$	$250\mu m$	rim	$>250\mu m$	rim	$200\mu m$
SiO_2	43.18	44.18	43.45	47.80	47.29	44.67	44.22	46.01	45.52	42.68	41.41	43.23	42.49	42.79	47.99	48.08	47.23
TiO_2	2.76	1.47	1.81	1.30	1.98	2.08	2.17	2.18	1.89	3.17	3.78	3.34	3.38	2.79	1.13	1.20	1.63
Al_2O_3	9.19	9.94	9.28	5.57	8.03	9.40	9.85	7.76	7.92	11.77	11.51	10.37	10.62	10.64	5.99	5.96	6.98
FeO	12.32	12.74	10.19	14.74	15.77	12.93	12.06	11.52	11.52	11.61	8.73	8.95	9.12	8.07	12.22	12.10	11.23
Fe_2O_3	4.32	3.32	6.10	2.45	0.00	1.25	1.66	4.50	5.23	0.97	5.70	5.13	5.22	6.23	4.77	4.48	5.35
FeO^*	16.21	15.73	15.68	16.95	15.77	14.05	13.55	15.57	16.22	12.48	13.86	13.57	13.82	13.68	16.52	16.13	16.05
MnO	0.32	0.33	0.20	0.48	0.28	0.19	0.18	0.25	0.37	0.16	0.19	0.19	0.23	0.28	0.60	0.55	0.32
MgO	11.98	13.10	13.71	13.48	13.12	13.73	14.11	13.21	13.12	13.81	13.28	13.89	13.74	13.96	13.99	14.09	13.34
CaO	10.32	10.77	10.94	10.87	10.71	10.73	10.66	10.91	10.73	11.24	11.20	11.13	11.17	11.35	10.33	10.39	10.90
Na_2O	2.30	1.57	1.81	0.98	1.56	1.60	1.67	1.49	1.45	1.89	2.01	1.94	1.90	2.02	0.95	1.04	1.10
K_2O	0.44	0.34	0.43	0.74	0.41	0.29	0.30	0.39	0.36	0.43	0.36	0.37	0.41	0.40	0.29	0.30	0.44
H_2O	1.68	1.74	1.88	1.96	1.92	1.91	1.90	1.85	1.71	1.92	1.93	1.95	1.91	1.97	2.00	1.96	1.96
F	0.59	0.54	0.21	0.04	0.24	0.21	0.25	0.34	0.60	0.24	0.17	0.17	0.22	0.10	0.00	0.12	0.12
Cl	0.07	0.09	0.08	0.19	0.09	0.05	0.02	0.06	0.07	0.02	0.01	0.03	0.01	0.03	0.12	0.07	0.07
Total	99.47	100.14	100.10	100.59	101.41	99.02	99.03	100.47	100.49	99.90	100.29	100.68	100.42	100.63	100.37	100.33	100.67
Cations																	
Si	6.46	6.53	6.42	7.04	6.89	6.62	6.54	6.74	6.69	6.27	6.08	6.29	6.22	6.24	7.01	7.02	6.88
Ti	0.31	0.16	0.20	0.14	0.22	0.23	0.24	0.24	0.21	0.35	0.42	0.37	0.37	0.31	0.12	0.13	0.18
Aliv	1.54	1.47	1.58	0.96	1.12	1.38	1.46	1.26	1.31	1.73	1.92	1.71	1.78	1.76	0.99	0.98	1.12
Alvi	0.09	0.26	0.03	0.01	0.26	0.27	0.26	0.08	0.07	0.31	0.07	0.07	0.05	0.07	0.04	0.05	0.08
Fe^{2+}	1.54	1.57	1.27	1.81	1.92	1.61	1.50	1.41	1.41	1.43	1.07	1.09	1.12	0.98	1.49	1.47	1.37
Fe^{3+}	0.49	0.37	0.67	0.28	0.00	0.14	0.18	0.50	0.59	0.11	0.64	0.56	0.57	0.69	0.53	0.50	0.59
Mn	0.04	0.04	0.03	0.06	0.04	0.02	0.02	0.03	0.05	0.02	0.02	0.02	0.03	0.04	0.07	0.07	0.04
Mg	2.67	2.89	3.02	2.96	2.85	3.03	3.11	2.88	2.88	3.02	2.90	3.01	3.00	3.03	3.05	3.07	2.90
Ca	1.66	1.71	1.73	1.72	1.67	1.70	1.69	1.71	1.69	1.77	1.76	1.74	1.75	1.77	1.62	1.63	1.70
Na(M4)	0.21	0.00	0.06	0.02	0.05	0.00	0.00	0.15	0.12	0.00	0.13	0.14	0.10	0.12	0.08	0.09	0.15
Na(A)	0.67	0.45	0.46	0.26	0.39	0.46	0.48	0.28	0.29	0.54	0.45	0.41	0.44	0.45	0.19	0.21	0.16
K	0.08	0.06	0.08	0.14	0.08	0.06	0.06	0.07	0.07	0.08	0.07	0.07	0.08	0.07	0.05	0.06	0.05
OH	1.70	1.73	1.88	1.93	1.87	1.89	1.88	1.83	1.70	1.88	1.92	1.91	1.90	1.95	1.97	1.93	1.93
Cl	0.02	0.02	0.02	0.05	0.02	0.01	0.01	0.02	0.02	0.01	0.00	0.01	0.00	0.01	0.03	0.02	0.02
F	0.28	0.25	0.10	0.02	0.11	0.10	0.12	0.16	0.28	0.11	0.08	0.08	0.10	0.05	0.00	0.06	0.06

Wt. %	3S090 glom	3S090a glom	3S090a 2nd pt	BPtA 250µm	BPta rim	BPtB >250µm	BPtb rim	BPtC 200µm	BPtc rim	BPtD 150µm	BPtd rim	BPbA 250µm	BPba rim	BPbB 200µm	BPbb rim	BPbC 250µm	BPbc rim
SiO2	41.45	42.21	42.72	43.17	42.54	42.10	41.35	42.15	43.20	41.42	41.35	41.70	42.18	41.71	42.47	41.64	40.55
TiO2	3.72	3.88	3.75	2.60	3.15	3.52	3.34	3.29	3.13	3.20	3.29	3.86	3.45	3.02	2.63	3.03	3.53
Al2O3	10.86	11.00	10.78	8.58	9.03	9.39	9.34	10.00	10.05	9.75	9.65	10.53	10.07	9.70	8.99	9.36	9.74
FeO	8.08	8.26	12.05	19.81	21.31	19.21	19.03	15.92	19.14	18.25	17.51	14.22	14.34	20.01	19.62	19.44	22.40
Fe2O3	4.03	3.93	0.00	3.00	3.54	2.37	2.61	3.62	0.00	3.30	3.71	3.95	4.24	4.24	4.15	4.12	3.08
FeO*	11.70	11.80	12.05	22.51	24.50	21.35	21.39	19.18	19.14	21.22	20.85	17.78	18.15	23.83	23.36	23.14	25.16
MnO	0.16	0.23	0.13	0.71	0.70	0.59	0.72	0.52	0.52	0.64	0.71	0.37	0.51	0.80	0.72	0.70	0.75
MgO	14.47	14.47	14.22	9.25	7.40	9.28	8.91	10.81	10.06	9.16	8.89	10.83	10.84	7.78	8.54	7.54	6.13
CaO	10.96	10.90	11.05	9.67	9.44	9.81	9.71	10.17	10.06	9.93	9.79	10.30	10.11	9.34	9.39	9.69	9.69
Na2O	2.27	2.50	2.50	2.02	2.13	2.17	2.10	2.22	2.07	2.31	2.13	2.26	2.12	2.19	1.96	2.16	2.21
K2O	0.32	0.35	0.35	0.40	0.37	0.32	0.33	0.29	0.28	0.32	0.34	0.32	0.28	0.31	0.31	0.35	0.38
H2O	1.93	2.02	1.96	1.92	1.89	1.89	1.80	1.88	1.77	1.94	1.93	1.87	1.79	1.83	1.88	1.82	1.88
F	0.14	0.00	0.13	0.08	0.10	0.14	0.26	0.21	0.46	0.00	0.00	0.24	0.39	0.22	0.13	0.22	0.05
Cl	0.03	0.03	0.04	0.08	0.08	0.06	0.06	0.04	0.05	0.05	0.05	0.01	0.03	0.07	0.07	0.03	0.07
Total	98.40	99.78	99.69	101.29	101.70	100.85	99.56	101.10	100.79	100.26	99.32	100.47	100.32	101.21	100.85	100.08	100.45

Cations

	3S090 glom	3S090a glom	3S090a 2nd pt	BPtA 250µm	BPta rim	BPtB >250µm	BPtb rim	BPtC 200µm	BPtc rim	BPtD 150µm	BPtd rim	BPbA 250µm	BPba rim	BPbB 200µm	BPbb rim	BPbC 250µm	BPbc rim
Si	6.16	6.18	6.29	6.52	6.45	6.37	6.35	6.29	6.48	6.31	6.33	6.23	6.31	6.34	6.45	6.39	6.29
Ti	0.42	0.43	0.42	0.30	0.36	0.40	0.39	0.37	0.35	0.37	0.38	0.43	0.39	0.35	0.30	0.35	0.41
Al iv	1.84	1.82	1.70	1.48	1.55	1.63	1.65	1.71	1.52	1.70	1.67	1.78	1.69	1.66	1.55	1.61	1.72
Al vi	0.06	0.08	0.17	0.04	0.07	0.05	0.05	0.05	0.26	0.05	0.08	0.08	0.08	0.08	0.06	0.09	0.06
Fe2+	1.00	1.01	1.49	2.50	2.72	2.44	2.44	1.99	2.40	2.34	2.24	1.77	1.79	2.55	2.49	2.48	2.89
Fe3+	0.46	0.44	0.00	0.35	0.39	0.27	0.31	0.41	0.00	0.37	0.43	0.45	0.48	0.49	0.48	0.49	0.37
Mn	0.02	0.03	0.02	0.09	0.09	0.08	0.09	0.07	0.07	0.08	0.09	0.05	0.07	0.10	0.09	0.09	0.10
Mg	3.20	3.16	3.12	2.08	1.67	2.09	2.04	2.10	2.25	2.08	2.03	2.41	2.42	1.76	1.93	1.73	1.42
Ca	1.74	1.71	1.75	1.56	1.53	1.59	1.60	1.63	1.62	1.62	1.61	1.65	1.62	1.52	1.53	1.59	1.61
Na(M4)	0.11	0.16	0.04	0.08	0.17	0.09	0.09	0.09	0.05	0.10	0.15	0.17	0.16	0.15	0.12	0.19	0.14
Na(A)	0.55	0.55	0.67	0.51	0.46	0.55	0.54	0.55	0.55	0.58	0.49	0.49	0.46	0.49	0.46	0.46	0.52
K	0.06	0.07	0.07	0.07	0.07	0.06	0.07	0.06	0.05	0.06	0.07	0.06	0.05	0.05	0.06	0.07	0.08
OH	1.93	1.99	1.93	1.94	1.93	1.92	1.86	1.89	1.77	1.99	1.99	1.88	1.81	1.88	1.92	1.89	1.96
Cl	0.01	0.01	0.01	0.02	0.02	0.02	0.02	0.01	0.01	0.01	0.01	0.01	0.01	0.02	0.02	0.01	0.02
F	0.07	0.00	0.06	0.04	0.05	0.07	0.13	0.10	0.22	0.00	0.00	0.11	0.18	0.11	0.06	0.11	0.03

Wt. %	BPbD >250µm	BPbd rim	BPbE 100µm	BPlA >250µm	BPla rim	BPlB >250µm	BPlb rim	BPlC 250µm	BPlc rim	LIA 200µm	LIa rim	LIB 250µm	LIb rim	LIC 200µm	LIc rim
SiO2	41.54	42.25	41.71	41.90	42.31	42.23	41.50	42.42	40.04	42.03	42.50	42.30	42.86	41.90	41.35
TiO2	3.85	3.50	2.96	2.97	2.92	3.03	2.80	2.98	3.32	2.73	2.76	3.23	2.75	3.33	3.47
Al2O3	10.29	10.22	9.44	9.17	8.78	8.60	8.70	8.79	9.88	8.61	9.23	9.28	9.81	9.86	10.07
FeO	14.95	13.38	20.70	19.12	19.65	22.86	21.89	20.66	20.10	21.10	18.92	17.33	19.82	17.00	16.55
Fe2O3	3.16	4.44	3.44	3.46	2.70	2.21	3.01	2.55	4.25	2.61	5.26	2.63	0.00	3.87	4.60
FeO*	17.80	17.38	23.79	22.24	22.08	24.85	24.59	22.95	23.92	23.45	23.65	19.70	19.82	20.48	20.69
MnO	0.51	0.40	0.75	0.75	0.65	0.74	0.93	0.73	0.78	0.81	0.69	0.67	0.58	0.57	0.46
MgO	10.85	11.05	7.94	8.32	8.70	7.69	7.08	8.74	6.31	8.21	7.75	10.28	9.98	9.36	8.85
CaO	10.35	10.40	9.53	9.94	9.76	9.18	9.43	9.42	9.63	9.80	9.16	10.06	9.85	9.99	9.99
Na2O	2.19	2.22	2.22	2.06	2.21	2.08	1.97	2.12	2.25	2.04	2.18	2.19	2.12	2.27	2.13
K2O	0.32	0.36	0.33	0.35	0.28	0.30	0.35	0.30	0.35	0.38	0.32	0.30	0.32	0.29	0.32
H2O	1.84	1.73	1.82	1.85	1.69	1.87	1.83	1.86	1.86	1.85	1.88	1.83	1.85	1.82	1.76
F	0.27	0.52	0.24	0.17	0.49	0.14	0.13	0.18	0.03	0.14	0.10	0.29	0.26	0.28	0.38
Cl	0.04	0.05	0.05	0.06	0.09	0.05	0.08	0.05	0.08	0.08	0.08	0.04	0.04	0.05	0.04
Total	100.17	100.52	101.12	100.10	100.21	100.97	99.70	100.80	98.90	100.37	100.83	100.42	100.23	100.59	99.96

Cations

Si	6.24	6.29	6.36	6.41	6.47	6.48	6.45	6.46	6.26	6.46	6.45	6.39	6.49	6.34	6.29
Ti	0.44	0.39	0.34	0.34	0.34	0.35	0.33	0.34	0.39	0.32	0.32	0.37	0.31	0.38	0.40
Aliv	1.76	1.71	1.64	1.59	1.53	1.52	1.55	1.54	1.73	1.54	1.55	1.61	1.51	1.68	1.71
Alvi	0.06	0.09	0.06	0.07	0.06	0.03	0.05	0.04	0.09	0.02	0.10	0.04	0.24	0.08	0.09
Fe2+	1.88	1.66	2.64	2.44	2.50	2.95	2.84	2.64	2.62	2.73	2.40	2.20	2.51	2.13	2.11
Fe3+	0.36	0.51	0.40	0.41	0.32	0.24	0.36	0.28	0.51	0.29	0.60	0.29	0.00	0.45	0.52
Mn	0.07	0.05	0.10	0.10	0.08	0.10	0.12	0.09	0.10	0.11	0.09	0.09	0.07	0.08	0.06
Mg	2.43	2.45	1.81	1.90	1.98	1.76	1.64	1.98	1.47	1.88	1.75	2.31	2.25	2.11	2.01
Ca	1.67	1.55	1.56	1.63	1.60	1.51	1.57	1.54	1.62	1.62	1.49	1.63	1.60	1.62	1.63
Na(M4)	0.11	0.19	0.11	0.12	0.12	0.06	0.09	0.08	0.20	0.04	0.25	0.08	0.02	0.17	0.19
Na(A)	0.53	0.45	0.55	0.49	0.54	0.55	0.50	0.55	0.48	0.56	0.40	0.57	0.61	0.50	0.44
K	0.06	0.07	0.06	0.07	0.06	0.06	0.07	0.06	0.07	0.08	0.06	0.06	0.06	0.06	0.06
OH	1.86	1.74	1.87	1.90	1.74	1.92	1.92	1.90	1.96	1.91	1.93	1.85	1.87	1.85	1.81
Cl	0.01	0.01	0.01	0.02	0.02	0.01	0.02	0.01	0.02	0.02	0.02	0.01	0.01	0.01	0.01
F	0.13	0.25	0.12	0.08	0.24	0.07	0.06	0.09	0.02	0.07	0.05	0.14	0.12	0.13	0.18

Appendix C-4: Composition of spinels determined through microprobe analysis. FeO, Fe$_2$O$_3$, and mol fraction ülvospinel (XŪsp) calculated using the method of Carmichael (1967). **Xlvd:** sample had visible exsolution lamallae.

	SiO2	TiO2	Al2O3	FeO	Fe2O3	MnO	MgO	Cr2O3	TOTAL	XŪsp
3SXBP	0.10	14.53	1.21	42.48	38.56	0.83	0.57	0.00	98.28	42.4
3SXBP	0.05	14.08	1.21	43.01	41.10	0.82	0.46	0.00	100.73	39.9
3SXBP 150μm	0.14	14.66	1.28	43.43	39.63	0.83	0.50	0.13	100.59	42.0
3SXBP 200μm	0.11	14.42	1.35	43.24	40.31	0.93	0.50	0.11	100.97	41.0
3SXBP 150μm	0.10	14.66	1.29	43.50	39.66	0.75	0.50	0.07	100.52	41.8
3SXBP 40μm	0.09	14.48	1.25	43.39	40.17	0.83	0.44	0.06	100.70	41.2
3SXBP 150μm	0.12	14.52	1.19	43.50	40.39	0.68	0.53	0.02	100.94	41.4
3SXBP 50μm	0.10	16.70	2.41	43.55	34.94	0.87	1.72	0.07	100.36	46.8
3S003	0.08	13.67	2.89	40.65	40.89	0.48	2.19	0.04	100.89	38.0
3S003	0.05	14.23	2.75	40.71	40.21	0.63	2.42	0.06	101.05	39.2
3S005 xlvd	0.10	12.74	1.90	40.45	41.66	0.64	1.08	0.06	98.64	36.8
3S005 xlvd	0.08	11.63	2.56	39.32	43.59	0.59	1.37	0.07	99.21	33.2
3S017 30μm	0.13	19.69	1.71	45.89	26.68	0.49	1.31	0.21	96.10	57.9
3S028	0.11	14.03	2.26	42.00	40.05	0.59	1.49	0.01	100.71	39.2
3S028	0.03	14.22	2.16	41.04	38.68	0.66	1.56	0.00	98.35	40.5
3S028 100μm	0.10	14.29	2.06	40.99	39.22	0.49	1.86	0.01	99.03	40.8
3S028 150μm	0.06	13.66	2.24	40.23	41.27	0.60	2.18	0.03	100.27	38.2
3S028 50m	0.09	14.33	2.29	42.24	38.77	0.51	1.19	0.08	99.49	40.8
3S028 100μm	0.06	14.51	2.26	41.08	38.44	0.63	1.85	0.05	98.88	41.2
3S030	0.05	18.39	1.40	44.13	31.01	0.44	2.18	0.96	98.56	52.1
3S036	0.11	16.54	1.83	45.48	35.53	0.53	0.56	0.00	100.58	46.9
3S042	0.04	13.56	0.97	41.70	39.45	0.61	0.39	0.00	96.89	39.8
3S042 20m	2.15	0.24	0.52	28.70	62.19	0.05	0.03	0.04	93.96	10.7
3S045 20μm	0.10	15.53	0.57	44.04	36.84	0.34	0.30	0.02	97.73	45.7
3S045 120μm	0.07	2.03	20.60	21.50	20.02	0.32	9.38	24.04	97.95	5.2
3S049 20μm	0.07	10.00	0.77	35.35	48.22	0.28	2.57	0.02	97.28	29.2
3S058 50μm	0.09	8.49	1.82	37.58	51.29	0.54	0.86	0.07	100.74	24.3
3S061 120μm xlvd	0.07	13.44	2.57	41.04	42.58	0.50	2.02	0.02	102.24	36.9
3S069 20μm	0.17	22.37	0.14	48.82	21.56	0.11	1.00	0.60	94.77	66.9
3S069 30μm	0.07	1.78	3.51	27.85	50.79	0.43	3.19	11.52	99.14	5.2
3S069 30μm	0.04	1.44	2.26	27.06	61.95	0.51	3.27	2.84	99.37	4.2
3S074 30μm	0.01	18.14	0.23	43.56	30.19	0.28	1.44	0.08	93.94	54.3
3S079 100μm	0.08	14.55	2.19	40.95	39.36	0.69	2.14	0.09	100.05	40.8
3S079 100μm	0.09	13.97	3.11	39.87	40.63	0.70	2.82	0.03	101.21	38.5
3S090 60μm	1.19	15.35	2.78	40.34	32.08	0.44	1.81	0.03	94.02	52.9
3S098 100μm	0.07	17.49	1.35	45.59	35.85	0.86	1.17	0.00	102.38	48.4
3S098 100μm	0.08	17.32	1.30	45.38	35.73	0.72	1.15	0.01	101.68	48.3
3S098 75μm	0.08	17.66	1.38	45.82	35.20	0.85	1.05	0.01	102.05	49.0
3S112 30μm	0.07	20.46	1.53	47.45	24.66	0.38	1.20	2.15	97.89	58.7
3S114 50μm	0.07	9.63	1.84	37.93	49.74	0.52	1.43	0.02	101.18	27.1
3S115 30μm	0.11	23.68	0.65	51.17	20.20	0.37	0.34	0.00	96.52	69.8
3S123 50μm	0.05	14.49	2.17	42.41	39.61	0.47	1.42	0.00	100.63	40.6
3S123 50μm	0.11	14.83	2.09	42.93	39.30	0.58	1.29	0.00	101.13	41.7
3S131 100μm	0.07	24.33	1.06	50.68	19.34	0.43	1.20	0.12	97.21	70.2
3S131 100μm	0.09	26.42	0.97	53.13	15.97	0.47	1.15	0.13	98.33	75.2
3S134 100μm	0.07	18.55	1.88	45.64	30.49	0.75	1.12	0.00	98.50	53.0
3S134 30μm	0.15	18.25	1.15	45.32	31.32	0.82	0.88	0.00	97.89	53.4
3S137 100μm	0.09	19.89	1.04	46.98	30.57	0.76	1.41	0.01	100.75	55.8
3S137 25μm	0.10	20.05	0.86	47.45	30.61	0.75	1.25	0.00	101.07	56.2
Lava Is xlvd	0.10	12.10	1.09	40.48	44.76	1.85	0.19	0.06	100.62	34.7
Lava Is xlvd	0.09	10.28	1.29	38.65	48.14	2.06	0.19	0.05	100.74	29.5

Appendix C-5: Composition of ilmenites determined through microprobe analysis. FeO, Fe$_2$O$_3$, and mol fraction of hematite component (XR$_2$O$_3$) calculated using the method of Carmichael (1967). **N/a:** not analyzed; **xlvd:** Sample had visible exsolution lamallae.

	SiO2	TiO2	Al2O3	FeO	Fe2O3	MnO	MgO	Cr2O3	Nb2O5	TOTAL	XR2O3
3S003 200μm	0.00	44.25	0.00	36.64	17.70	0.50	1.50	0.06	0.07	100.72	16.73
3S003 100μm	0.01	43.57	0.00	36.05	18.30	0.54	1.47	0.08	0.02	100.04	17.43
3S005 >200μm	0.03	48.90	0.00	39.96	6.31	0.63	1.92	0.11	0.08	97.94	6.16
3S005 300μm	0.00	48.90	0.00	39.98	7.83	0.74	1.86	0.00	n/a	99.30	7.42
3S005 10μm	0.06	49.62	0.00	40.98	6.55	0.69	1.69	0.00	n/a	99.59	6.19
3S005	0.01	49.07	0.00	39.97	8.99	0.80	1.88	0.02	0.10	100.84	8.40
3S009 xlvd	0.05	26.07	0.02	18.91	45.99	1.45	1.77	0.00	n/a	94.26	46.84
3S028 50μm	0.00	44.15	0.00	35.58	18.47	0.51	2.05	0.09	0.10	100.94	17.37
3S028 30μm	0.01	44.41	0.00	35.16	17.64	0.68	2.31	0.06	0.02	100.27	16.63
3S028 30μm	0.03	44.04	0.00	35.31	17.85	0.77	1.99	0.07	0.04	100.10	16.90
3S058 50μm	0.00	42.68	0.00	34.73	19.24	0.76	1.60	0.05	n/a	99.06	18.44
3S079 15μm	0.03	44.85	0.00	33.50	17.54	0.80	3.38	0.02	0.06	100.18	16.36
3S079 30μm	0.00	44.64	0.00	33.00	17.77	0.93	3.48	0.01	0.00	99.83	16.62
3S090 10μm	0.17	36.65	0.00	32.37	21.99	0.15	0.25	0.02	0.02	91.62	22.99
3S098 100μm	0.01	48.60	0.00	39.90	8.87	1.08	1.53	0.02	0.18	100.19	8.39
3S114 50μm	0.03	42.16	0.04	33.00	20.60	0.56	2.49	0.00	n/a	98.88	19.68
3S115 40μm	0.03	49.09	0.00	39.47	9.73	0.65	2.26	0.00	0.11	101.33	9.01
3S115 60μm	0.04	49.03	0.00	39.15	10.11	0.64	2.41	0.02	0.00	101.40	9.36
3S123 125μm	0.05	45.79	0.07	35.99	14.99	0.50	2.66	0.04	0.00	100.09	14.18
3S123 30μm	0.06	45.58	0.00	36.70	14.29	0.62	2.06	0.01	0.00	99.31	13.54
3S134 150μm	0.00	48.51	0.00	39.45	7.95	0.92	1.82	0.00	0.07	98.73	7.58
3S137 ≈200μm	0.05	48.02	0.00	38.23	11.08	0.93	2.25	0.00	0.10	100.66	10.34
3S137 ≈200μm	0.03	47.90	0.00	38.35	11.46	0.97	2.10	0.00	0.03	100.84	10.68
3SXBP 50μm	0.02	40.39	0.00	33.58	23.16	0.96	1.03	0.04	n/a	99.19	22.31
3SXBP	0.03	48.17	0.02	35.40	10.09	0.76	4.02	0.00	0.00	98.49	9.50
3SXBP	0.02	46.49	0.08	33.51	11.34	0.91	4.18	0.03	n/a	96.56	11.00
3SXBP 200μm,	0.03	47.68	0.09	35.09	11.58	0.84	3.95	0.01	n/a	99.27	10.95
3SXBP 100μm	0.03	49.69	0.00	40.99	6.40	1.42	1.29	0.08	0.24	100.13	6.12
3SXBP 50μm	0.02	49.03	0.00	38.12	9.83	1.03	2.80	0.14	0.08	101.05	9.23
Lava Is. xlvd	0.00	46.51	0.00	37.49	12.64	3.47	0.48	0.08	0.17	100.83	12.03

Appendix D-1: Compositions and locations of Quaternary rocks from the Three Sisters area. **Total** is the original XRF total; major elements reported as normalized to 100% anhydrous. **Blank space** indicates element was not analysed, **0** indicates not detected by XRF, **<** indicates upper limit of element in this sample by INAA. **La/Sm, Eu/Eu*** and total **HREE** use chondrite normalized values (Anders and Ebihara, 1982). **Label** is the symbol used in geochemical plots.

Sample	3S001	3S003	3S005	3S007	3S008	3S009	3S010	3S010X	3S011	3S012
SiO2	71.9	61.5	68.0	71.9	63.0	68.2	59.0	69.7	55.3	74.5
TiO2	0.21	1.28	0.72	0.25	1.12	0.61	1.08	0.44	1.28	0.15
Al2O3	16.4	17.6	15.6	15.3	16.7	16.1	17.4	15.1	17.6	14.1
FeO*	2.33	6.53	4.24	2.38	5.62	3.44	7.10	3.83	7.78	1.68
MnO	0.10	0.22	0.09	0.08	0.13	0.09	0.13	0.11	0.14	0.06
MgO	0.12	1.50	0.45	0.47	1.73	0.87	3.02	0.29	4.39	0.17
CaO	0.82	3.83	2.12	1.41	4.32	2.35	6.52	1.59	8.05	0.71
Na2O	3.73	5.16	4.64	4.02	6.06	5.56	4.11	5.97	4.69	5.06
K2O	3.49	1.65	3.25	3.14	1.82	2.58	1.29	2.76	0.98	3.46
P2O5	0.04	0.47	0.19	0.05	0.29	0.16	0.23	0.09	0.30	0.02
TOTAL	98.06	99.92	99.86	96.72	101.25	101.16	100.62	100.70	100.96	101.78
Rb	77	26	77	67	46	52	24	61	15	82
Ba	986	519	755	776	474	732	431	774	341	797
Sr	68	396	209	130	407	237	503	157	575	54
Cs	2.70	1.20	1.40	1.70	1.20	0.95	0.50	0.37	0.50	0.80
Sc	6.32	18.33	9.52	4.88	14.81	8.72	20.18	12.30	26.34	4.06
V	0	105	25	0	71	23	369	51	194	0
Co	4.93	11.60	5.87	1.54	8.11	3.72	18.00	1.27	23.80	0.54
Ni	18	7	12	13	4	8	13	10	16	12
Cr	4	4	3	2	0	0	14	0	63	0
Zn	69	108	66	69	70	65	62	105	59	88
La	27.4	20.8	25.2	21.8	18.9	25.9	16.7	25.5	15.6	23.0
Ce	62.7	49.8	57.2	44.9	38.0	57.7	33.1	58.9	34.1	48.1
Nd	26.1	23.9	27.1	20.7	21.3	26.0	18.5	31.0	17.8	20.8
Sm	5.69	6.13	6.27	4.71	5.28	6.02	4.34	7.15	4.54	4.26
Eu	0.75	1.71	1.49	0.78	1.39	1.40	1.27	1.66	1.46	0.59
Tb	0.85	0.88	0.97	0.71	0.81	0.88	0.65	1.23	0.68	0.70
Yb	4.0	2.9	3.7	3.1	2.8	3.7	2.1	4.8	2.3	3.1
Lu	0.56	0.43	0.51	0.48	0.45	0.53	0.34	0.72	0.36	0.47
La/Sm	3.04	2.14	2.54	2.92	2.26	2.72	2.43	2.25	2.17	3.41
ΣHREE	54.47	45.99	54.09	44.59	44.50	52.75	34.36	71.32	36.57	44.02
Eu/Eu*	0.40	0.86	0.72	0.50	0.80	0.71	0.89	0.68	0.98	0.41
Zr	264	203	293	253	173	277	158	285	152	218
Hf	7.1	5.2	7.9	6.1	4.6	7.5	3.8	8.5	3.7	6.1
Ga	23	20	24	19	19	20	20	20	19	22
Y	37	30	34	32	31	33	25	39	26	29
Nb	20.8	12.9	18.6	14.8	11.4	16.1	10.6	18.2	9.8	16.5
Ta	1.16	0.72	1.01	0.75	0.64	0.98	0.49	0.97	0.59	1.01
Th	7.6	3.3	7.5	5.5	4.1	5.8	2.2	5.9	1.9	7.7
U	2.5	1.2	2.6	1.8	1.4	1.9	0.8	1.8	<2	2.2
Series	TVC	TVC	TVC	TVC	BT	TVC	TVC	TVC	TVC	TVC
Label	+	+	+	+	+	+	+	+	+	+
Lat	44.10908	44.11018	44.10745	44.06482	44.04606	44.07912	44.09950	44.09950	44.10699	44.10996
-Long	121.4869	121.4891	121.4631	121.2865	121.5324	121.5522	121.5401	121.5401	121.5326	121.5319

3S001 Pumice lapilli on top of the Bull Sp. Inlier, = Hydrated Bend Pumice
3S003 Pumcie from Shevlin Park Tuff at W. margin of Bull Sp. Inlier
3S005 Pumice from Desert Spring Tuff on E. flank of Bull Sp. Inlier
3S007 Pumice lapilli @ base Pilot Bu; less evolved than Bottle Ck. 3S024
3S008 Main older An flow, Tumalo Ck. valley
3S009 Summit of Bearwallow Bu. dome
3S010 Triangle Hill, nonvesiculated part of bomb: Flow=3S073
3S010X Hb-bearing xenolith from Triangle Hill ejecta
3S011 Flow 0.75 mi ENE of Triangle Hill, under 5900'Cinder cone
3S012 Dome @ 5400', 3/4 mi ENE Triangle Hill

Sample	3S014	3S015	3S017	3S018	3S019	3S022	3S023	3S024	3S027	3S028
SiO2	67.6	57.4	58.4	71.6	67.7	56.0	67.8	71.4	65.9	58.5
TiO2	0.30	1.01	1.15	0.23	0.66	1.17	0.63	0.26	0.92	1.51
Al2O3	20.5	18.3	17.4	16.3	16.1	17.5	16.1	16.2	16.2	17.4
FeO*	3.03	6.69	7.25	2.36	3.64	7.16	3.59	2.51	4.67	7.88
MnO	0.10	0.12	0.13	0.07	0.10	0.13	0.10	0.08	0.11	0.16
MgO	0.20	3.30	3.13	0.22	0.88	5.08	0.90	0.22	1.05	2.26
CaO	1.03	7.70	6.59	1.02	2.50	7.64	2.48	1.16	2.82	5.36
Na2O	3.66	5.44	4.33	4.44	5.37	3.88	5.49	4.30	5.53	4.78
K2O	2.63	1.17	1.34	3.05	2.72	1.14	2.52	3.12	2.44	1.02
P2O5	0.06	0.22	0.31	0.04	0.19	0.26	0.17	0.04	0.21	0.37
TOTAL	95.58	100.06	101.57	98.23	99.63	100.92	101.25	98.13	100.67	100.09
Rb	62	23	27	73	56	26	56	74	52	16
Ba	1253	379	470	859	739	312	698	830	687	503
Sr	163	536	525	125	253	429	249	113	271	498
Cs	1.60	0.60	1.20	2.00	2.10	1.00	0.70	2.10	0.50	0.80
Sc	6.03	21.60	21.24	4.86	8.77	22.30	8.22	4.99	13.21	21.82
V	0	186	182	17	20	183	32	1	61	159
Co	1.08	19.33	21.00	0.85	3.60	25.90	3.79	1.05	6.88	15.38
Ni	13	15	11	9	5	64	7	11	9	3
Cr	0	33	16	0	0	111	<4	2	6	10
Zn	92	62	85	87	81	60	75	84	90	66
La	25.8	14.9	19.7	27.9	27.5	14.6	24.4	24.3	22.6	19.3
Ce	57.8	32.1	43.4	48.2	58.6	32.5	48.7	48.2	49.9	39.9
Nd	24.8	17.1	21.0	25.7	27.9	17.0	24.9	23.0	25.6	24.1
Sm	5.51	4.06	5.38	5.50	6.45	4.32	5.42	5.09	6.26	6.24
Eu	0.95	1.26	1.47	0.83	1.43	1.30	1.26	0.84	1.61	1.92
Tb	0.84	0.61	0.76	0.86	0.93	0.67	0.80	0.78	1.03	0.96
Yb	3.7	2.0	2.4	3.8	3.7	2.4	3.2	3.4	3.6	3.2
Lu	0.55	0.32	0.36	0.56	0.56	0.37	0.50	0.54	0.57	0.49
La/Sm	2.96	2.32	2.31	3.20	2.69	2.13	2.84	3.01	2.28	1.95
ΣHREE	52.38	32.41	38.74	53.73	54.74	37.14	47.79	49.69	56.80	51.02
Eu/Eu*	0.52	0.95	0.84	0.46	0.68	0.91	0.71	0.50	0.77	0.93
Zr	342	147	165	281	287	146	275	270	251	176
Hf	8.3	3.4	4.2	7.0	7.5	3.6	6.5	6.7	6.8	4.6
Ga	23	17	22	21	19	17	17	23	19	24
Y	36	22	25	38	35	24	32	34	37	32
Nb	19.7	9.1	11.0	15.6	17.9	11.9	17.3	15.7	16.4	9.5
Ta	1.05	0.46	0.54	0.89	1.04	0.58	0.84	0.86	0.83	0.61
Th	7.6	2.0	2.7	6.4	5.5	2.5	5.1	6.2	5.0	3.0
U	2.3	<2	1.1	2.3	2.0	0.9	1.8	2.2	1.7	0.9
Series	TVC	TVC	TVC	TVC	TVC	TVC	TVC	TVC	BT	TVC
Label	+	+	+	+	+	+	+	+	+	+

Lat	44.10882	44.10375	44.09579	44.09827	44.07912	44.05953	44.05549	44.06806	44.03800	43.97077
-Long	121.5522	121.5545	121.5558	121.5510	121.5522	121.5038	121.5459	121.6021	121.5225	121.5857

3S014 Pumice lapilli 1mi NW from Triangle Hill: Hydrated
3S015 Cinder cone @ 6260', 1 mi W of Triangle Hill
3S017 Cinder cone @ 6415', 1 mi SW of Triangle Hill
3S018 Pumice lapilli 0.5 mi W Triangle Hill, ≈3S024 but hydrated
3S019 Summit of dome 0.5 mi N of Bearwallow Butte
3S022 Cinder cone @ 5635', 2 mi ESE Bearwallow Bu.
3S023 Summit of dome 1.5 mi ESE of Bearwallow Butte
3S024 Poorly consolidated pumice lapilli @ 6600' on Bottle Ck.; hydrated
3S027 Whole rock analysis of welded ignimbrite in N. wall Tumalo Ck. @ 5200'
3S028 Mafic pumice from Century Drive Tuff, 2 mi NW of Wanoga Bu.

Sample	3S029	3S030	3S031	3S032	3S033	3S034	3S035	3S036	3S037	3S038
SiO2	69.2	54.3	55.3	74.5	56.0	74.7	74.7	64.9	69.6	55.5
TiO2	0.49	1.01	1.62	0.15	1.29	0.16	0.15	1.02	0.54	1.86
Al2O3	15.7	18.9	17.2	13.7	17.3	13.7	13.8	16.0	15.4	16.6
FeO*	3.39	7.14	9.15	1.70	8.26	1.57	1.57	4.94	3.31	9.06
MnO	0.10	0.13	0.16	0.06	0.15	0.06	0.06	0.11	0.07	0.16
MgO	0.44	4.72	3.33	0.00	3.80	0.02	0.00	1.33	0.36	3.60
CaO	1.90	9.00	7.28	0.71	7.49	0.72	0.70	3.43	1.64	7.24
Na2O	6.25	4.03	4.76	5.26	3.61	5.25	5.12	5.54	5.38	4.40
K2O	2.31	0.66	0.94	3.48	1.02	3.46	3.52	2.23	2.93	1.07
P2O5	0.11	0.14	0.28	0.02	0.31	0.02	0.02	0.33	0.11	0.42
TOTAL	100.33	100.26	100.01	99.92	99.53	100.17	99.76	100.53	100.22	99.89
Rb	43	12	16	86	16	82	83	41	59	18
Ba	598	203	304	796	383	818	802	649	736	321
Sr	215	565	471	52	611	50	49	363	181	474
Cs	0.30	0.60	0.70	1.50	0.60	1.60	1.10	0.50	0.90	0.90
Sc	9.18	25.67	25.45	4.25	22.71	4.28	4.03	13.60	8.73	28.16
V	9	198	264	0	203	2	1	58	15	259
Co	1.76	25.60	24.12	0.54	19.97	0.53	0.51	7.14	2.50	24.84
Ni	5	24	4	10	5	10	12	9	10	7
Cr	<5	100	5	<3	23	<3	<3	<5	<5	21
Zn	82	48	74	84	67	64	73	80	54	74
La	20.7	7.3	12.6	25.3	14.2	24.2	23.0	24.1	22.2	16.5
Ce	43.8	17.0	28.2	52.6	29.6	53.0	51.2	50.4	53.7	37.1
Nd	22.3	10.2	16.0	20.4	17.0	21.8	21.5	27.9	24.0	20.8
Sm	5.73	2.97	4.42	4.77	4.15	4.71	4.83	6.59	5.99	5.58
Eu	1.40	1.11	1.55	0.64	1.30	0.63	0.60	1.65	1.28	1.71
Tb	0.92	0.46	0.69	0.78	0.56	0.78	0.72	0.95	0.84	0.85
Yb	3.5	1.5	2.4	3.7	2.0	3.5	3.3	3.4	3.5	2.9
Lu	0.53	0.25	0.34	0.53	0.28	0.54	0.51	0.51	0.50	0.43
La/Sm	2.28	1.55	1.80	3.35	2.16	3.24	3.01	2.31	2.34	1.87
ΣHREE	52.46	24.67	36.64	50.62	30.11	50.12	46.92	52.10	50.02	45.21
Eu/Eu*	0.73	1.13	1.06	0.40	0.98	0.40	0.38	0.77	0.66	0.93
Zr	230	93	130	222	142	219	219	250	308	158
Hf	6.0	1.9	3.2	6.5	2.9	6.5	6.1	6.3	8.4	3.9
Ga	22	18	20	20	20	18	19	18	19	22
Y	34	16	26	31	24	32	30	34	30	30
Nb	13.1	5.5	8.5	17.8	8.3	18.0	17.8	15.7	16.8	12.1
Ta	0.64	0.29	0.45	1.00	0.39	1.04	0.98	0.80	1.00	0.66
Th	4.0	1.1	1.4	7.9	1.5	7.8	7.7	4.0	5.4	1.7
U	1.4	<1	0.7	2.7	0.8	2.5	2.3	1.6	2.2	<2
Series	TVC	NSMS	NSMS	TVC	TVC	TVC	TVC	TMR	TMR	TMR
Label	+	o	o	+	+	+	+	+	+	+
Lat	44.14281	44.17489	44.18962	44.15244	44.17484	44.17766	44.15535	44.09165	44.09669	44.09550
-Long	121.6828	121.6691	121.6654	121.5760	121.5944	121.6021	121.6090	121.6216	121.6176	121.6310

3S029 Dome at Squaw Creek Falls, 5600'
3S030 BaLa(33) under Shevlin Park Tuff, NF Squaw Ck @ 4800'
3S031 BaLa(32), N. Fork Squaw Ck, 4760'
3S032 3 Creek Butte, summit
3S033 Flow at southern base of 3 Creek Butte
3S034 Melvin Butte, summit
3S035 Summit of dome 1.25 mi S. of Melvin Butte
3S036 E. Tam MacArthur Rim, NW23, 6800'
3S037 N. side of saddle on E Tam Rim, 0.25 mi NE of 3S036
3S038 Flow exposed near SW bank of 3 Creeks Lake, 6700'

Sample	3S040	3S041	3S042	3S043	3S044	3S045	3S046	3S048	3S049	3S050
SiO2	69.4	68.1	74.5	69.5	66.6	56.0	69.5	69.4	53.0	68.9
TiO2	0.56	0.59	0.15	0.55	0.90	1.12	0.55	0.55	1.37	0.62
Al2O3	15.3	16.9	13.9	15.3	16.6	18.3	15.2	15.4	17.6	15.5
FeO*	3.39	3.61	1.64	3.33	5.10	7.40	3.30	3.37	8.06	3.32
MnO	0.09	0.10	0.06	0.09	0.15	0.13	0.09	0.09	0.14	0.11
MgO	0.54	0.49	0.03	0.48	1.29	3.66	0.54	0.46	6.11	0.65
CaO	1.97	1.87	0.67	1.85	3.17	7.70	1.85	1.81	8.41	2.04
Na2O	5.60	4.92	5.18	5.61	3.04	4.45	5.98	5.79	3.73	5.93
K2O	2.85	2.79	3.49	2.93	2.46	1.02	2.88	2.89	1.17	2.49
P2O5	0.12	0.12	0.02	0.11	0.27	0.28	0.11	0.11	0.41	0.15
TOTAL	100.71	97.99	100.27	100.52	97.10	100.47	101.27	100.49	100.70	100.64
Rb	60	58	83	61	42	15	60	59	21	51
Ba	715	701	788	707	573	364	740	753	475	711
Sr	194	174	49	184	295	719	182	182	675	220
Cs	2.50	1.60	1.50	1.70	0.90	0.60	1.90	1.90	0.40	1.50
Sc	9.65	9.28	4.56	9.13	12.42	22.34	9.45	9.30	23.01	10.36
V	19	0	8	7	36	183	1	19	187	4
Co	3.35	2.89	0.92	2.94	3.63	21.80	2.89	2.88	30.50	2.32
Ni	10	8	12	10	8	12	8	10	86	9
Cr	<5	<4	1	<5	3	40	<4	<5	138	<5
Zn	83	85	68	86	98	79	89	87	74	90
La	25.9	28.4	19.4	24.8	22.8	15.4	25.9	26.2	23.8	25.0
Ce	55.7	55.0	44.0	52.8	46.2	34.2	55.1	54.4	53.3	52.8
Nd	27.0	32.1	17.6	28.0	27.6	19.3	29.5	26.0	27.1	26.0
Sm	6.55	7.64	3.66	6.18	6.73	4.30	6.30	6.42	6.24	6.34
Eu	1.33	1.37	0.60	1.27	1.77	1.35	1.36	1.32	1.81	1.45
Tb	1.00	1.23	0.59	0.99	1.08	0.63	1.03	1.03	0.84	0.99
Yb	4.2	4.2	3.0	3.8	3.8	1.8	4.0	4.2	2.2	3.9
Lu	0.60	0.65	0.46	0.61	0.58	0.29	0.64	0.63	0.37	0.57
La/Sm	2.50	2.35	3.35	2.53	2.14	2.26	2.60	2.58	2.41	2.49
ΣHREE	59.85	66.34	41.27	58.09	59.08	30.95	60.73	61.51	39.80	57.19
Eu/Eu*	0.62	0.54	0.49	0.62	0.79	0.97	0.64	0.62	0.91	0.69
Zr	300	335	217	306	267	137	307	311	177	261
Hf	8.5	8.4	6.6	8.2	6.2	3.1	8.5	8.5	4.1	6.9
Ga	17	22	18	20	19	17	20	20	19	17
Y	37	45	24	37	44	20	37	39	26	36
Nb	16.3	18.6	16.3	16.9	18.7	7.0	17.7	17.0	16.2	15.8
Ta	1.01	0.96	1.00	0.88	0.85	0.50	0.92	0.97	0.80	0.91
Th	5.4	5.5	8.2	5.3	3.6	2.0	5.6	5.4	3.1	4.7
U	2.2	2.2	2.6	2.0	1.2	0.6	2.0	2.3	0.9	1.7
Series	TMR	TMR	TVC	BT	BT	TMR	TMR	TMR	BT	BT
Label	+	+	+	+	+	+	+	+	+	+

Lat	44.08856	44.09084	44.14904	44.07083	44.07349	44.09102	44.09242	44.09223	44.05410	44.03938
-Long	121.5932	121.6124	121.6241	121.6524	121.6535	121.6347	121.6364	121.6397	121.6615	121.6736

3S040 Glassy flow, 1.5 mi SE of 3 Creeks Lake, 6640'
3S041 Pumice lapilli from vent breccia on E. Tam Rim, 7000'
3S042 Dome 2 mi SW of Melvin Butte
3S043 Glassy base of flow in N. Fork Tumalo Ck, 7040'
3S044 Pumice lapilli from tuff cone in N. Fork Tumalo Ck, 7160'
3S045 Flow under 3S046 @ 7320', Tam Rim
3S046 Upper Tam Rim, black glassy flow @ 7400'
3S048 Pumice lapilli from vent breccia on upper Tam Rim, 7440'
3S049 Cinder cone 1 mi SE of Ball Butte, 7229'
3S050 Flow 1 mi ENE of Todd Lake, 6700', =BT-390

Sample	3S051	3S052	3S053	3S054	3S057	3S058	3S059	3S060	3S061	3S062
SiO_2	70.6	65.3	72.7	74.2	72.7	73.7	65.3	73.7	64.6	73.8
TiO_2	0.43	0.97	0.33	0.24	0.32	0.27	0.96	0.29	0.96	0.26
Al_2O_3	15.3	16.1	14.6	14.3	14.6	14.3	16.1	14.1	16.5	14.3
$FeO*$	2.92	4.70	2.02	1.58	2.00	1.73	4.75	1.75	4.82	1.71
MnO	0.08	0.10	0.05	0.05	0.05	0.05	0.10	0.05	0.11	0.05
MgO	0.33	1.40	0.50	0.23	0.51	0.29	1.35	0.41	1.52	0.26
CaO	1.40	3.73	1.90	1.20	1.88	1.39	3.64	1.62	3.98	1.37
Na_2O	5.77	5.14	4.60	4.53	4.52	4.83	4.88	4.38	4.92	4.64
K_2O	2.68	2.26	3.20	3.37	3.21	3.25	2.30	3.48	2.07	3.24
P_2O_5	0.08	0.28	0.08	0.05	0.08	0.06	0.27	0.07	0.26	0.06
TOTAL	100.61	100.79	100.65	100.95	100.63	100.35	100.23	100.64	101.00	100.53
Rb	54	46	76	74	76	73	47	85	40	68
Ba	706	608	783	840	775	831	633	809	584	812
Sr	148	344	224	144	221	165	338	185	386	162
Cs	0.60	1.60	1.90	1.30	1.80	1.60	1.30	2.20	1.50	1.20
Sc	8.94	12.36	3.80	2.51	3.69	2.73	11.91	3.29	12.44	2.60
V	3	70	16	3	17	3	84	20	85	17
Co	1.76	8.92	2.92	1.47	2.80	1.80	8.45	2.44	8.54	1.69
Ni	7	32	<1	<1	<1		7	<10	5	
Cr	<5	1	3	<2	2	<3	3	2	<7	<3
Zn	70	68	53	49	51	51	61	47	75	48
La	19.0	20.4	20.0	19.8	19.4	20.7	20.4	21.0	19.6	19.9
Ce	44.4	43.8	37.2	36.2	36.6	37.3	42.9	38.4	41.6	34.9
Nd	20.0	21.0	16.0	14.0	15.2	15.0	22.0	16.0	21.0	13.7
Sm	4.94	5.05	3.00	2.62	2.98	2.75	5.09	3.07	4.64	2.67
Eu	1.19	1.44	0.65	0.49	0.63	0.54	1.38	0.59	1.39	0.52
Tb	0.79	0.74	0.41	0.35	0.40	0.37	0.74	0.41	0.66	0.34
Yb	3.7	2.6	1.9	1.6	1.9	1.8	2.7	1.8	2.5	1.6
Lu	0.52	0.40	0.26	0.24	0.26	0.24	0.39	0.31	0.38	0.25
La/Sm	2.43	2.55	4.21	4.77	4.11	4.75	2.53	4.32	2.67	4.71
ΣHREE	50.62	40.51	25.82	22.50	25.61	23.87	40.68	26.89	37.71	22.59
Eu/Eu*	0.72	0.87	0.67	0.59	0.66	0.61	0.83	0.60	0.92	0.62
Zr	265	207	171	180	172	192	208	168	195	190
Hf	7.0	5.4	4.5	4.6	4.5	4.9	5.4	4.5	5.0	4.8
Ga	21	16	14	15	15	16	18	13	19	15
Y	32	27	19	16	19	17	26	18	24	16
Nb	16.7	11.1	11.5	11.5	11.8	10.9	11.7	12.1	12.9	11.5
Ta	0.81	0.76	0.76	0.77	0.78	0.74	0.75	0.79	0.77	0.73
Th	4.8	4.4	7.3	6.4	7.2	6.4	4.5	8.2	4.1	6.2
U	2.0	1.9	2.9	2.6	2.7	2.5	1.6	3.2	1.4	2.4
Series	BT	SS	SS	SS	SS	SS	SS	SS	SS	SS
Label	+	o	o	o	o	o	o	o	o	o

Lat	44.03220	44.03188	44.03361	44.03898	44.05077	44.05012	44.05280	44.05680	44.05075	44.04664
-Long	121.6724	121.7404	121.7555	121.7495	121.7572	121.7587	121.7702	121.8034	121.8001	121.7935

3S051 Flow 0.75 mi E. of Todd Lake, under 3S050, ≈BT-391
3S052 End of flow from SS, N. Sparks Lk. at Century Dr.
3S053 Southernmost Holocene Devils Hill Dome
3S054 SE flank of Devils Hill, 5800'
3S057 Northernmost Holocene Devils Hill Dome
3S058 Upper Devils Hill, next to Holocene Dome @ 6600'
3S059 Flow along Upper Moraine Lk. Trail, 6500'
3S060 Rock Mesa Holocene dome, SE margin
3S061 Columnar flow margin, 0.75 mi SE of LeConte cone
3S062 Kaleetan Butte, SW flank, 6200'

Sample	3S064	3S065	3S066	3S067	3S069	3S073	3S074	3S075	3S078	3S079
SiO2	62.7	63.1	54.5	64.2	51.8	58.6	55.6	74.9	73.7	67.0
TiO2	1.03	1.01	1.31	1.03	1.02	1.08	1.42	0.14	0.21	0.81
Al2O3	16.6	16.6	16.7	16.1	16.7	17.5	17.6	13.7	14.7	17.1
FeO*	5.63	5.45	7.89	5.44	8.39	7.04	8.46	1.56	1.62	4.12
MnO	0.11	0.11	0.14	0.11	0.15	0.13	0.14	0.05	0.06	0.13
MgO	1.97	1.94	6.43	1.73	8.79	3.07	3.67	0.08	0.24	0.83
CaO	4.73	4.65	7.58	3.88	9.14	6.57	7.88	0.66	1.49	2.39
Na2O	4.88	4.87	3.92	5.41	3.22	4.04	3.57	4.78	4.27	4.33
K2O	1.89	1.97	1.18	2.22	0.64	1.28	1.02	3.53	3.14	2.16
P2O5	0.23	0.23	0.33	0.30	0.21	0.23	0.35	0.02	0.06	0.16
TOTAL	100.34	100.15	99.94	101.68	100.31	100.99	100.27	101.28	99.81	98.01
Rb	37	39	21	49	11	24	17	87	66	44
Ba	530	539	343	633	173	441	350	801	826	616
Sr	408	403	437	304	439	494	578	42	192	278
Cs	1.30	1.30	0.70	1.60	0.60	0.60	0.60	1.60	1.50	1.60
Sc	14.67	14.48	21.55	14.40	27.74	20.73	27.75	4.34	1.98	11.05
V	136	120	161	106	187	178	219	9	8	36
Co	12.24	12.09	32.22	10.06	39.74	18.55	23.30	0.69	1.32	2.12
Ni	25	40	119	6	148	9	15	12	<1	7
Cr	6	6	217	3	451	17	45	<4	<3	3
Zn	60	67	65	78	54	68	60	71	60	87
La	17.9	18.1	15.7	24.9	9.5	16.0	17.6	19.4	19.2	19.8
Ce	37.7	38.8	34.9	55.0	21.2	33.3	36.2	43.4	36.1	39.9
Nd	17.0	18.5	17.9	28.4	11.3	19.0	21.0	17.5	13.0	22.1
Sm	4.28	4.38	4.49	6.41	3.18	4.41	5.12	3.84	2.65	6.06
Eu	1.28	1.30	1.41	1.58	1.12	1.28	1.67	0.54	0.56	1.37
Tb	0.62	0.66	0.68	0.99	0.51	0.68	0.77	0.64	0.35	0.87
Yb	2.0	2.3	2.2	3.7	1.6	2.2	2.6	3.1	1.6	3.4
Lu	0.33	0.37	0.35	0.54	0.28	0.35	0.38	0.46	0.24	0.50
La/Sm	2.64	2.61	2.21	2.45	1.89	2.29	2.17	3.19	4.57	2.06
ΣHREE	32.93	36.45	35.78	55.40	27.14	35.78	40.53	42.62	22.50	50.23
Eu/Eu*	0.92	0.90	0.96	0.75	1.06	0.88	0.99	0.42	0.66	0.70
Zr	176	179	156	248	105	160	161	201	158	231
Hf	4.5	4.6	3.7	6.7	2.3	3.8	3.8	6.1	4.0	5.5
Ga	17	20	15	18	15	17	21	22	17	21
Y	23	24	24	33	18	24	28	26	16	36
Nb	11.7	12.7	13.6	15.6	8.3	9.6	11.1	17.4	10.6	14.3
Ta	0.70	0.75	0.88	0.96	0.48	0.50	0.59	1.04	0.73	0.66
Th	3.9	4.0	2.2	5.0	1.2	2.4	2.0	8.0	5.8	3.8
U	1.3	1.5	0.8	1.6	0.5	0.9	0.6	2.3	2.3	1.4
Series	SS	SS	SS	BT	BT	TVC	TVC	TVC	NSMS	TVC
Label	o	o	o	+	+	+	+	+	o	+

Lat	44.02272	44.01727	44.02367	44.02404	44.02697	44.09801	44.11785	44.11552	44.21842	44.09376
-Long	121.7752	121.7729	121.7649	121.7215	121.7249	121.5211	121.5429	121.5510	121.8312	121.4315

3S064 Kokostick Butte, S flank, 5680'
3S065 Small dome 1 mi SSW of Kokostick, 5820'
3S066 LeConte Flow, 2.5 mi SE of vent, along Century Dr.
3S067 SW Flank TLV, 5600', along Century Drive
3S069 Cayuse flow, 2.5 mi SSW of vent, at Century Dr.
3S073 Flow 1 mi E. of Triangle Hill, 4900'
3S074 Cinder cone 1 mi NNW Triangle Hill, 5000'
3S075 Glaciated dome 1 mi NW Triangle Hill, 5400'
3S078 Summit of glaciated dome 1 mi SE of Condon Butte
3S079 Pumice lapilli from fall deposit under Shevlin Park Tuff in Columbia Canyon

Sample	3S085	3S086	3S090	3S091	3S092	3S093	3S094	3S095	3S096	3S097
SiO2	63.4	75.6	55.2	69.5	57.0	57.5	67.2	62.5	63.8	60.0
TiO2	1.13	0.13	1.14	0.54	1.39	1.25	0.79	1.34	1.18	1.33
Al2O3	16.1	14.2	19.2	15.3	16.9	17.4	16.0	15.8	16.2	16.8
FeO*	5.70	1.07	7.44	3.33	8.34	7.60	3.79	6.47	5.66	6.67
MnO	0.12	0.04	0.14	0.09	0.15	0.14	0.12	0.14	0.13	0.14
MgO	1.70	0.09	4.02	0.52	3.27	3.37	0.90	1.68	1.47	2.29
CaO	3.90	0.93	7.74	1.83	6.84	6.73	2.46	4.10	3.67	5.40
Na2O	5.44	4.22	3.85	5.96	4.67	4.63	6.15	5.26	5.56	5.22
K2O	2.11	3.40	0.88	2.88	1.12	1.17	2.27	2.09	1.87	1.49
P2O5	0.38	0.04	0.35	0.11	0.31	0.27	0.20	0.48	0.35	0.39
TOTAL	100.97	98.21	101.45	101.19	100.79	101.19	100.52	100.70	101.31	100.84
Rb	41	74	11	61	19	23	44	42	37	29
Ba	634	861	402	719	377	401	655	581	517	458
Sr	393	115	617	179	485	478	292	334	326	446
Cs	1.15	1.84	0.48	2.11	0.59	0.34	1.44	1.54	0.85	0.61
Sc	16.60	1.98	19.44	9.44	27.65	24.62	11.81	17.44	15.99	20.15
V	93	0	163	0	247	212	29	93	51	134
Co	10.52	0.92	22.24	2.90	22.54	21.66	2.18	10.70	7.66	12.65
Ni	5	11	42	10	4	9	8	2	6	5
Cr	7	4	60	4	22	41	2	<8	<6	13
Zn		58		145			163		200	
La	24.7	20.0	19.1	25.8	15.0	15.6	23.9	24.1	18.8	18.7
Ce	58.7	43.5	41.2	63.6	35.9	35.2	60.0	60.0	44.3	39.1
Nd	31.6	16.3	23.6	31.3	19.7	20.6	29.4	32.3	25.7	24.8
Sm	6.96	2.77	5.28	6.48	4.99	4.82	6.50	7.58	6.36	5.98
Eu	1.82	0.44	1.51	1.33	1.61	1.46	1.63	1.96	1.71	1.72
Tb	1.18	0.41	0.75	1.22	0.84	0.84	1.03	1.22	1.04	1.01
Yb	3.7	1.5	2.5	4.4	2.5	2.7	3.5	3.9	3.6	3.1
Lu	0.58	0.26	0.40	0.63	0.42	0.38	0.53	0.64	0.55	0.51
La/Sm	2.24	4.56	2.28	2.51	1.90	2.04	2.32	2.01	1.87	1.97
ΣHREE	60.68	23.92	40.25	66.41	42.78	42.49	54.99	64.34	56.30	52.04
Eu/Eu*	0.77	0.49	0.88	0.59	0.96	0.89	0.75	0.77	0.80	0.85
Zr	239	97	168	306	154	157	242	244	201	176
Hf	6.7	3.3	3.8	9.1	3.9	3.9	6.8	6.6	5.5	4.5
Ga	19	17	16	20	21	20	20	21	21	20
Y	35	16	25	36	26	25	36	38	33	31
Nb	13.3	10.9	10.9	16.4	10.2	11.6	15.7	16.6	14.3	11.8
Ta	0.79	0.69	0.59	0.93	0.53	0.51	0.78	0.94	0.71	0.59
Th	4.2	7.3	1.9	5.9	1.7	1.8	4.4	4.1	3.3	2.8
U	1.8	4.5	<3	1.9	<3	<3	1.7	1.5	1.4	<3
Series	TVC	SS	TVC	TVC	BT	BT	BT	BT	BT	BT
Label	+	o	+	+	+	+	+	+	+	+

```
Lat    44.12728 44.13327 43.93606 44.12042 44.10968 44.09774 44.09323 44.09194 44.09279 44.09439
-Long  121.5849 121.5873 121.5941 121.5706 121.6563 121.6661 121.6704 121.6743 121.6761 121.6813
```

3S085 Flow 1.5 mi SSW of 3 Creek Butte, 5400'
3S086 Reworked pumice lapilli 1.25 mi SSW of 3 Ck. Bu., 5400'
3S090 Edison Butte, SE flank, 5240'
3S091 Glaciated dome remnant, 2 mi NW of Triangle Hill
3S092 Ridge @7020',NE16, Snow Ck. cirque
3S093 Flow in Snow Creek Cirque, 7040'
3S094 Lapilli fall tuff, Snow Creek cirque, 7350'
3S095 Dike, Snow Creek cirque, 7560', AnId6
3S096 Flow, Snow Creek cirque, 7480', AnLa5
3S097 Dike, 1.25 mi NE BT, 7280', AnId4

Sample	3S098	3S099	3S100	3S101	3S102	3S103M	3S103S	3S104	3S105	3S106
SiO2	71.1	56.5	64.9	57.8	60.4	56.0	66.9	68.6	54.8	55.9
TiO2	0.40	1.54	0.97	1.21	1.36	1.65	0.80	0.62	1.22	0.99
Al2O3	14.9	16.7	16.3	17.3	16.1	16.8	16.7	15.8	18.9	18.3
FeO*	2.74	8.50	4.85	7.40	7.22	8.99	3.76	3.38	7.46	7.09
MnO	0.08	0.16	0.14	0.14	0.13	0.16	0.13	0.10	0.14	0.13
MgO	0.30	3.49	1.22	3.29	2.40	3.34	0.89	0.61	3.77	4.58
CaO	1.40	7.12	3.26	6.65	5.10	6.90	2.39	2.13	8.53	7.82
Na2O	6.13	4.49	6.22	4.81	4.99	4.84	5.92	6.09	4.16	3.98
K2O	2.77	1.02	1.99	1.17	1.78	1.02	2.23	2.43	0.81	0.93
P2O5	0.07	0.31	0.30	0.29	0.40	0.37	0.20	0.14	0.20	0.22
TOTAL	100.71	100.38	100.96	100.90	100.67	100.12	99.88	100.35	100.67	100.73
Rb	58	19	39	20	35	18	42	49	16	17
Ba	721	300	548	412	523	347	637	705	243	357
Sr	135	440	300	564	462	534	283	236	515	542
Cs	2.04	0.66	1.29	0.84	0.65	0.54	1.34	1.58	0.27	0.19
Sc	9.25	27.96	14.07	23.92	20.41	27.01	12.18	10.48	25.52	21.77
V	1	243	24	189	163	234	11	11	203	164
Co	1.59	21.63	3.84	20.17	16.37	22.45	2.23	2.44	22.90	25.44
Ni	10	7	6	7	12	2	7	5	21	50
Cr	2	27	4	37	12	7	3	4	73	92
Zn	135		207	104	170	118	158	87		
La	24.4	13.4	24.6	19.3	22.9	14.4	24.7	24.5	9.7	13.6
Ce	61.3	31.7	62.6	39.9	52.4	32.2	62.1	63.2	22.8	30.4
Nd	30.8	20.0	34.0	22.3	30.6	19.4	33.3	30.5	13.3	17.8
Sm	6.46	4.93	7.84	5.29	6.76	5.01	6.89	6.69	3.68	3.83
Eu	1.28	1.57	2.04	1.52	1.75	1.63	1.68	1.51	1.31	1.22
Tb	1.28	0.79	1.45	0.81	0.97	0.80	1.07	1.14	0.64	0.60
Yb	4.2	2.7	4.8	2.8	3.2	2.6	3.9	3.9	2.3	2.1
Lu	0.66	0.47	0.77	0.39	0.52	0.45	0.58	0.56	0.34	0.31
La/Sm	2.38	1.72	1.98	2.30	2.14	1.81	2.26	2.31	1.66	2.24
ΣHREE	67.67	44.22	77.55	42.64	51.98	43.33	59.29	60.16	35.10	32.36
Eu/Eu*	0.56	0.96	0.75	0.87	0.80	0.98	0.74	0.67	1.05	0.96
Zr	274	150	272	154	214	139	252	260	113	136
Hf	8.3	3.7	7.7	4.0	5.6	3.4	7.1	7.5	2.7	3.2
Ga	20	20	19	16	22	20	21	19	20	19
Y	37	27	42	28	32	27	37	36	22	19
Nb	15.5	10.6	20.0	9.4	13.0	10.4	16.9	15.7	7.7	8.4
Ta	0.90	0.46	1.03	0.45	0.66	0.40	0.85	0.91	0.35	0.37
Th	5.5	1.5	3.8	2.1	3.4	1.9	4.8	5.0	1.3	1.4
U	2.2	<2	1.3	0.9	1.2	<3	1.5	1.9	<3	1.3
Series	BT	BT	BT	BT	TVC	TVC?	TVC?	BT	BT	BT
Label	+	+	+	+	+	+	+	+	+	+

Lat	44.09975	44.09906	44.11087	44.09380	44.05756	43.92009	43.92009	44.04378	44.04255	44.04789
-Long	121.6817	121.6775	121.6897	121.6342	121.5622	121.5881	121.5881	121.6962	121.7003	121.7019

3S098 Flow along Squaw Creek, 7020', RdLa5
3S099 Flow along Squaw Creek, 7140'
3S100 Flow along Squaw Creek, 6600', DaLa2
3S101 Basal Tam Rim flow, W. shore of 3 Creek Lk, 6820'
3S102 Flow ridge @ 6212', 1.5 mi SSW of Bearwallow Bu.
3S103M Mafic pumice from ignimbrite 1.3 mi SSE of Edison Bu, 4900'
3S103S Silicic pumice from ignimbrite 1.3 mi SSE of Edison Bu, 4900'
3S104 Flow @ 6120',1 mi NNW Todd Lk., ≈3S050
3S105 Flow @ 6160', 1 mi NNW Todd Lk.
3S106 Flow @ Crater Ck. Falls, 6320'

Sample	3S107	3S108	3S109	3S110	3S111	3S112	3S113	3S114	3S115	3S116
SiO2	63.0	63.9	56.5	69.6	64.1	60.0	72.0	72.8	62.9	74.6
TiO2	1.10	1.20	1.37	0.62	1.04	1.24	0.34	0.34	1.24	0.15
Al2O3	16.2	15.7	17.1	15.3	16.2	16.7	14.8	14.5	16.3	13.9
FeO*	5.84	5.74	8.37	3.00	5.19	6.85	2.22	2.04	5.98	1.66
MnO	0.13	0.13	0.15	0.10	0.12	0.13	0.06	0.06	0.14	0.06
MgO	1.84	1.49	3.52	0.64	1.65	2.76	0.43	0.49	1.68	0.01
CaO	4.23	3.73	7.17	1.83	4.02	5.80	1.76	1.85	4.10	0.67
Na2O	5.45	5.42	4.61	6.24	5.26	4.76	5.09	4.70	5.59	5.40
K2O	1.87	2.19	0.95	2.60	2.05	1.58	3.15	3.22	1.71	3.46
P2O5	0.33	0.40	0.19	0.13	0.27	0.27	0.09	0.08	0.39	0.02
TOTAL	101.03	100.77	100.46	101.23	100.43	100.78	101.17	100.79	100.96	100.86
Rb	37	45	17	52	40	28	67	77	34	84
Ba	558	581	275	713	572	458	851	788	495	783
Sr	375	311	497	196	383	418	205	216	355	51
Cs	1.10	0.94	0.50	1.91	1.05	0.34	1.75	2.15	0.71	1.54
Sc	16.27	16.10	28.50	11.23	13.54	20.29	3.69	3.85	17.70	4.36
V	98	71	269	20	95	166	15	11	80	6
Co	9.63	8.71	24.90	1.95	8.89	19.13	2.35	2.92	9.24	0.73
Ni	4	3	3	10	15	13	24	<20	4	11
Cr	8	4	24	3	3	24	3	3	3	1
Zn	135	181		146	129		<20	82	180	89
La	21.8	23.8	10.0	26.6	20.0	16.3	22.5	20.8	20.5	23.0
Ce	51.5	62.2	23.9	68.7	44.5	36.4	49.8	44.9	48.7	73.4
Nd	28.6	33.9	13.8	34.3	20.5	20.2	19.5	14.7	28.8	18.4
Sm	6.50	7.47	3.75	7.00	4.88	4.59	3.48	3.19	6.55	4.39
Eu	1.58	1.86	1.36	1.55	1.40	1.45	0.75	0.66	1.86	0.66
Tb	1.00	1.36	0.61	1.25	0.84	0.73	0.56	0.49	1.18	0.84
Yb	3.6	4.4	2.3	4.4	2.7	2.7	2.1	1.9	3.5	3.2
Lu	0.51	0.61	0.31	0.63	0.37	0.39	0.34	0.28	0.56	0.51
La/Sm	2.12	2.01	1.68	2.40	2.59	2.24	4.08	4.12	1.98	3.31
ΣHREE	54.21	68.77	33.53	67.05	42.18	40.46	32.44	28.14	59.11	48.90
Eu/Eu*	0.74	0.72	1.08	0.65	0.85	0.95	0.65	0.63	0.83	0.43
Zr	222	247	116	271	198	172	223	172	191	217
Hf	5.8	7.3	2.8	8.3	5.3	4.4	6.3	5.0	5.9	7.2
Ga	21	24	22	19	20	17	13	18	18	21
Y	34	40	23	38	25	25	20	18	37	27
Nb	14.4	17.3	6.6	16.6	12.1	9.1	13.7	12.0	13.5	17.0
Ta	0.71	1.02	0.32	1.00	0.73	0.60	0.82	0.82	0.68	1.06
Th	3.3	4.3	1.6	5.6	4.1	3.0	6.6	8.0	3.2	8.5
U	1.5	1.7	<2	2.0	1.5	0.9	2.3	2.9	1.2	2.5
Series	BT	BT	BT	BT	SS	SS	SS	SS	BT	TVC
Label	+	+	+	+	o	o	o	o	+	+

Lat	44.04482	44.09182	44.09411	44.09658	44.11459	44.10692	44.09029	44.08407	44.06765	43.93969
-Long	121.7048	121.7167	121.7221	121.7246	121.7333	121.7293	121.7399	121.7361	121.7227	121.5987

3S107 Dike along Crater Ck., 6000' DaId10
3S108 Flow on NW arm BT, 7560' DaLa1
3S109 Dike NW arm BT, 7440', 0.5 mi NE Green Lk. AnId2
3S110 Dome NW arm BT 7200', 0.5 mi NE Green Lk. RdIp4
3S111 Flow on W. Fork Park Ck., 7040'
3S112 Flow 1 mi N. of Green Lk., 6990', on trail. AnLa1
3S113 Dome W. shore Green Lk., 6600'. RdLa3
3S114 Newberry Dome, E. flank @ Green Lk., 6600'
3S115 Flow on SW BT arm, 6800', 1 mi SE Green Lk. DaLa8
3S116 Edison Butte, W. flank near summit, 5440'

Sample	3S117	3S118	3S119	3S120	3S122	3S123	3S124	3S125	3S126	3S127
SiO2	74.3	73.8	65.8	63.4	73.6	63.5	72.7	64.4	73.4	72.7
TiO2	0.16	0.27	0.91	1.09	0.29	1.08	0.33	1.04	0.28	0.33
Al2O3	14.1	14.3	16.0	16.6	14.2	16.5	14.7	16.3	14.6	14.6
FeO*	1.64	1.72	4.49	5.46	1.80	5.42	2.01	5.07	1.84	2.01
MnO	0.06	0.05	0.10	0.11	0.05	0.11	0.06	0.12	0.06	0.06
MgO	0.07	0.30	1.35	1.72	0.44	1.73	0.37	1.45	0.33	0.52
CaO	0.70	1.41	3.52	4.29	1.65	4.21	1.52	3.80	1.52	1.84
Na2O	5.36	4.71	5.30	5.06	4.48	5.09	5.03	5.27	4.86	4.55
K2O	3.48	3.26	2.34	2.00	3.42	2.00	3.20	2.10	3.10	3.21
P2O5	0.02	0.06	0.26	0.29	0.07	0.29	0.07	0.33	0.07	0.08
TOTAL	101.56	100.63	100.80	100.60	100.82	100.83	100.88	100.46	101.11	101.68
Rb	86	72	46	38	84	38	66	40	62	76
Ba	785	818	653	597	834	575	850	608	808	763
Sr	50	165	329	393	191	388	181	356	180	217
Cs	1.35	2.00	1.27	0.65	2.45	0.61	0.99	1.16	1.39	2.11
Sc	4.52	2.73	11.45	14.50	3.40	14.47	3.60	13.23	3.18	3.78
V	0	13	67	104	14	95	21	53	17	16
Co	0.83	1.92	7.73	10.59	2.69	10.59	2.21	7.90	1.97	2.89
Ni	10	<20	<40	4	<30	26	12	<40	<20	14
Cr	2	2	5	4	3	3	2	<5	2	3
Zn	95	73	140	180	81	122	160	146	78	78
La	28.6	19.9	20.6	20.3	20.8	19.6	21.2	20.1	20.5	19.7
Ce	54.5	43.8	47.1	43.7	45.4	45.7	47.4	47.6	46.7	44.2
Nd	24.9	15.2	20.4	21.7	15.5	22.5	16.6	22.2	16.3	16.4
Sm	4.88	2.75	4.95	5.07	3.11	5.10	3.03	5.46	3.08	3.07
Eu	0.62	0.56	1.28	1.48	0.62	1.43	0.69	1.59	0.64	0.62
Tb	0.82	0.42	0.90	0.76	0.53	0.87	0.49	1.02	0.50	0.53
Yb	3.3	1.7	2.6	2.7	1.8	2.5	2.0	2.8	1.9	1.8
Lu	0.52	0.28	0.41	0.41	0.30	0.41	0.33	0.47	0.31	0.28
La/Sm	3.70	4.57	2.63	2.53	4.22	2.43	4.42	2.32	4.20	4.05
ΣHREE	49.26	25.70	44.22	41.72	29.14	43.11	30.17	49.59	29.28	28.52
Eu/Eu*	0.38	0.62	0.75	0.89	0.59	0.83	0.68	0.84	0.62	0.59
Zr	223	197	206	197	168	197	228	212	176	172
Hf	7.6	5.4	5.6	5.1	5.0	5.4	6.2	5.7	5.1	4.9
Ga	16	11	22	21	13	21	14	19	17	15
Y	25	16	26	27	18	26	17	29	16	18
Nb	18.3	11.9	10.9	11.7	10.8	12.0	13.7	12.7	12.5	10.4
Ta	1.04	0.73	0.74	0.70	0.61	0.69	0.82	0.72	0.81	0.73
Th	9.0	6.9	4.7	3.8	8.8	3.8	6.6	3.8	6.8	7.6
U	2.7	2.4	1.7	1.9	3.1	1.4	2.6	1.3	2.5	2.9
Series	TVC	SS	SS	SS	SS	SS	SS	SS	SS	SS
Label	+	o	o	o	o	o	o	o	o	o

Lat	43.95220	44.07730	44.07628	44.07624	44.07363	44.07574	44.07912	44.08730	44.07056	44.06664
-Long	121.6224	121.7651	121.7598	121.7757	121.7769	121.7870	121.7980	121.8187	121.7459	121.7429

3S117 Dome 1.5 mi NW of Edison Bu., 5730'
3S118 Flow 1 mi N. of Moraine Lk., 7380'
3S119 Flow 1 mi NNE of Moraine Lk., 7320'
3S120 Flow 0.3 mi N of Rock Mesa NE, 7000'
3S122 Rock Mesa NE, N. flank of dome
3S123 Flow 0.5 mi NNE of Rock Mesa, 6620'. WDaLa6
3S124 Flow(?) 1 mi NW of Rock Mesa, 6440'. WRdLa2
3S125 Lower flow, 1.5 mi NW of Rock Mesa, 5980'. WDaLa1
3S126 Dome on SE flank of SS, 6600' RdLa9
3S127 Goose Ck. Holocene dome, E. Flank, 6480'

Sample	3S128	3S130	3S131	3S132	3S133	3S134	3S135	3S136	3S137	3S138
SiO2	56.0	62.0	55.0	61.9	58.2	65.7	62.6	63.9	64.7	62.3
TiO2	1.76	0.75	1.74	1.10	1.30	0.73	1.18	1.01	0.92	1.25
Al2O3	16.5	16.5	16.8	17.2	17.2	16.2	16.6	16.4	16.2	16.4
FeO*	9.18	5.25	9.41	5.91	7.82	5.03	5.87	5.47	5.35	6.16
MnO	0.16	0.10	0.16	0.14	0.14	0.14	0.14	0.14	0.14	0.14
MgO	3.36	3.85	3.83	1.86	2.92	0.99	1.75	1.40	1.26	1.76
CaO	7.03	5.72	7.44	4.59	6.11	2.72	4.30	3.66	3.23	4.33
Na2O	4.69	4.08	4.60	5.52	4.86	6.26	5.60	5.80	6.09	5.62
K2O	0.97	1.64	0.86	1.47	1.23	1.89	1.59	1.72	1.79	1.65
P2O5	0.33	0.12	0.29	0.33	0.29	0.25	0.37	0.37	0.33	0.39
TOTAL	100.70	100.62	100.81	101.44	100.80	101.27	101.25	100.92	100.48	100.53
Rb	17	35	14	24	19	31	27	28	27	29
Ba	299	456	312	508	436	607	540	583	555	553
Sr	440	352	485	483	520	272	412	392	318	404
Cs	0.23	0.69	0.43	0.68	0.53	0.85	0.76	0.95	0.87	0.86
Sc	29.59	15.68	30.03	16.01	21.75	12.81	17.14	15.75	14.21	17.64
V	286	109	318	58	184	12	74	50	14	77
Co	23.73	20.66	27.16	9.76	19.01	3.56	9.04	7.12	4.74	9.30
Ni	2	49	10	<40	3	18	4	<40	<70	7
Cr	9	84	21	3	3	<6	4	3	<7	<9
Zn				152		208	100	181		
La	13.3	14.1	12.0	18.6	15.8	21.3	19.6	22.0	20.5	20.4
Ce	30.3	28.5	27.5	44.1	35.5	53.8	41.7	53.2	48.5	45.9
Nd	18.6	15.0	17.8	23.1	20.4	28.0	23.9	26.0	27.7	25.6
Sm	4.83	3.15	4.39	5.29	4.67	6.75	5.81	6.27	6.55	6.13
Eu	1.58	0.90	1.51	1.61	1.45	1.80	1.80	1.82	1.87	1.85
Tb	0.86	0.57	0.72	1.04	0.76	1.27	0.91	1.13	1.04	0.94
Yb	3.0	2.0	2.5	2.7	2.6	4.2	3.1	3.2	3.7	3.5
Lu	0.41	0.28	0.37	0.41	0.36	0.62	0.45	0.49	0.58	0.50
La/Sm	1.74	2.83	1.73	2.22	2.14	1.99	2.13	2.22	1.98	2.10
ΣHREE	45.28	30.32	38.68	47.68	39.70	66.22	48.06	54.45	57.70	52.15
Eu/Eu*	0.95	0.83	1.03	0.86	0.93	0.77	0.93	0.84	0.86	0.92
Zr	145	110	134	176	154	241	190	203	225	196
Hf	3.6	2.9	3.3	4.6	3.7	7.0	5.0	5.8	6.1	5.3
Ga	19	13	20	20	18	21	22	20	23	24
Y	28	19	25	27	24	38	31	32	35	31
Nb	9.8	7.4	8.1	10.2	8.2	12.7	12.3	11.9	14.3	11.1
Ta	0.56	0.45	0.45	0.54	0.48	0.62	0.62	0.59	0.69	0.58
Th	1.5	3.0	1.1	2.3	1.8	2.9	2.6	2.6	2.7	2.6
U	0.5	1.1	<2	0.9	0.7	1.3	1.0	1.2	1.2	1.3
Series	BT	NSMS	NSMS	MS	NSMS	MS	MS	MS	MS	MS
Label	+	o	o	x	o	x	x	x	x	x

Lat	44.06570	44.16157	44.15917	44.13528	44.14319	44.15447	44.15859	44.16345	44.16512	44.17088
-Long	121.7356	121.8175	121.8165	121.8048	121.8190	121.8264	121.8073	121.8079	121.8036	121.8040

3S128 Flow along Fall Ck., 6200'. AnLa7
3S130 Flow 0.5 mi SSW of Obsidian Falls, 6560'
3S131 Flow 0.75 mi SSW Obsidian Falls, 6580', on trail
3S132 Flow 1 mi E. of Linton Sp., 7000'
3S133 Flow on N. Fork of Linton Ck., 6580'
3S134 Lane Mesa, E. margin, 6460'
3S135 Flow 1 mi SSE of Sister Sp., 6980'
3S136 Platy flow 0.5 mi SE of Sister Sp., 6800'
3S137 Flow 0.5 mi ESE of Sister Sp., 7040'
3S138 Flow 0.5 mi E. of Sister Sp., 6880'

Sample	3S139	3S140	3S143	3S145	3S146	3S147	3S148	3S149	3S150	3S151
SiO2	76.1	73.7	73.3	71.8	59.9	64.8	72.5	56.7	65.4	65.8
TiO2	0.14	0.26	0.29	0.35	1.28	0.89	0.33	1.18	0.85	0.94
Al2O3	13.4	14.2	14.4	14.9	16.1	16.3	14.5	17.8	16.1	16.0
FeO*	1.16	1.95	2.07	2.20	7.29	5.13	2.06	7.31	4.53	4.56
MnO	0.04	0.09	0.06	0.07	0.14	0.14	0.06	0.13	0.09	0.10
MgO	0.11	0.31	0.35	0.53	3.37	1.19	0.61	4.06	1.72	1.31
CaO	0.97	1.43	1.56	2.11	5.33	3.23	1.86	7.16	4.10	3.50
Na2O	4.46	4.42	4.13	4.61	4.69	6.07	4.77	4.18	4.73	5.40
K2O	3.41	3.21	3.14	3.09	1.59	1.78	3.15	1.00	2.25	2.31
P2O5	0.04	0.06	0.07	0.09	0.29	0.32	0.07	0.25	0.20	0.27
TOTAL	101.99	100.90	100.73	100.67	100.70	101.28	100.85	100.80	101.24	101.08
Rb	79	70	69	73	30	29	71	19	48	47
Ba	876	813	785	755	432	550	742	310	609	629
Sr	119	168	179	251	380	325	193	504	335	331
Cs	1.94	1.60	1.50	1.93	0.91	0.75	2.02	0.53	1.42	1.30
Sc	1.63	2.66	3.10	3.92	19.56	14.25	4.60	20.17	12.24	12.12
V	9	16	19	29	164	20	31	169	87	57
Co	0.58	1.96	2.09	3.53	19.51	4.53	3.75	22.45	11.14	7.80
Ni	<10	<10	<10	16	17	<70	9	32	26	6
Cr	1	11	11	7	43	4	9	58	16	3
Zn	64	56	53	90			180		96	
La	20.0	19.1	18.9	18.8	16.0	20.6	19.2	11.6	17.2	21.2
Ce	44.6	35.9	34.2	43.1	36.0	49.6	38.6	25.5	41.7	44.6
Nd	14.9	13.5	14.0	16.7	18.6	26.3	17.4	14.2	16.9	21.7
Sm	2.63	2.84	2.74	2.97	5.04	6.38	3.06	3.85	4.05	5.23
Eu	0.42	0.54	0.60	0.70	1.43	1.90	0.64	1.29	1.11	1.39
Tb	0.39	0.38	0.38	0.54	0.79	1.09	0.41	0.57	0.68	0.74
Yb	1.5	1.7	1.8	1.7	2.8	3.8	1.9	2.2	2.1	2.9
Lu	0.24	0.27	0.26	0.27	0.40	0.58	0.29	0.30	0.34	0.42
La/Sm	4.80	4.25	4.36	4.00	2.00	2.04	3.96	1.90	2.68	2.56
ΣHREE	22.87	24.54	24.71	27.94	42.53	59.24	26.75	31.89	34.99	42.56
Eu/Eu*	0.49	0.59	0.68	0.68	0.86	0.88	0.65	1.02	0.81	0.82
Zr	96	167	174	168	182	224	153	143	185	211
Hf	3.2	4.3	4.3	4.6	4.6	6.2	4.5	3.4	5.1	5.6
Ga	15	16	16	16	16	20	17	17	16	20
Y	15	17	18	17	27	34	18	20	21	26
Nb	10.0	11.5	10.7	10.6	10.5	13.0	8.7	8.1	10.4	12.9
Ta	0.74	0.75	0.75	0.68	0.53	0.68	0.67	0.40	0.67	0.71
Th	7.3	6.1	5.7	7.2	2.7	2.7	7.0	1.6	4.7	4.5
U	2.6	2.5	2.3	2.6	1.1	1.0	2.4	0.7	1.5	1.8
Series	MS	SS	SS	SS	SS	MS	SS	SS	SS	SS
Label	x	o	o	o	o	x	o	o	o	o

Lat	44.17746	44.12136	44.08801	44.12244	44.11236	44.12094	44.12735	44.09796	44.12165	44.13126
-Long	121.8157	121.7546	121.7726	121.7629	121.7642	121.7941	121.7876	121.7670	121.7595	121.7649

3S139 Obsidian Cliffs, by Prouty Plaque, 6560'
3S140 W. flank of largre dome, easternmost Chambers Lakes, 7600'
3S143 Dome at terminus of Clark Glacier, SS, 8400'
3S145 Holocene dome 0.5 mi NW of Carver Lk., 7500',BT-205
3S146 Flow on W. flank of Prouty Glacier, SS, 8300'. WAnLa2
3S147 E. arm of flow, W. Chambers Lk., 7600'. TS-1603
3S148 Dome W. Chambers Lk, 7600'. TS-1601
3S149 Dike near SS summit, 9300', TS-1712
3S150 Flow at E. Chambers Lk, 7440'. WDaLa2, TS-1716
3S151 Flow on SE flank of SS at 9800', TS-1711

Sample	3S152	3S157	3S159	3S162	3SXBP	Misc. Analyses 3S071	3S063
SiO2	63.6	53.6	52.9	64.4	74.2	71.7	65.2
TiO2	1.08	1.07	1.62	0.72	0.16	0.31	0.66
Al2O3	16.4	18.4	15.8	15.8	14.2	14.5	16.6
FeO*	5.42	7.49	9.55	5.17	1.82	3.47	4.32
MnO	0.11	0.14	0.17	0.10	0.07	0.12	0.09
MgO	1.63	5.20	5.66	1.65	0.08	0.00	1.94
CaO	4.26	9.00	8.21	3.87	0.81	0.62	4.38
Na2O	5.13	3.77	3.60	4.90	4.46	5.68	4.82
K2O	2.05	0.62	0.71	2.01	3.47	2.79	1.92
P2O5	0.30	0.18	0.28	0.28	0.03	0.03	0.16
TOTAL	100.54	99.47	98.50	98.90	99.63	100.35	101.78
Rb	40	7	13	73	84	54	39
Ba	564	276	264	611	794	750	575
Sr	389	550	466	349	65	76	388
Cs	1.16				3.10	0.40	0.90
Sc	14.86				4.29	11.54	10.47
V	94				0	0	88
Co	10.60	68	74	25	0.50	0.27	11.26
Ni	23	72	10	2	11		
Cr	2	93	113	7	1	2	23
Zn		76	94	73	105	130	71
La	19.8				28.7	37.0	17.6
Ce	44.9				59.7	53.7	33.7
Nd	20.5				26.5	48.0	16.2
Sm	5.13				5.95	10.62	3.53
Eu	1.52				0.83	1.81	0.99
Tb	0.80				0.94	1.74	0.48
Yb	2.7				4.2	6.0	1.9
Lu	0.41				0.58	0.94	0.30
La/Sm	2.44				3.05	2.20	3.15
ΣHREE	42.57				57.77	94.69	28.55
Eu/Eu*	0.89				0.42	0.51	0.87
Zr	200				231	336	167
Hf	5.4				6.7	9.1	4.2
Ga	21				20	22	17
Y	27				36	63	19
Nb	11.5				16.9	19.9	10.2
Ta	0.77				1.20	1.02	0.60
Th	3.9				8.1	4.2	3.6
U	1.1				2.7	2.1	1.2
Series	SS	NS	MS	SS	TVC	NBRY	SC
Lbl	o	o	x	o	+	N	C
Lat	44.12443	44.18055	44.13120	44.13844	44.04200	43.93800	43.85802
-Long	121.7700	121.7470	121.7676	121.7199	121.3330	121.4130	121.7840

3S152 Flow at Chambers Lk., 7480'. DaLa3, TS-1718
3S157 N. Sister flow, E. flank, 7080' UO AA data, 7/90
3S159 Flow on S. flank of MS at 7160'. UO AA data, 7/90
3S162 Flow 3 mi NE of SS @ 5800', SF Squaw Ck. UO AA data, 7/90
3SXBP Bulk Bend Pumice, fresh interiors, quarry ≈1mi SW Bend

Miscellaneous analyses from the Oregon central Cascades:

3S071 Benham Butte; Main dome at parking pad along Deschutes River
3S063 E. flank of Benchmark Butte, near Crane Prarie along Century Drive

Appendix D-2: Compositions and locations of Deschutes Formation rocks in the Three Sisters-Bend area.

Sample	3S002	3S006	3S077	3S080	3S087	3S088M	3S088S	3S141	3S142	3S144
SiO2	54.9	59.3	68.2	68.7	54.3	57.8	67.4	65.7	69.9	67.1
TiO2	1.87	1.13	0.70	0.59	1.85	1.49	0.78	0.87	0.59	0.69
Al2O3	16.8	17.1	15.9	16.3	16.5	16.7	16.0	16.0	15.9	16.3
FeO*	9.25	7.31	3.65	3.48	10.46	8.08	3.71	4.55	3.35	4.45
MnO	0.16	0.14	0.14	0.14	0.16	0.15	0.12	0.16	0.08	0.10
MgO	3.20	2.79	0.61	0.67	3.28	3.04	0.96	1.19	0.48	0.37
CaO	7.30	6.11	1.78	2.17	7.40	6.32	2.45	2.91	1.61	2.24
Na2O	4.61	6.23	5.50	4.28	4.33	4.83	5.98	5.50	3.04	6.16
K2O	1.15	1.40	2.75	2.83	0.97	1.25	2.34	2.12	3.82	2.23
P2O5	0.54	0.25	0.18	0.14	0.59	0.32	0.19	0.25	0.11	0.18
TOTAL	100.18	100.82	100.52	98.95	100.05	100.29	99.41	100.48	98.42	100.98
Rb	17	30	45	64	17	21	45	31	56	44
Ba	413	468	946	850	429	367	650	768	740	805
Sr	686	485	240	304	574	497	288	316	135	289
Cs	0.70	0.90	1.10	1.60	<.7	0.81	1.43	1.40	1.70	0.64
Sc	27.06	20.45	12.32	10.28	32.96	25.88	11.89	12.56	7.37	13.78
V	188	192	7	9	281	211	18	38	28	5
Co	17.90	19.60	2.24	1.19	25.90	20.92	2.23	4.52	2.49	1.65
Ni	0	8	8	11	3	3	8	6	11	7
Cr	1	7	<3	<3	8	11	4	2	3	<6
Zn	73	76	96	109		107	89	100	55	
La	13.4	18.8	25.5	24.9	18.9	15.2	23.8	25.5	22.4	22.9
Ce	29.5	37.8	70.1	50.8	38.8	37.6	60.1	57.5	44.9	49.2
Nd	19.3	19.7	31.8	29.5	23.0	20.9	30.5	32.0	25.0	26.9
Sm	5.31	4.71	7.35	7.09	6.93	5.14	6.42	7.35	5.69	6.41
Eu	1.83	1.40	2.35	1.76	2.42	1.65	1.64	2.01	1.00	2.05
Tb	0.77	0.70	1.30	1.06	1.19	0.84	1.16	1.13	0.84	1.01
Yb	2.2	2.6	4.5	4.0	2.9	2.7	3.9	4.5	3.9	3.5
Lu	0.34	0.37	0.65	0.61	0.45	0.46	0.61	0.65	0.58	0.50
La/Sm	1.59	2.52	2.19	2.22	1.72	1.87	2.34	2.19	2.49	2.26
ΣHREE	37.39	38.73	69.02	60.53	53.06	44.97	62.14	65.59	54.40	53.64
Eu/Eu*	1.06	0.91	0.93	0.76	1.03	0.96	0.74	0.83	0.54	0.96
Zr	118	163	278	240	136	153	241	269	365	244
Hf	2.6	4.2	7.5	5.7	3.3	4.1	6.9	7.1	7.7	7.1
Ga	19	19	22	21	23	16	22	21	22	23
Y	28	28	47	44	30	28	35	43	43	31
Nb	7.7	10.9	17.8	16.1	10.6	8.6	15.8	16.9	18.3	15.5
Ta	0.36	0.57	1.13	0.80	0.48	0.57	0.83	0.89	0.85	0.81
Th	1.3	2.8	5.1	4.4	1.3	4.3	4.6	2.7	4.0	4.0
U	<2	<3	0.8	1.6	<3	<3	1.4	0.8	1.5	2.3
Series	DF	DF	DF	DF	DF	DF	DF	DF	DF	DF
Label	>	>	>	>	>	>	>	>	>	>

Lat	44.11051	44.10129	44.13000	44.09803	44.10604	44.11393	44.11393	44.29165	44.28996	44.10994
-Long	121.4869	121.4659	121.4200	121.3407	121.3466	121.3387	121.3387	121.4068	121.4088	121.4638

3S002 Upper Pmag-reversed flow, Bull Sp. Inlier
3S006 Lower pmag-normal flow, Bull Sp. Inlier
3S077 Lapilli from devitrified ignimbrite at S wall of Tumalo Dam
3S080 Lapilli from ignimbrite remnant on NNW flank of Awbrey Butte, 3460'
3S087 Pmag-normal flow under Bend Pumice, Coates gravel pits, N. Awbrey Bu.
3S088M Mafic pumice from ignimbrite at Tumalo Ck-Des.R. junction, 3420'
3S088S Silicic pumice from ignimbrite at Tumalo Ck-Des.R. junction, 3420'
3S141 Pumice lapilli from Buckhorn Canyon Tuff, Hwy 26, Deep Cyn Grade. HB-14
3S142 Pumice lapilli from Deep Canyon Tuff, Hwy 26., 3020'. HB-28
3S144 Flow on E. flank of Bull Sp. Inlier. B-65

Appendix E-1: Compilation of mineral/matrix distribution coefficients for calc-alkaline and mildly alkaline rocks. Rare earth element distribution coefficients reported in appendix E-2.

PLAGIOCLASE

Sample	Rb	Ba	Sr	Cs	Zr	Hf	Nb	Ta	Th	U	Sc	V	Co	Ni	Cr	Zn	Mol An	Reference
XI	0.08		1.50								0.02		0.05	0.04				Irving, 1978
D-Kyu	0.46	1.43	7.0	0.78		0.07		0.05	0.03		0.15		0.29		0.67	0.49	49	Dudas et al., 1971
D-GlPk	0.06	0.79	6.0	0.03		0.13		0.03	0.03		0.03		0.06		0.06	0.51	41	Dudas et al., 1971
HB-39	0.03	0.33	2.04	0.03													70	Hart & Brooks, 1974
SP-19	0.06	0.26	1.77														79	Schnitzler & Philpots, 1968
PS-225	0.14	0.59	2.75														46	Philpots & Schnitzler, 1970
HN-225	0.02	0.30	2.87															Higuchi & Nagasawa, 1969
D-34b	0.30		1.67			0.02			0.01	0.01								Dostal et al., 1983
PS-208	0.03	0.15	1.36														65	Philpots & Schnitzler, 1970
H-688MS	0.05	0.21	1.98	0.06	0.05	0.01		0.01			0.02	0.03	0.04	0.05	0.05		61	Hughes, 1983
PS-204	0.19	0.24	1.66														87	Philpots & Schnitzler, 1970
LC-11		0.08				0.02					0.02					0.13	71	Luhr & Carmichael, 1980
PS-240	0.03	0.06	1.30														97	Philpots & Schnitzler, 1970
PS-233	0.07	0.14	1.31														93	Philpots & Schnitzler, 1970
PS-184	0.04	0.13	1.66														80	Philpots & Schnitzler, 1970
PS-271	0.06	0.20	1.83														77	Philpots & Schnitzler, 1970
LC-6		0.08				0.01					0.02					0.25	58	Luhr & Carmichael, 1980
LC-7		0.10				0.02					0.02					0.16	60	Luhr & Carmichael, 1980
PS-218	0.05	0.36	2.84														51	Philpots & Schnitzler, 1970
D-SHy	0.18	0.34	4.5	0.13		0.17		0.08	0.07		0.05		0.06		0.06	0.26	44	Dudas et al., 1971
BD-PlA	0.30	0.27	3.40	0.03	0.20	0.03		0.03	0.01		0.01		0.07		0.01	0.44		Bacon & Druitt, 1988
NC-15	0.19	1.20	10.5	0.09	0.05	0.06		0.03	0.05	0.07	0.10					0.44	41	Nash & Crecraft, 1985
NC-12	0.09	1.20	8.7	0.10	0.05	0.05		0.04	0.03	0.06	0.10					0.40	42	Nash & Crecraft, 1985
NC-6	0.07	0.41	4.0	0.16	0.08	0.14		0.03	0.03	0.10	0.01					1.70	39	Nash & Crecraft, 1985
BD-PlR	0.30	0.48	4.40	0.03	0.20	0.03		0.03	0.01		0.01		0.15		0.01	0.48		Bacon & Druitt, 1988
NS-1P	0.04	0.31	4.4															Nagasawa & Schnetzler, 1971
NS-2P	0.02	0.30	3.9															Nagasawa & Schnetzler, 1971
D-Tum	0.07	0.92	24.3	0.10		0.16		0.09	0.09		0.17		0.51		0.15	0.39	23	Dudas et al., 1971

CLINOPYROXENE

Sample	Rb	Ba	Sr	Cs	Zr	Hf	Nb	Ta	Th	U	Sc	V	Co	Ni	Cr	Zn	Mol En	Reference
XI	0.00	0.00	0.10	0.00			0.02		0.01	0.01	2.00	1.00	1.00	5.00	2.50			Irving, 1978
PS-193	0.02	0.01	0.15															Philpots & Schnitzler, 1970
SP-25	0.02	0.02	0.11															Schnitzler & Philpots, 1968
HB-39	0.00	0.00	0.08	0.00														Hart & Brooks, 1974
SP-19	0.02	0.02	0.12															Schnitzler & Philpots, 1968
On-b		0.00	0.11						0.01	0.02	2.9		1.1					Onouma et al., 1968
D-34b						0.30					2.9	1.6	1.2	4.2	28.0	0.3		Dostal et al., 1983
PS-204	0.00	0.00	0.08	0.00														Philpots & Schnitzler, 1970
LC-11		0.04				0.26					6.9	1.1		5.7	42.9	9.5	43	Luhr & Carmichael, 1980

CLINOPYROXENE (cont.)

Sample	Rb	Ba	Sr	Cs	Zr	Hf	Nb	Ta	Th	U	Sc	V	Co	Ni	Cr	Zn	Mol En	Reference
PS-271	0.01	0.04	0.07															Philpots & Schnitzler, 1970
LC-6		0.05				0.23					12.5	3.2		5.0	145.0	8.9	44	Luhr & Carmichael, 1980
LC-7		0.02				0.29					12.3	2.8		6.0	126.0	10.6	44	Luhr & Carmichael, 1980
BD-CpxA		0.10				0.46		0.50	0.10		17.0		5.5		30.0	2.0		Bacon & Druitt, 1988
NC-15						0.50		0.13	0.12		30.6							Nash & Crecraft, 1985
NC-12						0.84		0.09	0.09		30.0							Nash & Crecraft, 1985
NC-6						0.91		0.46	0.22		25.1							Nash & Crecraft, 1985
PS-266	0.03	0.13	0.52															Philpots & Schnitzler, 1970
BD-CpxR		0.10				0.29		0.50	0.10		33.0		17.0		30.0	2.0		Bacon & Druitt, 1988

ORTHOPYROXENE

Sample	Rb	Ba	Sr	Cs	Zr	Hf	Nb	Ta	Th	U	Sc	V	Co	Ni	Cr	Zn	Mol En	Reference
XI		0.01	0.02							0.01	1.40	3.40	1.30	3.00	5.00			Irving, 1978
On-c											1.2		2.1					Onouma et al., 1968
PS-203	0.00	0.00	0.00															Philpots & Schnitzler, 1970
PS-271	0.02	0.01	0.02															Philpots & Schnitzler, 1970
PS-184	0.03	0.01	0.01															Philpots & Schnitzler, 1970
LC-6		0.23				0.22			0.22		3.9	1.5		7.0	21.0	3.9	71	Luhr & Carmichael, 1980
LC-7		0.04							0.05		3.7	99.0		20.0	110.0	3.9	71	Luhr & Carmichael, 1980
BD-OpxA	0.01	0.10	0.01	0.01	0.11	0.11		0.11	0.14		4.3		12.0		10.0	3.7		Bacon & Druitt, 1988
NC-15				0.40		0.20		0.19	0.14	0.16	12.00							Nash & Crecraft, 1985
NC-12				0.76		0.17		0.12	0.11	0.11	10.0							Nash & Crecraft, 1985
BD-OpxR	0.01	0.10	0.01	0.01	0.11	0.11		0.11	0.14		7.1		38.0		10.0	6.0		Bacon & Druitt, 1988
NS-1H	0.00	0.00	0.01															Nagasawa & Schnetzler, 1971
NS-2H	0.00	0.00	0.05															Nagasawa & Schnetzler, 1971

HORNBLENDE

Sample	Rb	Ba	Sr	Cs	Zr	Hf	Nb	Ta	Th	U	Sc	V	Co	Ni	Cr	Zn	Reference
HN-3											2.2						Higuchi & Nagasawa, 1969
SP-29	0.43	0.42	0.55														Schnitzler & Philpots, 1968
D34-b	0.33		0.48			0.50			0.50	0.10	3.2	3.4	2.0	6.8	12.5	0.4	Dostal et al., 1983
PS-233	0.05	0.10	0.19														Philpots & Schnitzler, 1970
LC-6		0.17				0.34			0.18		10.3	7.0		14.0	51.3	5.0	Luhr & Carmichael, 1980
LC-7		0.16				0.45			0.14		9.5	6.5		14.0	89.8	8.7	Luhr & Carmichael, 1980
BD-HbA		0.30				0.54		0.59	0.16		13.0		6.1		40.0	1.6	Bacon & Druitt, 1988
BD-HbR		0.30				0.52		0.43	0.16		14.0		37.0		40.0	2.3	Bacon & Druitt, 1988
NS-1Hb	0.01	0.04	0.02														Nagasawa & Schnetzler, 1971.
NS-2Hb	0.01	0.05	0.09														Nagasawa & Schnetzler, 1971.

OLIVINE

Sample	Rb	Ba	Sr	Cs	Zr	Hf	Nb	Ta	Th	U	Sc	V	Co	Ni	Cr	Zn	Mol Fo	Reference
LS-48											0.18		2.75		1.06		88	Leeman & Scheidegger, 1977
SP-25	0.01	0.01	0.02															Schnitzler & Philpots, 1968
LS-15											0.22		4.19		3.06		72	Leeman & Scheidegger, 1977
LS-36											0.15		3.24	17.6	1.23		87	Leeman & Scheidegger, 1977
LS-44											0.14		3.24	16.1	2.70		87	Leeman & Scheidegger, 1977
HB-39	0.00	0.00	0.00	0.00													86	Hart & Brooks, 1974
LS-82											0.14		4.11	23.5	1.65		88	Leeman & Scheidegger, 1977
LS-5											0.15		3.49	19.0	2.92		85	Leeman & Scheidegger, 1977
PS-19	0.01	0.01	0.01															Schnitzler & Philpots, 1968
D-SvG												0.06	6.60	22.0	0.70	1.20		Dostal et al., 1983
H-688MS								0.1	0.1		0.39	0.08	7.70	47.2	2.5		75	Hughes, 1983
LC-11		0.01		0.01		0.01				0.0	0.30	0.08		58.0	34.0	1.5	75	Luhr & Carmichael, 1980

MAGNETITE

Sample	Rb	Ba	Sr	Cs	Zr	Hf	Nb	Ta	Th	U	Sc	V	Co	Ni	Cr	Zn	Xusp	Reference
D-34b												26.0	7.4	29.0	153	3.1		Dostal et al., 1983
LC-11		0.40				0.62					1.7	8.7		9.6	93	5.4	61	Luhr & Carmichael, 1980
LC-6		0.13				0.31					3.2	38.7		15.0	165	12.6	63	Luhr & Carmichael, 1980
LC-7		0.20				0.37					2.5	34.3		13.0	133	11.8	69	Luhr & Carmichael, 1980
NC-15						2.80		13.0	0.2	0.5	8.0				40	50.0		Nash & Crecraft, 1985
NC-12						1.70		5.6	0.1	0.2	7.4				30.0	50.0		Nash & Crecraft, 1985
NC-6						0.90		7.9	0.3	0.8	4.6				50.0	60.0		Nash & Crecraft, 1985
BD-MgtR					0.24	0.24		1.2			5.0		80.0		30.0	15.0		Bacon & Druitt, 1988

ILMENITE

Sample	Rb	Ba	Sr	Cs	Zr	Hf	Nb	Ta	Th	U	Sc	V	Co	Ni	Cr	Zn	Reference
NC-6						3.00		20.0	7.3	3.0	2.3				3.0	75.0	Nash & Crecraft, 1985
XI					0.27		0.80					12			6		Irving, 1978

APATITE

Sample	Rb	Ba	Sr	Cs	Zr	Hf	Nb	Ta	Th	U	Sc	V	Co	Ni	Cr	Zn	Reference
XI		1.00							1.50	0.50							Irving, 1978
F-1					0.64	0.73											Fujimaki, 1986

ZIRCON

Sample	Rb	Ba	Sr	Cs	Zr	Hf	Nb	Ta	Th	U	Sc	V	Co	Ni	Cr	Zn	Reference
F-1						958											Fujimaki, 1986

Appendix E-2: Published rare earth element phenocryst/matrix distribution coefficients.

PLAGIOCLASE

Sample	La	Ce	Nd	Sm	Eu	Tb	Yb	Lu	An	Reference
D-Kyu	0.28	0.16	0.16	0.12	0.75	0.12	0.07	0.06	49	Oudas et al., 1971
D-GlPk	0.49	0.40	0.29	0.11	1.78	0.15	0.09	0.07	41	Oudas et al., 1971
SP-19		0.08	0.11	0.10	0.35	0.09			79	Schnitzler & Philpots, 1968
PS-225		0.11	0.07	0.04	0.39	0.02	0.01		46	Philpots & Schnitzler, 1970
HN-225	0.14	0.09	0.04	0.04	0.32	0.03	0.02			Higuchi & Nagasawa, 1969
PS-208		0.02	0.02	0.02	0.23	0.01	0.03	0.04	65	Philpots & Schnitzler, 1970
H-688MS	0.06	0.06		0.03	0.30	0.03		0.01	61	Hughes, 1983
PS-204		0.28	0.20	0.17	0.44	0.20	0.30	0.24	87	Philpots & Schnitzler, 1970
LC-11	0.13	0.12	0.13	0.07	0.36	0.05	0.01	0.01	71	Luhr & Carmichael, 1980
PS-240		0.08	0.02	0.03	0.06	0.01			97	Philpots & Schnitzler, 1970
PS-184		0.06	0.05	0.01	0.19	0.03	0.02	0.03	80	Philpots & Schnitzler, 1970
PS-271		0.20	0.14	0.11	0.73	0.05	0.03	0.03	77	Philpots & Schnitzler, 1970
LC-6	0.21	0.14	0.16	0.10	0.63	0.05	0.01	0.01	58	Luhr & Carmichael, 1980
LC-7	0.20	0.18	0.15	0.10	0.70	0.08	0.01	0.01	60	Luhr & Carmichael, 1980
PS-218		0.24	0.17	0.13	2.11	0.09	0.08	0.06	51	Philpots & Schnitzler, 1970
O-SHy	0.49	0.22	0.14	0.13	0.97	0.18	0.11	0.10	44	Oudas et al., 1971
AB-BP1		0.18	0.17	0.10	0.80	0.07	0.06	0.05		Arth & Barker, 1976
BO-PlA	0.18	0.12	0.09	0.06	0.75	0.15	0.10	0.10		Bacon & Oruitt, 1988
NS-6P		0.12	0.08	0.96	0.40	0.30	0.29			Nagasawa & Schnetzler, 1971.
NC-15	0.39	0.27	0.18	0.16	3.40	0.10	0.07	0.07	41	Nash & Crecraft, 1985
NC-12	0.38	0.26	0.20	0.16	3.50	0.11	0.06	0.05	42	Nash & Crecraft, 1985
NC-6	0.38	0.29	0.24	0.19	3.20	0.15	0.10	0.09	39	Nash & Crecraft, 1985
BO-PlR	0.30	0.22	0.19	0.12	2.00	0.15	0.10	0.10		Bacon & Oruitt, 1988
NS-1P		0.27	0.19	0.13	2.35	0.06	0.04	0.04		Nagasawa & Schnetzler, 1971
NS-2P		0.11	0.06	0.05	0.82	0.03	0.02	0.02		Nagasawa & Schnetzler, 1971
O-Tum	0.30	0.22	0.19	0.17	4.20	0.21	0.11	0.11	23	Oudas et al., 1971
NS-8P		0.35	0.24	0.15	2.81	0.08	0.07	0.07		Nagasawa & Schnetzler, 1971
NS-4P		0.28	0.29	0.14	2.49	0.08	0.56	0.54		Nagasawa & Schnetzler, 1971

CLINOPYROXENE

Sample	La	Ce	Nd	Sm	Eu	Tb	Yb	Lu	Mol En	Reference
XI	0.15	0.20	0.30	0.50	0.40	0.65	0.60	0.60		Irving, 1978
PS-193		0.10	0.18	0.26	0.26	0.30	0.23			Philpots & Schnitzler, 1970
SP-25		0.18	0.32	0.43	0.48	0.57	0.48			Schnitzler & Philpots, 1968
SP-19		0.12	0.26	0.38	0.39	0.48	0.43			Schnitzler & Philpots, 1968
On-b	0.08	0.07	0.38	0.74	0.75	0.97	1.01	0.95		Onouma et al., 1968
O-34b	0.14	0.18		0.80	0.55	0.68	0.65	0.60		Oostal et al., 1983
PS-204		0.04	0.07	0.09	0.09	0.10	0.09	0.07		Philpots & Schnitzler, 1970
LC-11	0.14	0.20	0.43	0.78	0.72	1.11	0.96	0.86	43	Luhr & Carmichael, 1980
PS-271		0.51	0.65	0.95	0.68	1.40	1.30			Philpots & Schnitzler, 1970
LC-6	0.14	0.24	0.64	0.96	1.07	1.48	0.97	0.95	44	Luhr & Carmichael, 1980
LC-7	0.16	0.36	0.68	1.26	1.19	1.66	1.33	1.38	44	Luhr & Carmichael, 1980
BO-CpxA	0.28	0.47	0.86	1.60	1.10	2.70	2.00	2.00		Bacon & Oruitt, 1988
NS-6Au		0.36	0.94	1.50	1.10	2.60	2.01	1.81		Nagasawa & Schnetzler, 1971.
NC-15	0.76	1.20	2.10	3.30	2.20	4.40	3.50	3.30		Nash & Crecraft, 1985
NC-12	0.68	1.10	2.00	3.20	2.20	4.00	3.20	3.00		Nash & Crecraft, 1985
NC-6	1.50	2.50	4.50	6.90	2.60	10.3	9.50	8.80		Nash & Crecraft, 1985
PS-266		0.65	1.28	1.81	2.01	1.30	1.14	1.28		Philpots & Schnitzler, 1970
BO-CpxR	0.52	0.84	1.40	2.90	2.50	3.80	3.00	3.00		Bacon & Oruitt, 1988

ORTHOPYROXENE

Sample	La	Ce	Nd	Sm	Eu	Tb	Yb	Lu	Mol En	Reference
XI	0.005	0.010		0.02	0.02	0.03	0.15			Irving, 1978
On-c		0.00		0.01	0.02	0.05	0.11	0.11		Onouma et al., 1968
PS-203		0.02	0.05	0.10	0.07	0.19	0.40	0.45		Philpots & Schnitzler, 1970
PS-271		0.04	0.06	0.10	0.08	0.23	0.67	0.84		Philpots & Schnitzler, 1970
PS-184		0.03	0.03	0.05	0.05	0.09	0.24			Philpots & Schnitzler, 1970
LC-6	0.30	0.33	0.43	0.43	0.42	0.48	0.56	0.68	71	Luhr & Carmichael, 1980
BO-OpxA	0.26	0.31	0.47	0.16	0.34	0.69	0.77	0.71		Bacon & Oruitt, 1988
NS-6H		0.08	0.12	0.16	0.13	0.33	0.73	0.76		Nagasawa & Schnetzler, 1971
NC-15	0.74	0.87	1.20	1.40	0.54	1.70	2.10	2.10		Nash & Crecraft, 1985
NS-3H		0.26	0.34	0.38	0.27	0.55	0.99	0.92		Nagasawa & Schnetzler, 1971.
NC-12	0.65	0.79	1.10	1.40	0.56	1.60	1.90	1.90		Nash & Crecraft, 1985
BO-OpxR	0.40	0.46	0.60	0.78	0.61	0.85	0.91	0.90		Bacon & Oruitt, 1988
NS-1H		0.17	0.26	0.34	0.21	0.51	0.78	0.78		Nagasawa & Schnetzler, 1971
NS-4H		0.10	0.15	0.21	0.09	0.30	0.93	1.14		Nagasawa & Schnetzler, 1971

HORNBLENDE

Sample	La	Ce	Nd	Sm	Eu	Tb	Yb	Lu	Reference
HN-3	0.17	0.34		0.93	1.11	1.02	0.98	0.82	Higuchi & Nagasawa, 1969
SP-29		0.12	0.16	0.24	0.26	0.30	0.23		Schnitzler & Philpots, 1968
D34-b	0.25	0.32		1.40	1.20	1.30	1.20	1.10	Oostal et al., 1983
PS-233		0.09	0.19	0.34	0.36	0.58	0.46	0.44	Philpots & Schnitzler, 1970
LC-6	0.14	0.33	0.79	1.31	1.66	1.93	1.18	1.07	Luhr & Carmichael, 1980
LC-7	0.19	0.32	0.73	1.51	1.79	1.91	1.43	1.41	Luhr & Carmichael, 1980
AB-BP1		0.90	2.80	3.99	3.44	5.80	4.90	4.51	Arth & Barker, 1976
BO-HbA	0.31	0.53	1.20	2.00	1.90	2.00	2.10	2.00	Bacon & Oruitt, 1988
NS-3Hb		1.38	4.03	7.10	5.00	12.5	9.0	6.3	Nagasawa & Schnetzler, 1971.
BO-HbR	0.36	0.68	1.60	2.30	3.20	2.40	1.80	1.80	Bacon & Oruitt, 1988
NS-1Hb		1.42	4.25	8.20	5.90	13.5	8.7	5.9	Nagasawa & Schnetzler, 1971.
NS-2Hb		0.43	1.06	1.61	1.39	2.3	1.9	1.8	Nagasawa & Schnetzler, 1971.
NS-8Hb		1.77	4.49	8.00	4.53	13.0	7.5		Nagasawa & Schnetzler, 1971.

OLIVINE

Sample	La	Ce	Nd	Sm	Eu	Tb	Yb	Lu	Mol Fo	Reference
LS-48				0.009					88	Leeman & Scheidegger, 1977
SP-25		0.009	0.007	0.006	0.006	0.009				Schnitzler & Philpots, 1968
LS-15				0.009					72	Leeman & Scheidegger, 1977
LS-36				0.003					87	Leeman & Scheidegger, 1977
LS-44				0.009					87	Leeman & Scheidegger, 1977
LS-82				0.009					88	Leeman & Scheidegger, 1977
LS-5				0.015					85	Leeman & Scheidegger, 1977
PS-19		0.009	0.010	0.011	0.010	0.013	0.023			Schnitzler & Philpots, 1968
HN-4	0.003			0.003	0.005	0.005	0.009	0.014		Higuchi & Nagasawa, 1969
H-688MS	0.008			0.012	0.008		0.070	0.300	75	Hughes, 1983
LC-11				0.010			0.030		75	Luhr & Carmichael, 1980

MAGNETITE

Sample	La	Ce	Nd	Sm	Eu	Tb	Yb	Lu	%üsp	Reference
LC-11	0.45	0.42	0.43	0.45	0.41	0.48	0.47	0.44	61	Luhr & Carmichael, 1980
LC-6	0.37	0.35	0.55	0.53	0.42	0.67	0.29	0.32	63	Luhr & Carmichael, 1980
LC-7	0.38	0.31	0.42	0.54	0.35	0.53	0.38	0.41	69	Luhr & Carmichael, 1980
NC-15	0.89	1.10	1.60	1.90	0.25	1.90	1.10	1.10		Nash & Crecraft, 1985
NC-12	0.74	0.99	1.30	1.70	0.32	1.70	0.89	0.84		Nash & Crecraft, 1985
NC-6	1.70	2.40	3.00	3.50	1.20	3.50	1.60	1.20		Nash & Crecraft, 1985
BO-MgtR	0.66	0.71	0.93	1.20	0.91	1.30	0.11	0.30		Bacon & Oruitt, 1988

ILMENITE

Sample	La	Ce	Nd	Sm	Eu	Tb	Yb	Lu	Reference
NC-6	6.20	6.80	6.30	5.50	1.00	4.80	3.10	2.10	Nash & Crecraft, 1985

APATITE

Sample	La	Ce	Nd	Sm	Eu	Tb	Yb	Lu	Reference
XI	8.00	9.00	11.00	11.00	10.0	8.00	4.00	3.50	Irving, 1978
F-1	14.5	21.1	32.8	46.0	25.5	38.0	15.4	13.8	Fujimaki, 1986
N-6A		18.0	27.4	29.3	20.5	25.0	13.1	11.2	Nagasawa, 1970
NS-2A		16.6	21.0	20.7	14.5	18.0	9.4	7.9	Nagasawa & Schnetzler, 1971
N-1A		52.5	81.1	89.8	50.2	75.0	37.0	30.0	Nagasawa, 1970
N-4A		33.6	61.3	69.6	23.8	60.0	23.2	20.1	Nagasawa, 1970

ZIRCON

Sample	La	Ce	Nd	Sm	Eu	Tb	Yb	Lu	Reference
F-1	3.11	3.49	3.80	4.72	4.23	35	254	333	Fujimaki, 1986
N-1A		3.00	2.43	3.70	5.22	40	299	366	Nagasawa, 1970
N-4A		2.29	1.97	2.58	1.07	20	242	281	Nagasawa, 1970